VOLUME B66 Nos. 1, 2
MARCH (II) 1992

To be followed by
issues B63 No. 4 and
B65 Nos. 1–4

NIMBEU B66 (1, 2) 1–306 (1992)
ISSN 0168-583X

Nuclear Instruments & Methods in Physics Research

Editor-in-Chief: Kai Siegbahn

Section B

Beam Interactions with Materials and Atoms

Editors: H. H. Andersen & L. E. Rehn

Proceedings of the Third International Conference on
Chemical Analysis
Namur, Belgium, 8–12 July 1991

North-Holland

NUCLEAR INSTRUMENTS AND METHODS IN PHYSICS RESEARCH

Editor-in-Chief: Kai Siegbahn

SECTION B: BEAM INTERACTIONS WITH MATERIALS AND ATOMS

Editors: H.H. Andersen & L.E. Rehn

Editorial Board:

M. AONO (Saitama)
B.R. APPLETON (Oak Ridge)
R.S. AVERBACK (Urbana)
J.L. CAMPBELL (Guelph)
N.N. GERASIMENKO (Novosibirsk)
G. GÖTZ (Jena)
J. GYULAI (Budapest)
P. HEMMENT (Guildford)
G.J.F. LEGGE (Melbourne)
J.W. MAYER (Ithaca)
P. MAZZOLDI (Padova)
S.T. PICRAUX (Albuquerque)
P.B. PRICE (Berkeley)
J.P. RIVIERE (Poitiers)
B. STRITZKER (Augsburg)
I.S.T. TSONG (Tempe)
E. UGGERHØJ (Aarhus)
F. VAN DER VEEN (Amsterdam)
Zhong-Lie WANG (Beijing)
G. WEYER (Geneva)
Y. YAMAZAKI (Tokyo)

Information for Authors

Section B of Nuclear Instruments and Methods in Physics Research (NIM B) has been formed to provide a special forum for the discussion of all aspects of the interaction of energetic beams with atoms, molecules and aggregate forms of matter. This includes ion beam analysis and ion beam modification of materials as well as studies of the basic interaction mechanisms of importance for this work. The editors invite submission of both theoretical and experimental papers of original research in this area.

Contributions should be in English and should be submitted in duplicate directly to the editors. To assist in minimizing publication time, it is suggested that manuscripts originating from Europe, India, The Middle East and Africa be sent to Prof. Andersen, and manuscripts from The Americas, The Far East (China and Japan) and Australasia to Dr. Rehn.

Prof. H.H. Andersen
Physics Laboratory, H.C. Ørsted Institute
Universitetsparken 5, DK-2100 Copenhagen Ø, Denmark
Tel. +45 31 353133, ext. 322 FAX: +45 31 350628

Dr. L.E. Rehn
Materials Science Division, Bldg 223, Rm S231
Argonne National Laboratory, 9700 South Cass Avenue
Argonne IL 60439, USA.
Tel. +1 708 2529297 FAX +1 708 2523308

Short contributions of less than 1500 words and not subdivided into sections may be published as Letters to the Editor in a shorter time than regular articles as the proofs will normally be corrected by the publisher.

Correspondence with the publisher regarding articles accepted for publication or the return of corrected proofs should be addressed to: NIM B Editors, Elsevier Science Publishers B.V., P.O. Box 103, 1000 AC Amsterdam, The Netherlands
FAX: +31 20 5862 775 telex: 10704 ESP OM tel. +31 20 5862 488

There are no page charges to individuals or institutions for publication of an article in this journal. 25 reprints of each article will be supplied free of charge. Further reprints can be ordered from the publisher on the Order Form sent out with the proofs.

Subscriptions

Nuclear Instruments and Methods in Physics Research – A is published semi-monthly and Nuclear Instruments and Methods in Physics Research – B, monthly. For 1992, 13 volumes of NIM A and 10 volumes of NIM B have been announced. The subscription price for a combined subscription to the journal (NIM A + B: 23 volumes) is Dfl. 12075.00 (US $6598). Postage and handling amount to Dfl. 713.00 (US $390). Therefore the total price for a combined subscription is Dfl. 12788.00 (US $6988). Separate subscriptions are available for each section of the journal at a total price (including postage and handling) of Dfl. 7878.00 (US $4305) for NIM A (13 volumes) and of Dfl. 6060.00 (US $3311) for NIM B (10 volumes). In all cases the Dutch Guilder price is definitive, the currency equivalent being for guidance only. Subscriptions should be sent to the publisher, Elsevier Science Publishers B.V., Journals Department, P.O. Box 211, 1000 AE Amsterdam, The Netherlands, or to any subscription agent.

Journals are sent by surface delivery to all countries, except the following countries where SAL air delivery (Surface Airlifted Mail) is ensured: USA, Canada, Japan, Australia, New Zealand, The People's Republic of China, Israel, India, Brazil, Malaysia, Singapore, South Korea, Taiwan, Pakistan, Hong Kong, South Africa. Air mail rates for other countries are available upon request.

Claims for missing issues should be made within three months of the date of publication. The publisher expects to supply missing issues free only when losses have been sustained in transit and the reserve stock will permit.

Information for Advertisers

Advertising orders and enquiries can be sent to the Advertising Manager, Elsevier Science Publishers B.V., Advertising Department, P.O. Box 211, 1000 AE Amsterdam, The Netherlands, tel. +31 20 5803714, telex: 18582 ESPA NL, FAX: +31 20 5803769.

UK: T.G. Scott & Son Ltd (Michael White), 30-32 Southampton St., London WCE 7HR, tel. (71) 240 2032, telex 299 181, FAX: +44 (71) 379 7155.

USA, Canada: Weston Media Associates, Daniel S. Lipner, P.O. Box 1110, Greens Farms, CT 06436-1110, USA, tel. (203) 261 2500, FAX: (203) 261 0101.

Elsevier Science Publishers B.V.: All rights reserved. No part of this publication may be reproduced, stored in a retrieval system or transmitted in any form or by any means, electronic, mechanical, photocopying, recording or otherwise, without the written permission of the publisher Elsevier Science Publishers B.V., Copyright & Permissions Department, P.O. Box 521, 1000 AM Amsterdam, The Netherlands.

Special regulations for authors – Upon acceptance of an article by the journal, the author(s) will be asked to transfer copyright of the article to the publisher. This transfer will ensure the widest possible dissemination of information.

Submission to this journal of a paper entails the author's irrevocable and exclusive authorization of the publisher to collect any sums or considerations for copying or reproduction payable by third parties (as mentioned in article 17 paragraph 2 of the Dutch Copyright Act of 1912 and in the royal Decree of June 20, 1974 (S. 351) pursuant to article 16b of the Dutch Copyright Act of 1912) and/or to act in or out of Court in connection therewith.

Special regulations for readers in the USA – This journal has been registered with the Copyright Clearance Center, Inc. Consent is given for copying articles for personal or internal use, or for the personal use of specific clients. This consent is given on the condition that the copier pays through the Center the per copy fee stated on the first page of each article for copying beyond that permitted by Sections 107 or 108 of the US Copyright Law. The appropriate fee should be forwarded with a copy of the first page of the article to the Copyright Clearance Center, Inc., 21 Congress St., Salem, MA 01970, USA. If no code appears on an article, the author has not given consent to copy and permission to copy must be obtained directly from the author. All articles published prior to 1981 may be copied for a per copy fee of US $2.25, also payable throught the Center. (N.B. For review journals this fee is $0.25 per copy per page.) This consent does not extend to other kinds of copying, such as for general distribution, resale, advertising and promotion purposes, or for creating new collective works. Special written permission must be obtained from the publisher for such copying.

No responsibility is assumed by the Publisher for any injury and/or damage to persons or property as a matter of products liability, negligence or otherwise, or from any use or operation of any methods, products, instructions or ideas contained in the materials herein. Although all advertising material is expected to conform to ethical standards, inclusion in this publication does not constitute a guarantee or endorsement of the quality or value of such product or of the claims made of it by its manufacturer.

Published monthly

Printed in The Netherlands

Nuclear Instruments & Methods in Physics Research
B: Beam Interactions with Materials and Atoms

EDITORIAL BOARD

M. AONO (Saitama)
B.R. APPLETON (Oak Ridge)
R.S. AVERBACK (Urbana)
J.L. CAMPBELL (Guelph)
N.N. GERASIMENKO (Novosibirsk)
G. GÖTZ (Jena)
J. GYULAI (Budapest)
P. HEMMENT (Guildford)
G.J.F. LEGGE (Melbourne)
J.W. MAYER (Ithaca)
P. MAZZOLDI (Padova)
S.T. PICRAUX (Albuquerque)
P.B. PRICE (Berkeley)
J.P. RIVIERE (Poitiers)
B. STRITZKER (Augsburg)
I.S.T. TSONG (Tempe)
E. UGGERHØJ (Aarhus)
F. VAN DER VEEN (Amsterdam)
Zhong-Lie WANG (Beijing)
G. WEYER (Geneva)
Y. YAMAZAKI (Tokyo)

Nuclear Instruments & Methods in Physics Research

Editor-in-Chief: Kai Siegbahn

Section B

Beam Interactions with Materials and Atoms

VOLUME B66
1992

Editors: H.H. Andersen & L.E. Rehn

North-Holland

© 1992 Elsevier Science Publishers B.V. All rights reserved.

No part of this publication may be reproduced, stored in a retrieval system or transmitted in any form or by any means, electronic, mechanical, photocopying, recording or otherwise, without the written permission of the Publisher, Elsevier Science Publishers B.V., Copyright & Permissions Department, P.O. Box 521, 1000 AM Amsterdam, The Netherlands.

Special regulations for authors – Upon acceptance of an article by the journal, the author(s) will be asked to transfer copyright to the publisher. This transfer will ensure the widest possible dissemination of information.

Submission to this journal of an article implies the transfer of the copyright from the author(s) to the publisher and entails the author's irrevocable and exclusive authorization of the publisher to collect any sums or considerations for copying or reproduction payable by third parties (as mentioned in article 17 paragraph 2 of the Dutch Copyright Act of 1912 and in the Royal Decree of June 20, 1974 (S. 351) pursuant to article 16b of the Dutch Copyright Act of 1912) and/or to act in or out of Court in connection therewith.

Special regulations for readers in the U.S.A. – This Journal has been registered with the Copyright Clearance Center, Inc. Consent is given for copying of articles for personal or internal use, or for the personal use of specific clients. This consent is given on the condition that the copier pays through the Center the per-copy fee stated in the code on the first page of each article for copying beyond that permitted by Sections 107 or 108 of the U.S. Copyright Law. The appropriate fee should be forwarded with a copy of the first page of the article to the Copyright Clearance Center, Inc., 21 Congress Street, Salem, MA 01970, U.S.A. If no code appears in an article, the author has not given broad consent to copy and permission to copy must be obtained directly from the author. All articles published prior to 1981 may be copied for a per-copy fee of US $02.25, also payable through the Center. (N.B. For review journals this fee is $0.25 per copy per page.) This consent does not extend to other kinds of copying, such as for general distribution, resale, advertising and promotion purposes, or for creating new collective works. Special written permission must be obtained from the Publisher for such copying.

No responsibility is assumed by the Publisher for any injury and/or damage to persons or property as a matter of products liability, negligence or otherwise, or from any use or operation of any methods, products, instructions or ideas contained in the materials herein. Although all advertising material is expected to conform to ethical standards, inclusion in this publication does not constitute a guarantee or endorsement of the quality or value of such product or of the claims made of it by its manufacturer.

This volume is printed on acid-free paper

Printed in The Netherlands

MICROANALYSIS OF LIGHT ELEMENTS (HYDROGEN TO NEON) USING CHARGED PARTICLE ACCELERATORS

Proceedings of the Third International Conference on Chemical Analysis
Namur, Belgium, 8–12 July 1991

Editor

G. DEMORTIER

LARN, Facultés Universitaires Notre-Dame de la Paix
Namur, Belgium

1992

NORTH-HOLLAND

The Manuscript of the Proceedings
was received by the Publisher: mid-October to mid-November 1991

Preface

The first meeting in the field of Chemical Analysis by Charged Particle Bombardment organized in Namur was held in September 1971, only one year after the first proton beam was produced by our Van de Graaff accelerator. Works and research at the LARN had begun in 1970. The LARN was created by Professor G. Deconninck and all the staff members present from the start (i.e. 22 years ago) are still there today: Prof. F. Bodart who conducts works on ion implantation, Mr. Y. Morciaux our powerful technician, and myself. F. Bodart and myself are Ph.D. students of Prof. Deconninck, This basic staff has then been progressively reinforced with Dr. G. Terwagne, also a Ph.D. of Prof. Deconninck, Mrs. Ch. Honhon, our efficient secretary, and Mr. J. Nackers, our second technician. We also supervise 6 to 10 graduate and Ph.D. students permanently.

The subject of the 1971 meeting was very wide: all aspects of elemental analysis using charged particle bombardment were accepted for presentation. They included: Auger spectroscopy, secondary ion mass spectroscopy (SIMS), charged particle activation analysis, PIXE, PIGE, RBS, NRA, etc. This first meeting was attended by 70 persons and the Proceedings were published in J. Radioanal. Chem. 12 (1972) 1–385.

The second meeting in September 1981 was entirely devoted to nuclear microprobes. Twenty-three laboratories using a nuclear microprobe were represented and I think it was the first Symposium on Nuclear Microprobes well before the First Official International Conference held in 1987 in Oxford. With this more specific subject we also welcomed about 70 participants and the Proceedings were published in Nucl. Instr. and Meth. 197 (1982) 1–258.

To keep a relatively low number of participants in order to encourage discussion, the field of the present meeting was still narrower. We have only accepted papers relating to the analysis of very light elements: from hydrogen to neon. The meeting took place the week following the Tenth International Conference on Ion Beam Analysis (IBA), Eindhoven, the Netherlands (Proceedings published in Nucl. Instr. and Meth. B64 (1992)).

The subject of the next meeting (to be held in next millenium if we maintain the same interval of ten years) has not yet been decided on but, in order to keep a low number of attendees, it is likely to be: "The Analysis of Elements Emitting a γ-ray Between 435 and 445 keV Under Charged Particle Bombardment". All the current participants will certainly be on our mailing list and will receive all useful information in due time.

Four laboratories represented at both meetings of 1971 and 1981 have also sent attendees to our recent conference

- the Nuclear Center of Harwell, represented by Dr. J. McMillan,
- the laboratory of the Ecole Normale Supérieure of Paris, represented by Dr. G. Amsel and several of his students,
- the School of Physics of the University of Birmingham, represented by Prof. L. Earwaker and three coworkers,
- the Study Centre for Atomic Energy of Saclay, with Ph. Massiot, J.P. Frontier, A. de Chateau-Thierry and J. Tirira.

Other research staffs were represented for the second time: the Faure laboratory of South Africa (Dr. A. Pillay), the Institute of Nuclear Physics of Villeurbanne (Dr. N. Moncoffre and Mr. B. Roux).

I thank the invited speakers who accepted to give a speech on each of the ten lightest elements. They were selected for their qualification in the field, but also to get a varied range of different citizenships. All of them were very enthusiastic in accepting my invitation. The speakers were: Dr. W. Lanford (USA)

for hydrogen, Dr. F. Paszti (Hungary) for helium, Dr. J. Räisänen (Finland) for lithium, Dr. N. Moncoffre (France) for boron, Prof. R. Vis (Holland) for carbon, Prof. K. Bethge (Germany) for nitrogen, Dr. D. Cohen (Australia) for oxygen, Dr. G. Coote (New Zealand) for fluorine, and Prof. G. Deconninck (Belgium) for neon.

My special thanks are given to Prof. Deconninck, who is the appreciated teacher of all the LARN staff for accepting a difficult subject: the analysis of neon. Neon is probably one of the less studied elements, and it was certainly not an easy task for my friend Gaston to review the spare litterature on it. The eleventh invited speaker was Dr. G. Amsel who suggested a contribution on Resonant Nuclear Reactions on light elements with low energy beams and very high resolution. G. Amsel finally proposed to let Dr. I. Vickridge, one of the coauthors, present the paper. Prof. L. Earwaker gave the address during the conference banquet.

The LARN is part of the Facultés Universitaires Notre-Dame de la Paix, Namur. This University is one of the oldest in Belgium, but the decision to deliver Ph.D.s dates only from the 60s. One goal of each university is to give young scientists the opportunity to meet specialists in their own field. Thanks to two main sponsors, the Crédit Communal de Belgique and NEW (Namur Europe Wallonie), who have attributed ten grants covering the full registration fees of ten graduate or newly promoted Ph.D. students. Several of them were faced with an international audience for the first time.

We also thank Charles Evans and Associates, Canberra, Cameca and Rivac Technology for their financial support and the Fonds National de la Recherche Scientifique, a Belgian foundation, for the facilities given to invite well-known speakers.

All sessions were held in the historic building of the Arsenal. It was erected on the direction of Vauban, the military architect of Louis the XIV, at the end of the 17th century. The inside of the building was completely restored in 1982 and layed out as the university restaurant.

All the contributed papers were presented as posters, but we suggested that every one who wished could give a short oral presentation. These presentations were limited to ten minutes, excluding discussion. A lot of time was then let for discussion during the poster sessions. Each oral contributed paper was given right after the invited speech on the subject.

Three workshops were also organized on subjects suggested in a questionnaire filled by the registered participants before the meeting. The selection was not easy to make due to a large scattering of wishes. The final choice made by the local committee was:

(a) The usefulness of analyses of light elements in metallurgy and the need for confident reference samples. The discussion was organized by F. Degrève (Péchiney, France) and D. Cohen (ANSTO, Australia).

(b) The second one, scheduled for an entire afternoon, was devoted to cross sections of various nuclear reactions induced by the bombardment of light elements with charged particles. This workshop was chaired by G. Amsel (Paris) and myself, with the efficient help of I. Vickridge (DSIR, Australia), G. Battistig (Paris) and W. De Coster (IMEC, Heverlee). The summary was written by I. Vickridge and is published as the last contribution in these Proceedings.

(c) The third one, coinciding with the last session of the meeting, was devoted to the analysis of hydrogen, the element which has been chosen by more than 30 people of the audience. It was chaired by W. Lanford (Albany, USA) and G. Ross (INRS Energie, Canada).

For the good organization of these workshops, each participant had the opportunity to fill in sheets to specify his special wishes. During each workshop, each question and comment was written as a short summary to be later summarized in a document distributed to all participants.

All the papers were submitted to two referees: one present at the meeting, the other one chosen in the international community among users of IBA. I thank all of them for their pertinent advice and specially Ms. H. Brading, Mr. M. Briggs and Prof. L. Earwaker for their valuable help for the correction of the english in several contributions.

I have appreciated the active participation of each attendee. This five days meeting was suspended during a half day for a barbecue and a short trip to Brussels. Several of the photographs are published in this issue of NIM. I hope that this bound volume will be used in the future as a reference book for IBA of light elements.

The whole work performed before, during and after the conference (to organize the publication of these Proceedings) was a team job. The advice and scientific aid of Professor F. Bodart and Dr. G. Terwagne, the technical and graphical experience of Yvon Morciaux and Jules Nackers, the disponibility of our Ph.D. students: Daniel Decroupet, Serge Mathot and Stéphane Lucas, and of young graduate students: Catherine Steuckers, Benoît Deconninck, Michel Closset, Patrice Clément and Christophe Soumoy, were highly appreciated. I specially thank Chantal Honhon, our efficient secretary, who cared for everything to enable all participants to have a pleasant stay in Namur. She devoted a lot of her time to prepare the circulars, the programme, the book of abstracts, the booking of rooms. She and Anne Deconninck were also continuously present during the meeting to welcome and help the attendees. Chantal has also been very methodical in organizing the processing of the Proceedings.

Professor G. Demortier
Guest Editor

1. N. Moncoffre
2. J. Räisänen
3. G. Amsel
4. M. Strathman
5. H.E. Zschau
6. F. Plier
7. Ch. Neelmeijer
8. F. Paszti
9. M.F. Da Silva
10. L.G. Earwaker
11. W.A. Lanford
12. I. Vickridge
13. W.H. Schulte
14. M. Closset
15. G. Demortier
16. K. Bethge
17. S. Gujrathi
18. Mrs. McMillan
19. J.W. McMillan
20. G. Otto
21. A. Sole
22. M. Respaldiza
23. Ph. Massiot
24. F. Sommer
25. A. de Chateau-Thierry
26. J. Chaumont
27. A. Pillay

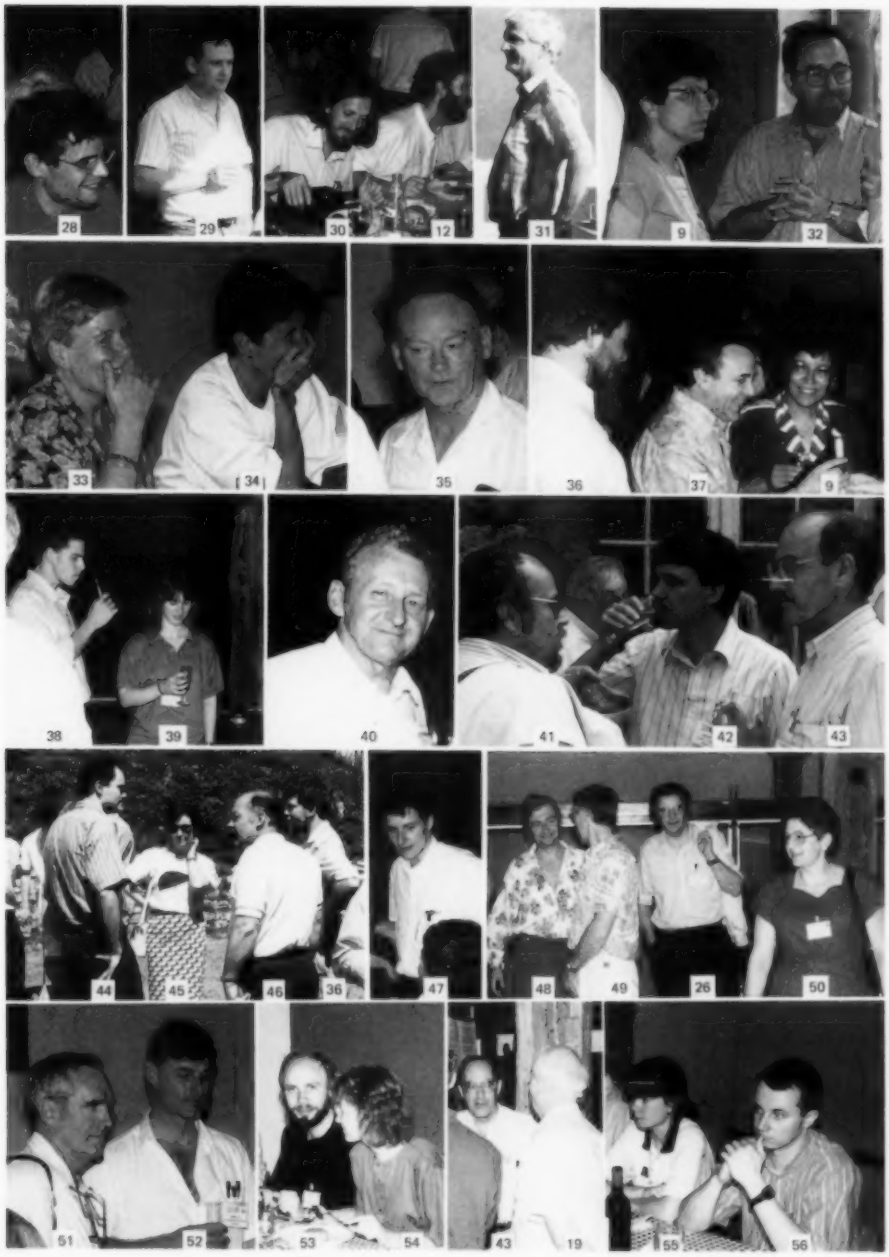

28. B. Roux
29. S. Mathot
30. G. Ross
31. R.D. Vis
32. J. Ferrero
33. Mrs. A. Deconninck
34. Mrs. Ch. Honhon
35. G.E. Coote
36. G. Terwagne
37. F. Bodart
38. M.C. Briggs
39. H. Brading
40. G. Deconninck
41. M. Uhrmacher
42. Th. Laursen
43. J.S. Forster
44. S. Lucas
45. Mrs. Demortier
46. J. Nackers
47. B. Deconninck
48. J.P. Frontier
49. Y. Morciaux
50. Mrs. Morciaux
51. L. McIntyre
52. D. Cohen
53. K. Bourdelle
54. Mrs. Bourdelle
55. C. Steuckers
56. M. Piette
57. J. Knox

Organizing Committee

Prof. F. Bodart
Prof. G. Demortier, Chairman
Prof. R. Gijbels, UIA Antwerpen
Dr. G. Terwagne

Sponsors

Namur Europe Wallonie
Crédit Communal de Belgique
Fonds National de la Recherche Scientifique
Province de Namur: Administration de l'Enseignement et de la Culture
Facultés Universitaires Notre-Dame de la Paix, Namur

With the financial support of:

Canberra Packard Benelux
Cameca
Charles Evans & Associates
Rivac Technology

Nuclear Instruments and Methods in Physics Research 66 (1992) xiii–xv
North-Holland

Contents

Preface vii

Conference photographs x

Organizing Committee/Sponsors xii

Section I. General methods of analysis of light elements

A very narrow resonance in $^{18}O(p, \alpha)^{15}N$ near 150 keV: Application to isotopic tracing. II. High resolution depth profiling of ^{18}O
Battistig, G., G. Amsel, E. d'Artemare and I. Vickridge 1

Novel applications of high-energy resolution ion beams
Schulte, W.H., H. Ebbing, H.W. Becker, S. Wüstenbecker, M. Berheide, M. Buschmann, C. Rolfs, G.E. Mitchell and J.S. Schweitzer 11

Nuclear microanalysis by means of 350 keV Van de Graaff accelerator
Ros, G.G., L. Leblanc, B. Terreault, J.F. Pageau and P.A. Gollier 17

Characterisation of thin layers in processed silicon
Earwaker, L.G., M.C. Briggs, M.I. Nasir, J.P.G. Farr and J.M. Keen 23

Non-Rutherford scattering of protons by light elements
Knox, J.M. 31

The influence of surface topography on the depth resolution of the PIGE depth profiling technique
Plier, F., H.-E. Zschau and G. Otto 38

The application of high energy prompt gamma-ray spectrometry to ^{3}He activation analysis of light elements
Pillay, A.E. and M. Peisach 43

Ion microbeam analysis with superconducting AMS minicyclotron as the analyzing instrument
Subotic, K.M., M.K. Pavicevic and D. Novkovic 48

Twenty years of analysis of light elements at the LARN
Demortier, G. 51

Section II. Review papers on analysis of individual elements

Analysis for hydrogen by nuclear reaction and energy recoil detection
Lanford, W.A. 65

Microanalysis of the He using charged particle accelerators
Pászti, F. 83

Analysis of lithium by ion beam methods
Räisänen, J. 107

Acceleator methods for the determination of beryllium
McMillan, J.W. 118

Analysis of boron by charged particle bombardment
Moncoffre, N. 126

0168-583X/92/$05.00 © 1992 – Elsevier Science Publishers B.V. All rights reserved

On the determination of carbon using charged particle accelerators
Vis, R.D. 139
Ion beam analysis of nitrogen
Betghe, K. 146
Analysis of oxygen by charged particle bombardment
Cohen, D.D. and E.K. Rose 158
Ion beam analysis of fluorine: Its principles and applications
Coote, G.E. 191
Analysis of neon by particle accelerators
Banse-Lefebvre, A., G. Deconninck, M. Dubus and G. Terwagne 205

Section III. Contributed papers on the analysis of individual elements

Hydrogen decoration of defects produced by Na implantation into polycrystalline Cr and Ta
Keinonen, J., A. Kehrel, K.P. Lieb and M. Uhrmacher 209
Depth profiling of hydrogen isotopes in thin, low-Z films by scattering recoil coincidence spectrometry
Forster, J.S., J.R. Leslie and T. Laursen 215
Determination of boron using the B(α, p)C nuclear reaction at incident energies near 3 MeV
McIntyre Jr., L.C., J.A. Leavitt, M.D. Ashbaugh, Z. Lin and J.O. Stoner Jr. 221
Some studies on nuclear methods for boron determination
Pillay, A.E. and M. Peisach 226
The structure and composition of plasma nitrided coatings on titanium
Brading, H.J., P.H. Morton, T. Bell and L.G. Earwaker 230
Nitrogen profiling in nitride films and nitrogen-implanted samples using the ^{14}N(α, α) and ^{14}N(α, p) reactions at 6 MeV incident energy
Artigalas, H., A. Chevarier, N. Chevarier, M. El Bouanani, E. Gerlic, N. Moncoffre, B. Roux, M. Stern and J. Tousset 237
Ion beam analysis of steel surfaces modified by nitrogen ion implantation
Neelmeijer, C., R. Grötzschel, E. Hentschel, R. Klabes, A. Kolitsch and E. Richter 242
Simultaneous determination of ^{14}N and ^{15}N by elastic backscattering and nuclear reaction: application to biology
Massiot, Ph., F. Sommer, M. Thellier and C. Ripoll 250
Location of protein bands in cellulose acetate electrophoretograms measuring nitrogen distributions by the ^{14}N(p,p'γ)^{14}N nuclear reaction
Szökefalvi-Nagy, Z. and J. Räisänen 258
High resolution depth profiling of nitrogen in AlN layers
Terwagne, G., S. Lucas and F. Bodart 262
Polarized nitrogen beams at LISOL
Vanderpoorten, W., J. Wouters, P. de Moor, P. Schuurmans, N. Severijns, J. Vanhaverbeke, L. Vanneste and J. Vervier 267
Oxygen measurements by elastic backscattering
Bourdelle, K.K. 274
Location of oxygen in leached UO_2 single crystals by resonant scattering of He ions
Turos, A., Hj. Matzke, J. Chaumont and L. Thomé 280
Depth profiling of light-Z elements with elastic resonances: Oxygens profiling with the 3.045 MeV ^{16}O(α, α)^{16}O resonance
De Coster, W., B. Brijs and W. Vandervorst 283
PIGE – Resonance profiling applied to a clinical test of fluoride varnishes
Zschau, H.E., F. Plier, G. Otto, C. Wyrwich and A. Treide 292
The investigation of the fluorine uptake in tooth enamel after the application of a NaF containing varnish
Plier, F., H.E. Zschau and G. Otto 295

Fluorine enrichment phenomena in coal combustion cycle
Caridi, A., E. Cereda, S. Fazinic, M. Jaksic, G.M. Braga Marcazzan, O. Valkovic and V. Valkovic 298

A workshop on cross-section data bases for IBA
Vickridge, I.C. 303

Section I
General methods of analysis of light elements

Nuclear Instruments and Methods in Physics Research B66 (1992) 1–10
North-Holland

Nuclear Instruments & Methods in Physics Research
Section B

A very narrow resonance in $^{18}O(p, \alpha)^{15}N$ near 150 keV: Application to isotopic tracing. II. High resolution depth profiling of ^{18}O *

G. Battistig [1], G. Amsel and E. d'Artemare

Groupe de Physique des Solides, Universités Paris 7 et Paris 6, Tour 23, 2 place Jussieu, 75251 Paris Cedex 05, France

I. Vickridge

Institute of Nuclear Sciences, P.O. Box 31312, Lower Hutt, New Zealand

Various depth profiling experiments illustrating the high depth resolutions obtained are presented for Ta_2O_5 and SiO_2 layers with sharp ^{18}O–^{16}O interfaces in depth ranges up to some hundreds of angstrom. A further increase of depth resolution is reached by resorting to glancing geometry with respect to the beam. The depth sensitivity of this resonance is actually so high that it is the energy straggling induced by the ubiquitous hydrocarbon contamination layer on the sample surface that limits the near-surface resolution. The experimental curves are interpreted with the stochastic theory of energy loss. The results are compared to those obtained with the previously used resonances for ^{18}O depth profiling. Applications of these techniques to the isotopic tracer study of the microscopic growth mechanisms of SiO_2 on silicon are shown. Operated in UHV this method may yield potentially nanometric or even subnanometric near surface depth sensitivities, as illustrated by detailed theoretical calculations corresponding to ideal but realistic experimental conditions. These results illustrate the usefulness for very high resolution depth profiling of low energy narrow resonances in general due to the corresponding large dE/dx values.

1. Introduction

In the first part of this work, referred to here after as "Part I" [1], we showed that, according to our experimental results, the most probable value of the width of this resonance is $\Gamma = 50$ eV, while neither ≈ 30 eV nor ≈ 100 eV may be unequivocally excluded. In this paper we present further experimental and theoretical results illustrating the possible applications of this resonance to depth profiling ^{18}O in various types of samples. According to the depth domains considered, surface, intermediate or deep regions, distinct properties of this resonance are beneficial and different experimental problems show up. The very narrow width found is mainly important for enhancing the near-surface depth resolution, and may be taken full advantage of only if the measurements can be carried out without surface contamination, in UHV and with a very high beam energy definition, as illustrated in Part I. It then becomes important to determine whether the resonance width is closer to 100 or 30 eV, as will be shown. In the intermediate depth range two features of this resonance are the most important: small width and high dE/dx at this low energy. For thick targets the fact that this resonance is the first and isolated is its main quality, while the large beam energy variations required for the measurements pose some experimental problems and we must begin to question the validity of the classical theory used to interpret the data. In all cases grazing incidence geometry may be used to improve depth resolution. Multiple scattering processes, which increasingly limit the corresponding gain with depth, will be discussed.

2. Experimental

Most of the experimental details were described in Part I. Let us recall that the proton beam diameter was 2 mm and its intensity around 200 nA. The Gaussian beam energy spread, including the Doppler effect at room temperature was $G = 100$ eV FWHM. In normal incidence geometry an annular detector subtending 0.93 sr was used. We now describe details of the experiments carried out in grazing incidence geometry

* Work supported by the Centre National de la Recherche Scientifique (GDR 86), France and DSIR, New Zealand.

[1] On leave from: Central Research Institute for Physics, H-1525 Budapest, Hungary, with a fellowship from the Ministère de la Recherche et de la Technologie, France.

0168-583X/92/$05.00 © 1992 – Elsevier Science Publishers B.V. All rights reserved

which allowed us to improve the depth resolution markedly.

With the target tilted to $\psi = 70°$ or more (i.e., the plane of the target to less than 20° from the beam) it is possible to put a large area detector close to the impact spot with its plane parallel to the beam. In our grazing incidence experiments a 3 cm^2 ORTEC detector was mounted at 1.5 cm from the center of the spot, at a 90° detection angle. The α-particle yields are independent of the detection angle, the angular distribution at resonance being isotropic [2]. The detection conditions are similar to those with the annular detector used in perpendicular geometry, the solid angles being comparable, although not identical for two reasons: the mechanical layout differs slightly and the solid angle itself depends on the shape of the elongated impact spot.

The beam size perpendicular to the tilting axis should be small enough in this geometry to limit the elongation of the spot with increasing ψ. In our case we could not use such collimation, the beam density from our Van de Graaff accelerator being too low around 150 keV, as pointed out in Part I. The elongated spots were up to ~ 8 mm wide and sufficiently large samples were therefore required for such experiments. With an ion implantation type accelerator like that of Münster [3] there is no problem obtaining such low energy beams with intensities of several μA. Let us emphasize that for large ψ, beam current integration must be devised very carefully as secondary electron suppression is increasingly difficult. Special choppers, positioned after the beam defining slits may be used or, if this is impossible, an RBS based monitoring system might be set up.

The resonance being weak, the highest beam current should be used. The only limitations in intensity are set by target heating, not too stringent a condition at these low energies, and by radiation damage effects which depend on the nature of the target. It seems reasonable to assume that, with accelerators of the type mentioned above, beam currents 10 to 20 times larger than with a Van de Graaff accelerator, i.e., 2 to 4 μA might be applied to many inorganic targets. This may represent counting rates up to several hundreds of counts per second, at the peaks of the excitation curves, for samples of the type studied below.

It should be noted that the detrimental effects of hydrocarbon contamination on effective beam energy spread increase with ψ. Therefore UHV conditions and well cleaned targets are specially important in grazing geometries.

When investigating deep ^{18}O profiles, or films of intermediate thickness but measured with large ψ, the energy must be varied in a wide range, up to 60 keV before the next resonance is reached. This is not possible for a Van de Graaff accelerator with the hysteresis-free electrostatic energy scanning system used in Part I: the magnet setting must be changed manually. This problem is probably easier to solve for ion implantation type accelerators. It should also be noted at this point that for such large energy variations the assumptions underlying the stochastic energy loss theory implemented in the program SPACES [4] break down. However alternative programs for deep regions are presently under development.

For optimal near-surface depth resolution it might be necessary to minimize the Doppler broadening by cooling the targets to liquid nitrogen temperatures, as illustrated in ref. [3]. Note that the machine described in this reference presents a beam energy spread around 15 eV FWHM.

3. Depth profiling capability

In all the excitation curve fittings and theoretical simulations that follow we used the value $\Gamma = 75$ eV for the resonance described by a Breit–Wigner line shape. In this way, whether Γ is equal to 50 or 100 eV, the fits and simulations will be reasonably representative.

3.1. Normal incidence

The depth profiling capabilities of this resonance were first studied with 98% ^{18}O enriched Ta_2O_5 anodic oxide films prepared and their thickness measured as described in Part I. Fig. 1 shows excitation curves recorded with the annular detector for $Ta_2^{18}O_5$ targets

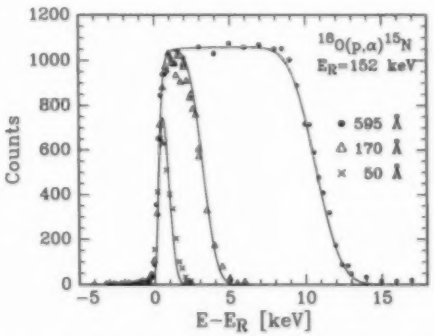

Fig. 1. Excitation curves for 98% ^{18}O-enriched Ta_2O_5 targets. Annular detector with solid angle 0.93 sr; 20 μC per point; origin at resonance energy $E_R = 152$ keV. The solid lines represent theoretical fits obtained with the parameters: resonance width $\Gamma = 75$ eV; gaussian beam energy spread including Doppler broadening $G = 100$ eV FWHM; surface hydrocarbon contamination $T = 0.4$ μg/cm^2. Let us emphasize that these measurements are background-free: the origin of the ordinate scale corresponds hence to zero count.

of increasing thicknesses. The experimental data corresponding to the 595 and 170 Å thick films were shown in Part I, fig. 2; they were used to determine the width of the resonance. The curves were fitted here using the stochastic theory of energy loss as implemented with SPACES. The mid point $E_{1/2}$ of the rise of the curves is slightly shifted with respect to E_R due to the energy loss in the hydrocarbon contamination layer. The falling edge corresponding to the 595 Å film was fitted with a Gaussian approximation, a procedure complementing SPACES for targets too thick to be interpreted with its autoconvolution sum algorithm. The parameters of the calculations with SPACES, extracted from the width and falling edge of the curve labeled 595 Å, are: $dE/dx = 210$ keV/mg cm^{-2} (17.8 eV/Å); straggling root constant $S = 5.7$ keV(mg cm^{-2})$^{-1/2}$ (real straggling to Bohr straggling root mean square deviation ratio of 0.64). The fit of the curve for the 50 Å thick film is slightly too narrow and too high. It is possible that this is due to some mixing, during growth, between the ^{18}O atoms in this very thin isotopically labeled film and the ^{16}O atoms in the underlying 35 Å thick natural spontaneous oxide on the tantalum substrate. The possibility of such a short-range mixing cannot be ruled out according to ref. [5]; with the precision level in depth profiling reached with this resonance we could now investigate this question further.

In fig. 2 we compare the results in fig. 1 to those shown in refs. [6] and [7], corresponding to the high yield but 2.1 keV wide resonance at 629 keV, classically used for ^{18}O depth profiling. We may observe that while the counting rates are much higher, the broadening of the excitation curve with thickness is much slower, saturation being reached around 1000 Å compared with around 170 Å in fig. 1. The shape of the saturated curves is not rectangular and the base line of the curves increases proportionally to the overall ^{18}O content due to the asymmetrical resonance line shape and to the high off-resonance cross section.

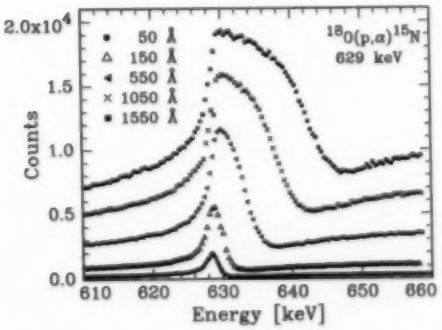

Fig. 2. Excitation curves for 75% ^{18}O-enriched Ta_2O_5 targets measured with the classically used 2.1 keV wide $^{18}O(p, \alpha)^{15}N$ resonance at 629 keV, shown for comparison with fig. 1. 384 eV/channel, 0.08 sr, detection angle 150°. Automatic energy scanning with beam dose per channel: 50 Å, 20 μC; 150 Å, 15 μC; 550 Å, 6 μC; 1050 Å, 5 μC; 1550 Å, 3 μC. The curves were normalized to the same charge; the real counts are those for the 1550 Å thick film. From ref. [6] and [7].

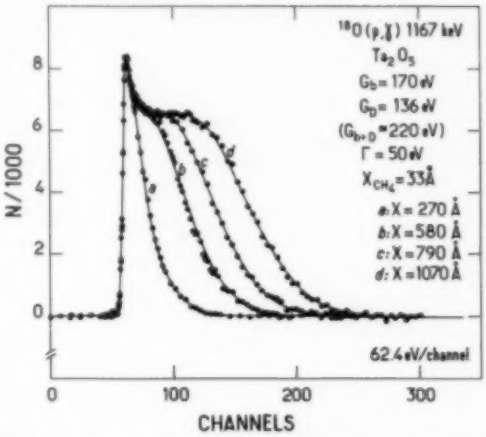

Fig. 3. Excitation curves for 90% ^{18}O-enriched Ta_2O_5 targets measured with the $\Gamma = 50$ eV $^{18}O(p, \gamma)^{19}F$ resonance at 1167 keV, shown for comparison with fig. 1. G_{b+D} is the beam energy spread including Doppler broadening. 100 μC/channel, 3" × 3" NaI(Tl) detector near 0° at ~1 cm from the target. The curves were shifted to the same base line to compensate for the yield from the off-resonance cross section. The solid lines are theoretical fits. Note the strong overshoot due to the Lewis effect. From ref. [7].

Fig. 3 shows results similar to those in fig. 1 measured with the very narrow resonance at 1167 keV, observed here through the (p, γ) channel. The 152 and 1167 keV resonances present similar widths Γ, around 50 eV, and the counting rates at saturation are also analogous in the respective experimental conditions used. It is therefore important to discuss in detail the relative merits for depth profiling of these two resonances.

For a rectangular depth profile of thickness x let ΔE be the FWHM and $L_{1/2}$ the 88% to 12% width of the falling edge of the corresponding excitation curve in the saturated case. The sharper the fall of this curve as compared to its width the better the image it gives of the depth profile. For thick enough films we may define a target thickness independent factor of merit m of a resonance by: $\Delta E/L_{1/2} = m\sqrt{x}$. In fact m is the ratio of dE/dx to S. The parameters describing the slowing down of protons around 1167 keV extracted from the experimental data [6], are: $dE/dx = 83.6$ keV/mg cm^{-2} (6.7 eV/Å); $S = 6.8$ keV (mg cm^{-2})$^{-1/2}$ (real straggling root to Bohr straggling root mean square deviation ratio of 0.77). At 152 keV, $m = 37$ and

at 1167 keV, $m = 12.2$. The ratio ≈ 3 of these figures of merit reflects the intrinsic advantage of the low-energy resonance in depth profiling experiments as far as the proton slowing down process is concerned. Another advantage of low resonance energies is the faster convergence with film thickness of the energy-loss spectra towards symmetrical and eventually gaussian-like shapes as illustrated by the various falling edges in fig. 1 and 3. This aspect corresponds to the fact that the maximum energy transfer U_{max} from a proton to an electron in a single collision is 0.3 and 2.5 keV, respectively, for the two resonances.

At 1167 keV a strong Lewis effect shows up, conferring a high surface sensitivity to this resonance, an intuitive concept which will be defined more precisely in section 5. This effect does not appear on the excitation curves around 152 keV both because at this energy it is intrinsically smaller and also because of the stronger smearing effect of the hydrocarbon contamination, much more effective with the larger dE/dx at low energies. The absence of the Lewis effect in our experimental results at 152 keV does not mean that the surface sensitivity is smaller than at 1167 keV. In fact the stronger smearing effect of the contamination layer reflects an even better potential surface sensitivity at low energies. This will be illustrated in detail in the theoretical section 5.

Let us also observe that saturation is reached at a smaller thickness in fig. 1 than in fig. 3, as illustrated by the curves corresponding to 595 and 580 Å, respectively. At the other end of the depth ranges which might be of interest, the 1167 keV resonance may be useful insofar as thicker targets can be studied in favorable cases, the next resonance being far away and the dE/dx being smaller.

A fundamental advantage of the 152 keV resonance is the much larger admissible target beam current as discussed in section 2, which may be taken advantage of with an implantation-type accelerator. Let us note at this point that while the results shown in fig. 1 may be improved in every respect with a machine of this type, those in fig. 3 were obtained in almost ideal conditions around 1.2 MeV (nearly the best potential stability for a Van de Graaff accelerator, close to the maximum admissible target beam current, around 1 μA).

Other advantages of the 152 keV resonance with respect to that at 1167 keV are related to nuclear physics, detection and background problems. The (p, α) channel of the 1167 keV resonance may be used only under very stringent experimental conditions. As the range of the α-particles is shorter than that of the backscattered protons here, the latter cannot be stopped in an absorber and, except for self supporting thin targets, special ultrahigh speed amplification must be used to keep pulse pileup under control, as in ref. [6] for the study of $Al_2^{18}O_3/Al$ films. Even that is possible only with moderate beam currents and for low-Z target backings like silicon, for which it is a necessity, as in this case the beam induced γ-ray background would prevent any measurement with the (p, γ) channel. Moreover the α-particles must be detected at 170°, as the yield of this resonance decreases abruptly below 170°. Finally the off-resonance cross section in the (p, α) channel is rather large and induces strong thickness dependent backgrounds. For high enough Z target backings the (p, γ) channel is much easier to use but the natural γ-ray background remains a limiting factor in sensitivity, in contrast with the background-free α-particle detection at 152 keV. Last but not least the low energy resonance is the first and may therefore be used for near surface depth profiling even for thick ^{18}O-labeled films, as there is no contribution from the bulk below the resonance. This may be most useful, for example in the study of oxygen transport in high-T_c superconductors.

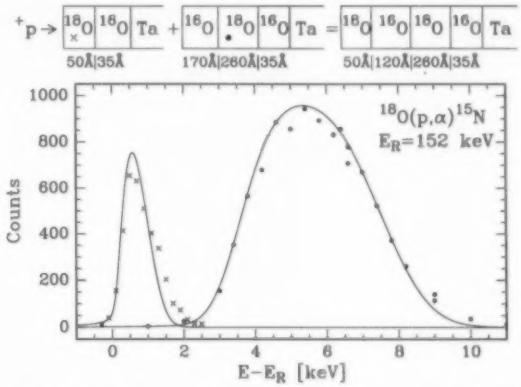

Fig. 4. Excitation curves of a thin $Ta_2^{18}O_5$ layer and a buried $Ta_2^{18}O_5$ layer under a $Ta_2^{16}O_5$ layer. The sum of these two curves is equivalent to the excitation curve of a $Ta_2^{18}O_5/Ta_2^{16}O_5/Ta_2^{18}O_5$ sandwich, as indicated. Experimental conditions and the parameters of the theoretical fits represented by solid lines are the same as for fig. 1.

Fig. 4 shows how the excitation curve is shifted when the corresponding ^{18}O-enriched layer is buried under an unlabeled one. The separation between the two peaks is practically total for a 170 Å thick overlayer, which induces a slower rise of the shifted peak due to energy straggling. Fig. 5 shows a similar experiment carried out with the 1167 keV resonance. The comparison between these two results is most illustrative. At high energy the relative shift is much smaller and the curves present much longer asymmetrical tails. The latter aspect was already noticed above in connection with fig. 3 as related to the high value of U_{max}, 2.5 keV at 1167 keV.

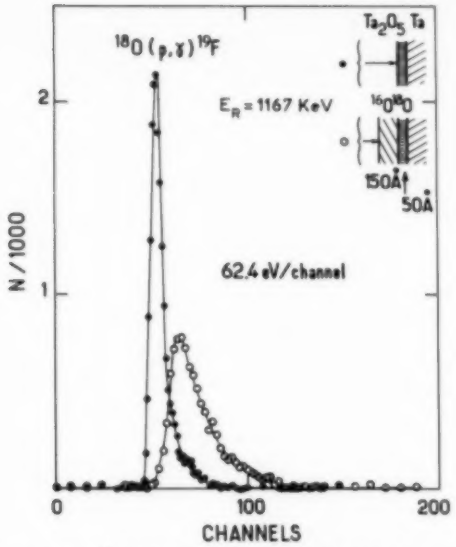

Fig. 5. Buried ^{18}O-labeled layer experiment similar to that in fig. 4, carried out with the 1167 keV resonance. Experimental conditions similar to those in fig. 3. From ref. [7].

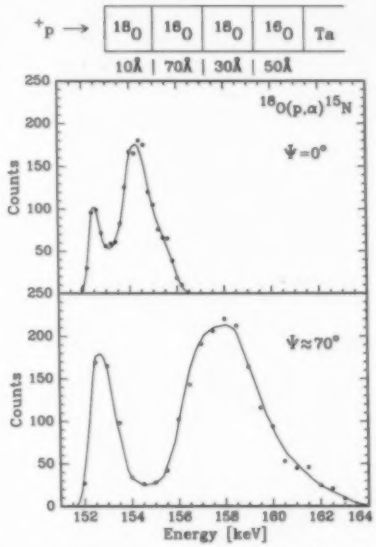

Fig. 7. Excitation curves for a thin ^{18}O–^{16}O–^{18}O Ta_2O_5 sandwich sample measured with $\psi = 0°$ and $\psi \approx 70°$ tilts. The solid lines were drawn for guiding the eye.

Let us note that in both figs. 4 and 5 the sum of the two peaks is equivalent to the excitation curve corresponding to a $Ta_2^{18}O_5/Ta_2^{16}O_5/Ta_2^{18}O_5$ sandwich with respective thicknesses 50 Å/120 Å/260 Å and 50 Å/100 Å/50 Å. It is clear that while such a sandwich is well resolved at 152 keV it is not at all at 1167 keV. In this connection it is interesting to show an excitation curve (fig. 6) recorded with the broader 629 keV resonance for such an isotopic sandwich, with an intermediate ^{16}O oxide layer 820 Å thick; even though this separation is 7 times larger, the peak to valley ratio is markedly less favorable than in fig 4.

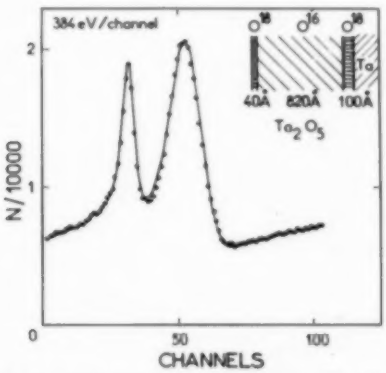

Fig. 6. Typical depth profiling experiment on a ^{18}O–^{16}O–^{18}O Ta_2O_5 sandwich measured with the broad resonance illustrated in fig. 2, shown for comparison with fig. 4. 30 μC/channel, 0.08 sr, channel zero at 616.7 keV. From ref. [7].

3.2. Grazing incidence geometry

A real isotopic Ta_2O_5 sandwich of this type, but much thinner, was prepared by alternate anodic oxidation of tantalum in 98% ^{18}O-enriched and natural water (0.204% ^{18}O) and its total ^{18}O and ^{16}O contents were checked as described in Part I. The corresponding depth profile was measured with the 152 keV resonance, as shown in fig. 7. The excitation curve recorded with normal incidence exhibits a clear although not complete separation. We tried to improve the depth resolution by resorting to grazing incidence with a tilt $\psi \approx 70°$, which increases the effective thicknesses traversed by the protons by a factor $(1/\cos \psi) \approx 3$. The corresponding curve in fig. 7 shows a reasonable separation of the two labeled layers only 70 Å apart, illustrating how powerful may be the combination of grazing incidence geometry with resonance depth profiling. Let us observe that the boundaries between such thin ^{18}O and ^{16}O anodic oxide layers are probably not ideally sharp, as pointed out in connection with fig. 1. It seems difficult to produce thin isotopic sandwich test samples with boundaries known a priori to be better defined. The ultimate near surface depth resolving capability of this resonance may only be determined by theoretical calculations, as will be shown in section 5.

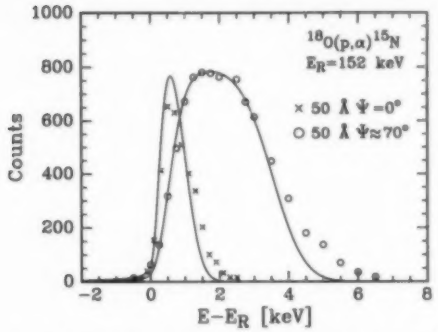

Fig. 8. Excitation curves and theoretical fits for a thin $Ta_2^{18}O_5$ layer measured in normal and grazing incidence geometries. Experimental conditions and the parameters of the theoretical fits are the same as for fig. 1, except for the case of the tilted sample where the apparent thicknesses of both the hydrocarbon contamination layer and the oxide layer are multiplied by the factor $1/\cos\psi$. Note that the solid angles are not exactly the same.

Fig. 8 presents a comparison of depth profiling in normal and grazing incidence geometries. The thin target used in fig. 1 was remeasured with $\psi \approx 70°$. At this tilt angle the excitation curve nearly saturates. The solid lines are calculated with the same parameters except that the thickness of the ^{18}O labeled oxide film as well as that of the hydrocarbon contamination layer ($x = 50$ Å, $T = 0.4$ μg/cm^2) were multiplied by 3.4 for the tilted case. The agreement is satisfactory, the experimental tails being due probably to the isotope mixing effects considered above. We may conclude that target tilting may be used most efficiently to improve depth resolution, except very near the surface where the effect of the apparent increase of the thickness of the contamination limits the possible gains. For deep regions multiple scattering may limit the maximal values of ψ, which may be even larger than $\approx 70°$, as will be discussed in section 5.

4. A typical application

The microscopic mechanisms of oxygen transport during the thermal oxidation of silicon have been investigated in our laboratory for many years by the group headed by S. Rigo. A particularly important effort has been devoted to the ^{18}O isotopic tracing study of oxidation processes in dry oxygen [8,9]. In the recent period this effort was applied to very thin SiO_2 films, in the range below 100 Å. It has been shown that when silicon is oxidized first in $^{16}O_2$ and then in $^{18}O_2$, most of the ^{18}O is found at the SiO_2/Si interface, while a smaller amount of ^{18}O is fixed at the surface of the silica film grown. The deep component is due to growth through permeation of the SiO_2 film by molecular oxygen, while the near surface component is due to defect induced exchange and diffusion processes depending on the heat treatment conditions: the shape and relative area of the near surface profile is still under investigation, in particular in the case of very thin films. For sufficiently thick films the ^{18}O depth profiles were determined with the 629 keV resonance. For the thinner films the depth resolution of the known $^{18}O(p, \alpha)^{15}N$ resonances was insufficient and a step by step dissolution technique was used [10], the profile being extracted by differentiation of the ^{18}O content versus remaining thickness curve. It is our aim to apply the high depth resolution technique described in this paper to the isotopic tracing study of such processes, with the inherent advantages of a direct, nondestructive and nondifferential method.

We present here the first results of this program, obtained on old samples from experiments carried out in our laboratory. Fig. 9 shows the curves obtained for a medium thickness SiO_2 layer where a 200 Å thick ^{16}O film was retreated in 98% enriched $^{18}O_2$ at 930°C and 10 mbar for 18 h. The two peaks are well resolved even with normal incidence; the separation is complete with $\psi \approx 70°$. A thicker SiO_2 film was also investigated in grazing geometry (fig. 10). The separation is spectacular, the counts falling actually to zero around 160 keV. This is not surprising if we consider the results in refs. [8]–[10] according to which no ^{18}O is fixed in the

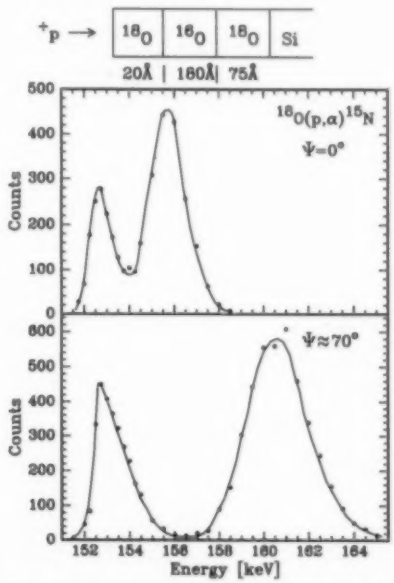

Fig. 9. Excitation curves similar to those in fig. 8 but for a thin ^{18}O–^{16}O–^{18}O SiO_2 sandwich grown by thermal oxidation of silicon in natural and 98% ^{18}O-enriched dry oxygen.

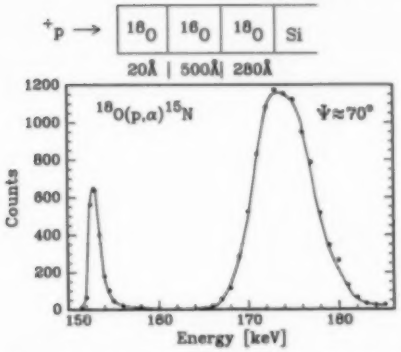

Fig. 10. Experimental result obtained like in fig. 9 but for a thicker SiO_2 isotopic sandwich. Note the complete separation of the peaks, the counts between them approaching zero, as they should considering the natural isotopic abundance of ^{18}O, 0.204%, in the "^{16}O" layer.

bulk of the oxide in these experimental conditions. Let us note however that the latter conclusion could not be drawn with the precision reached in fig. 10 and its confirmation by this new technique may be considered as its first contribution to this subject.

Fig. 11 shows for comparison a depth profiling experiment with the 629 keV resonance applied to an isotopic sandwich with a depth profile similar to that in fig. 10. This meausurement was also carried out in grazing incidence geometry with nearly the same tilting angle. The two peaks are distinguishable but there is a complete overlap between them and not much can be

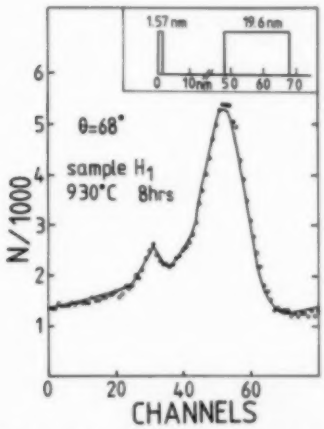

Fig. 11. SiO_2 isotopic sandwich very similar to that of fig. 10, depth profiled in nearly the same grazing geometry but with the 2.1 keV wide 629 keV resonance. 384 eV/channel, detection angle 150°. The comparison between this curve and that of fig. 10 speaks for itself. Reprinted with permission of the publisher. From ref. [9].

deduced about the amount of ^{18}O fixed in the middle region of the film.

5. Ultimate resolution limits

In this section we make a theoretical investigation of the best performance that may be expected of the 152 keV resonance in SiO_2. We have assumed ideal but achievable experimental conditions: Gaussian beam energy spread (including Doppler effect) of $G = 40$ eV, implying a target cooled to around liquid nitrogen temperature, and no surface contamination, which implies UHV conditions and a nondestructive in-situ surface cleaning method. SPACES [4] has been used for all the calculations. We have assumed $dE/dx = 475$ keV/mg cm^{-2}, and have used a value for S of 7.25 keV (mg cm^{-2})$^{-1/2}$ based on an approximation in [6]. For low Z, as is the case here, this approximation falls very close [11] to the values of Chu [12], and Bonderup and Hveplund [13]. We intend to measure both the stopping power and the straggling constant in specially prepared oxides of known thicknesses, however the present predictions should not be very sensitive to small variations in these values. These theoretical predictions should nevertheless be treated with some caution, since the use of a simple truncated $1/u^2$ form for the primary energy loss function becomes questionable for the prediction of such high resolution excitation curves and it is possible that we may be obliged to adopt a more realistic form to interpret such experiments correctly. It may also become necessary to try and include the "half-atom" effect [6,14] to account for the fact that all protons which contribute a count to the excitation curve will have had their last interaction with an atom at zero impact parameter.

5.1. Surface sensitivity

By surface sensitivity, or more precisely surface composition sensitivity, we mean sensitivity of the shape of the excitation curve to the presence of surface layers devoid of reacting nuclei. Such layers may be due to unwanted surface contamination, or to composition variations deliberately induced for the purpose of studying them. In fig. 12 we compare theoretical excitation curves corresponding to a homogeneous ^{18}O-labeled oxide buried beneath 10 Å of natural oxide with those corresponding to an uncovered homogeneous ^{18}O-labeled oxide. The curves have been shifted on the energy scale so that the mid-points of the rises occur at the same place. Our first remark is that the observed Lewis effect is strongly influenced by the presence of the inert surface oxide layer, completely disappearing when only 10 Å of natural oxide covers the labeled oxide. In addition, we have done the calcu-

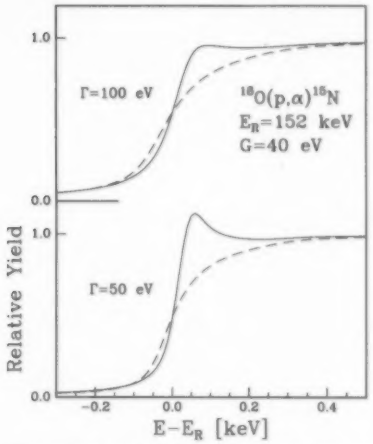

Fig. 12. Theoretical excitation curves for the 152 keV resonance in SiO_2 calculated for ideal experimental conditions (no hydrocarbon contamination, $G = 40$ eV). The solid curves correspond to a constant concentration from the surface into the sample, whilst the broken curves correspond to a sample in which the first 10 Å of SiO_2 is not ^{18}O-labeled. The curves have been slightly shifted in the energy scale so that the half-heights of the rises cross at zero energy. The Lewis effect is very sensitive to the resonance width, disappearing for $\Gamma = 100$ eV, whilst being readily visible for $\Gamma = 50$ eV. To be able to use the sensitivity of the Lewis effect confidently Γ must be known as precisely as possible. The presence of even 10 Å of superficial oxide free of ^{18}O completely annihilates the Lewis peak.

lations for two different values of Γ for the resonance width, and we can note that the difference between the excitation curves of the surface and buried oxides is rather strongly dependent on Γ. This highlights the practical importance of measuring Γ with as great a precision as possible. In fact with sufficiently good thick targets and a suitable experimental setup, such as that at Münster [3], it is possible to exploit the Lewis effect to measure Γ with the necessary precision.

5.2. Surface depth resolution

The usual definitions of depth resolution break down when depth profiling very near the surface, since the instrument function is neither Gaussian nor of fixed, or even slowly varying width. We may consider the instrument function to be composed of three parts: the natural resonance line shape (Lorentzian in the present case); a Gaussian component, which represents the beam energy spread and the Doppler effect, and the straggling function $g(u; x)$. The straggling component is highly asymmetrical in the vicinity of the surface, and has a FWHM that varies virtually linearly with x for small depths [15], and a standard deviation σ that varies as $x^{1/2}$ (implying a rate of increase of σ that is infinitely large at the surface). For narrow enough resonances and sufficiently good beam energy resolution, which is assumed to be the case here, $g(u; x)$ is central to a useful definition of resolution at the surface.

When, as is presently the case, the instrument function is unimodal, the resolution R at depth x_0 is classically defined as the smallest value of Δx for which the response to two delta functions of concentration, one at x_0 and the other at $x_0 + \Delta x$, has a point of zero slope and positive second derivative. In fig. 13 we have plotted the excitation curves corresponding to $C(x) = \delta_0 + \delta_{\Delta x}$ for various values of Δx, and it is clear that the theoretical surface depth resolution is around 30 Å. This is to be compared with the well-known "naive" definition which is the FWHM of the instrument function at the surface – in this case 95 eV – divided by the stopping power, which gives a rather optimistic resolution estimate: 9 Å. As demonstrated in the experimental section above, the depth resolution may be improved by tilting the target, and on fig. 13 we have indicated the degree of tilting that would be necessary to increase the seperation of two deltas 10 Å apart to that corresponding to the figure. At 70° of tilt, therefore, we would expect to have a depth resolution of about 10 Å. However this number has only

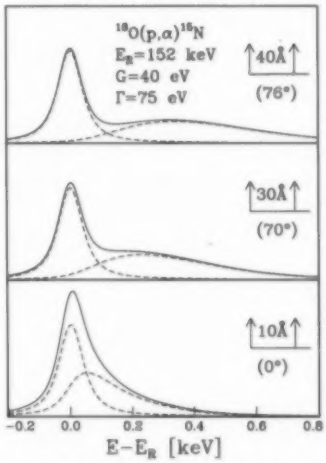

Fig. 13. Theoretical excitation curves for the same ideal experimental conditions as in fig. 12 but with $\Gamma = 75$ eV, corresponding to concentration profiles which are simply two delta-functions; one on the surface, and the other at some depth in the sample. The numbers in brackets indicate the target tilt angle ψ necessary to increase the seperation of two deltas 10 Å apart to that in the figure. The broken curves are the excitation functions corresponding to each delta seperately, and the solid curves simply their sum. The surface depth resolution at normal incidence is seen to be about 30 Å.

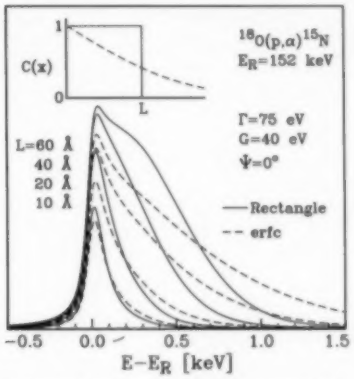

Fig. 14. Theoretical excitation curves in normal incidence for the same ideal experimental conditions as in fig. 13 corresponding to finite homogeneous (full curves) and complementary error function (broken curves) ^{18}O concentration profiles $C(x)$ of the same surface concentration and containing the same total numbers of atoms.

nominal meaning, since the idea of continuous depth profiles over depths of the order of 10 Å or so needs modification to account for the fact that at this scale matter itself may no longer be thought of as continuous.

5.3. Near surface depth profiling

As a final example of what we may hope to achieve under suitable conditions with this resonance we have calculated the excitation curves for $\psi = 0°$ corresponding to finite homogeneous ^{18}O-labeled oxides of various thicknesses L, and to the same number of ^{18}O atoms distributed in an erfc function (of unit surface concentration), shown in fig. 14. erfc-type concentration profiles could result from experiments in which a natural SiO_2 is re-oxidised in $^{18}O_2$. In this case the lack of any background under the resonance (in contrast to the 1167 keV resonance) gives good discrimination between these two types of concentration profiles since the difference in the tails, even for $L = 20$ Å, should be measurable. As erfc-type profiles may be distinguished from rectangular ones the corresponding diffusion coefficients might be measured directly, and the profiles may provide the information necessary to distinguish between different models for diffusion and surface exchange effects.

5.4. Multiple scattering induced limitations on tilting angle

Let us consider what happens at a given depth x measured perpendicularly to the sample surface which we assume is ideally flat. Let t be the length along the beam axis up to x, $t = x/\cos\psi$. Due to multiple scattering the particle trajectories have a fluctuating shape which, for given t, results in a spread of the angle α of the particle trajectories with respect to their initial direction and in a fluctuation of the length of the trajectories up to x, which depends strongly on ψ. In normal incidence these trajectory length fluctuations are negligible as long as $\cos\alpha \approx 1$. In grazing incidence geometry they become an important limiting factor of depth resolution enhancement. They induce an extra energy spread which combines with the ordinary energy straggling considered so far; the latter is inherent to the statistical nature of the slowing down process, while multiple scattering induced energy spread is geometrical in nature and is proportional to dE/dx. For given ψ the effect increases with depth and with the atomic number of the species in the film being analyzed. The treatment of the general problem is out of the scope of this paper: a detailed theoretical and experimental investigation is required. In this section we merely present some rough estimates for the case of SiO_2, based on classical multiple scattering and lateral spread theory. We shall consider that multiple scattering induced energy spread may be overlooked for given t (and SPACES may be applied to the interpretations), if it is less than half of the FWHM of the straggling function $g(u; t)$ for at least 85% of the beam particles. With this criterion we find the following typical limitations. For $t = 120$ Å we may tilt up to $\psi = 87°$, meaning that theoretically we may stretch out a thickness x of 7 to 120 Å. More realistically for $\psi = 80°$ the resolution of 30 Å found in fig. 13 is reduced to ≈ 5 Å in the near surface region. For $t = 600$ Å our criterion leads to 76°, showing that we may explore a depth x of 150 Å with an amplification of 4 while straggling effects still dominate. For $\psi = 70°$ this corresponds approximately to the case of fig. 9. For $t = 1200$ Å our criterion limits ψ to 67°, a more severe limitation, but which still allows an amplification by a factor 2.5, i.e., the exploration of a ~ 500 Å thick layer without multiple scattering playing an appreciable role. For $t = 2400$ Å ψ should be less than 48° to respect our criterion. However fig. 10, where $t \approx 2400$ Å and $\psi = 70°$, shows that we still may have excellent excitation curves in these conditions, except that the falling edge corresponding to the deepest interface is slightly broader as compared to the case in fig. 9 than the prediction of pure straggling theory.

These conclusions are hence probably pessimistic our criterion being severe and because we considered the angles α in space while we should have used angles projected onto a plane containing the beam axis, a lengthy calculation procedure. The values above illustrate however that while in the near surface region grazing incidence may be used with large tilting angles, caution should be exercised for depths x greater than some hundreds of angstrom in SiO_2.

6. Conclusions

The results illustrate the merits of low energy narrow resonances in general for very high resolution depth profiling, due to the corresponding large dE/dx values. Resonances around 300 keV on ^{23}Na, ^{26}Mg, ^{27}Al among others are good candidates for such experiments [3]. For profiles of intermediate and large depth the ultimate limits of depth resolution enhancement in grazing incidence geometry set by multiple scattering induced trajectory length fluctuations should be investigated both theoretically and experimentally in various materials. A comparison for such profiles of resonance depth profiling with SIMS techniques in ^{18}O isotopic tracing would be useful.

The method described here may have many applications to the ^{18}O isotopic tracer study of oxidation processes in addition to the case of the thermal oxidation of silicon considered above. Thus the thermal oxidation of Si_3N_4 or SiC films on silicon has received renewed attention in the recent period [16]. Two aspects of these problems may be considered: a fundamental one, to understand the corresponding growth and exchange mechanisms, in particular the formation of oxynitrides; a more applied one, in connection with the production of oxidation resistant materials, ceramics and encapsulation layers in microelectronics for example. An interesting inverse problem is that of the nitridation of thin SiO_2 films. All these processes may be studied with classical thermal treatments, or one of the growing number of alternative techniques such as rapid thermal annealing, plasma treatments, etc. Many other fields of application spring to mind. The study of oxygen transport and exchange processes in high-T_c superconductors for example is a domain which may benefit from the ^{18}O depth profiling method presented here.

Acknowledgements

We wish to thank S. Rigo and I. Trimaille for providing us with the ^{18}O-labeled SiO_2 isotopic sandwich samples. Enlightening discussions with them and with J.J. Ganem on the applications of this resonance to the study of the oxidation processes of silicon were most appreciated. An exchange of ideas with F. Rochet on other possible applications of this analytical technique is gratefully acknowledged. We greatly benefited from A. L'Hoir's advice on the role of multiple scattering processes in grazing incidence ^{18}O depth profiling. The technical assistance during the measurements of J. Moulin and E. Girard was always most helpful. We also thank W.H. Schulte from Münster for his interest in this work.

References

[1] G. Battistig, G. Amsel, E. d'Artemare and I. Vickridge, Nucl. Instr. and Meth. B61 (1991) 369.
[2] H. Lorenz-Wirzba, P. Schmalbrock, H.P. Trautwetter, M. Wiescher, C. Rolfs and W.S. Rodney, Nucl. Phys. A313 (1979) 346.
[3] S. Wüstenbecker, H. Ebbing, W.H. Schulte, H. Baumeister, H.W. Becker, B. Cleff, C. Rolfs, H.P. Trautvetter, G.E. Mitchell, J.S. Schweitzer and C.A. Peterson, Nucl. Instr. and Meth. A279 (1989) 448.
[4] I. Vickridge and G. Amsel, Nucl. Instr. and Meth. B45 (1990) 6.
[5] J.P.S. Pringle, J. Electrochem. Soc. 120 (1973) 1391.
[6] B. Maurel, Thesis, Université de Paris 7, France (1980).
[7] B. Maurel, G. Amsel and J.P. Nadai, Proc. 2nd Int. Conference on Chemical Analysis, Namur, September 1981, Nucl. Instr. and Meth. 197 (1982) 1.
[8] E. Rosencher, A. Straboni, S. Rigo and G. Amsel, Appl. Phys. Lett. 34 (1979) 254.
[9] F. Rochet, B. Agius, and S. Rigo, J. Electrochem. Soc. 131 (1984) 914.
[10] I. Trimaille and S. Rigo, Appl. Surf. Sci. 39 (1989) 65.
[11] I. Vickridge, Thesis, Université de Paris 7, France (1990).
[12] W.K. Chu, Phys. Rev. A13 (6) (1976) 2057.
[13] E. Bonderup and P. Hvelplund, Phys. Rev. A4 (2) (1971) 562.
[14] W.H. Schulte, H. Ebbing, H.W. Becker, S. Wüstenbecker, M. Berheide, M. Buschmann, C. Rolfs, G.E. Mitchell and J.S. Schweitzer, submitted to Proc. 10th Int. Conf. on Ion Beam Analysis, Nucl. Instr. and Meth. B64 (1992).
[15] I. Vickridge and G. Amsel, Nucl. Instr. and Meth. B45 (1990) 16.
[16] H. Du, C.A. Houser, R.E. Tressler, K.E. Spear and C.G. Pantano, J. Electrochem. Soc. 137 (1990) 741.

Nuclear Instruments and Methods in Physics Research B66 (1992) 11–16
North-Holland

Nuclear Instruments & Methods in Physics Research
Section B

Novel applications of high-energy resolution ion beams *

W.H. Schulte, H. Ebbing, H.W. Becker and S. Wüstenbecker
Institut für Kernphysik, Universität Münster, Münster, Germany

M. Berheide, M. Buschmann and C. Rolfs
Institut für Experimentalphysik III, Universität Bochum, Bochum, Germany

G.E. Mitchell
North Carolina State University, Raleigh, NC, USA and Triangle Universities Nuclear Laboratory, Durham, NC, USA

J.S. Schweitzer
Schlumberger-Doll Research, Ridgefield, CT, USA

Improvements in targetry and ion beam energy resolution permit the observation of novel effects using narrow nuclear resonances as a probe. For the 400 kV Münster accelerator the ion-beam energy resolution was reduced to 15–20 eV at full ion-beam current. The development of UHV, vapor, and gas target systems allowed the use of very clean targets with variable density and temperature. With the energy spread of the ion beam approaching the eV level, the dynamics of the nuclear environment (atomic shells and solid material) become observable. Some novel applications in nuclear, atomic, molecular, and solid state physics are discussed.

1. Introduction

A wide range of phenomena in pure and applied physics can be studied with narrow nuclear resonances ($\Gamma_R \ll E_R$, $\Gamma_R \leq 100$ eV). The topics range from the observation of chaos in nuclear spectra to depth profiling measurements. Improvements in the energy resolution of ion beams ($\Delta E/E$) and the quality of targets enable the observation of very weak resonances and improve the sensitivity of applications such as depth profiling. Most importantly for the present discussion, good energy resolution ($\Delta E/E \approx 10^{-5}$) permits investigation of a variety of effects which are not observed with moderate or poor energy resolution ($\Delta E/E \approx 10^{-3}$).

When the energy spread of ion beams (ΔE) approaches the eV level, the dynamics of the nuclear environment (atomic shells and solid material) become observable with narrow nuclear resonances, since the energies in the atomic or solid-state interactions are comparable [1]. For example, a compound nuclear state is actually a quasistationary state of an entire compound nuclear atom. Therefore in a nuclear collision it might be possible to observe replicas (or echoes, or satellites) of very sharp nuclear resonances, displaced in energy by the atomic excitation energies. Similarly, the lattice vibrations in a solid target lead to a broadening of a nuclear resonance due to the Doppler motion, which in turn can be used to measure the Debye temperature of the surface layer of the solid. Here we briefly describe technical improvements to the 400 kV Münster accelerator, and to the ion-beam handling, data acquisition, and target systems. Results for a few novel applications in pure and applied physics are then presented. It should be pointed out that these applications involving the interface between the nucleus and its environment are just beginning and that no comprehensive framework has yet been developed.

2. Ion-beam energy resolution and data acquisition

The energy resolution of ion beams is of central interest at all energies. From various technical consid-

* Supported in part by Deutsche Forschungsgemeinschaft (Ro429/16-2), US Department of Energy, Office of High Energy and Nuclear Physics (Grant no. DE-FG05-88ER40441), NATO Scientific Affairs Division (Grant no. 86-0485), Minister für Wissenschaft und Forschung des Landes NRW (IVA5-10600387), NC Board of Science and Technology, and Friedrich-Flick Förderungsstiftung.

0168-583X/92/$05.00 © 1992 – Elsevier Science Publishers B.V. All rights reserved

erations we concluded [2] that a Dynamitron tandem accelerator appears to be ideal. However, initially we have focused our efforts on a low-energy machine – the 400 kV Munster cascade accelerator. We wished first to demonstrate the efficacy of high-ion-beam resolution in various applications, before embarking on a more extensive program of technical development and research at higher energies and using various types of ion beams. We felt that the disadvantages of the restriction to low energy and light ions (protons and ^{4}He) would be outweighed by the advantages of extremely good energy resolution. Details of the 400 kV accelerator including investigation of the ion beam specifications have been described recently [3]. The accelerator provided proton beams of up to 300 μA at the target with an energy spread $\Delta E_i \leq 20$ eV, when the high voltage (HV) ripple was reduced to $\Delta E_{HV} = 4$ eV. The major contribution to ΔE_i arose from the ion source (ΔE_{IS}); recent measurements [4] indicate $\Delta E_{IS} = 15$–20 eV, and thus $\Delta E_i/E < 5 \times 10^{-5}$. The energy stability and reproducibility was better than ±3 eV over a time period of eight days [3,4].

The data acquisition and accelerator energy scanning system (fig. 1) were controlled by a personal computer [4]. An IEC bus system allowed automatic variation of the accelerator energy, which was set first manually near the value of interest. The energy variation (ranging up to 4 keV) was performed in small steps (as small as 0.4 eV) by applying a control voltage to the external control input of the HV power supply. This control voltage was produced by a digital to analog converter (DAC) controlled by the IEC bus. The HV setting was recorded by reading the voltage display of a $6\frac{1}{2}$ digit voltmeter (DVM), directly connected to the precision voltage dividing resistor chain of the HV power supply. In addition to the actual HV value at each energy, the counting rate of a nuclear detector (here: γ-ray detector) was converted to logic signals via a single channel analyser (SCA) and registered by an IEC bus controlled counter. Similarly, the charge collected on the Faraday cup, converted to logic signals by a current to frequency converter, was also monitored in a counter. When an energy scan was completed, all data were written to a file. Further scans were then added to improve the statistics. The system provided on-line data manipulation and analyzing capability as well as a display of the energy dispersion of the data being recorded. To keep the beam current constant on target during an energy scan, the setting of the switching magnet of the accelerator also was controlled via the DAC output. This procedure led to a target current change of less than 2% for an energy variation of up to 4 keV. In some experiments, the remaining ripple of the HV terminal was amplified appropriately

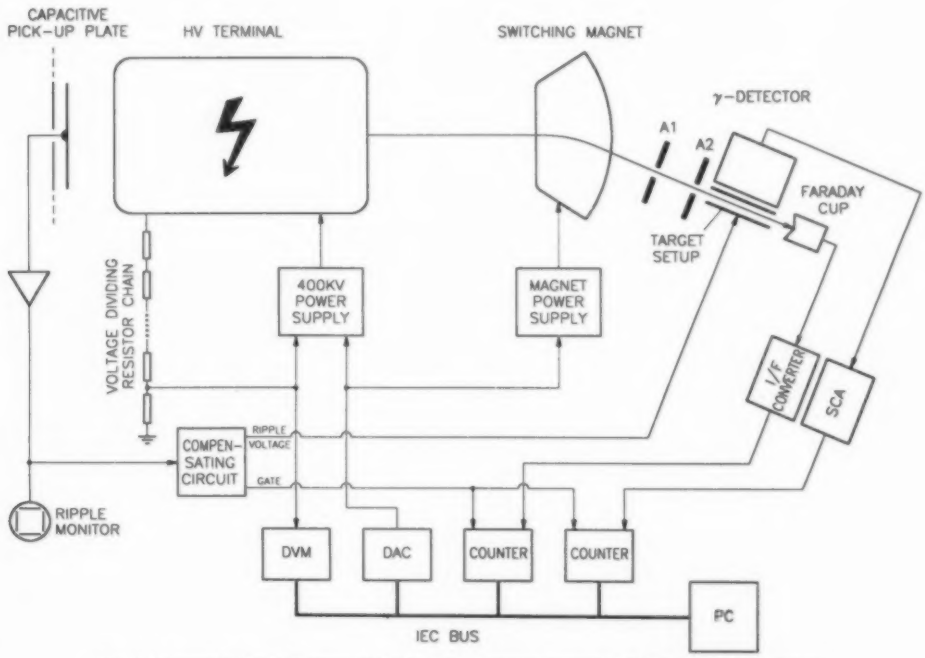

Fig. 1. Schematic block diagram of the ion-beam energy control and data acquisition system.

and applied via a ripple-compensating circuit to the target, thus compensating for the ripple-induced energy spread. The IEC bus gated off all data acquisition, when the HV ripple exceeded a given standard value (e.g. in the case of a spark).

3. Targets

For high-resolution investigations using narrow nuclear resonances, the quality of the target is extremely important. For this reason an UHV system has been developed which allows in-situ fabrication of extremely clean targets of variable thickness. The target temperature T can also be varied. This system [3] was used for studies of solid state effects. For other investigations, such as concurrent atomic and nuclear excitations, windowless gas and vapor targets of variable thickness and temperature have been developed [4–6]. These systems permitted the utilization of extremely thin targets (less than one monolayer thickness: $N_t < 1 \times 10^{15}$ atoms/cm^2), with significantly reduced Doppler broadening.

4. Concurrent atomic and nuclear excitations

For simplicity, consider a monoenergetic projectile with energy E_p incident on a target atom (monolayer target). The projectile excites a narrow nuclear resonance which is observed via the characteristic nuclear radiation. Since each projectile initiating a nuclear resonance must pass through the electron cloud of the target atom, it can with some probability excite or knock out an electron. This process results in echoes, or satellites, of the nuclear resonance at higher energies ($E_p > E_R$), corresponding to emission of K, L, M, ... electrons before (or at the same time as) the resonance is formed. The "replica" resonances are displaced in energy by the respective atomic excitation energies and have a $1/E^2$ tail describing the ionization into the continuum. The impact parameter b on the atomic scale is obviously very small and it is usually permissible to assume $b = 0$. The yield of the replica resonances relative to the total yield reflects the corresponding atomic excitation probabilities $P_{K,L,M}(b = 0)$. In real experiments, these structures are broadened due to contributions from the finite energy spread of the ion beam (ΔE_i) and from Doppler broadening of the target atoms (ΔE_D): $\Delta E_{eff} = (\Delta E_i^2 + \Delta E_D^2)^{1/2}$. Therefore one expects to observe an asymmetric high energy shoulder at $E_p \geq E_R$ which may still reflect the individual atomic excitations.

Fig. 2a shows data obtained at the $E_R = 272$ keV resonance in ^{21}Ne(p, γ)^{22}Na. One sees clearly an asymmetric high-energy shoulder superimposed with

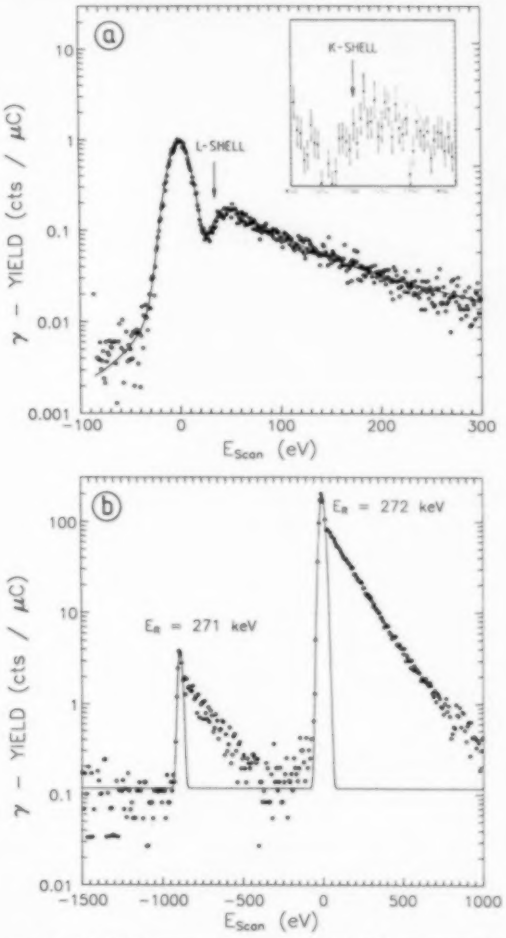

Fig. 2. (a) Yield curve of the $E_R = 272$ keV resonance in ^{21}Ne(p, γ)^{22}Na. The curve through the data points are fit results using Voigt profiles, with an $1/E^2$ dependence above the L- and K-shell thresholds. (b) Larger energy scan around the $E_R = 272$ keV resonance revealing a new resonance at $E_R = 271$ keV. The Voigt profiles (solid curves) have been calculated only in the region of the two resonances.

edges at $E_L = 34 \pm 3$ eV and $E_K = 1150 \pm 50$ eV, corresponding fairly well to $L_{2,3}$(2p)- and K(1s)-shell ionisation of the compound atom Na, respectively. The curve through the data points is a fit using Voigt profiles, with a $1/E^2$ dependence at energies above the L-shell edge. The deduced atomic excitation probabilities are $P_L(b = 0) = 0.42 \pm 0.04$ and $P_K(b = 0) = (1.0 \pm 0.5) \times 10^{-3}$, consistent with available atomic physics data [10]. Similar results were also obtained for other resonances in ^{21}Ne(p, γ)^{22}Na [4], as well as for

the $E_R = 309$ keV resonance in $^{23}Na(p, \gamma)^{24}Mg$ (here M-shell excitation could also be observed [5]) and for the $E_R = 184$ keV resonance in the α–α scattering [6].

Fig. 2b shows data indicating the existence of a nuclear doublet, at $E_R = 271$ and 272 keV, separated by $\Delta E_R = 889 \pm 5$ eV, with total widths of $\Gamma_R \leq 5$ and ≤ 3 eV, respectively. Previous investigations reported only one resonance with $\Gamma_R \leq 100$ eV. This example demonstrates the potential of high-resolution ion beams for nuclear physics research, i.e., resolution of potential doublets (or multiplets) and measurement of resonance widths in the range $\Gamma_R = 1$ to 100 eV, which are inaccessible (or difficult) with other techniques.

5. Molecular physics

The $E_R = 126$ keV resonance in $^{21}Ne(p, \gamma)^{22}Na$ was investigated using both a proton beam ($E_p = 126$ keV) and a H_2 molecular beam ($E_{H_2} = 252$ keV). The resulting yield curves (fig. 3) are drastically different: the very broad structure observed with the molecular beam probably arises from the Coulomb explosion of the molecule. Again, a high-resolution ion beam amplifies enormously the effects of this process. Such experiments and their analyses may contribute to solutions of some open questions in molecular physics.

6. Energy-loss (collision) spectrum

At the projectile energies of the present work ($E_p = 120$ to 310 keV), the energy loss of the projectiles in a target is dominated more than 99% by electronic energy-loss mechanisms [7]. The projectile (mass m_p) transfers an energy Q to the electrons (mass m_e). This energy transfer varies between Q_{min} (i.e., the binding energy of the electrons in the target) and $Q_{max} = 4E_p m_e/m_p$ (i.e., the classical recoil energy). It involves all atomic impact parameters b (both close and distant collisions) and is discrete, varying between Q_{min} and Q_{max} with probability $W(Q)$, which is called the collision spectrum. For free electrons, $W(Q)$ is described by the Thompson law

$$W(Q)\,dQ = \text{const}\,dQ/Q^2,$$

and the energy loss per unit path length, dE/dx, is

$$dE/dx = \text{const}\,\ln[Q_{max}/Q_{min}].$$

However, the electrons cannot be considered as free for all values of Q (at least not for Q near Q_{min}) and Q_{min} also can not be calculated reliably. For these reasons, one usually takes Q_{min} as an adjustable parameter to fit the observed dE/dx value [7]. A detailed knowledge of $W(Q)$ is not only important for the microscopic understanding of the stopping power, but also for the Lewis effect (see below).

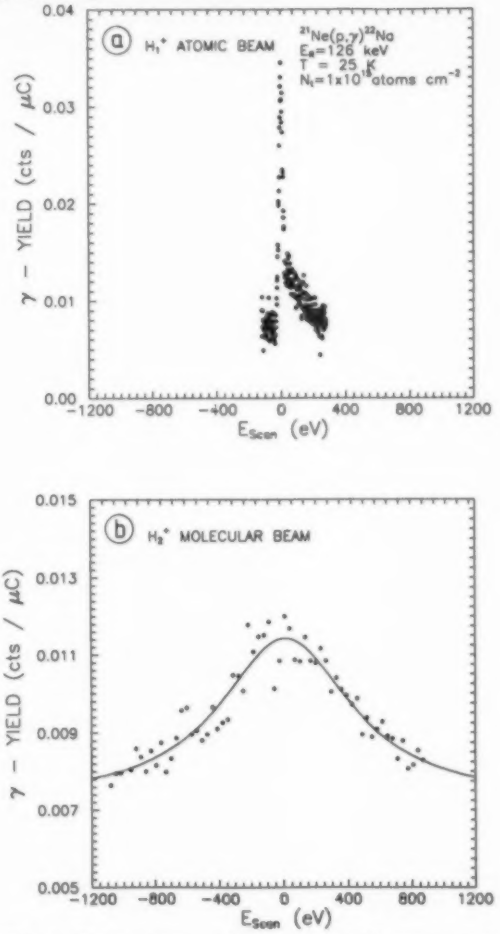

Fig. 3. Yield curves at the $E_R = 126$ keV resonance in $^{21}Ne(p, \gamma)^{22}Na$ obtained with (a) a proton beam and (b) a H_2 molecular beam.

Measurements of $W(Q)$ were performed in two ways: (i) comparison (subtraction) of yield curves obtained for a target of monolayer thickness with that obtained for a thicker target; and (ii) comparison of yield curves with and without energy loss of the beam, produced in a windowless gas cell filled with Neon gas prior to the monolayer target [4]. An illustrative example is shown in fig. 4. The subtracted yields have to be deconvoluted to correct for energy resolution of the ion beam and the Doppler broadening. One sees an energy-loss spectrum with a mean value of about 100 eV, consistent with the mean reported ionization value from dE/dx fitting [7,8].

7. The Lewis effect

The quantized character of the energy loss of energetic-charged particles penetrating through matter is manifested in the Lewis effect on the thick-target yield curves of narrow resonances. The standard signature is a peak (the Lewis peak) near E_R, followed by the usual plateau. Since the charged particles lose energy Q in discrete steps (between Q_{min} and Q_{max}), some particles with an energy $E_p > E_R$ will "jump over" the resonance and do not contribute to the yield; for projectiles incident at $E_p = E_R$, however, all have a chance to react. The thick-target yield is given by the expression

$$Y^*(E_p) = \int_0^{\Delta} Y(E_p - Q) W^*(Q)\, dQ,$$

where Δ is the target thickness (in units of eV) and $Y(E_p - Q)$ is the thin-target (monolayer) yield curve including information on Γ_R, ΔE_I, ΔE_D, and atomic excitations at impact parameter $b = 0$. The yield curve $Y^*(E_p)$ is thus the integrated convolution of $Y(E_p - Q)$ with the collision spectrum $W^*(Q)$, which can be derived from the single encounter collision spectrum $W(Q)$ [9]. Therefore, $W(Q)$ is the key quantity in the description of the Lewis effect.

The thick-target yield curve obtained at the $E_R = 272$ keV resonance in ^{21}Ne(p, γ)^{22}Na using a windowless gas target (fig. 5a) shows clearly the Lewis peak followed by a plateau with damped oscillations. Folding and integrating the measured functions $Y(E_p - Q)$ and $W(Q)$ (figs. 2a and 4), the resulting curve reproduces the data fairly well. For comparison, data are shown in fig. 5b at the $E_R = 309$ keV resonance in ^{23}Na(p, γ)^{24}Mg obtained with a solid target. The Lewis peak is also clearly visible but it is smaller in magnitude, mainly due to the existence of the lattice motion of the solid (zero point vibrations) leading to a value of $\Delta E_D = 41$ eV [3]. This Doppler width can in turn be used to extract a value for the Debye temperature of the phonon spectrum at the target surface. Thus, high-resolution ion beams can be used to measure solid-state properties.

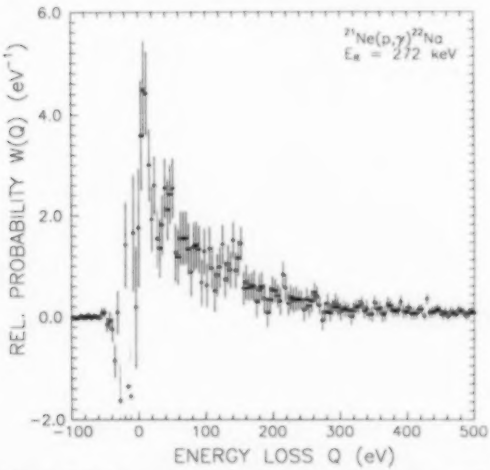

Fig. 4. Collision spectrum obtained from yield curves at the $E_R = 272$ keV resonance in ^{21}Ne(p, γ)^{22}Na.

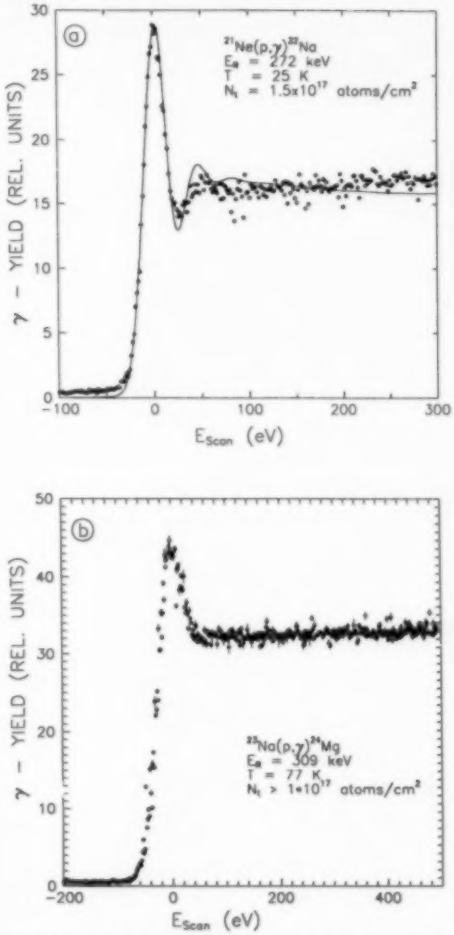

Fig. 5. (a) Thick-target yield curve for the $E_R = 272$ keV resonance in ^{21}Ne(p, γ)^{22}Na using a windowless gas target ($T = 25$ K). The calculated curve through the data points is based only on experimental data. (b) Thick-target yield curve for the $E_R = 309$ keV resonance in ^{23}Na(p, γ)^{24}Mg using a solid target ($T = 77$ K).

References

[1] E. Merzbacher, in: X-Ray and Atomic Inner-Shell Physics – 1982, ed. B. Crasemann (American Institute of Physics, New York, 1982) p. 1.

[2] S. Wustenbecker et al., Nucl. Instr. and Meth. A256 (1987) 9.
[3] S. Wustenbecker et al., Nucl. Instr. and Meth. A279 (1989) 448.
[4] W.H. Schulte et al., to be submitted.
[5] H. Ebbing, Thesis, Universität Bochum (1992).
[6] S. Wüstenbecker, Thesis, Universität Bochum (1992).
[7] J. Ziegler, J. Biersack, and U. Littmark, The Stopping Power and Range of Ions in Solids (Pergamon, New York, 1985).
[8] J.W. Butler, in: Ion Beam Surface Layer Analysis, Vol. 1, eds. O. Mayer, G. Linker and F. Käppeler (Plenum Press, New York, 1976).
[9] N. Meier, Diplomarbeit, Universität Münster (1989); I. Vickridge and G. Amsel, Nucl. Instr. and Meth. B45 (1990) 6.
[10] D.L. Matthews, C.F. Moore and D. Schneider, Phys. Lett. 48A (1974) 27.

Nuclear Instruments and Methods in Physics Research B66 (1992) 17–22
North-Holland

Nuclear Instruments & Methods in Physics Research
Section B

Nuclear microanalysis by means of 350 keV Van de Graaff accelerator

G.G. Ross, L. Leblanc, B. Terreault, J.F. Pageau and P.A. Gollier
INRS-Energie, Université du Québec, C.P. 1020, Varennes, Québec, Canada J3X 1S2

An inexpensive and quantitative method to depth profile hydrogen and helium isotopes in low-Z materials ($Z \leq 25$) by ERD $E \times B$ and, simultaneously, elements heavier than the substrate by RBS, has been developed. It uses a 350 keV He^+ beam, low-noise ion-implanted detectors and a filter built out of crossed magnetic and electric fields. Typically, with this setup, the depth resolution (which depends significantly on the materials) is ~4 nm at the surface degrading to ~15 nm at a depth of 100 nm, while the depth probed is ~100 nm for H and He and ~500 nm for heavier elements. The sensitivity is ~1 at.% for H and He, ≈0.1 at.% for other light elements (e.g.: C, N, O, etc.) and 1 ppm for heavier elements such as gold. It is also possible to use a 350 keV $^1H^+$ beam to simultaneously depth profile heavier elements by RBS and identify them by PIXE. These combined techniques are especially useful to detect elements with neighbouring Z, such as stainless steel components.

1. Introduction

Quantitative depth profiling of elements in materials has many applications in science. For example, to characterize thin film deposits, to perform archaeological dating, to identify the elements making up a compound and many others. Our interest concerns the plasma–wall interaction in thermonuclear devices. Quantitative depth profiling of H, He and heavier elements is an essential tool to study the erosion of the wall surrounding the plasma, the transport of eroded particles in the plasma "scrape-off layer" (SOL) and their codeposition (with H and/or He) onto other parts of the wall. Depth profiling of H and/or D is crucial for the understanding of gas recycling, wall inventories and irradiation effects to be expected in future machines. For example, the depth profiles of H and heavier elements trapped in samples exposed during a given time in the SOL of a tokamak, give information, on one hand, about the energy distribution and the fluxes of incident atoms and, on the other hand, allow one to establish the plasma composition in the SOL.

Ion beam analysis usually necessitates an expensive nuclear installation. Also, there are few techniques which can depth profile simultaneously H (or He) and heavier elements with sufficient sensitivity and depth resolution. To overcome these difficulties, we have developped and inexpensive, quantitative depth profiling technique which uses a 350 kV accelerator and low-noise ion-implanted detectors with a resolution (standard deviation) of 3 keV. The H and He isotopes are depth profiled by elastic recoil detection (ERD) induced by a $^4He^+$ or a $^3He^+$ beam. The backscattered He are energy-analyzed and depth profiles of heavier elements are also obtained from them. A 350 keV $^1H^+$ beam is used to simultaneously depth profile heavier elements by Rutherford backscattering (RBS) and identify them by means of proton induced X-ray emission (PIXE). These combined techniques are especially useful to detect elements with neighbouring Z. In this paper, our nuclear microanalysis installation will be described. Some examples will be presented and the advantages as well as the limitations of this setup will be discussed and compared to other techniques.

2. Brief description of the techniques used

2.1. ERD $E \times B$

H depth profiling by means of the ERD $E \times B$ method was developed several years ago [1] and has been extended to the depth profiling of D, T, ^3He and ^4He [2]. A schematic diagram of our setup is shown in fig. 1. A 350 keV $^4He^+$ or $^3He^+$ beam is incident at an angle of 65° with respect to the normal to the surface. The recoils R^+ (H^+, D^+, T^+, $^3He^+$ or $^4He^+$) are energy-analyzed at an angle of 45° to the beam. Scattered projectiles and other elastic recoils emerging in various charge states are eliminated by means of an appropriate adjustment of an achromatic filter using crossed magnetic and electric fields. The procedure to adjust this filter depends on the detected recoil and is described in detail elsewhere [2]. The R^+ spectrum is corrected for the undetected R^0 and/or R^- and/or R^{2+} fractions [3] and it is then deconvoluted into a depth profile with a computer code which uses the

0168-583X/92/$05.00 © 1992 – Elsevier Science Publishers B.V. All rights reserved

stopping powers of Andersen and Ziegler [4]. Typically, the sensitivity is ~0.5% for H isotopes and ~2% for He isotopes.

The 3 keV resolution (standard deviation) of the ion-implanted detector limits the depth resolution at the surface to ~4 nm. Deeper in, straggling and principally multiple scattering degrade it. The last has been evaluated approximately, by means of the LSS expression [5] for the screened Coulomb cross section. The details of the calculations were described earlier [6,7]. The depth resolution (standard deviation) δx (which depends on the material and on the detected recoil) at a depth x can be calculated by:

$$\delta^2 x = \delta^2 x_d + \delta x_{c1} x + \delta_{c2} x^2, \quad (1)$$

where $\delta^2 x_d$, the detector contribution, and δx_{c1} and δ_{c2}, the straggling and multiple scattering contribution, respectively, are given in tables of ref. [2] for different materials and for either ^{3}He or ^{4}He beam. Typically at 100 nm depth the resolution is 12 nm in Be and 20 nm in Si for H isotopes and, 16 nm in Be and 25 nm in Si for He isotopes. The ion-beam-induced desorption may also be another inaccuracy source [8]: depth profiles may be modified and the absolute quantity may be underestimated. It is recommended to use the correction curves given in ref. [8] and/or to use very low current beam (~5 nA) and to perform many analyses at different positions (if there is no spatial irregularity) limiting each analysis to a beam charge of ~1 μC.

2.2. RBS

RBS analysis is usually performed simultaneously with ERD $E \times B$ analysis. The backscattered He particles are detected at an angle $\phi = 157.5°$ to the beam. The grazing incident angle (65° to the normal to the surface) allows better sensitivity and depth resolution but limits the depth probes to ~250 nm. When the thickness of the analyzed layer is large, the atomic numbers Z of the probed elements have to be distant from each other in order to avoid overlapping of signals corresponding to each element. To discriminate overlapping signals, an incident angle of 10° is sometimes used and the depth probed is then increased to ~500 nm.

The raw data is deconvoluted into a depth profile with our own computer code which uses the stopping powers of Andersen and Ziegler [4]. This code can do many iterations using the preceding profile (with a more correct sample composition) to compute the true energy lost in the sample. The sensitivity increases with the atomic number Z. Typically, with a ^{4}He beam incident at 65° relative to the normal of the target, it is ~0.5% for C, ~0.2% for O, ~200 ppm for Si, ~100 ppm for Fe, ~30 ppm for Mo and ~10 ppm for Au. The depth resolution at the surface is also limited by the detector resolution (3 keV). It is typically ~5 nm in C, ~3.3 nm in Si and ~1.5 nm in Mo and Au. Deeper in, multiple scattering and principally strag-

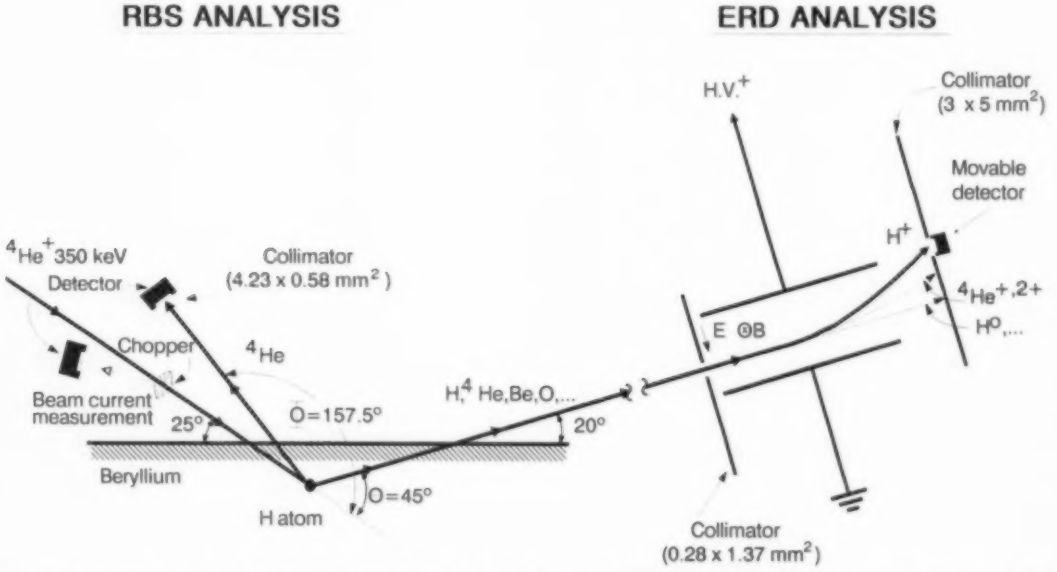

Fig. 1. Schematic diagram of the combined ERD $E \times B$ and RBS methods showing the ERD and RBS interaction geometries, the $E \times B$ filter, collimator positioning, the detectors and the beam current measurement.

Table 1
Values of $\delta^2 x_d$, δx_{c1} and δ_{c2} for the depth-resolution of profiles obtained by RBS (350 keV ^{4}He beam) calculated with the equation $\delta^2 x = \delta^2 x_d + \delta x_{c1} x + \delta_{c2} x^2$

Material	$\delta^2 x_d$ [nm^2]	δx_{c1} [nm]	δ_{c2}
Be	58.98	0.422	45.3×10^{-4}
C	22.18	0.233	22.7×10^{-4}
Al	11.09	0.197	8.68×10^{-4}
Si	10.50	0.159	9.51×10^{-4}
Cu	3.46	0.255	10.5×10^{-4}
Mo	1.88	0.136	13.3×10^{-4}
Au	2.16	0.292	29.94×10^{-4}

gling degrade it. For example, at 250 nm depth, the resolution is ~ 15 nm in C, ~ 11 nm in Si and Mo and ~ 16 nm in Au. Depth resolution δx as a function of the depth x can be calculated with equation 1 [7]. Values of $\delta^2 x_d$, δx_{c1} and δ_{c2} are given in table 1 for some typical elements. It is interesting to note that for low-Z materials such as Be and C, multiple scattering affects significantly the depth resolution while for high-Z materials such as Mo and Au, it is negligible. This is due to the large difference in energy of the backscattered ^{4}He. Detailed description of RBS analysis is available in the literature.

2.3. PIXE

PIXE measurements are done by means of a 350 keV $^1H^+$ beam incident at right angle and we usually perform RBS analysis simultaneously. PIXE is used to identify elements with atomic numbers $14 < Z < 35$ in matrices of similar or higher Z, by detecting the K-shell X-rays (it is possible to identify higher-Z elements by detecting L-shell X-rays). It is also useful to identify elements with neighbouring Z, such as stainless steel components or to discriminate overlapping RBS signals. Although feasible [9], we have not done any depth profiling by means of PIXE up to now. The computer code GUPIX [9] is used to deconvolute the raw data. Typically, the sensitivity is $\sim 2 \times 10^{14}$ S/cm^2, $\sim 1 \times 10^{15}$ Fe/cm^2 and $\sim 1 \times 10^{16}$ Ge/cm^2 with K-shell X-rays. One can find good discussions on the use of a 350 keV H beam for PIXE analysis in the literature (e.g., ref. [10]).

3. Experimental setup

Our apparatus is based on a 400 kV Van de Graaff accelerator (from HVEC), with several home-made improvements. The beam line consists of an Einzel lens, X–Y deflectors, a quadrupole doublet lens, a first set of cooled collimators located at a focal point, a 90° analyzing magnet and a second set of collimators. These two last elements insure an energy beam stability of ~ 2 keV. The beam current is measured by a Faraday cup and, during analysis, by the backscattering yield from a rotating bicycle wheel-like tungsten target. Typically, on the target the beam size is 1 mm^2. The whole beam line is built out of ultrahigh-vacuum components and is pumped by a 360 l/s and two 50 l/s turbomolecular pumps.

The 60 cm diameter stainless steel analysis chamber is pumped by a 450 l/s turbomolecular pump. A liquid-nitrogen-cooled plate is used to reduce the water vapour pressure. The base pressure is $\sim 5 \times 10^{-9}$ mbar while in operation the typical pressure is $\sim 2 \times 10^{-8}$ mbar. Referring to fig. 1, the $E \times B$ filter ($B = 1$ kG, E variable from 0 to -5 kV/cm) and the detector are in a separate vacuum chamber, isolated by a gate valve, which is evacuated separately by a 80 l/s turbomolecular pump. A 0.28×1.37 mm^2 collimator is located at the entrance of the $E \times B$ filter, at a distance of 475 mm (imposed on us by the dimensions of the vacuum chamber) from the target, defining a solid angle of 1.70×10^{-6} sr (a shorter distance would increase the solid angle and so, the sensitivity). The detector is movable from outside and a 3 mm wide collimator is located just in front of it. Another movable half-collimator is used to reduce, when necessary, the detector aperture.

The detector for RBS analysis is also located in a separate vacuum chamber, isolated by a gate valve, and evacuated separately by a 50 l/s turbomolecular pump. A 4.23×0.58 mm^2 collimator is located in front of this detector, at a distance of 426 mm from the target, defining a solid angle of 1.35×10^{-5} sr.

The recoils and the backscattered particles are energy-analyzed by means of uncooled low-noise thin-window ion-implanted silicon detectors (from Enertec–Schlumberger) which are exposed every night to dry air at 1 bar to avoid increase of their reverse current. A way to reduce the reverse current is to increase the bias potential (from ~ 60 to ~ 110 V) for several hours.

The X-rays for PIXE measurements are detected in a Si(Li) detector at an angle $\eta = 135°$. The detector is located behind a 25 μm Be window (blocking the scattered ions) at a distance of 385 mm from the sample, defining a solid angle of 5.30×10^{-4} sr. In this case also, the sensitivity is strongly limited by the dimension of our setup. The solid angle could be increased by a factor of ten (and even more) and, consequently the sensitivity would be improved.

4. Examples

Examples of depth profiles of H and He isotopes implanted in materials and analyzed by means of the

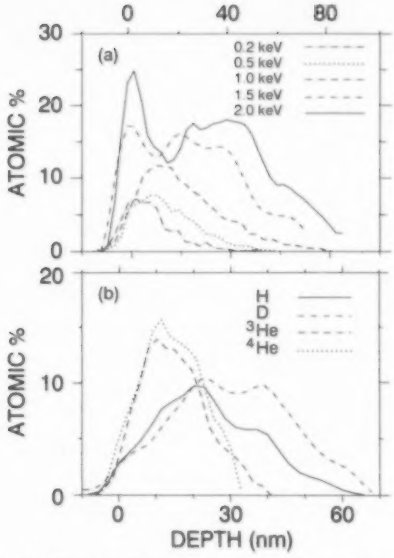

Fig. 2. (a) Depth profiles of H implanted at different low energies in Si as measured by the ERD $E \times B$ method. (b) Depth profiles of H, D, ^{3}He and ^{4}He implanted at 1 keV in Be (at different concentrations), as measured by the ERD $E \times B$ method.

ERD E × B method, are shown in fig. 2. All the profiles are resolution-broadened. In Fig. 2a, H was implanted at different low energies (0.2, 0.5, 1.0, 1.5 and 2.0 keV) in ⟨100⟩ oriented Si. Implantations, were performed at an angle of 22.5° to avoid channeling. A large surface H peak is present on the profiles of H implanted at 1.5 and 2.0 keV because these profiles were done under a poor vacuum without using any liquid-nitrogen-cooled plate. This allows us to check that the widths of these surface H peaks are consistent with the calculated resolution at the surface. The profiles of H implanted at lower energies were done with the setup as described in section 2 and the H surface peak measured on a virgin sample corresponded to ~ 2 at.%. One can easily subtract it.

The goal of these implantations was to measure mean ranges and variances of H implanted into Si. It is shown that the depth resolution is sufficient to perform these measurements at a energy as low as 200 eV (and even lower) which gives an excellent tool to do such a study. As expected, mean ranges and variances increase with the implantation energy. The values are in fair agreement with the code TRIM-90 [11]. More detailed results and discussion on this subject will be published in a future paper.

Fig. 2b shows depth profiles of H, D, ^{3}He and ^{4}He implanted at 1 keV in Be but at different doses. As expected, mean ranges and profile widths are higher, one the one hand, in H isotopes than in He isotopes and, on the other hand, in D than in H as well as in ^{4}He than in ^{3}He. The measured mean ranges and variances are in fair agreement with Andersen–Ziegler's compilation. However, contrary to results of H implanted in Si, mean ranged and variances of H implanted in Be disagree with TRIM-90 [11] computations, as already reported in a preceding paper [3] for the measurements of D-projected ranges and variances in Be and C.

Depth profiles of Al samples with 100 nm Cu deposits and with 100 nm Au deposits are shown in fig. 3a and 3b, respectively. These profiles were obtained by the RBS of 350 keV $^1H^+$ incident at right angles and simultaneously, PIXE measurement was performed. These profiles were done to calibrate and adjust the PIXE measurement (not shown here) for different deposit layer thicknesses. The flatness of the Al profiles indicates that one can measure depth profiles up to a depth of ~ 1 μm.

The two last examples are from the analysis of samples exposed to plasma discharges in TdeV (Tokamak de Varennes). Fig. 4 shows depth profiles of H and impurities deposited and/or implanted on/in a Be sample exposed to ≈ 1500 plasma discharges of ≈ 700 ms each. The sample was fixed at the position of the wall surrounding the plasma. So, it represents a coupon of the wall and gives many information on the plasma–wall interaction. As shown in fig. 4, C, F, O and "Ni", in fact Ni ≈ 50%, Cr ≈ 28% and Fe ≈ 22%, as measured by Auger electron spectroscopy [12], as well as 8×10^{14} Al/cm^2 and some traces of Mo were

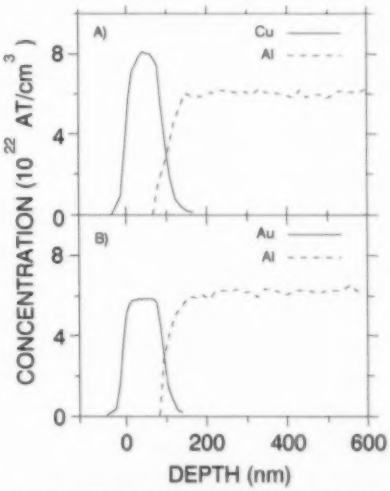

Fig. 3. Depth profiles of Al samples with (a) 100 nm Cu deposits and with (b) 100 nm Au deposits, as measured by RBS of 350 keV $^1H^+$ beam.

detected on the collected probe. C, O and Ni are expected impurities eroded from the graphite limiters and/or the neutralization plates, from water vapour and oxides, and from the Inconel and stainless steel walls surrounding the plasma, respectively. These impurities travelled in the plasma edge to be deposited elsewhere onto the wall. However, the presence of F is more surprising. It was also detected by AES [12]. There are some probable F sources such as the ceramics widely used in our machine to isolate some electric components, vacuum greases and Viton seals. It is also known that X-rays radiated from the plasma can remove fluorine from these materials.

H was also detected in the collector probe. However, the H profile is different from those of impurities. This is due to the fact that while some H was codeposited at low incident energy along with the impurities, additionnal H came from the plasma core by charge exchange, with an energy equivalent to the ion temperature, and were thus deeply implanted in our sample. Using the H profile width and subtracting the codeposition contribution, an ion temperature of ~ 540 eV [13,14] was estimated.

Sometimes, the deposits are too thick to be measured by means of RBS. In such cases, the impurity concentration was obtained by PIXE. An example is shown in fig. 5. Coupon of Be was exposed ~ 5 mm behind an outboard graphite limiter, facing the plasma, during 112 plasma discharges [14]. Concentrations of 1.3×10^{14} Ti/cm^2, 3.1×10^{15} Cr/cm^2, 1.3×10^{16} Fe/cm^2 and 2.8×10^{15} Ni/cm^2, as well as some traces of K, S, Si and Al were measured by PIXE. When this experiment was performed, the plasma was surrounded

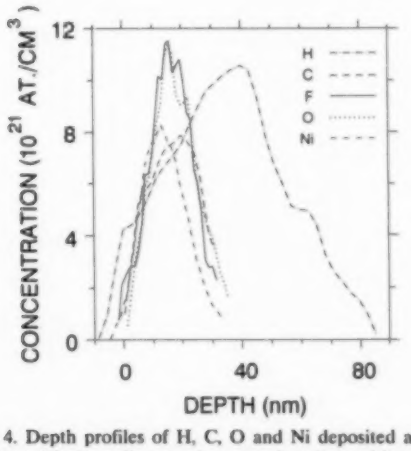

Fig. 4. Depth profiles of H, C, O and Ni deposited and/or implanted in/on a Be sample exposed at the position of the wall to ~ 1500 plasma discharges of ~ 700 ms each in TdeV. These profiles were obtained by the combined ERD $E \times B$ (for H) and RBS methods.

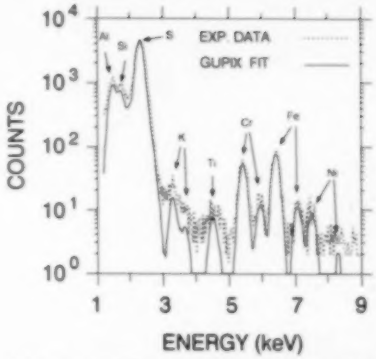

Fig. 5. PIXE measurement of a Be sample exposed to plasma discharges in TdeV at a distance of ~ 5 mm from the plasma.

by two stainless steel guard limiters and consequently, the Fe concentration was higher. Also, a TiC test limiter was used for some discharges and it is the Ti source [14].

5. Discussion and conclusion

The possibility of doing depth profiling of H, He and heavier elements simultaneously and routinely is a great advantage of our combined ERD $E \times B$ and RBS techniques. These techniques are inexpensive, quantitative and accurate. They have excellent depth resolution, good sensitivity and do not necessitate an expensive nuclear installation. RBS and PIXE analyses by means of 350 kV accelerators were used in many other laboratories (e.g., ref. [9,10]) before we installed them. They complement the ERD $E \times B$ method allowing us to depth profile and/or quantify heavier elements included or implanted in materials. However, the ERD $E \times B$ method is particularly attractive because it compares favourably with many other more expensive techniques by its depth resolution, and the possibility of depth profiling quantitatively all the H and He isotopes. For example, ERD with 2 MeV ^{4}He and 30 MeV ^{35}Cl have a depth resolution ~ 25 nm and 8 nm, respectively. The ^{1}H(^{15}N, $\alpha\gamma$)^{12}C technique has an excellent depth resolution of ~ 2 nm but it requires higher energy and it cannot be used for depth profiling other elements. The D(^{3}He, α)p is widely used because it needs only a modest accelerator; however, it can be used only for D (and ^{3}He) profiling and its depth resolution is limited to ~ 15 nm.

The ERD $E \times B$ technique has also some weaknesses. The depth probed is limited to ~ 100 nm, the depth resolution degrades with depth and depth profiling is limited to low-Z materials. Also, the sensitivity of 0.5 to 2% could be improved by decreasing the dis-

tance between the target and the collimator at the entrance of the $E \times B$ filter [2]. The surface of the sample has to be flat when grazing angles are used. The roughness of the surface affects the depth resolution and the sensitivity because the relationship between the path length of the beam and detected particles and the depth of interaction is strongly modified. Also the measurement may be not quantitative because the elements in the shadow of the beam remain undetected.

Finally, an attractive possibility would be to perform all the three methods (ERD $E \times B$, RBS and PIXE) simultaneously. The difficulty is due to the low cross section of X-rays production by a 350 keV He beam.

Acknowledgements

The authors wish to thank G. Gobeil for his excellent operation of the accelerator and the National Science and Engineering Research Council for financial support.

References

[1] G.G. Ross, B. Terreault, G. Gobeil, G. Able, C. Boucher and G. Veilleux, J. Nucl. Mater. 128/129 (1984) 730.

[2] G.G. Ross and L. Leblanc, Depth profiling of hydrogen and helium isotopes by means of the ERD $E \times B$ technique, Nucl. Instr. and Meth., in press.

[3] G.G. Ross and B. Terreault, Nucl. Instr. and Meth. B15 (1986) 146;
G.G. Ross and L. Leblanc, Nucl. Instr. and Meth. B48 (1990) 134.

[4] H.H. Andersen and J.F. Ziegler, Hydrogen Stopping Powers and Ranges in All Elements (Pergamon, New York, 1977);
J.F. Ziegler, Helium Stopping Powers and Ranges in All Elements (Pergamon, New York, 1977).

[5] J. Linhard, V. Nielsen and M. Scharff, K. Dan. Vidensk. Selsk. Mat. Fys. Medd. 36 (1968) no. 10;
J. Lindhard, M. Scharff and H.E. Schiott, ibid. 33 (1963) no. 14.

[6] G.G. Ross and B. Terreault, Nucl. Instr. and Meth. B15 (1986) 61.

[7] L. Leblanc, G.G. Ross and B. Terreault, internal report, NRG-609, in French.

[8] G.G. Ross and I. Richard, Influence of the ion beam induced desorption on the quantitative depth profiling of hydrogen and helium isotopes in a variety of materials, Proc. 10th Int. Conf. on Ion Beam Analysis, 1–5 July 1991, Eindhoven, The Netherlands, Nucl. Instr. and Meth. B64 (1992).

[9] J.A. Maxwell, J.L. Campbell and W.J. Teesdale, Nucl. Instr. and Meth. B43 (1989) 218.

[10] G. Linder, Nucl. Instr. and Meth. B3 (1984) 130;
G. Brunner and V. Rössiger, Nucl. Instr. and Meth. B3 (1984) 275.

[11] J.P. Biersack and L.G. Haggmark, Nucl. Instr. and Meth. 174 (1980) 257.

[12] R.W. Paynter, private communication.

[13] R. Becerra-Acevedo and B. Terreault, Nucl. Instr. and Meth. B28 (1987)1.

[14] G.G. Ross, R.W. Paynter and D. Michaud, J. Nucl. Mater. 176/177 (1990) 962.

Nuclear Instruments and Methods in Physics Research B66 (1992) 23–30
North-Holland

Nuclear Instruments & Methods in Physics Research
Section B

Characterisation of thin layers in processed silicon

L.G. Earwaker, M.C. Briggs and M.I. Nasir
School of Physics and Space Research, The University of Birmingham, Birmingham B15 2TT, UK

J.P.G. Farr
School of Metallurgy and Materials, The University of Birmingham, Birmingham B15 2TT, UK

J.M. Keen
Defence Research Agency, Electronics Division, RSRE, Great Malvern, Worcs, UK

Rutherford backscattering spectrometry (RBS), elastic recoil detection analysis (ERDA) and nuclear reaction analysis (NRA), are routinely used in the analysis of electronic materials. Application of these techniques together provides both light and heavy elemental concentration profiles to a depth of several microns. Examples are given of the analysis of layers of CVD produced Si_3N_4 and metallised porous silicon using RBS, ERDA and (d, p)-NRA, with elemental depth profiles being extracted to a depth of about 5 μm. Computer simulations of (d, p) spectra from carbon, nitrogen and oxygen, illustrating the expected proton energy distributions, are also presented.

1. Introduction

Electronic devices constructed on optically flat silicon wafers are built up of thin layers which have received many processing steps to produce different materials such as doped silicon, oxides, nitrides, metals and silicides. In general, the thickness and composition of a layer is well defined by the materials used to produce it and the overall aim for the device dimensions, usually of the order of microns. All these features make silicon structures ideal candidates for analysis by nuclear reaction analysis (NRA), Rutherford backscattering spectrometry (RBS) and elastic recoil detection analysis (ERDA), where elemental depth profiling is possible with minimal interference to the layers themselves [1]. This paper describes the ways in which these techniques have been applied to characterise silicon wafers processed to produce the above surface layers. Probably the most used analysis technique in semiconductor characterisation is RBS because silicon is a relatively light element, and therefore, the backscattered signal from implanted heavy dopant elements or metallised sections stand out clearly above the silicon signal. In many materials, however, the light element content is also important and in these cases NRA is often used as it is largely sensitive to light elements, particularly in the presence of heavy elements. Many of the processing steps leave hydrogen in the new material. Therefore, it is important to have a clear idea of its distribution and ERDA is used to provide rapid depth profiles of hydrogen isotopes in the near surface regions.

One of the major advantages of RBS is that the interaction cross section follows the well known Rutherford analytical form (with some exceptions for light elements at high energies). It is therefore possible to calculate expected yields and hence arrive at elemental number densities in samples. Interpretation of spectra is relatively straightforward, providing the full range of elements present in the sample is known. RBS is best used to profile the distributions of trace concentrations of heavy elements in matrices composed of light elements. The depth range attainable with the conventional 2 MeV alpha scattering experiment is limited to roughly the top micron depending on the material. However, the depth resolution is reasonably good with around 10 nm being routinely achievable in the near surface region.

Information can often be obtained to a much greater depth using NRA where nuclear reactions with a positive Q value can give products with quite high energy and hence penetration. The penalty paid for this penetrability is a poor depth resolution when compared with RBS. Unfortunately, NRA cross sections are usually not well behaved, often varying markedly with reaction energy, and are usually poorly quantified. The main virtue of NRA is that often the technique is totally free from interference from reactions with high

0168-583X/92/$05.00 © 1992 – Elsevier Science Publishers B.V. All rights reserved

atomic number nuclei where the Coulomb barrier inhibits reactions. Hence NRA is ideal for profiling the elemental distributions that RBS is particularly insensitive to, such as small concentrations of light elements distributed throughout matrices composed of heavy elements.

Kinematically it is impossible for conventional alpha RBS to detect directly the presence of hydrogen isotopes. However, if hydrogen is present in a matrix it is possible to profile its depth distribution using the ERDA technique. Here the alpha beam is introduced to the target at a glancing angle and the forwardly scattered hydrogen recoil is detected. The glancing geometry implies that the absolute depth that can be analysed with a 2.5 MeV beam is limited to about 500 nm and because of straggling in the stopper foil placed in front of the detector the depth resolution is limited to approximately 50 nm. Nevertheless, ERDA provide a fast nondestructive method for determining the hydrogen concentration in the near surface of materials.

When RBS, ERDA and NRA are used together, elemental depth profiles can be constructed over a depth of many microns with good depth resolution near the surface, where compositions often change rapidly. NRA, RBS and ERDA measure specifically the number of atoms present in layers of materials. It is not possible without further information to convert this measurement into a linear thickness, as it is well accepted that the density of a thin layer is often different from that of the bulk material [2]. Having generated a composite depth profile, therefore, it is necessary to provide additional information, from other analysis techniques, to establish the absolute linear thickness. In many such techniques, depth profiles are generated by sputtering away layers of the sample, raw data is provided as a sputter time, and absolute depth scales are provided from visual or mechanical measurements on the analysis "crater".

2. (d, p) analysis of carbon, nitrogen and oxygen

Carbon, nitrogen and oxygen depth profiles in processed silicon are routinely analysed in our laboratory using the (d, p) nuclear reaction. The ground state reaction for nitrogen has a very high Q value which allows this proton group to be clearly observable in the presence of most competing reactions. However, both carbon and oxygen have relatively low Q values which cause problems when the analysis of silicon based materials is attempted because silicon produces a large number of proton groups, some with relatively high Q values. Table 1 shows the deuteron induced nuclear reactions used to analyse carbon, nitrogen and oxygen, their Q values, and their product energy, for the detection geometry of 150° and incident deuteron beam energy of 1.1 MeV, before and after passing through a 12 μm Al foil. In all cases the cross sections vary considerably with energy. For the case of thin layer analyses it is sufficient to design the experiment so that a proton group is produced at an incident deuteron energy where the cross section is relatively flat. For thick layer analyses (several microns) a low deuteron energy is chosen (1.1 MeV) where most of the silicon reactions are suppressed by the Coulomb barrier. Use is then made of the published cross sections [3] to simulate (d, p) spectra and extract depth profiles from fits to experimental data. In general, absolute cross section data is known to be unreliable. However, cross section shapes tend to be reasonably reliable and it is therefore usually sufficient to normalise cross sections so that good fits to spectra from the standard materials are obtained and to use these values in the analysis of unknown samples.

Table 1
A compliation of the nuclear reactions used in these analyses, their Q values, and the reaction product energy, determined at 150°, for incident 1.1 MeV deuterons before and after passing through a 12 μm Al absorber foil

Reaction	Q value [MeV]	Reaction product energy [MeV]	Reaction product energy after stopper foil [MeV]
Carbon			
$^{12}C(d, p_0)^{13}C$	2.722	3.065	2.65
Nitrogen			
$^{14}N(d, p_0)^{15}N$	8.609	8.485	8.40
$^{14}N(d, p_{1,2})^{15}N$	3.319	3.619	3.48
$^{14}N(d, p_3)^{15}N$	2.281	2.761	2.45
$^{14}N(d, p_4)^{15}N$	1.449	2.020	1.66
$^{14}N(d, p_5)^{15}N$	1.229	1.887	1.47
$^{14}N(d, p_6)^{15}N$	1.039	1.658	1.22
$^{14}N(d, \alpha_0)^{12}C$	13.574	9.851	8.55
$^{14}N(d, \alpha_1)^{12}C$	9.144	6.705	4.76
Oxygen			
$^{16}O(d, p_0)^{17}O$	1.917	2.500	2.15
$^{16}O(d, p_1)^{17}O$	1.046	1.715	1.29

A simulation code, written in this laboratory by J.C.B. Simpson [4], is used to simulate RBS, ERDA and NRA. A proposed target surface structure, consisting of layer thicknesses and elemental number densities, is supplied to the routine. Simulations are then compared with experimental data using residual differences and the proposed layer structure altered until a good fit is obtained. A facility is also available which allows slowly varying concentrations to be simulated by specifying a layer thickness and the elemental number densities at the front and back of a given layer. The program then makes a linear interpolation of the concentration values within this layer. Cross sections taken

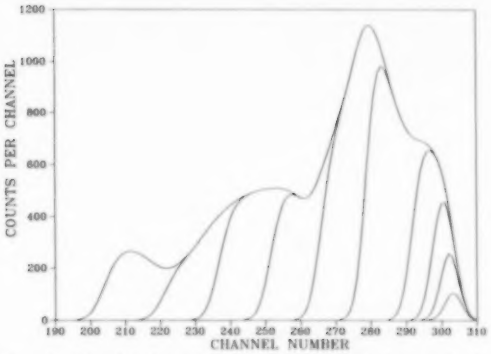

Fig. 1. Simulated proton energy distributions of the $^{16}O(d, p_0)^{17}O$ group for the 1.1 MeV deuteron bombardment of thin SiO_2 layers. Spectra correspond to layer thicknesses of 0.1, 0.25, 0.5, 1.0, 2.0, 3.0, 4.0, 5.0, 6.0 and 7.0 μm, measured at a laboratory angle of 150° and with a 12 μm Al absorber foil placed over the detector. The energy width of each channel is 7.395 keV.

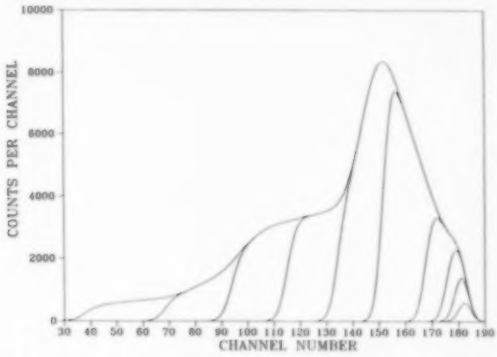

Fig. 2. Simulated proton energy distributions of the $^{16}O(d, p_1)^{17}O$ group for the 1.1 MeV deuteron bombardment of thin SiO_2 layers. Spectra correspond to layer thicknesses of 0.1, 0.25, 0.5, 1.0, 2.0, 3.0, 4.0, 5.0, 6.0 and 7.0 μm, measured at a laboratory angle of 150° and with a 12 μm Al absorber foil placed over the detector. The energy width of each channel is 7.395 keV.

from the compilation of Jarjis [3] are presented to the program in tabular form. Unfortunately this compilation is a University of Manchester internal report, which is out of print, and is not now generally available. It is useful therefore to quote here the references used by Jarjis. Cross sections for the $^{12}C(d, p_0)$ reaction were taken from Debras and Deconninck [5], T.W. Bonner et al. [6], Cords et al. [7], Kashy et al. [8], McEllistrem et al. [9], and Katman et al. [10]. Cross sections for the $^{14}N(d, p)$ (p_0 to p_7) and $^{14}N(d, \alpha)$ (α_0 and α_1) reactions were taken from Amsel and David [11], Gomes-Porto et al. [12] and Debras and Deconninck [5]. Cross sections for the $^{16}O(d, p)$ (p_0 and p_1) were taken from Debras and Deconninck [5], Seiler et al. [13], Dietzsch et al. [14] and Amsel and Samuel [15].

Examples of simulated spectra from the (d, p) reactions from oxygen in normal density SiO_2 layers of various thickness have been produced and the results for the p_0 and p_1 groups are shown in figs. 1 and 2. An incident beam energy of 1.1 MeV was assumed. In real analyses backscattered deuterons are not allowed to enter the detector because the high count rate distorts the spectra and their signal would mask low energy proton groups. A 12 μm Al absorber foils is therefore placed in front of the detector. The protons contributing to the signal in these simulations are assumed to have passed through such an absorber foil. The shape of the proton energy distributions follows closely the differential cross sections and it is clear that layers up to about 5 μm thick can be satisfactorily measured. A similar set of curves is shown in fig. 3 for the $^{12}C(d, p_0)$ reaction. Here it has been assumed that the carbon is uniformly distributed throughout an SiO_2 layer at a 1% atomic density. The reason for choosing this composition is that it is similar to the small carbon depth distributions found in the analysis of processed silicon layers. The maximum analysis depth for carbon in SiO_2 is about 4 μm. Analysis of nitrogen using the $^{14}N(d, p)$ reaction is a rather more complex situation because many more proton groups are available (fig. 4). The p_0 group has a very high energy and therefore suffers very little interference from competing reactions. However, the cross section is not well known, and because of the high energy the depth resolution is poor. The p_{1+2} groups are much lower in energy and are often clear of competing reactions. In this case two proton groups,

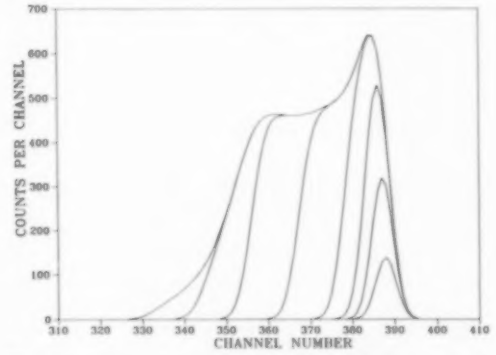

Fig. 3. Simulated proton energy distributions of the $^{12}C(d, p_0)^{13}C$ group for the 1.1 MeV deuteron bombardment of thin SiO_2 layers containing 1% atomic ^{12}C nuclei. Spectra correspond to layer thicknesses of 0.1, 0.25, 0.5, 1.0, 2.0, 3.0, 4.0 and 5.0 μm, measured at a laboratory angle of 150° and with a 12 μm Al absorber foil placed over the detector. The energy width of each channel is 7.395 keV.

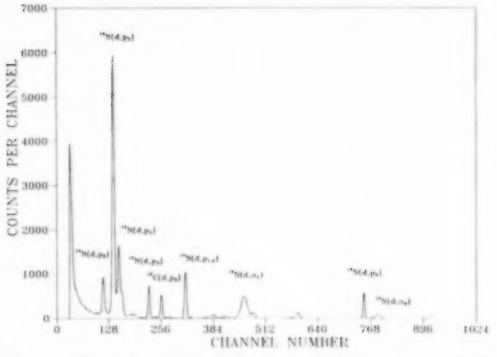

Fig. 4. The charged particle spectrum from the 1.1 MeV deuteron bombardment of a thin layer of Si_3N_4 measured at a laboratory angle of 150°. Peaks arising from nitrogen (and carbon) are labelled. Other peaks arise from silicon. The energy width of each channel is 10.75 keV.

which are too close in energy to be easily resolved, contribute to the yield. However, it is perfectly possible to use a composite cross section in simulating the proton energy distribution. Fig. 5 shows the expected spectrum shape for the $p_{1,2}$ groups for various thickness Si_3N_4 layers. In this case depth profiling down to about 7 μm is possible. The $^{14}N(d, \alpha)$ groups also offer the possibility of depth profiling but unfortunately the absorber foil before the detector tends to degrade the higher resolution potentially available with alpha particles.

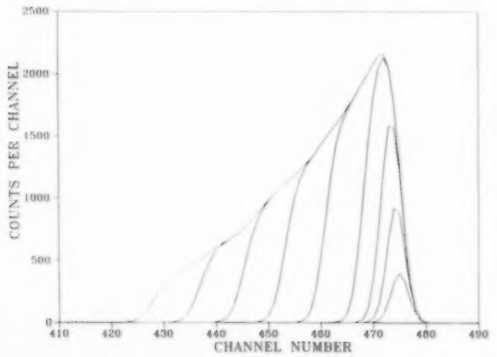

Fig. 5. Simulated proton energy distributions of the $^{14}N(d, p_{1,2})^{15}N$ group for the 1.1 MeV deuteron bombardment of thin Si_3N_4 layers. Spectra correspond to layer thicknesses of 0.1, 0.25, 0.5, 1.0, 2.0, 3.0, 4.0, 5.0, and 6.0 μm, measured at a laboratory angle of 150° and with a 12 μm Al absorber foil placed over the detector. The energy width of each channel is 7.395 keV.

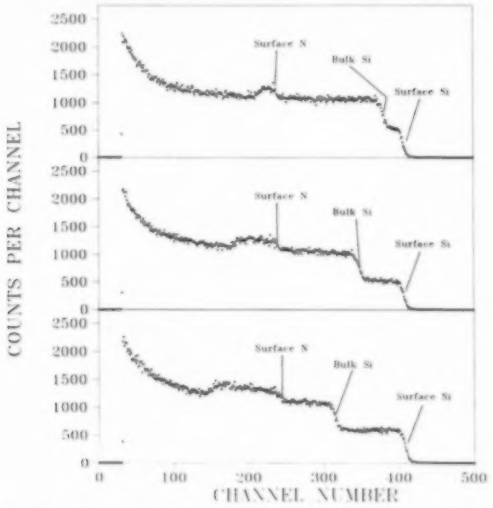

Fig. 6. RBS spectra, measured at 150° with 2 MeV incident He ions, for Si_3N_4 films of thickness 106, 233 and 339 μm on a silicon substrate. The energy width of each channel is 3.685 keV.

3. CVD-produced Si_3N_4 layers

Silicon nitride is used as an insulating and protective layer on silicon and has many applications in

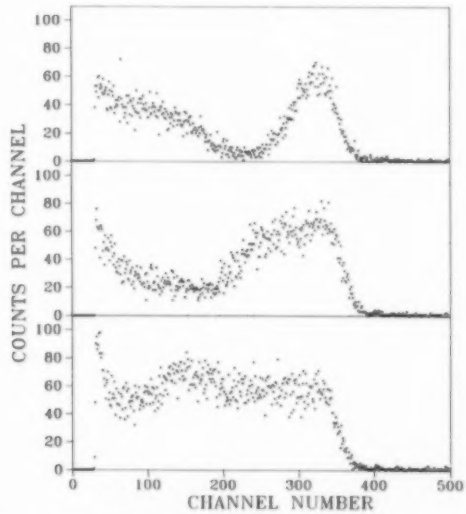

Fig. 7. ERDA hydrogen recoil spectra from Si_3N_4 films of thickness 106, 233 and 339 nm on a silicon substrate. A 2.5 MeV He ion beam was incident on a target placed at 15° to the beam with recoil protons detected at 30°. The energy width of each channel is 1.65 keV.

silicon processing. One route to producing thin nitride layers is low-pressure chemical vapour deposition (LPCVD) where ammonia is reacted with SiH_2Cl_2 to produce a layer of Si_3N_4, which also contains significant levels of hydrogen. A series of nitride layers with thicknesses in the range 100–400 nm and produced in two different nitriding kits has been analysed by NRA, RBS and ERDA. RBS analysis with 2 MeV He ions gave a measure of the uniformity and thickness of the nitride layers and showed that the chlorine content was negligible. Residual hydrogen was measured using ERDA with 2.5 MeV He ions and was found to be uniformly distributed throughout the layer at 16% atomic. Typical RBS spectra, measured at 150° to the incident beam, are shown in fig. 6 and elastic recoil proton spectra, detected at 30° to the incident beam and measured with the sample at an angle of 15° to the incident beam, are shown in fig. 7. The shapes of these spectra are consistant with uniform composition layers of silicon nitride containing hydrogen. Fits to the RBS data, made using tabulated nitrogen and silicon stopping powers were used to derive the nitrogen areal number density and a linear thickness was calculated assuming a bulk nitride density of 3400 $kg\,m^{-3}$ [16]. The average result for four samples in each of the three thickness groups is shown in column 2 of table 2. Alternative measurements were made of layer thickness using the reflected intensity of light with wavelength in the range 400–800 nm ("Nanospec") and the scattering of polarised light ("Ellipsometer") and the results of these measurements are tabulated in column 1. The difference is rather large and an explanation was sought in the accuracy of the density assumed in the RBS calculations. Assuming a uniform nitride cover over the Si wafers, a layer density was calculated from a measure of the weight gained during processing and the results shown in column 3. A value significantly lower than the book value for bulk nitride was obtained and if this new value is used with the RBS data a corrected thickness is derived and is presented in column 4. Finally, it should be noted that the stopping power for nitrogen in Si_3N_4 is reported to be about 6% lower than that measured for the gaseous value which is usually tabulated [17] and if this revised value is used in simulating the data good agreement is achieved with the optical measurements as shown in column 5. These data amply illustrate the difficulty of obtaining linear thickness measurements using nuclear techniques alone.

4. Metallised porous silicon

Porous silicon is produced when silicon is electrochemically anodised in HF acid in a process which removes very fine "cylinders" of material along the electric field direction, leaving a form of "porous silicon" whose density can be reduced to approximately half that of bulk silicon [18]. Such material has a very high surface area to volume ratio and is very chemically reactive. In addition, as the anodising process is sensitive to the resistivity and type of dopant in the silicon, complex distributions of porous material both on the surface and in buried layers can be produced by doping different regions in the appropriate manner. The porous layer can easily be converted to oxide, nitride or oxynitride to form good dielectric layers or can be converted to metal or silicide to produce conducting layers or paths both between and under particular structures [19].

A wafer of silicon was anodised to produce a porous layer 5 μm thick and this was processed in a chemical vapour deposition rig to induce metal or silicide depositions which where analysed by 2 MeV RBS and 1.1 MeV (d, p) NRA. Because porous silicon has such a large surface to volume ratio, even a monolayer of oxide will produce a significant oxygen content. Also, because of the complex structure, the material tends to getter gaseous molecules containing carbon from the atmosphere, and from the processing and metallisation environment. Therefore, in any assessment of the metallisation process, it is essential to measure the light element content.

Two different metallisation processes have been investigated with porous silicon samples. In both cases metal is expected to have penetrated into the pores

Table 2
Results of analysis of Si_3N_4 layers using optical and nuclear techniques

	Si_3N_4 thickness Ellipsometry/ Nanospec [nm]	RBS thickness ($\rho = 3400$) [nm]	Ellipsometry/ Nanospec ρ [$kg\,m^{-3}$]	RBS thickness (corr ρ) [nm]	RBS thickness (corr ρ) (corr ϵ) [nm]
Group 1	106.9 ± 1.4	82 ± 4	2920	100 ± 5	106 ± 5
Group 2	238.7 ± 3.3	181 ± 9	2960	220 ± 11	233 ± 11
Group 3	369.6 ± 4.7	278 ± 1	3060	320 ± 16	339 ± 16

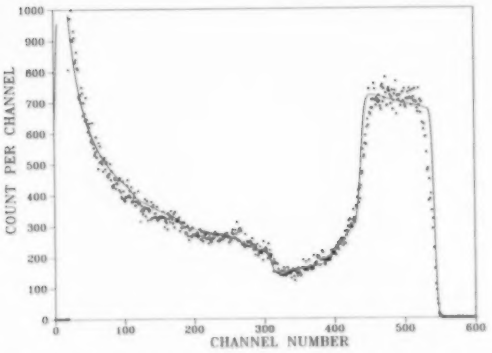

Fig. 8. RBS spectrum measured at 150° with 2 MeV incident He ions, from a 5 μm thick porous silicon layer metallised with cobalt in a chemical vapour deposition kit. The solid curve is a computer simulation assuming a 300 nm thick surface layer of Co containing 20% atomic light elements. Beneath this layer the porous silicon contains about 15% Co and 30% light element atoms (See also fig. 10). The energy width of each channel is 2.875 keV.

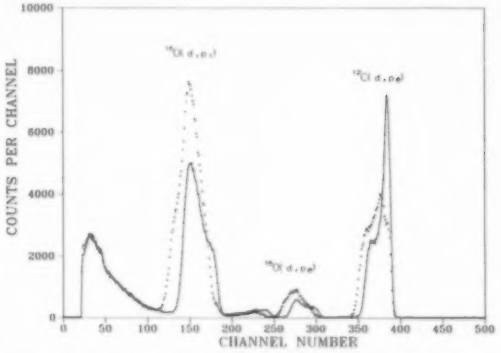

Fig 9. Proton spectra from 1.1 MeV deuteron bombardment of metallised porous silicon samples. The Spectrum of dots was from a sample metallised with cobalt and that of lines from a sample metallised with a CoSi silicide process. Protons were measured at a laboratory angle of 150° using a detector covered by a 12 μm Al absorber foil. The energy width of each channel is 7.395 keV.

and also, possibly, to have built up on the surface. In addition the samples were expected to contain carbon and oxygen. In the first sample CVD deposition of Co was desired. The RBS spectrum for this sample is shown in fig. 8 where it is clear that a metal layer of about 300 nm thick has built up on the surface in addition to penetrating the pores. The surface layer is found also to contain about 20% atomic light elements (carbon and oxygen) but the silicon edge suggests that the layer has been grown on top of the silicon. The cobalt content inside the pores is rather low at about 10% atomic. The RBS simulations give a reasonable measure of the elemental content down to a depth of about 700 nm. Light element contents were measured using (d, p) reactions with 1.1 MeV deuterons as illustrated in the dotted spectrum shown in fig. 9. Computer simulations of the RBS and NRA data indicate that the 0.3 μm surface metal layer contains 10% carbon and 10% oxygen atoms. Below this layer, the top regions of the porous silicon contain 10% carbon atoms reducing to 6% atoms at the back interface and 40% oxygen rising to 50% at the back interface. Elemental depth profiles, derived from the combined RBS and NRA data, are shown in fig. 10 where the depth scale has been derived from a knowledge of the thickness of the porous silicon (5 μm) and the cobalt thickness from the RBS spectrum assuming a bulk cobalt number density with added oxygen and carbon atoms.

An enlarged view of the $^{16}O(d, p_0)^{17}O$ group is shown in fig. 11 together with the response from an as-produced porous silicon sample and a simulated response from a fully dense 5 μm layer of SiO_2. The oxygen in the as-produced sample appears to be less than 2 μm thick. However, as the layer is only half normal density the signal actually indicates about 10% oxygen atoms spread throughout a 5 μm porous layer. The porous microstructure has typical dimensions in the range 5–10 μm and should therefore have only an averaging effect on the RBS and NRA spectra. The spectrum from the metallised sample, as illustrated by the dotted curve shows clearly the increase in the oxygen content toward the back interface and the suppressed signal in the cobalt surface layer.

Another set of samples was metallised by a CVD precursor which was designed to deposit CoSi silicide. A typical RBS spectrum is shown in fig. 12 where it is seen that a thin surface CoSi layer 90 nm thick has

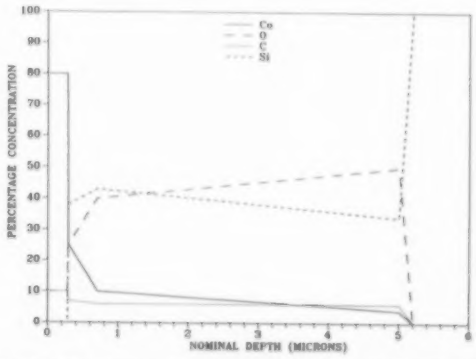

Fig. 10. The elemental depth profile for the cobalt metallised sample of porous silicon derived from the combined RBS and (d, p) measurements. The depth scale has been derived from a knowledge of the thickness of the porous silicon (5 μm).

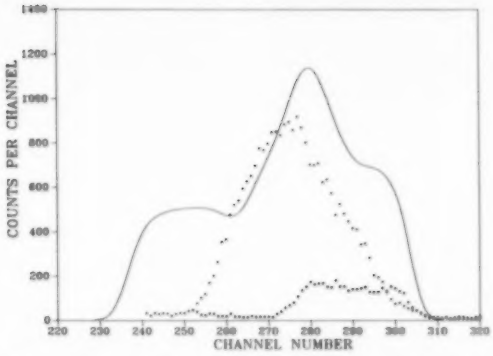

Fig. 11. A section of a (d, p) spectrum showing the $^{16}O(d, p_1)^{17}O$ group for three different samples. A measured spectrum from a lightly oxidised 5 mm thick porous layer is plotted as stars, while a measured spectrum from a more heavily oxidised 5 μm porous layer which has a 0.3 μm overlayer of cobalt is plotted in dots. A computer simulated prectrum for a 5 μm layer of fully dense SiO_2 is shown as a continuous curve. The energy width of each channel is 7.395 keV.

been formed and that CoSi has penetrated the pores (probably as CoSi). The (d, p) spectrum for this sample is shown as lines in fig. 9. In this case the oxygen and carbon content is slightly lower. However, in the surface layer both oxygen and carbon contents are significantly higher. The depth profile derived from the RBS and NRA spectra is given in fig. 13 where the depth scale has been derived from a knowledge of the thickness of the porous silicon (5 μm) and the CoSi thickness from the RBS spectrum assuming the number density for CoSi with added oxygen and carbon atoms.

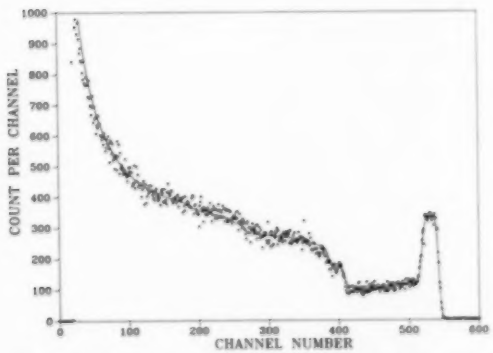

Fig. 12. RBS spectrum measured at 150° with 2 MeV incident He ions, from a 5 μm thick porous silicon layer metallised with cobalt silicide in a chemical vapour deposition kit. The solid curve is a computer simulation assuming a 9 run surface layer of CoSi containing 50% light element atoms. The porous silicon beneath this layer contains 8% Co atoms and 35% light atoms. (See also fig. 13). The energy width of each channel is 2.84 keV.

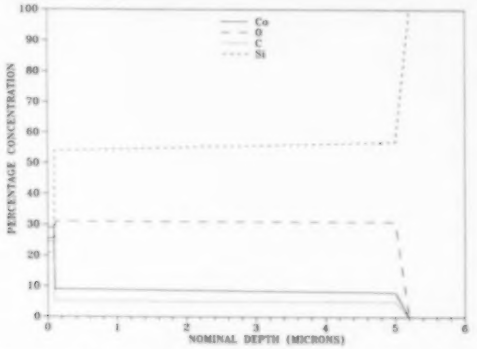

Fig. 13. The elemental depth profile for the cobalt silicide coated sample of porous silicon derived from the combined RBS and (d, p) measurements. The depth scale has been derived from a knowledge of the thickness of the porous silicon (5 μm).

5. Conclusions

The power of RBS, NRA and ERDA in analysing processed layers in silicon has been confirmed and the difficulty of translating the atomic number densities so obtained into linear thicknesses demonstrated. It is recommended that any reported nuclear measurements of linear thickness be accompanied by full details of assumptions made about stoichiometry or porosity.

Elemental depth profiles to a depth of about 5 μm have been measured on metallised porous silicon using a combination of RBS and NRA. Good depth resolution is obtained from RBS near the surface where concentrations are changing rapidly, whilst NRA provides information to a much greater depth. Again the difficulty of working with materials which contain small voids has been highlighted.

Acknowledgements

This work is published with the permission of the director of RSRE Malvern. We wish to acknowledge DTI/SERC support through the IED 1625 programme.

References

[1] J.R. Bird and J.S. Williams, eds., Ion Beam Analysis of Materials (Academic Press New York, 1989).

[2] Electrochem. Soc. Ext. Abstr. 3 (1966). Over 20 papers discussing- difficulties of producing stoichiometric thin-film nitrides.
[3] R.A. Jarjis, Nuclear Cross Section Data for Surface Analysis, vols. 1–3, University of Manchester, Department of Physics Internal Report (1979).
[4] J.C.B. Simpson and L.G. Earwaker, Nucl. Instr. and Meth. B15 (1986) 502.
[5] G. Debras and G. Deconninck, J. Radioanal. Chem. 38 (1977) 198.
[6] T.W.A Bonner, J.T. Eisinger, A.A. Kraus, Jr. and J.B. Marion, Phys. Rev. 101 (1956) 209.
[7] H. Cords, G.H. Din and B.A. Robson, Nucl. Phys. A127 (1969) 95.
[8] E. Kashy, R.R. Perry and J.L. Risser, Phys. Rev. 117 (1960) 1289.
[9] M.Y. McEllistrem, K.W. Jones, R.E.N. Chiba, R.A. Douglas, D.F. Herring and E.A. Silverstein, Phys. Rev. 104 (1956) 1008.
[10] T.S. Katman, N.R. Fletcher, D.R. Tilley and R.M. Williamson, Nucl. Phys. 80 (1966) 449.
[11] G. Amsel and D. David, Rev. Phys. Appl. 4 (1969) 383.
[12] V. Gomes-Porto, N. Ueta, R.A. Douglas, O. Sala, D. Wilmore, B.A. Robson and P.E. Hodgson, Nucl. Phys. A114 (1968) 330.
[13] R.F. Seiler, C.H. Jones W.J. Anzick, D.F. Herring and X.W. Jones, Nucl. Phys. 45 (1963) 647.
[14] O. Dietzsch, R.A. Douglas, E. Farrelly Pessoa, V. Gomes-Porto, E.W. Hamberger, T. Polga, O. Sala, S.M. Perez and P.E. Hodgson, Nucl. Phys. A114 (1968) 330.
[15] G. Amsel and D. Samuel, Anal. Chem. 39 (1967) 1689.
[16] Handbook of Chemistry and Physics (CRC Press, Boca Raton, 1986).
[17] J.F. Ziegler, W.K. Chu and J.S.-Y. Feng, Appl. Phys. Lett. 27 (7) (1975) 387.
[18] K. Barla, G. Bomchill, R. Herino and A. Monray, IEEE Circuits and Devices 3 (4) (1987) 11.
[19] K. Barla, G. Bomchill and R. Herino, Electron. Lett. 22 (1986) 1291.

Nuclear Instruments and Methods in Physics Research B66 (1992) 31–37
North-Holland

Nuclear Instruments & Methods in Physics Research
Section B

Non-Rutherford scattering of protons by light elements

J.M. Knox
Physics Department, Idaho State University, Pocatello, ID 83209, USA

The use of H^+ beams with a few MeV of energy allows the analyst to probe much deeper into a sample than would be possible with a similar helium beam. The price one pays for this greater depth is a loss of mass resolution. For the light elements (lithium to neon) being discussed here, there is an additional problem and benefit: the scattering cross section, in several instances, deviates significantly from the Rutherford formula; very often this deviation enhances the sensitivity of the analysis. This paper reviews the available experimental cross section data for lithium to neon and discusses one method of modeling these cross sections.

1. Introduction

The typical backscattering experiment consists of a beam of ions incident on a sample the elemental composition and structure of which may be unknown. The usual ions used for this work are He^+ or He^{2+}. In certain circumstances heavier ions may be used, e.g., in elastic recoil spectroscopy, or, for greater analysis depth, a proton beam may be used. Often the sample may be tilted to provide better resolution of the near-surface layer(s). In this standard experiment, the incident ions are thought to interact with the Coulomb potential of the various nuclei in the sample. For the lower mass ion beams, the scattered ion distribution is not isotropic; most of the ions are scattered in the backward direction, i.e., toward the incoming beam. Thus a detector such as a silicon surface barrier detector placed at as large a back angle as possible (normally around 160°) will collect the largest number of scattered ions in a unit solid angle per unit of charge incident on the target.

In this review we consider the ion beam analysis of materials containing light elements ($Z = 3$–10); the incident ions are moderate energy (2 MeV or less) proton beams. Protons have two advantages over helium and heavier ions in that their probing depth is much larger and the cross section for elastically scattered protons from these light elements is often large enough, due to nuclear contributions, that the sensitivity of the analysis is improved. For example, in an energy region near 1.0 MeV where proton scattering from carbon is nonresonant, the proton cross section is nearly 180 mb/sr while the helium cross section is somewhat less: about 150 mb/sr at 165°. At the resonant proton energy of 1.735 MeV, the comparative values are 940 and 51 mb/sr, respectively. This enhancement of proton scattering compared with helium scattering is particularly useful when the signal due to helium ions scattered by the heavier elements within the sample masks the signals from helium scattered by the lighter elements.

The price one pays for the improved sensitivity with protons is that the depth resolution is reduced and the cross section no longer follows the well-known E^{-2} dependence of the Rutherford model. This is due to the penetration of the Coulomb barrier by the protons and, therefore, nuclear potential and energy levels of the compound nucleus must be considered in the scattering problem. The details of proton backscattering have been reviewed recently by Rauhala [1] and need not be discussed further here.

Often the effects on the elastic scattering cross section of nuclear potential and nuclear resonant scattering processes are to enhance the scattering cross sections by factors from 2 or 3 times the Rutherford value to as much as 2 or 3 orders of magnitude over the Rutherford value. However, there are some situations where the actual cross section may be less than the Rutherford value. When the analyst is aware of these contributions, one may take advantage of the enhancements, whether resonant or nonresonant, to increase sensitivity by carefully choosing the energy of the incident ion beam. It is then very useful to have the correct cross section available in the modeling program used to assist in the analysis.

The present paper reviews the data available for protons scattering from the most common isotope of the elements lithium through neon and, using a fitting function similar in form for each element, obtains multiparameter fits to these cross sections. This function is then readily inserted in modeling programs such as RUMP [2] which assist in the analysis of the sample. While we have not fit the stable isotopes of lesser abundance, notes on the general shape of their cross

0168-583X/92/$05.00 © 1992 – Elsevier Science Publishers B.V. All rights reserved

section are provided where appropriate. We have restricted this review to data taken at a large laboratory scattering angle (150–170°) and to protons with energy less than 2 MeV.

2. Theory

The form of the fitting function used for all of the cross sections has been described previously [3] as a summation of successive Fermi steps with each step requiring three parameters:

$$\sigma(E) = \frac{A}{D(E)},$$

where A is an adjustable overall scaling parameter and $D(E)$ is given by

$$D(E) = 1 + \sum_i \frac{B_i}{1 + \exp\left(\frac{E - E_i}{W_i}\right)}.$$

In this expression, the B_i give the height and direction (up or down) of the step; the E_i give the energy position of the step; and the W_i give the step width. The fit is accomplished with standard, nonlinear, least squares routines [4]. In order to avoid finding a false minimum in the multidimensional parameter space, the parameters provided to the fitting routine are obtained in a short modeling session on a PC with a spreadsheet configured to plot the data and the proposed fit.

3. Data

The input values for the proton elastic scattering cross section have come from a variety of sources: recent data from this laboratory [5] and the laboratory at the University of Helsinki [6,7] plus published data from 1953–1970. The older published data are normally presented as a graph which must then be enlarged so that numerical values may be obtained to use as input data to the fitting procedure. This process of enlarging and reading values from the plot necessarily introduces some additional error into the data used in the fit. Thus the fitting parameters are not as accurate as they are when the cross section data is presented in tabulated form. However, the fit fo this "estimated" cross section leads to a considerable improvement in the analysis of materials containing light elements as compared to using only the Rutherford values for the cross section. In the following, we will consider the data available for each element in turn. All scattering angles are given in the laboratory system.

3.1. Lithium

The mass seven isotope comprises about 92% of natural lithium; the other 8% is ^{6}Li. Note that the exact percentage may vary somewhat with the source of the material. We have used our own data [8] taken at 160° along with the data of Bashkin and Richards [9] at 164°. The data of Warters et al. [10] was not used for two reasons: (1) our measurements [8] and the earlier work [9] are in good agreement with each other but some 25 to 50% smaller than Warters' values; (2) the energy range covered (0.373–1.398 MeV) by Warters et al. is not high enough to meet our needs here. Note that the ^{6}Li cross section rises from the Rutherford value at 400 keV to a broad (600 kev) resonance at approximately 1.75 MeV that is 29 times larger than the Rutherford cross section [11].

3.2. Beryllium

The most recent data we could find in the given energy range and with a good back angle is that of Mo and Hornyak [12] at 158.7°. Earlier work [13], plotting the ratio of the cross section to the Rutherford value, is reasonably consistent with ref. [12]. Mo and Hornyak were able to obtain a physically based theoretical fit using R-matrix theory with several resonance levels included in the model. This fit was not used here because it is different in functional form and parameterization than the fit used for the other elements' cross sections.

3.3. Boron

Elastic proton scattering for ^{11}B, which is 80.2% of naturally occurring boron, has been measured by Tautfest and Rubin [14] at approximately 150° from 0.600 to 2.0 MeV. Data on ^{10}B (19.8% of natural boron) [15] at an angle or 154° has not been modeled in this work. However, it should be noted that for ^{10}B the cross section between 0.2 and 1.4 MeV is seen to increase linearly from the Rutherford value at 200 keV to approximately three times Rutherford at 1.4 MeV. At 1.50 MeV and at 2.1 MeV very large resonances are displayed which are also shown to be very strongly scattering-angle dependent.

3.4. Carbon

The data for ^{12}C (98.89% of natural carbon) come from three sources. We have used Rauhala's [6] data for proton energies greater than 1 MeV and an average of data from Goldhaber and Williamson [16] and Jackson et al. [17] for proton energies less than 1 MeV. Scattering angles are 170, 164, and 169.2°, respectively.

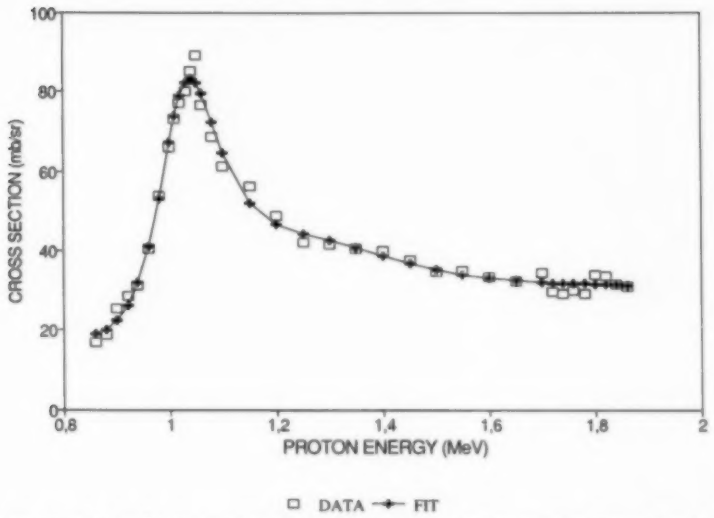

Fig. 1. The measured cross section for ^{7}Li (squares) in mb/sr is plotted versus incident proton energy. The fit, using the parameters in table 1, is given by the plus symbols; the pluses are connected by a line which is only an aid to viewing the fit.

3.5. Nitrogen

As with the carbon data, the nitrogen 14 data was discussed previously [3]; ^{14}N comprises 98.63% of natural nitrogen. The data come from Rauhala [6] above 1.4 MeV incident proton energy and an average of Olness et al. [18] and Bashkin et al. [19] at lower energies. The scattering angles are 170°, 168.1° and 160.9° respectively. These data are also consistent with that of Tautfest and Rubin [14] taken at 150°.

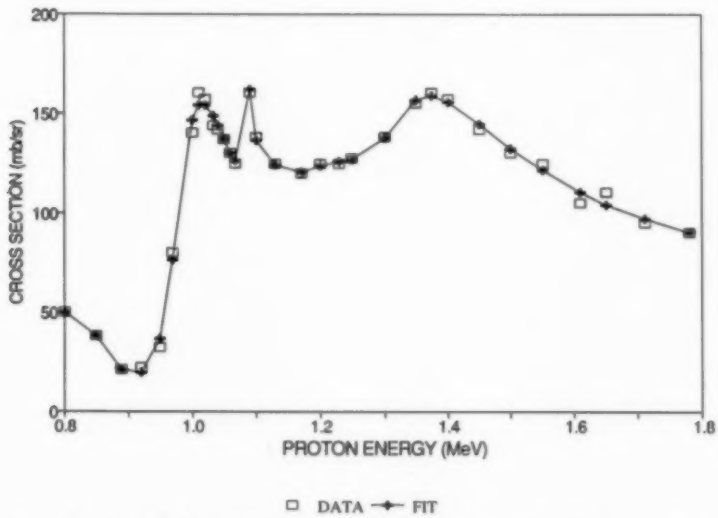

Fig. 2. The measured cross section for ^{9}Be (squares) in mb/sr is plotted versus incident proton energy. The fit, using the parameters in table 1, is given by the plus symbols; the pluses are connected by a line which is only an aid to viewing the fit.

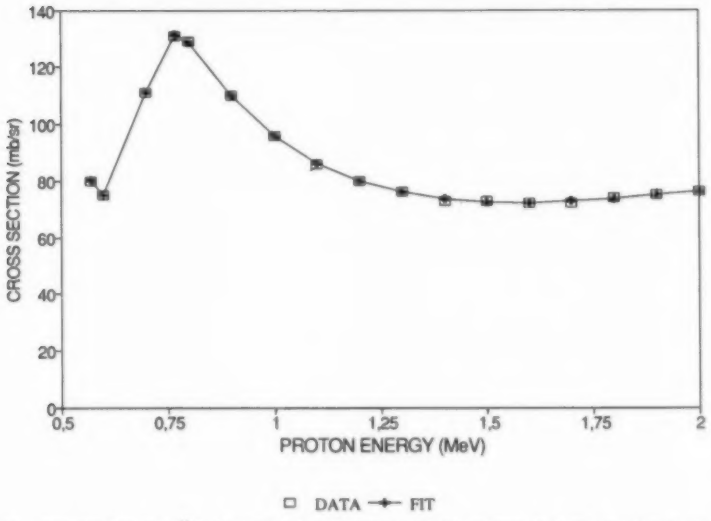

Fig. 3. The measured cross section for ^{11}B (squares) in mb/sr is plotted versus incident proton energy. The fit, using the parameters in the table 1, is given by the plus symbols; the pluses are connected by a line which is only an aid to viewing the fit.

3.6. Oxygen

Luomajärvi et al. [7] have published measured cross section values for ^{16}O (99.76% of natural oxygen) at 170° over the applicable energy range. While the shape of the cross section is somewhat similar to the Rutherford E^{-2} dependence, upon comparison, it is clear that there is a considerable difference in magnitude at

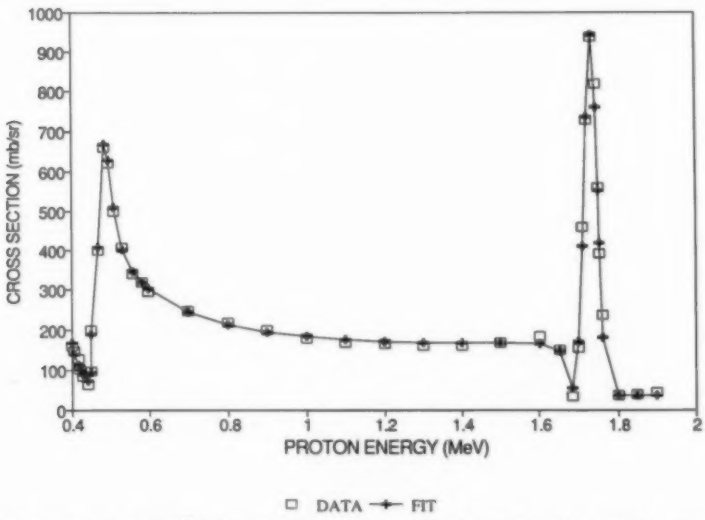

Fig. 4. The measured cross section for ^{12}C (squares) in mb/sr is plotted versus incident proton energy. The fit, using the parameters in table 1, is given by the plus symbols; the pluses are connected by a line which is only an aid to viewing the fit.

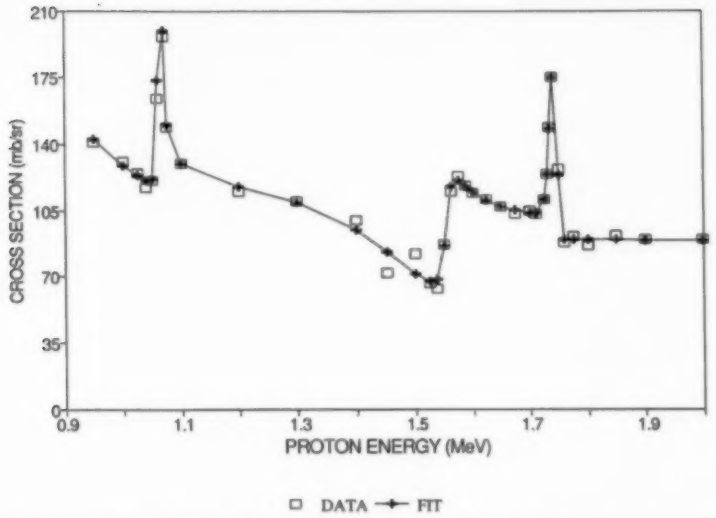

Fig. 5. The measured cross section for ^{14}N (squares) in mb/sr is plotted versus incident proton energy. The fit, using the parameters in table 1, is given by the plus symbols; the pluses are connected by a line which is only an aid to viewing the fit.

these energies. The data is easily fit with a polynomial; however, for consistency we have retained the Fermi step form as discussed earlier with regard to beryllium.

3.7. Fluorine

The data is taken from our previous work [5] with a scattering angle of 165° below 1 MeV and 153° above 1 MeV.

3.8. Neon

There are two stable isotopes of neon with significant abundance: ^{20}Ne and ^{22}Ne appear at 90 and 10% respectively. Due to the narrowness and number of the resonances, we have not modeled either isotope of neon. Bloch et al. [20] have studied ^{20}Ne and Keyworth et al. [21] have studied ^{22}Ne using scattering angles of

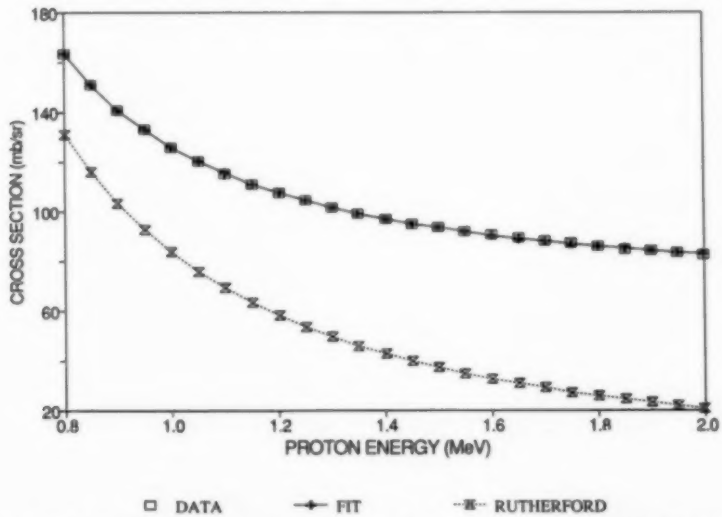

Fig. 6. The measured cross section for ^{16}O (squares) in mb/sr is plotted versus incident proton energy. The fit, using the parameters in the table 1, is given by the plus symbols; the pluses are connected by a line which is only an aid to viewing the fit.

Table 1
The table gives the parameters used to obtain the fits to the proton scattering cross sections for the light elements discussed. The number of steps and the overall amplitude or scaling factor required are given. The position (E_i), height (B_i) and width (W_i) are given for each step in the fitting function

Element	^{7}Li	^{9}Be	^{11}B	^{12}C	^{14}N	^{16}O	^{19}F
Steps	4	8	4	7	8	1	15
Amplitude [A]	14.54	72.25	82.11	34.60	70.05	75.37	31.95
Position, E_i	0.9389	0.8820	0.5278	0.4213	0.8927	−0.7969	0.8517
[MeV]	1.055	0.9429	0.6495	0.4753	1.062		0.8580
	1.179	1.094	0.8311	0.5870	1.068		0.8869
	1.48×10^{15}	1.088	1.724	0.4504	1.490		0.9126
		1.098		1.656	1.550		0.9515
		1.312		1.688	1.864		0.9595
		1.164		1.769	1.733		1.365
		1.555			1.750		1.381
							1.391
							1.417
							1.420
							1.428
							1.696
							1.720
							1.875
Height, B_i	1.648	−3.386	−2.552	−0.6758	−0.6009	−7.046	−0.2926
	−2.582	4.470	1.795	0.1345	0.7026		0.1274
	1.062	−0.6592	−1.351	−0.1952	−0.6164		0.04754
	−0.5311	0.3924	0.3674	0.4699	−0.6076		−0.2024
		−0.1836		−0.8261	0.5739		0.07865
		0.2417		1.002	−0.4278		−0.06879
		0.3128		−0.9667	0.3463		−0.2531
		−0.7982			−0.4375		−0.4402
							0.4399
							−0.3986
							−0.5695
							1.055
							−0.4889
							0.3888
							−0.4649
Width, W_i	47.91	18.09	72.73	26.79	134.1	640.3	14.84
[keV]	127.7	14.48	43.56	6.126	3.100		1.374
	83.02	40.24	284.6	191.5	3.272		0.5393
	3.59×10^{12}	6.468	281.6	0.5881	56.47		110.1
		0.9901		1.864	5.054		0.8505
		26.45		7.529	5196		0.5405
		28.45		5.492	4.591		89.15
		203.7			0.8534		3.049
							1.149
							2.533
							28.24
							3.926
							41.84
							11.79
							33.53

141 and 160°, respectively. The Bloch study is at a smaller angle than included in this review and presents the cross section measurements only within a few hundred eV of the four observed resonances at 1.169, 1.311, 1.504, and 1.955 MeV. These resonances are very narrow: approximately 250, 1000, 250, and 6000

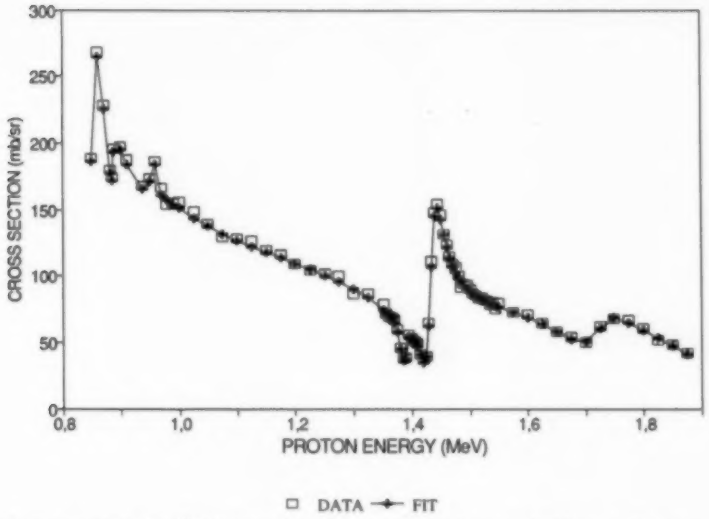

Fig. 7. The measured cross section for ^{19}F (squares) in mb/sr is plotted versus incident proton energy. The fit, using the parameters in the table 1, is given by the plus symbols; the pluses are connected by a line which is only an aid to viewing the fit.

eV, respectively. They are also no more than 2.5 times the Rutherford value. Thus it is not clear that these resonances will be observed when a 15 keV resolution surface barrier detector, such as commonly used in ion beam analysis, is used for data acquisition. The situation is somewhat similar with ^{22}Ne as there are some 27 anomalies in the measured cross section between 0.8 and 2.1 MeV [21]. Some of these are a few kilovolts wide, but most are only a few electron volts in width.

4. Results and conclusions

The measured cross section data and the resulting fits are plotted in figs. 1–7. The number of steps required along with the parameters used in each of the fits are displayed in table 1. As can be seen, the multiparameter fit using a summation of Fermi steps successfully models the experimental data. These fits may then be incorporated into a backscattering modeling program to provide the analyst with a much more accurate portrayal of the sample. The techniques used here are readily extended to other angles and energy ranges as appropriate for different accelerator and analysis facilities.

References

[1] E. Rauhala, Nucl. Instr. and Meth. B40/41 (1989) 790.
[2] L.R. Doolittle, Nucl. Instr. and Meth. B9 (1985) 344; B15 (1986) 227.
[3] J.M. Knox, R.J. McLeod, D.R. Mayo and X. Qian, Nucl. Instr. and Meth. B45 (1990) 26.
[4] P.R. Bevington, Data Reduction and Error Analysis for the Physical Sciences (McGraw–Hill, New York, 1969).
[5] J.M. Knox and J.F. Harmon, Nucl. Instr. and Meth. B44 (1989) 40.
[6] E. Rauhala, Nucl. Instr. and Meth. B12 (1985) 447.
[7] M. Luomajärvi, E. Rauhala and M. Hautala, Nucl. Instr. and Meth. B9 (1985) 255.
[8] S. Banerjee, Low Energy Scattering Cross Section of Protons on ^{7}Li, M.S. Thesis, Idaho State University, Pocatello, Idaho, 1990.
[9] S. Bashkin and H.T. Richards, Phys. Rev. 84 (1951) 1124.
[10] W.D. Warters, W.A. Fowler and C.C. Lauritsen, Phys. Rev. 91 (1953) 917.
[11] J.A. McCray, Phys. Rev. 130 (1963) 2034.
[12] T. Mo and W.F. Hornyak, Phys. Rev. 187 (1969) 1220.
[13] F.S. Mozer, Phys. Rev. 104 (1956) 1386.
[14] G.W. Tautfest and S. Rubin, Phys. Rev. 103 (1956) 196.
[15] J.C. Overly and W. Whaling, Phys. Rev. 128 (1962) 315.
[16] G. Goldhaber and R.M. Williamson, Phys. Rev. 82 (1951) 495.
[17] H.L. Jackson, A.I. Galonsky, F.J. Eppling, R.W. Hill, E. Goldberg and J.R. Cameron, Phys. Rev. 89 (1953) 365.
[18] J.W. Olness, J. Vorona and H.W. Lewis, Phys. Rev. 112 (1958) 475.
[19] S. Bashkin, R.R. Carlson and R.A. Douglas, Phys. Rev. 114 (1959) 1552.
[20] R. Bloch, T. Knellwolf and R.E. Pisley, Nucl. Phys. A123 (1969) 129.
[21] G.A. Keyworth, P. Wilhjelm, G.C. Kylar, Jr., H.W. Newson and E.G. Bilpuch, Phys. Rev. 176 (1968) 1302.

Nuclear Instruments and Methods in Physics Research B66 (1992) 38–42
North-Holland

Nuclear Instruments & Methods in Physics Research
Section B

The influence of surface topography on the depth resolution of the PIGE depth profiling technique

F. Plier, H.-E. Zschau and G. Otto
Department of Physics, University of Leipzig, Linnéstrasse 5, Leipzig, O-7010, Germany

When calculating the depth resolution of the PIGE depth profiling technique, it can often be assumed that the target has an ideal smooth surface. However for many targets (enamel, ceramics) the surface roughness must be taken into consideration. A model of a rough surface was procuded and was used to calculate the influence of experimental arrangement on the depth resolution. An approximate formula is given, from which the depth resolution of the depth profiling technique, applied to a rough surface (incidence angle $\vartheta_i = 0°$), can be calculated.

1. Introduction

In PIGE (particle induced gamma-ray emission spectrometry) depth profiling of an ideal smooth target, an estimate can be made of the depth region, in which incident particles (incidence energy E_0) excite the resonance of a nuclear reaction (resonance energy E_R). The total energy spread across this region has been calculated using ref. [1].

$$\Gamma^2 = \Gamma_R^2 + \Gamma_B^2 + \Gamma_S^2, \tag{1}$$

where Γ, Γ_B and Γ_S are expressed in keV and represent the FWHM of the excited depth region, the FWHM of the nuclear reaction resonance, the FWHM of the beam energy resolution, and the FWHM of the straggling distribution, respectively.

The so called depth resolution Δt of the profiling technique can be estimate by means of Γ:

$$\Delta t = \frac{\Gamma}{\rho S(E_R)}, \tag{2}$$

where $S(E_R)$ in keV/(g cm^{-2}) is the stopping power of the target at the proton of energy E_R and ρ in (g/cm^3) is the mass density.

But which formula is valid for a target with surface roughness? The aim of this work is to describe the influence of surface roughness on the depth resolution of the depth profiling measurements.

2. Methods

The study of the influence of surface roughness on the depth resolution was made using theoretical simulations.

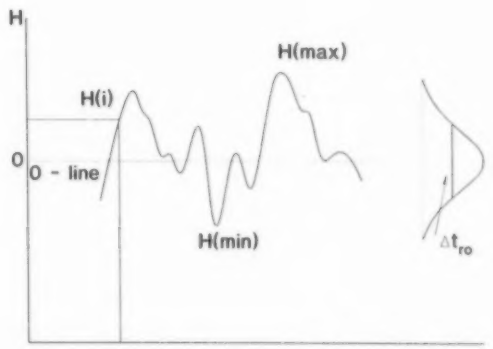

Fig. 1. Description of the parameters for the target with surface roughness.

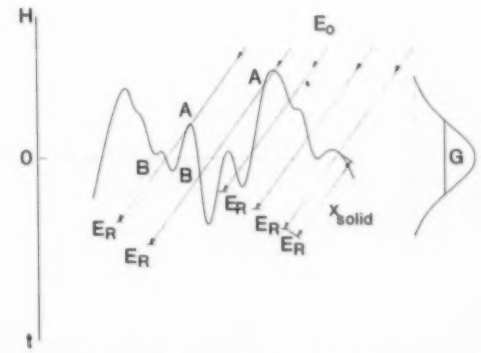

Fig. 2. Penetration of incident protons (E_0) in a target with rough surface.

0168-583X/92/$05.00 © 1992 – Elsevier Science Publishers B.V. All rights reserved

Measurements were carried out on aluminum layers to prove the theoretical results.

In order to describe the rough surface, the surface line (fig. 1) was divided into N equidistant intervals, each defined by a high point $H(i)$ in the middle of the interval. The assumption was made that a Gaussian approximation can be used to describe the distribution of these high points around the surface line of an ideal smooth target (0-line, fig. 1) [2]. This $H(i)$-distribution (FWHM = Δt_{ro}) describes the probability distribution of high points. This rough surface model can be used to calculate the penetration depths of particles in a solid. Fig. 2 shows that protons hitting the target surface under defined experimental conditions (ϑ_i, E_0) attain the resonance energy E_R at different depth t due to surface roughness. These differences in depth were caused by the additional regions of surface structure encountered by protons, like those between A and B (fig. 2), and also by the different heights H at which the protons hit the target surface. For each high point,

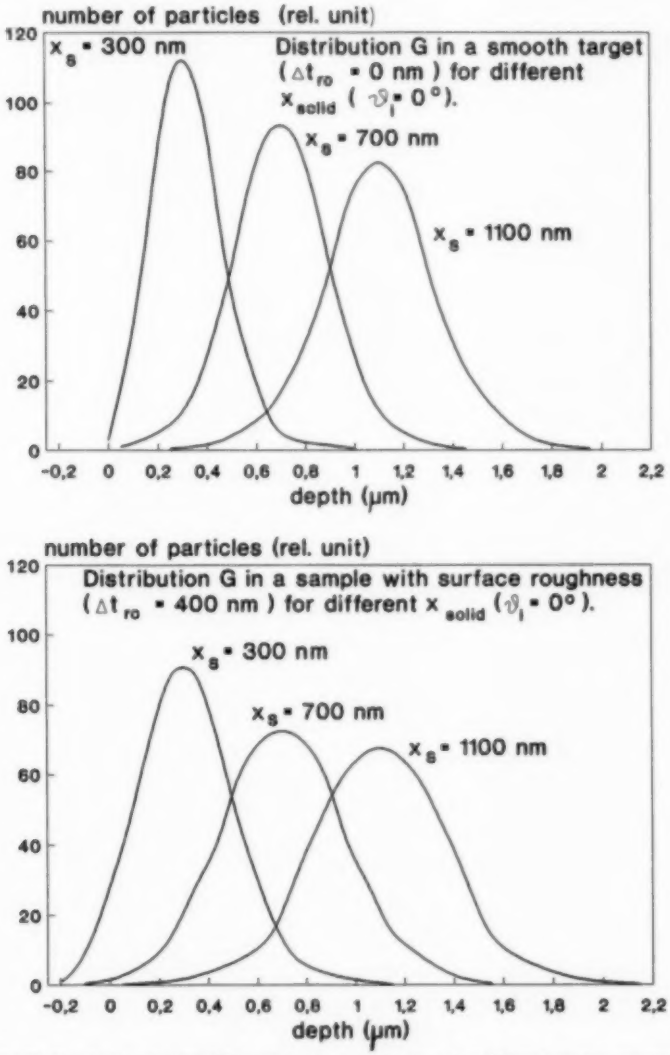

Fig. 3. Total proton distribution in targets with different surface roughnesses, for different proton penetration depths x_{solid} and for $\vartheta_i = 0°$ (E_R = 935 keV, $^{19}F(p, p'\gamma)^{19}F$ reaction, Γ = 8 keV).

the possible penetration depths of a proton lie in the interval Δx

$$\Delta x = x_{\text{solid}} \frac{H(i) - H(\min)}{\cos \vartheta_i},$$

with

$$x_{\text{solid}} = \int_{E_0}^{E_R} S(E)^{-1} \, dE.$$

Now a probability distribution $p(x[H(i)])$ was evaluated for every high point $H(i)$, which described every possible penetration depth which existed for each $H(i)$. The function $p(x[H(i)])$ depends on the incidence angle ϑ_i, the spreading Δt_{ro} of the high point distribution and of $H(i)$ itself:

$$p(x[H(i)]) = f(\vartheta_i, \Delta t_{ro}, H(i)). \quad (3)$$

By means of $p(x[H(i)])$ an estimate was made for every high point of all the possible penetration depths in the interval Δx; we got a proton distribution function $d(p(x[H(i)]))$. The summation of $d(p(x[H(i)]))$, estimated for all high points, described the proton distribution P in the target with surface roughness defined by Δt_{ro}. This distribution p exists additionally. The total proton distribution G in a target with rough

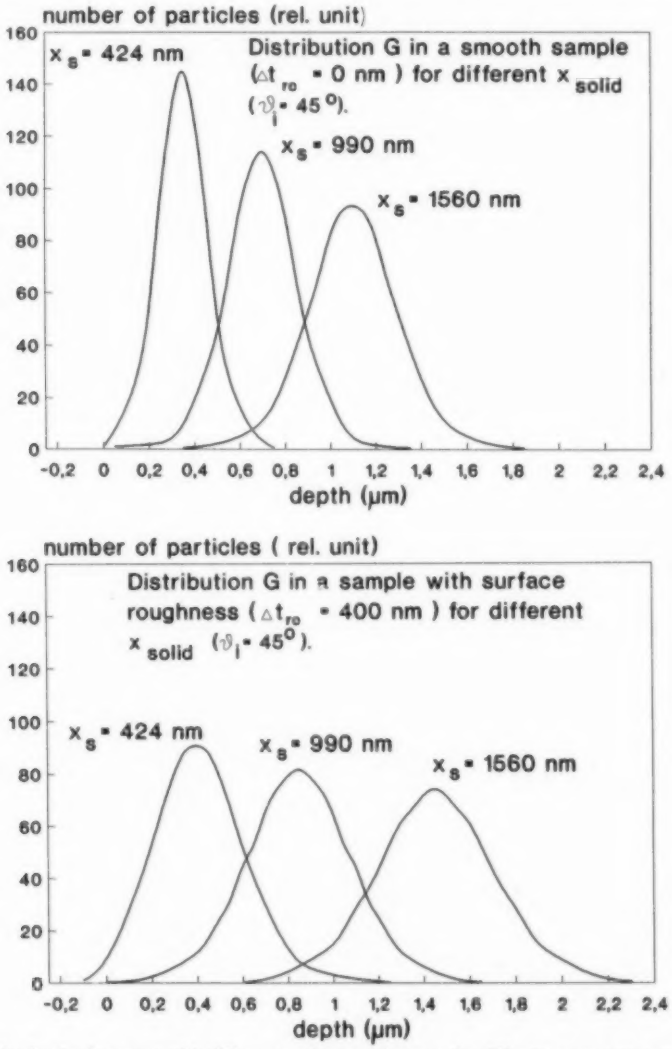
number of particles (rel. unit)
Distribution G in a smooth sample
(Δt ro = 0 nm) for different x solid
(ϑi = 45 °).
x s = 424 nm
x s = 990 nm
x s = 1560 nm
depth (μm)
number of particles (rel. unit)
Distribution G in a sample with surface
roughness (Δt ro = 400 nm) for different
x solid (ϑi = 45°).
x s = 424 nm
x s = 990 nm
x s = 1560 nm
depth (μm)

Fig. 4. Total proton distribution in targets with different surface roughnesses, for different proton penetration depths x_{solid} and for $\vartheta_i = 45°$ ($E_R = 935$ keV, $^{19}F(p, p'\gamma)^{19}F$-reaction, $\Gamma = 8$ keV).

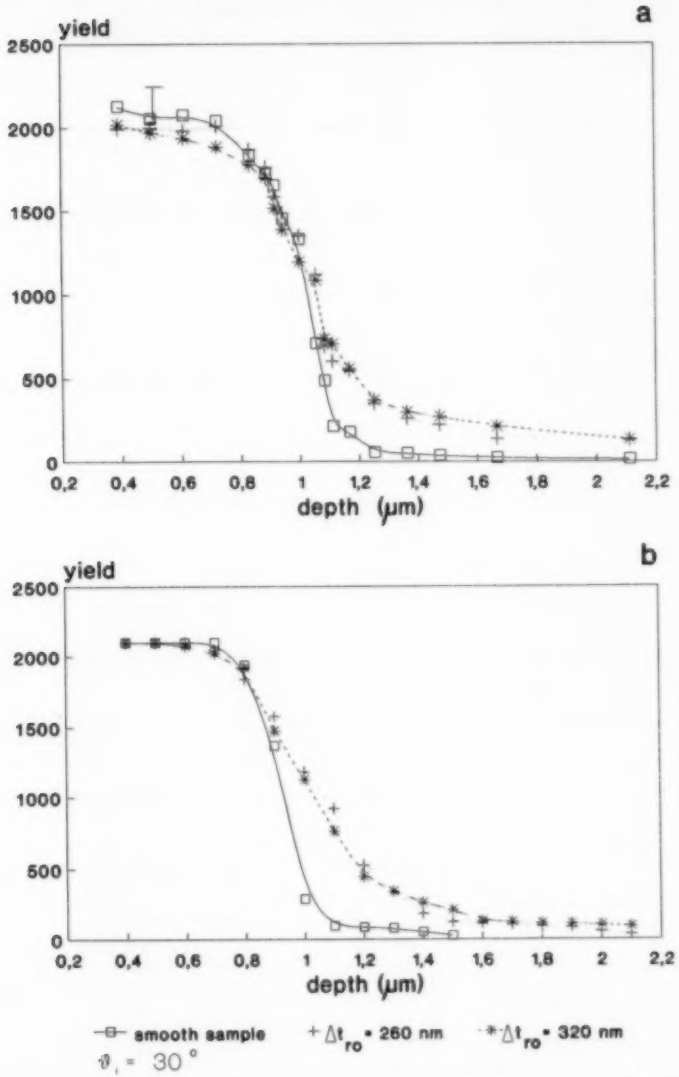

Fig. 5. Comparison between measured (a) and calculated (b) aluminum depth profiles for targets with different surface roughnesses (thickness $d = 500$ nm, Δt_{ro} in the range 260–320 nm, $^{27}Al(p, p'\gamma)^{27}Al$; $E_R = 1520$ keV; $E_\gamma = 843$ keV).

surface was calculated from the convolution of both proton distributions.

3. Results

Figs. 3 and 4 show the total proton distributions G obtained for different experimental arrangements, supposing the resonance $E_R = 935$ keV of the $^{19}F(p, p'\gamma)^{19}F$ nuclear reaction. In fig. 3 the total proton distribution G were compared for a smooth target and for a target with surface roughness ($\Delta t_{ro} = 400$ nm), and also for an incidence angle $\vartheta_i = 0°$ and for different incidence energies E_0. From this it can be seen that for an increase of the surface roughness (Δt_{ro}) the maximum of the proton distribution decreases, but its spreading Δt_{total} increases. On the other hand (fig. 4) when an incidence angle of $\vartheta_i = 45°$ occurs in addition to the changes discussed before, the maximum of the total proton distribution shifts to a

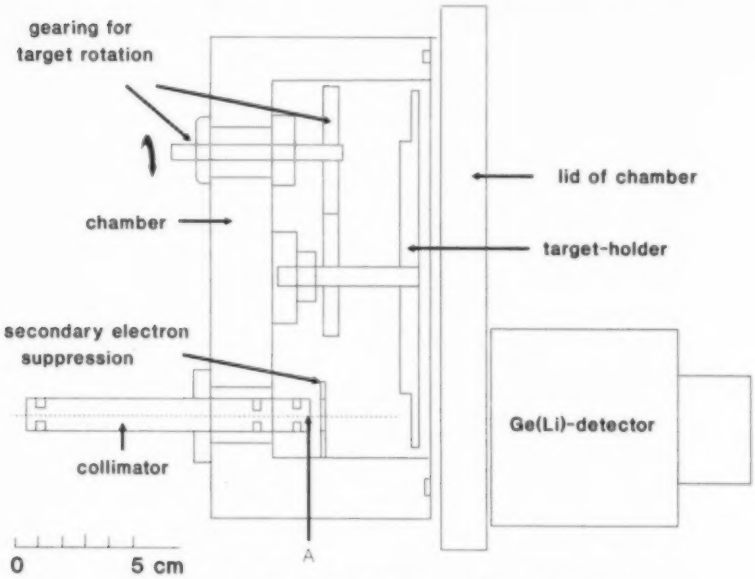

Fig. 6. The new chamber used for depth profiling measurements.

deeper target region in relation to a smooth target measured under the same experimental conditions.

Fig. 5a shows the aluminum depth profiles (thickness of layer $d = 500$ nm) measured for targets with different surface roughness (Δt_{ro} in the range 260–320 nm, $^{27}Al(p, p'\gamma)^{27}Al$, $E_R = 1520$ keV, $E_\gamma = 843$ keV) and fig. 5b shows aluminum depth profiles calculated for the same experimental conditions and targets ($d =$ 500 nm and Δt_{ro} in the range 260–320 nm).

4. Discussion

The computation showed that the width of the total proton distribution and the position of its maximum depended on the scale of the surface topography, the experimental geometry and the incidence energy. Two especially important results of the simulation were the shift in the maximum of the total proton distribution towards deeper regions of the rough target with growing incidence angle ϑ_i in relation to the ideal smooth target, and the increase in Δt_{total} of the total proton distribution with increasing Δt_{ro} of the surface high point distribution of the target. This means that, for depth profiling measurements on rough samples false results are obtained for the depth scaling and calculation of the excited depth region if a flat target situation was supposed when analysing the experimental data. The correctness of this statement was examined in PIGE-resonance profiling measurements on aluminum layers with different surface roughnesses. The changes in the depth profiles measured at $\vartheta_i = 0°$ characterized the increase in Δt_{total} of the total proton distribution with increasing Δt_{ro} of the surface high point distribution.

As a consequence of these results a new chamber was built for PIGE-measurements, in which the incident particles hit the target perpendicular to the surface. Fig. 6 shows the new chamber used for depth profiling measurements.

In a similar manner to that, used in the calculation of the total proton distribution, we described the region in which the resonance reaction was excited (incidence angle $\vartheta_i = 0°$) by

$$\Gamma^2 = \Gamma_R^2 + \Gamma_B^2 + \Gamma_S^2 + \Gamma_T^2,$$

with

$$\Gamma_T = \frac{\Delta t_{ro} \rho S(E_R)}{\cos \vartheta_i}.$$

References

[1] G. Deconninck, Introduction to Radioanalytical Physics (Akad. Kiado, Budapest, 1987).
[2] J.L. Campbell et al., Nucl. Instr. and Meth. B12 (1985) 402.

Nuclear Instruments and Methods in Physics Research B66 (1992) 43–47
North-Holland

Nuclear Instruments & Methods in Physics Research
Section B

The application of high energy prompt gamma-ray spectrometry to ^{3}He activation analysis of light elements

A.E. Pillay [1] and M. Peisach

National Accelerator Centre, P.O. Box 72, Faure, 7131 South Africa

Prompt high energy gamma rays induced by moderate beam currents of 2 MeV $^3He^+$ ions on thick targets of boron, carbon, nitrogen and oxygen were evaluated for analytical purposes. Gamma rays were observed from (^{3}He, p), (^{3}He, α) and Coulomb excitation reactions. Interference-free determination of boron, and carbon was achieved at concentrations of a few parts per thousand. At these concentrations a precision of about 10% was attainable. The technique was tested by determining carbon in standard steel specimens.

1. Introduction

There is a widespread need for methods to determine light elements at all levels of concentration. It is generally accepted that wet chemical methods are tedious and unsuitable for routine quantitative determination of the light elements [1], while instrumental methods such as PIXE, XRF or neutron activation are suitable for elements with atomic numbers greater than 11. Probably one of the few instrumental methods that are capable of handling such problems is ICP, but it is a destructive method, the sample pre-treatment of which is time-consuming especially if interfering components of the matrix have to eliminated by chemical complexation. The matrices in which light elements have to be determined vary greatly. Boron forms a vital component of glasses, is used in nuclear reactor materials, forms an essential element of some semiconductor devices and is used in metallurgy. Carbon, nitrogen and oxygen are essential elements in biochemical and physiological systems and their determination is important in studies of the environment and its pollution.

Low energy gamma rays, from activation by protons, deuterons and $^4He^+$ ions, have been widely studied for analytical use [2–5], but the sensitivity is often affected by the level of the background and the intensity of the annihilation radiation of 511 keV. In the case of activation with $^3He^+$ ions, the reactions of interest are highly exoergic, resulting in the emission of energetic prompt gamma rays where background interference is much reduced. The analytic potential of lower energy gamma rays has already been evaluated [6].

[1] Department of Chemistry, University of the Witwatersrand, P.O. Wits, 2050 South Africa.

2. Experimental

2.1. Materials for analysis

Targets of boron and carbon were prepared by compressing powders in a 10 ton press to produce tablets of 13 mm diameter and about 2 mm thickness. Targets of oxygen and nitrogen were similarly prepared by using powders of Y_2O_3 and GaN or BN respectively. The heavy element component in these targets were not expected to interfere since the calculated Coulomb barriers [7] for Y and Ge were about 15.6 and 31.2 MeV respectively, which was far in excess of the energy used for the investigation (see below). In addition, a target disc of Al was bombarded, because the beam tube and scattering chamber material consisted mainly of aluminium, from which a background of gamma rays was expected.

2.2. Irradiation and measurement

Targets were mounted on a remote-controlled vertical ladder, that operated through a geared stepping motor at the rate of 150 steps per mm, which enabled each target to be mounted with a precision of about 7 μm. The ladder fitted into a multipurpose scattering chamber [8], where a constant geometrical arrangement of target and detector was rigidly maintained. Beams of 2 MeV $^3He^+$ were obtained from the 6 MV Van de Graaff accelerator at Faure, and beam currents were adjusted so that the dead time of the entire counting assembly did not exceed 10%. Gamma-ray spectrometry was carried out with a 80 cm^3 Ge(Li) detector mounted outside the scattering chamber at 45° to the bombarding beam, where the aluminium chamber wall was thinned to reduce absorption of low

0168-583X/92/$05.00 © 1992 – Elsevier Science Publishers B.V. All rights reserved

energy radiation. In an attempt to reduce the background due to the interaction between scattered particles and the aluminium walls of the scattering chamber, a Perspex sleeve, perforated to allow entrance to the beam, was mounted around the target assembly. Data were recorded on magnetic tape and processed off-line.

3. Results and discussion

Energetically, all (^{3}He, γ), (^{3}He, n), (^{3}He, p), (^{3}He, d) and (^{3}He, α) reactions on the stable isotopes of boron, carbon, nitrogen and oxygen are possible, with a bombarding beam of 2 MeV ^{3}He ions, with the exception of ^{12}C(^{3}He, d)^{13}N, ^{16}O(^{3}He, n)^{18}F and ^{16}O(^{3}He, d)^{17}F, which are endoergic with $Q < -3$ MeV. Because most reactions are highly exoergic, the reaction products are produced from highly excited states with the result that the gamma ray spectra are complex. The high energy prompt gamma rays which have analytical potential are those for which interference from other matrix components is unlikely. Since the Coulomb barrier [7] reaches about 3 MeV for $Z = 10$ (neon) the main interferences are likely to come from the light elements themselves, or from secondary nuclear effects generated by the very energetic protons and alpha particles produced in the reactions with the light elements under investigation.

3.1. Boron

The high energy region of a typical gamma ray spectrum obtained from the bombardment of a boron target is shown in fig. 1. In this and subsequent figures, the gamma rays are labelled according to the Chemists' Convention, which lays most stress on the target nuclide [9]. The most prominent peak in the spectrum is due to the Doppler-broadened 4450 keV gamma ray from the Coulomb excitation of boron-11. Since the Q-values for the (^{3}He, p) and (^{3}He, α) reactions on boron-11 are very high (13.185 and 9.122 MeV respectively) and the corresponding reactions on boron-10 have even higher Q-values, a flux of high energy particles is generated within the boron target. Under these conditions, Coulomb excitation occurs producing the 4450 keV gamma rays. Other relatively intense gamma rays are those from the reaction ^{11}B(^{3}He, p)^{13}C. The spectrum is complicated by the escape peaks, but even these may be used for analyses.

3.2. Carbon

Fig. 2 shows the high energy region of the gamma ray spectrum obtained from the bombardment of graphite. The most prominent peaks are due to the 5106 keV ^{12}C p(4, 0) gamma rays. From the same reaction, the 4915 keV ^{12}C p(2, 0) gamma rays were detected, while the other prominent peak is due to the 2799 keV ^{12}C α(3, 1) gamma ray. The importance of

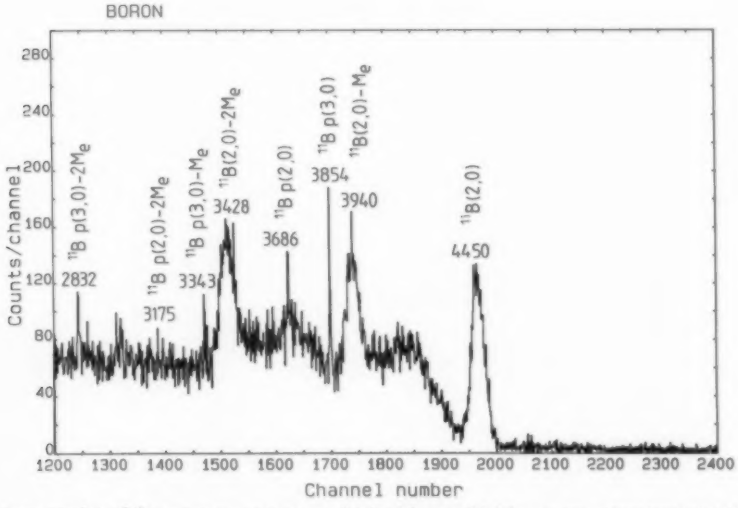

Fig. 1. The high energy portion of the gamma-ray spectrum obtained from a thick boron target bombarded with 2 MeV ^{3}He$^+$ ions.

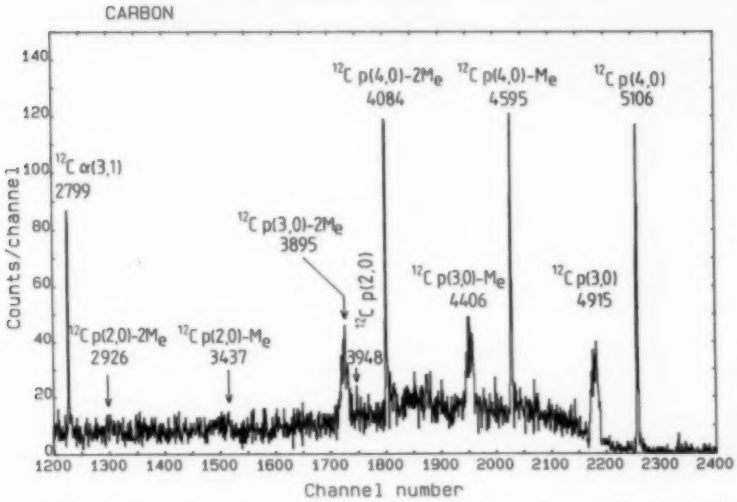

Fig. 2. The high energy portion of the gamma-ray spectrum obtained from a thick target of graphite bombarded with 2 MeV $^3He^+$ ions.

the relatively intense gamma rays lies in the fact that they can be measured without interference.

3.3. Nitrogen

While several low energy gamma rays are suitable for analysis [6], the only prominent peaks due to nitrogen are those due to the 6130 keV ^{14}N p(2, 0) gamma rays, as is shown in fig. 3. A very low intensity peak was observed from the 6917 keV ^{14}N p(3, 0) gamma ray, which may be useful for analysis when high energy $^3He^+$ ions are used. The importance of the 6130 keV gamma ray lies in the fact that the background against which it has to be measured is very low.

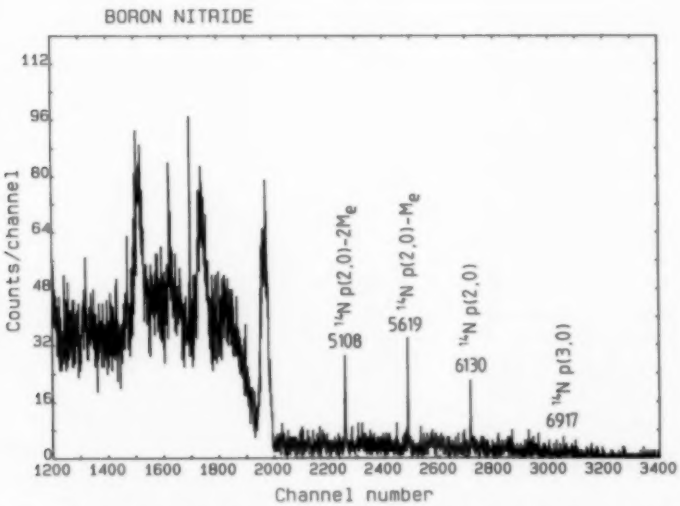

Fig. 3. The high energy portion of the gamma-ray spectrum obtained from a thick target of boron nitride bombarded with 2 MeV $^3He^+$ ions. Peaks due to boron have not been labelled.

Table 1
Analytically useful ^{3}He-induced prompt high energy gamma rays

Target element	E_{γ} [keV]	Assignment	Sensitivity [gmC]
Boron	3684	^{11}B p(2, 0)	37 mg
	3854	^{11}B p(3, 0)	17 mg
	4450	^{11}B (2, 0) [a]	1.8 mg
Carbon	2799	^{12}C α(3, 1)	10 mg
	3948	^{12}C p(2, 0)	75 mg
	4915	^{12}C p(3, 0)	5.2 mg
	5106	^{12}C p(4, 0)	3.1 mg
Nitrogen	6130	^{14}N p(2, 0)	20 mg
	6917	^{14}N p(3, 0)	47 mg
Oxygen	nil		

[a] Coulomb excitation by secondary radiation.

3.4. Oxygen

No high energy gamma rays were observed from the bombardment of yttrium oxide. However, low energy gamma rays, mainly from the reaction $^{16}(^{3}He, p)^{18}F$ have been suggested as of use for analysis [6].

3.5. Sensitivities

Table 1 lists the main high energy gamma rays observed from thick targets bombarded with 2 MeV $^{3}He^{+}$ ions. The sensitivity attainable with each listed radiation was calculated as the weight of element which will produce a signal equivalent to about 3.29 times the square root of the background value over that energy region [10]. Obviously the sensitivity will be a function of the integrated beam current. The values given in table 1 were calculated for 1 mC. Under such conditions, and using the gamma ray which gives the best sensitivity for each element, concentrations of B, C and N greater than a few parts per thousand can readily be determined without interference.

Table 2
Carbon content of some standard steels

Steel	Counts [μC]	Carbon content [%]			Relative error [%]
		Known	Found	Error	
1262	2.14 ± 0.40	0.160	0.183	+0.023	+14.4
1263	3.97 ± 0.45	0.62	0.541	−0.079	−12.7
1264	5.92 ± 0.81	0.870	0.920	+0.050	+5.9

3.6. Steel analysis

Standard reference materials Low-Alloy Steels 1262, 1263 and 1264 obtained from the U.S. National Bureau of Standards, Washington, DC, were analysed for their carbon content. Because the matrix elements had high Coulomb barriers towards the low energy $^{3}He^{+}$ beam, the gamma-ray yield from the samples was low and beam currents of up to 100 nA could readily be used. Fig. 4 shows a typical spectrum from a steel sample, in which the carbon lines were observed at a level of

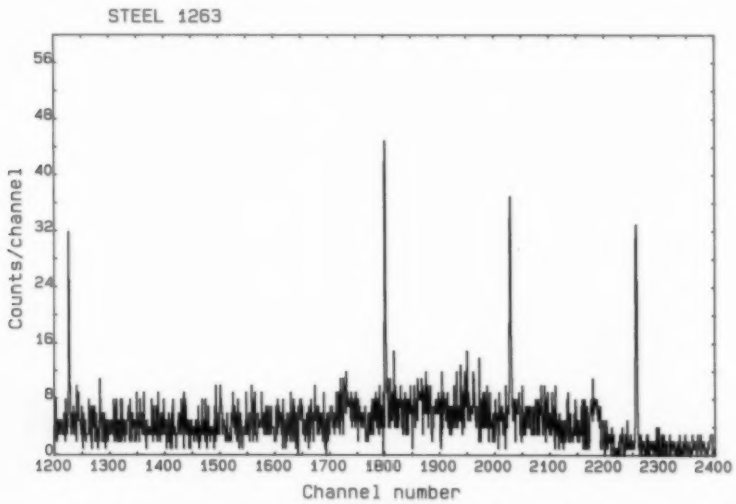

Fig. 4. The high energy portion of the gamma-ray spectrum obtained from the reference standard Low-Alloy Steel 1263 containing 0.62% C by mass, showing the prominent peaks due to carbon.

0.62% by mass. The results of analyses of the steels, using the combined areas under the three peaks from the 5106 keV gamma ray, are given in table 2. The error ranges refer to 2σ errors based on the counting statistics only. The analyses were acceptably accurate, with a relative precision of about 11% as given by the relative root mean square error.

4. Conclusion

The potential for analysis of the high energy prompt gamma ray excited by 2 MeV $^3He^+$ ions has been evaluated for the light elements B, C, N and O. Boron, carbon and nitrogen yielded gamma rays of practical importance. The application of the technique to high purity metallurgical matrices has shown that the method is adequate for quantitative analysis at minor concentration levels, in thick samples containing a homogeneous distribution of the element under consideration. The sensitivity could be improved through the use of a more efficient detector.

References

[1] H. Willard, L. Merritt, J. Dean and F. Settle, Instrumental Methods of Analysis (Wadsworth, Belmont, California, 1988) p. 226.
[2] C. Olivier and M. Peisach, J. Radioanal. Chem. 49 (1979) 265.
[3] I.S. Giles and M. Peisach, J. Radioanal. Chem. 50 (1979) 307.
[4] D. Gihwala, Analytical Application of Proton-Induced Prompt Photo Spectrometry, Ph.D. Thesis, University of Cape Town (1983).
[5] A.E. Pillay, Application of Nuclear Methods to Chemical and Isotopic Analysis, Ph.D. Thesis, University of London (1982).
[6] A.E. Pillay and M. Peisach, Proc. Int. Conf. on Activation Analysis and its Applications, Beijing, China, October 1990, to be published in J. Radioanal. Nucl. Chem. (1992).
[7] J.B. Marion and F.C. Young, Nuclear Reaction Analysis (North-Holland, Amsterdam, 1968) p. 108.
[8] I.S. Giles and M. Peisach, J. Radioanal. Chem. 32 (1976) 105.
[9] M. Peisach, J. Radioanal. Chem. 12 (1972) 251.
[10] L.A. Currie, Anal. Chem. 40 (1968) 586.

Nuclear Instruments and Methods in Physics Research B66 (1992) 48–50
North-Holland

Nuclear Instruments & Methods in Physics Research
Section B

Ion microbeam analysis with superconducting AMS minicyclotron as the analyzing instrument

K.M. Subotic [a], M.K. Pavicevic [b] and D. Novkovic [a]

[a] *Boris Kidrich Institute, P.O.B. 522, 11001 Beograd, Yugoslavia*
[b] *Faculty of Mining and Geology, Laboratory for Electron Microanalysis, P.O.B. 241, 11001 Beograd, Yugoslavia*

The advantages of the usage of the cyclotron based accelerator mass spectrometer (AMS) as an analyzing instrument in the characterization of materials are discussed. Superconducting minicyclotron design criteria leading to the improvement of the analytical sensitivity and isotope resolution are considered. In particular the detection limits of Be and C measurements are discussed.

1. Introduction

The sensitivity and resolution demonstrated by accelerator mass spectrometry (AMS) in the areas of archeological and geological dating make the use of this technique for the characterization of materials, bulk analysis and depth profiling extremely attractive. This paper discusses the possible improvements of the use of the superconducting minicyclotron in characterization methods as the AMS analyzing instrument [1].

Conventional secondary ion mass spectrometry (SIMS) is extensively used for these purposes. In SIMS oxygen (cesium) ions are used for sample sputtering to produce positive (negative) ion currents from the sample. Due to the inefficient phyical basis of the phenomena determining SIMS detection limits, tandem AMS data, when compared with those from SIMS measurements for the characterization of semiconductor materials [2], show 10–100 times better sensitivities.

Tandem based AMS implies the usage of the negative ion primary beam. Cyclotron based AMS, however, enables the use of both the positive and negative ion primary beams. Positive ion techniques produce more intense beam currents as well as much higher ion charge states, imposing much lower rigidity demands. The background-free extraction of the in-phase beam component combined with aforesaid features gives the possibility to attain significantly higher sensitivities.

Fig. 1 shows the principle of the instrument for ion microbeam analysis with a superconducting minicyclotron. Ion source system (1) produces either positive or negative ions of different gases accelerated up to energies of 20 keV which bombard the investigated sample (2). The ion-optical system enables to adjust the beam diameter from 1 to 500 μm on a sample, producing ion currents for the sample ranging from several to fifty mA/cm^2. Inspection of spots that have to be analyzed can be made using an optical microscope (3). The ion-optical system (4) transfers the spattering ions through the axial injection line (5) and a spiral inflector (6) into the superconducting minicyclotron (7).

The cyclotron as an AMS rejects non-resonant particles due to the phase slip induced by mass differences of the beam constituents. The mass resolution $R = m/\delta m$ is proportional to the product of the harmonic number of the applied rf frequency and the number of executed cyclotron turns necessary to resolve the resonant particle trajectory from the non-resonant background.

A small low energy cyclotron, in the conventional room temperature version, has been designed and built at Berkeley [3] for the detection and dating of ^{14}C. The required mass resolution criteria are easily satisfied with such a machine. However in order that ^{10}Be and ^{10}B measurements could be made avoiding the isobar interference, the mass resolution should be increased by an order of magnitude. High field settings available only in superconducting cyclotron magnetic fields should be used to achieve this goal. The superconducting minicyclotron project is under development at the Nuclear Physics Laboratory in Belgrade [4]. Evaluation of the most essential performances of the AMS superconducting minicyclotron used as an analyzing instrument for characterization purposes is reported here.

2. Cyclotron AMS

Ions that have to be analyzed are produced in an external ion source, and axially injected into the cy-

0168-583X/92/$05.00 © 1992 – Elsevier Science Publishers B.V. All rights reserved

clotron median plane. The trajectories of the ions of mass $m = \gamma m_0$, charge q and impuls p in the homogeneous cyclotron magnetic field, whose center of symmetry coincides with the machine center, are stable circular equilibrium orbits of radius $r = p/qB$. The frequency of the particle motion along these orbits, $\omega = qB/m$, is constant, determined at a given field value only by the particle q/m ratio.

Cyclotrons are inherently high mass resolution devices. When tuned for a given atomic mass, they are detuned for isobars and molecules of the same atomic mass number but different true masses, due to the acceleration phase slip. Principles of cyclotron based AMS are determined by the phase slip equation.

If we have a two-component beam and the rf frequency is tuned for the q/m ratio of one of the components, the other beam component will experience a phase slip, Φ, determined by

$$\sin \Phi = 2\pi h n \frac{df}{f}$$

$$= 2\pi h n (dq/q + dB/B - dm_0/m_0 - d\gamma/\gamma), \quad (1)$$

where h is the harmonic number, n the number of executed particle turns, f the eigenfrequency of the reference beam component and df the difference of the beam eigenfrequencies of the beam components. After executing the sufficient number of orbits at the given harmonic of the rf field, the out-of-phase beam component will experience a phase slip higher than 90°, will be decelerated and fall toward the machine

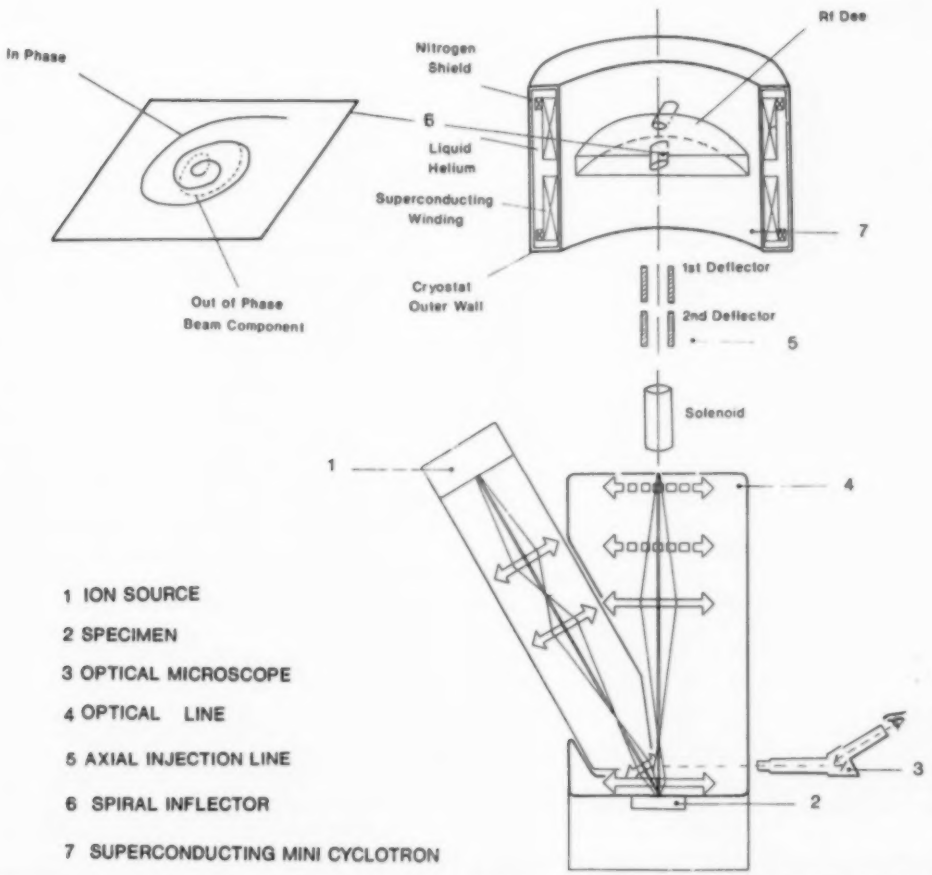

Fig. 1. Schematic representation of the principle of work of the system for ion microbeam analysis with an AMS superconducting minicyclotron as the analyzing instrument.

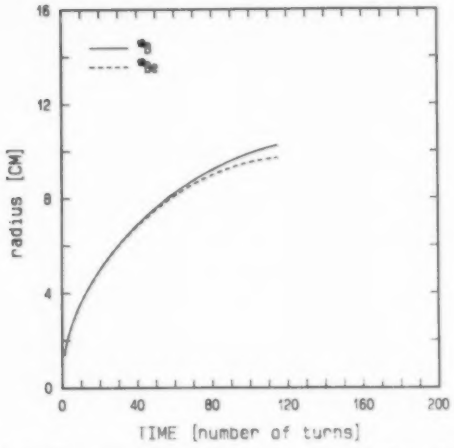

Fig. 2. Changes of the orbit radius as a function of the executed number of turns for the $^{10}B^{1+}$ and $^{10}Be^{1+}$ ion species at a field of 3.1 T, requiring a resolution R of 17000. Trajectories which may not be discriminated at a field level of 1.08 T are resolved at 3.1 T after 120 turns of the mass-10 ion species.

center. The in-phase beam component, however, may be accelerated up to the energies suitable for extraction and particle identification.

3. Device resolution and detection limits

An AMS dedicated cyclotron characterized by a high resolution $R = \pi hn$ value may have a small radius (in the 10–20 cm range). Operating the superconducting cyclotron magnet in the persistent mode the only power consumption would be that used to operate the rf accelerating system and the ion source. The demand for high particle turn number means very low rf power requirements. The relaxed design criteria for dee structure may be employed and cheap commercial components in power supply circuits may be used. The relevant design parameters of an AMS superconducting minicyclotron are given elsewhere [4].

The number of particles that can be safely transmitted depends on the maximum beam current determined by the cyclotron space charge limit:

$$I_0 = \epsilon_0 A\omega \frac{h^2 \sin \Phi}{4R} \frac{\mathrm{d}\Phi \, \mathrm{d}E}{2\pi q},$$

where ϵ_0 is the permitivity, A the full beam aperture, $\mathrm{d}\Phi$ the beam phase width and $\mathrm{d}E$ the energy gain per turn.

Cyclotron orbit calculations are used to establish the dependence of the device resolution power on the applied cyclotron magnetic field. Numerical calculations for ^{14}C, $^{13}CH^-$ and $^{12}CH_2^-$ ions show that respective trajectories may be discriminated in an AMS minicyclotron at a field of 1.08 T. However the final energy of 42 keV for ^{14}C at this field level is not high enough to make the detection of ^{14}C nuclei and the background species in standard nuclear detectors feasible [4].

Table 1
Analyzing performance

Cyclotron resolution	$\mathrm{d}f/f = \pi nh = 100000$
Secondary beam current	$2\mu A = 1.2 \times 10^{13}$ p/s
Cyclotron transparency	10%
Detection limit	$D_0 = 10^{-12}$ at 3% statistics in 10^3 s
Detection limit	$D_1 = 10^{-16}$ at 20% statistics in 24 h

Fig. 2 depicts the results of orbit caculations for ^{10}Be and ^{10}B ions accelerated with harmonic number $h = 5$ at a field of 3.1 T in a superconducting minicyclotron with injection radius $r = 2.66$ cm and extraction radius $r = 10$ cm.

Numerical calculations demonstrate that the unavoidably present isobar interference problems in the case of ^{10}B and ^{10}Be detection may be solved by accelerating these ion species in a sufficiently high cyclotron field. Trajectories which may not be discriminated at the conventional cyclotron field level of 1.08 T are easily resolved at 3.1 T. The required mass resolution R of 17000 is attained after 120 turns of the mass 10 ion species.

The maximum intensity ratio of in-phase I and out-of-phase I_0 cylotron beam components is determined by

$$I/I_0 = [N/N_0]_c,$$

where $[N/N_0]_c$ is the ratio of the respective concentrations in the analyzed sample.

The cyclotron charge space limit calculations show that at 10% cyclotron transparency, an internal current of $2\mu A$ may be easily achieved. The respective evaluations of detection limits of the SIMS method in which an AMS superconducting minicyclotron is used as the analyzing instrument are given in table 1.

References

[1] K.M. Subotic and M. Pavicevic, Proc. 2nd Europian Workshop EMAS'91, Dubrovnik, 1991, in press.
[2] J.M. Anthony and D. Donahue, Nucl. Instr. and Meth. B29 (1987) 77.
[3] K.J. Bertsche at al., Nucl. Instr. and Meth. B29 (1987) 105.
[4] K.M. Subotic et al., Nucl. Instr. and Meth. B50 (1990) 267.

Nuclear Instruments and Methods in Physics Research B66 (1992) 51–64
North-Holland

Nuclear Instruments & Methods in Physics Research
Section B

Twenty years of analysis of light elements at the LARN

Guy Demortier

Laboratoire d'Analyses par Réactions Nucléaires (LARN) and Institute for Studies in Interface Sciences (ISIS), Facultés Universitaires Notre-Dame de la Paix, 22 Rue Muzet, B-5000 Namur, Belgium

We review the applications of ion beam analysis of light elements performed in the LARN during the last twenty years.

The works mainly concern: helium bubbles in aluminum foils, Li in aluminum alloys, carbon in high purity MgO crystals and in olivines, nitrogen bubbles in glass and implanted nitrogen in iron and aluminum, oxygen in YBaCuO superconductors, fluorine in tooth enamel and implanted fluorine in metals.

1. Introduction

Set up in 1969 by a staff directed by Professor G. Deconninck, the LARN has been involved in analytical studies of many elements and particularly of light ones. Various accelerator based methods have been developed and progressively improved to achieve better limits of detection and sensitivity: they include resonant and nonresonant nuclear reactions, (p,γ), Rutherford and non Rutherford backscattering. The laboratory is equipped with a 3 MeV Van de Graaff accelerator (delivering four beam lines specially equipped for PIGE, PIXE, RBS, microprobe and an external beam), and a 300 keV accelerator initially used for fast neutron activation analysis and now converted for ion implantation. A Mössbauer spectrometer is routinely used for the chemical characterization of iron compounds. Table 1 summarizes the references of works on light elements published by members of the laboratory since 1972. Extensive measurements of He, Li, C, N, O, F, Ne have been performed in various fields: biology, medicine, glasses, metals and alloys; Be and B were scarcely studied.

Experimental works in these fields were performed during Ph.D. theses at the Facultés Universitaires of Namur: J. Baijot, G. Debras, S. Van Den Broek, A Lefebvre, M. Piette and S. Lucas under the supervision of Prof. G. Deconninck, Prof. F. Bodart and Dr. G. Terwagne, and also presented at the University of Köln: H. Wengeler, G. Oberheuser, H. Kathrein and R. Knöbel under the supervision of Prof. F. Freund and Prof. G. Demortier.

General information on the physical methods of analysis developed at the LARN may be found in the book by G. Deconninck [1] and in a review paper on PIGE published by the IAEA [2].

Numerous measurements have also been performed on industrial materials and are only recorded in confidential reports. Detailed LARN reports are regularly edited: they contain data usually not included in published works.

2. Helium bubbles in metals

The behavior of inert gases implanted into metal surfaces has been a subject of interest particularly since the importance of gas–metal interactions in the fusion reactor first wall was recognized. In this context, the study of the formation of helium bubbles, in He irradiated materials with the subsequent blistering and flaking of the bombarded surface, gained importance.

From the point of view of blister formation, many authors suggested that the formation of surface blister-

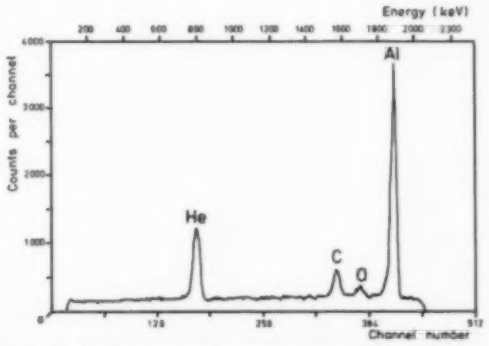

Fig. 1. Typical proton backscattering spectrum for a 55.5 μg cm^{-2} aluminum film containing 2.65 at.% He (proton energy: 2.2 MeV; backscattering angle: 150°) [3].

0168-583X/92/$05.00 © 1992 – Elsevier Science Publishers B.V. All rights reserved

Table 1
Ion beam analysis of light elements; experimental parameters and fields of application

	Reaction	Energy [MeV]	Matrix	Analytical results		Refs.
				Major and minor elements	Traces	
Helium	resonant BS	2.2	Al		implanted He	[3,4]
Lithium	(p,γ) and (p,α)	various	Al	special phases		[5,6]
	(^{3}He,γ)	2.0	metals	1%		[7]
	(p,γ)	2.0	minerals	ion exchange		[8]
	(p,γ)	various	metals	×	×	[9]
Beryllium	(^{3}He,γ)	2.0	metals	1%		[7]
Boron	(^{3}He,γ)	2.2	metals	×		[7]
	(p,α)	0.5–0.8	glass		×	[10–12]
	(p,α)	0.45, 0.7	biological		×	[13]
Carbon	(^{3}He,γ)	2.2	metals	1%		[7]
	(p,γ)	0.47	metals	1%		[7,12]
	(d,p)	1	glass		×	[11,12]
	(d,pγ)	2.5	biological	×		[11,25]
	(d,p)	1.0–1.8	MgO		profiling	[14–19]
	(d,p)	1.0–1.8	olivine, CaO, SrO		profiling	[20,21]
	RBS α	2.4	biological	×		[22]
	RBS α	2.4	iron			[23]
	(p,γ)	0.5	biological	×		[24,25]
Nitrogen	(p,αγ)	⩾ 1.8	biological	×		[12,13,23,24]
	(d,pγ)	2.5	biological	×		[16,26]
	(d,α)	1.0	glass		×	[27,28]
	^{14}N(α,γ)	1.531	iron		N implanted	
	^{15}N(p,αγ)	0.429	iron		N implanted	[29–31,34]
	^{15}N(p,αγ)	0.429	AlN		N implanted	[35–40]
Oxygen	(^{3}He,γ)	2.2	metals	×		[7]
	(p,γ)	2.2–2.7	biological	×		[11,12,24]
	(d,p)	1.0–2.0	glass	×		[11,27]
	RBS α	2.4	biological	×		[22]
	RBS α	2.4	iron		×	[23]
	(d,p)	2.0	YBaCuO	microprobe		[43]
	RBS α	2.0	YBaCuO	×		[45]
	(d,p)	2.0	zeolites	×		[46]
	(d,p)	2.0	gold alloys			[47]
Fluorine	(p,γ)	various	teeth	×	×	[10,45,46]
	(p,γ)	2.0	teeth and chemicals]	×	×	[12,41,54,56,57]
	(p,αγ)	2.0, 2.2	biological		ppm	[13,24]
	RBS α	2.0	iron		implanted	[23]
	(p,γ)	0.935	glass	profiles		[28]
	(p,αγ)	0.34	iron		implanted	[32,55]
	(p,αγ) and (p,γ) (p,γ)]	2.0	teeth		×	[48,51,53,54]
	(p,αγ)	0.87	iron		implanted	[55]
	(p,γ)	various		WD spectroscopy		[58–60]
Neon	(p,γ)	1.170	iron		implanted	[32]
	(α,X-rays)	2.8	Al		implanted and WD spectrometry	[61–63]

×: Elemental analysis (bulk)

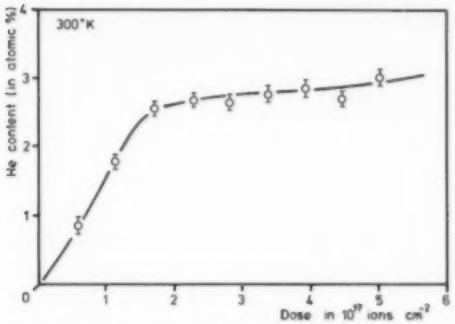

Fig. 2. Retention curve for helium implantation at room temperature in a 55 $\mu g\ cm^{-2}$ Al foil [4].

ing on metals is explained by coalescence of small helium bubbles (1–2 nm in diameter); the condition for coalescence being satisfied when the bubbles are large enough to touch. The internal pressure in the resulting bubble increases for each coalescence to a value where deformation of the material can be seen and creates blisters.

The atomic concentration of helium retained was measured by proton backscattering with a beam energy of 2.2 MeV. The sensitivity for helium is sufficient to measure as little as 0.2 at.% He in reasonable measuring times. The choice of the proton energy is important because at 2.2 MeV there is an elastic resonance for proton scattering on helium ($^4He + p \rightarrow {}^5Li^* \rightarrow {}^4He + p$) which causes an enhancement of the scattering cross section by a factor of 400 as compared to the Rutherford value. A typical backscattering spectrum for a specimen containing 2 at.% He is shown in fig. 1.

By using the proton microbeam facility, it was possible to measure the lateral variation of helium concentration with a spatial resolution of $3 \times 3\ \mu m^2$ at the

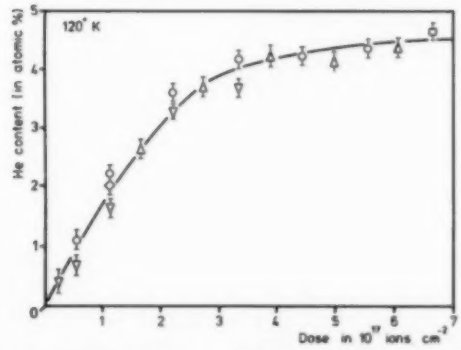

Fig. 3. Retention curve for helium implantation at 120 K (implantation and backscattering carried out at 120 K): (○), (△), and (▽) correspond to different specimens [4].

surface of helium implanted Al foils where blisters of 10 μm or less are present [3,4].

Fig. 2 illustrates the retention curve for helium implanted at 5 keV, normal incidence, into an aluminum film with a mass thickness of 55.5 $\mu g\ cm^{-2}$ at room temperature. The dose rate was 2.5×10^{14} ions $cm^{-2}\ s^{-1}$. Even at doses well below saturation, the gas retention is fairly low. In this case it is only 19% of the incident dose. By cooling the sample down to 120 K the retention rises up to a maximum of 30% (fig. 3). Various complementary techniques have been used to explain [3] the diffusive process of helium after implantation.

3. Al–Li alloys

Depending on the alloy composition, numerous constituent particles are likely to be present in complex ternary or quaternary Al–Li alloys for aerospace applications. Beside the phase recognition and the structure determination by X-ray and electron diffraction, the study of the composition of such intermetallic compounds for the establishment of complex equilibrium phases diagrams needs a combination of microanalytical techniques. Conventional techniques (SEM, EPMA) routinely performed in an industrial laboratory using secondary X-ray emission cannot detect Li due to the associated high wavelength. However, micrographs using backscattered electrons (BSE) in the SEM give a mean atomic number contrast and may indicate the possible presence of Li. This contrast can also be quantitatively exploited by densitometry. Complementary methods are necessary to detect, visualize and analyze Li in phases.

Qualitatively, SIMS offers the ability to visualize Li in combination with any other element in solid solutions or in intermetallic phases. Due to the important matrix effects at high concentration (> 1%), the quantification is difficult if standard samples of similar composition are not available. Quantitative microanalysis of major elements, particularly Li, can be performed with a high accuracy with a nuclear microprobe.

Nuclear reactions: $^7Li(p,p'\gamma)^7Li$ and $^7Li(p,\alpha_0)^4He$ have been used to determine the Li loss profile in the superficial region of Al–Li sheets, i.e. essentially in the solid solution.

For characterization of (Al–Li–Zn) alloys we chose the 472 keV γ-rays from Li nucleus excitation, the 843 and 1013 keV γ-rays for Al and the 8.6 and 9.6 keV K X-rays from Zn (all included by 2.8 MeV protons in the first 5–8 μm under the irradiated surface) as characterization signals. The depth at which they are produced and their energies allow us to certify the negligible absorption of these photons in this light Al

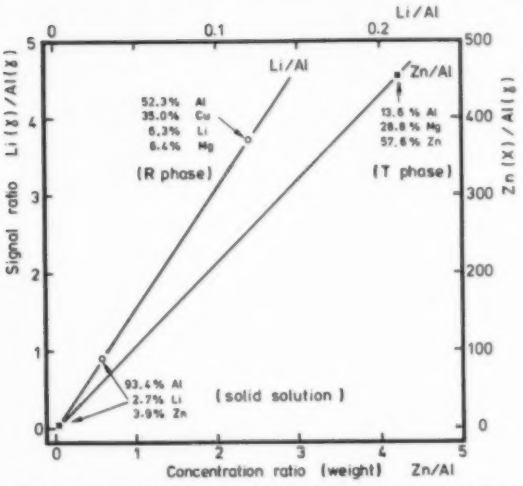

Fig. 4. Linear variation of the signals detected in the analysis of Li and Zn in aluminum using a nuclear microprobe vs concentration ratio. The bulk composition of samples is given for each point [6].

matrix [5]. For three reference samples, fig. 4 illustrates the variation of the normalized signals Li/Al and Zn/Al versus the corresponding concentration ratios. As expected, the γ-signals of Li and Al, and X-signals of Zn vary linearly with the concentration. The line passes through the experimental points and through the origin [6]. A comparison of SIMS and nuclear microprobe results for the study of the depleted Li concentration at both faces of a 3 mm thick Al–Li (3%) sheet is given in fig. 5.

Other measurements of Li in metals and minerals (after ion exchange experiments) have also been performed by (p,γ) and (^{3}He,γ) reactions [7–9].

Determinations of Be in alloys [7], boron in glasses [10–12], metals [7] and biological materials [13] have also been reported.

4. Carbon in high-purity alkaline earth oxide single crystals

Supposedly high-purity MgO, CaO and SrO single crystals, grown by the submerged arc fusion method, were found to contain carbon up to 10000 ppm at the surface, probably atomically dissolved in the oxide lattice. Carbon was nondestructively analyzed by means of the nuclear reaction $^{12}C(d,p)^{13}C$ using 1.0 or 1.7 MeV deuterons. Concentration profile analyses (using the proton spectroscopy in nonresonant reactions) indicate that the carbon content near the surface is much higher than in the bulk. Heating the crystals in air to 800°C increases the carbon content in the upper 1–5 μm surface layer and decreases it in the bulk. Heating in vacuum leads to soot formation at the surface and carbon depletion inside the crystals. Special care was taken to avoid accumulation of carbon arising from oil vapours of the pumping system during the nuclear analysis. Two gold foils with a total thickness of 1.2 mg cm^{-2} were installed at 20 cm in front of the target. These foils collect all the molecules trapped in a deuteron beam tube 8 m long. Additionally, a collector cylinder at liquid nitrogen temperature between the Au foils and the target ensures condensation of residual oil vapours [14–16].

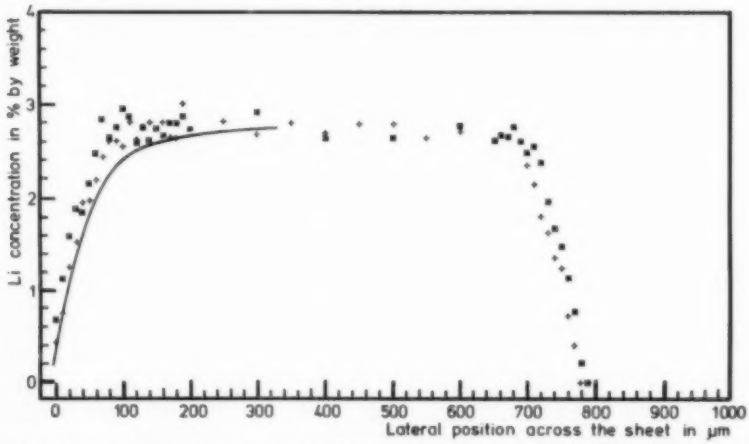

Fig. 5. Comparison of nuclear microprobe (■ and +) and SIMS (full line) for the analysis of lithium concentration across an Al–Li sheet (790 μm thick).

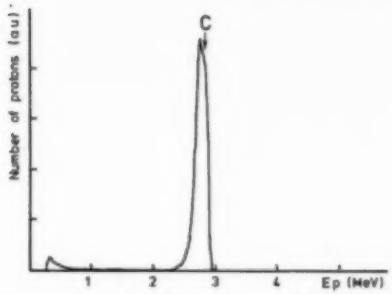

Fig. 6. Proton spectrum obtained by irradiation of a graphite sample with 1 MeV deuterons [16].

The selection of the incident deuteron energy and the position of the surface barrier detector were dictated by interferences with other nuclear reactions induced in the major elements in the sample: mainly Mg in the case of MgO samples. Figs. 6 and 7 show that the p_0 peak on C (at surface) coincides with the p_6 peak on ^{24}Mg. The limit of sensitivity for C identification in MgO lies around 50 μg/g (fig. 8).

The usable depth range for carbon analysis in MgO lies around 4 μm. In CaO and SrO the incident deuteron energy may be raised to 1.7 MeV to increase the depth to analyze. No nuclear reactions on Ca and Sr intrefere due to the large Coulomb barrier of these high Z nuclei. At 1.7 MeV, the spectrum is no longer a single asymmetrical line as with 1.0 MeV deuterons, but has a more complex structure due to variable cross sections. However, the $^{16}O(d,p_0)^{17}O$ reaction cannot be avoided with either 1.0 or 1.7 MeV deuterons. This reaction limits the depth range to 6 μm in CaO and SrO [17,18].

In MgO, carbon sets up steep concentration gradients in the 0–1 μm subsurface layer. It disappears and reappears as a function of heat treatments between 300 and 1170 K in ultrahigh vacuum [19]. By heating in O_2 carbon can be burnt out of the subsurface zone, but

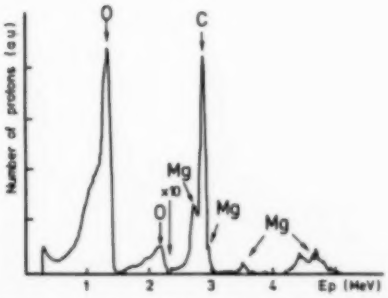

Fig. 7. Proton spectrum obtained by irradiation of a MgO sample (0.8% C at surface) irradiated with 1 MeV deuterons [16].

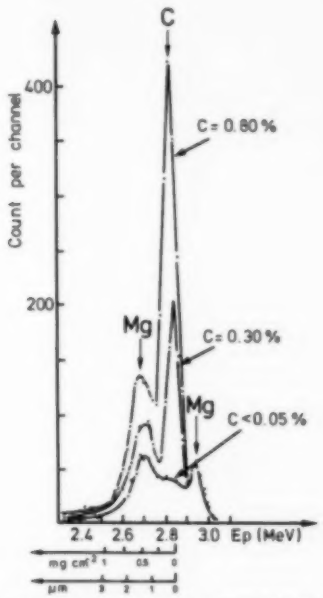

Fig. 8. Selected regions of proton spectra obtained by irradiation with 1 MeV deuterons of 3 MgO samples containing various concentrations of carbon at the surface [16].

upon isothermal annealing at 470 K, carbon starts to diffuse from the bulk back into the subsurface zone within minutes, giving rise to fluctuating concentration variations which last for hours with periodicities of about 45 min. After quenching samples previously heated in O_2 to 80 K and reheated linearly at 2 K/min, the onset temperature of carbon mobility was found to be as low as 140 K. From these experiments and other techniques listed in refs. [14–19], it is concluded that carbon is atomically dissolved in the MgO. The C atoms probably occupy extrinsic cation vacancies introduced in the MgO by co-dissolved "water", but at the same time they must also be on interstitial sites where they acquire an extremely high mobility.

Similar behavior has been observed in other alkaline earth oxides and in natural olivines [20,21].

Carbon subsurface concentration profiles in olivine single-crystals from San Carlos, Arizona, and the Sergebet Island, Red Sea, containing total carbon between 60–180 wt. ppm, were analyzed by means of the $^{12}C(d,p)^{13}C$ nuclear reaction and by X-ray induced photoelectron spectroscopy (XPS) in combination with acid etching and with Ar^+ ion sputtering respectively, between 200–930 K. The (d,p) analysis reveals equilibrium subsurface C profiles extending on 1–2 μm or more in the bulk. Their steepness is function of temperature. Typical mean C concentrations at 300 K in the resolvable sublayers from 0 to 1.2 μm decrease

from 1.8 and 0.6 wt.%, corresponding to an enrichment factor over the mean bulk C concentration of 30–100. In the topmost atomic layers also analyzed by XPS, carbon appears to be enriched by a factor of the order of 1000 and decreases with rising temperature. These results suggest that the carbon is in a truly dissolved state, highly mobile and subject to a reversible subsurface segregation.

RBS, (^{3}He,γ), (p,γ) and (d,pγ) reactions on carbon have also been used to measure the progressive degradation of biological materials studied for ion exchange [22], bulk concentration in alloys [7,12,23], certification of the total composition of a biological reference material [24,25], and determination of C/N ratio in protein rich biological specimens [11,26].

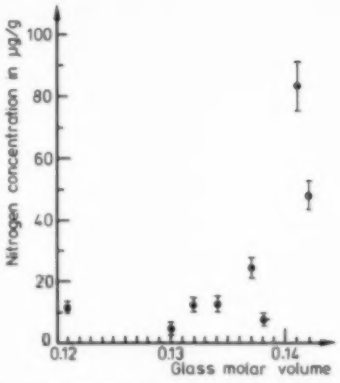

Fig. 9. Nitrogen concentration in a glass as a function of the binding number of oxygen (Y) by unit of molar glass volume (V_m) [27].

5. Nitrogen in glasses and implanted in metals

The problem of gaseous inclusions and bubbles is very important for glass manufacture since the objective has always been to obtain bubble-free glass. It has been shown that nitrogen gas was a predominant component of defects. Additionally the refining process consisting in eliminating gaseous inclusions requires high temperature as a consequence on acceleration of this phase results in energy economy. The structure of glass is characterized by its random network of silicon oxygen tetrahedra. Holes of different sizes are present in this structure. These holes are often found filled with glass. Relatively large amounts of nitrogen can be chemically dissolved in glass under suitable experimental conditions. Chemically dissolved nitrogen may exist in glass melts mainly as nitrogen–hydrogen groups and dissolved nitrides.

The industrial methods commonly used for the identification of dissolved nitrogen in glass are hot extraction followed by gas chromatography or mass spectrometry for physical solubility, hot extraction and chemical analysis (Kjeldahl method) after dissolution of glass in hydrofluoric acid for chemically dissolved nitrogen. These methods allow us to distinguish the two forms of solubility; however they are destructive. Gas absorption by evaporated alkalis is a limitation for these methods.

Prompt nuclear methods involving deuteron beams for trace analysis of nitrogen in glass have several advantages: they are nondestructive, have a high sensitivity, and may give information in the μm range in 3D with microbeams, but cannot distinguish between the two forms of solubility. G. Debras has used the following experimental conditions [11,27,28].

The main characteristics are:

(a) Nuclear reaction: $^{14}N(d,\alpha_0)^{12}C$, α-particles detected at 135°.
(b) Incident particle energy of 1.55 MeV: for low energies, high-Z nuclei contribute weakly to nuclear reactions owing to the Coulomb repulsion.
(c) Beam current: 10 nA.
(d) Time of measurement: 2 h for a sample containing 10 ppm of nitrogen (for an accuracy of 15% when interference with B may be avoided).
(e) Reference materials: AlN and Si_3N_4

Fig. 9 shows the measured amount of dissolved nitrogen as a function of the binding number of oxygen (Y) by unit molar glass volume (V_m); one observes that this nitrogen content increases with the ratio Y/V_m. This phenomenon is explained by the fact that more and more holes are filled with alkali ions. The increasing amount of network modifiers induces a rise in the activation energy for the diffusion process corresponding to the filling of the holes, then making nitrogen migration more difficult. It has been also shown that the residual concentration of N decreases from 20 to 8 ppm when the ratio of refining agents $NaNO_3/As_2O_3$ is increased [11].

A large program of study on nitrogen implanted in metals is still running under the direction of Prof. F. Bodart. Nitrogen implantation is known to enhance the tribological properties of steels [29] (reduction of wear and increase of hardness). The implantation energies range is 30–300 keV, and the ion doses range is 5–10^{16}–5×10^{17} cm^{-2}. In order to minimize the implantation time, very high currents have been developed in ion implanters used in the industry.

The depth profiles were measured using the $^{15}N(p,\alpha\gamma)^{12}C$ nuclear resonant reaction at $E_p = 429$ keV and quantified via a TiN standard (natural nitrogen) [30,31]. The change in the local stopping power (related to the local composition) has been taken into account in quantifying the nitrogen content of the

sample. The measurement and deconvolution techniques used have been described in details in refs. [32,33].

The depth profile of nitrogen implanted in pure iron shows a surface peak whose area increases with the temperature of the sample during implantation. The nitrogen depth profiles have been measured on a set of iron samples (99.5% purity) implanted with 100 keV N_2^+ ions at different doses (2×10^{16}–5×10^{17} ions cm^{-2}) and at different temperatures (20–200°C).

In order to explain the shape of the depth profiles and, particularly the existence of the surface peak and its dependence on implantation temperature, a numerical model has been developed by M. Piette [29]. This model takes the following elements into account: preferential sputtering, ion beam mixing, thermal diffusion, radiation-enhanced diffusion (RED), radiation-induced segregation (RIS), secondary phase precipitation and radiolytic decomposition of the precipitates. The surface peak cannot be explained by RED or RIS alone but is the consequence of an enhanced precipitation near the surface of the sample. Samples of copper, molybdenum and nickel have also been investigated in order to confirm that hypothesis and to show that there is a correlation between the presence of the surface peak and the formation energy of the corresponding nitrides. The ion deposition profiles, sputtering yields, ion beam mixing and radiolytic decomposition of the precipitates were calculated with the TRIDYN program. Fig. 10 shows the experimental nitrogen depth profiles obtained in polycrystalline pure

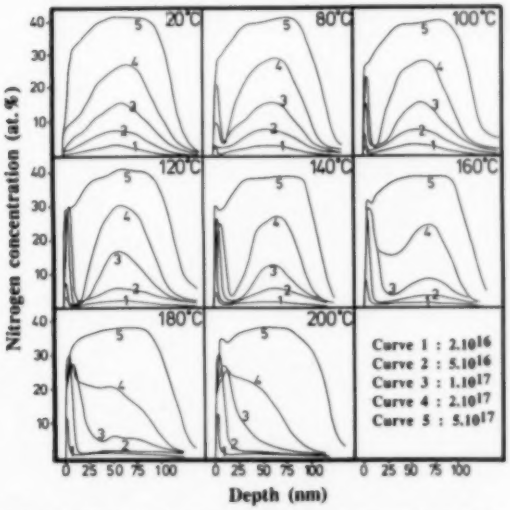

Fig. 10. Nitrogen depth profiles in N-implanted iron (after deconvolution). Each figure corresponds to a different implantation temperature. The different curves in the same figure correspond to different ion doses [29].

(99.5%) iron samples implanted with 100 keV $^{15}N_2^+$ ions. The sample preparation techniques and the implantation conditions have been widely described in ref. [30] and in the Ph.D. thesis of M. Piette (see appendix).

At low temperatures, nitrogen is not mobile enough to diffuse far away from the depth where it has been stopped. At higher temperatures nitrogen is allowed to diffuse and to precipitate; near the surface, the enhanced precipitation (higher concentration in nucleation sites) reduces the concentration of free nitrogen (it should be noted that only free nitrogen is assumed to be able to diffuse). Therefore, there is a concentration gradient of free nitrogen toward the surface region. Nitrogen from the bulk precipitates and the surface peaks builds up. When no iron at the surface remains free for further precipitation, an iron nitride layer grows toward the bulk [29,34].

Nitrogen implantation into aluminum also increases the hardness of the aluminum surface due to the formation of crystalline aluminum nitride. In order to produce large thicknesses of the aluminum nitride formed during nitrogen implantation in pure aluminum, the samples were implanted with $^{15}N_2^+$ ions successively at different energies between 100 and 320 keV. The implanted specimens were investigated by nuclear reaction analysis, Rutherford backscattering spectroscopy and scanning electron microscopy. Implantations of ^{14}N and ^{15}N were performed in various conditions in order to follow the mechanism of nitride formation. Post-irradiations with Kr^+ ions at doses of 10^{17} ions cm^{-2} and an energy of 500 keV were also performed, and it was shown that bombardment with krypton redistributed the implanted nitrogen to give a more homogeneous aluminum nitride layer.

Details may be found in refs. [35–39], in these Proceedings [40] and in the Ph.D. Thesis of S. Lucas (see appendix).

Other applications of nitrogen analysis using various nuclear reactions for investigations in biological materials are given in refs. [12,13,23–25,41].

6. Oxygen in high T_c superconductors

Since the initial paper of Bednorz and Müller who reported the possibility for La-Ba-Cu-O multiphase materials to behave as high temperature (above 30 K) superconductors, the synthesis and superconductive properties of Y-Ba-Cu-O or many RE-Ba-Cu-O compounds (RE being a rare earth element) with various stoichiometries, have been extensively investigated.

We have explored [42] different preparation routes of $YBa_2Cu_3O_{6.5+x}$ from solid reactant powders Y_2O_3, $BaCO_3$ and CuO, heated, annealed and cooled under various atmospheres. Their qualitative superconducting

character (or its absence) at liquid nitrogen temperature was assessed according to the occurrence of the Meissner effect, on pelletized or sintered samples. Precursors were made by mixing in water, stoichiometric amounts of finely grounded powders of analytical grade Y_2O_3 (Janssen), $BaCO_3$ (UCB) and CuO (Merck). The mixture (wet slurry) was ground up (homogenized) in an agate mortar, prior to a subsequent drying at 100°C for several hours. They are used as a reference material for further stoichiometric characterization by ion probe techniques.

In addition to measurements of thermal and electrical properties of superconducting materials, rapid and nondestructive analytical techniques involving milliprobes and microprobes facilities were developed for the search of the best conditions of their synthesis and to test the stoichiometric composition of the bulk material: PIXE for the determination of Ba, Cu, Y, RBS of α-particles to check the homogeneity in the 3 μm layer and $^{16}O(d,p)$ reaction for O analysis [43]. Materials showing the strongest Meissner effect at liquid nitrogen temperature are also those showing the best homogeneity in Cu, Ba and Y concentrations in analyzed regions of $5 \times 5 \times 5$ μm (fig. 11). Inhomogeneities in O concentration cannot be correlated with the presence (or absence) of specific oxides (CuO, Y_2O_3, BaO, etc.).

Ternary diagrams of three of the four components (Y, Ba, Cu, O) indicate that the local discrepancies from the ideal YBa_2Cu_3 composition is mainly observed in the Y composition, the reason lies only in the poor statistical accuracy on YK signals [43]. The distribution of the points in diagrams involving O (fig. 12) is not statistical: the local concentration of oxygen shows

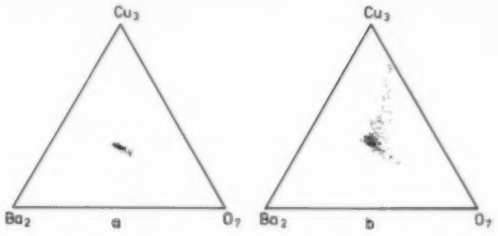

Fig. 12. Ternary diagrams of Cu, Ba and O concentrations (from figs. 11a and 11b) showing that oxygen is nonhomogeneously distributed even in the apparently homogeneous material (fig. 11a) [43].

variations of about 10% around the expected value of 6.7. The reason could be due to the presence of copper in different valence states. Total oxygen determination by classical chemical methods provides highly quantitative and accurate results [44].

Sputtering techniques are widely used in the thin film technology of high T_c superconductors, but problems of homogeneity due to the different sticking coefficients of the elements of the YBaCuO compounds are not completely solved yet. The oxygen content is particularly critical and as annealing is often required to achieve the superconducting phase, a detailed investigation of the stoichiometry in thin films at the different stages of the process has been performed. The use of RBS for oxygen determination in thin films of YBaCuO has also been investigated [45].

Thin films (500–1200 nm) of YBaCuO superconductors are sputtered onto magnesia and sapphire coated with a carbon interlayer (of about 500 nm). This

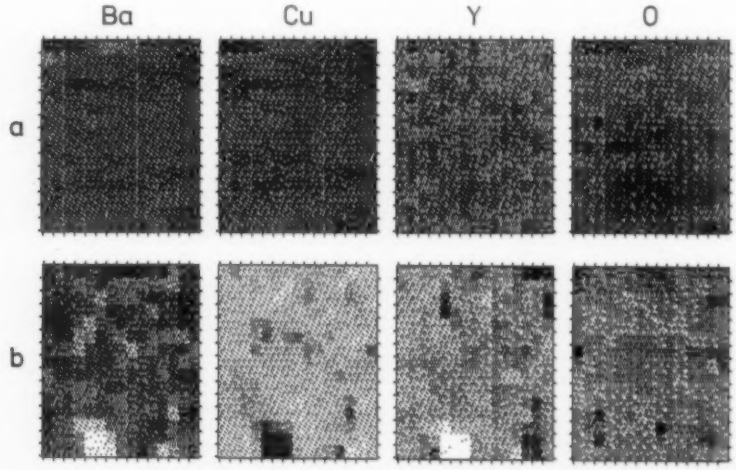

Fig. 11. Cu, Ba, Y and O concentration maps simultaneously determined by PIXE and nuclear reaction with a deuteron microbeam of 5 μm in diameter on a bulk sample of YBaCuO; (a) homogeneous; (b) non-homogeneous [43].

interlayer makes it possible to separate oxygen (RBS signals: α-particles) induced in the superconducting film from that produced by the MgO and Al_2O_3 substrates. They are analyzed after the different stages of the preparation process in order to investigate the influence of the presence of oxygen during the sputtering operation, as well as the effects of annealing and post-oxidation (oxygen content, interdiffusion) [45]. The primary target is a sintered $YBa_2Cu_3O_{7-x}$ material, obtained by the classical solid preparation route. The sputtering process is realized in vacuum (10^{-7} Torr) as well as in O_2 atmosphere (10^{-4} Torr), in order to study the influence of the preparation on the oxygen content.

For α-particles of energy ranging from 2.55 to 2.95 MeV, the actual cross section at 170° is non-Rutherford but the deviation from the Rutherford value is constant. The true oxygen cross section has been calculated using a sample of 3000 Å of Al_2O_3 layer on a Al substrate irradiated in the same conditions as those used for YBaCuO analysis, using the Bragg rule for the calculation of the stopping power by the classical RUMP program (fig. 13). With those data the composition of a homogeneous film, whose RBS spectrum is reproduced in fig. 14, gives $Y_{1.5\pm0.05}Ba_{2.0+0.05}Cu_{3.2+0.1}O_{9.4\pm0.2}$ using both PIXE and RBS data for the heavy elements and only RBS for oxygen. The α-BS technique (with the appropriate correction on cross section for oxygen) is used for the determination of oxygen with an accuracy of 3% in conditions involving no oxygen signal from the substrate.

Using (^{3}He,γ) oxygen has also been determined as a minor element in metals [7], using (d,p) reaction it has been analyzed in glass [11,27], in zeolites [46] and in gold-cadmium alloys produced by Cd diffusion from CdS pellets [47]. It has also been studied by RBS in thin metallic films [23], and to control the stability of biological material in PIXE analysis of heavy ions [22], finally using (p,γ) reactions for the characterization of a biological reference sample [11,12,24].

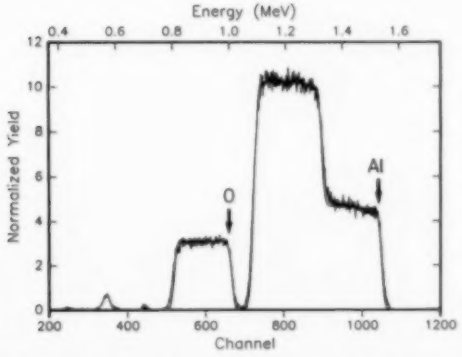

Fig. 13. RBS spectrum of 2.75 MeV α-particles on a reference sample of 3000 Å Al_2O_3 layer on Al and the corresponding calculation by RUMP.

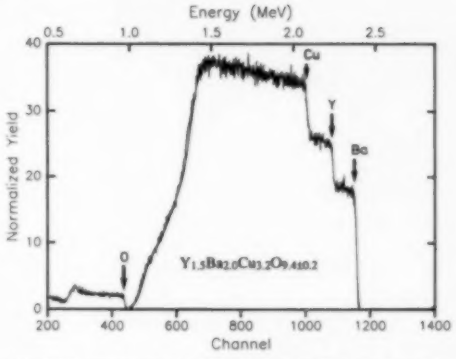

Fig. 14. RBS spectrum of a YBaCuO thin film produced in an oxygen atmosphere and its comparison with RUMP calculation.

7. Fluorine in tooth enamel and implanted in metals

Various studies of fluorine migration in extracted teeth [48–52] and in vivo analyses [53] of fluorine after application of various fluorides have been performed. The reaction $^{19}F(p,p'\gamma)^{19}F$ ($E_\gamma = 110$ and 197 keV), for the measurement of the total fluorine content [48–53] and resonant nuclear reaction $^{19}F(p,\alpha\gamma)^{16}O$ (E_γ = 5–7 MeV) induced by 872 keV protons for the depth profiling [48,51] have been experimented. This resonance at 872 keV was chosen for its high intensity. The high energy γ-rays were detected with a high efficiency 4 × 4 in. NaI crystal and the low energy γ-rays in a Ge(Li) detector.

The important problem of dental caries following dissolution of the enamel structure under the action of acid substances has been studied for many years using different analytical techniques: the fluorine ion plays an important part in the inhibition of enamel dental caries. The dental enamel is at 95% layer of apatite, 500 μm thick, in which the OH radicals are partly substittued with fluorine ions giving a concentration of 1–5‰ of fluorine. Resonant nuclear reactions are an unvaluable probe in dental enamel analysis since X-ray techniques (electron microprobe) are subjected to large errors from strong absorption of soft X-rays. Another advantage of nuclear reactions is the possibility of nondestructive depth profile analysis with very small diameter beams. NMR studies indicate that the fluorine ion would migrate along the C axis of the hydroxiapatite crystal, preventing further migration of OH^- ions. However, the enamel structure is very different

from the single crystal model, X-ray diffraction spectra show a widening of X-ray lines, which indicates that the sample is a superposition of crystallites, the size of which ranges between 300 and 400 Å. The intervals between these crystallites are filled with an organic network in which the F^- ion can also migrate. Therefore, measurements have to be done on tooth enamel rather than on apatite crystals, and they should be as close as possible to real life. Fluoride treatments were made in vivo and the tooth was extracted directly before measurements by the nuclear method. The measured fluorine concentration is highly variable from place to place on the same tooth and much more from tooth to tooth. A large amount of data was collected before drawing significant conclusions. The results of fig. 15a show that in the treated region a large enrichment in fluorine is detected to a depth of 0.1–0.3 μm. In a second run of measurements, teeth are left in mouth during 10 days before extraction: no appreciable difference is detected between polished and fluoridated regions (fig. 15b). A similar phenomenon is observed when teeth are kept in distilled water. The general conclusion of the studies on extracted teeth may be summarized as follows: fluorine migration in teeth enamel is measured after the rough surface is eliminated by polishing and then treated with different fluoridated compounds. This fluoridation does not disappear when the tooth is kept in dry atmosphere. On the contrary, the enrichment effect is practically absent after a few days when the tooth is kept in contact with saliva. It is then supposed that the atoms of fluorine are eliminated by ion exchange phenomena in saliva. The hypothesis of exchange with chlorine ions was put forward and the Cl concentration was measured by PIXE, but no appreciable variation was observed. Another explanation of the fluorine exchange would be that the fluorine ions introduced by the treatment do not appreciably migrate into the crystallites but are simply introduced between the crystallites through the organic matrix.

Using higher protons energies (2–3.5 MeV), the total fluoride concentration below the surface can also be rapidly measured. The $^{19}F(p,p'\gamma)^{19}F$ reaction is then used giving γ-rays of 110 and 197 keV. The maximum analyzed depth is about 45 μm, but the average value on the analyzed depth lies somewhere between 20 and 25 μm. Such nuclear analyses take only 1 min of bombardment. The tooth fragment was mounted in the vacuum and an electron spraying is needed to avoid charging effects.

One of the most spectacular applications of the $^{19}F(p,p'\gamma)^{19}F$ reaction is the in vivo analysis of a human tooth. This technique was elaborated in our laboratory and has been extensively used for the study of topical applications of fluoridated compounds [50]. To date, there is no other example of the application of the technique from any other laboratories. The problem of radiation damage and radiation hazard has been investigated carefully. Calculations and experiments show that the radiation emitted during the bombardment of protons and measured at different levels is extremely low and is well below the security limits which are normally accepted for the general population [54]. The technique is as follows. A 3 MeV proton beam enters the atmospheric air through a tantalum window 5 mg cm^{-2} thick and the tooth is placed 1 cm

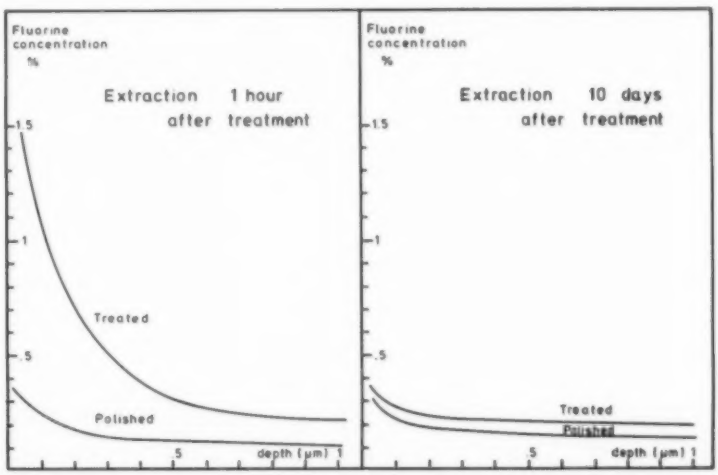

Fig. 15. (a) Concentration profile of fluorine in tooth enamel. Comparison between polished and fluoridated tooth regions (average values on more than 10 different teeth). (b) Same as (a) but teeth are extracted 10 days after treatment (average values) [51].

behind the window. For in vivo analysis a special mouth piece is designed for each case, allowing accurate reproductible geometry in successive irradiations before and after treatment. The tooth is irradiated with a 30 nA proton beam, 110 and 197 keV γ-rays are detected, and their intensity is related to the fluorine content of the irradiated area of enamel. The results are average values of the concentrations in the 20 μm thick layer of enamel. Gels are applied during 4 min using a special mouth piece, solutions are applied with a cotton tip during the same time. The fluorine concentrations were measured at different intervals after the fluoride application and the F enrichments are calculated by comparison with the F content before treatment. Typical results are given in fig. 16. Measurements at longer intervals after the treatment indicate that the loss follows a nearly exponential curve to reach the initial F concentration (before treatment) after 2–3 weeks for APF gels, 6 weeks for AmF solution. Additional measurements of other elements (Na, P, Ca, Fe, Cu, Zn, Sr and Pb) have also been performed on extracted teeth [52].

Diffusion of F in iron after implantation has been finely analyzed using the 483.8 keV resonance. The chemical bounding of F in iron may be analyzed by Mössbauer spectroscopy [55].

Commercial laminated iron foils have been implanted with 2×10^{16} and 2×10^{17} ions/cm^2. Depth profiling was performed using both the 340.6 and 483.6 keV resonances. The samples were then heated to different temperatures and under different conditions. The technique was found to be non-destructive and repeated measurements on a given sample yield the

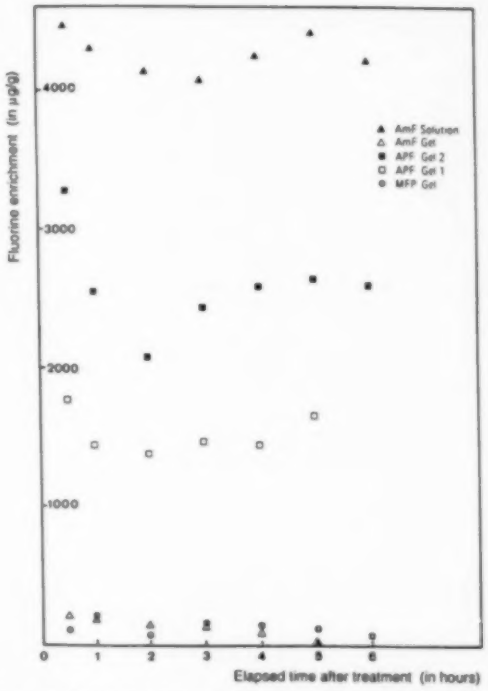

Fig. 16. Mean enrichment in fluorine with time after application of 5 various fluorine compounds on a total of 74 teeth analyzed in vivo [53]: AmF solution: 1% F^-, pH = 5.03; AmF gel: 1% F^-, pH = 5.93; APF Gel 1: 1.2% F^-, pH = 5.40; APF Gel 2: 1.2% F^-, pH = 5.00; MFP Gel: 1.8% F^-, pH = 6.25.

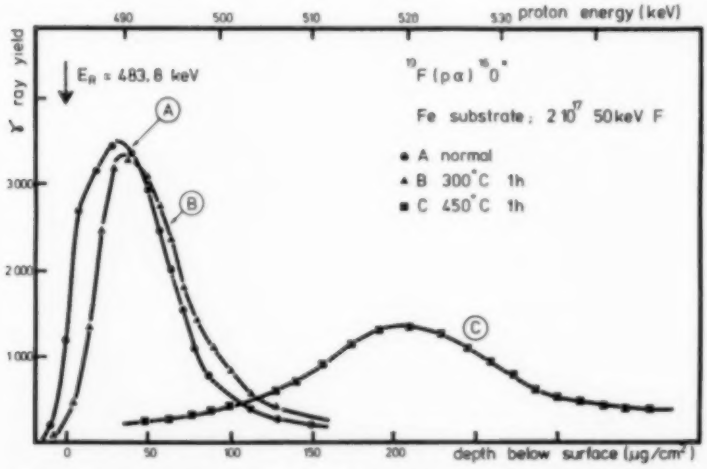

Fig. 17. Excitation curves measured after thermal treatment of fluorine implanted iron at atmospheric pressure. Curve C indicates a deep migration of fluorine and the presence of a large background (attributed to the 596.8 keV resonance) [55].

same results, allowing investigation of temperature-dependent effects on a given sample, a performance which cannot be achieved with Auger spectroscopy.

Results of measurements performed with the 483.6 keV resonance are shown in fig. 17. The excitation curve shows a bell-shape distribution with a FWHM of 900 Å and present a sharp edge on the low energy side. During thermal treatment, the front of the distribution moves rapidly toward large depth. This movement is accelerated between 300 and 450°C where the fluorine atoms are found in a broad distribution centered around 4000 Å. An important background attributed to the third resonance is observed in the excitation curve corresponding to the fluorine density profile after treatment at 450°C. Further measurements have shown that an oxide layer is formed on the surface, the position and the shape of the density curve show that the fluorine cluster has been translated toward large depths. The presence of oxygen has been identified by backscattering of 3050 keV α-particles on ^{16}O.

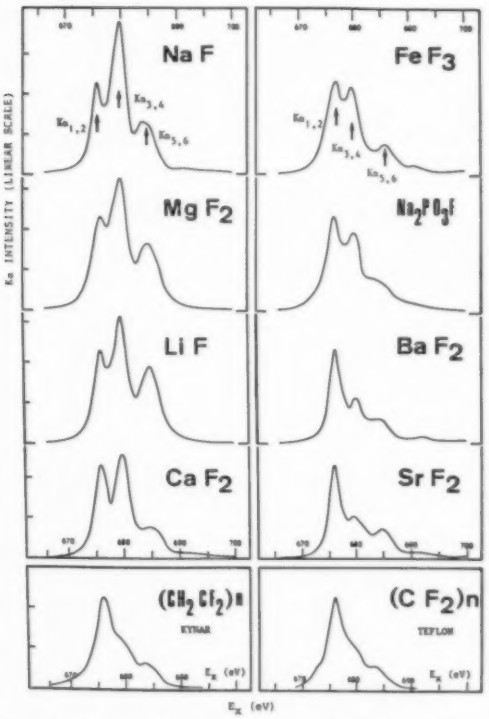

Fig. 18. Fluorine K X-ray emission during irradiation of fluoride solid samples with 2 MeV $^4He^+$ ions. The spectra are normalized to the $K_{\alpha_{1,2}}$ peak amplitude and are presented with decreasing $K_{\alpha_{3,4}}$ amplitudes [60].

Other applications of F analysis has been reported for biological materials [13,24], in glass [28] and metals [23].

Energy shifts and change in relative intensities following the ionization of shells involved in the chemical energy bound were investigated by charged particle bombardment to produce ionization of the K-shell by light projectiles (protons and α-particles). High intensity chemical effects were measured in fluorine compounds where L electrons are directly involved in the binding. Special attention has been attached to the $K_{\alpha_{3,4}}$ satellites corresponding to a double ionization of the 2p shell in the final state; a situation which is also seen in the KLL Auger electron emission [58]. Compounds of fluorine are powdered, then cylindrical disc samples (20 mm in diameter) are obtained by compression. These samples are bombarded with a beam of 2 MeV α-particles, F X-rays from K-shell ionization are detected at a take-off angle of 45° from the surface. X-rays are analyzed with a Bragg spectrometer using a thallium acid phthalate crystal (TlAP). The overall energy resolution is 1.2 eV for F K X-rays. The description of this technique is given in detail in ref. [59].

The results on: NaF, MgF_2, LiF, CaF_2, FeF_3, KF, Na_2PO_3F, BaF_2, SrF_2, $(CF_2\text{-}CH_2)_n$ (Kynar), $(CF_2)_n$ (Teflon) and other polymers are reported in fig. 18. It is obvious that the spectrum shape is very sensitive to the chemical bond. The $K_{\alpha_{3,4}}$ satellite peak, which is prominent in NaF, is completely washed out in substances like Teflon and other polymers.

An important decrease of the $K_{\alpha_{3,4}}$ amplitude is observed when going from ionic to covalent bond. The case of KF remains completely unexplained and does not follow this simple rule. A correlation is found between spectra of satellite from double ionization and KLL Auger electron spectra, making further theoretical investigations possible for a better knowledge of double-hole states in the second-row elements and the structure of p-bands in alkali halides and other fluorine compounds. In many cases, X-ray satellite spectroscopy shows features which are not seen in photoelectron spectroscopy (ionic compounds) and more pronounced than in KLL Auger electron spectra. This spectroscopy can be considered as a new tool for the identification of fluorine compounds, particularly well adapted to the study of surface layers [58,60].

8. X-ray emission from neon implanted into metals

The physical state of neon implanted into different metals has been studied by means of soft X-ray emission spectroscopy [61].

Metal samples (beryllium, aluminum, titanium, chromium, iron, copper, zinc, molybdenum, silver, tungsten, gold, lead and bismuth) are implanted with

50 keV neon ions ($^{20}Ne^{+}$) and subsequently irradiated with 4 keV electrons to excite the neon X-ray fluorescence which is analyzed with a flat-crystal spectrometer. A considerable broadening of the atomic K X-ray line is observed for all samples, showing the existence of a band structure. The observed 2p band width W ranges between 1.95 and 4.07 eV depending on the host metal (compared with 1.3 eV for solid neon at atmospheric pressure). X-ray fluorescence analysis yields two observations (the total width W and the spectrum shape) which should be related to the following macroscopic parameters: the average metal shear modulus μ and the internal pressure [62]. A plot of W versus the shear modulus shows a relation which can be approximated by a straight line (where W is in eV and μ in GPa): $W = (0.017\mu + 1.3)$. Using the relationship between the shear modulus and pressure, it is thus possible to relate W to the pressure. This effect is documented in the review paper by Banse-Lefebvre et al. in these Proceedings [63].

Appendix

Ph.D. Theses related to analyses of light elements by charged particle bombardment totally or partially made at the LARN:

J. Baijot-Stroobants: Etude par réactions nucléaires de la migration du fluor dans l'émail dentaire humain après application topique in vivo.

G. Debras: Analyse quantitative et profil de concentration d'éléments légers par méthodes nucléaires promptes. Application à l'étude de la solubilité et de la diffusion de l'azote dans le verre.

S. Van Den Brook: Effets d'état solide dans l'émission du rayonnement X satellite du fluor observé lors de l'irradiation avec des particules chargéees.

M. Piette: L'implantation d'azote dans le fer: étude expérimentale et modélisation.

S. Lucas: L'implantation d'azote dans l'aluminium: caractérisation des profils et mesures de nanodureté.

A. Banse-Lefebvre: Spectroscopie d'émission X du néon fluide et solide.

H. Kathrein: Struktur und Eigenschaften der an Kohlenstoff und Wasserstoff gebundenen Defekte in Magnesiumoxid.

H. Wengeler: Einbau von atomarem Kohlenstoff und Wasserstoff in hochschmelzende Oxide.

G. Oberheuser, Kohlenstoff, Exzess-Sauerstoff und OH^{-} Ionen in Olivin-Einkristallen.

References

[1] G. Deconninck, Akadémiai Kiado, Budapest (Elsevier, Amsterdam, 1978).

[2] G. Deconninck, G. Demortier and F. Bodart, At. Energy Rev. Suppl. 2 (1981) 151.

[3] S.E. Donnelly, F. Bodart, K. Barfoot, R. Werz and R.P. Webb, Thin Solid Films 94 (1982) 289.

[4] F. Bodart and S.E. Donnelly, Nucl. Instr. and Meth. 218 (1983) 529.

[5] F. Degrève, J.M. Lang, F. Bodart and G. Demortier, Proc. 5ème Cong. Soc. Franç. Spectrométrie de Masse, Grenoble (1986).

[6] F. Degrève, B. Dubost, A. Dubus, N.A. Thorne, F. Bodart and G. Demortier, J. Phys. (Paris), Colloque C3, supplément au no. 9, 48 (1987) 505.

[7] G. Deconninck and G. Demortier, Nuclear Techniques in the Basic Metal Industries, IAEA-SM (1973) 573.

[8] G. Demortier and G. Hoffelt-Fontaine, in: Clays and Clay Minerals, vol. 24 (Pergamon, Oxford, 1976) pp. 69–78.

[9] F. Bodart and G. Demortier, Radiochem. Radioanal. Lett. 31 (4–5) (1977) 215.

[10] G. Deconninck, J. Radioanal. Chem. 17 (1973) 29.

[11] G. Debras and G. Deconninck, Int. J. Radioanal. Chem. 38 (1977) 193.

[12] G. Demortier, Spectra 2000, 48 (1979) 51.

[13] G. Demortier, Radiochem. Radioanal. Lett. 16 (1974) 329.

[14] F. Freund, B. Lindner, G. Demortier and L. Thone, Proc. Int. Clay Conf., Mexico (1975) p. 92.

[15] F. Freund, G. Debras and G. Demortier, J. Cryst. Growth 38 (1977) 277.

[16] F. Freund, G. Debras and G. Demortier, J. Am. Ceram. Soc. 61 (9–10) (1978) 429.

[17] H. Wengeler, R. Knobel, H. Kathrein, G. Demortier, H.J. Heinen and F. Freund, Mater. Res. Bull. 15 (1980) 1011.

[18] F. Freund, H. Kathrein, H. Wengeler, R. Knobel, G. Oberheuser and G. Demortier, Nucl. Instr. and Meth. 197 (1982) 27.

[19] H. Wengeler, R. Knobel, H. Kathrein, G. Demortier, G. Wolff and F. Freund, J. Phys. Chem. Solids 43 (1) (1982) 59.

[20] H. Kathrein, H. Wengeler, R. Knobel, F. Freund, G. Demortier and H. Gonska, High Temp.–High Press. 15 (1983) 353.

[21] G. Oberheuser, H. Kathrein, G. Demortier, H. Gonska and F. Freund, Geochim. Cosmochim. Acta 47 (1983) 1117.

[22] G. Demortier, J. Lefebvre and C. Gillet, J. Radioanal. Chem. 12 (1972) 277.

[23] I.V. Mitchell, W. Maenhaut, H. Raemdonck and F. Bodart, Nucl. Instr. and Meth. 197 (1982) 51.

[24] G. Demortier, Radiochem. Radioanal. Lett. 20 (1975) 197.

[25] J. Baijot-Stroobants, G. Debras and G. Demortier, Radiochem. Radioanal. Lett. 27 (1976) 271.

[26] F. Bodart, G. Deconninck, and J. Mengeot, Proc. Int. Symp. on Nuclear Activation Techniques in Life Sciences, Vienna, Austria, IAEA-SM-227/98, pp. 37–45.

[27] G. Debras, M. Pieret, L. Van Cangh and G. Deconninck, Silicates Industriels 3 (1979) 59.

[28] G. Debras, G. Deconninck and F. Bodart, Verres et Réfractaires 35 (1981) 88.

[29] M. Piette, G. Terwagne, W. Moller and F. Bodart, Mater. Sci. Eng. B2 (1989) 189.
[30] G. Terwagne, M. Piette, P. Bertrand and F. Bodart, Mater. Sci. Eng. B2 (1989) 195.
[31] F. Bodart, G. Terwagne and M. Piette, Mater. Sci. Eng. 90 (1987) 111.
[32] G. Deconninck and B. Van Oystaeyen, Nucl. Instr. and Meth. 218 (1983) 165.
[33] G. Terwagne, M. Piette and F. Bodart, Nucl. Instr. and Meth. B19/20 (1987) 145.
[34] G. Terwagne, M. Piette and F. Bodart, Mater. Sci. Eng. A115 (1989) 25.
[35] S. Lucas, F. Bodart, G. Terwagne, G. Sorensen and H. Jensen, Mater. Sci. Eng. B2 (1989) 183.
[36] G. Terwagne, S. Lucas, F. Bodart, G. Sorensen and H. Jensen, Mater. Sci. Eng. A116 (1989) 59.
[37] G. Terwagne, S. Lucas, F. Bodart, G. Sorensen and H. Jensen, Nucl. Instr. and Meth. B45 (1990) 95.
[38] S. Lucas, G. Terwagne and F. Bodart, Nucl. Instr. and Meth. B50 (1990) 401.
[39] S. Lucas, G. Terwagne, F. Bodart and M. Benmallek, Proc. Int. Conf. Applications Nuclear Techniques, eds. G. Vourvopoulos and Th. Paradellis (World Scientific, Singapore, 1991) p. 166.
[40] G. Terwagne, S. Lucas and F. Bodart, these Proceedings (3rd Int. Conf. on Chemical Analysis, Namur, Belgium, 8–12 July 1991), Nucl. Instr. and Meth. B66 (1992) 262.
[41] G. Deconninck and F. Bodart, Nucl. Instr. and Meth. 149 (1978) 609.
[42] Z. Gabelica, G. Demortier, G. Deconninck, F. Bodart, A.A. Lucas, M. Renier, Ph. Lambin, J.P. Vigneron and E.G. Derouane, Solid State Commun. 64 (8) (1987) 1137.
[43] G. Demortier, F. Bodart, G. Deconninck, G. Terwagne, Z. Gabelica and E.G. Derouane, Nucl. Instr. and Meth. B30 (1988) 491.
[44] Z. Gabelica, E.G. Derouane, J.P. Vigneron, Ph. Lambin, M. Renier, A.A. Lucas, G. Deconninck, F. Bodart and G. Demortier, Solid State Commun. 64 (9) (1987) 1221.
[45] De Decroupet and G. Demortier, Proc. MRS Fall Meeting 1990, Symp. H, Materials Issue in Applications of Ceramic Superconductors (1990) p. H.8.89.
[46] D. Decroupet, H. Meurisse and G. Demortier, Zéolites 7 (1987) 540.
[47] D. Decroupet, S. Mathot, G. Demortier and G. Blaise, Vacuum 42 (13) (1991) 831.
[48] G. Deconninck, Surface and Colloid Phenomena: Methodology (IRL Press Ltd., 1982) pp. 27–39.
[49] G. Deconninck, J. Radioanal. Chem. 12 (1972) 182.
[50] J. Baijot-Stroobants and J. Vreven, Caries Res. 13 (1979) 211.
[51] J. Stroobants, F. Bodart, G. Demortier, G. Deconninck and G. Nicolas, Ion beam Surface Layer Analysis, vol. 2, eds. O. Meyer, G. Linker and F. Käppeler (Plenum, New York, 1975) pp. 933–943.
[52] F. Bodart, G. Deconninck, and M.Th. Martin, IEEE Trans. Nucl. Sci. NS-28 (2) (1981) 1401.
[53] J. Baijot-Stroobants and J. Vreven, Proc. Int. Symp. on Nuclear Activation Techniques in Life Sciences, Vienna, Austria, IAEA-SM-227/99, pp. 395–406.
[54] J. Baijot-Stroobants, F. Bodart, G. Deconninck and J. Vreven, Health Phys. 36 (1979) 423.
[55] F. Bodart and G. Deconninck, Nucl. Instr. and Meth. 197 (1982) 59.
[56] G. Deconninck, Proc. 4th Conf. on Scientific and Industrial Applications of Small Accelerators, eds. J.L. Duggan and I.L. Morgann, 76CH 1175-9 NPS (1976) pp. 533–542.
[57] G. Deconninck, J. Stroobants, W.E.E. Stone and H. Charlier, Radiochem. Radioanal. Lett. 24 (1976) 331.
[58] G. Deconninck and S. Van den Broek, J. Phys. C13 (1980) 3329.
[59] G. Deconninck, Z. Szokefalvi-Nagy and S. Van den Broek, J. Appl. Phys. 17, suppl. 17-2 (1978) 357.
[60] G. Deconninck and S. Van den Broek, IEEE Trans. Nucl. Sci. NS-28 (2) (1981) 1404.
[61] A. Lefebvre and G. Deconninck, Nucl. Instr. and Meth. B15 (1986) 616.
[62] G. Deconninck and A. Lefebvre, Mater. Sci. Eng. 90 (1987) 167.
[63] A. Banse-Lefebvre, G. Deconninck, M. Dubus and G. Terwagne, these Proceedings (3rd Int. Conf. on Chemical Analysis, Namur, Belgium, 8–12 July 1991), Nucl. Instr. and Meth. B66 (1992) 205.

Section II
Review papers on analysis of light elements

Nuclear Instruments and Methods in Physics Research B66 (1992) 65–82
North-Holland

Nuclear Instruments & Methods in Physics Research
Section B

Analysis for hydrogen by nuclear reaction and energy recoil detection

W.A. Lanford

Department of Physics, SUNY Albany, Albany, NY 12222, USA

The use of MeV ion beams to measure hydrogen concentration profiles is reviewed. Both nuclear reaction analysis (NRA) and energy recoil detection (ERD) methods are discussed. Details of experimental approaches used and the effects of these different approaches on the analytic characteristics obtained are considered. The use of Doppler spectroscopy in both NRA and ERD to study the bonding of hydrogen in solids is briefly reviewed. The different methods are compared in terms of their advantages and disadvantages for certain analytic characteristics including accuracy, beam damage effects, sensitivity, and depth resolution.

1. Introduction

The use of MeV ion beams to analyze materials for hydrogen has been more interesting and more important than even the early researchers in this field had realized. The reasons for this are simple: hydrogen is probably the most common contaminant element, especially in thin film materials; hydrogen has important effects on the chemical, physical, and electrical properties of many materials; and, the analysis for hydrogen is difficult or impossible by most traditional analytical methods.

The purpose of the present paper is to briefly review what experimental approaches have been developed to utilize MeV ion beams to probe for hydrogen and to try to give some perspective on the advantages and disadvantages of the different approaches for particular applications. Generically, these techniques fall into one of two categories: One is nuclear reaction analysis (NRA), in which MeV ions bombard a sample inducing nuclear reactions between the bombarding ion and hydrogen in the target with the number of nuclear reactions induced used to determine the amount of hydrogen in the target. The second is energy recoil detection (ERD) in which MeV ions bombard a sample and through elastic collisions cause hydrogen ions to recoil out of the sample with the number of these recoils used to determine the amount of hydrogen in the target.

1.1. Historical

In 1914, Ernest Marsden, who had been a student working with Rutherford and Geiger on the classic alpha particle scattering experiments that led to our current understanding of the structure of atoms, observed long ranged particles coming from foils being bombarded with alpha particles [1]. He identified these long ranged particles as protons being knocked out of the target by the alpha particles. He apparently was surprised by the large amount of hydrogen present in these foils implied by these results.

These observations, published almost 80 years ago, are probably the first use of MeV ion beams as a probe for the presence of hydrogen in materials. The utility of this approach was not recognized by Marsden or others until much later when B. Cohen at Pittsburgh [2] published the first modern paper on the subject. It is perhaps interesting to note that two of the observations made independently by many workers in this field over the years are already implied by Marsden's 1914 result: One is that hydrogen is present in surprisingly high concentrations in many materials; and the second is that cross sections for probing for hydrogen can be remarkably large.

In 1972, B. Cohen and coworkers [2] described a recoil method for measuring hydrogen concentration versus depth in foils with thickness on the order of 0.1 mm, or thinner. This method is described in more detail below, but the authors were able to demonstrate sensitivities on the order of 10 ppm (atomic) and concluded that sensitivities several orders of magnitude higher were possible. They also observed the universal presence of large amounts of surface hydrogen on their samples and measurable amounts of hydrogen contaminations in the bulk of these samples with the possible exception of their measurements on an iron foil. While these authors described a powerful technique with many potential applications, this method has not been widely utilized.

In the following year, papers began to be published utilizing nuclear reactions to probe for hydrogen. D. Leich and T. Tombrello [3] demonstrated the use of a resonant nuclear reaction between ^{19}F and ^{1}H to

0168-583X/92/$05.00 © 1992 – Elsevier Science Publishers B.V. All rights reserved

measure concentration versus depth in any sample that can be placed in a vacuum. This work was motivated by Tombrello's interest in learning about the history of the solar wind by measuring the resulting hydrogen profile on exposed surfaces of lunar rock. However, in addition to applying this method to this one special case, he also began to demonstrate the general utility of this approach by making measurements in other materials, including the hydration of obsidian [4].

It is at this time that large numbers of researchers began to publish on nuclear methods for hydrogen analysis. P. Adler and coworkers at Grumman [5] published work on the ^{7}Li induced nuclear reaction. E. Ligeon and Guivarc'h in Grenoble published on the ^{11}B induced nuclear reaction [6].

All of these were probes are sensitive to ^{1}H. However, at this time there was also work done on analysis for deuterium (D). This includes the work by Chu and Friedman at Brookhaven National Laboratory the D(D, n)^{3}He reaction to measure implantation profiles of D in Au and Al [7]. Much more widely followed was the work of Pronko and Pronko who proposed using the ^{3}He(d, p)^{4}He reaction to measure D profiles [8].

By the mid-1970s Lanford at Yale (and later at Albany) working with Zielger at IBM and coworkers developed the ^{15}N resonant nuclear reaction [9]. For most problems, this technique is generally agreed to have the best analytic characteristics. With this development, Lanford undertook a program to see this technique utilized in as wide a variety of problems as practical. This resulted in contributions to fields from basic physics (e.g. containment of ultracold neutrons [10]), to energy (H in amorphous Si solar cells [11]), to radioactive waste (durability of rad-waste glasses [12]), to glass science (surface reactions on glasses [13]), to electronic materials (H in plasma deposited materials, semiconductors and insulators [14]), to H in superconductors [15], to applications in art history and archaeology (dating glasses [16]).

Others have undertaken similar programs utilizing NRA to measure hydrogen in a wide variety of materials including Tombrello at Cal Tech, Kalbitzer at Heidelberg, Rauch at Frankfurt, Doyle at Sandia, Thomas at Lyon, and Bottiger at Aarhus among others.

It was at this same time that the Montreal group of J. L'Ecuyer and coworkers [17] demonstrated that the energy recoil detection (ERD) method, even without the coincidence technique of Cohen, could be a very powerful and general way to profile surfaces for all light elements. They typically used a bombarding beam of 30 MeV Cl and could simultaneously analyze for all elements oxygen and lighter.

In 1976–77, J. Ziegler's famous interlaboratory comparison of hydrogen profiling methods took place leading to the workshop on hydrogen profiling held at the Georgetown IBA Conference in 1977 and the paper [18] summarizing these results. This paper [18] is still a good source of information on hydrogen profiling techniques. As evidence of the power of Montreal's recoil method, they were the only group that participated in Ziegler's interlaboratory comparison that reported analysis for both H and D in these samples.

In spite of the power of the method developed at Montreal, much like the experience with Cohen's coincidence recoil method, this method was not immediately widely adopted by others. Part of the reason for this is the fact that most groups using ion beams for materials characterization did not have easy access to accelerators with 30 MeV heavy ions. To some extent, the lack of access to accelerators with ^{15}N and ^{19}F beams also hindered the use of nuclear reaction profiling technique based on these beams.

However, all ion beam analysis laboratories had access to MeV He beams and 1979 B. Doyle and P. Peercy of Sandia demonstrated that these beams could be used in an ERD mode to measure hydrogen profiles [19]. Since the equipment used for He ERD was so similar to that used in Rutherford backscattering, this development allowed most ion beam analysis laboratories to do hydrogen profiling. This greatly broadened the interest in routine hydrogen analysis.

As recoil analysis for hydrogen became more popular, the technique also has been greatly refined. Ross and coworkers [20] demonstrated that one can do very high resolution work even at low energies (350 keV) with He ERD when an electromagnetic (nonstraggle-inducing) filter is used to remove the elastically scattered particles, rather than the more common absorber foil. And more recently, R. Groleau and coworkers in Montreal [21] have combined high energy heavy ion ERD with a particle identifying counter telescope to measure separate profiles of all light elements at one time. In principal, this procedure is an enormous advantage, one that is now being exploited by a number of groups arround the world.

2. Nuclear reaction analysis

While other nuclear reactions have been used (and many others are possible) by far the reactions most commonly used to probe for ^{1}H in material are those induced by ^{15}N [9] and ^{19}F [3]. These reactions are similar in many ways: both have low energy isolated resonances at about 6.4 MeV and both have higher energy resonances above 10 MeV [22]. Another reaction which is capable of profiling much deeper into samples uses a ^{7}Li beam [5]. The important parameters for these reactions are given in table 1.

The use of the ^{15}N reaction as a probe for hydrogen will be given as an illustration of this approach. Other resonant nuclear reactions can be used in the same

general way with differences (and, hence, different analytic characteristics) due to differences in the parameters given in table 1.

The ^{15}N nuclear reaction method is illustrated in fig. 1. The nuclear reactions is

$$^{15}N + {}^{1}H \rightarrow {}^{12}C + {}^{4}He + \text{gamma-ray}.$$

To use this reaction to probe for hydrogen, a beam of ^{15}N ions is incident on the sample being analyzed and the yield of characteristic gamma-rays is measured. Because this is a resonance reaction, the cross section is large at the resonance energy (E_{res}) and small off resonance. Hence, if a sample is bombarded with ^{15}N ions at the resonance energy, the yield of gamma-rays is proportional to the hydrogen on the surface of the sample. If the beam energy is raised above the resonance energy, there are no longer reactions with surface hydrogen (because the ^{15}N ions are above the resonance energy) but as the ions loose energy penetrating the sample, they reach the resonance energy at some depth. Now the yield of gamma-rays is proportional to the hydrogen content at this depth. Hence, by measuring the yield of characteristic gamma-rays versus beam energy, the hydrogen concentration versus depth is determined.

Fig. 2 shows a schematic of the chamber that we have been using for this analysis for many years. There are a few comments that should be made about such chambers.

First, note that there are no beam defining slits near the sample. Otherwise, hydrogen present on such slits would give a background count rate, limiting the sensitivity of the analysis. F. Rauch at Frankfurt [23] has solved this problem differently. He has a set of slits near the target that are kept nearly hydrogen free by keeping them hot.

Second, note that the whole chamber is a Faraday cage with electron suppression at the insulated coupling where this chamber attaches to the beam line. In

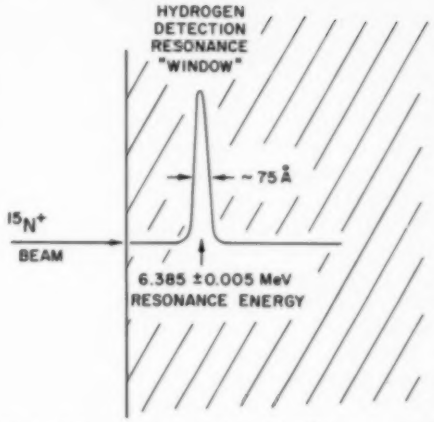

Fig. 1. A schematic representation of the ^{15}N nuclear reaction profiling method.

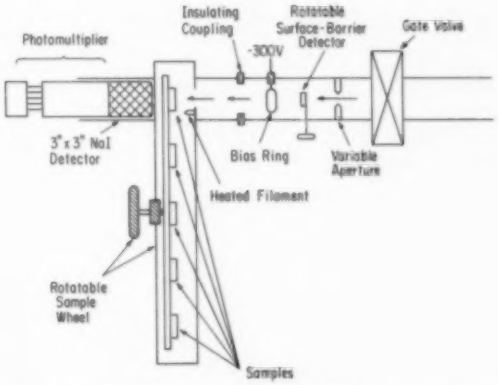

Fig. 2. A schematic representation of the chamber used at Albany for nuclear reaction analysis. Many samples can be mounted on the circumference of the sample wheel to allow for rapid changing of samples.

Table 1
Nuclear reaction cross section characteristics [a,b]

Reaction	$^{7}Li+H$	$^{15}N+H$	$^{15}H+H$	$^{19}F+H$	$^{19}F+H$
Resonance energy [MeV]	3.07	6.385	13.35	6.418	16.44
Cross section (σ_0) at resonance [mb]	4.8	1650	1050	88	440
Resonance width (Γ) [keV]	81	1.8	25.4	44	86
$\sigma_0\Gamma$ [mb·keV]	389	2970	26700	3870	37800
Relative yield	0.13	1.000	9.0	1.3	12.7
dE/dx in Si [MeV/μm]	0.442	1.45	1.35	1.94	1.94
$(\Gamma)/dE/dx$ [μm]	0.183	0.0012	0.0188	0.0226	0.0443
Energy of next resonance [MeV]	7.11	13.35	18.0	9.1	17.6
Gamma-ray energy [MeV]	17.7, 14.7	4.43	4.43	6.13, 6.98, 7.12	6.13, 6.98, 7.12

[a] The ^{7}Li results are from Trocellier and Engelmann (ref. [5]).
[b] The ^{15}N and ^{19}F results are from Xiong et al. (Ref. [22]).

addition to the bias ring (shown), there is also a permanent magnet (not shown) mounted to stop electrons from passing between the Faraday chamber and the beam line. We have found that both electric and magnetic suppression are needed to get sub 1% reproducibility for beam current integration, regardless of the nature of the sample (e.g. metals versus insulators).

Because we do a lot of work with insulators, we have installed a heated filament near the samples. If during analysis, an insulating sample begins to charge up, the filament provides enough electrons to neutralize this charge. Because the filament is battery powered with the batteries (electrically) part of the Faraday cage, the presence of the heated filament has no effect on the beam current integration system. (Note, this system is just a flash-light bulb with the glass removed and the filament coated to reduce the work function.)

In a typical run, the variable aperture will be opened wide. A beam viewer will be positioned in the target position and the ion beam will be focused to a small spot. A raster supply on the beam line will then be turned on to raster the analyzing beam over a square several millimeters on a side.

The characteristic gamma-rays from the reaction are detected by a scintillation detector (NaI or BGO) located about 2 cm behind the samples. This detector is outside the vacuum chamber and is not electrically part of the Faraday cage.

The samples are mounted nearly normal (actually six degrees away from normal to avoid accidental channeling) to the ion beam. This is done so that if the beam moves laterally on the sample, it does not change the distance from the sample to the gamma-ray detector significantly. In an earlier design [9] with the samples at 45 degrees to the beam, we found that lateral motions of the beam caused important changes in the detection efficiency.

As an illustration, fig. 3 shows examples of both the raw data (gamma-ray yield versus beam energy) and final result (hydrogen concentration versus depth).

The conversion of the raw data to hydrogen concentration is simple in these cases. First, it is usually a good approximation that the energy loss (dE/dx) of the incident ion is independent of energy over the energy range of interest. Hence, the depth of a measurement (x) is given simply by

$$x = (E - E_{res})/(dE/dx). \tag{1}$$

The gamma-ray yield is proportional to the energy integrated area under the Breit–Wigner formula for a resonant cross section, i.e. proportion to $(\pi/2)\sigma_0\Gamma$, where σ_0 is the cross section at the resonance energy and Γ is the width of the resonance. The yield of gamma-rays is also inversely proportional to the energy loss of the incident ions. This is because the yield of

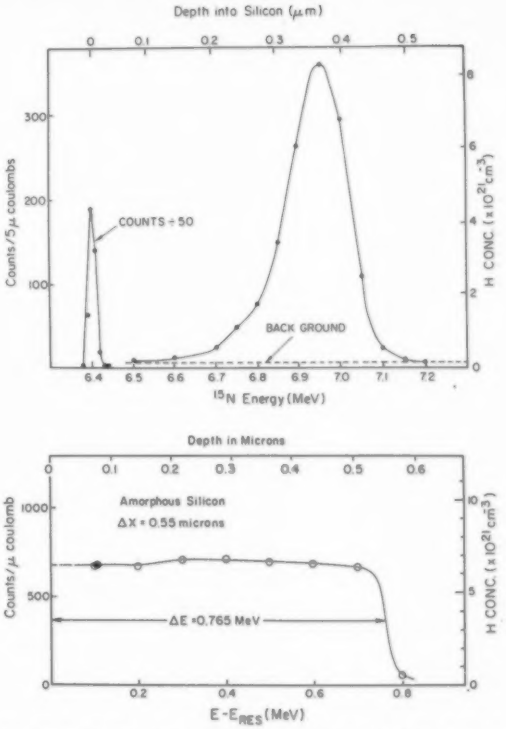

Fig. 3. (top) The NRA profile of a sample of Si implanted with 10^{16} H/cm^2 at 40 keV. Both raw data (counts versus beam energy) and final results (H concentration versus depth) are shown. (bottom) The NRA profile of a plasma deposited silicon sample on a Si substrate. The solid datum is a repeat measurement after the profile of the thin film was completed.

gamma-rays is proportional to the amount of H/cm^2 within the resonance detection window (i.e. when the energy is on resonance) and this is proportional to the thickness of the resonance detection window. But this thickness is inversely proportional to dE/dx.

$$\begin{aligned} &\text{Or: } Y = (\text{hydrogen concentration})/\text{K}\, dE/dx, \\ &\text{or: hydrogen concentration} = KY\, dE/dx, \end{aligned} \tag{2}$$

where Y is the gamma-ray yield (counts/C of incident ions), and K is a constant which depends on the reaction cross section, detector efficiency, etc., *but is independent of the material being analyzed*.

In summary, in resonant nuclear reaction profiling, a measurement of the number of nuclear reactions versus incident energy is made and eqs. (1) and (2) are used to convert the raw data to concentration profiles. The constant K is usually determined for a particular setup by measuring some sample of known hydrogen content (e.g. ion implanted with known dose, compounds of known stoichiometry, other standard sam-

ples). It is important to emphasize the K is independent of the material being analyzed and has only to be determined once. All the matrix dependent effects are contained in dE/dx.

The procedure outlined above is the way most NRA hydrogen profiles are actually carried out. However, there are both real and potential complications that can enter and need to be considered.

2.1. Depth resolution

Let us define the depth resolution (Δx) of this method to be what the measured full width at half maximum (FWHM) of the hydrogen profile would be if measured for an infinitely thin layer of hydrogen at some depth in a sample. This is then determined by the width of the reaction resonance (Γ) and the fluctuations in the energy (ΔE) of the bombarding ions *at this depth in the sample*. ΔE has contributions from the energy spread in the incident ion beam (ΔE_b), energy straggle (ΔE_s), and Doppler energy broadening (ΔE_D). Since in most cases these are all Gaussian distributions, the total energy width is obtained by adding them in quadrature:

$$\Delta E^2 = \Delta E_b^2 + \Delta E_s^2 + \Delta E_D^2. \quad (4)$$

The the nuclear reaction cross section is not a Gaussian function of the beam energy, and, hence, the width of the resonance does not simply add in quadrature to E above, but must be numerically convoluted. This convolution is available in graphical form in a paper by Amsel and Maurel [24]. In the case of the ^{15}N low energy resonance, the nuclear reaction width is so narrow as to be always small compared to the other contributions in eq. (4). In this case, Γ and ΔE add linearly. See ref. [24].

Hence, for the ^{15}N nuclear reaction method, the depth resolution is given by

$$\Delta x = (\Delta E + \Gamma)/(dE/dx). \quad (5)$$

For other cases, the resonance width has to be combined appropriately with ΔE above. See reference [24].

2.2. Straggling

As the pioneering work of Amsel and coworkers at Paris have demonstrated, a proper treatment of straggling is very important when proton induced NRA is carried out. However, straggling is usually much less important when hydrogen profiling with heavy ion induced nuclear reactions. The basic reason for this is simply that the ratio of energy straggle to energy loss of an ion penetrating a solid decreases with increase M (and Z) of the ion. Hence, while the influence of straggle can be dramatic in proton resonant profiling data, it is usually a small perturbation in ^{15}N nuclear reaction profiling data.

When straggling is taken into account, it is usual to use the Bohr formula [25]

$$\Delta E_s = 2.355(4\pi e^4 z^2 ZNx)^{1/2}, \quad (3)$$

where z and Z are the atomic numbers of the projectile and target atoms, respectively and N is target atomic density (atoms/volume) and x is the distance into the target. To put these numbers into perspective, for the ^{15}N NRA case, in Si, the energy straggle given by eq. (3) is 75 keV $\sqrt{\mu m}$, or the contribution of straggle to the depth resolution (a Gaussian full width at half maximum) is 50 nm $\sqrt{\mu m}$.

2.3. Doppler effects

It is a fact that hydrogen atoms in materials are not stationary but vibrate, typically in the zero point motion of an atom trapped in the lowest state of an harmonic oscillator potential well. For a narrow nuclear resonance, this motion can shift the reaction on and off resonance [26]. For example, the width of the ^{15}N resonance is 1.8 keV, whereas the Doppler broadening is in the range of 5 to 15 keV, depending on the strength of the hydrogen bond. This will be discussed further below. For the present purposes, it should be noted that this contribution is usually small compared to straggle, except when analyzing very thin hydrogen surface layers where Doppler effects are usually the dominant source of broadening.

2.4. Beam energy spread

This is a difficult topic to discuss in general because it is so dependent on the nature of the accelerator and its energy control and stability systems. However, experience suggests that if it has not been measured carefully, it is not known and it may be larger than simple estimates suggest.

2.5. Off-resonance contributions

The ideal nuclear reaction for profiling would be one with an infinitely narrow resonance reaction with a zero cross section off resonance. The ^{15}N nuclear reaction is nearly this ideal. The cross section is shown in fig. 4 [27]. Note that the off resonance cross section is more than four orders of magnitude smaller than the peak resonance cross section. For other resonance reactions, the off resonance cross sections a generally much larger.

However, even in this very favorable case, there are situations where the nonzero off resonance cross section needs to be taken into account. This occurs when

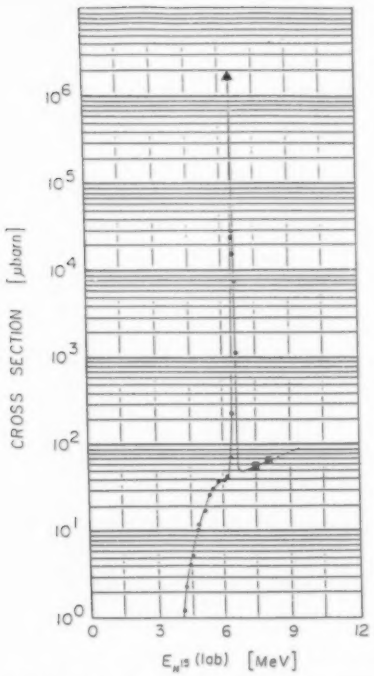

Fig. 4. The $^{15}H + {}^1H \rightarrow {}^{12}C + {}^4He$ + gamma-ray cross section. From ref. [27]. Note that the peak cross section at the resonance is more than four orders of magnitude greater than the off resonance cross section.

a profile is being measured through a surface layer containing large amounts of hydrogen and into a low hydrogen containing material. When the ^{15}N ions are on resonance deep into the material, the off resonance cross section with the large amount of near surface hydrogen may result in significant counts. The extreme example was used to measure this off resonance contribution. Namely, a layer of nominally TiH_2 on clean Si was profiled [27]. The results of this profile are shown in fig. 5. The counts above 7.2 MeV essentially all come from the off resonance cross section.

The correction for such off resonance effects are simple. Since the off resonance yield is proportional to the on resonance energy integrated gamma-ray yield (i.e. the yield curve between 6.4 and 7.2 MeV in fig. 5) times the off resonance cross section, once the proportionality constant is known, one simply subtracts these off resonance counts from the total counts. In the case of ^{15}N NRA, this correction is

$$Y_{\text{off res.}} = (1.28 \times 10^{-5}) I,$$

where I is the energy integrated on resonance yield (in counts · keV) [27].

In the case of the ^{19}F high energy nuclear reaction, there is another resonance at slightly higher energy [3]. The presence of this other resonance makes profiling anything other than rather thin layers very difficult because of "off-resonance" contributions from this second resonance.

2.6. Energy loss rate

As indicated above, all the matrix dependent effect in nuclear reaction analysis appear only in the rate of energy loss of the bombarding ions in the target. This is one of the great advantages of many nuclear methods of analysis. Because of it, the phrase "quantitative without reference to standards" is often used in describing these methods.

However, this phrase is only true to the extent that one knows dE/dx for the target. Fortunately, while dE/dx is a very complicated subject with no complete theoretical solution available, dE/dx is known to approximately 5 or 10% for most ions of interest in NRA from a combination of theory and experiment [28].

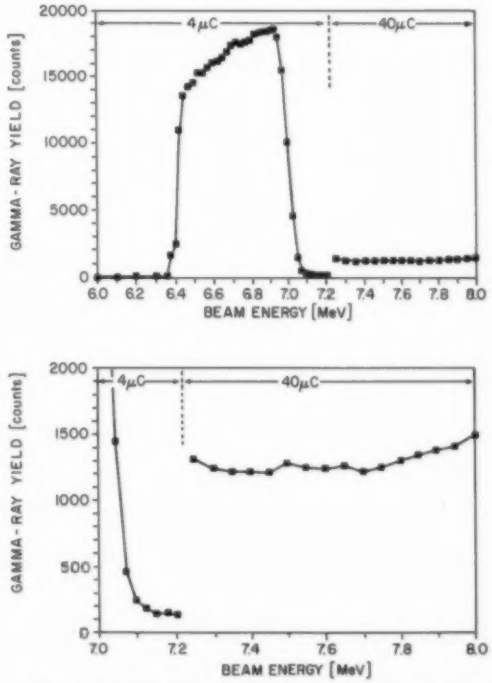

Fig. 5. The raw data (counts versus beam energy) for a sample of TiH_2 on Si. Both plots are of the same data with the lower plot expanded in order to see the off-resonance counts clearly. The counts above 7.2 MeV come from the off-resonance cross section. From ref. [27].

Most materials being analyzed are not single element targets. Hence, one needs to know how to combine elemental dE/dx to obtain the dE/dx for compound targets. The usual procedure is to assume (the Bragg rule) that each atom in a target contributes the same energy loss as it would in a single element target, i.e. that dE/dx is not sensitive to how elements are bonded in a sample. This is known not to be always accurate. One can do much better. For example, Ziegler and Manoyan [29] have shown accuracy of a few percent can be obtained for dE/dx in compound targets by making appropriate corrections to the Bragg rule. While these corrections are not typically made, they should be.

2.7. Channeling

When working with single crystal samples, channeling can have huge effects on NRA measurements. It can be a great asset when employed to learn about lattice locations. However, "accidental channeling" can also limit the accuracy of NRA depth profile measurements. As Andersen and coworkers have shown [30] these effects can also be very important in polycrystalline samples that have preferred crystal orientations (e.g. evaporated films). See ref. [30].

It is not the possible to discuss channeling in detail here. The only point that needs to be made is to beware of channeling effects when working with crystalline targets. In some single crystals, it is difficult to find any direction that is "random" in a channeling sense.

2.8. Backgrounds and sensitivity

When making NRA measurements where the reaction product is a high energy gamma-ray, the gamma-ray detectors are also sensitive to other background radiations, such as cosmic rays and, in some cases, accelerator generated radiation. This background is what limits the sensitivity of such NRA. There are several ways in which sensitivity can be improved. The first is to increase the beam current. Since, the background us usually independent of beam current whereas the real count rate increases linearly with beam current, sensitivity improves linearly with beam current. However, this approach can be used only up to the limit of the beam current available at a particular accelerator or the limit of beam current that a particular sample will withstand.

When the beam current is sample limited, it is now common practice in some laboratories to raster the ion beam over a large target area in order to reduce the effects of the beam.

An approach that would be possible if pulsed ion beams were available would be to blank electronically the detector except when the beam pulse was on target. Such an approach with the same average beam current would improve the sensitivity by the ratio of the pulse repeat time to the length of the beam pulse. As far as we are aware, this approach has not been utilized.

An approach that has been used at a number of laboratories is to build material and electronic shields to reduce the background in the gamma-ray detectors [31–33]. This approach is much easier with the advent of bismuth germinate (BGO) scintillation detectors as a replacement for NaI. BGO detectors are much more efficient (for a given size) than NaI but are much less sensitive to cosmic ray neutrons [32,33]. Hence, BGO detectors need much less material shielding than NaI. Experience suggest that one can obtain about an order of magnitude improvement in sensitivity using this approach. A variety of these systems are described in the literature [31–33].

3. Nuclear reactions for other isotopes of hydrogen

While the bulk of work on hydrogen profiling involves analysis for ^{1}H, there has also been considerable work on other isotopes. Indeed, one of the first publications of NRA was a study of range profiles of ion implanted D into gold and aluminum. In this work, the $D + D \rightarrow {}^3He + n$ reaction was used, with neutrons detected [7].

We will not attempt to describe here all the different possible reactions for deuterium (D) and tritium (T) analysis. Some of the reactions that have been used include: $D + D \rightarrow T + p$ [34], $D + D \rightarrow {}^3He + n$ [7], $^3He + D \rightarrow p + {}^4He$ [8,35], $T + D \rightarrow {}^4He + n$ [36], and $T + H \rightarrow {}^3He + n$ [37,38]. The reader is referred to the literature for discussion of these various reactions.

The most widely used reaction for deuterium analysis is the $^2H(^3He, p)^4He$ reaction [8,35] which has a very positive Q-value (18.35 MeV) making identification of the reactions products very easy. The depth information is obtained by the energy loss of the outgoing ^{4}He particles. The cross section for this reaction is not large (70 mb at 0.75 MeV) compared to the elastic cross section, so one has to worry about count rate problems.

4. Energy recoil detection (ERD)

4.1. Transmission coincidence

The 1971 paper of Cohen and coworkers [2] describes a method for hydrogen profiling in relatively thick (on the order 100 μm) self-supporting foils. The authors demonstrated ppm sensitivity, outlined how to

improve this sensitivity by an order of magnitude or more, and pointed out that with a microbeam, full three dimensional profiling could be achieved. While this method has not been widely adopted, it seems capable of solving some still outstanding hydrogen profiling problems. Hence, this method will be briefly described here.

The basic approach of this method, as outlined in fig. 6, makes use of the proton–proton elastic scattering. The sample to be analyzed is bombarded with protons (in Cohen's case at 17 MeV) and the incident proton and a recoiling proton are detected in coincidence by two detectors at plus and minus 45 degrees to the beam direction. The key reason that this technique works is that for every proton detected on one detector which comes from an elastic scattering from a hydrogen in the target there *must be a proton also detected in coincidence in the other detector*. Hence, it is the requirement that there must be two protons detected simultaneously in the two detectors that selects out the scattering from hydrogen from the scattering for all the other atoms in the target.

The depth information comes from the fact that the total energy lost in the target depends on where in the target a scattering occurred. See fig. 6. To make use of this information, the energy detected in both detectors is summed. The highest energy events observed come from scattering at the back edge of the foil and the lowest energy events come from scattering at the front side.

Fig. 7 shows a typical result for analysis of a foil with a very low hydrogen concentration. The count rate in the center of this foil corresponds to 10 ± 10 ppm (atomic), with the sensitivity limited by the tails of the surface hydrogen peaks. Background caused by tails of surface peaks is a common sensitivity limitation in

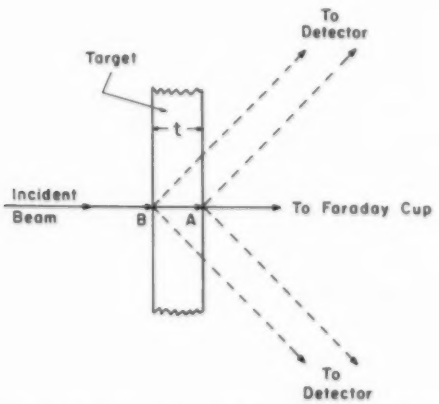

Fig. 6. A schematic representation of Cohen's transmission coincidence method for H profiling in self supporting foils. From ref. [2].

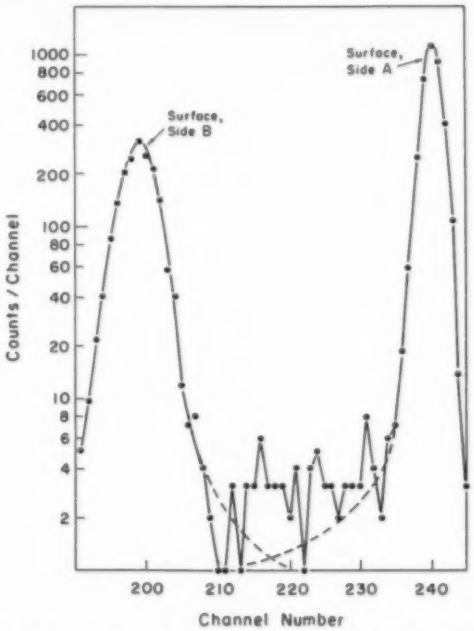

Fig. 7. Results for H content versus depth in a 50 μm iron foil measured by Cohen's p–p transmission coincidence method. From ref. [2].

recoil methods. However, it is worth noting that the foils used by Cohen had unusually high surface hydrogen contaminations, perhaps because of the way they were manufactured, perhaps because of Cohen's vacuum conditions. For example, the surface peaks in fig. 7 correspond to 1.2×10^{18} H/cm^2 (side A) and 0.24×10^{18} H/cm^2 (side B). This is 10 to 100 times more surface hydrogen than is commonly found on samples. Lowering this surface hydrogen would immediately improve the sensitivity.

The advantage of this method would seem to be that of high sensitivity, probably well below 1 ppm (atomic) is good cases. It utilizes low beam currents (a few nanoamperes) of a lowly ionizing particle. Hence, beam induced effects on the target material should be small. With microbeams, there Is the possibility of full 3 dimensional imaging.

The disadvantage of this method is that it requires samples that are thin enough to transmit the protons. At the energies that Cohen worked, this corresponds to maximum thickness on the order of a few tenths of millimeters. It also requires a relatively high energy proton beam which is not commonly available to the IBA community.

One area of research that might benefit from application of this method is the study of hydrogen in minerals. This problems was discussed in detail by G.

Rossman at the last IBA conference [39]. It would seem that standard geologic thin sections (removed from their backing) would be suitable targets. This application needs high sensitivity along with minimum beam effects on the samples. Imaging with a microprobe to look at different hydrogen concentrations in different phases or at different regions in a single crystal would also be useful.

4.2. Heavy ion ERD

Heavy ion energy recoil analysis uses precisely the same physics as Rutherford backscattering spectrometry but chooses a geometry to detect the recoiling target atoms rather than the backscattered incident ion [17]. By doing this, the method becomes sensitive to exactly those atoms that are difficult to detect in RBS, light atoms. Within this general framework, there is a large amount of freedom to choose different experimental conditions to optimize for different goals (best depth resolution, or maximum count rate, or sensitivity to many light elements, ...).

Fig. 8 shows a common arrangement used in ERD. There is an beam of ions incident on the sample and a detector sensitive to the recoiling target atoms. This figure shows the more commonly used geometry (glancing angle) but for thin samples a transmission geometry can be very useful.

Fig. 9 shows a spectrum of recoil particles recorded by the Montreal group using 30 MeV ^{35}Cl beam incident on a thin copper sample coated with Li and implanted with He [17]. This spectrum illustrates both the power and the limitation of this method. First, it is powerful in that it gives information on all the light elements present in the sample from H to carbon. In this case, depth profiles for both the front (F) and back (B) are determined. The limitation of this method is that (as in RBS) the spectra for all the different elements are superimposed. For example, the H profile data are on top of a large carbon peak. For H analysis alone, this is not a very serious limitation because one can usually choose a projectile mass and energy so that the H signal is kinematically separate from everything else. However, a better solution is to use a counter telescope to identify the M or Z or the recoil particles. This is discussed below.

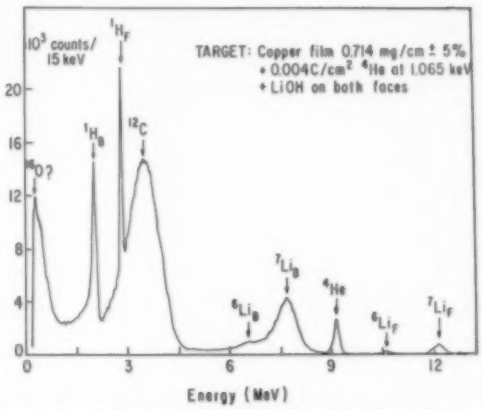

Fig. 9. The ERD spectrum recorded by the Montreal group for 30 MeV ^{35}Cl beam incident on a target of LiOH on Cu implanted with He. F and B refer to front and back of the target. From ref. [17].

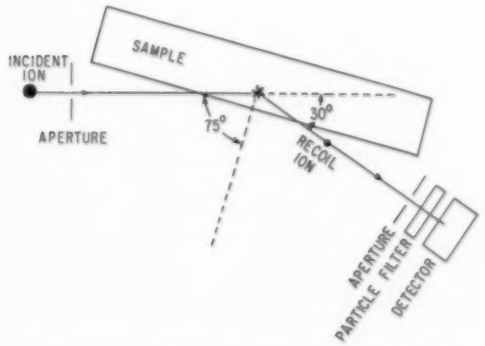

Fig. 8. A schematic representation of the usual ERD method for glancing geometry. From ref. [19].

One of the main considerations in designing a recoil setup is how are the recoiling target atoms going to be separated from the elastically scattering incident ions. The most common approach is the one shown in fig. 8. Namely, an absorber foil (particle filter) is placed in front of the detector. This absorber foil is chosen to be thick enough to stop all the elastically scattered incident particles but thin enough to pass the recoiling atoms.

The use of absorber foils has the big advantage of being simple but has the disadvantage of introducing straggle into the energy of the detected particle. Since, as in RBS, the depth information is contained in the energy of the detected particle, this straggle degrades the depth resolution of this method. Because of its simplicity, the foil absorber method is widely used. Paszti and coworders in Budapest have carefully studied optimization of parameters to obain the best possible depth resolution in this approach. They report that using a ^{4}He beam, a depth resolution of 10 nm can be optained [40].

A second approach is to eliminate the elastically scattered particles kinematically [41]. This can be done by moving the detector to a large enough angle that it is beyond the kinematically allowed maximum scattering angle for the particular beam/target combination

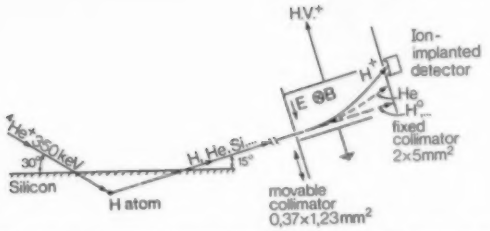

Fig. 10. A schematic representation of the recoil method as developed by Ross and coworkers. Here the absorber foil is replaced with a electromagnetic filter that passes the recoil particles but not the elastically scattered particles. This method does not add straggle to the recoils. From ref. [20].

in question. In this situation, only the recoils are possible at the detector. Unfortunately, since targets with only light elements are not common, this approach has had few applications.

A far better approach is to install an electromagnetic particle filter in front of the detector. This could be a full magnetic spectrometer or it could be a rather crude electromagnetic filter that passes the recoil particles but not the elastically scattered particles. Ross and coworkers at the University of Quebec [20] have demonstrated the utility of the latter approach. Fig. 10 shows this situation. As shown in this figure, their electromagnetic filter disperses the particles by their mass. By placing the detector at the position of H^+ particles, that is all that they detect. This process introduces no straggle in the energy of the detected particle, greatly improving the depth resolution over that obtained with absorber foils. Fig. 11 shows a hydrogen profile measured by this technique. As seen in this figure, the depth resolution can be very good, on the order of a few nm.

Ross's filter is a rather simple and inexpensive device with crossed electric and magnetic fields. A much more powerful (and expensive) solution is to use a magnetic spectrometer to detect the recoils. Gossett at NRL [42] has done this and obtained 8 nm depth resolution using 3 MeV He as the bombarding ion. The use of magnetic spectrometers to measure hydrogen profiles in ERD would seem to have enormous potential. This approach should have very high depth resolution, and since sensitivity in ERD is almost always limited by tails of surface hydrogen peaks, this approach should give very high sensitivity.

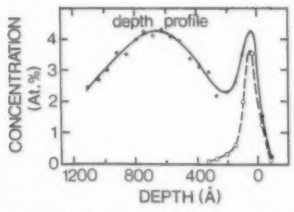

Fig. 11. An example of a H profile measured using 350 keV He beam with the electromagnetic filter shown in fig. 10. The depth resolution is approximately 10 nm at the surface. From ref. [20].

4.3. Glancing or transmission geometry

Most ERD work is done in a glancing angle geometry. This is because most samples are not thin and self-supporting. However, for some types of problems, there are large advantages of using transmission geometry where the recoiling hydrogen passes through the sample and is detected at or near zero degrees from the incident beam direction. Zero degrees is both the angle where the recoils have the maximum energy and the angle where the change in recoil energy with angle ($dE/d\theta$) is a minimum. In fact, $dE/d\theta$ is 0 at zero degrees. Hence, one has both high energy particles and one can use a large solid angle and still preserve reasonable depth resolution.

Hence in cases where high count rates per incident projectile are needed, transmission geometry may be the best solution. For example, ppm sensitivity can be obtained in favorable cases in transmission geometry in UHV [43]. In another example, we used a large solid angle transmission geometry (shown in fig. 12) in order to measure the redistribution of H under changes in strain [44]. Since the changes in hydrogen concentration expected were relatively small (10% or less), a method that gave high statistical accuracy quickly was needed. By using this geometry, count rates of 5000 counts/s were obtained with 7 nA of beam current on samples contain 23% H. Fig. 13 shows an example of the use of this method to measure the hydrogen near the surface of Ta depending on the stress applied (by bending the sample). H content decreases under compression and increases under tensile stress. Transmission geometry can even be used to obtain useful hydro-

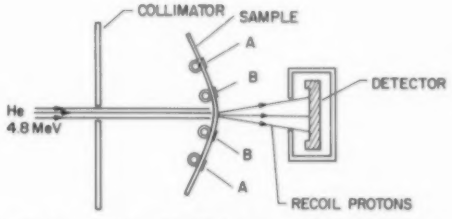

Fig. 12. An example of ERD in transmission geometry to get very large count rates of recoil H with small incident beams. This was used in an experiment to measure the change in hydrogen content with stress (as obtained by bending the sample in situ). From ref. [44].

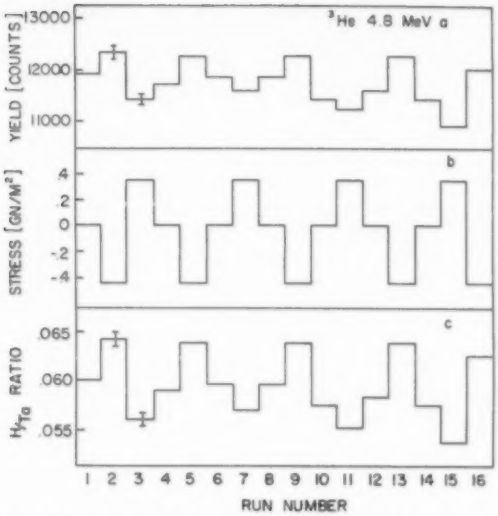

Fig. 13. Recoil data recorded with the apparatus shown in fig. 12. Hydrogen is seen to move from regions under compression to regions under tension. From ref. [44].

gen profile data in ERD using radioactive alpha sources, although long run times are needed [45].

In sum, the very large count rate per incident particle possible in a recoil geometry provides a number of unique analytic possibilities that might solve problems that are otherwise unsolvable.

4.4. M or Z dispersive ERD

ERD is fundamentally very much like RBS and is usually practiced much like RBS. Namely a single energy sensitive detector is used and mass of the detected particle is determined only by its energy [17]. If analysis is desired only for hydrogen isotopes, they are so different in mass from other nuclei that this simple kinematic determination is usually sufficient. However, overlap of masses is this single recoil spectrum can and commonly does occur. See for example fig. 9.

ERD has one large fundamental advantage over RBS in that the detected particle has the M and Z of the target element being profiled. Hence, if a simple energy sensitive detector is replaced with a counter telescope that can measure the M or Z (or both) of the recoiling atoms as well as their energy, one has the possibility of determining in a single run separated, nonoverlapping depth profiles of all light elements in the target. This is clearly a very desirable goal.

Counter telescopes which can determine the isotope of the detected particle have been known and utilized in nuclear physics for decades. There are two common types: one measures energy loss (ΔE) in a thin detector as well as total energy (E). The other type measures time-of-flight (TOF) of the detected particle as well as its energy. An energy loss telescope is capable of uniquely determining both the M and Z of the recoiling particle at reasonable energies. A TOF telescope determines the mass of the recoils. For IBA purposes, either is normally sufficient [21,46–48].

4.5. Kinematically corrected counter telescope

One of the difficulties of ERD is that in order to preserve the depth resolution of this method, the scattering angles accepted by the detector have to be carefully restricted. Otherwise, because the energy of the recoils changes so rapidly with scattering angle, the depth resolution of the method is rapidly degraded. This problem can be solved to a limited extent by carefully designing the slits [49]. However, if a counter telescope is to be used to identify the recoil isotope, it is possible to also make kinematic corrections.

Fig. 14 shows the schematic of the ΔE ion chamber telescope. It consists of an ion chamber (with a Frisch grid) ΔE detector in front of a standard surface barrier detector. There are actually two ΔE chambers for redundancy. This a rather thin ΔE counter, with the entrance window about 30 $\mu g/cm^2$, operated with 100 $\mu g/cm^2$ of isobutane.

This detector is mounted on its side (i.e. the figure shown is in the scattering plane) so that electrons from particles at large scattering angles have to drift farther to the collector electrodes than electrons from smaller scattering angles. By measuring the time it takes these electrons to drift to from the ion path to the Frisch grid, one has a measure of the scattering angle which can be used to make kinematic corrections to data. This can be done, for example, by feeding this drift time data, event by event, into a computer along with

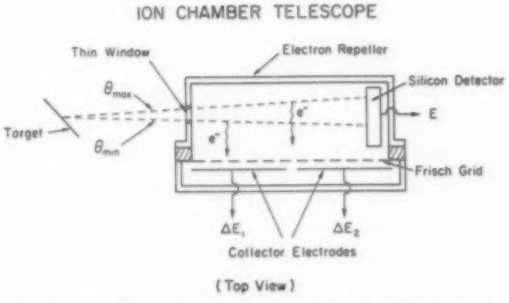

Fig. 14. A schematic representation of a ion chamber telescope that can measure energy loss (to identify recoiling element), energy (for depth information) and scattering angle (to make kinematic corrections). The scattering angle is determined by measuring the electron drift time from the ion track to the collector.

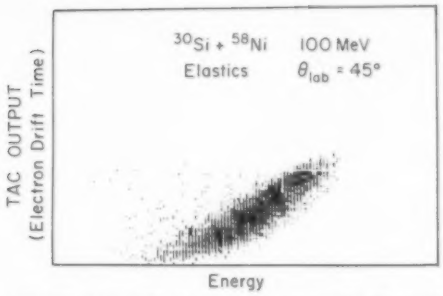

Fig. 15. Electron drift time versus energy for Si elastically scattering from Ni. By making kinematic correction, the effective energy resolution was improved by a factor of 3.

the ΔE and E data. We have done it by simply taking the output of the TAC used to determine the drift time, carefully adjusting the gain of the TAC output and simply adding it to the E signal, i.e. making kinematic corrections with fixed wire linear electronics.

Fig. 15 shows a plot of TAC out put versus energy of the particle. The large peak is just of elastic scattering of Si off Ni. The tilted line in the plot results from simple kinematics. By making the kinematic correction outlined above, the energy resolution of this elastic scattering was improved by a factor of 3.

Since M and Z Dispersive ERD are much more general analytical methods than simply ways to probe a sample for hydrogen, they will not be discussed in more detail here. They clearly have great potential but require higher energy heavy ion beams than are generally available in IBA laboratories. They are also relatively new and only time will tell if this approach competes effectively with other analytical approaches.

5. Foreward alpha scattering technique (FAST)

Another method to measure H and other light elements in thin samples is simply to detect elastically scattered partiles with a detector at foreward angle and use the energy of the detected particle to deduce the mass from which it scattered. T. Cahill at Davis [50] uses this method with a 30 MeV ^{4}He beam to measure H, C, O, and N in aersols. The method gives only the areal density (atoms/cm^2). Fig. 16 shows a typical spectrum with the peaks identified by the element from which the particles scattered [50].

This method is well suited to be used in conjunction with particle induced X-ray measurements (PIXE). The PIXE is sensitive to all heavier elements and the FAST gives the light elements. See [50].

6. Doppler spectroscopy

As pointed out in a series of papers by the Heidelberg group of Zinke-Allmang, Kalbitzer, and coworkers [51], the 6.385 MeV resonance in the $^{15}N + ^1H$ nuclear reaction is so narrow that motion (usually ground state zero point motion) of H bound in a target can shift the reaction on and off resonance. This broadening effect can then be used to learn about how H is bound in the solid [51]. Consider a hydrogen atom bound in a solid or a molecule which has a velocity, v. The energy of the ^{15}N ion incident on such a moving proton is Doppler shifted. The proton sees the energy of the incident ^{15}N as

$$E = M(V_N + v)^2/2$$
$$= MV_N^2/2 + MvV_N + Mv^2/2, \quad (4)$$

where V_N is the velocity of the ^{15}N ion (9.1×10^6 m/s at 6.4 MeV) and M is mass of the ^{15}N ion.

In eq. (4), the first term is 6.385 MeV (the laboratory ^{15}N energy). The second "Doppler" term is on the order of 5 keV, depending on how the H is bonded in the target. The third term is on the order of the binding energy of the proton in the solid and is negligible here. If one can measure the Doppler term, one has a rather direct measure of the strength with which the hydrogen is bonded in the solid [51–54].

The velocity of a H atom is sometimes toward and sometimes away from the direction of the incident ^{15}N ion. Hence, the effect of this term is to add to the beam energy (measured in the laboratory) a fluctuating term that has the magnitude of the Doppler term in eq. (4). That means, for example, that when measuring the nuclear reaction gamma-ray yield versus beam energy for an infinitely thin H target, the width of the yield curve would not be the 1.8 keV width of the nuclear resonance but rather the convolution of the 1.8

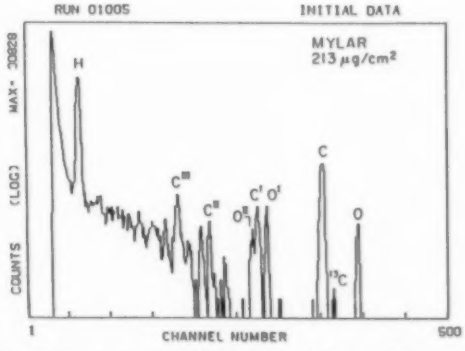

Fig. 16. Spectrum of He ions scattered from a 213 mg/cm^2 mylar film. The labels on the peaks identify the elements in the target. From ref. [50].

keV Breit–Wigner shape with a Gaussian whose width was given by the Doppler term and is in the range of 5–15 keV (FWHM), depending on the bond strength. Hence a measurement of this yield curve for a thin target determines the bond strength. Fig. 17 gives some Doppler widths expected for some known hydrogen bonds [54].

Since this method is only sensitive to the strength of the H bond in the direction of the incident ion, this method is capable of measuring bond strength as a function of angle, for example of hydrogen bonded to a single crystal surface. This is unique information not available from other experimental measurements.

Doppler spectroscopy has been demonstrated in a few cases [51–55]. One of the potential experimental problems associated with this measurement is the effect of radiation damage from the analyzing beam on the way H is bonded to a surface. To avoid this problem, Horn and coworkers [53,54] demonstrated the effect by measuring the Doppler broadening for H_2 and methane gases using a windowless gas cell for a target. Since the target was continually refreshed, this avoided radiation damage effects. In addition, because the target thickness could be easily and continually varied, this allowed for careful determination of both straggle and energy loss effects. Iwata and coworkers have measured the Doppler broadening of H on W (001) [52].

However, perhaps the physically most interesting results are not measurements made on single crystal samples but on hydrogenated carbon samples [55]. Kalbitzer's group published the first measurements on Doppler broadening [51] working with surfaces coated with thin layers of hydrocarbons. His group has continued to work with carbon containing H. Shown in fig. 18 are some very interesting results of Doppler broadening for this case [51]. These are thick target yields and the Doppler broadening results in the yield curve rising more slowing than it would without this effect. The interesting point is that the Doppler broadening measured at the beginning of the analysis of a sample gave a width of 14.6 keV (FWHM) whereas the same sample, after long exposure to the ^{15}N beam has a reduced Doppler width of 8.3 keV. Hence, what is being ob-

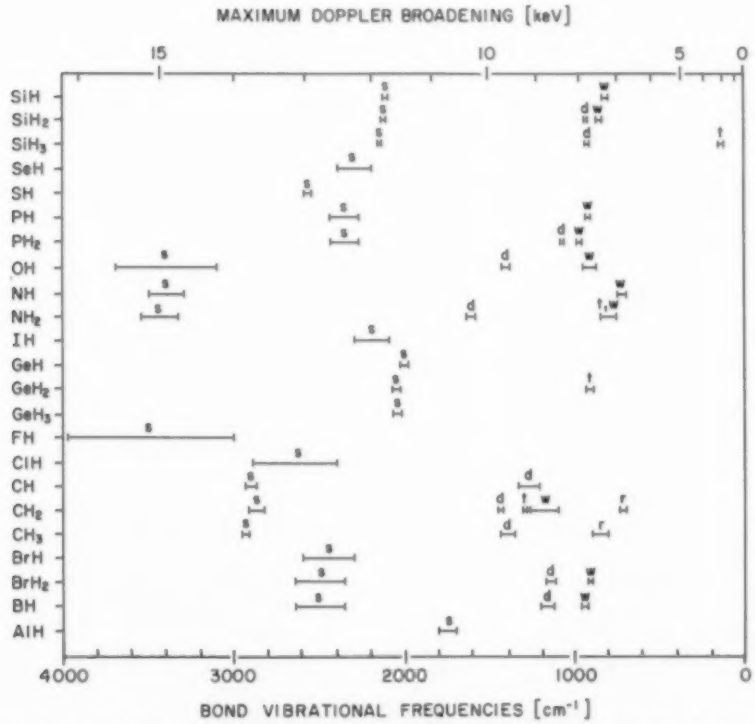

Fig. 17. Compilation of expected Doppler broadening for some X–H bonds. S = stretch, R = rock, D = deformation, T = twist, and W = wagging. From ref. [54].

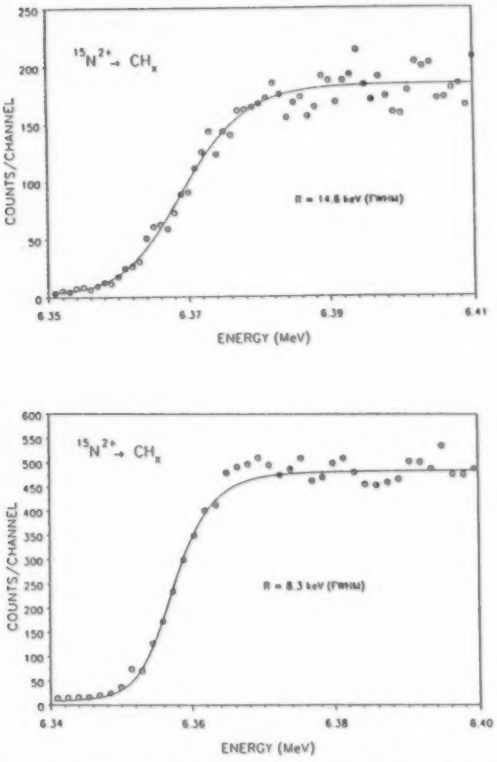

Fig. 18. Measurement of Doppler broadening for H in thick carbon films. The upper data were measured first and show a Doppler width of 14.6 keV. The lower data were measured after exposing the sample to ^{15}N beam for a long time. Now the Doppler width has decreased to 8.3 keV. This change is caused by changes in the H bonding caused by the beam irradiation. From ref. [55].

served is change in the way the H is bound to C as a result of the ion beam irradiation. This may be the result of conversion of C–H bonds to H–H bonds [55].

6.1. ERD doppler spectroscopy

While to the best of our knowledge, Doppler broadening has been used to study bond strengths only in the context of NRA with very narrow resonances, it is more general than that. For example, the motion of a bonded proton also effects the energy of a recoiling proton subject to ERD.

In particular, let there be a projectile of mass M with velocity V incident on a proton of mass m and velocity v and work in one dimension. (Note, the expression for the full three dimensional case is given in ref. [51c].) If $v = 0$ (proton at rest), the recoil energy is given by

$$E_{\text{recoil}} = \{(4Mm)/(M+m)^2\}E_0, \tag{5}$$

where E_0 is the incident energy of M. If v is not 0

$$E_{\text{recoil}} = \{(4Mm)/(M+m)^2\}\{M(V-v)^2/2\} + \{mv^2/2\} + \{2mMv(V-v)/(M+m)\}, \tag{6}$$

which, in the limit that v is much less than V becomes approximately

$$E_{\text{recoil}} = \{(4mM)/(m+M)^2\}\{E_0 - (M-m)Vv/2\}. \tag{7}$$

The second term now becomes the "Doppler" term (E_D). To compare the size of this effect with the NRA Doppler term, consider the ratio of E_D to the incident energy E_0.

NRA: $E_D/E_0 = 2v/V_N$,

ERD: $E_D/E_0 = -\{4mM/(m+M)^2\} \times \{(M-m)/M\}v/V$.

As can be seen, both these are comparable, with the ERD ratio typically 1/2 to 1/4 the NRA ratio.

To put some numbers in to see how big this effect is, lets consider ^4He ERD at 1.7 MeV (the same velocity as 6.4 MeV ^{15}N), if the Doppler broadening was 15 keV in NRA, then it would be 1.0 keV in ERD, which is small but it should be measurable.

7. Comparison of different approaches for H profiling

A number of different ways to measure hydrogen concentration profiles are outlined above. While they are very different in some ways, it is important to remember that they all share the important property that they are MeV ion beam methods that rely on nuclear properties and are insensitive (except through channeling and stopping powers) to the matrix effects that make other methods, such as secondary ion mass spectrometry, so difficult to quantify. Hence, they all share the important characteristic that they are easy to make quantitative without reference to standards.

7.1. General light element probe

Heavy ion ERD is fundamentally different from the other methods discussed in that *it is a general method that gives information about all light elements present in a sample*. This can be an enormous advantage, just as it is in RBS. Many times RBs spectra are recorded to study some particular element in a sample and the

analysis points out some totally unexpected features in the target. This can lead to major discoveries. Heavy ion ERD gives information not only about H but also about C, N, and O and having all this information may provide insights that looking at just one element cannot give.

7.2. Comparison of H probes

Our experience has been that by far the most common analytic need for hydrogen analysis is to provide a quantitative measure of the hydrogen content versus depth in some sample or set of samples. Examples would be a study of CVD thin film materials (amorphous Si, silicon nitride, silicon carbide, boron nitride, silicon dioxide, diamond-like amorphous carbon, copper, high temperature superconductors,...) or studies of the water based corrosion of materials (e.g. radiation-waste glasses, obsidian or other archaeological glasses, Zr alloys used in reactors,...). For most such measurements, as long as the hydrogen levels are high enough and the layers thick enough, any of these methods will work fine. One should simply choose that method which is easiest to implement given the laboratory resources available.

The distinction between which methods are better depends on responding to certain analytic challenges. Below are listed some generic analytic challenges along with comments on the advantages or disadvantages of different approaches.

7.3. Quantitative accuracy

The method that is easiest to make quantitatively accurate is the method that is the simplest and allows for the most precise determination of the critical parameters. In this respect, NRA is the best. To make quantitatively accurate NRA measurements requires that you can reliably measure the quantity of beam incident on the target, and that the gamma-ray detector has'a constant efficiency. Since in NRA the detector is removed from the analysis chamber, there is essentially complete freedom to design a very effective Faraday cage. If the geometry with the sample normal to the beam with the detector at zero degrees (as shown in fig. 2) is chosen, even if the incident beam wanders a little in position, the detector efficiency does not change significantly. In ERD, charge integration is more difficult because the detector has to be in the analysis chamber and the beam/sample/detector geometry has to be maintained very precisely in order not to change either scattering angles (and hence cross sections) or detector solid angles.

In addition, analysis of NRA data relies only on a single cross section (the reaction cross section at the resonance energy) whereas ERD depends on knowing the recoil cross section at all energies at which recoils occur. Since the ERD cross sections commonly used are distinctly not Rutherford, they have to be measured as a function of energy and detection angles used. Just the determination of ERD cross sections has resulted in a large number of publications and the question is still not settled [56–59].

ERD is similarly more sensitive to stopping powers as a function of energy [60]. In NRA, the equation converting raw data to hydrogen concentration (eq. (2)) depends only on the stopping power at the resonance energy whereas ERD depends on stopping powers at all energies at which recoils occur.

Hence, NRA is easier to make quantitatively accurate both because it is easier to make the needed measurements accurately and because analysis of the date relies on fewer parameters such as cross sections and stopping powers as a function of energy.

7.4. Beam damage effects

However, accuracy can be obtained in any of these methods only if the hydrogen content of the sample is not significantly altered during a measurement. For many materials, hydrogen can be lost from a sample during ion beam irradiation. A good example is the measurement of the hydrogen content of a plastic such as polyethylene which rapidly looses a large fraction of its hydrogen content under beam irradiation.

There are at least two approaches to minimize this problem. One is to use an analysis beam which minimizes irradiation effects, i.e. proton or helium beams in an ERD mode rather than high energy heavy ions in NRA mode. The other is to raster the analysis beam over a large area of the sample. While rastering is commonly done is NRA, it generally cannot be done in ERD (in glancing geometry) because of the need to control the scattering geometry carefully. Rastering can be done is ERD in a transmission geometry.

Either of these approaches can be used effectively in many cases. However, in the limit of measuring a sample that has a low hydrogen content and that is sensitive to beam effects, ERD in a transmission geometry is clearly the best technique. Recoil cross sections are very large and in a transmission geometry, detector solid angles can also be very large. The principal disadvantage of this approach is that it requires relatively thin samples.

7.5. Sensitivity

Sensitivity is difficult to discuss without carefully specifying what type of sample is being considered. How much beam will the sample take? (How much is available?) How large is the sample? Is it flat with a smooth surface? How much surface hydrogen does the

sample have? Can the surface hydrogen be cleaned without changing the hydrogen in the bulk? Is the sample available as a thin self-supporting film?

The first point to make is that all these methods have sufficient signal to see ppm hydrogen and below. The problem of sensitivity is one of backgrounds. In NRA, backgrounds come from cosmic rays in the gamma-ray detector and while this can be reduced by shielding (material and electronic) it remains an important limit. In ERD and in some cases in NRA, the backgrounds come from hydrogen that is not in the region of analytical interest. In ERD, the sensitivity limit is almost always the tail of the ever present surface hydrogen peak. Since depth resolution in ERD is usually not very good (especially if the samples are not both flat and smooth), this is a significant problem, often limiting the practical sensitivity to 1 ppt or worse. An obvious approach is to clean sample surfaces, and to a point this can be done. However, at least in some metals, there is a dynamic equilibrium between surface hydrogen and bulk hydrogen. Hence, the surface cannot be effectively cleaned without changing the hydrogen content in the bulk.

In some situations, particularly when analyzing small samples, there can be a similar source of background in NRA. Namely, one has to be certain that the *analyzing beam hits the target and only the target*. One cannot use beam defining slits near the target because H in them will be a source of background. Yet if any of the beam misses the sample or hits the edge of the sample, it is likely to produce signals from hydrogen not in the region of analytical interest.

Since the background in ERD is from surface contaminations, it would seem that if experiments were done with D instead of H, the background would be greatly reduced. This has been demonstrated [43]. Fig. 19 shows an ERD spectrum recorded with 4 MeV He beam incident on a 13 μm Ni foil. The large peak is due to surface H contamination. The counts in the D region correspond to an average concentration 500 ppb of D in the first micron within the foil.

It is difficult to give simple statements as to what method has the highest practical sensitivity. To date, NRA has produced more useful high sensitivity data than recoil. Yet recoil (using a transmission geometry in UHv) has demonstrated better sensitivity in ideal cases.

7.6. Depth resolution

Depth resolution is one area where NRA is generally far superior to ERD, as commonly practiced. Namely, ^{15}N NRA profiling has a depth resolution at the surface of a sample (Gaussian FWHM) of about 8 nm in Si and about 3 or 4 nm in a heavy metal. It is limited by the Doppler broadening effect. Deeper into the target, it is limited by straggle of the nitrogen beam. In ERD, at least when an absorber foil is used, there is always straggle of the recoil protons in this foil which translates into poor depth resolution. ERD is glancing geometry also has to account for kinematic broadening of depth resolution. Namely, the finite sized detector accepts recoil protons at different scattering angles and, hence, different energies even if they originated at the same depth in the sample.

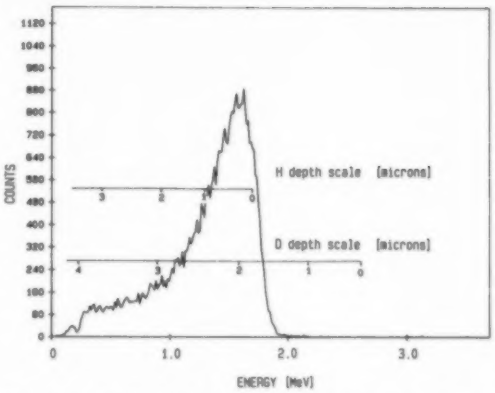

Fig. 19. An ERD profile for D in a 13 μm Cu film measured in transmission geometry with a 4 MeV He beam. The counts in the D region correspond to an average concentration of 500 ppb of D in the first micrometer of this film. From ref. [43].

In sum, depth resolution in NRA is typically several times better than in ERD, and, as indicated above, this effects the practical sensitivity of ERD. However, it should be emphasized that this is not a fundamental limitation of ERD. If a nonstraggling filter (such as Ross's electromagnetic filter) [20] is used along with a kinematically corrected detector, ERD can also have very good depth resolution. A better solution would be to use a magnetic spectrometer which is without straggle, kinematically corrected, and capable of very good energy resolution [42].

7.7. Other comparitive reviews

MeV ion beam analysis for H has now been practiced for about 20 years and a number of publications have described different approaches and commented on advantages and disadvantages of particular procedures. Probably the first of these is by Bottiger, Picraux and Rud at the Second International Conference on Ion Beam Analysis held in Karlsruhe in 1975 [61]. At the next Ion Beam Analysis Conference held in Georgetown in 1977, Ziegler organized a workshop on H analysis in connection with a round-robin comparison of all the available techniques for measuring H in materials. The publication describing that comparison

is still very useful [18]. There have also been some single laboratory comparisons of some of these methods. Xiong et al. made some detailed comprisons of both the low and high energy resonances in ^{15}N and ^{19}F [22]. Trocellier and Engelmann made comparitive measurements of ^{7}Li with other nuclear reactions [5].

Recently, Khabibullaev and Skorodumov have published a book Determination of Hydrogen in Materials Nuclear Reaction Methods [62]. This includes descriptions of most MeV ion beam techniques (such as those discussed here) as well as some nuclear methods not well known in the West. One potentially important example is the measurement of H profiles by elastic recoil detection induced by monoenergetic neutron beams.

8. Conclusions

Above are described a number of ways that MeV ion beams can be used to measure hydrogen concentration profiles. These methods are easy to make quantitative without reference to standards and are now practiced in a number of laboratories around the world and are making substantial contributions to a wide variety of fields.

The techniques fall into one of two categories: nuclear reaction analysis and energy recoil detection. Depending of the needs of a particular problem, both of these methods have advantages.

In good cases, ppm sensitivity and depth resolutions of a few nanometers are possible. However, the practical limits achievable is dependent on the nature of the sample being analyzed and on the facilities available.

The development of Doppler spectroscopy to measure how H is bound to surfaces in NRA and possibly in ERD provides a new and useful probe of H on surfaces.

Historically, NRA has been used in many more studies of hydrogen in materials. However, because of the wide availability of facilities for He ERD and because of the potential of high energy heavy ion ERD, this method seems to becoming more popular.

References

[1] E. Marsden, Philos. Mag. 27 (1914) 824; E. Marsden and W.C. Lantsberry, Philos. Mag. 28 (1914) 240.

[2] B.L. Cohen, C.L. Fink and J.H. Degnan, J. Appl. Phys. 43 (1972) 19.

[3] D.A. Leich and T.A. Tombrello, Nucl. Instr. and Meth. 108 (1973) 67.

[4] R.R. Lee, D.A. Leich, T.A. Tombrello, J.E. Ericson and I. Friedman, Nature 250 (1974) 44.

[5] P.N. Adler, E.A. Kamykowski and G.M. Padawer in: Hydrogen in Metal (ASM, Metals Park, OH, 1974) p. 623. Also see, P. Trocellier and Ch. Engelmann, J. Radioanal. Nucl. Chem. 100 (1986) 117.

[6] E. Ligeon and A. Guivarc'h, Radiat. Eff. 22 (1974) 101.

[7] Y.Y. Chu and L. Friedman, Nucl. Instr. and Meth. 38 (1965) 254.

[8] P.A. Pronko and J.G. Pronko, Phys. Rev. 9B (1974) 2870.

[9] W.A. Lanford, H.P. Trautvetter, J.F. Ziegler and J. Keller, Appl. Phys. Lett. 28 (1976) 566.

[10] W.A. Lanford and R. Golub, Phys. Rev. 39 (1977) 1509.

[11] M.H. Brodsky, M.A. Frisch, J.F. Ziegler and W.A. Lanford, Appl. Phys. Lett. 30 (1977) 561.

[12] W.A. Lanford, IEEE Trans. Nucl. Sci 26 (1979) 1795.

[13] W.A. Lanford, K. Davis, P. LaMarche, T. Laursen, R. Groleau and R.H. Dormus, J. Non-Cryst. Solids 33 (1979) 249.

[14] W.A. Lanford and M.J. Rand, J. Appl. Phys. 49 (1978) 2473.

[15] W.A. Lanford, P.H. Schmidt, J.M. Rowell, J.M. Poate, R.C. Dynes and P.D. Dernier, Appl. Phys. Lett. 32 (1978) 339.

[16] W.A. Lanford, Science 196 (1977) 975.

[17] J. L'Ecuyer, C. Brassard, C. Cardinal, J. Chabbal, L. Deschenes, J.P. Labrie, B. Terreault, J.G. Martel and R.St. Jacques, J. Appl. Phys. 47 (1976) 381.

[18] J.F. Ziegler, C.P. Wu, P. Williams, C.W. White, B. Terreault, B.M.U. Scherzer, R.L. Schulte, E.J. Schneid, C.W. Magee, E. Ligeon, J. L'Eecuyer, W.A. Lanford, F.J. Kuehne, E. A. Kamykowski, W.O. Hofer, A. Gauivarc'h, C.H. Filleaus, V.R. Deline, C.A. Evans, C. Brassard, R.S. Blewer, R. Behrisch, B.R. Appleton and D.D. Allred, Nucl. Instr. and Meth. 149 (1978) 19.

[19] B.L. Doyle and P.S. Peercy, Appl. Phys. Lett. 34 (1979) 811.

[20] G.G. Ross, B. Terreault, G. Gobeil, G. Abel, C. Coucher and G. Veilleus, J. Nucl. Mater. 128/129 (1978) 730.

[21] R. Groleau, S.C. Gujrathi and J.P. Martin, Nucl. Instr. and Meth. 218 (1983) 11.

[22] F. Xiong, F. Rauch, C. Shi, Z. Zhou, R.P. Livi and T.A. Tombrello, Nucl. Instr. and Meth. B27 (1987) 432. Also, see C.A. Barnes, J.C. Overly, Z.E. Switzkowski and T.A. Tombrello, Appl. Phys. Lett. 31 (1977) 239.

[23] F. Rauch, Institut für Kernphysik der Johann Wolfgang Goethe Universitat, Frankfurt am Main, Germany, private communication.

[24] G. Amsel and B. Maurel, Nucl. Instr. and Meth. 218 (1983) 183.

[25] N. Bohr, K. Dan Viden Selsk. Mat.-Fys. Medd. 18 (1948) 1.

[26] G. Amsel and B. Maurel, Nucl. Instr. and Meth. 218 (1983) 183.

[27] K.M. Horn and W.A. Lanford, Nucl. Instr. and Meth. 29 (1988) 609.

[28] See Stopping and Ranges of Ions in Matter (especially vol. 5), ed. J.F. Ziegler (Pergamon, New York, 1985).

[29] J.F. Ziegler and J.M. Monoyan, Nucl. Instr. and Meth. B35 (1988) 215.

[30] H.H. Andersen, K.N. Tu and J.F. Ziegler, Nucl. Instr. and Meth. 149 (9178) 247.

[31] H. Damjantschitsch, M. Weiser, G. Heusser, S. Kalbitzer and H. Mannsperger, Nucl. Instr. and Meth. 218 (1983) 129.
[32] D. Kuhn, R. Fauch and H. Baumann, Nucl. Instr. and Meth. B45 (1990) 253.
[33] K.M. Horn and W.A. Lanford, Nucl. Instr. and Meth. B45 (1990) 256.
[34] W. Moller, H. Hufschmidt and D. Kamke, Nucl. Instr. and Meth. 140 (1977) 157.
[35] D. Dieumegard, D. Dubreuil and G. Amsel, Nucl. Instr. Meth. 166 (1979) 431.
[36] M. Caterini, D.A. Thompson, P.T. Wan and J.A. Swaicki, Nucl. Instr. and Meth. B15 (1986) 535.
[37] J.C. Davis, H.W. Lefevre, C.H. Poppe, D.M. Drake and L.R. Veeser, Nucl. Instr. and Meth. 149 (1978) 41.
[38] L.G. Earwaker, J.B.A. England and D.J. Goldie, Nucl. Instr. and Meth. B24/25 (1987) 711.
[38] G.R. Rossman, Nucl. Instr. and Meth. B45 (1990) 41.
[40] F. Paszti, E. Szilagyi and E. Kotai, Nucl. Instr. and Meth. B54 (1991) 507.
[41] G. Ross and B. Terreault, J. Appl. Phys. 51 (1979) 1259.
[42] C.R. Gossett, Nucl. Instr. and Meth. B15 (1986) 481.
[43] L. Wielunski, R. Benenson, K. Horn and W.A. Lanford, Nucl. Instr. and Meth. B15 (1986) 469.
[44] L. Wielunski, R. Benenson and W.A. Lanford, Nucl. Instr. and Meth. 218 (1983) 120.
[45] W.A. Lanford, L. Wielunski and R.E. Benenson, J. Appl. Phys. 58 (1985) 4.
[46] H.J. Whitlow, in: High Energy and Heavy Ion Beam in Materials Analysis, eds. J.R. Tesmer, C.J. Maggiore, M. Nastasi, J.C. Barbour and J.W. Mayer (Materials Research Society, Pittsburgh, 1990) p. 73.
[47] M. Alurralde, E. Garcia, D. Abriola, A. Filevich, G. Garcia Bermudez, M. Aucouturier, and J. Siejka, in: High Energy and Heavy Ions Beams in Materials Analysis, eds. J.R. Tesmer, C.J. Maggiore, M. Nastasi, J.C. Barbour and J.W. Mayer (Materials Research Society, Pittsburgh, 1990) p. 119.
[48] B. Gebauer, D. Fink, P. Goppelt, M. Wilpert and Th. Wilpert, in: High Energy and Heavy Ion Beams in Materials Analysis, eds. J.R. Tesmer, C.J. Maggiore, M. Nastasi, J.C. Barbour and J.W. Mayer (Materials Research Society, Pittsburgh, 1990) p. 257.
[49] D.K. Brice and B.L. Doyle, Nucl. Instr. and Meth. B45 (1990) 265.
[50] T.A. Cahill, Y. Matsuda, D. Shadoan, R. Eldred and B.H. Kusko, Nucl. Instr. and Meth. B3 (1984) 263.
[51] (a) M. Zinke-Allmang, S. Kalbitzer and M. Weiser, Z. Phys. A320 (1985) 697.
(b) M. Zinke-Allmang and S. Kalbitzer, Z. Phys. A323 (1986) 251.
(c) M. Zinke-Allmang, S. Kalbitzer and M. Weiser, Mater. Res. Soc. Proc. 82 (1987) 59.
[52] Y. Iwata, F. Fujimoto, E. Vilalta, A. Ootuka, K. Komaki, K. Kobayashi, H. Yamashita and Y. Murata, Jpn. J. Appl. Phys. 26(6) (1987) L1026.
[53] K.M. Horn and W.A. Lanford, Nucl. Instr. and Meth. B29 (1988) 609.
[54] K.M. Horn, Application of the ^{15}N Nuclear Reaction to Study the Bond Energy and Dirction of Bound Hydrogen, Thesis, University at Albany, 1987.
[55] K. Izsak, S. Kalbitzer, M. Weiser and M. Zinke-Allamng, Nucl. Instr. and Meth. B33 (1988) 578.
[56] R.E. Benenson, L.S. Wielunski and W.A. Lanford, Nucl. Instr. and Meth. B15 (1986) 453.
[57] J.A. Wawicki, Nucl. Instr. and Meth. B30 (1988) 123.
[58] J. Tirira, P. Trocellier, J.P. Frontier and P. Trouslard, Nucl. Instr. and Meth. B45 (1990) 203.
[59] F. Besenbacher, I. Stennsgaard and P. Vase, Nucl. Instr. and Meth. B15 (1986) 459.
[60] B.L. Dolye and D.K. Brice, Nucl. Instr. and Meth. B35 (1988) 301.
[61] J. Bottiger, S.T. Picraux and N. Rud, in: Ion Beam Surface Layer Analysis, eds. O. Meyer, G. Linker and F. Kappeler (Plenum, New York, 1975).
[62] P.K. Khabibullaev and B.G. Skorodumov, Determination of Hydrogen in Materials Nuclear Physics Methods (Springer, Berlin, 1989).

Nuclear Instruments and Methods in Physics Research B66 (1992) 83–106
North-Holland

Nuclear Instruments & Methods in Physics Research
Section B

Microanalysis of He using charged particle accelerators

F. Pászti
Central Research Institute for Physics, P.O.B. 49, H-1525 Budapest, Hungary

Accumulation of the nuclear reaction product He in fusion and fission reactor components leads to severe problems. During investigation of these problems, microanalysis of He in solids has special importance. The present paper will give a review of analytical methods, especially those based on interactions of energetic charged particles. Some of these are based on elastic scattering (proton elastic scattering, elastic recoil detection, scattering combined with coincidental detection of both scattered and recoiled ions), while others are related to nuclear reactions (i.e., ^{3}He(d, p)^{4}He). Some other methods will also be presented (i.e., thermal desorption spectroscopy, VUV absorption spectroscopy, electron energy loss spectroscopy). Special attention will be paid to the progress made during the last 10 years.

1. Introduction

Helium is a noble gas that is basically insoluble in solids. However, via natural processes such as cosmogenical evolution, a decay of radioisotopes, β decay of tritium or exposure to solar wind, minerals contain different amounts of the two stable He isotopes. From absolute determination of these, one may draw important conclusions.

In conventional fission reactors and especially in fast reactors neutrons generate a considerable amount of ^{4}He in the reactor components via (n, α) reactions. The a decay of fission fragments is another He source. The He accumulates at the grain boundaries of the metallic alloys causing embrittlement.

In the seventies much work started in controlled nuclear fusion projects. It became obvious that the goal, an operating fusion reactor, could not be reached without solving the problems that will be faced when the first wall of the device will be subjected to the severe bombardment of different particles originating from the fusioning D–T plasma. Among others, α particles from the

$$D + T \rightarrow {}^4He\ (3.52\ MeV) + n\ (14.1\ MeV) \qquad (1)$$

fusion reaction and thermalized He ions or neutrals of several keV energy will be implanted into the upper few μm of the first wall components. Helium also will be produced in the bulk material as a result of (n, α) reactions and β decay of the incorporated tritium fuel.

Extensive research was initiated to explore the phenomena that will be caused by He at different concentration levels in solids; this research drastically increased the interest towards microanalysis of He. This is why a lot of different He analytical methods were developed in those years.

The subject has been reviewed several times [1–7]. The main goal of this paper is to give a wider and more up to date survey. Special attention will be paid to methods based on MeV energy charged particle beams or to methods that, because of their outstanding features, gained widespread application. We will try to compare the different methods on the basis of their: (1) performance: sensitivity, depth resolution and maximum accessible depth; (2) versatility: the cost of the necessary instrumentation, the work and time that must be devoted to carry out an experiment and the additional information that can be obtained from one measurement; (3) reliability and precision; and (4) special features: information about the surroundings of He, lattice localization, etc.

The performance data are rather uncertain, so we will refer to representative values only. For example, the depth resolution can be improved by a factor of 10 using glancing incidence or detection angles in the ion beam techniques (see e.g. [8]). This is also valid for the detection limits in ion beam techniques. By increasing the detector acceptance angle, the number of incident ions, or decreasing the background using different tricks, the detection limit can be considerably improved. The probing depth strongly depends on incident energy and incident and/or detection angles.

We tried to collect applications of the different methods as well. The reference list is not complete, however. For instance, the publications that are not easily accessible are frequently missing. We will not go into details, the reader can find them in the references. The same is valid for figures and expressions.

0168-583X/92/$05.00 © 1992 – Elsevier Science Publishers B.V. All rights reserved

Table 1
List of acronyms of the different analytical methods

AES	Auger electron microscopy
EELS	electron energy loss spectrometry
ERD	elastic recoil detection
ERD/$E \times B$	ERD with $E \times B$ filter
ERD/F	ERD with foil filter
ERD/K	ERD with kinematic separation
ERDC	elastic recoil detection in coincidence
ERDC/A	ERD with asymmetric coincidence
ERDC/S	ERD with symmetric coincidence
GES	gas emission spectrometry
HREM	high resolution electron microscopy
LEED	low energy electron diffraction
NMR	nuclear magnetic resonance
NR	neutron radiography
NRA	nuclear reaction analysis
PA	positron annihilation
PAC	perturbed angular correlation
PES	proton elastic scattering
RBS	Rutherford backscattering spectroscopy
SANS	small angle neutron scattering
SAXS	small angle X-ray scattering
SEM	scanning electron microscopy
SIMS	secondary ion mass spectrometry
SRCS	scattering recoil coincidence spectroscopy
STM	scanning tunnel microscopy
TDS	thermal desorption spectrometry
TEM	transmission electron microscopy
VES	vacuum extraction spectrometry
VPS	vibro polishing spectrometry
VUVAS	VUV absorption spectrometry
XRRS	X-ray reflection spectrometry

The different analytical methods will be divided arbitrarily into two main groups: methods to detect He using MeV energy beams and the other ones.

For convenience, a list of acronyms of the different analytical methods is included in table 1.

2. Nonaccelerator based methods

To give proper background to the accelerator based techniques, the other methods will be presented first. They might be divided into three subgroups: mass spectrometer based methods, resonance based methods and indirect methods. We will deal only with methods that are primarily developed to analyze solid samples. It is quite probable that we were not lucky enough to explore all of them, but all the methods that were met during an extensive search in the literature are presented. Not only direct analytical methods are included, but there are some that are not really sensitive to the He gas itself, but can give information about its density or pressure.

Methods like TEM or SEM that show bubbles and punched out dislocation loops, or the resulting macroscopic surface deformations are not included here because they do not give information on the He itself. The very recent methods like STM or HREM were not yet applied, to our best knowledge, to investigate He in solids, but we hope they will soon gain interesting applications in this field.

2.1. Mass spectrometer based methods

These methods use magnetic or electrostatic mass analysis and are able to distinguish the atomic or molecular ions that have masses differing by at least 1 amu (atomic mass unit). Those that only differ in a small fraction of amu (i.e., D_2 and ^{4}He) are only distinguishable by- more selective special devices. From the point of view of ^{4}He and ^{3}He, if there is no D contamination in the UHV (ultrahigh vacuum) chamber of the instrument, these methods are almost background free (apart from the electronic noise). So a common feature of them is the relatively high sensitivity for He isotopes. In addition, they are relatively inexpensive compared to accelerator based methods. The same instrument can also be used to analyze other elements. Other techniques like AES or LEED can be carried out in the same chamber.

2.1.1. Secondary ion mass spectrometry (SIMS)

In this analytical method the surface layer of the specimen is continuously sputtered away by a low (several keV) energy medium mass ion beam (typically Ar^+). A considerable part of the sputtered atoms or molecular fragments is ionized (either positively or negatively) and, using a proper electric field, is directed into the entrance slit of the mass analyzer. SIMS has around a monolayer depth resolution, but, because the sputtering yield and the ionization probability are strongly dependent on the chemistry at the sample surface, the precision and reliability of the quantitative results are rather poor. These can be improved using sophisticated theoretical models or standard sample series. The sample is completely destroyed at the measured spot.

Helium and other noble gases do not form negative ions, and their first ionization potentials are sufficiently high to decrease positive ion formation probability to a relatively low value. Helium has the highest first ionization potential in the periodic table (24.58 eV), and is the least detectable positive atomic ion using SIMS. The presence of oxygen on the sputtering surface enhances the formation of positive secondary ions, so using oxygen ion bombardment, the yield of positive He ions can be increased. Also, it is necessary to use a basically sensitive instrument. This way He was successfully depth profiled in Si and GaAs (see fig.

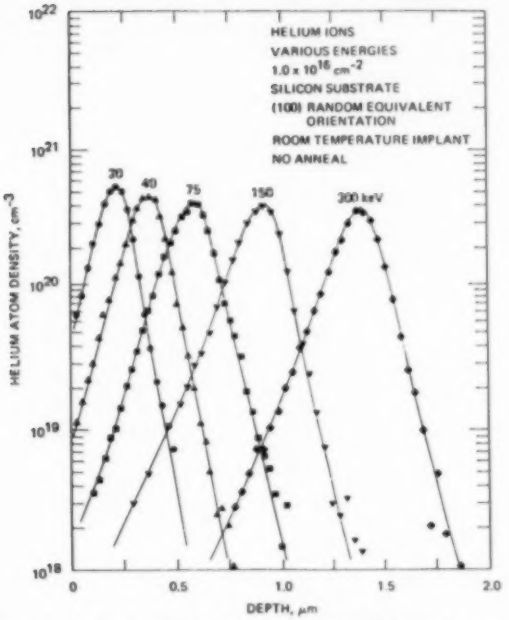

Fig. 1. He depth distributions in implanted Si determined by SIMS using oxygen ions (various energies, 10^{16} He/cm^2 fluence) [9].

1) [9]. He concentrations down to ~20 ppm were measured. The depth resolution is not mentioned, but it has to be lower than in the case of other impurities, because, under the ion mixing caused by the beam, the insoluble He might migrate in the near surface layer. A depth resolution of ~3 nm can be assumed.

He incorporation into Al from a low temperature He–H plasma was also successfully investigated by SIMS [10]. In this case the sputtering ion beam consisted of 7 keV Ar^+ ions, so the ionization probability was not enhanced by the oxygen trick. Sensitivity or depth resolution are not reported here and cannot be guessed from the presented data.

2.1.2. Gas emission spectrometry (GES)

This technique is quite similar to SIMS. The main difference is that here, instead of collecting the ions produced in the sputtering process into the mass analyzer, the residual gas of the vacuum chamber is monitored using a conventional mass spectrometer. No application of GES to He was reported. To gain some impression of GES we refer the work of Freeman and Latimer [11] where the method was applied to investigate implanted D depth profiles in Al and Au targets. Here the depth resolution and sensitivity were far from the accessible optimum. The depth resolution has to be

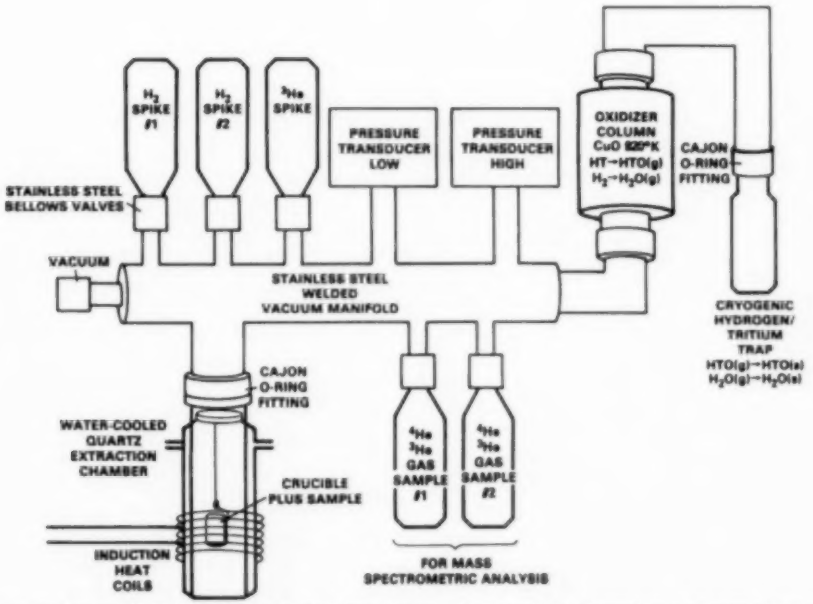

Fig. 2. Vacuum extraction manifold [12]. He is extracted from the samples by melting, cleaned by a cryogenic H trap and analyzed by transferring the "gas sample" bottles to a mass spectrometer. The "^{3}He spike" bottle serves calibrational purposes.

inferior to SIMS because of the finite He evacuation time.

2.1.3. Vacuum extraction spectrometry (VES)

This mass spectroscopy based method measures the total ^{3}He and ^{4}He content of solid (liquid) samples without giving any information about the depth distribution. To assure rapid release of the trapped gases the sample is completely melted and the residual gas of the vacuum chamber is monitored by a mass spectrometer (see fig. 2) [12–14]. The sensitivity might be improved by orders of magnitude applying the "static mode operation", where the mass spectrometer tube is isolated from the vacuum system before allowing the extracted gas to enter it [14]. This way a detection limit of 0.01 ppb can be reached, that corresponds to 10^9 atoms in the case of 1 mg samples.

VES is precise and reliable and the instrument might frequently be calibrated by gas puffs of well known quantities.

2.1.4. Vibro polishing spectrometry (VPS)

This is a unique method. Here the total He content of the samples is measured similarly to VES. The method is depth sensitive, however, using a special trick. First a whole series of practically identical samples is produced, then, by careful vibro polishing, layers of increasing thicknesses are removed from the front side of the different samples. From the difference in the total remaining He content one can deduce He concentrations at the corresponding depths.

The performance of VPS was successfully demonstrated by measuring the depth distribution of a 3×10^{11} at./cm^2 dose of 100 keV ^{4}He$^+$ ions implanted into Ni (see fig. 3) [15]. The sensitivity of VPS was considerably improved by separating the vacuum chamber from the pumps during gas extraction and mass spectroscopy reaching the 10 ppb level. The minimum detectable amount was $\sim 10^{10}$ at./cm^2 at a depth resolution of $\sim$ 10 nm.

The total He content of a specimen might be determined with high precision through calibration by injecting a known amount of gas as in VES. The precision of the thickness of the removed layer from the different samples might contain a considerable uncertainty, resulting in a scatter in the measured He concentrations at different depths. While VPS is relatively inexpensive, too much work is needed to obtain a single depth profile. The technique is "super destructive", destroying one sample for every depth profile point.

2.1.5. Thermal desorption spectrometry (TDS)

This method, in contrast to the other four mass spectrometry based methods, is widely applied in nuclear reactor related research [16–31]. This is related

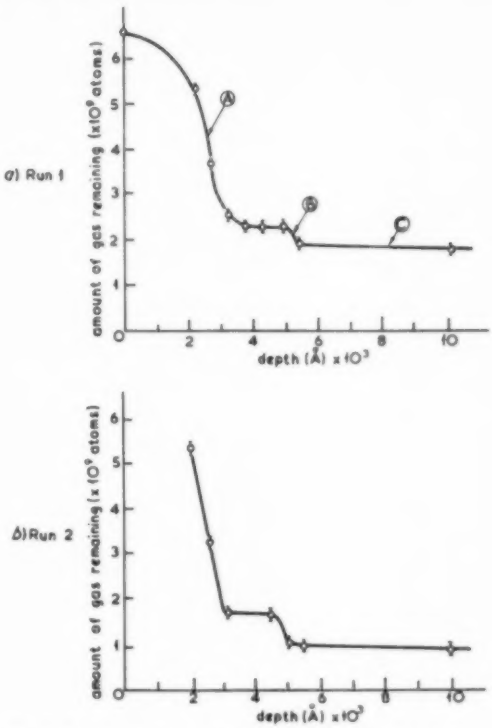

Fig. 3. Integral range profiles of He implanted into polycrystalline Ni (100 keV, 3×10^{11} He/cm^2) as measured by VPS [15]. The different points were obtained from mass spectrometric measurements on samples from which layers of different thickness were removed by vibro polishing.

to its simplicity and the special feature of determining the atomic position of He in solid matrices.

The principle of TDS is as follows. He (and also H) are very mobile interstitially in the matrices of most materials. So they can move fast until being trapped in different kinds of lattice imperfections. They can only leave the trap when having a kinetic energy large enough to overcome the binding energy and the potential barrier of the trap. The necessary kinetic energy can be ensured by heating the sample. Continuously increasing the temperature, one can observe the He groups trapped in defect clusters of different kinds as abrupt increases of the He partial pressure in the vacuum chamber. Traps of that given kind will, however, soon be emptied and the He release stopped. As a result, the He pressure decreases in accordance to the pumping speed. The resulting He partial pressure peaks are monitored with a mass spectrometer tuned to ^{4}He or ^{3}He, and one can clearly see which type of traps are present and how much He was trapped in

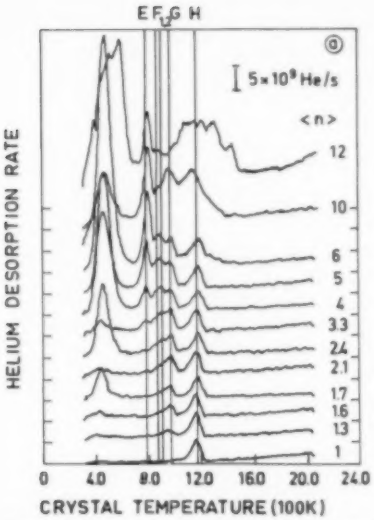

Fig. 4. Thermal desorption spectra of sub-threshold energy (50 eV) He – implanted Mo single crystals [30]. As the He to vacancy concentration ratio n increases from 1 to 12 He/V, new peaks appear. These peaks correspond to different bonding energies of He to He_nV_1-complexes (H, G, etc. for $n = 1, 2, \ldots$).

them. The principles are reviewed in more details in ref. [21].

Using this method, it was possible to determine: 1) the He binding energies to vacancy–He clusters of different He and vacancy multiplicity [18–20,27,30]; 2) the diffusion constant of He (e.g. [29] and a review is given in ref. [7]) and; 3) many other important parameters.

This is the most effective method to investigate the evolution of vacancy–He clusters into bubbles and macroscopic surface deformations [22–24,30–31].

TDS is especially effective when the He atoms are introduced into the material without causing lattice damage. Two ways are frequently used: implantation with energies low enough to prevent even the highest energy recoils to be displaced from their original position in the lattice ("sub-threshold energy implantation", see fig. 4) and the "tritium trick". In this latter, the material is filled up with T. After several months aging, a considerable part of T transforms into ^{3}He by β-decay while the energy of the recoiled ^{3}He is not enough to cause any damage. This way it becomes possible to introduce He and damage into the sample separately in a well controlled way [18–20,30].

The sensitivity of TDS is $\sim 10^9$ at./cm^2 for a given cluster type (assumed from ref. [30]). There is no depth profiling possibility. The probed depth is restricted to ~ 100 nm because of retrapping by the defects.

2.2. Resonance based methods

These methods are connected to resonant energies or frequencies that are characteristic for He. They are sensitive to He, but without depth profiling. No absolute He content measurements are reported. Instead, the methods were applied to determine He densities in bubbles that are formed at relatively high He concentration levels.

2.2.1. Vacuum ultraviolet absorption spectrometry (VUVAS)

This method is based on the fact that when transmitting VUV radiation through a foil containing He, there is a resonant absorption at energies corresponding to the 1S–2P transition in the electronic shell structure of He. If the He is practically free of interactions (gas, or liquid at low pressure), the absorption line is sharp at 21.23 eV. The pressure, and consequently the density, of He in bubbles can be rather high (several GPa, up to 2–3 He atom/vacancy). At this pressure the shell structure of the atom is distorted, and as a consequence the transition energy is shifted by up to 3 eV towards higher energies. This shift can be calculated theoretically [32–36] and a one to one correspondence can be given between the blue shift energy and the He density. Unfortunately, the different theories give results differing by a factor of at least two [36].

VUVAS is excellent for measuring relative He densities. There is hope that the calibration difficulties will soon be resolved, either with more reliable theoretical calculations or calibration measurements. The latter is not trivial because of the lack of a more reliable alternative method. VUVAS is widely applied to follow the gas bubble evolution in Al foils during implantation or a subsequent heating or cooling process [37,39,40]. The detection limit is ~ 0.1 at.%, or ~ 10^{14} at./cm^2. Because of absorption problems, only a few materials (e.g., Al) can be investigated and the thickness of the foil cannot exceed ~ 300 nm. To obtain monochromatic VUV radiation of high enough intensity, a synchrotron radiation facility is needed.

2.2.2. Electron energy loss spectrometry (EELS)

This method is closely related to VUVAS. The energy of the same 1S–2P transition in Helium is determined from the energy loss spectrum of an electron beam of ~ 100 keV energy during its penetration through the sample foil. The typical foil thickness is ~ 100 nm. This method, in contrast to VUVAS is not restricted to Al. Because it measures the same quantity as VUVAS, it gives very similar experimental results and suffers from the same problems of calibration. It was applied to determine He densities in bubbles in Al

and Ni [33,37,40–46]. From the spectra a detection limit similar to that in VUVAS can be assumed.

2.2.3. Nuclear magnetic resonance (NMR)

In principle, the NMR spin–lattice and spin–spin relaxation times are directly related to the physical state of the resonant-spin species. The difference between rigid and mobile atoms is dramatic, the relaxation times change 2–4 orders of magnitude [47]. Analyzing the frequency and temperature dependence of the relaxation times one can distinguish between wall interactions in microscopic gas bubbles and bulk diffusion in a solid lattice.

Experiments made on UT_3 [47], LiT, $TiT_{1.9}$ and UT_3 [48] and $PdT_{0.62}$ samples containing ^3He [49] and $^3He^+$ implanted Pd [50] show that the ^3He is somewhere between the free state and the bound state, i.e., in bubbles of high pressure. To deduce a quantitative value for the gas pressure is almost impossible because the method is sensitive to the state of the matrix and local magnetic fields distort the measured relaxation properties. The detection limit is rather high, ~ 0.1 at.% or ~ 10^{19} at./cm^2.

2.3. Indirect methods

The common feature of these methods is that they do not observe the He itself; instead they are sensitive to the defects in the host material. If these defects are filled or decorated with He, the measured signal changes, and one can deduce information about the amount or density of He.

2.3.1. Small angle X-ray scattering (SAXS)

Small angle scattering is a diffuse elastic scattering with short scattering vectors. It does not appear for pure ideal crystals. He bubbles are imperfections in the crystal lattice and, since all atomic scattering amplitudes of the host matrix cannot cancel out totally, a diffuse scattering at small angles is observed. There are two reasons for this diffuse scattering. First, for each vacancy in the bubble, the scattering amplitude of the host atom is replaced by a different one. Second, the phases of the scattering amplitudes of all the surrounding atoms are altered since both surface tension and He pressure displace them from their regular lattice positions (lattice relaxation). The magnitude of the elastic diffuse scattering signal is proportional to the bubble concentration and to the square of the scattering amplitude per bubble. The angular distribution of the small angle scattering gives information on the distribution of bubbles (i.e., there will be bright interference spots if the bubbles are ordered into a superlattice). The lattice relaxation is not symmetrical along different crystal directions. This results in an asymmetry in the small angle scattering. The pressure inside the bubbles can directly be determined from the extent of the asymmetry [51].

Using SAXS, the bubble size, bubble density and He gas pressure inside were determined in He irradiated Ni single crystal foils [51,52]. The lowest He concentration during the measurements was 0.06 at.%, so the detection limit has to be considerably better than this value, ~ 100 ppm. Because this concentration was produced in a 10 μm thick layer by multiple energy implantation, the detection limit can also be expressed as ~ 10^{16} at./cm^2.

SAXS gives a variety of information from one measurement. It is not specific to He, so impurities and damage might confuse the interpretation. No expensive instrument is needed.

2.3.2. X-ray reflection spectrometry (XRRS)

While He does not interact strongly with X-rays, its effect on the density of the material can be well traced with the change in the critical angle in the glancing angle refection of X-rays. For example, if the density of Au decreases 25% from its original value, the critical angle decreases from ~ 0.7° to 0.6° [53]. XRRS was applied to determine He density in bubbles in combination with RBS [53].

XRRS is not specific to He, and voids cause the same effect as the He filled bubbles. The probing depth is 5–10 nm depending on the wavelength.

2.3.3. Small angle neutron scattering (SANS)

In conventional applications of SAXS and SANS the scattering pattern is measured to determine the number, size and shape of particles in the sample. A new application, the contrast variation method, makes it possible to determine the He density inside the bubbles [54,55]. This method is based on the fact that identical He bubbles can be measured in specimens of different contrast. This situation can be achieved for instance, if identical bubble distributions are created in Ni^{58} and Ni^{60} isotope specimens whose coherent neutron scattering lengths are about one order of magnitude different. By a simple theoretical approximation, it can be determined how the ratio of scattered intensities from the two isotopic samples depends on the relative density of Ni and He [55]. SANS is rather sensitive to relative densities between 0.93 and 4.8 He/vacancy, but the same intensity ratios can also be obtained if the real value falls out of this interval. This ambiguity can be avoided and the region of sensitive density ratio can be widened by investigating other Ni isotopes, as well.

SANS requires a monoenergetic neutron beam, i.e., a dedicated reactor channel, and isotopic samples, therefore with this method routine applications are impossible. For the special experiments in ref. [55] 100 μm thick Ni foils were doped uniformly with He up to

a 1200 ppm level. The detection limit can be assumed to be ~ 100 ppm, that is 10^{17} at./cm^2.

2.3.4. Neutron radiography (NR)

This method is based on the fact, that the absorption cross section of ^{3}He for thermal neutrons is extremely high (5333 b) as compared to that of T (1.7 b) or various metals (~ 20 b). Consequently, the neutron flux after penetrating a specimen strongly depend on its ^{3}He content. The flux can easily be monitored by placing a Gd converter foil – photographic film sandwich behind the sample.

NR is a sensitive tool to determine ^{3}He lateral distribution in foil samples. Lateral resolution of 16 μm and a detection limit of 200 ppm (10^{18} at./cm^2) were reported in 1 mm thick Ta samples [56]. Because of its high detection limit NR is not fit for ion implanted samples. Wide applications on reactor components can be foreseen (especially related to T handling in fusion reactors).

2.3.5. Positron annihilation (PA)

Positrons after slowing down in the material easily become trapped by vacancy-like defects, then annihilate. From the characteristics of the annihilation (lifetime, angular correlation of the two 511 keV annihilation γ-rays and their Doppler-broadening) the PA method gives information on the surroundings of the trap position.

In the classical PA method the positrons are emitted by a radioactive source having a wide energy distribution in accordance with the principles of β-decay. Maximum positron energies range from 0.5 to 1.5 MeV for various isotopes. Thus the penetration depth of the positrons in the sample is of the order of 100 μm, and correspondingly homogeneous samples of similar thicknesses are needed. There is a more effective version of PA, however. Here the positrons are thermalized first in a suitable metal, and the reemitted slow positrons of 1–2 eV energy are then accelerated to the needed energy. For example, the device – presented in ref. [61] provides a positron beam of variable energy in the range of 0.15–28 keV. The corresponding penetration depth is 0.1–1000 nm. In this way depth profiles of defect concentrations produced by ≤ 50 keV He implantation can be determined [58,59,62,64].

There is one group claiming that they are able to detect He itself using variable energy PA [62]. This statement is based on the observation that the Doppler broadening-depth profiles of He implanted samples differ from those obtained on virgin samples even after annealing enough to remove all the defects from the sample. We are convinced that what they really see are the voids stabilized by the included He. The effect of ~ 10^{13} at./cm^2 (~ 10 ppm) He implantation is already detectable [62].

In connection with He PA is frequently applied to investigate He-vacancy interactions and the evolution of He filled bubbles [57–63]. Hansen et al. [51] were able to determine the He density in the bubbles formed in Al using positron lifetime measurements.

2.3.6. Perturbed angular correlation (PAC)

During the radioactive decay of ^{111}In ($T_{1/2}$ = 2.8 days) two γ particles are emitted with a short delay. Their directions are also correlated. Due to the precession of the nucleus under the effect of the local electric and/or magnetic fields, the direction of the second emitted γ also rotates with the precession frequency. If one uses the detection of the first and second γ as start and stop signals for a time to amplitude converter, the precession frequency will appear in the collected intensity versus delay-time spectrum as a weak oscillation. The frequency is characteristic of the defect structure at the position of the probe nucleus. From the frequency distribution one can deduce which type of defects are trapped at the probe nucleus and with what probability. In the case of He implanted samples, captured vacancies, He atoms and He–vacancy complexes will appear. By implanting He and ^{111}In to different depths, PAC becomes a powerful way to investigate He diffusion and the early stages of bubble nucleation [65–70]. In this latter case, however, the effect of the probe nucleus itself cannot be ignored.

The detection limit is probably better than 10^{15} at./cm^2. Special accelerators and implanters are needed to produce and implant ^{111}In.

3. Methods using MeV ion beams

These methods require expensive MeV energy accelerators. They have widespread applications, however, because the same accelerator can be used to solve a lot of other scientific and technological problems. A variety of accelerator based analytical methods can be applied simultaneously or in succession to the same sample. These methods are nondestructive in the sense that the samples maintain their integrity during the analysis. The damage caused by high energy ions cannot be neglected in some cases. Because most features of these techniques are encountered in the simplest elastic scattering methods, we will detail them there.

3.1. Elastic scattering based methods

In principle all the following methods except NRA are based on the elastic scattering of probing ions from the atomic nuclei of the target. We will divide these methods into three different groups, however, of increasing experimental complication: RBS/PES, ERD, and coincidence techniques.

All these methods are based on the following principles. Because of energy and momentum conservation laws, the energy of both the scattered and the recoiled particles is strictly determined by the energy of the incident ion, the scattering/recoil angles and the masses of the ion and recoiling atom. In most of the experimental setups, surface barrier or ion implanted solid state detectors of ~ 10 keV energy resolution are used to determine the energy spectra of the scattered and/or recoiled particles. Additional filters (foils, electrostatic and magnetic fields, etc.), if applied, will be mentioned at the given technique. The peaks in the energy spectra appearing at energies corresponding to the atoms of different masses in the target are used to determine the elemental (in some cases also isotopic) composition of the sample. The energy separation of neighboring masses ($\Delta E/\Delta M$) is determined by the scattering kinematics. The peak area depends on the amount of the given element or isotope, on the experimental parameters, and on the cross section.

If the sample is thick, both the incident ion and the scattered atom will loose energy. As a result, the peaks will be distributed toward smaller energies corresponding to the depth distributions of the given elements. In this case the spectrum height corresponding to a specific depth will be determined by the concentration of the given atom and the stopping power of the target there. The energy loss rate (the stopping power) is relatively well known for the cases of interest, so it is possible to restore, from the measured energy spectrum, depth profiles. Sophisticated computer codes are now available to speed up the evaluation.

It is worth noting that the signal corresponding to a given element is smeared in energy because of the detector resolution, the variations in the scattering angle corresponding to the finite beam spot and detector solid angle (geometrical contribution). Due to the statistical character of the stopping processes (energy straggling) and multiple scattering of both incident and scattered or recoiled ions in the sample, there is a further energy spread contribution in the signals corresponding to greater depths. If there is a filter foil (i.e. ERD/F) the energy straggling, multiple scattering in the foil and the inhomogeneity of the foil thickness give other contributions. These processes together with $\Delta E/\Delta M$ and the stopping powers determine the mass and depth resolutions of the different methods. As an example, one can find a detailed analysis on depth resolution of ERD/F in ref. [8].

Only typical energies and types of incident ions will be mentioned in sections 3.1., 3.2 and 3.3. because they can be almost freely changed to have the best experimental parameters for a given analytical problem. The limitations are as follows:

(1) The maximum energy is determined first of all by the accelerator itself. Another limit is the appearance of unwanted non-Rutherford cross sections, resonances and nuclear reactions. In some cases the depth resolution needed also limits the energy.
(2) The minimum energy is determined by the detector system (filters, detector and electronics) and the need to separate the different constituents in the sample.
(3) The incident and detection angles can be perpendicular at most. Glancing angles may increase the depth resolution and detection limit in the at./cm^2 sense. The surface roughness of the sample and the multiple scattering contribution for higher depths, however, limit these parameters. When glancing incidence is used, narrow beam shape and little distance between the final beam defining aperture and the sample are crucial and the conventional current integration methods fail in determining the number of incident ions. Possible solutions are given in ref. [71]. The angles are finally determined by the necessary depth resolution and accessible depth.

Almost the same considerations can be applied for NRA; the differences will be detailed there.

3.1.1. Rutherford backscattering (RBS)

This is the most straightforward method in the case of heavy impurities in a lighter substrate. The ions scattered in the backward directions are detected. The most frequently used ion is the 2 MeV $^4He^+$. In this case the cross sections are determined by the Rutherford formula, resulting in a relatively simple and reliable evaluation. RBS fails to detect He, because the ions cannot backscatter from atoms having masses smaller or equal to the incident ion.

It is not hopeless, however, to apply RBS to indicate He. In the spectrum corresponding to the host material, a yield loss due to the He content of the sample will appear. This is caused by the increased stopping power related to the same amount of host atoms (see fig. 5).

RBS is not specific to He; other light impurities can cause the same yield loss. The detection limit is ~ 10 at.%; the depth resolution is about 10 nm. The probing depth is in the μm range, and it can be enhanced by a factor of ~ 4 using H ions instead of He. In spite of its weak performance, the method is frequently applied [53,72–74].

3.1.2. Proton elastic scattering (PES)

Protons can backscatter from heavier isotopes like D, T, ^{3}He and ^{4}He. For thick samples, however, the He signal will appear on the top of a relatively high background corresponding to the protons backscattered from the deeper regions of the host material. Fortunately the cross sections for He isotopes are more than two orders of magnitude higher than the Ruther-

ford value [4,75–79]. The background in most cases is smooth, because the occasional resonances in the scattering cross section of the host material components are smeared out by multiple scattering and straggling (the same energy corresponds to much deeper regions for heavier elements than that for He). This way a detection limit of ~ 1 at.% can be reached with 2–4 MeV energy protons [25,26,78,80,90]. The depth resolution is ~ 100 nm while depths up to ~ 5 μm can be probed.

The detection limit can be improved by a factor of ~ 10 using thin foil samples and an effective beam trap behind the sample (the background will be diminished) [38–41,43,91–95]. The method is rather simple and its performance is good enough to investigate He migration and escape at higher concentration levels (e.g., during macroscopic surface deformations, see figs. 6 and 7).

3.2. Elastic recoil detection (ERD)

The problem that the probing ion cannot backscatter from atoms having the same or lighter mass than itself can be resolved by detecting the recoiled atoms. These atoms recoil to forward directions, so it is obvious to use a transmission geometry in case of thin foil samples. Thick samples can also be profiled using grazing incident and detection angles. However, the forward scattered beam ions give rise to an inadmissible background when detected. The irradiation damage that is caused by these particles in the detector has to be also minimized. This is why at least one of the different filter techniques are always used with ERD. For simultaneous detection of the heavy constituents ERD is almost always combined with other techniques (i.e. RBS).

3.2.1. ERD with foil filter (ERD / F)

In this case the incident ions have higher atomic numbers than the atoms to be analyzed. The scattered ions and the recoiled heavy target atoms are completely stopped in a filter foil of proper thickness placed in front of the detector. The light recoils have smaller energy than the scattered ions, but, because

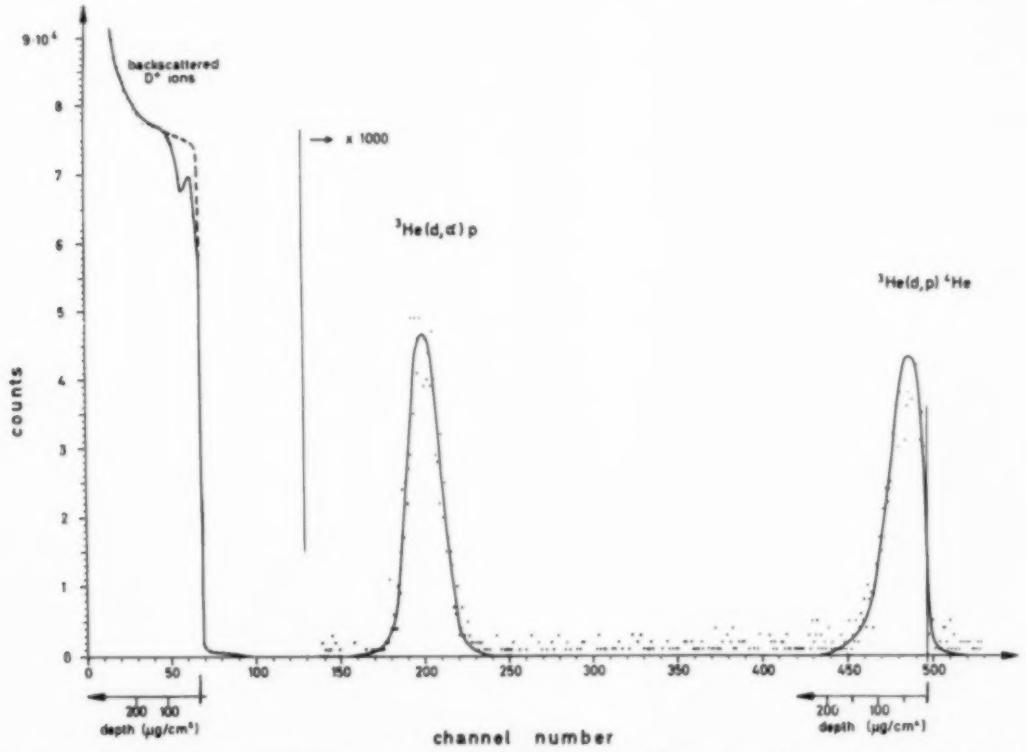

Fig. 5. Energy spectrum of d, α and p particles from elastic backscattering (RBS), ^{3}He(d, α) and ^{3}He(d, p) reactions [73]. The Nb target was first implanted with 15 keV ^{3}He up to a fluence of 10^{18} ^{3}He/cm^2, then analyzed with 500 keV d ions (sample tilt 12°, scattering angle 93°). The He depth profile can be determined from either the RBS yield loss or the α and/or p energy distributions.

their stopping power in the foil is considerably smaller, they can still get through the foil [96]. This way a backgroundless detection of high sensitivity can be performed. The price is that the filter foil will decrease the depth and mass resolutions and the maximum probing depth. Another problem is that light recoils of different masses can have the same energy after leaving the foil: the lighter ones have a small energy because of kinematics, the heavier ones because they loose more energy in the foil.

In case of He, the probing ions must have an atomic number of 6 or higher. A widely applied method uses ions of atomic number around 17 and energy of several 10 MeV (from a tandem accelerator). In this case all the light elements up to oxygen or beyond can be detected (see fig. 8) [6,96–101]. The reported depth resolutions are about 30 nm; the probing depth is a few μm. The detection limit is 0.1 at.%, 10^{15} at./cm^2.

ERD/F can be used even with Van de Graaff accelerators. ERD/F measurements were carried out using 8 MeV ^{16}O ions (see fig. 9) [102]. In this case the depth resolution for He is 20 nm and the probing depth is 150 nm. According to our calculations, with 2.5 MeV ^{12}C ions a probing depth of ~ 20 nm can be reached.

3.2.2. ERD with kinematic separation (ERD / K)

There is an elegant way to avoid the use of the filter foil. In the collisions of heavy projectiles on lighter substrate atoms, there is a maximum scattering angle equal, e.g., to 15° for ^{35}Cl atoms on ^{9}Be. If the detector is placed at a scattering angle higher than this

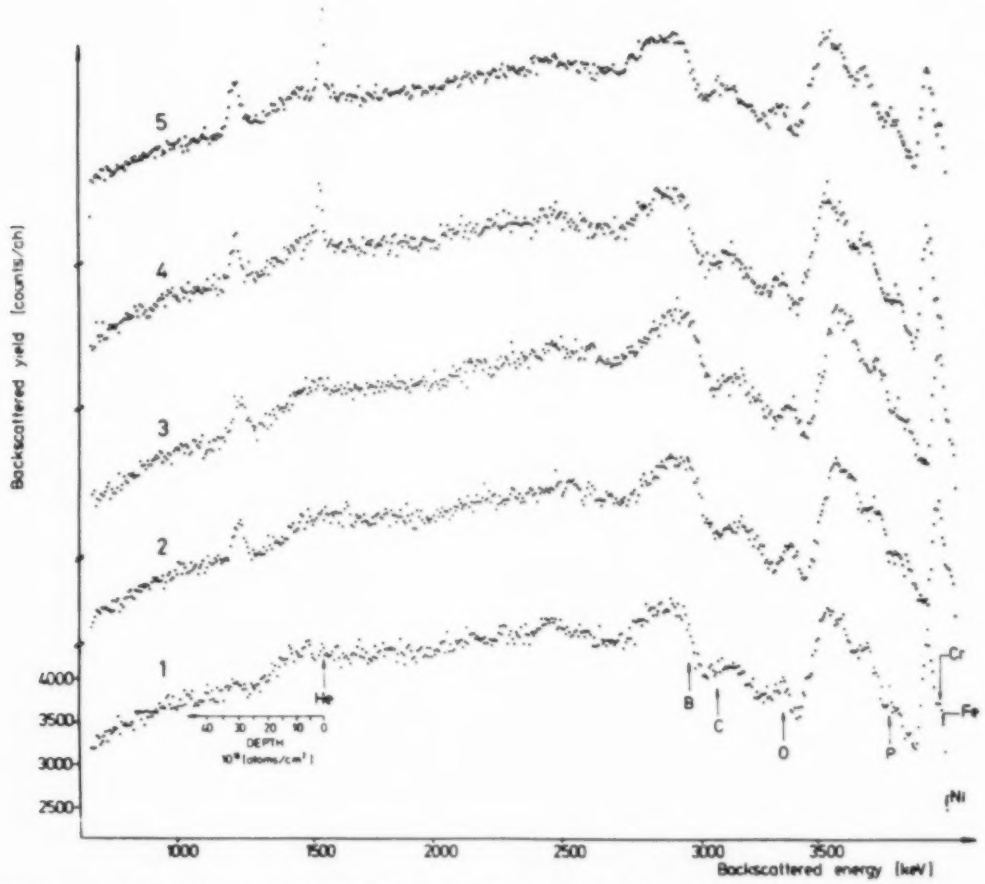

Fig. 6. Proton elastic scattering spectra of 2 MeV ^{4}He implanted $Fe_{32}Ni_{36}Cr_{14}P_{12}B_6$ samples (tilt 0°, scattering angle 165°, incident p energy 4250 keV) [85]. The fluences were 0 (1), 6×10^{17} (2, 3) and 2.34×10^{18} ^{4}He/cm^2 (4, 5). Peaks around 1200 and 1500 keV correspond to implanted and near-surface He, respectively. This latter appears when the layer above the implanted He flakes off.

limit, for that substrate no scattered ions can reach it, thus eliminating the greatest part of the background. The recoiled substrate atoms will still be detected, so the method is not background free.

The idea and its experimental application can be found in [103] (see fig. 10). Here a 30 MeV ^{35}Cl beam was applied to detect He in Be. Approximately 10 nm depth resolution at a depth of ~ 100 nm and a sensitivity of 10^{16} at./cm^2 were obtained. The maximum probing depth is ~2 μm. The main disadvantage of ERD/K is that it can work only on light substrates. The background of the substrate recoils can be filtered out by a suitable foil, but in this case we get back to the ERD/F case.

3.2.3. ERD with $E \times B$ filter (ERD / $E \times B$)

There is another way to avoid the use of the filter foil. In this case an $E \times B$ filter is mounted in front of the detector. This filter consists of an entrance slit, placed in a position where the detector aperture would be in the case of the conventional ERD/F method, followed by a zone where a constant magnetic field deflects the entering ions into one direction and a variable electric field deflects them into the opposite direction. In this way, at the end of this zone the ions for which the electric field was tuned will pass at nearly the same angle of deflection independently of their energy. The detector is placed at this deflection angle behind another aperture. With proper adjustment of the electric field and the detector position one can achieve background-free detection for the selected ion [104–106]. It is natural that the incident ions must be different from the atoms to be analyzed (i.e., $^3He^+$ ions for ^4He and vice versa).

There is a problem, however. Not all the recoiled atoms will have the selected charge state. There will be $^4He^0$, $^4He^+$ and $^4He^{2+}$ particles for instance. The solution is to choose the ion fraction of highest probability and make a correction to take into consideration the undetected fractions. Charge fraction measurements are reported in ref. [107].

ERD/$E \times B$ can be applied even at sub-MeV energies. The first applications were made with 0.35 MeV energy $^4He^+$ ions (see figs. 11 and 12) [104–106].

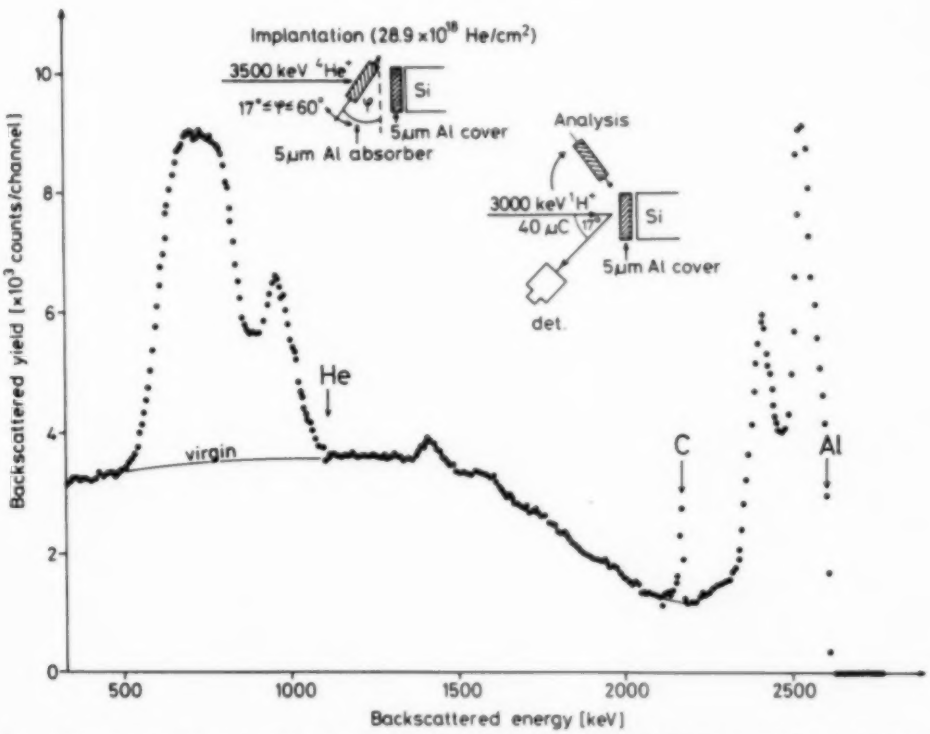

Fig. 7. Proton elastic scattering spectrum of a 5 μm Al foil covered Si sample [88]. The double peaked He distribution indicates that a part of the implanted gas escaped from the Al cover foil but not from the Si. The most important experimental conditions are inserted.

Approximately 10 nm depth resolution and ~1 at.% detection limit was reported. The probing depth was found to be ~100 nm for H in the given case.

The method is very promising. The detection limit and maximum probing depth can easily be improved an order of magnitude by using a smaller distance between the target and the entrance aperture and higher incident energy than those in the original works. Separate measurements are needed for all different atoms.

3.3. Elastic recoil detection in coincidence (ERDC)

In these methods the scattered ions and the recoils are detected in coincidence. This way the background is almost completely eliminated and excellent detection limits can be reached. These methods can be applied to thin foils only. More complicated electronics are needed than in the case of other ion beam techniques and the detectors are not protected against radiation damage. These are the common drawbacks of these methods.

3.3.1. Symmetric coincidence (ERDC / S)

This is the simplest ERDC technique. In this case the two detectors are placed symmetrically at 45° scattering angles. This way only the recoils having the same mass as the incident ions will be detected. The two detected energies are summed to improve the resolution. ERDC/S was applied for H [108–111] and ^{4}He [60,112] detection (see fig. 13). 0.5–17 MeV energy protons and 18–70 MeV He ions were applied. The high energy is crucial when analyzing thicker foils.

A common problem of these measurements is that, after the scattering event, a second scattering of either the recoil or the scattered ion will defeat the coincidence. As a result, for increasing depths (measured from the backside of the foil) an increasing multiple scattering correction has to be applied during the evaluation of the spectra. Because this correction has a strong dependence on the target material, the precision and reliability of the measurements is good only for small depths. A second measurement of the same sample from the other side may significantly improve this situation.

Approximately 1 ppm detection limits and ~0.1 μm depth resolutions are reported. The maximum probing depth is determined by multiple scattering; it is ~5 μm for 18 MeV ^{4}He$^+$. ERDC/S can be applied also at small Van de Graaff accelerators, but in this

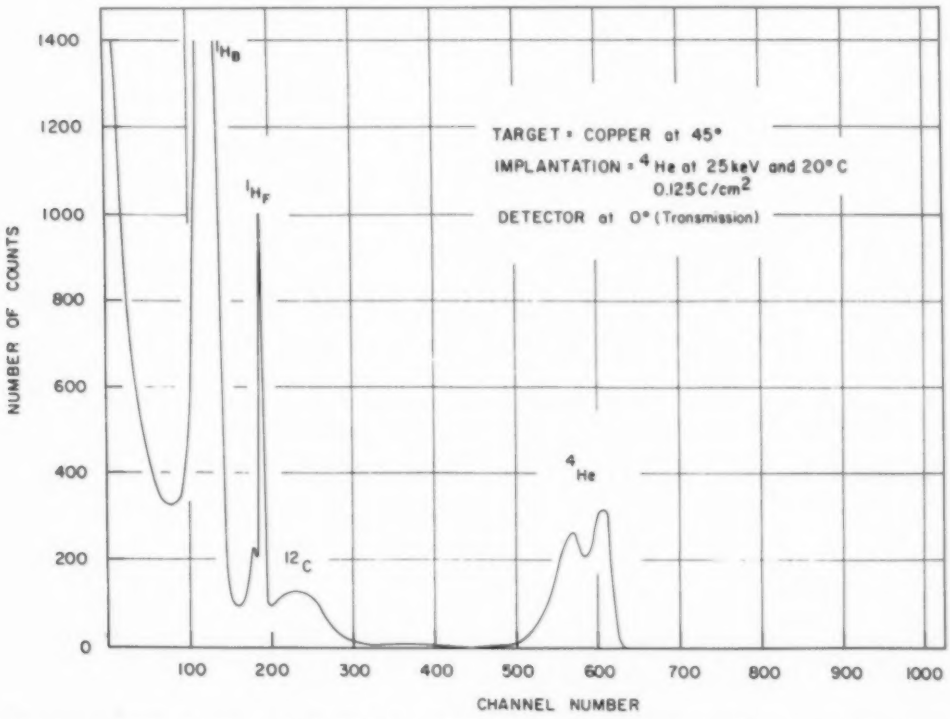

Fig. 8. Transmission ERD/F spectrum of a 7×10^{17} ^{4}He/cm^2 25 keV implanted Cu foil (30 MeV ^{35}Cl ions, 10 μm Mylar filter foil) [96]. The He depth distribution is double peaked because of He reemission during blister formation.

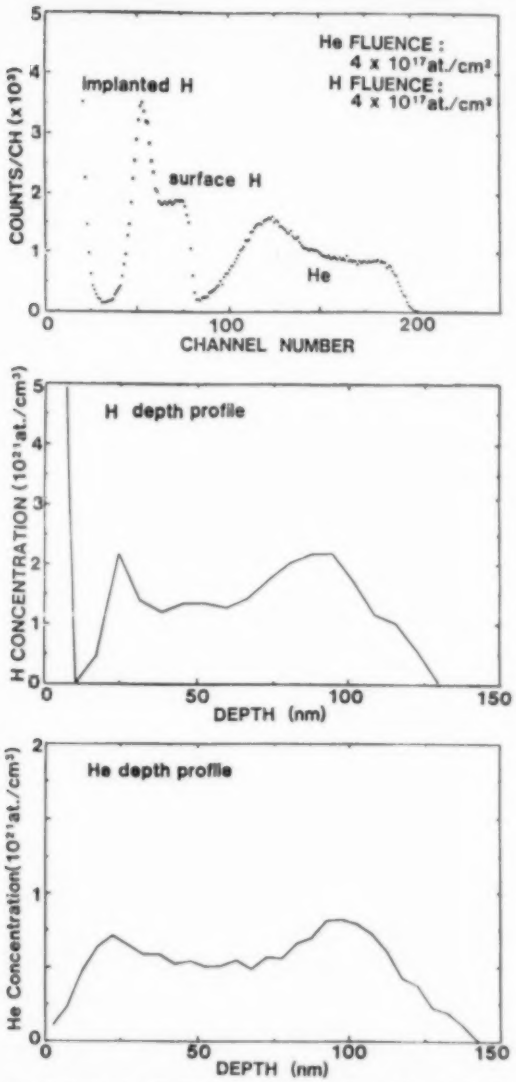

Fig. 9. Reflection ERD/F spectrum and the evaluated depth profiles of a He and H implanted stainless steel sample (8 MeV ^{16}O ions, 75° tilt, 30° scattering angles, 2.2 μm Havar filter foil) [102].

case the foil thickness has to be much smaller (just a few tenths of μm).

3.3.2. Asymmetric coincidence (ERDC/A)

This is an extension of ERDC/S for recoils of masses different from that of the incident ions. In this case the scattered ions are detected near 90° scattering angle. Moving the other detector through the different scattering angles, the whole mass spectrum of recoils can be scanned (at higher masses the mass discrimination is rather poor). ERDC/A was applied to detect ^{12}C, ^{13}C, ^{16}O and ^{27}Al with 30 Mev α particles [113] and ^{16}O and ^{24}Mg as well as ^{39}K and ^{63}Cu using 15–20 MeV oxygen and 40 MeV chlorine ions, respectively [114].

The performance of ERDC/A for He isotopes would be similar to the ERDC/S case.

3.3.3. Scattering recoil coincidence spectroscopy (SRCS)

SRCS is the most sophisticated ERDC technique. Its principles are presented in ref. [115], while a real experiment with 2 MeV $^4He^+$ ions to detect B, C, O and Si atoms can be found in [116] (see fig. 14).

The basic idea of SRCS is as follows. If one does not sum the two measured energies or use only one of them as in the case of the other two ERDC techniques, but instead collects into a two dimensional array (as in the case of $\Delta E/E$ telescopes), the solid angle of the detectors can be increased a thousand times (i.e., two ring detectors covering different scattering angle regions). In this case the recoils of different masses will be represented in the two dimensional spectrum as separated groups that extend along different curves corresponding to depth distributions in the sample. These groups will be widened due to the different scattering angles, but this can be handled with a suitable data evaluation step based on the kinematics and knowledge of the stopping process. Of course, the recoil must be identified first. The groups will be smeared out due to other contributions like multiple scattering, straggling, etc. which then define the resolution of the method.

The detection limits seem to be even better than in the case of other ERDC methods. But this is not the case; to prevent accidental coincidences the counting rate cannot be higher than the one for the other two methods. The sensitivity can really be increased if the beam current is as large as permitted by the accelerator or the heating of the foil. SRCS is superior to the other methods due to its smaller radiation damage. The data evaluation is however rather complicated.

3.4. Nuclear reaction analysis (NRA)

Let us denote a general nuclear reaction as

$$A(a, b_1 b_2 b_3 \ldots)B. \qquad (2)$$

The nucleus A is bombarded with the projectile a, and as a result, after emission of particles b_1, b_2, b_3,... nucleus B will be formed. After the reaction the total kinetic energy differs from the original value with a well known energy Q characteristic of the different nuclear reactions.

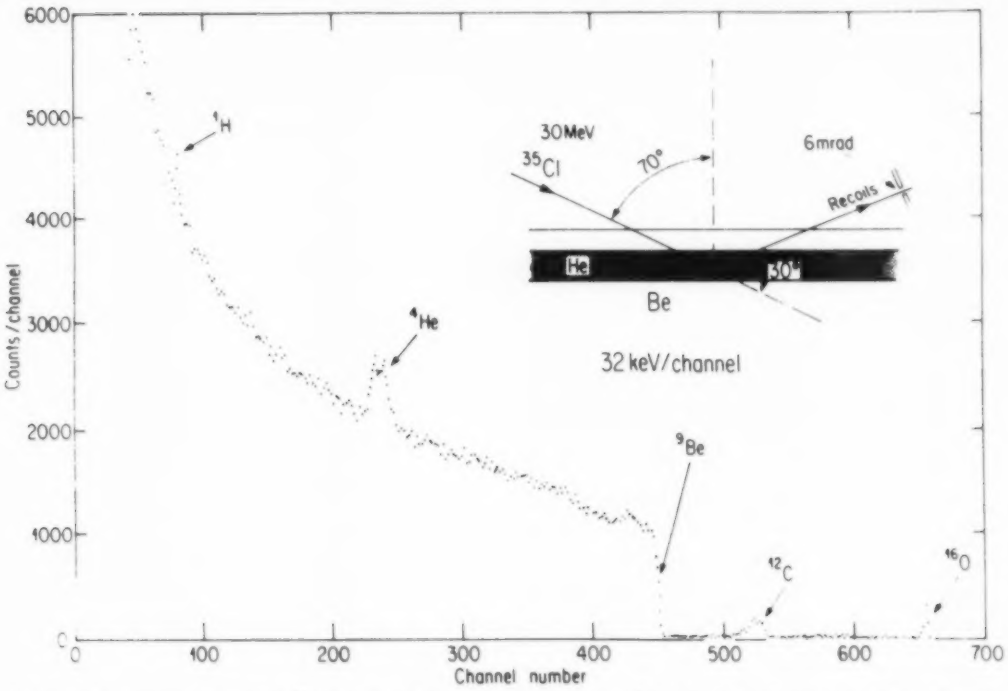

Fig. 10. ERD/K spectrum of 30 MeV ^{35}Cl ions from a 20 keV 2.7×10^{17} He/cm^2 implanted Be foil [103]. No filter foil is needed, because the heavy ^{35}Cl cannot scatter into 30° from the light sample constituents.

The principle of NRA is that if the specimen containing A is bombarded with a projectiles of suitable energy, reaction (2) takes place with a known cross section and via detection of one (or more) of the emitted b particles, the A content of the specimen can be determined. For NRA a is an ion (most frequently p, d, ^{3}He) that can be accelerated to the desired energy with an accelerator. The detected b particle is also an

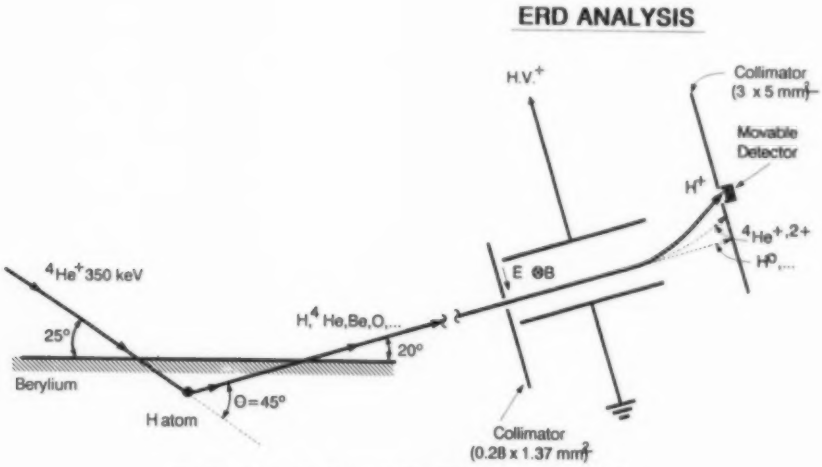

Fig. 11. Schematic diagram of ERD/$E\times B$ method [104].

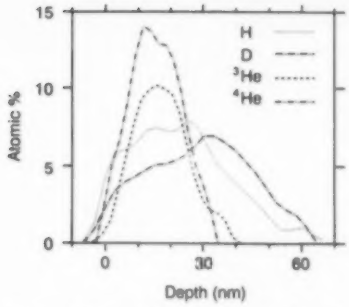

Fig. 12. H, D, ^{3}He and ^{4}He depth profiles obtained by ERD/$E \times B$ (1 keV implants into Be) [104].

ion (p, d, t, ^{3}He, α, etc.) in the case of charged particle reactions.

NRA can also be used for depth profiling. The two basic ways are the *energy distribution* method and the *resonance* method. The energy distribution method can easily be applied in the case of charged particle reactions. This is completely similar to methods based on elastic scattering, with the only exception that the kinematics is a bit different due to the Q value of the reaction. As a result, one can determine the depth profile of A in the sample simply from the energy distribution of b or the recoiled B. In the resonance method, there is a sharp resonance in the cross section at energy E_r. The projectiles originally have an energy $E \geq E_r$ and the reaction will take place with a high cross section only at the depth where the projectiles are slowed down to E_r. This means that each value of E is characteristic of a particular depth. By varying E, the depth profile of A can be mapped. This is the only depth profiling method if the detected particle b is γ

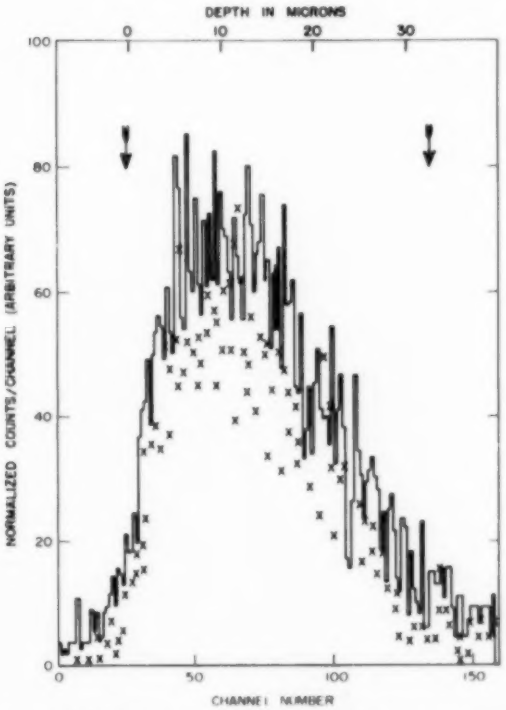

Fig. 13. ERDC/S spectra of 33 μm thick V foils containing 64 ppm He peak concentration [60]. The arrows identify the front and back surfaces of the foils.

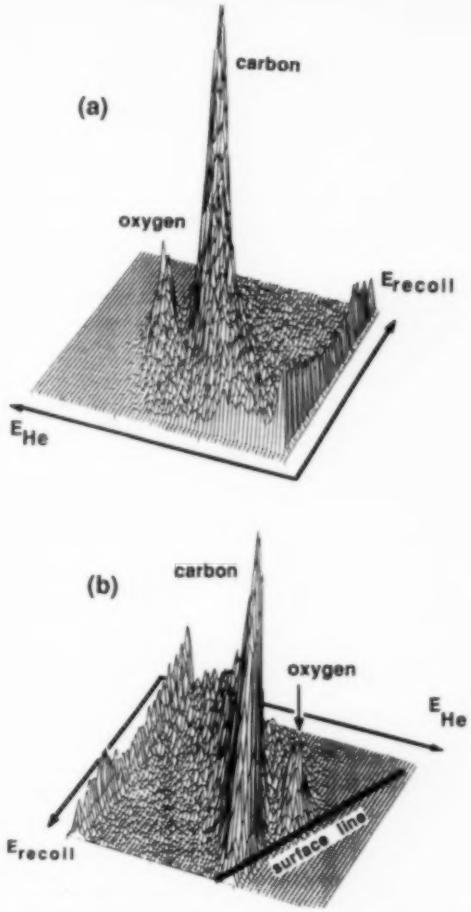

Fig. 14. SRCS spectrum of a < 2 μm thick polycarbonate foil [116]. The coincidence counts are plotted from two different view points (a, b) as a function of the energy of scattered ^{4}He and the recoiled light elements (2 MeV incident energy, 70° scattering, 50° recoil angles). The method can be adapted to He depth profiling as well.

or n. (It is difficult to measure the energy spectrum of neutrons).

We will include here also a neutron induced nuclear reaction based He profiling method. The reason is that the technique is very similar to the energy distribution methods; only neutrons are used instead of charged particles. As a result, only the energy loss of the emitted charged particle has to be taken into consideration when the energy-depth relation is determined.

3.4.1. ^{3}He(d, α)H

The ^{3}He(d, α)H NRA method is based on small Van de Graaff accelerators. It has outstanding performances but it cannot be applied for ^{4}He detection, and cannot easily be combined with other methods.

Perhaps, this is the only NRA method that is widely known in He analysis. The method is the reciprocal of the also frequently used D profiling NRA method based on the D(^{3}He, α)H. ^{3}He(d, α)H has another peculiarity. Both reaction products are light charged particles, and as a result they are alternatively used for NRA (see fig. 5). This is why the reaction is also called ^{3}He(d, p)^{4}He. The label used depends on which particle is evaluated from the measured spectra.

If protons are detected, higher probing depths can be obtained. This is especially true if one uses it as a resonance method [117–119], based on the fact, that there is a wide (FWHM = 350 keV) resonance around 430 keV in the cross section (see fig. 15) [117,119,120–125]. In this case the probing depth is ~ 10 μm with a poor depth resolution of ~ 1 μm. The detection limit is assumed to be ~ 10 ppm [119]. ^{3}He(d, α)H is frequently used to determine only the total amount of near surface ^{3}He without any depth profiling [89,110,126,127]. If the energy distribution method is applied, 0.1 μm depth resolution, ~ 4 μm probing depth and ~ 100 ppm detection limit can be achieved [128].

If one detects the α particles [22,23,28,73, 89,126,127,129–138], due to their much higher stopping power, the depth resolution is much better: ~ 10 nm that can be improved down to ~ 2 nm by glancing detection angles (see fig. 16) [132]. The probing depth is ~ 1 μm. The detection limit is normally ~ 100 ppm. One can eliminate, however, the different background contributions: (1) protons from (d, p) reactions of other light impurities by a thin effective detector thickness (~ 5 V detector voltage); (2) α particles from interfering (d, α) reactions on N and O with a well chosen scattering angle (~ 70°); (3) pile up counts from the intense low energy scattered deuterons with a filter foil (4 μm Mylar).

Applying all these precautions, together with a large detector solid angle, 10 ppm detection limit was achieved (compare figs. 17 and 18) [133,135]. The depth resolution in this case was only 50 nm.

In principle, all the MeV energy ion beam based methods can be used to determine lattice location by channeling measurements. This is especially useful, if the detection limit is low enough (≤ 0.1 at.%), because in this case the He is not yet accumulated into big

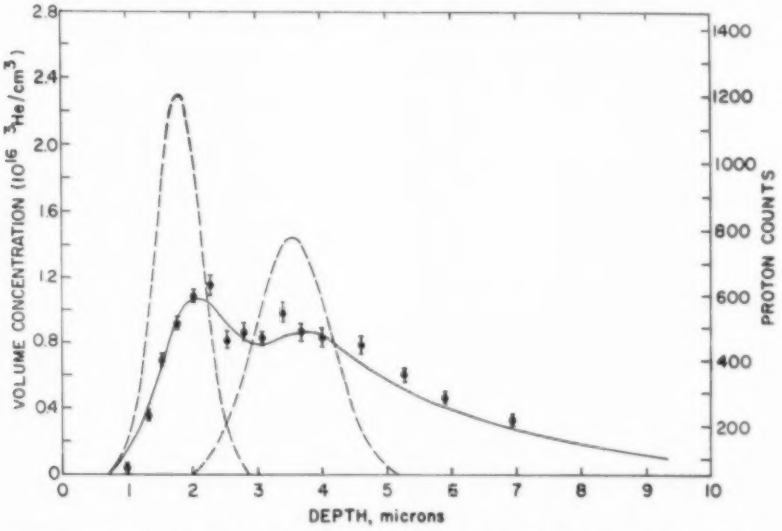

Fig. 15. ^{3}He depth distribution determined by the ^{3}He(d, p) resonance depth profiling method. The Nb sample was implanted first with 1 and 2 MeV ^{3}He ions (2×10^{16} ^{3}He/cm^2 each) then measured at 75° tilt angle (dots and solid line) [117]. Dashed lines indicate theoretical depth distributions corresponding to the two implantations.

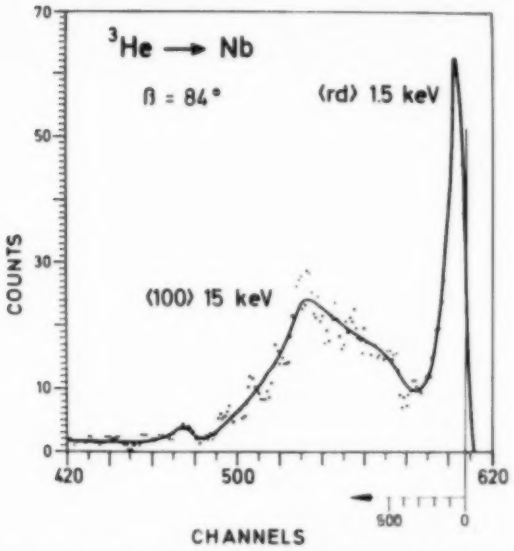

Fig. 16. Grazing detection angle (6° to the surface) ^{3}He(d, α) nuclear reaction spectrum taken on a 1.5 keV (6×10^{16} ^{3}He/cm^2 random) and 15 keV (1.5×10^{17} ^{3}He/cm^2 ⟨100⟩) implanted Nb single crystal [132].

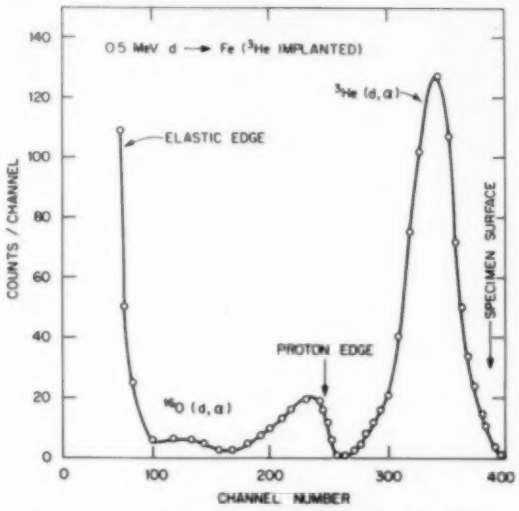

Fig. 18. Energy spectrum obtained applying the different background suppression methods (4 μm Mylar filter foil, 5 V detector bias, 70° scattering angle) for ^{3}He(d, α) depth profiling technique (500 keV incident d energy, 200 keV ^{3}He implanted Fe target) [135].

bubbles. To our knowledge, the only channeling measurement made was based on the ^{3}He(d, α)H NRA method (see fig. 19) [136]. We do not want to go too deeply into a description of the channeling technique. The very basic principle of it is that when a single crystal is oriented with respect to the ion beam, so that the direction of the ions coincide with an axis or plane of the crystal of low Miller index, the positively charged ions will be trapped into the "channels" that are surrounded by the rows or planes of the positively charged nuclei of the matrix atoms. This way the ions can

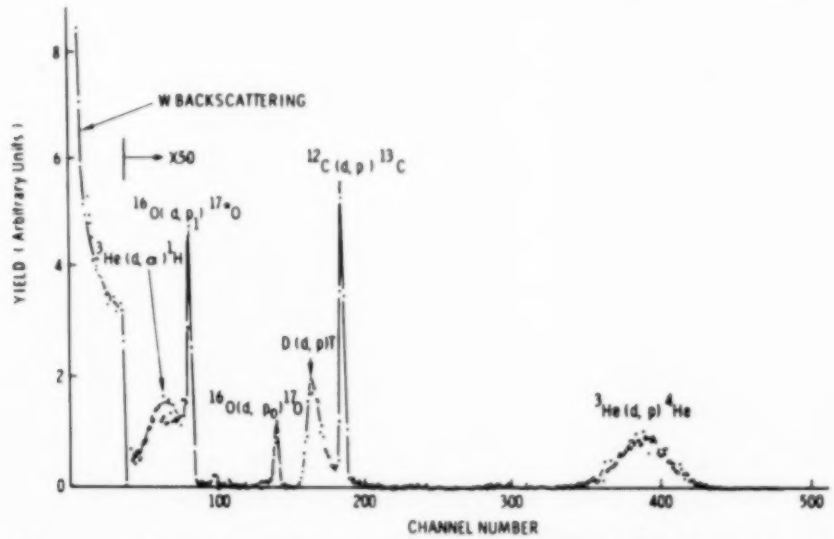

Fig. 17. Energy spectrum showing some of the possible background contributions in ^{3}He(d, α) reaction measurements [1].

penetrate almost without interactions (i.e., nuclear reactions) with the nuclei that are inside these rows or planes. The interaction probability with atoms that are inside the channels depends on their relative displacement from the center of the channels and the precision of the alignment. By increasing the misalignment between the beam direction and the crystal axis or plane, the ions moving through the channels will reach atoms with higher and higher displacements from the center of the channel. Observing the reaction yield as a function of incident angle around the different axes and planes, it is possible to determine the lattice localization of the investigated atoms with a precision of ~0.01 nm.

3.4.2. $^3He(n, p)T$

This is the second NRA method that is applied in practice to detect He (see fig. 20) [72,139–143]. This again, like $^3He(d, \alpha)H$, is sensitive only for ^3He. The specimen is irradiated with thermal neutrons from a nuclear reactor (10^9 n/cm^2 s). The neutrons produce protons all having the same energy (580 keV) independently of depth, but as the protons leave the sample, their energy is decreased corresponding to the stopping process.

Approximately 10 nm depth resolution can be reached when optimizing the detection angle [140]. The maximum probing depth is ~2 μm. The cross section is very high (5327 b) and a detection limit of 10 ppm (10^{11} at./cm^2) can be reached. (n, p) reactions on other light elements (Li, Be, B, Na, N, O, S and Cl) give a background.

$^3He(n, p)T$ can be applied for lattice localization [140] due to its high sensitivity and practically damage-

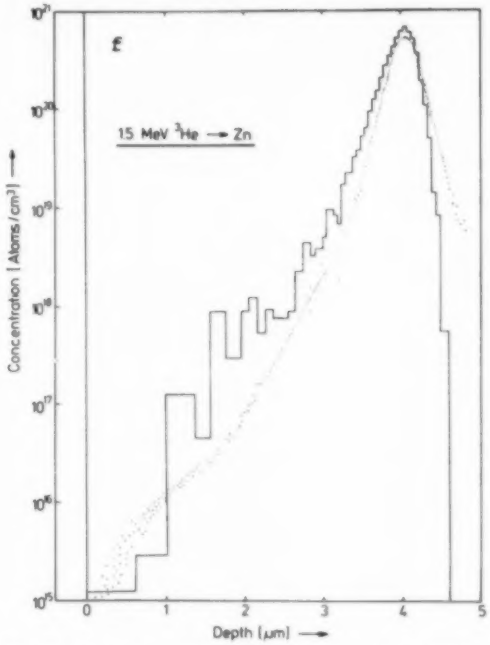

Fig. 20. Comparison of TRIM [148] (solid curve) and $^3He(n, p)$ (dots) depth profiles for ^3He implanted Zn [143].

less depth profiling characteristic. In this case, however, the channeling method cannot work (there are no channels for neutral neutrons). Instead, its reciprocal, the blocking method, has to be applied. This is based on the fact that the atomic rows and planes deflect the

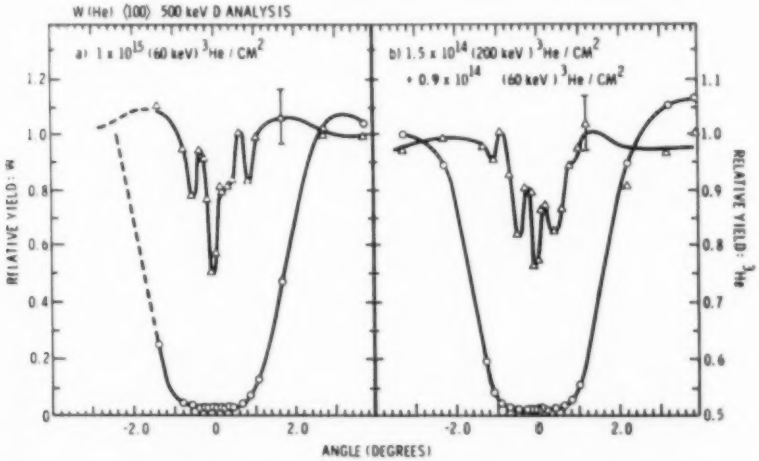
W (He) ⟨100⟩ 500 keV D ANALYSIS
a) 1 x 10^{15} (60 keV) ^{3}He / CM^2
b) 1.5 x 10^{14} (200 keV) ^{3}He / CM^2
+ 0.9 x 10^{14} (60 keV) ^{3}He / CM^2
RELATIVE YIELD: W
RELATIVE YIELD: ^{3}He
ANGLE (DEGREES)

Fig. 19. Channeling measurements using both $^3He(d, p)$ and $^3He(d, \alpha)$ nuclear reactions (both p and α pulses were counted in the same spectrum) [136]. Axial ⟨100⟩ angular scans, 135° scattering angle, 12 μm Mylar absorber foil.

emitted charged particles if they originate inside them and are emitted in a direction close to them. As a result, there will be forbidden directions for the emitted particles ("blocking pattern"). Blocking experiments would need position sensitive detectors and several weeks measurement time.

3.4.3. $^3He(^{12}C, \alpha\gamma)^{11}C$

This method was developed to measure the local density around ^{3}He atoms by the Doppler-shift attenuation method [144–146]. The principle is the following. The excited $^{11}C^*$ isomer produced by the ^{3}He

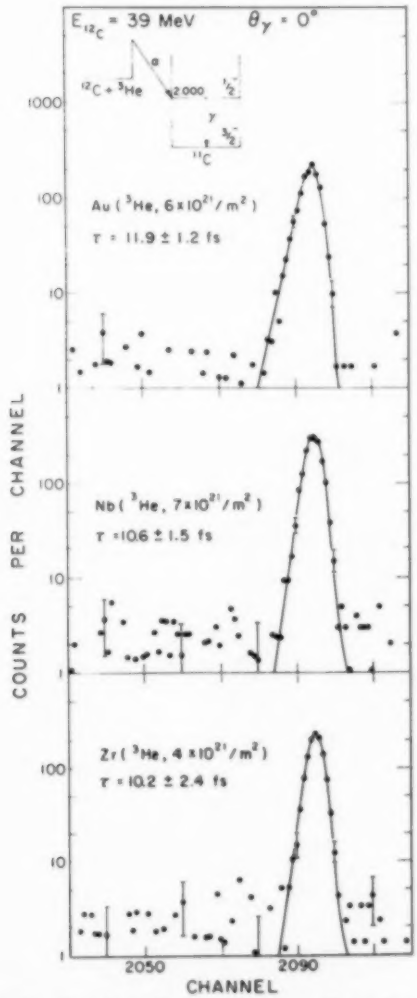

Fig. 21. Doppler-shift broadened γ lines from the $^3He(^{12}C, \alpha\gamma)$ reaction for various target materials (incident energy 39 MeV) [145].

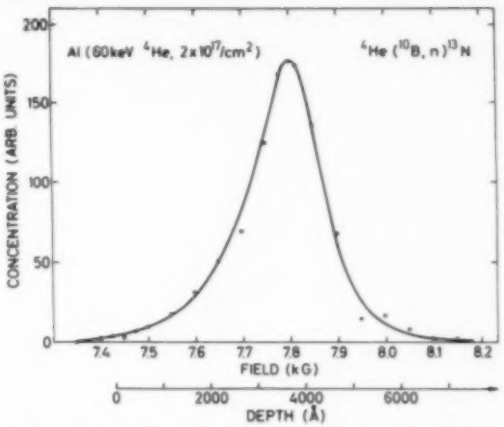

Fig. 22. He depth profile determined by the $^4He(^{10}B, n)$ resonant nuclear reaction method [2].

$(^{12}C, \alpha)^{11}C^*$ reaction is recoiled; as a consequence the γ line emitted by it will be broadened by the Doppler-shift. The broadening depends on the mean energy of the recoil at the moment of the γ emission. Because the mean lifetime of $^{11}C^*$ is just a few fs, they cannot slow down completely before the γ emission, their average speed will depend on the stopping power of the surrounding material. Because this latter is determined by the density of the material, there is a correspondence between the density and the width of the observed γ line. Its peculiarity is that the density is measured directly in the implanted layer (see fig. 21).

Otherwise the reaction is not very convenient for ^{3}He depth profiling, because the impinging ions must have 39 MeV energy (a big tandem machine is involved), and the sensitivity is rather low ($\sim 2 \times 10^{16}$ at./cm^2).

3.4.4. $^4He(^{10}B, n)^{13}N$

This method seems to be not directly published. We were able to find references on it as "to be published" only [1,2]. This is a resonance method using 3.5–5.0 MeV energy ^{10}B beam (the resonance energy is 3.77 MeV). The detected particle is the ~3 MeV energy n, the depth-resolution is ~60 nm and the maximum probing depth is ~1 μm (see fig. 22). A detection limit of 1 at.% was reached. If one compares the difficulties with the performance, it is clear that it cannot compete with the elastic scattering methods.

3.4.5. $^4He(^7Li, \gamma)^{11}B$

The method was invented in 1978 [147], but it seems to be never applied in practice. This is a resonant reaction at 1.68 MeV ^{7}Li energy producing 4.83 and 4.44 MeV energy γ lines. There is a weaker resonance in the cross section at 1.44 MeV producing γ lines of

Table 2
Methods to determine the amount, depth profile and microscopic surroundings of He isot
the others are as follows: instr. (instrument), det. (detection), at. fra. (atomic fraction), r
(microstructure), appl. (application), destr. (destruction), R (resonance method), E (en
(synchrotron), isotope (isotope producing facility), VdG (Van de Graaff accelerator), com
refl. (reflection) and ann. annihilation. Detection limit values in brackets are assumed
energies given with more than 1 digit precision); they are mentioned for orientation only

Method	Reaction	Energy	Large instr.	Det. limit		Depth res.	Max. depth
				at. fra.	at/cm^2		
SIMS	I sputt.	5–20 keV	–	20 ppm	(10^{11})	3 nm	3 μm
GES	I sputt.	5–20 keV	–	1%	(10^{14})	3 nm	3 μm
VES	melting	–	–	(10^{-11})	10^{8}	–	–
VPS	polishing	–	–	10 ppb	10^{10}	10 nm	1 mm
TDS	annealing	–	–	(10 ppb)	10^{9}	–	100
VUVAS	VUV abs.	~ 20 eV	synchr.	(1%)	10^{14}	–	–
EELS	He(e^-, e^-)	~ 100 keV	–	(1%)	10^{14}	–	–
NMR	resonance	–	–	(0.1%)	10^{19}	–	–
SAXS	X scatt.	~ 10 keV	–	(100 ppm)	10^{16}	–	–
XRRS	X refl.	~ 10 keV	–	1%	(10^{13})	–	10 nm
SANS	n scatt.	λ = 0.68 nm	reactor	(100 ppm)	10^{17}	–	–
NR	^{3}He(n, –)	thermal	reactor	(200 ppm)	10^{18}	–	–
PA	e^+ ann.	0.1–30 keV	–	10 ppm	(10^{13})	10 nm	1 μm
		0–1.5 MeV				–	100
PAC	γ emission	–	isotope	(0.1%?)	$< 10^{15}$	–	–
RBS	He(I, I)	0.5–3 MeV	VdG	10%	10^{16}	10 nm	5 μm
PES	He(p, p)	2–4 MeV	VdG	1%	10^{16}	100 nm	5 μm
				0.1%	10^{15}		
ERD/F	He(Cl, Cl)	30 MeV	tandem	0.1%	10^{15}	30 nm	5 μm
	He(O, O)	8 MeV	tandem			20 nm	150
	He(C, C)	2.5 MeV	VdG			5 nm	20 nm
ERD/K	He(Cl, Cl)	30 MeV	tandem	1%	10^{16}	10 nm	2 μm
ERD/ $E \times B$	He(I, I)	350 keV	VdG	1%	10^{16}	10 nm	100
ERDC /S	He(He, He)	5–70 MeV	tandem	1 ppm	10^{12}	0.1 μm	5μm
ERDC /A	He(I, I)						
SRCS							
NRA							
R	^{3}He(d, p)	0.43–2 MeV	VdG	10 ppm	10^{14}	1 μm	10 μ
E				100 ppm	10^{14}	100 nm	4 μm
E	^{3}He(d, α)			100 ppm	10^{14}	2 nm	1 μm
				10 ppm	10^{13}	50 nm	1 μm
E	^{3}He(n, p)	thermal	reactor	10 ppm	10^{11}	10 nm	2 μm
?	^{3}He(^{12}C, αγ)	39 MeV	tandem	?	10^{16}	?	?
R	^{4}He(^{10}B, n)	≥ 3.77 MeV	VdG	1%	10^{16}	60 nm	1 μm
R	^{4}He(^{7}Li, γ)	≥ 1.68 MeV	VdG	1%	10^{16}	30 nm	5 μm

He isotopes in solids. The abbreviations of the names of the methods can be found in table 1, ion), res. (resolution), max. depth (maximum probing depth), thick. (thickness), microstruct. E (energy distribution method), I (ion), ~ (possible or it was tried a few times), synchr.), compl. (complete destruction), cont. (contamination), sputt. (sputtering), scatt. (scattering), amed from the other type of detection limit. The values are uncertain (except the incident n only

Max. depth	Foil thick.	Reliability in He det.	Micro-struct.	Routine appl.	Sample destr.	Notes
3 μm	–	weak	–	~	spot	standards are needed
3 μm	–	weak	–	–	spot	standards are needed
–	–	excellent	–	+	compl.	–
1 mm	–	weak	–	–	compl.	too much work
100 nm	–	weak	+	+ + +	compl.	a basic method
–	300 nm	weak	+	~	no	aluminum only
–	100 nm	weak	+	+	no	–
–	–	weak	+	–	no	–
–	10 μm	no	+	–	no	not specific
10 nm	–	no	+	–	no	not specific
–	100 μm	no	+	–	no	not specific
–	1 mm	good	–	~	no	not specific
1 μm	–	no	+	~	no	not specific
100 μm						
–	1 mm	no	+	–	cont.	disturbed situation
5 μm	–	weak	–	~	damage	not specific
5 μm	–	good	–	+ + +	damage	a basic method
5 μm	–	good	–	+	damage	–
150 nm				–		
20 nm				–		
2 μm	–	good	–	–	damage	light substrates only
100 nm	–	medium?	–	–	damage	complicated
5μm	5 μm	medium	~	~	damage	for 1 isotope only
				–		element scan possible
				–		less damage/complicated
10 μm		good	~	+ +	damage	frequently fixed energy
4 μm	–		–	~		–
1 μm			–	+ + +	–	
1 μm			~	+ +		most sensitive version
2 μm	–	medium	~	+	no	–
?	–	medium	+	–	damage	density measurement
1 μm	–	weak	–	–	damage	–
5 μm	–	weak	–	–	damage	–

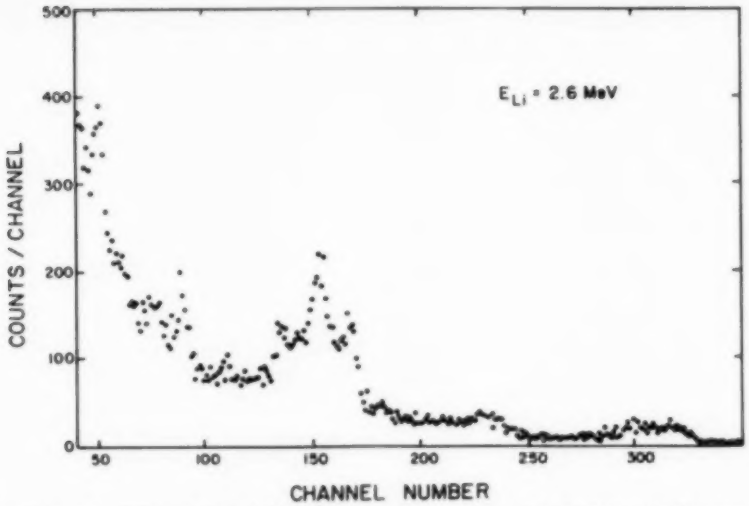

Fig. 23. γ spectrum accumulated using the ^{4}He(^{7}Li, γ) reaction (gas target, 2.6 MeV incident ^{7}Li energy) [147].

very similar energy (4.75 and 4.44 MeV). So one has to choose either to detect all the γ lines together with a high sensitivity detector and do an unfolding, or to detect the 4.83 MeV energy line separately with a high resolution (and low sensitivity) detector. Both solutions were presented and compared in ref. [147]. The depth resolution and probing depth are 30 nm and a few μm, respectively. The detection limit is ~ 1 at.%. C, Li and B impurities in the specimen can adversely affect the detectability. Similarly to the previous reaction, this is also not competitive with the elastic scattering based methods.

4. Conclusions

There is a great variety of methods that are able to determine the amount, the depth profile and the microscopic surroundings of He isotopes in the solids. To make their comparison more convenient they, together with their most important features, are listed in table 2.

References

[1] J. Bøttiger, J. Nucl. Mater. 78 (1978) 161.
[2] J. Bøttiger, S.T. Picraux and N. Rud, in: Ion Beam Surface Layer Analysis, eds. O. Meyer, G. Linker and F. Käppeler (Plenum, New York, 1976) p. 811.
[3] S.E. Donnelly, Radiat. Eff. 90 (1985) 1.
[4] L.C. Feldman and S.T. Picraux, in: Ion Beam Handbook for Material Analysis, eds. J.W. Mayer and E. Rimini (Academic Press, New York 1977) p.178.
[5] B. Terreault, Proc. 9th Int. Vacuum Congress – 5th Int. Conf. on Surface Science, Madrid, 1983, p. 599.
[6] B. Terreault, J.G. Martel, R.G. St-Jacques and J. L'Ecuyer, J. Vac. Sci. Technol. 14 (1977) 492.
[7] G.J. Thomas, Radiat. Eff. 78 (1983) 37.
[8] F. Pászti, E. Szilágyi and E. Kótai, Nucl. Instr. and Meth. B54 (1991) 507.
[9] R.G. Wilson, V.R. Deline and C.G. Hopkins, Appl. Phys. Lett. 41 (1982) 929.
[10] M.E. Gurevich, A.D. Krasjuk, L.H. Larikov and A.V. Rjasnuj, Phys. Met. 9/6 (1987) 94.
[11] N.J. Freeman and I.D. Latimer, Can. J. Phys. 46 (1968) 467.
[12] D.L. Baldwin and G.W. Hollenberg, J. Nucl. Mater. 141/143 (1986) 305.
[13] J. Dietrichs and G.H. Frischat, Proc. 5th Int. Conf. on Rapidly Quenched Metals, vol. 1, Wurzburg, Germany, 1984 (North-Holland, Amsterdam, 1985) p. 891.
[14] H. Farrar IV and B.M. Oliver, J. Vac. Sci. Technol. A4 (1986) 1740.
[15] S.E. Donnelly, D.S. Whitmell and R.S. Nelson, Radiat. Eff. 33 (1977) 145.
[16] H. Atsumi, S. Tokura, T. Yamaguchi and S. Yamanaka, J. Nucl. Mater. 141/143 (1986) 258.
[17] H. Atsumi, S. Yamanaka, P. Son and M. Miyake, J. Nucl. Mater. 133/134 (1985) 268.
[18] P. Bailey, D.G. Armour, D.S. Karpuzov and G. Carter, Radiat. Eff. 78 (1983) 133.
[19] W.Th.M. Buters and A. van den Beukel, J. Nucl. Mater. 137 (1985) 57.
[20] W.Th.M. Buters, A. van Veen and A. van den Beukel, Phys. Status Solidi A100 (1987) 87.
[21] G. Carter, D.G. Armour, S.E. Donnelly, D.C. Ingram and R.P. Webb, Radiat. Eff. 53 (1980) 143.
[22] J. Ehrenberg, B.M.U. Scherzer and R. Behrisch, Radiat. Eff. 78 (1983) 405.

[23] W. Jäger and J. Roth, Nucl. Instr. and Meth. 182/183 (1981) 975.
[24] E.V. Kornelsen and A.A. Van Gorkum, J. Nucl. Mater. 92 (1980) 79.
[25] R.A. Langley, in: Ion Beam Surface Layer Analysis, eds. O. Meyer, G. Linker and F. Käppeler (Plenum, New York, 1976) p. 201.
[26] R.A. Langley, R.S. Blewer and J. Roth, J. Nucl. Mater. 76/77 (1978) 313.
[27] W.T. Moore and E.V. Kornelsen, Radiat. Eff. 90 (1985) 141.
[28] W. Möller, B.M.U. Scherzer and J. Ehrenberg, J. Nucl. Mater. 111/112 (1982) 669.
[29] V. Sciani and P. Jung, Radiat. Eff. 78 (1983) 87.
[30] A. Van Veen, J.H. Evans, W.Th. M. Buters and L.M. Caspers, Radiat. Eff. 78 (1983) 53.
[31] V.F. Zelenskij, I.M. Neklyudov, V.V. Ruzhitskij, V.F. Rybalko, V.I. Bendikov and S.M. Khazan, J. Nucl. Mater. 151 (1987) 22.
[32] W. Jäger, R. Manzke, H. Trinkaus, R. Zeller, J. Fink and G. Crecelius, Radiat. Eff. 78 (1983) 315.
[33] A.A. Lucas, S.E. Donnelly, J.P. Vigneron and J.F. Rife, Surf. Sci. 126 (1983) 66.
[34] A.A. Lucas, J.P. Vigneron, S.E. Donnelly and J.C. Rife, Phys. Rev. B28 (1983) 2485.
[35] A.A. Lucas, J.P. Vigneron, Ph. Lambin, S.E. Donnelly and J.C Rife, Radiat. Eff. 78 (1983) 349.
[36] P.R. Taylor, Chem. Phys. Lett. 121 (1985) 205.
[37] S.E. Donnelly, A.A. Lucas, J.P. Vigneron and J.C. Rife, Radiat. Eff. 78 (1983) 337.
[38] S.E. Donnelly, J.C. Rife, J.M. Gilles and A.A. Lucas, J. Nucl. Mater. 93/94 (1980) 767.
[39] S.E. Donnelly, J.C. Rife, J.M. Gilles and A.A. Lucas, IEEE Trans. Nucl. Sci. NS-28 (2) (1981) 1820.
[40] J.C. Rife, S.E. Donnelly, A.A. Lucas, J.M. Gilles and J.J. Ritsko, Phys. Rev. Lett. 46 (1981) 1220.
[41] W. Jäger, R. Manzke, H. Trinkaus, G. Crecelius, R. Zeller, J. Fink and H.L. Bay, J. Nucl. Mater. 111/112 (1982) 674.
[42] R. Manzke and M. Campagna, Solid State Commun. 39 (1981) 313.
[43] R. Manzke, G. Crecelius, J. Fink, H. Trinkaus and W. Jäger, J. Phys. F12 (1982) 279.
[44] R. Manzke, G. Crecelius and J. Fink, Phys. Rev. Lett. 51 (1983) 1095.
[45] R. Manzke, G. Crecelius, W. Jäger, H. Trinkaus, R. Zeller and J. Fink, Radiat. Eff. 78 (1983) 327.
[46] R. Manzke, W. Jäger, H. Trinkaus G. Crecelius, R. Zeller and J. Fink, Solid State Commun. 44 (1982) 481.
[47] R.C. Bowman Jr. and A. Attalla, Phys. Rev. B16 (1977) 1828.
[48] R.C. Bowman, Nature (London) 271 (1978) 531.
[49] G.C. Abell and A. Attalla, Phys. Rev. Lett. 59 (1987) 995.
[50] H.T. Weaver and W. Beezhold, J. Nucl. Mater. 53 (1974) 346.
[51] H.G. Haubold, Radiat. Eff. 78 (1983) 385.
[52] H.G. Haubold and J.S. Lin, J. Nucl. Mater. 111/112 (1982) 709.
[53] F.H. Cocks and J.T.A. Pollock, Phys. Status Solidi A95 (1986) 141.
[54] D. Schwahn, W. Kesternich, S. Spooner, H. Schroeder, H. Ullmaier and J. Schelten, Proc. IFF-ILL Workshop, Jülich, Germany, 1985 (Springer, Berlin, 1986) p. 197.
[55] D. Schwahn, H. Ullmaier, J. Schelten and W. Kesternich, Acta Metall. 31 (1983) 2003.
[56] T. Buchberger, H. Rauch and E. Seidl, Kerntechnik 53 (1989) 215.
[57] H.E. Hansen, H. Rajainmäki, R. Talja, M.D. Bentzon, R.M. Nieminen and K. Petersen, J. Phys. F15 (1985) 1.
[58] G. Kögel and W. Triftshäuser, Radiat. Eff. 78 (1983) 221.
[59] K.G. Lynn, D.M. Chen, B. Nielsen, R. Pareja and S. Myers, Phys. Rev. B34 (1986) 1449.
[60] F.A. Smidt Jr. and A.G. Pieper, J. Nucl. Mater. 51 (1974) 361.
[61] W. Triftshäuser, G. Kögel and J. Bohdansky, J. Nucl. Mater. 111/112 (1982) 687.
[62] A. Uedono, S. Tanigawa and H. Sakairi, Phys. Lett. A129 (1988) 249.
[63] B. Viswanathan, W. Triftshäuser and G. Koegel, Radiat. Eff. 78 (1983) 231.
[64] S. Tanigawa, Y. Iwase, A. Uedono and H. Sakairi, J. Nucl. Mater. 133/134 (1985) 463.
[65] M. Deicher, G. Grübel and Th. Wichert, Nucl. Instr. and Meth. 209/210 (1983) 817.
[66] G. Grübel, M. Deicher, R. Keller, T. Korinth, W. Reiner, E. Recknagel and T. Wichert, 7th Int. Conf. Hyperfine Interactions, Bangalore, India (1986); Hyp. Inter. (Switzerland) 35 (1987) 609.
[67] F. Pleiter, A.R. Aren and H. De Waard, Phys. Lett. A77 (1980) 81.
[68] H. Sekiguchi, H. Watanabe, I. Sakamoto, Y. Nishihara, E. Tanaka, S. Hayashibe and M. Fujioka, J. Nucl. Mater. 133/134 (1985) 468.
[69] H. De Waard, Nuclear and Electron Resonance Spectroscopies Applied to Materials Science, eds. E.N. Kaufman and G.K. Shenoy (North-Holland, Amsterdam, 1981) p. 199.
[70] Th. Wichert, Radiat. Eff. 78 (1983) 177.
[71] F. Pászti, A. Manuaba, C. Hajdu, A.A. Melo and M.F. da Silva, Nucl. Instr. and Meth. B47 (1990) 187.
[72] D. Fink, J.P. Biersack, H. Grawe, J. Riederer, K. Müller and R. Henkelmann, Nucl. Instr. and Meth. 168 (1980) 453.
[73] J. Roth, R. Behrisch, W. Eckstein and B.M.U. Scherzer, Ion Beam Surface Layer Analysis, eds. O. Meyer, G. Linker and F. Käppeler (Plenum, New York, 1976) p.47.
[74] J. Roth, R. Behrisch and B.M.U. Scherzer, Appl. Phys. Lett. 25 (1974) 643.
[75] G. Freier, E. Lampi, W. Sleator and J.H. Williams, Phys. Rev. 75 (1949) 1345.
[76] L. Kraus and I. Linck, Nucl. Phys. A224 (1974) 45.
[77] R.A. Langley, Proc. Int. Conf. on Radiation Effects and Tritium Technology for Fusion Reactors, vol. 4, eds. J.S. Walson and F.W. Wiffen (Conf-750989, U.S. Dept. of Commence, Springfield, 1976) p. 158.
[78] R.A. Langley, Bull. Am. Phys. Soc. 20 (1975) 499.

[79] T.A. Tombrello, C. Miller Jones, G.C. Phillips and J.L. Weil, Nucl. Phys. 39 (1962) 541.
[80] R.S. Blewer, Nucl. Instr. and Meth. 149 (1978) 47.
[81] R.S. Blewer and R.A. Langley, J. Nucl. Mater. 63 (1976) 337.
[82] M. Fried, L. Pogány, A. Manuaba, F. Pászti and C. Hajdu, Phys. Rev. B41 (1990) 3923.
[83] M.I. Guseva, V. Gusev, U.L. Krasulin, Yu.V. Martynenko, S.K. Das and M. Kaminsky, J. Nucl. Mater. 63 (1976) 245.
[84] A. Manuaba, F. Pászti and E. Kótai, J. Nucl. Mater. 175 (1990) 158.
[85] A. Manuaba, F. Pászti, L. Pogány, M. Fried, E. Kótai, G. Mezey, T. Lohner, I. Lovas, L. Pócs and J. Gyulai, Nucl. Instr. Meth. 199 (1982) 409.
[86] N.T. My, F. Pászti, G. Mezey, A. Manuaba, E. Kótai and J. Gyulai, J. Nucl. Mater. 165 (1989) 222.
[87] F. Pászti and A. Manuaba, Int. Conf. on Physics of Irradiation Effects in Metals, May 20, 1991, Siófok, Hungary.
[88] F. Pászti, A. Manuaba, L. Pogány, Gy. Vízkelethy, M. Fried, E. Kótai, H.V. Suu, T. Lohner, L. Pócs and G. Mezey, J. Nucl. Mater. 119 (1983) 26.
[89] B.M.U. Scherzer, H.L. Bay, R. Behrisch, P. Børgesen and J. Roth, Nucl. Instr. and Meth. 157 (1978) 75.
[90] L. Yupu, W. Peixuan, L. Jiarui, Z. Peiran, Y. Feng, Z. Guoguang and M. Ruzhang, Nucl. Tech. (China) 12 (11) (1989) 653.
[91] R.S. Blewer, Appl. Phys. Lett. 23 (1973) 593.
[92] R.S. Blewer, in: Applications of Ion Beams to Metals, eds. S.T. Picraux, E.P. EerNisse and F.L. Vook (Plenum, New York, 1974) p. 557.
[93] R.S. Blewer, J. Nucl. Mater. 53 (1974) 268.
[94] L.R. Mervine, R.C. Der, R.J. Fortner, T.M. Kavanagh and J.M. Khan, Report UCRL-73087 (1971).
[95] F. Pászti, M. Fried, A. Manuaba, G. Mezey, E. Kótai and T. Lohner, J. Nucl. Mater. 114 (1983) 330.
[96] J. L'Ecuyer, C. Brassard, C. Cardinal and B. Terreault, Nucl. Instr. and Meth. 149 (1978) 271.
[97] J. L'Ecuyer, C. Brassard, C. Cardinal, J. Chabbal, L. Deschênes, B. Terreault, J.G. Martel and R.G. St-Jacques, J. Appl. Phys. 47 (1976) 381.
[98] B. Terreault, G. Abel, J.G. Martel, R.G. St-Jacques, J.P. Labrie and J. L'Ecuyer, J. Nucl. Mater. 76/77 (1978) 249.
[99] B. Terreault, R.G. St-Jacques, G. Veilleux, J.G. Martel, J. L'Ecuyer, C. Brassard and C. Cardinal, Can. J. Phys. 56 (1978) 235.
[100] B. Terreault, J.G. Martel, R.G. St-Jacques, G. Veilleux, J. L'Ecuyer, C. Brassard, C. Cardinal, L. Deschênes and J.P. Labrie, J. Nucl. Mater. 63 (1976) 106.
[101] B. Terreault, J.G. Martel, R.G. St-Jacques, G. Veilleux, J. L'Ecuyer, C. Brassard, C. Cardinal, L. Deschênes and J.P. Labrie, J. Nucl. Mater. 68 (1977) 334.
[102] Q. Qiu, K. Kurimoto, M. Nakajima, M. Ogawa and E. Arai, Nucl. Instr. and Meth. B45 (1990) 186.
[103] G.G. Ross and B. Terreault, J. Appl. Phys. 51 (1980) 1259.
[104] G.G. Ross and L. Leblanc, to be submitted to Nucl. Instr. and Meth.
[105] G.G. Ross, L. Leblanc, B. Terreault, J.F. Pageau and P.A. Gollier, these Proceedings (3rd Int. Conf. on Chemical Analysis, Namur, Belgium, 8–12 July 1991), Nucl. Instr. and Meth. B66 (1992) 17.
[106] Ross, B. Terreault, G. Gobeil, G. Abel, C. Boucher and G. Veilleux, J. Nucl. Mater. 128/129 (1984) 730.
[107] G.G. Ross and B. Terreault, Nucl. Instr. and Meth. B15 (1986) 146.
[108] B.L. Cohen, C.L. Fink and J.H. Degnan, J. Appl. Phys. 43 (1972) 19.
[109] P. Paduschek and P. Eichinger, Appl. Phys. Lett. 36 (1980) 62.
[110] A.G. Pieper and R.B. Theus, NRL Memo Report 2394, Naval Research Laboratory, Washington DC (1972).
[111] M.F.C. Willemsen, A.M.L. Theunissen and A.E.T. Kuiper, Nucl. Instr. and Meth. B15 (1986) 492.
[112] L. Shabason and W.J. Choyke, Nucl. Instr. and Meth. 138 (1976) 533.
[113] S.S. Klein, Nucl. Instr. and Meth. B15 (1986) 464.
[114] J.A. Moore, I.V. Mitchell, M.J. Hollis, J.A. Davies and L.M. Howe, J. Appl. Phys. 46 (1975) 52.
[115] W.K. Chu and D.T. Wu, Nucl. Instr. Meth. B35 (1988) 518.
[116] H.C. Hofsäss, N.R. Parikh, M.L. Swanson and W.K. Chu, Nucl. Instr. and Meth. B45 (1990) 151.
[117] P.P. Pronko, J. Nucl. Mater. 53 (1974) 252.
[118] P.P. Pronko and J.G. Pronko, Bull. Am. Phys. Soc. 18 (1973) 367.
[119] P.P. Pronko and J.G. Pronko, Phys. Rev. B9 (1974) 2870.
[120] C.J. Altstetter, R. Behrisch, J. Bøttiger, F. Pohl and B.M.U. Scherzer, Nucl. Instr. and Meth. 149 (1978) 59.
[121] T.W. Bonner, J.P. Conner and A.B. Lillie, Phys. Rev. 88 (1952) 473.
[122] G. Freier and H. Holmgren, Phys. Rev. 93 (1954) 825.
[123] W.E. Kunz, Phys. Rev. 97 (1955) 456.
[124] W. Möller and F. Besenbacher, Nucl. Instr. and Meth. 168 (1980) 111.
[125] J.L. Yarnell, R.H. Lovberg and W.R. Stratton, Phys. Rev. 90 (1953) 292.
[126] R. Schulz, R. Behrisch and B.M.U. Scherzer, Nucl. Instr. and Meth. 168 (1980) 295.
[127] R. Schulz, R. Behrisch and B.M.U. Scherzer, J. Nucl. Mater. 93/94 (1980) 608.
[128] W. Möller, M. Hufschmidt and D. Kamke, Nucl. Instr. and Meth. 140 (1977) 157.
[129] R. Behrisch, J. Bøttiger, W. Eckstein, U. Littmark, J. Roth and B.M.U. Scherzer, Appl. Phys. Lett. 27 (1975) 199.
[130] R. Behrisch, J. Bøttiger, W. Eckstein, J. Roth and B.M.U. Scherzer, J. Nucl. Mater. 56 (1975) 365.
[131] J. Bøttiger, J.S. Williams and P.S. Jensen, Nucl. Instr. Meth. 151 (1978) 241.
[132] W. Eckstein, R. Behrisch and J. Roth, in: Ion Beam Surface Layer Analysis, eds. O. Meyer, G. Linker and F. Käppeler (Plenum, New York, 1976) p. 821.
[133] M.B. Lewis, J. Nucl. Mater. 149 (1987) 143.
[134] M.B. Lewis, Nucl. Instr. and Meth. B22 (1987) 499.
[135] M.B. Lewis and K. Farrell, Nucl. Instr. Meth. B16 (1986) 163.

[136] S.T. Picraux and F.L. Vook, in: Applications of Ion Beams to Metals, Eds. by S.T. Picraux, E.P. EerNisse and F.L. Vook (Plenum, New York, 1974) p. 407.
[137] J. Roth, S.T. Picraux, W. Eckstein, J. Bøttiger and R. Behrisch, J. Nucl. Mater. 63 (1976) 120.
[138] B.M.U. Scherzer, J. Ehrenberg and R. Behrisch, Radiat. Eff. 78 (1983) 417.
[139] J.P. Biersack, Radiat. Eff. 78 (1983) 363.
[140] J.P. Biersack, D. Fink, R. Henkelmann and K. Müller, Nucl. Instr. and Meth. 149 (1978) 93.
[141] J.P. Biersack, D. Fink, P. Mertens, R.A. Henkelmann and K. Müller, Int. Symp. on Plasma–Wall Interaction, Jülich, Germany, 1976 (Pergamon, Oxford) p. 421.
[142] D. Fink, J.P. Biersack, M. Städele, K. Tjan and V.K. Cheng, Nucl. Instr. and Meth. 218 (1983) 817.
[143] D. Fink, J.P. Biersack, K. Tjan and V.K. Cheng, Nucl. Instr. and Meth. 194 (1982) 105.
[144] T.K. Alexander, G.C. Ball, W.G. Davies and J.S. Forster, Nucl. Phys. A313 (1979) 425.
[145] T.K. Alexander, G.C. Ball, W.G. Davies and I.V. Mitchell, J. Nucl. Mater. 96 (1981) 51.
[146] J.S. Forster, T.K. Alexander, G.C. Ball, W.G. Davies, I.V. Mitchell and K.B. Winterbon, Nucl. Phys. A313 (1979) 397.
[147] R.L. Schulte, Nucl. Instr. and Meth. 149 (1978) 65.
[148] J.P. Biersac and L.G. Haggmark, Nucl. Instr. and Meth. 174 (1980) 257.

Nuclear Instruments and Methods in Physics Research B66 (1992) 107–117
North-Holland

Nuclear Instruments & Methods in Physics Research
Section B

Analysis of lithium by ion beam methods

J. Räisänen

Accelerator Laboratory, Department of Physics, University of Helsinki, 00170 Helsinki, Finland

Analysis methods of lithium based on charged particle bombardment are reviewed. Special interest is paid to the parameters related to experimental arrangements and to the results obtained under the experimental conditions. The applicability of the methods in various fields is surveyed. The ion beam methods are compared with various other physical and chemical analysis methods used for Li detection.

1. Introduction

Lithium consists naturally of two stable isotopes; ^{6}Li (6.43%) and ^{7}Li (93.57%). Lithium isotopes are of interest from the viewpoint of astrophysics, geochemistry and cosmochemistry. Perhaps lithium may be used as a fusion reactor first blanket material. It is also a common element in optical waveguide and fiber optic materials. Furthermore, Al–Li base alloys have many potential applications, particularly in the aerospace industry, because of their high strength-to-weight ratio. On the other hand, lithium is a therapeutic agent for manic-depressive illnesses. The clinical aim of the therapy is maintenance of blood concentration levels within the range 6–7 μg/ml. For these determinations accurate analysis methods are needed.

A number of nuclear techniques are known for the determination of lithium. In the present review the accelerator based techniques are surveyed first, then neutron induced methods, and last, some other analytical techniques are summarized for comparison. The methods are briefly introduced and typical applications are given. Exact numbers describing the usability of the methods was of special interest. The literature was surveyed by a computer code search with the main interest being in the literature published after 1980. The important data concerning the methods and applications is summarized in tables. Finally a general comparison of the methods is given.

2. Charged particle accelerator based methods

In selecting the analysis method the highest possible sensitivity is required to ensure reasonable measuring time. Also possible interference should be kept at a minimum. Sensitivity may be optimized by selecting a nuclear reaction with a high cross reaction and by maximizing the beam current. By passing the particle beam through a thin exit foil into gas at atmospheric pressure the measurement capabilities of the methods are increased considerably (these are referred to as external beam studies in this review). In the following the methods are divided into prompt and activation method groups.

2.1. Prompt methods

The best known accelerator based prompt methods for elemental analysis are particle induced X-ray emission (PIXE), nuclear reaction analysis (NRA), Rutherford backscattering spectrometry (RBS) and elastic recoil detection analysis (ERDA). Of these methods PIXE and RBS are not useful in practical Li analyses. Proton induced reaction analysis is discussed separately from other ion induced reactions as protons are used most frequently.

2.1.1. Proton induced reactions

The proton induced reactions used for Li analysis are based either on prompt gamma ray or charged particle emission.

2.1.1.1. Proton induced gamma ray emission. In proton induced gamma-ray emission (PIGE) the prompt gamma rays from various reactions are detected during the irradiation. The reaction ^{7}Li(p, p′γ)(E_γ = 478 keV) is most frequently used and yields the best sensitivity. Due to the short lifetime of the deexciting state and the high recoil of the light nucleus, a clear Doppler broadening occurs in the 478 keV peak [1]. The reaction ^{7}Li(p, γ) may be used for depth profiling of lithium. The information found in the literature is collected in table 1. Courel et al. [2] have compared microbeam and macrobeam analyses of light elements in minerals and glasses (see table 1). Boni et al. have

0168-583X/92/$05.00 © 1992 – Elsevier Science Publishers B.V. All rights reserved

used the (p, p'γ) reaction in many studies [3–6]. Differential cross section data for the reaction ^{7}Li(p, p'γ), which are essential in the analysis of samples of thin and intermediate thicknesses, have been provided. The proton energy region studied was 2.7–3.8 MeV [3]. For thin sample analysis an energy spread proton beam is used to smooth the fluctuations in the excitation functions. The method is described in ref. [4]. Hall [7] has

Table 1
Analysis of Li by the PIGE method

Proton energy [MeV]	E_γ	I [nA]	t_{mean} [min]	Sample	Det. limit [ppm]	Remarks	Ref.
^{7}Li(p, p'γ)^{7}Li							
1.7–2.0	478 keV	300	30	organic	0.15	external beam	[14]
		40	30	geological	0.5	gamma ray background high	[14]
1–1.5		q = 1 mC		rock + 10%C	1.0		[15]
3		15	10	vesicles on Nuclepore filter	0.05 μg/cm^2	external beam	[16]
1.03		q = 1 mC		rock + 10%C	0.69		[17]
4.0		60	10	tree rings	1.6	PIXE/PIGE simultaneously, external beam, dry ashing sample prep. technique	[7]
2.5		50	3	drill cores	~ 40	PIXE/PIGE simultaneously, external beam	[11]
3.1		q = 60 μC		thin fly ash	0.030 μg/cm^2	PIXE/PIGE simultaneously	[5]
				thin coal	0.015 μg/cm^2		
				thick fly ash	10		
				thick coal	25		
3.52		q = 60 μC		thin particulate matter	0.001 μg/cm^2	PIXE/PIGE simultaneously	[4]
3.5				Li_xNi_{1-x} thin film	15 ng/cm^2	PIXE/PIGE	[6]
2.5		5–100		coal	2	simultaneously	[18]
		q = 100 μC		fly ash	10		
				rock	10		
1.2–2.0		2 μA/mm^2	15–30	glass	45	microbeam	[2]
		2×10^{-2} μA/mm^2		glass	10	macrobeam	[2]
1.8		150	33	calcite	~ 6		[8]
1.2		100	120	blood serum	< 0.3		[8]
^{7}Li(p, γ)^{8}Be	Q = 17.3 MeV [a]						
0.44	14.7 MeV 17.6 MeV			Cu–Ag–Li alloy brazed joint	4	for depth profiling, depth resol. 0.15 μm, max. depth 50 μm	[19]
0.44		1000		Al	500	for depth profiling, depth resol. in Al 0.2 μm, max. depth 7 μm	[20]
1.03	18.15 MeV 15.25			Al	250		[20]

[a] Ref. [86].

investigated different sample preparation methods of tree rings and analyzed various elements including Li by external beam PIXE/PIGE.

Boulton and Ewan [8] showed the advantage of using a low proton energy of 1.2 MeV for the bombardment to reduce the sensitivity of sodium, which yields a gamma ray peak at 440 keV and thus interferes with the Li analysis. Lithium has been analyzed, e.g., in pottery and glasses [9], geological samples [10,11], desert varnish [12] and Al–Li alloys [13] by various investigators. In ref. [14] Li analyses by the ^{7}Li(p, p′γ) and ^{7}Li(p, α) reactions is compared for external beam systems. A clear optimum for Li analyses via the ^{7}Li(p, p′γ) reaction was observed at E_p = 1.7–2.0 MeV. At increasing proton energies the gamma ray yields increase but the background in the spectra also increases significantly. At high proton energies the neutron yield from the matrix and the experimental system becomes the major drawback. If a conventional paraffin shield is used for the gamma ray detector it should be kept in mind that a strong peak at 478 keV is introduced from the reaction ^{10}B(n, α)^{7}Li.

The PIGE method is a multielemental method suitable for light element detection. A disadvantage is that the sensitivity depends strongly on the sample composition, mainly on the concentrations of Li, B, Na and F for which the proton induced γ-ray yields are the highest (see table 4 for references).

2.1.1.2. Particle–particle reactions (p, α) and (p, n). In the (p, α) method the alpha particles emitted from the reaction ^{7}Li(p, α) are detected, e.g., by a silicon surface barrier detector. As the backscattered proton flux is much higher than the flux of α-particles, an absorber foil of a suitable thickness must be used to prevent too high counting rates. Simultaneously, during the detection of the α-particles, the RBS spectrum of the protons is often taken for beam current monitoring with another detector. The (p, α) method allows the depth profiling of Li by deducing directly the profile from the energy spectrum of the emitted α-particles. Absolute thick target yields of α-particles following the proton bombardment are given in ref. [21] for 0.7 and 1.0 MeV energies.

When the (p, α) measurements are performed in He gas with an external beam volatile samples may also be analyzed and no problems arise due to charging effects. In ref. [14] the optimum conditions for Li analyses by an external beam (p, α) system are presented. The bombarding energy and the absorber foil thickness have been optimized. The optimum energy found was about 2.5 MeV with a 55 μm thick absorber

Table 2
Analysis of Li by (p, α) and (p, n) reactions

Proton energy [MeV]	I	t_{meas} [min]	Absorber foil	Sample	Detection limit [ppm]	Remarks	Ref.
^{7}Li(p, α)^{4}He	Q = 17.3 MeV [a]						
0.5–1.0		120	Al 7 μm	Be foil	0.1	interference free, microbeam	[30]
2.3	1.5 μA	5–10	Mylar 51 μm	human bone, blood serum, geological	0.10	external beam used with He gas	[14]
3.0/1.1				steel, B_4C	100	depth profiles, microbeam 10×10 μm^2, depth range → 5 μm	[31,32]
3.0	few nA			glass	~ 0.1 at.%	external beam, depth profiles, depth resolution ~ 1 μm, depth range → 30 μm	[33]
1.5	4–10 μA/cm^2 q ~ 1 mC		Mylar 25 μm	Al–Li, Cu–Li alloys	400 at surface	depth profiles, beam size ~ 2 mm^2, depth resol. ~ 1 μm, depth range → 17 μm	[34,35]
1.0	2 μA/mm^2	15–30		glass	20	microbeam	[2]
	2×10^{-2} μA/mm^2			glass	80	macrobeam	[2]
^{7}Li(p, n)^{7}Be	Q = −1.6 MeV [a]						
2.0	q = 100 μC			rock	100	K and Cl interfering elements	[29]
				diamond	~ 2		[28]

[a] Ref. [86].

foil (Mylar) for organic samples. The corresponding detection limit value is given in table 2.

Heck [22] has performed three-dimensional Li microanalysis in stainless steel with 3 MeV protons and a beam spot of ~ 2.5 μm diameter. Simultaneous (p, α), RBS and PIXE measurements were performed. Wen et al. [23] have determined trace amounts of Li in ZnO films by employing the (p, α) reaction. The RBS spectrum was also simultaneously taken. In the coincidence measurement of complementary particles method (CMCP) used by Pretorius et al. [24–26] the two particles are measured in coincidence with one another. The main limitation of this method is that samples must be thin enough to transmit both product particles. Pallon and Kristiansson [27] use the ^{7}Li(p, α) reaction for thin target thickness monitoring by employing a LiCl foil as a source of the α-particles. A high signal-to-noise ratio is obtained by using a coincidence technique to measure the induced α-particles pairwise.

The advantage of the (p, α) method is that the sensitivity does not depend on the sample composition as is the case, e.g., for the PIGE method. When the (p,α) method is used in its normal mode thick samples may also be analyzed. The disadvantage of this method is that only one element may be determined per run under optimum conditions (although also B, F and N may be determined at the same time if the best sensitivity is not needed). On the other hand, fluorine is the only element which may produce possible overlap in the dominant part of the Li spectrum with typical detection angles of 105° and 170° relative to the beam and with incident proton energies of 700–2700 keV as used in the studies of refs. [14] and [21]. The ^{7}Li(p, n) reaction has also been used, although not as extensively as the (p, α) reaction. The reaction threshold energy is 1.88 MeV. Sellschop et al. [28] have used the (p, n) reaction to analyze impurities in diamond and obtained a detection limit value of 2 ppm. Sippel and Glover [29] have analyzed sedimentary rock by the (p, n) reaction. A BF_3 counter was used for n detection. An estimated limit of detection was 100 ppm. Details of the results are given in table 2.

2.1.2. d, t, ^{3}He, ^{4}He and ^{35}Cl-ion induced reactions

Deuterons. The most frequently used deuteron induced reaction for Li analysis is ^{6}Li(d, α)^{4}He. Pretorius et al. [36] used it with the coincident measurement of the complementary particles. The LiF samples were prepared on thin carbon foils by evaporation and spraying techniques. A disadvantage of the method is that thin samples are needed. Möller et al. [37] used the ^{6}Li(d, α) reaction for depth profiling of lithium in nickel samples. Brown et al. [38] have determined the isotopic composition of lithium by employing the reactions ^{6}Li(d, α)^{4}He, ^{7}Li(d, α)^{5}He(n)^{4}He and ^{7}Li(d, n)^{8}Be(α)^{4}He.

Tritons. Borderie and Barrandon [39] have studied the use of tritons in prompt gamma ray spectrometry. Incident ion energies of 2 and 3 MeV were used. The

Table 3
d, t, ^{3}He, ^{4}He and ^{35}Cl-ion induced reactions

Reaction	Q [a] [MeV]	Ion energy [MeV]	I (μA)	t_{meas} [min]	Sample	Det. limit [ppm]	Remarks	Ref.
^{6}Li(d, α)^{4}He	22.4	2	1	1–30	Ni	0.5 at.%	α-particles detected, depth profiles, F interfering element, depth resol. 0.03–0.35 mg/cm^{2}	[37]
^{7}Li(t, t′γ)^{7}Li		2	0.5	120	Nb	3	gamma rays detected, Na interfering element	[39]
		3	0.5	120	Nb	2		[39]
^{7}Li(^{3}He, p)^{9}Be	11.2	2.5	q = 2 μC		Al–Li alloy	100	protons detected, depth profiles, spatial resol. ~ 100 μm, probing depth 4–6 μm	[40,41]
^{7}Li(α, α′γ)^{7}Li		2.4	10		volcanic stone	0.45	gamma rays detected	[44]
^{7}Li(α, α′γ)^{7}Li		3.5	0.1	30	quartz	1		[43]
		3.5	0.5	120	Nb	0.165		[39]
^{7}Li(α, α′γ)^{7}Li		5			LiF	30		[42]
^{7}Li(α, α′γ)^{7}Li		5	0.5	120	Nb	0.05		[15]
^{7}Li(^{35}Cl, np)^{40}K	4.6	55	0.5	120	Nb	10	gamma rays detected	[45]
^{7}Li(^{35}Cl, n)^{41}Ca	12.9	55	0.5	120	Nb	8	gamma rays detected	[45]

[a] Ref. [86].

reaction usable for Li analysis is ^{7}Li(t, t′γ) (see table 3 for more details).

^{3}He particles. For bombardment with ^{3}He particles the reaction ^{7}Li(^{3}He, p)^{9}Be has been employed in the analysis of lithium. Schulte et al. [40,41] have used a finely collimated beam of 2.5 MeV ^{3}He ions for depth profiling of Li in Al–Li alloys. In the measurements a 125 μm thick Kapton foil was used as an absorber for the elastically scattered ^{3}He particles.

^{4}He particles. Alpha particles are the second extensively used particles for Li analysis after protons. This is because alpha particles may be considered to be included in the normal routine use of ion accelerators. The reaction involved is ^{7}Li(α, α′γ) and Li may be determined by detecting the 478 keV prompt gamma rays. The Doppler broadening of the 478 keV gamma ray peak is useful in identifying the origin of the peak as Li only produces one gamma ray line with α-energies upto at least 5 MeV [42]. This method is often called the alpha particle induced gamma-ray emission (AIGE) method.

Giles and Peisach [42] have determined the thick target gamma ray yields of Li for 5 MeV alpha particles. Borderie et al. [43] for 3.5 MeV α-particles and Lappalainen et al. [44] for 2.4 MeV α-particles. The results are summarized in table 4. The low α-energies used in the above studies limit nuclear reactions to the lighter elements. A clear advantage of α-particles over protons is the lower gamma ray background. Another advantage of using alpha particles rather than protons is the possibility to determine Li from samples containing, e.g., Na, Mg, Al as major components for which the gamma ray yields with protons are high. This limits considerably the sensitivity obtainable with protons.

^{35}Cl ions. Borderie et al. [45] have used 55 MeV ^{35}Cl ions for the analysis of ^{7}Li in Nb by prompt gamma ray detection. The results obtained are given in tables 3 and 4. Two different reactions were observed: ^{7}Li(^{35}Cl, np) and ^{7}Li(^{35}Cl, n).

Table 4
Thick target gamma-ray yields for Li

Particle	Ion energy [MeV]	Reaction	E_γ [keV]	Yield/ [μC sr]	Ref.
Proton	1.0	^{7}Li(p, p′γ)	478	6.5×10^{5}	[46]
	3.1			5.6×10^{7}	[47]
	4.0			4.9×10^{8}	[48]
	5.0			5.7×10^{8}	[48]
	6.0			6.2×10^{8}	[48]
	9.0			2.1×10^{9}	[49]
Triton	2.0	^{7}Li(t, t′γ)	478	3.6×10^{6}	[39]
Alpha	2.4	^{7}Li(α, α′γ)	478	9.6×10^{5}	[44]
	3.5			6.5×10^{6}	[39]
^{35}Cl	55	^{7}Li(^{35}Cl, np)	892	4.1×10^{4}	[45]
	55	^{7}Li(^{35}Cl, n)	1584	7.1×10^{4}	

The use of particle–particle reactions is more complicated than that of radiative reactions. The advantage of radiative reactions is the high penetrability of the gamma rays which minimizes matrix effects. With deuteron bombardment only ^{6}Li may be determined. Of the ions listed in table 3 ^{4}He ions seem to yield the best sensitivity. If we compare the thick target gamma ray yields of Li obtainable with different ions and energies it may be noted from table 4 that the highest yield is clearly that obtained by protons. The background yield and thus the sensitivity, however, are in each case dependent on the sample matrix. General recommendations for the choice of ions and energies can not be given.

2.1.3. Elastic recoil detection analysis

Elastic recoil detection analysis (ERDA) involves the detection of ions recoiling elastically from a sample on bombardment by heavy ions of high energy. The technique is particularly useful for the detection of light elements at the surface of a heavy material. It

Table 5
Elastic recoil detection analysis of Li

Ion	Energy [MeV]	I [nA]	t_{meas} [h]	Absorber foil	Sample	Depth resol. at surface [nm]	Maximum acc. depth [μm]	Det. limit [atoms/cm^2]	Ref.
^{20}Ne	18	30	1	Mylar 7 μm	Al bulk	23	0.3	1.9×10^{15}	[51]
	18	20	9	Mylar 7 μm	Al bulk			5×10^{13}	[51]
^{35}Cl	30	30	1	Mylar 7 μm	Al bulk			7.4×10^{14}	[51]
^{40}Ar	18	30	1	Mylar 7 μm	Al bulk			1.9×10^{14}	[51]
^{35}Cl	35	10		Ni 5–7 μm	Cu/C backing evap. LiF	30		10^{14}	[50]

Table 6
Charged particle activation analysis of Li

Ion/energy [MeV]	Reaction	Q [a] [MeV]	I [μA]	$t_{1/2}$ of product	t_{irr}
p/6	$^{7}Li(p, n)^{7}Be$	−1.6	1.5	53.4 d	30 min
p/1.8					
4.5					
p/14			10		2 h
d/15	$^{7}Li(d, 2n)^{7}Be$	−3.9	10		2 h
	$^{6}Li(d, n)^{7}Be$	3.4			
d/4.8	$^{6}Li(d, n)^{7}Be$	3.4	0.15		$q = 400$ μC
d/20	$^{7}Li(d, p)^{8}Li$	−0.2	2	850 ms	1 ms–10 s, 100 irr./ counting sequence
$^{6}Li/7$	$^{6}Li(^{6}Li, n)^{11}C$	9.5	1	20.4 min	10 min
	$^{7}Li(^{6}Li, 2n)^{11}C$	2.2			
$^{9}Be/13.5$	$^{6}Li(^{9}Be, 2n)^{13}N$	4.0	1	10 min	5 min
$^{12}C/12$	$^{7}Li(^{12}C, n)^{18}F$	6.0	1	110 min	1 h
$^{14}N/12.5$	$^{6}Li(^{14}N, d)^{18}F$	6.1	1	110 min	1 h
	$^{7}Li(^{14}N, t)^{18}F$	2.0			20 min
$^{18}O/25$	$^{7}Li(^{18}O, \alpha n)^{20}F$	3.6	0.1	11.4 s	10 s cycle repeated for 10 times

[a] Ref. [86].

t_{meas}	Sample	Det. limit [ppm]	Remarks	Ref.
15 h	rock		interfering elements with protons; B, Be, C, N, see ref. [52] for reaction thresholds	[52]
	Al-fuel tubes			[53]
5 h	Nb, Ta	0.8 ppb	interference-free chemical separation of ^{7}Be, destructive	[54,55]
5 h	Nb, Ta		interfering elements with deuterons; B, Be, C, N, see ref. [52] for reaction thresholds	[54,55]
	LiOH, LiF		E_d below the threshold for the ^{7}Li(d, 2n) reaction (4.97 MeV). Only interfering element B	[56]
r./	silicon	0.9	irr. carried out in air	[57]
ce	glass	6	(25 μm Ta exit foil), non-destructive, interfering element Ca, a quasi-prompt method	
	glass	0.5	boron-free sample, interfering element B, non-destructive	[58]
	glass		method was not suitable for Li determination	[59]
	glass	0.5	interference due to B and C, non-destructive	[59]
5 min	rock	0.3	destructive	[60]
5 min	glass	2	non-destructive, interfering element Be	[60]
30 s	alloys, glass, environmental samples	5	interference-free values, non-destructive, generally interference from B, N, F, Na, det. limit 1 ppm for 40 MeV ^{18}O ions	[61]

may be noted that by conventional Rutherford backscattering analysis the determination of Li is not possible in practice. The ERDA method makes it possible to analyze Li. In ERDA, it is necessary to screen the detector from the high flux of the scattered beam ions in order to detect the small flux of the light recoil ions which are ejected in the forward direction. Generally Mylar foils are used for this purpose. The typical target–detector separation is 10–20 cm and the solid angle subtended by the detector about 10^{-4} sr. The typical scattering angle which has been used in most experiments is 30°. An important feature of this method is the possibility of depth profiling. Typical values obtained by ERDA are given in table 5.

L'Ecuyer et al. [50] investigated the use of various beams (^{19}F, ^{35}Cl, ^{79}Br) and concluded that the 35 MeV ^{35}Cl beam yielded the best depth resolution. Moreau et al. [51] have considered the beams of ^{20}Ne, ^{35}Cl and ^{40}Ar. As may be concluded from table 5, the best sensitivity in their study was obtained by the ^{40}Ar beam. However, the mass dispersion with the ^{40}Ar ions is not as good as with the ^{20}Ne and ^{35}Cl ions.

2.2. Charged particle activation analysis

Lithium has been determined successfully with charged particle activation [52–61] by employing various projectiles. The nucleus produced in the activation with the charged particles is used as an indicator radionuclide for the determination of the element in question. A difficulty in the activation method is that different reactions with the matrix nuclei may lead to the same product nucleus. For the most sensitive determinations elaborate radiochemical separation procedures must be performed if the matrix induces interfering activities. In these cases the method is clearly destructive. A summary of the various possibilities of detecting Li by charged particle activation analysis is given in table 5.

3. Neutron induced methods

3.1. (n, α) spectrometry

In these methods the element being determined undergoes a nuclear reaction (^{6}Li(n, α)^{3}H) with thermal neutrons. The means for detecting the reaction products vary with the different methods. By measuring the charge particles from neutron induced reactions depth profiling of Li is also possible [62,63]. The applications of the methods are many and varied [64,65].

3.1.1. Track etch method

In nuclear track detection the sample and the nuclear track detector are irradiated together in a reactor. The prompt alpha particles from the reaction ^{6}Li(n, α) produce nuclear tracks which are revealed by chemical etching. The track density is then inspected. A comparison of the measured track density produced in the sample with that of a standard of known composition is used to determine the elemental concentration. When several elements that have nuclides undergoing thermal neutron induced charged particle emission (e.g. ^{10}B, ^{17}O) are present in the sample, the use of the alpha particle track counting technique becomes difficult. For these samples the Li content must be determined by observing the tracks produced by the ^{3}H particles. The detection limit for Li is then much

Table 7
Neutron induced methods

Method	n flux [n/(cm^2 s)]	Sample	Det. limit [ppm]	Remarks	Ref.
^{6}Li(n, α) reaction					
Track etch		geological, glass	> 1	time-consuming method	[72]
		glass	0.1	interference-free	[73,74]
		glass	10	interference due to B	[73,74]
Mass spectrom.	3.3×10^{11}	whole blood, biol. ref. mater.	< 0.01	highly thermalized neutron flux	[68]
Reaction chain	1.5×10^{13}	geological material	0.4 μg	irr. 15 min, 30 min decay, 2000 s measurement	[69]
Coincidence technique		Mylar foil	10^{-6}	only thin samples, depth distributions, long determinations	[70]
		Si wafer	10^{-2}–10^{-3}		
^{7}Li(n, γ) reaction					
NAA	10^{13}	water, biol. material, geochem. ref. samples	0.05	fast irradiations, < 10 s	[71]

poorer (see table 7). In the work of Martini et al. [66] the problems related to the track etch method are discussed. Generally a fission reactor is used in these studies, but also a Ra–Be neutron source may be used as pointed out by Kjellman et al. [67]. The irradiation times varied from 3 to 10 days for mineral samples. The sensitivity of this method is clearly poorer than those of the reactor based methods.

3.1.2. Mass-spectrometric measurement of ^{3}He

In the work of Clarke et al. [68] a mass-spectrometric assay of ^{3}He from the decay of ^{3}H produced in the reaction ^{6}Li(n, α)^{3}H was performed. Several sample types were studied with good sensitivity. See table 7 for details.

3.1.3. Reaction chain method

The tritons produced in the reaction ^{6}Li(n, α) induce some secondary reactions which may be applied as an indirect method for Li analyses. The reactions ^{16}O(t, n)^{18}F and ^{18}O(t, α)^{17}N have been employed. In the work of Cohen et al. [69] the reaction ^{32}S(t, n)^{34m}Cl is used. The isotope produced has a convenient half-life and may be detected easily via gamma spectroscopy.

3.1.4. Coincidence technique

The standard method has been developed further especially at the Hahn–Meitner Institute [70]. In this method the background is reduced by a simple coincidence circuit. The method has been used for depth profiling of Li in numerous sample types. The method is extremely sensitive as may be noted from table 7. A disadvantage of the method is that only thin samples (a few μm thick) may be analyzed.

3.2. Instrumental neutron activation analysis

A clear difficulty in conventional NAA is that lithium does not have a radioactive isotope of convenient half-life. For example Heydorn et al. [71] have, however, determined Li by employing the reaction ^{7}Li(n, γ)^{8}Li ($t_{1/2} \sim 0.84$ s). They analyzed biological material and geochemical reference material. The relevant results are given in table 7.

4. Other analytical techniques

Several sensitive non-nuclear techniques have also been applied for the determination of lithium. Among them the most common methods are atomic emission spectrometry (AES), atomic absorption spectrometry (AAS) and inductively coupled plasma (ICP) methods. Nearly all non-nuclear techniques are destructive methods. In the following the methods used successfully for Li detection are briefly summarized. Typical values related to the methods are given in table 8.

(A) Atomic absorption spectrometry (AAS)

Atomic absorption spectrometry is one of the most extensively used analysis methods. It may be used easily in routine laboratory work. The problems related to AAS are discussed, for example, in ref. [75].

(B) Atomic emission spectrometry (AES)

This method has been the classical approach for simultaneous multielement determinations. The method has lost some of its importance to the AAS method.

(C) Inductively coupled plasma (ICP)

Several kinds of plasmas have been considered for analytical instrumentation, but the one most widely used is the inductively coupled plasma. Different ICP methods have been developed which may also be used for Li detection. The inductively coupled plasma atomic emission spectrometry (ICP-AES) techniques have brought simultaneous multielement capabilities. Also a

Table 8
Other analytical techniques

Method	Sample	Detection limit	Remarks	Ref.
AAS flame	biological	0.3 μg/l		[75]
AAS furnace		~ 2 μg/l	assuming a 20 μl sample	[79]
AES flame	biological reference materials and human hair	1 μg/l		[80]
ICP-AFS	water	0.3 μg/l	multielemental determination	[81]
ICP-AES	organic	0.05 ppm		[82,83]
ICP-MS		0.09 μg/l		[82]
SIMS	geological	0.005 ppm	good depth resolution	[84]
LAMMA	sucrose matrix with LiCl	2×10^{-19} g	high lateral resolution (spot size ~ 0.7 μm)	[85]
EELS	Al–Li alloy	~ 2.7 wt.%		[77]
PDMS	glass	100 ppm	non-destructive	[78]

Table 9
Comparison of various Li detection methods

Method	Sample	Detection limit [ppm]	Remarks
PIGE	organic	0.15	external beam
(p, α) method	human bone, blood serum, geological	0.10	external beam
AIGE	Nb	0.05	
ERDA (^{20}Ne)	Al	~1	depth profiling
Charged particle activation (^{14}N)	rock	0.3	destructive, chemical treatment of sample
(n, α) mass spectrometry	blood	< 0.01	destructive, long irradiation
(n, α) coincidence	Mylar foil	10^{-6}	only thin samples
AAS	organic	0.0003	destructive
ICP	organic	0.0003	destructive
SIMS	geological	0.005	destructive

rapid, simultaneous multielement technique is the inductively coupled plasma atomic fluorescent spectrometry (ICP-AFS). The inductively coupled plasma mass spectrometry (ICP-MS) is an accurate method to measure stable isotope ratios (^{6}Li/^{7}Li, ref. [76]). The disadvantage of these methods is that they generally need rather compiicated sample preparations.

(D) Secondary ion mass spectrometry (SIMS)

In this method the secondary ions produced by primary low energy ion bombardment are analyzed with a mass spectrometer. The method is generally extremely sensitive, but the quantitative interpretation of spectra requires a knowledge of the chemical state of the lithium (e.g. LiO_2, LiOH, Li_2O_3, etc.). This state is generally unknown and consequently quantitative measurements cannot be performed in these cases. SIMS has an excellent depth resolution but it has the disadvantage of being a destructive method [84].

(E) Laser microprobe mass analysis (LAMMA)

Laser induced mass spectrometry has become an important microanalytical technique with good relative and absolute detection limits. One of the problems related to LAMMA is the difficulty in obtaining a realistic estimation of the analytical microvolume or the analytical micromass. This method is also destructive.

In addition to the methods mentioned above, several others have been used for lithium determination. One of them is electron energy loss spectrometry (EELS). This method is, however, rather insensitive to lithium. For example, Chan and Williams [77] have analyzed Li from Al–Li alloys with a detection limit of about 2.7 wt.%. Schweikert et al. [78] have used fission fragments of 252 Cf (84 MeV Kr) for bombardment of glasses and plastics. The desorbed ions following the surface bombardment are detected with a time-of-flight mass spectrometer. The detection limit obtained for Li in glass by this particle induced desorption mass spectrometry (PDMS) method was 100 ppm.

5. Conclusions

A clear advantage of most charged particle based methods is the possibility of performing depth profile measurements. Other advantages of the techniques are their non-destructiveness and that they are generally fast and often no chemical sample preparation steps are needed. Furthermore, the nuclear methods are independent of the chemical and physicochemical properties of the samples. As may be noted from the varying detection limit values given in the tables, the sensitivities of the methods are generally very dependent on the sample matrix. Therefore an accurate comparison of the methods is difficult, but for general purposes the (p, α) and AIGE methods seem to yield the best sensitivities for lithium (table 9).

The (n, α) method used with the coincidence technique is clearly the most sensitive method which also offers the possibility of depth profiling of Li. The limitations of the method are that only thin samples may be analyzed and that a high flux reactor is needed.

The conventional methods of AAS and ICP are more sensitive than the ion beam methods. They are routinely used in most laboratories. The shortcomings of these methods are their destructiveness and that depth profiling is not possible.

References

[1] R. Hänninen, J. Räisänen and A. Anttila, Radiochem. Radioanal. Lett. 44 (1980) 201.
[2] P. Courel, P. Trocellier, M. Mosbah, N. Toulhoat, J. Gosset, P. Massiot and D. Piccot, Nucl. Instr. and Meth. B54 (1991) 429.

[3] C. Boni, E. Cereda, G.M. Braga Marcazzan and V. De Tomasi, Nucl. Instr. and Meth. B35 (1988) 80.
[4] C. Boni, E. Caruso, E. Cereda, G.M. Braga Marcazzan and P. Redaelli, Nucl. Instr. and Meth. B40/41 (1989) 620.
[5] C. Boni, A. Caridi, E. Cereda, G.M. Braga Marcazzan and P. Redaelli, Nucl. Instr. and Meth. B49 (1990) 106.
[6] C. Boni, A. Caridi, E. Cereda, G.M. Braga Marcazzan, F. Parmigiani and M. Scagliotti, Nucl. Instr. and Meth. B50 (1990) 243.
[7] G.S. Hall, Nucl. Instr. and Meth. B49 (1990) 60.
[8] R.B. Boulton and G.T. Ewan, Anal. Chem. 49 (1977) 1297.
[9] D. Gihwala, L. Jacobson, M. Peisach and C.A. Pineda, Nucl. Instr. and Meth. B3 (1984) 408.
[10] L-E. Carlsson, Nucl. Instr. and Meth. B3 (1984) 206.
[11] K.G. Malmqvist, H. Båge, L-E. Carlsson, K. Kristiansson and L. Malmqvist, Nucl. Instr. and Meth. B22 (1987) 386.
[12] P. Duerden, D.D. Cohen, D. Dragovich and E. Clayton, Nucl. Instr. and Meth. B15 (1986) 643.
[13] F. Degreve, B. Dubost, A. Dubus, N.A. Thorne, F. Bodart and G. Demortier, J. Phys. Colloq. (France) 48 (1987) C505.
[14] J. Räisänen and R. Lappalainen, Nucl. Instr. and Meth. B15 (1986) 546.
[15] B. Borderie, Nucl. Instr. and Meth. 175 (1980) 465.
[16] G.R. Palmer, J.D. MacArthur and M.A. Singer, Nucl. Instr. and Meth. B45 (1990) 337.
[17] P.J. Clark, G.F. Neal and R.O. Allen, Anal. Chem. 47 (1975) 650.
[18] J.R. Bird and E. Clayton, Nucl. Instr. and Meth. 218 (1983) 525.
[19] M.D. D'Agostino, E.A. Kamykowski, F.J. Kuehne, G.M. Padawer, E.J. Schneid, R.L. Schulte, M.C. Stauber and F.R. Swanson, J. Radioanal. Chem. 43 (1978) 421.
[20] I. Golicheff, M. Loeuillet and Ch. Engelmann, J. Radioanal. Chem. 12 (1972) 233.
[21] R. Lappalainen, J. Räisänen and A. Anttila, Nucl. Instr. and Meth. B9 (1985) 55.
[22] D. Heck, Nucl. Instr. and Meth. B30 (1988) 486.
[23] L-B. Wen, Y-W. Huang and S-B. Li, J. Appl. Phys. 62 (1987) 2295.
[24] R. Pretorius, P.P. Coetzee and M. Peisach, J. Radioanal. Chem. 16 (1973) 551.
[25] P.P. Coetzee, R. Pretorius and M. Peisach, Nucl. Instr. and Meth. 131 (1975) 299.
[26] R. Pretorius and M. Peisach, Nucl. Instr. and Meth. 149 (1978) 69.
[27] J. Pallon and P. Kristiansson, Nucl. Instr. and Meth. B49 (1990) 70.
[28] J.P.F. Sellschop, H.J. Annegarn, R.J. Keddy, C.C.P. Madiba and M.J. Renan, Nucl. Instr. and Meth. 149 (1978) 321.
[29] R.F. Sippel and E.D. Glover, Nucl. Instr. and Meth. 9 (1960) 37.
[30] I.G. Berzina, É.B. Gusev, A.V. Drushchits, V.S. Kulikauskas and A.F. Tulinov, Sov. At. Energy 53 (1982) 648.
[31] C.R. Allen, G. Dearnaley and N.E.W. Hartley, in: Ion Beam Surface Layer Analysis 2, eds. O. Meyer, G. Linker and F. Käppeler (Plenum, New York, 1976) p. 901.
[32] J.W. McMillan, F.C.W. Pummery and P.M. Pollard, Nucl. Instr. and Meth. 197 (1982) 171.
[33] B.L. Doyle, Nucl. Instr. and Meth. 218 (1983) 29.
[34] A. Sagara, K. Kamada and S. Yamaguchi, Nucl. Instr. and Meth. B34 (1988) 465.
[35] A. Sagara, K. Kamada, T.A. Sasaki and Y. Baba, Nucl. Instr. and Meth. B44 (1990) 373.
[36] R. Pretorius, Radiochem. Radioanal. Lett. 10 (1972) 297.
[37] W. Möller, M. Hufschmidt and D. Kamke, Nucl. Instr. and Meth. 140 (1977) 157.
[38] L. Brown, R.S. Rajan, R.B. Roberts, F. Tera and D.J. Whitford, Nucl. Instr. and Meth. 156 (1978) 541.
[39] B. Borderie and J.N. Barrandon, Nucl. Instr. and Meth. 156 (1978) 483.
[40] R.L. Schulte, J.M. Papazian and P.N. Adler, Nucl. Instr. and Meth. B15 (1986) 550.
[41] J.M. Papazian, R.L. Schulte and P.N. Adler, Metall. Trans. A17 (1986) 635.
[42] I.S. Giles and M. Peisach, J. Radioanal. Chem. 50 (1979) 307.
[43] B. Borderie, M. Basutcu, J.N. Barrandon and J.L. Pinault, J. Radioanal. Chem. 56 (1980) 185.
[44] R. Lappalainen, A. Anttila and J. Räisänen, Nucl. Instr. and Meth. 212 (1983) 441.
[45] B. Borderie, J.N. Barrandon, B. Delaunay and M. Basutcu, Nucl. Instr. and Meth. 163 (1979) 441.
[46] A. Anttila, R. Hänninen and J. Räisänen, J. Radioanal. Chem. 62 (1981) 293.
[47] Á.Z. Kiss, E. Koltay, B. Nyakó, E. Somorjai, A. Anttila and J. Räisänen, J. Radioanal. Nucl. Chem. 89 (1985) 123.
[48] D. Gihwala, Analytical Applications of Proton-Induced Prompt Photon Spectrometry, Ph.D. Thesis, University of Capetown (1982).
[49] J. Räisänen, T. Witting and J. Keinonen, Nucl. Instr. and Meth. B28 (1987) 199.
[50] J.L'Ecuyer, C. Brassard, C. Cardinal, J. Chabbal, L. Deschênes, J.P. Labrie, B. Terreault, J.G. Martel and R. St.-Jacques, J. Appl. Phys. 47 (1976) 381.
[51] C. Moreau, E.J. Knystautas, R.S. Timsit and R. Groleau, Nucl. Instr. and Meth. 218 (1983) 111.
[52] J. Hoste and C. Vandecasteele, Nucl. Instr. and Meth. B40/41 (1989) 1182.
[53] S. Shibata, S. Tanaka, T. Suzuki, H. Umezawa, J.G. Lo and S.J. Yeh, Int. J. Appl. Radiat. Isotopes 30 (1979) 563.
[54] C.S. Sastri, R. Caletka and V. Krivan, J. Radioanal. Chem. 70 (1982) 273.
[55] C.S. Sastri, R. Caletka and V. Krivan, Anal. Chem. 53 (1981) 765.
[56] J. Asher and M.T. Swinhoe, Nucl. Instr. and Meth. 213 (1983) 503.
[57] J.R. McGinley and E.A. Schweikert, Anal. Chem. 47 (1975) 2403.
[58] B.D. Lass, J.F. Ojo and E.A. Schweikert, J. Radioanal. Chem. 60 (1980) 255.
[59] B.D. Lass, N.G. Roché, A.O. Sanni, E.A. Schweikert and J.F. Ojo, J. Radioanal. Chem. 70 (1982) 251.
[60] B.D. Lass, C. Friedli and E.A. Schweikert, J. Radioanal. Chem. 57 (1980) 481.
[61] C. Friedli, Th. Diaco and P. Lerch. J. Radioanal. Nucl. Chem. 112 (1987) 403.

[62] R.G. Downing, R.F. Fleming, J.K. Langland and D.H. Vincent, Nucl. Instr. and Meth. 218 (1983) 47.
[63] R.G. Downing, J.T. Maki and R.F. Fleming, J. Radioanal. Nucl. Chem. 112 (1987) 33.
[64] D. Fink, Nucl. Instr. and Meth. 218 (1983) 456.
[65] P.N. Shukla and P.S. Goel, Geochim. Cosmochim. Acta 43 (1979) 1865.
[66] F. Martini, C. Heurteaux, J.C. Wissocq, M. Thellier and A. Stampfler, J. Radioanal. Nucl. Chem. 91 (1985) 3.
[67] N. Kjellman, K. Kristiansson and L. Malmqvist, Nucl. Instr. and Meth. A235 (1985) 193.
[68] W.B. Clarke, M. Koekebakker, R.D. Barr, R.G. Downing and R.F. Fleming, Int. J. Appl. Radiat. Isotopes 38 (1987) 735.
[69] I.M. Cohen, C. Magnavacca and G.B. Baró, J. Radioanal. Nucl. Chem. 112 (1987) 387.
[70] D. Fink, J.P. Biersack, C. Stumpff and S. Schlosser, Nucl. Instr. and Meth. B15 (1986) 740.
[71] K. Heydorn, P.Z. Skanborg, R. Gwozdz, J.O. Schmidt and M.E. Wacks, J. Radioanal. Chem. 37 (1977) 155.
[72] A.E. Liehu, Nucl. Instr. and Meth. 147 (1977) 93.
[73] B.S. Carpenter and L.J. Pilione, Anal. Chem. 52 (1980) 2452.
[74] L.J. Pilione and B.S. Carpenter, Nucl. Instr. and Meth. 188 (1981) 639.
[75] G.F. Kirkbright, in: Elemental Analysis of Biological Materials, IAEA Technical Reports 197 (IAEA, Vienna 1980) p. 141.
[76] X.F. Sun, B.T.G. Ting, S.H. Zeisel and M. Janghorbani, Analyst 112 (1987) 1223.
[77] H.M. Chan and D.B. Williams, Philos. Mag. B52 (1985) 1019.
[78] E.A. Schweikert, W.R. Summers, M.U.D. Beug-Deeb, P.E. Filpus-Luyckx and L. Quiñones, Anal. Chim. Acta 195 (1987) 163.
[79] W. Slavin, Anal. Chem. 58 (1986) 589A.
[80] H. Matusiewicz, J. Anal. At. Spectrom. 4 (1989) 265.
[81] R.F. Sanzolone and A.L. Meier, Analyst 111 (1986) 645.
[82] W. Maenhaut, in: Control and Fate of Atmospheric Trace Metals, eds. J.M. Pacyna and B. Ottar (Kluwer, Dordrecht, 1989) p. 259.
[83] S. Takács, F. Ditrói, M. Pankotai and P. Fodor, Nucl. Instr. and Meth. B49 (1990) 195.
[84] I.M. Steele, R.L. Hervig, I.D. Hutcheon and J.V. Smith, Am. Mineralogist 66 (1981) 526.
[85] P. Wieser, R. Wurster and H. Seiler, J. Phys. Colloq. (France) 45 (1984) C261.
[86] K.A. Keller, J. Lange and H. Münzel, in: Landolt-Börnstein, New Series I/5a, ed. H. Schopper (Springer, Berlin, 1973).
C. Maples, G.W. Goth and J. Cerny, Nucl. Data A2 (1966) 429.

Nuclear Instruments and Methods in Physics Research B66 (1992) 118–125
North-Holland

Nuclear Instruments & Methods in Physics Research
Section B

Accelerator methods for the determination of beryllium

J.W. McMillan

Process Services Division, B220, Harwell Laboratory, AEA Technology, Didcot, Oxfordshire OX11 0RA, UK

Accelerator methods for the determination of beryllium are reviewed. Three principal techniques are discussed, namely, prompt methods, mainly based on nuclear reactions, activation analysis methods, again based on nuclear reactions, and finally, accelerator mass spectrometry. Illustrative applications are quoted. Accelerator methods and other techniques for beryllium are briefly compared.

1. Introduction

Beryllium is used in a number of industries. In the nuclear industry its properties as a neutron moderator have been valued for many years. More recently it has been found to have beneficial properties in fusion devices, such as the Joint European Torus, as a coating on graphite tiles. Its good transmission for X-rays encourages its wide use as a window material for detectors and generators. The addition of beryllium to aluminium, nickel and copper improves their hardness and resistance to fatigue. The incorporation of beryllium into microelectronic devices improves their properties. The toxicity of beryllium is well known, consequently, its presence in the work place must be strictly controlled. The cosmogenic isotope, ^{10}Be, is finding wide use as a tracer for chemical and physical processes in the atmosphere, oceans and the earth's crust.

Accelerator methods of analysis can be applied to the determination of stable and radioactive isotopes of beryllium. In this review of accelerator methods they are broadly divided into three groups.

(a) Charged particle activation analysis methods.
(b) Prompt methods of analysis.
(c) Accelerator mass spectrometry.

These are reviewed in an exemplary rather than exhaustive manner, so that the range of techniques is indicated with illustrative applications. Finally, an indication is given of the value of accelerator methods at a time when a widening range of modern instrumental methods of analysis has become available.

2. Charged particle activation analysis methods

The analysis of materials by charged particle activation analysis, otherwise known as ion activation analysis, has been generally reviewed in articles by Hoste and Vandecasteele [1] and Engelmann [2]. The subject is discussed in detail in a book, "Activation Analysis with Charged Particles", by Vandecasteele and published in 1988 [3]. A further useful source of information is the book "Ion Beams for Materials Analysis" edited by Bird and Williams and published in 1989 [4].

Beryllium may be determined by a number of reactions involving irradiation with light or heavy, energetic ions.

2.1. Analysis with light ions

Light ion reactions used for the determination of beryllium by charged particle activation analysis include

(1) ^{9}Be(t,p)^{11}Be ($Q = (-)$ 1.166 MeV),
(2) ^{9}Be(α,2n)^{11}C ($Q = (-)$ 13.020 MeV),
(3) ^{9}Be(^{3}He,n)^{11}C ($Q = 7.558$ MeV).

In principle, the first reaction, studied by Borderie et al. [5], is the most attractive for the nondestructive determination of beryllium as the short lived product ^{11}Be, $t_{1/2} = 14$ s, emits an energetic gamma-ray at 2125 keV. A detection limit of ca. 1 $\mu g g^{-1}$ is achievable. However, the higher degree of activation of many other light elements discourages beryllium analysis by this reaction

In common with many reactions induced by charged particle irradiation [2,5,6,7] the product of the second and third reactions is solely a positron emitter, ^{11}C. Its identity can be confirmed by decay curve analysis or by chemical separation which is readily achievable for this relative long lived nuclide, $t_{1/2} = 20.3$ min.

A problem often encountered in charged particle activation analysis is interference from reactions on

Elsevier Science Publishers B.V.

other light nuclides that produce the same active product nuclide. This occurs in the case of reaction two by reactions on ^{10}B, ^{11}B and ^{12}C [2,7].

$^{10}B(\alpha,t)^{11}C$ ($Q = (-)$ 11.124 MeV),
$^{11}B(\alpha,tn)^{11}C$ ($Q = (-)$ 22.579 MeV),
$^{12}C(\alpha,\alpha n)^{11}C$ ($Q = (-)$ 18.722 MeV).

While ^{4}He irradiation has an interference free sensitivity of ca 10 $\mu g g^{-1}$ this is difficult to realise in practice because of inevitable doubts concerning interference from boron and carbon. Little can be gained by adjusting the irradiation energy because the reaction threshold energies are not dissimilar.

An exactly parallel problem occurs when using ^{3}He activation, as in reaction (3) [6,7]. Interfering reactions occur with ^{10}B, ^{11}B and ^{12}C.

$^{10}B(^{3}He,d)^{11}C$ ($Q = 3.196$ MeV),
$^{11}B(^{3}He,t)^{11}C$ ($Q = (-)$ 2.000 MeV),
$^{12}C(^{3}He,\alpha)^{11}C$ ($Q = 1.856$ MeV).

The interference free sensitivity is again ca. 10 $\mu g g^{-1}$. However, the probability of interference from carbon and boron is high and severely restricts the applicability of the reaction for beryllium determination. It is interesting to note that Debrun et al. [6] dismissed ^{3}He activation as unsuitable for trace element analysis because of the frequent formation of nuclides decaying by positron emission.

2.2. *Analysis with heavy ions*

A number of heavy ion reactions can be used for the determination of beryllium by charged particle activation analysis and include

(1) $^{9}Be(^{6}Li,2n)^{13}N$ ($Q = 3.945$ MeV),
(2) $^{9}Be(^{11}B,2n)^{18}F$ ($Q = 3.000$ MeV),
(3) $^{9}Be(^{14}N,\alpha n)^{18}F$ ($Q = 2.842$ MeV),
(4) $^{9}Be(^{15}N,2\alpha)^{16}N$ ($Q = 0.917$ MeV),
(5) $^{9}Be(^{18}O,2\alpha)^{19}O$ ($Q = 2.383$ MeV).

Studies of the activation of light elements by 7 MeV ^{6}Li ions [8,9] indicated that ^{9}Be and ^{12}C were the only nuclides to produce ^{13}N, the latter by the reaction $^{12}C(^{6}Li,\alpha n)^{13}N$. While the sensitivity for beryllium, 2 μg, is superior to that for carbon, 10 μg, the presence of significant amounts of carbon in many materials discourages use of the technique to measure beryllium.

Beryllium can be determined with great sensitivity, ca. 1 μg, by irradiating samples with 10 MeV ^{11}B ions to induce the reaction $^{9}Be(^{11}B,2n)^{18}F$ and subsequent measurement of the ^{18}F product [10]. Limited interference can occur from reactions on boron, $^{10}B(^{11}B,t)^{18}F$, carbon, $^{12}C(^{11}B,\alpha n)^{18}F$, fluorine, $^{19}F(^{11}B,^{12}B)^{18}F$, and magnesium, $^{24}Mg(^{11}B,^{17}O)^{18}F$.

The technique has been successfully applied to determine beryllium in a number of standard materials, NBS-SRM C1123 a Cu–Be alloy and three glass standards NBS-SRM 610, 612 and 614. By increasing the ^{11}B ion energy to 15 MeV the sensitivity of the method can be increased to 0.2 μg [11]. Other ^{11}B induced reactions also occur, for example, $^{9}Be(^{11}B,\alpha)^{16}N$, but they are accompanied by interfering reactions on lithium, boron, carbon and fluorine, the first being dominant. To determine beryllium through the production of ^{16}N the preferred reaction is $^{9}Be(^{15}N,2\alpha)^{16}N$ which is discussed later.

Beryllium may also be determined by irradiation with 12.5 MeV ^{14}N ion beams through the reaction $^{9}Be(^{14}N,\alpha n)^{18}F$ with a sensitivity of ca. 2 μg [9,12]. However, the sensitivity is identical for the determination of lithium through the reactions $^{6}Li(^{14}N,d)^{18}F$ and $^{7}Li(^{14}N,t)^{18}F$, demonstrating the strong mutual interference between these two elements. To determine beryllium in two standard rocks, USGS BCR-1 and CANMET SY-2, it was chemically separated prior to activation and successful measurement. Non-destructive measurements were made of beryllium in two standard glasses NBS-SRM 610 and 612 with tolerable success.

Irradiation of beryllium with 20 MeV ^{15}N ions permits its determination by the reaction $^{9}Be(^{15}N,2\alpha)^{16}N$ [13]. Measurement of ^{16}N, $t_{1/2} = 7.13$ s, via its 6129 keV gamma-ray avoids interference from gamma-emitting nuclides induced in the sample matrix. A sensitivity of 4 μg is achievable. While ^{16}N can be formed from other elements, notably hydrogen, lithium, carbon and fluorine, the sensitivities are much lower and beryllium determination will only be hindered significantly in organic samples. Using a cyclic irradiation system, beryllium was successfully determined in several standards, NBS-SRM C1123 a Cu–Be alloy, and two glass standards NBS-SRM 610 and 612.

A further reaction that has been used for the determination of beryllium is $^{9}Be(^{18}O,2\alpha)^{19}O$ [14]. The short lived product ^{19}O, $t_{1/2} = 27.1$ s, is measured through its 197 keV gamma-ray, during cyclic irradiation. The yield of ^{19}O increases upto an incident ion energy of ca. 30 MeV. Minor interference arises through the production of ^{19}O from lithium and carbon. However, a sensitivity of ca. 1 μg is achievable. Beryllium was measured in a wide range of standard materials with reasonable success.

3. Prompt methods of analysis

A large number of analytical methods have been drawn together under this heading. Prompt nuclear

reactions are most suitable for the determination of light elements, including beryllium, and allow bulk composition and depth distributions to be determined. While scattering methods are generally less suitable for light element determination, they have been applied to measure beryllium and elastic recoil analysis has excellent potential for the determination of this element. General information on prompt methods of analysis is available in books on accelerator methods of analysis such as "Introduction to Radioanalytical Physics" by Deconninck [15], "Ion Beams for Materials Analysis" edited by Bird and Williams [4] and "Backscattering Spectrometry" by Chu, Meyer and Nicolet [16]. Useful reviews have been written by Bird, Campbell and Price [17], Deconninck, Demortier and Bodart [18], and Peisach [19].

3.1. Nuclear reaction methods

3.1.1. Particle emission methods

A number of nuclear reactions that involve the measurement of emitted charged particles or neutrons have been studied for the determination of beryllium [20–25].

$^{9}Be(p,\alpha)^{6}Li$ ($Q = 2.126$ MeV),
$^{9}Be(p,d)^{8}Be$ ($Q = 0.559$ MeV),
$^{9}Be(d,p)^{10}Be$ ($Q = 4.857$ MeV),
$^{9}Be(d,t)^{8}Be$ ($Q = 4.592$ MeV),
$^{9}Be(d,\alpha)^{7}Li$ ($Q = 7.152$ MeV),
$^{9}Be(^{3}He,p)^{11}B$ ($Q = 10.322$ MeV),
$^{9}Be(\alpha,n)^{12}C$ ($Q = 5.701$ MeV).

The reactions $^{9}Be(d,p)^{10}Be$ and $^{9}Be(\alpha,n)^{12}C$ were both used by McMillan et al. [20] for the nuclear microprobe determination of beryllium diffusion profiles in copper. A compromise between sensitivity and selectivity was reached by using 1.3 MeV deuterons for the first reaction. Beryllium concentrations below 100 ppm could be measured but other light elements caused minor interference, particularly boron and nitrogen. Although the optimum sensitivity for the (α,n) reaction was achieved with incident ^{4}He ions of 2.6 MeV it was three times less sensitive than the (d,p) reaction. However, it can be made essentially specific as the Q value, 5.701 MeV, for the (α,n) reaction on ^{9}Be, is higher than for any other nuclide. Specificity was achieved by employing an energy sensitive neutron detector and setting a neutron energy discrimination level that rejected neutrons from other (α,n) reactions. The two methods produced results that agreed, that fitted theoretically calculated diffusion profiles and that produced diffusion coefficients that obeyed the Arrhenius relationship.

To measure elemental distributions close to the surface of materials, perhaps to a depth of a few micrometers, reactions are often selected that have cross sections containing resonances. Pronko et al. [21] recommended the reaction $^{9}Be(p,\alpha)^{6}Li$ for the high resolution determination of beryllium distributions near surfaces but favoured the reaction $^{9}Be(p,d)^{8}Be$ for the determination of moderately deep profiles, to ca. 1 μm, in nickel and copper. They applied the reactions to study the influence of irradiation on the segregation of beryllium in the surface of a nickel – 0.7% beryllium alloy and a copper – 7% beryllium alloy when treated at high temperature. Analysis comprised irradiation with 300 keV protons and observation of the emitted deuterons and alpha particles, at 150°, with or without a 2.5 μm mylar foil to remove backscattered protons, the former usually being favoured. For the nickel alloy, nickel ion bombardment, to a dose of 26 dpa, at 625°C, caused significant beryllium segregation, induced by point defect flows to the surface. The segregation was readily observed by both reactions.

An extensive range of nuclear reactions was used by Reichle, Behrisch and Roth [22], as well as scattering, to examine beryllium coated carbon tiles from the Joint European Torus, JET, fusion experiment. The objective was to study changes that occurred during their use including beryllium redistribution, and the formation of beryllium carbide and oxide. The reactions studied for the depth profiling of beryllium or determining its surface loading included $^{9}Be(p,d)^{8}Be$, $^{9}Be(p,\alpha)^{6}Li$, $^{9}Be(d,p)^{10}Be$, $^{9}Be(d,t)^{8}Be$, $^{9}Be(d,\alpha)^{7}Li$ and $^{9}Be(^{3}He,p)^{11}B$. Good depth distributions were obtained by irradiating with 0.35 MeV protons and observing the emitted deuterons from the reaction $^{9}Be(p,d)^{8}Be$, or alpha particles from the reaction $^{9}Be(p,\alpha)^{6}Li$. Irradiation with 0.9 MeV deuterons and observation of either the α_0 or α_1 particle groups emitted by the reaction $^{9}Be(d,\alpha)^{7}Li$ also allowed the determination of the depth distribution of beryllium. The thickness of the beryllium layer could be determined by observation of the protons emitted by the reaction $^{9}Be(d,p)^{10}Be$ under identical irradiation conditions. Finally, beryllium surface loadings could be determined by irradiation with 2.5 MeV $^{3}He^{+}$ ions and detection of the protons from the reaction $^{9}Be(^{3}He,p)^{11}B$. Further information on beryllium, carbon and oxygen distributions could be obtained principally from scattering using 1.3 MeV protons and 2.6 MeV $^{4}He^{+}$ ions. Simpson et al. [23,24] have also used irradiation with $^{3}He^{+}$ ions, 4 MeV initially and ca. 2.5 MeV at the target, to measure beryllium and deuterium distributions in graphite limiter tiles. They employed an external beam method and glove box handling techniques to avoid the beryllium toxicity hazard.

Hubler, Comas and Plew [25] have measured profiles of ion-implanted beryllium in gallium arsenide

using the reaction $^{9}Be(p,\alpha)^{6}Li$ and utilising the high energy resolving power of a magnetic spectrometer to detect the emitted alpha particles. The objective of the work was to confirm that unusual beryllium distributions observed, for high fluence implantations, using secondary ion mass spectrometry, SIMS, were real rather than an analysis artefact. Profiles measured by the two methods agreed well. The nuclear reaction method was superior for measurements very near the surfaces, < 100 nm, but was restricted in sensitivity to ca. 0.1 at.% and tended to be prohibitively slow.

Prompt nuclear reactions induced by heavy ions have some potential for the determinaton of beryllium. L'Ecuyer et al. [26] demonstrated the wide range of particles emitted when a beryllium target was bombarded with 6.5 MeV ^{6}Li ions.

3.1.2. Gamma emission methods

Many ion interactions with nuclides lead to prompt gamma-ray emission, notably radiative capture, inelastic scattering and so-called rearrangement collisions [18]. Collectively particle induced gamma-ray emission methods are referred to as PIGME or PIGE methods. Generally they are most sensitive for light element analysis and have been catalogued extensively [18,27–34]. A compact, graphical summary of many detection limits has been published recently [35] for proton, triton, alpha particle and ^{35}Cl ion interactions.

The reaction $^{9}Be(\alpha,n\gamma)^{12}C$ has the highest sensitivity for the determination of beryllium by PIGE, ca. 1 ppm (weight) [27,29]. In a systematic study of absolute thick target yields of prompt gamma-rays for light elements following bombardment with 2.4 MeV $^{4}He^{+}$ ions, Lappalainen et al. [29] used the 4439 keV gamma-ray to measure beryllium in volcanic rock. The measured concentration, 8.3 ppm (weight), was readily observed and was in reasonable agreement with expectation. The superiority of ^{4}He ion bombardment over proton bombardment for beryllium determination by PIGE, a factor of 100, was emphasised, and largely based on an earlier systematic study by the same authors [30].

Beryllium has been determined for many years [36,37] by the reaction $^{9}Be(\alpha,n\gamma)^{12}C$ using isotopic sources of alpha particles. Recently Chyong and coworkers [38] described a method, employing irradiation with ^{210}Po (3×10^{8} Bq) and neutron/gamma coincidence counting, to measure beryllium with a sensitivity of 0.1 μg, adequate for air monitoring.

Proton irradiation of beryllium leads to gamma-ray emission by two principal reactions, namely, $^{9}Be(p,\gamma)^{10}B$ and $^{9}Be(p,\alpha\gamma)^{6}Li$ [18,30]. Anttila and coworkers [30] demonstrated that gamma-rays from the reaction $^{9}Be(p,\gamma)^{10}B$ predominate at incident proton energies of 1.0 and 1.7 MeV, but at 2.4 MeV the 3562 keV gamma-ray, from the reaction $^{9}Be(p,\alpha\gamma)^{6}Li$ becomes prominent. Gihwala and Peisach [28] claim that beryllium can be determined, under interference free conditions, at 500 $\mu g\,g^{-1}$, by irradiating with 4.5 MeV protons. Even so, proton based PIGE is not a method widely recommended for the measurement of beryllium. Lappalainen et al. [29] prefer methods based on alpha irradiation. Deconninck, Demortier and Bodart [18] suggested that PIGE methods for beryllium were rarely applied because of low sensitivity and observation of emitted particles from nuclear reactions was often preferred.

3.2. Scattering methods

3.2.1. High energy scattering

The use of high energy scattering methods for the measurement of light elements is often limited by their relatively low scattering cross-sections compared to higher atomic number elements [16]. However, for materials containing mainly light elements this limitation is less constraining and their light element contents, including beryllium, have been measured [22,39,40].

The toxicity of beryllium is well known and its concentration in air is restricted to ca. 1 $\mu g\,m^{-3}$ or less. Hudson and co-workers [39,40] have described the development and application of a proton scattering method to measure beryllium collected from air by a streak sampler. Initially they established that the elastic scattering cross section for protons with energies between 13.5 and 16.0 MeV was nonresonant. For beryllium on a 1 $\mu g\,cm^{-2}$ Nucleopore backing a detection limit equivalent to 50 $ng\,m^{-3}$ of air was attained [39]. They subsequently reported the application of the method to samples taken in a factory manufacturing alloys containing beryllium [40]. Beryllium concentrations as high as 3.5 $\mu g\,m^{-3}$ were detected, prior to improvements in the air exhaust system. Results for samples taken by an impact cascader indicated that beryllium and copper only appear in large particles readily removable by simple face masks.

In an earlier section the use of scattering, by Reichle et al. [22], was briefly mentioned, for the measurement of beryllium, carbon and oxygen profiles at the surface of beryllium coated tiles from the JET fusion experiment. Enhanced elastic backscattering of 1.3 MeV protons provided an almost direct measure of the depth profiles for beryllium and carbon. Although the surface peak for beryllium sat on the carbon scattering plateau these could be readily resolved mathematically to produce depth profiles. To obtain information on the distribution of oxygen, the oxygen elastic scattering peak needed to be resolved from the emitted deuteron peak, from the reaction $^{9}Be(p,d)^{8}Be$, as they overlapped. While Rutherford backscattering with 2.6

MeV $^4He^+$ ions appeared attractive it proved to be susceptible to large systematic errors.

3.2.2. Elastic recoil analysis

In principle, elastic recoil analysis, ERA, is a method with good potential for the determination of beryllium. L'Ecuyer and coworkers [26] drew attention to the possibility of determining beryllium and other light elements by ERA using 30 MeV ^{35}Cl ions. Gujrathi et al. [41] indicate that, using 30 MeV ^{35}Cl ions, and time-of-flight detection, ^9Be should be detectable in a silicon matrix at a concentration of 5×10^{14} atoms cm^{-2} but a value at least ten times greater is more realistic.

In practice ERA appears to have been applied to a vanishingly small degree for the determination of beryllium. This perhaps reflects some of the difficulties associated with the technique which include the need for energetic heavy ion beams, the critical alignment of the glancing angle target geometry, ion beam induced target damage and the influence of surface roughness.

3.2.3. Low energy scattering

Low energy ion scattering, LEIS, provides information on the composition of the outermost surface layer of a solid, through the scattering of ions normally of < 10 keV. The technique has been applied to examine beryllium at the surface of metals [43,44].

Creemers, Van Hove and Neyens [43] used LEIS to study the segregation of beryllium and tin in alloys with copper. From examination of beryllium, beryllium–copper alloy and copper, using LEIS with 600 eV He^+ ions, it was concluded that surface oxidation causes segregation of beryllium to the surface of the alloy. The surface was found to be completely covered with oxidised beryllium atoms whereas the bulk concentration was only 12.5 at.% beryllium.

Difficulties can be encountered in quantifying surface coverage in LEIS. When studying the scattered He^+ ion yield from beryllium adsorbed on tungsten it was found to be nonlinear by Niehus and Bauer [44]. While the substrate signal decreased monotonically with coverage it was nonlinear. The beryllium signal reached a maximum at a coverage of 0.6 monolayers and then decreased, probably because of structural rearrangement of the surface.

4. Accelerator mass spectrometry

4.1. High energy mass spectrometry

The long-lived, cosmogenic beryllium isotope, ^{10}Be, has recently become of considerable interest as a natural, geophysical tracer for chemical and physical processes in the atmosphere, oceans and the earth's crust [45,46]. The half-life of ^{10}Be, 1.6×10^6 years, is so long and its specific activity so low, that its determination by radioactive counting is inadequately sensitive [45]. The advent of accelerator mass spectrometry, which measures the total number of ^{10}Be atoms rather than the small proportion undergoing radioactive decay, allows the measurement of small numbers of ^{10}Be atoms with much greater sensitivity, ca. 10^5 atoms [45], and with high isotopic and isobaric discrimination, ca. 10^{15}. The high energy mass analysis is frequently based on the use of a tandem accelerator.

The state of development of accelerator or high energy mass spectrometry is well illustrated in recent reviews by Elmore and Phillips [45], and by Kutschera [46]. Although accelerator mass spectrometry was initially employed in 1939 by Alvarez and Cornog [47] to measure ^3He abundances in natural helium, its use for detecting long-lived nuclides was simultaneously suggested in 1977 by Muller [48] and Purser et al. [49]. By 1978 a report appeared on the measurement of ^{10}Be at Grenoble [50]. Since that time this cosmogenic nuclide has been measured widely [45,46], and a number of specific applications will be detailed later, after a broad description of its measurement.

Accelerator mass spectrometry systems essentially comprise four parts [45].

1. Negative ion injector.
2. Tandem accelerator.
3. Positive ion analyser.
4. Detector system.

Because discrimination against isobaric interference from ^{10}B is the major objective of accelerator mass spectrometric measurement of ^{10}Be, chemical separation from boron is an important aspect of the preparation of a BeO target for the ion injector system. Negative ions, $^{10}Be^{16}O^-$ are formed by sputtering a BeO target typically with 20 keV Cs ions. Interfering isobaric negative ions also formed are $^{10}B^{16}O^-$ and $^9BeO^{17-}$. These are extracted, analysed magnetically, and possibly electrostatically, and preaccelerated for injection into the tandem accelerator.

After acceleration, to perhaps 10 MV, at the central terminal of the tandem accelerator the negative ions undergo electron stripping by passage through a thin foil or gas. Most molecular ions dissociate. The resulting Be ions of high positive charge state, +3 or, perhaps, +4, are then further accelerated before transfer to the positive ion analysis system.

In the positive ion analysis system any surviving molecular ions with positive charge states can be discriminated against by mass/charge analysis backed up by electrostatic analysis and, possibly, velocity selection. This ensures the removal of particles with a different mass but the correct mass–energy product. The system may incorporate beam monitors for the measurement of intense beams such as ^9Be.

The detection system for ^{10}Be ions often comprises a foil to remove ^{10}B ions, and a dE/dx and total energy detector to identify ^{10}Be ions. Time of flight analysers and gas filled magnets may also be used to enhance ion identification.

Lanford and coworkers at Yale [51] have applied accelerator mass spectrometry to determine the growth rate of a manganese nodule from the Rio Grande Ridge in the South Atlantic Ocean. The amount of ^{10}Be in the nodule varied with depth from about 3×10^{10} atom g^{-1} near the surface of the nodule to a tenth of that value 25 mm from its surface. The growth rate was calculated to be 4.5 mm every million years, confirming the very slow growth of manganese nodules.

The precipitation of ^{10}Be from the atmosphere has been studied by Imamura et al. [52] for rain water collected in Tokyo. The measured rate was ca. 0.1 atom $cm^{-2} s^{-1}$ which corresponds to a global rate of ca. 0.3 atom $cm^{-2} s^{-1}$ which is in reasonable agreement with other workers. Comparison with ^{7}Be and ^{137}Cs indicated that ^{10}Be precipitation correlates with the former but no the latter.

The relationship between solar activity and climate is a fundamental but controversial subject [53]. The correlation between ^{10}Be production and fractional changes in stable isotope ratios for hydrogen and oxygen caused by changes in surface temperature could help to address this question. Cosmogenic ^{10}Be is rapidly deposited on the Earth's surface, in ca. one year. Consequently changes in its production rate are reflected in its deposition rate. Comparison of ^{10}Be deposited in polar ice cores with $^{14}C:^{12}C$ ratios in tree rings shows good correlation. Consequently, ^{10}Be deposition is a good indicator of solar activity. However, no correlation of ^{10}Be deposition was found with changes in hydrogen isotope ratios, and, consequently, no relationship found between solar activity and climate.

Considerable numbers of applications of accelerator mass spectrometry involving the measurement of ^{10}Be are now published annually. Access to the literature can be gained through the reviews mentioned earlier [45,46] and to the proceedings of specialist conferences on accelerator mass spectrometry [54,55].

4.2. Particle induced desorption mass spectrometry

Ions and neutral species can be desorbed from targets by bombarding with heavy energetic ions [56]. The yield increases with the square of the stopping power of the target, hence the atomic number of the projectile to the fourth power [57]. Suitable ions, with energies between 0.5 and 1 MeV per mass unit can be obtained from accelerators or conveniently from ^{252}Cf isotope sources as fission fragments. Schweikert [56] has described the application of a ^{252}Cf source and a time-of-flight mass spectrometer for particle or plasma induced desorption mass spectrometric analysis of several NBS glass standards. The highly sensitive measurement of lithium isotopes was illustrated with simultaneous detection of beryllium. While this technique has been applied to the determination of large involatile biomolecules, it clearly has other possible applications.

5. Accelerator methods in perspective

The value of accelerator methods of analysis must be judged against other modern techniques of analysis, not only in terms of technical performance but also in terms of cost and convenience. Recently Maenhaut [58] extensively compared particle induced X-ray emission methods with other techniques on this basis. While beryllium is not practically determinable by X-ray based methods, Maenhaut's review gives a valuable and extensive picture of the comparative value of modern methods of analysis. Generally accelerator methods are expensive when judged on the basis of instrument cost, although unit analysis cost can be low and competitive. Unless accelerator methods have technical advantages their selection as the preferred method is in considerable doubt.

The performance of a number of modern methods of analysis is detailed in Table 1.

The determination of the bulk concentration of beryllium in materials can frequently be undertaken with sensitivities of ca. 1 $\mu g g^{-1}$ by atomic absorption and plasma source emission spectroscopy. While these methods are normally used for the analysis of solutions, with the inconvenience inherent in dissolving solid samples and the possible introduction of contamination, their performance essentially matches that of charged particle activation methods. The performance of these techniques is clearly bettered by plasma source mass spectrometry. When the technique is used with laser ablation of solid samples, spatial information is obtainable.

The direct determination of bulk beryllium concentrations in solids can be achieved with extremely high sensitivity by glow discharge mass spectrometry. This method is of great value in the examination of high purity materials such as silicon, however, samples must be conducting or made to be conducting. The sputtering process in the source allows some measure of the variation of the surface composition of conducting samples.

Accelerator methods tend to have advantages when the distribution of light elements, such as beryllium, need to be measured in materials. The ease of quantification of the results when using accelerator methods gives them some advantage compared with their princi-

Table 1
Comparative data for modern analysis methods for the determination of beryllium

Method	Sensitivity	Conditions
1. Atomic absorption		
(a) Flame	2×10^{-9} g ml^{-1}	Solution
(b) Graphite furnace	5×10^{-13} g	Solution
2. Inductively coupled plasma emission spectroscopy	2×10^{-10} g ml^{-1} 2×10^{-7} g g^{-1}	Solution Silicate rock
3. Inductively coupled plasma mass spectrometry		
(a) "Plasma quad"	5×10^{-11} g ml^{-1}	Solution
(b) "Plasma quad" with electrothermal vaporisation	10^{-13} g ml^{-1}	Solution
(c) "Plasma quad" with laser ablation	ca. 10^{-8} g g^{-1}	Silicon nitride
(d) "Plasma trace" (high resolution MS)	10^{-13} g ml^{-1}	Solution
4. Atomic fluorescence; hollow cathode excitation with plasma source	10^{-9} g ml^{-1}	Solution
5. Glow discharge mass spectroscopy	10^{-8}–10^{-10} g g^{-1}	Solids (UO_2, Si, In)
6. Auger electron spectroscopy	0.1–1.0 at.%	Solids (surface)
7. X-ray photoelectron spectroscopy	0.1–1.0 at.%	Solids (surface)
8. Secondary ion mass spectrometry	10^{14}–10^{15} atom cm^{-3} (10^{-8}–10^{-9} g g^{-1})	Solids

pal competitor, secondary ion mass spectrometry. The latter tends to be more convenient, faster and more sensitive, although, its quantification is always problematic. The introduction of secondary neutral mass spectrometry will probably overcome this difficulty. For measurements at surfaces Auger electron spectroscopy or X-ray photoelectron spectroscopy will frequently be preferred to low energy ion scattering, or may be used in a complementary manner.

At present the sensitivity and selectivity of accelerator mass spectrometry is unrivalled for the determination of ^{10}Be. However, there are expectations that methods based on resonance ionisation with laser photons will ultimately achieve a sensitivity and selectivity that surpass accelerator mass spectrometry [57].

Acknowledgements

The data on sensitivity was obtained through personal experience (AAS, ICP/OES) and consultation with colleagues and Fisons Instruments (Dr. K. Robinson). The consultations were with Dr. H.E. Bishop (SIMS, AES, XPS and SNMS), R.M. Brown (ICP/MS), Dr. A.W. McMahon (Resonance Ionisation), and Dr. K. Robinson (ICP/MS and GDMS). Their help and advice is gratefully acknowledged.

References

[1] J. Hoste and C. Vandecasteele, J. Radioanal. Nucl. Chem. 110 (1987) 427.
[2] C. Englemann, At. Energy Rev. 19 (1981) 107.
[3] C. Vandecasteele, Activation Analysis with Charged Particles (Ellis Horwood Ltd., Chichester, UK, 1988).
[4] J.R. Bird and J.S. Williams, eds., Ion Beams for Materials Analysis (Academic Press Australia, Marrickville, Australia, 1989).
[5] B. Borderie, J.N. Barrandon and J.L. Debrun, J. Radioanal. Chem. 37 (1977) 297.
[6] J.L. Debrun, D.C. Riddle and E.A. Schweikert, Anal. Chem. 44 (1972) 1386.
[7] C. Englemann, J. Radioanal. Chem. 7 (1971) 89.
[8] B.D. Lass, J.F. Ojo and E.A. Schweikert, J. Radioanal. Chem. 60 (1980) 255.
[9] B.D. Lass, N.G. Roché, A.O. Sanni, E.A. Schweikert and J.E. Ojo, J. Radioanal. Chem. 70 (1982) 251.
[10] M. Colin, C. Friedli and P. Lerch, J. Radioanal. Nucl. Chem. Lett. 119 (1987) 477.
[11] C. Friedli, M. Colin and P. Lerch, J. Radioanal. Nucl. Chem. Art. 120, (1988) 253.
[12] B.D. Lass, C. Friedli and E.A. Schweikert, J. Radioanal. Chem. 57 (1980) 481.
[13] C. Friedli, M.E. Colin and P. Lerch, J. Radioanal. Nucl. Chem. Art. 122 (1988) 115.
[14] C. Friedli, Th. Diaco and P. Lerch, J. Radioanal. Nucl. Chem. Art. 112 (1987) 403.
[15] G. Deconninck, Introduction to Radioanalytical Physics (Elsevier, Amsterdam, 1978).
[16] W.K. Chu, J.W. Meyer and M.A. Nicolet, Backscattering Spectrometry (Academic Press, New York, 1978).
[17] J.R. Bird, B.L. Campbell and P.B. Price, At. Energy Rev. 12 (1974) 275.
[18] G. Deconninck, G. Demortier and F. Bodart, At. Energy Rev., 19 (1981) 151.
[19] M. Peisach, J. Radioanal. Chem. 61 (1981) 24.
[20] J.W. McMillan, P.M. Hirst, F.C.W. Pummery, J. Huddleston and T.B. Pierce, Nucl. Instr. and Meth. 149 (1978) 83.
[21] P.P. Pronko, P.R. Okamoto and H. Wiedensich, Nucl. Instr. and Meth. 149 (1978) 77.
[22] R. Reichle, R. Behrisch and J. Roth, Nucl. Instr. and Meth. B50 (1990) 68.
[23] J.C.B. Simpson, J.P. Coad and J. Partridge, Nucl. Instr. and Meth., to be published.

[24] A.T. Peacock, J.P. Coad, F. Lama, R. Behrisch, A.P. Martinelli, B.E. Mills, M. Pick, J. Partridge, J.C.B. Simpson and Y.K. Zhu, J. Nucl. Mater. 176/177 (1990) 326.
[25] G.K. Hubler, J. Comas and L. Plew, Nucl. Instr. and Meth. 149 (1978) 635.
[26] J. L'Ecuyer, C. Brassard, C. Cardinal and B. Terreault, Nucl. Instr. and Meth. 149 (1978) 271.
[27] B. Borderie and J.N. Barrandon, Nucl. Instr. and Meth. 156 (1978) 483.
[28] D. Gihwala and M. Peisach, J. Radioanal. Chem. 70 (1982) 287.
[29] R. Lappalainen, A. Antilla and J. Räisänen, Nucl. Instr. and Meth. 212 (1983) 441.
[30] A. Antilla, R. Hänninen and J. Räisänen, J. Radioanal. Chem. 62 (1981) 293.
[31] J.L. Debrun, J.N. Barrandon and P. Benaben, Anal. Chem. 48 (1976) 167.
[32] J.N. Barrandon, P. Benaben and J.L. Debrun, Anal. Chim. Acta. 83 (1976) 157.
[33] I.S. Giles and M. Peisach, J. Radioanal. Chem. 50 (1979) 307.
[34] B. Borderie, J.N. Barrandon, B. Delaunay and M. Basutcu, Nucl. Instr. and Meth. 163 (1979) 441.
[35] J.R. Bird, in: Ion Beams for Materials Analysis, eds. J.R. Bird and J.S. Williams (Academic Press Australia, Marrickville, Australia, 1989) p. 189.
[36] R. Gold, Nucleonics 15 (1957) 114.
[37] J.M. McKibben, Nucl. Appl. Technol. 4 (1968) 260.
[38] Fam Ngok Chyong, G.M. Ter-Akop'yan and A.P. Kabachenko, At. Ehnergy 61 (1986) 129.
[39] G.M. Hudson, H.C. Kaufmann, J.W. Nelson and W.J. Courtney, Nucl. Instr. and Meth. 149 (1978) 307.
[40] G.M. Hudson, H.C. Kaufmann, J.W. Nelson and M.A. Bonacci, Nucl. Instr. and Meth. 168 (1980) 259.
[41] S.C. Gujrathi, P. Aubry, L. Lemay and J.-P. Martin, Can. J. Phys. 65 (1987) 950.
[42] J.R. Bird, R.A. Brown, D.D. Cohen and J.S. Williams, in: Ion Beams for Materials Analysis, eds. J.R. Bird and J.S. Williams (Academic Press Australia, Marrickville, Australia, 1989) table 14.11.
[43] C. Creemers, H. Van Hove and A. Neyens, Appl. Surf. Sci. 7 (1981) 402.
[44] H. Niehus and E. Bauer, Surf. Sci. 47 (1975) 222.
[45] D. Elmore and F.M. Phillips, Science 236 (1987) 543.
[46] W. Kutschera, Nucl. Instr. and Meth. B50 (1990) 252.
[47] L.W. Alvarez and R. Cornog, Phys. Mod. Rev. 56 (1939) 379 and 613.
[48] R.A. Muller, Science 196 (1977) 1487.
[49] K.H. Purser, R.B. Liebert, A.E. Litherland, R.P. Beukus, H.E. Gove, C.L. Bennett, H.R. Clover and W.E. Sondheim, Rev. Phys. Appl. 12 (1977) 1487.
[50] G.M. Raisbeck, F. Yiou, M. Fruneau and J.M. Loisaux, Science 202 (1978) 215.
[51] W.A. Lanford, P.D. Parker, K. Bauer, K.K. Turekian, J.K. Cochran and S. Krishnaswami, Nucl. Instr. and Meth. 168 (1980) 505.
[52] M. Imamura, H. Nagai, M. Honda, K. Kobayashi, K. Yoshida, H. Yoshikawa and T. Kobayashi, J. Radioanal. and Nucl. Chem. Art. 138 (1990) 261.
[53] G.M. Raisbeck, F. Yiou, J. Jouzel and J.R. Petit, Philos. Trans. R. Soc. London A330 (1990) 463.
[54] W. Woelfi, H.A. Polach and H.H. Anderson, eds., Proc. 3rd Int. Conf. on Accelerator Mass Spectrometry, Zurich, 1984, Nucl. Instr. and Meth. B5 (1984) 91–448.
[55] H.E. Gove, A.E. Litherland and D. Elmore, eds., Proc. 4th Int. Symp on Accelerator Mass Spectrometry, Niagra-on-the-Lake, 1987, Nucl. Instr. and Meth. B29 (1987) 1–455.
[56] R.D. Macfarlane and D.F. Torgerson, Science 191 (1976) 920.
[57] E.A. Schweikert, Analyst 114 (1989) 269.
[58] W. Maenhaut, Nucl. Instr. and Meth. B49 (1990) 518.

Nuclear Instruments and Methods in Physics Research B66 (1992) 126–138
North-Holland

Nuclear Instruments & Methods in Physics Research
Section B

Analysis of boron by charged particle bombardment

N. Moncoffre

Institut de Physique Nucléaire de Lyon, IN2P3-CNRS et Université Claude Bernard 43, Bd du 11 Novembre 1918, F-69622 Villeurbanne Cedex, France

The determination of boron concentration in thin films, semiconductors or other materials requires techniques providing good depth resolution and high sensitivities. For this purpose nuclear analysis techniques can be powerful tools and this paper presents a review of the nuclear reactions essentially with charged particles (p, α, d) that have been used (including charge particle activation analysis). Irradiation with neutrons is also considered, in particular with the very sensitive $^{10}B(n,\alpha)^{7}Li$ reaction due to the strong absorption of neutrons by boron. With the aim to search for reactions producing better depth resolutions, elastic recoil detection based techniques (ERDA, ERCS) on boron are discussed. The performances of these nuclear reactions are compared with other methods, in particular with SIMS, AES, XPS and, using recent developments, the electronic microprobe.

1. Introduction

In the field of semiconductors boron is a very extensively used dopant and secondary ion mass spectrometry (SIMS) is a common technique for profiling such a light ion impurity. However boron analysis using nuclear reaction techniques can be of great interest and it is our purpose in this paper to emphasize their analytical applications. For instance, as mentioned by Scanlon et al. [1] the production of very shallow junctions makes it more and more difficult to determine the narrow implantation profile of boron. This puts forward the necessity to use analysis techniques providing excellent surface depth resolutions often at the expense of sensitivity. In particular, with SIMS it is difficult to establish the initial sputtering rate and the range of the sputter ions.

Of course boron implantation concerns not only semiconductors but also other materials like metals in which it can significantly improve surface properties. A typical example is given by Henriksen et al. [2] of the boron implantation in single crystal or polycrystalline copper samples and of the boron implantation profiles using the ^{11}B (p,α) nuclear reaction. So in all these cases where the accurate knowledge of boron concentration profiles is required, the analysis by nuclear reactions can offer both the quantitative determination and the lateral and depth profiling.

In this paper, we will try to review surface analysis techniques using mainly charged particle bombardment, which can be used for analytical applications either on ^{10}B or on ^{11}B and the literature on this subject is important. The abundance of the two isotopes of boron is respectively 19.8 and 80.2% and there is inherent advantage in using methods based on the more abundant isotope.

The analysis by nuclear reaction spectroscopy (NRS) can be made either by detecting charged particles or prompt γ-rays and more rarely neutrons. We will distinguish the reactions providing good depth resolutions or high sensitivities, the choice of the appropriate reaction depending on the research aim. We will underline the possibility of investigating lattice localization with the help of channeling techniques as well as of using microprobe facilities to determine boron lateral distribution. The way chosen to classify these nuclear reactions depends on the nature of the incident particle.

Charged particle activation analysis remains however very interesting for the determination of traces despite the great number of interferring reactions with other light elements, in particular oxygen and carbon. This technique, which allows to obtain excellent sensitivities, will be also discussed.

More recent developments of charged particle detection allowing light element profiling can significantly improve depth resolutions. Such is the case for the elastic recoil detection analysis (ERDA) applied, for instance, by Gossett [3] to identify C, O, B and N elements or for the elastic recoil coincidence spectroscopy (ERCS) [4,5]. Both techniques will be considered in this review.

We will also focus on the $^{10}B(n,\alpha)^{7}Li$ reaction although it concerns irradiations with neutrons since it combines both an excellent sensitivity and depth resolution and it has been extensively applied in many different fields. Finally the performance of these nuclear reactions will be compared with other methods,

0168-583X/92/$05.00 © 1992 – Elsevier Science Publishers B.V. All rights reserved

which can provide complementary information such as chemical information. These techniques are mainly SIMS, X-ray photoelectron spectroscopy (XPS), Auger electron spectroscopy (AES), glow discharge optical spectroscopy (GDOS) and, under more difficult and limiting conditions, the electron microprobe.

2. The $^{10}B(n,\alpha)^{7}Li$ nuclear reaction

Although the incident particle is not a charge particle, this reaction giving rise to α particles has to be mentioned since it has been extensively used in several fields, in particular for medical and biological applications, for its very interesting features. This reaction is based on the very high absorption cross section of thermal neutrons by ^{10}B ($\sigma = 3840$ b) and is thus extremely sensitive. It yields α-particles of 1776.8 and 1472.8 keV for α_0 and α_1 respectively with an α_1/α_0 ratio of 6.7.

This reaction can be used in different ways:

(a) Simply by measuring the attenuation coefficient of the incident neutron flux using a scintillation counting during neutron bombardment from an isotope source (for example Am–Be) [6,7]. The analysis is quick and reproducible, and allows for example to control production of industrial alloys or to determine boron concentration in water samples with rather good sensitivity.

(b) By detecting the prompt γ-rays of 478 keV coming from the first excited state of ^{7}Li in 93.5% of the decays [8]. The detection limits are 10^{-2} to 1 $\mu g\ g^{-1}$ [9]. It is possible to use the influence of the Doppler effect on the γ energy in order to increase the detection sensitivity. In the medical field, the boron neutron capture therapy (BNCT) using the $^{10}B(n,\alpha\gamma)^{7}Li$ reaction can be mentioned. This technique is based on the biological efficiency of α-particles and implies the boron concentration knowledge in tissues at very low level. Via the detection of the prompt 478 keV γ-rays, the technique is however not sensitive to detect ng amounts in μl samples [10].

(c) By detecting during the neutron irradiation the emitted α-particles. Photographic emulsions have been used as detectors in the past, but dielectric detectors such as cellulose nitrate films are more convenient [11] and images of the boron distribution at the sample surface can thus be obtained. Further concerning the BNCT technique Fleisher et al. [12] found that cellulose esters could detect charged α-particles in the presence of γ-rays and thermal neutrons and so by track etching lower concentrations could be detected (the lower limit for boron determination in cells is $\simeq 1$ μg B/g).

Using the thermal neutrons from a neutron guide tube (fluxes up to 10^{10} cm^2/s of pure thermal neutrons) of the high flux reactor of the I.L.L. in Grenoble, Fink et al. [13], who examined boron and lithium distributions in glaze of ancient pottery, could measure ^{10}B concentration profiles in depth intervals of μm with depth resolution as good as 5–10 nm and down to concentrations of a few ppm. Also, Behar et al. [14] determined the profiles of ^{10}B implants in silicon using a Si surface barrier diode to detect the 1473 keV α-particles. With this reaction they could, for instance, compare the TRIM calculated profiles with the experimental distributions of 50 keV implanted boron ($R_p \simeq$ 200 nm).

In conclusion, the use of the (n,α) reaction is especially interesting for light elements such as B and Li which have no radioisotope with a convenient period. This reaction is very sensitive as well as allows depth profile determination, but the necessity to use intense neutron beams is however a limiting factor.

3. Charged particle activation analysis of boron (CPAA)

CPAA is a powerful method and a very convenient technique for the determination of light elements like B, C, N and O. It is based on the production of artificial radioactive nuclei, often positron emitters easily detectable by their annihilation radiation. In a general book on CPAA. Vandecasteele [15] gives an overview of the possible nuclear reactions for the determination of boron and of the interference reactions (see table 1). The interference reactions are those producing the same element as the one on which the analysis is based. From this table, it appears that the activation with the various charged particles (p, d, α, ^{3}He) often leads to the production of the pure positron emitters ^{13}N and ^{11}C (of respectively 9.96 and 20.38 min of half-life). The selective detection of these pure β^+ emitters necessitates chemical separations. The risk of interferences, not always overcome, due to the creation of the same element from the stable atoms present (C,N,O,etc.) requires a judicious choice of both the nature and the energy of the incident particles. For instance the interference with nitrogen, when analyzing boron, increases when the proton energy is high [16].

In general, the best selectivity is obtained with the deuterons, which avoid interferences if the energy is lower than 6 MeV. The deuteron induced nuclear reaction $^{10}B(d,n)^{11}C$ is suitable to determine traces of boron. Its maximum cross section amounts to 230 mb at E_d of 2.2 MeV. Michelmann et al. [17] have measured the excitation function of this reaction, together with that of the $^{12}C(d,n)^{13}N$, with high accuracy in order to analyze simultaneously boron and carbon traces, between 0.5 and 6 MeV.

An accurate knowledge of the boron concentration is necessary to control the refining process in Al and Al–Mg alloys used as construction materials in nuclear industry [15]. For that purpose, Mortier et al. [18] have developed an industrial control method using the $^{10}B(d,n)^{11}C$ reaction. This method was developed mainly for the analysis of reference materials to be certified by the community bureau of reference of the Commission of the European Communities. This reaction on ^{10}B is almost always mentioned in recent publications dealing with the determination of boron in metals and semiconductors. This is also the case for the nuclear reactions leading to ^{7}Be which emits 477.6 keV γ-rays. For instance, with the $^{10}B(p,\alpha)^{7}Be$ and $^{10}B(d,\alpha n)^{7}Be$ reactions, the long half-life of ^{7}Be(52.23 d) allows a simple analysis when Li is not present in the target [15,8].

The best sensitivities are generally obtained with the protons [16] and in particular the $^{11}B(p,n)^{11}C$ reaction yields the highest sensitivity but with the drawback of the $^{14}N(p,\alpha)^{11}C$ interference reaction. Pillay et al. [8] show that the $^{10}B(p,n)^{10}C$ reaction can be a sensitive analytical technique: by using the β–γ coincidence detection between the β-particles above 1 MeV and the 717 keV γ-rays from the ^{10}C excited level they could detect boron levels below 100 μg g^{-1} in matrices such as high purity aluminum.

It can be mentioned that Friedly et al. have analyzed boron using the $B(^{18}O,x)^{27}Mg$ reaction with 125 MeV ^{18}O ions! [19]. In addition, one can notice that ^{10}B has been used for hydrogen analysis by CPAA with the $^{1}H(^{10}B,\alpha)^{7}Be$ reaction, allowing to detect 30 to 100 μg of hydrogen per g of titanium for example.

The activation using 3.5 MeV tritons on light elements ($Z \leq 34$) has been studied, in particular by J.N. Barrandon and coworkers, using (t,p), (t,d), (t,2n), (t,α) reactions. It appears that for elements with $Z \leq 16$, the sensitivity can be excellent (10^{-9} to 5×10^{-8} g/g). The penetration depth of 3.5 MeV t being relatively low (~ 30 μm), it is possible to realize localized analysis [20,21].

Table 1
From ref. [15]: Nuclear reactions for the determination of boron. The threshold energy is given in brackets

Nuclear reaction		Interference reaction	
$^{11}B(p,n)^{11}C$	(3.0)	$^{14}N(p,\alpha)^{11}C$	(3.1)
$^{10}B(d,n)^{11}C$	($Q > 0$)	$^{12}C(d,t)^{11}C$	(14.5)
$^{11}B(d,2n)^{11}C$	(5.9)	$^{14}N(d,\alpha n)^{11}C$	(5.8)
$^{10}B(^{3}He,d)^{11}C$	($Q > 0$)	$^{9}Be(^{3}He,n)^{11}C$	($Q > 0$)
$^{11}B(^{3}He,t)^{11}C$	(2.5)	$^{12}C(^{3}He,\alpha)^{11}C$	($Q > 0$)
		$^{14}N(^{3}He,\alpha d)^{11}C$	(10.2)
		$^{16}O(^{3}He,2\alpha)^{11}C$	(6.3)
$^{10}B(\alpha,n)^{13}N$	($Q > 0$)	$^{12}C(\alpha,t)^{13}N$	(23.8)
$^{11}B(\alpha,2n)^{13}N$	(14.2)	$^{14}N(\alpha,\alpha n)^{13}N$	(13.6)
		$^{16}O(\alpha,\alpha t)^{13}N$	(26.7)
		$^{16}O(\alpha,^{7}Li)^{13}N$	(28.2)
		$^{19}F(\alpha,2\alpha 2n)^{13}N$	(34.5)
		$^{19}F(\alpha,^{10}Be)^{13}N$	(19.5)
$^{10}B(p,\alpha)^{7}Be$	($Q > 0$)	$^{7}Li(p,n)^{7}Be$	(1.8)
$^{11}B(p,\alpha n)^{7}Be$	(11.2)	$^{9}Be(p,t)^{7}Be$	(14.9)
		$^{12}C(p,p\alpha n)^{7}Be$	(28.5)
		$^{14}N(p,2\alpha)^{7}Be$	(11.3)
$^{10}B(d,\alpha n)^{7}Be$	(1.3)	$^{6}Li(d,n)^{7}Be$	($Q > 0$)
$^{11}B(d,\alpha 2n)^{7}Be$	(14.8)	$^{7}Li(d,2n)^{7}Be$	(5.0)
		$^{9}Be(d,tn)^{7}Be$	(21.5)
		$^{12}C(d,\alpha p2n)^{7}Be$	(33.3)
		$^{14}N(d,2\alpha n)^{7}Be$	(14.5)

4. Nuclear reactions on boron induced by low energy protons

The analytical applications of nuclear reactions induced by protons of energies ranging from 400 to 1500 keV on light elements have been reviewed by Golicheff et al. [22] and as developed by Ligeon et al. [23], in the case of ^{11}B analysis, the reactions induced by protons have the largest cross sections and the minimum competing interferences with the semiconductor matrices (Ge,Si). Fig. 1 gives a schematic representation of the different possible reactions between protons and ^{11}B at low energies. The ones more interesting and used for analytical applications have been underlined with thicker lines.

Among these reactions the ^{11}B $(p,\gamma)^{12}C$ at 163 keV (fig. 1(1)) is particularly interesting for depth profile analysis due to its narrow resonance ($\Gamma = 5.5$ keV) and, for instance, has been used to determine ^{11}B implanted profiles in silicon by Behar et al. [14]. The emission percentage of the γ-rays is the following: 4.43 MeV (96.5%), 11.68 MeV (96.5%), 16.11 MeV (3.5%). The 4.43 MeV peak is easily identified despite some possible interference reactions. However the low cross section ($\sigma = 0.157$ mb) results in a small peak-to-background ratio.

Pruppers et al. [24] have determined boron concentrations in thin films of hydrogenated amorphous silicon by means of this resonance. They obtained a depth resolution better than 50 nm and could measure concentrations of dopant down to 100 ppm by detecting the 4.43 MeV γ-rays.

The PIGE (proton induced γ-ray emission) technique based on the detection of γ-rays emitted from (p,γ), (p,p′γ) reactions is also very suitable for the analysis of light elements like Li, B, F, Na, Mg and Al [25,26]. Boni et al. [25] have plotted the excitation functions of the $^{10}B(p,\alpha_1\gamma)^{7}Be$ and $^{11}B(p,p_1\gamma)^{11}B$ for

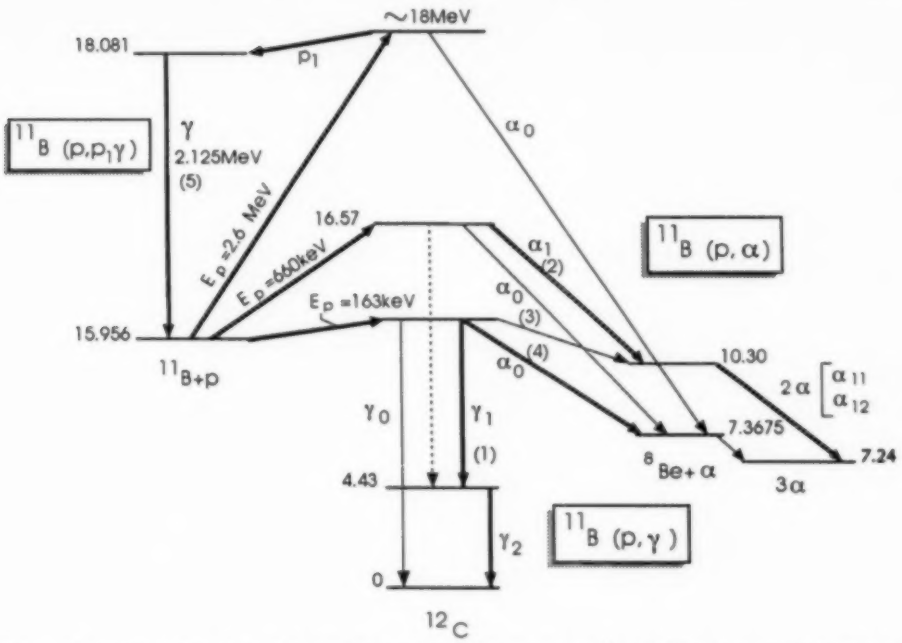

Fig. 1. Schematic representation of possible nuclear reactions with protons on ^{11}B. Thicker lines emphasize the origins of the nuclear reactions that can be used for analytical applications.

respectively, the 429 and 2125 keV γ-rays emitted between 2.6 and 3.8 MeV incident proton energies. The purpose of their work was to find out an energy region where the γ yield was high and constant so as to set up an analytical system for multielemental analysis of samples of unknown thickness and composition. In spite of a higher cross section for the 429 keV γ-rays, the 2125 keV ones are more interesting when Li is present due to identical γ energy emission.

With the $^{11}B(p,\alpha)$ reaction the sensitivity is much

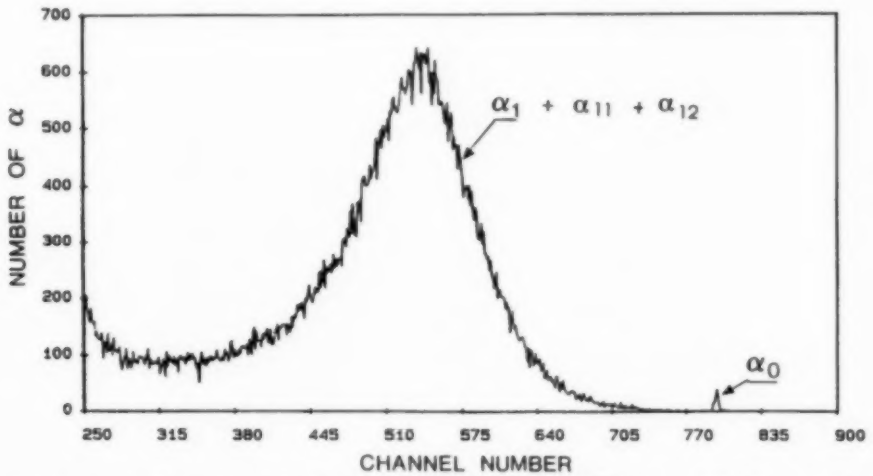

Fig. 2. Energy spectrum of α-particles emitted from the $^{11}B(p,\alpha)2\alpha$ reaction at 660 keV, on a 30 keV boron implanted steel.

better. Several reactions have to be considered. First, let us consider the $^{11}B(p,\alpha)$ at 660 keV. At this energy the resonance is large ($\Gamma = 300$ keV) and so does not provide any depth resolution. However the $^{11}B(p,\alpha)2\alpha$ reaction (fig. 1(2)) can be a powerful method for the detection of trace quantities of boron due to its high cross section ($\sigma = 300$ mb). The α-particles produced belong to several groups: the α_1-particles which have a 3.63 MeV energy at 172° and the α_{11}- and α_{12}-particles with energies varying from 4.48 MeV to 6.2 keV. In fact the 3α are detected together. A typical spectrum of such α particle detection from this reaction used to analyze a boron implanted steel is displayed in fig. 2 (from ref. [27]).

The applicability of this reaction at this energy has been studied by Lappalainen et al. [28] who were able to go down to detection limit values of 0.1 wt. ppm for B analysis in biological samples. Compared with other nuclear reactions, the (p,α) is interference free and allows quick measurements with very good sensitivities (at the ppm level or even below).

Because of its high sensitivity, this reaction has been used by Vickridge et al. [29] with a nuclear microprobe facility (beam spots of 30–80 μm diameter) to obtain boron distributions in coals. These authors used protons in the range 700–850 keV. An example of the maps they obtained is displayed in fig. 3.

It can be noticed that this resonance at 660 keV was also used by Henriksen et al. for lattice location analysis of implanted boron atoms in single crystal samples of copper [2].

The $^{11}B(p,\alpha_0)^8Be$ reaction at 660 keV (fig. 1(3)) has a very low sensitivity compared with the $^{11}B(\alpha_1)$ and is not interesting.

An appropriate reaction for depth profiling is the $^{11}B(p,\alpha)$ at E_p of 163 keV due to the narrow energy width of the resonance ($\Gamma = 6$ keV) (fig. 1(4)). This reaction has been chosen by Henriksen et al. [2] to profile boron in copper up to depths of 500 nm. Other authors [30–32] have measured implanted boron in silicon wafers with this resonance by detecting only the α_0-particles from the $^{11}B(p,\alpha_0)^8Be$ reaction. In fact the ^8Be is an unstable nucleus which decays with a half-life of about 10^{-16} s to two α-particles and Scanlon et al. [30] shows that the α_0 peak detection (5.5 MeV) is convenient since it is well isolated from the other α. By tilting the target they could significantly improve the resolution down to 10nm. Li Xiting et al. [33] have used a more energetic resonance at 2.62 MeV incident proton energy of the $^{11}B(p,\alpha_0)^8Be$ reaction. They obtained a surface depth resolution of about 50 nm and could profile boron on 4 μm depths in silicon (fig. 1(5)).

It may be added that ^{11}B is used to analyze hydrogen by the inverse nuclear reaction $^1H(^{11}B,\alpha)^8Be$ at 1793 keV.

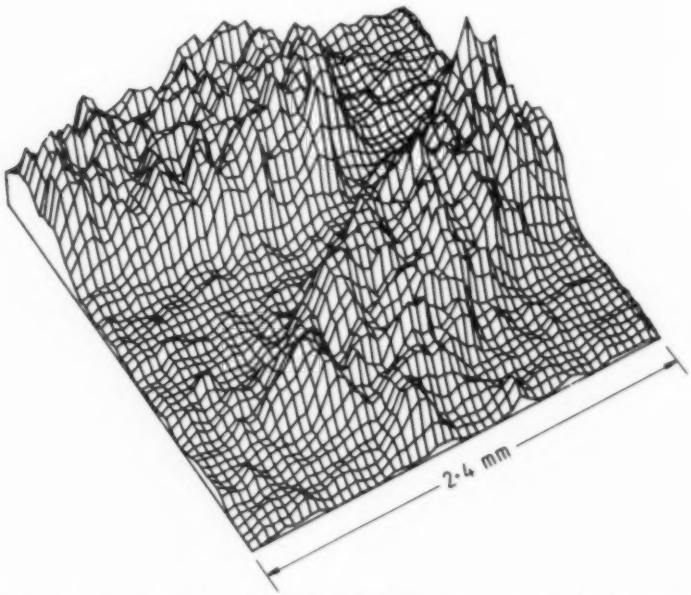

Fig. 3. From ref. [29]: Boron distribution in a polished section of Waikato coal measured by the nuclear microprobe using the 660 keV broad resonance of the $^{11}B(p,\alpha)2\alpha$ reaction (beam spot ≃ 30–80 μm diameter).

5. Deuteron-induced nuclear reactions

Reactions with deuterons are often very exoergic and consequently the emitted particles can be easily measured. In the case of (d,p) reactions, a stripping process occurs due to the low binding energy between the p and the n inside the deuterium nucleus and the deuterons do not give rise to resonant reactions (there is no formation of a compound nucleus). In general, due to the low stopping powers of protons, the depth resolutions resulting from these reactions are poor. In addition, the necessity to use sometimes an absorber to stop backscattered deuterons also contributes to diminish the depth resolutions.

The advantage of the reactions with deuterons is their good sensitivity especially with the (d,p) reactions. The most likely reactions yielding prompt charge particles when bombarding with deuterons of a few MeV are the (d,p) and (d,α) reactions (table 2 from ref. [34]).

Olivier et al. [35] who analyzed boron by prompt proton spectrometry showed that with 2.7 MeV deuterons the $^{10}B(p_0)$ reaction displayed an almost constant cross section and this reaction was chosen for analytical purpose since it allowed to obtain the least interference. Concentrations down to 0.2% could be determined. Coetzee et al. [34] have used the $^{10}B(d,p)^{11}B$ and $^{11}B(d,\alpha)^{9}Be$ reactions using 4 MeV incident beams and a coincidence setup detecting the recoil nuclei (see section 8 on recoil nuclei). They could thus establish the isotopic $^{10}B/^{11}B$ ratio in boric oxide samples. In order to facilitate the escape of the product nucleus without excessive loss of energy, the targets were very thin. This technique, which allows an excellent specificity with almost no interference, was able to give a relative precision in the determination of isotopic concentration of 2.5%.

Table 2
From ref. [34]: Some nuclear reactions induced during deuteron irradiation of boron.

Reaction	Q value [MeV]
$^{10}B(d,p)^{11}B$	9.2314
$^{10}B(d,\alpha)2\alpha$	17.8192
$^{11}B(d,p)^{12}B$	1.14444
$^{11}B(d,\alpha)^{9}Be$	8.0283
$^{11}B(d,\alpha n)2\alpha$	6.3632

6. α-particle-induced nuclear reactions

The main possible analytical applications of the α induced nuclear reactions on ^{10}B and ^{11}B are presented in figs. 4 and 5 respectively and are reviewed here successively.

Among these reactions, those inducing γ-rays allow high accuracy analysis. In fact the α-particles are the most appropriate to produce a limited number of reactions giving high energy γ-radiation and consequently to reduce the Compton background. These reactions have been in particular investigated by Borderie et al. [36,37] to analyze light elements like Li, F, O, Na and B in different materials (geological materials, pottery, rocks, boron carbides, etc.). They used 3.5 MeV α-par-

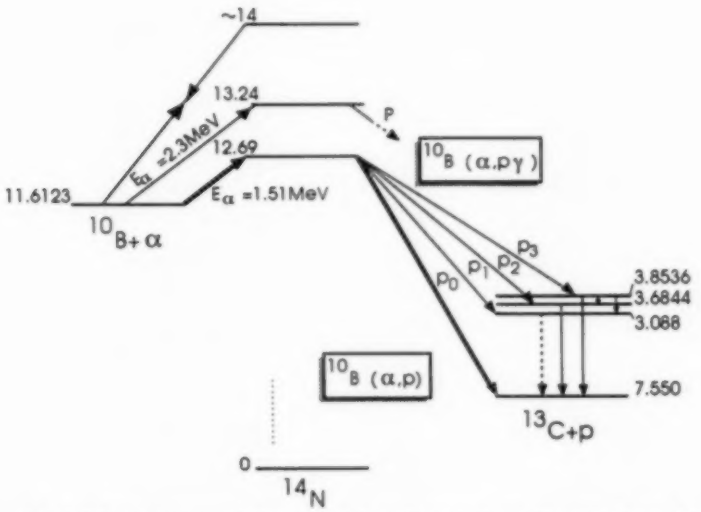

Fig. 4. Schematic representation of possible nuclear reactions with α-particles on ^{10}B.

Table 3
From ref. [36]: Reactions on boron used for elemental analysis using 3.5 MeV α-particles

Nuclear reaction	Emitting nucleus	γ-ray energy [keV]	Experimental detection limit [ppm]	
			in Nb	in quartz
$^{10}B(\alpha,p\gamma)$	^{13}C	169	15	90
$^{10}B(\alpha,\alpha\gamma)$	^{10}B	717	25	160

ticles in order to limit the nuclear reactions to very light elements and detected the produced γ-rays with a Ge(Li) detector.

The nuclear reactions occurring on boron are given in the table 3 (from ref. [36]), as well as the detection limits and the detected γ-ray energies.

The γ detection, with the main advantages of being rapid, simple and nondestructive, allows a quantitative analysis with a precision better than 5%.

In the case of high energy ion implantation, of increasing interest in semiconductor technology, there is no real necessity to use nuclear reactions giving good depth resolution, the sensitivity being a more interesting requirement. Such characteristics are obtained with the $^{11}B(\alpha,n)^{14}N$ reaction used in particular by Oosterhoff [38] and Vos et al. [39]. These authors have profiled implanted B in the energy range from 0.1 to 1.5 MeV in silicon wafers. In ref. [39] the depth profile was measured using the 2060 keV resonance which has no neighbouring resonance within a few hundred of keV. The Q value of the reaction is 0.1574 MeV resulting in a neutron energy of 2.07 MeV at 0°. The neutrons are detected with an organic scintillator detector. The width of the resonance peak is 45 ± 3 keV, which provides a depth resolution in silicon of the order of 200 nm. This performance, as mentioned above is not very good but sufficient compared with the range of the 1 MeV implanted boron ions (up to 2 μm). The detection limit is around $10^{19}/cm^3$, i.e. approximately 100 ppm.

McIntyre and co-workers have investigated the use of the (α,p) reaction on both isotopes of boron [40] with incident α-particle energies below 4 MeV for determining the boron content in thin films and show that many broad resonances exist between 1.4 and 3.5 MeV in the relative yield of ground state protons of this (α,p) reaction. They have used the 2.3 MeV resonance on ^{10}B to determine the boron content in thin films. The (α,p) reaction had already been used by Olivier et al. [41] to determine boron distribution in metal samples using a nuclear microprobe, also on both isotopes. The incident α-particle energy chosen was 2.67 MeV. Irradiations on steels of known boron content allow calibration of the technique. The microprobe facility (beam ≃ 16 μm) allows to establish

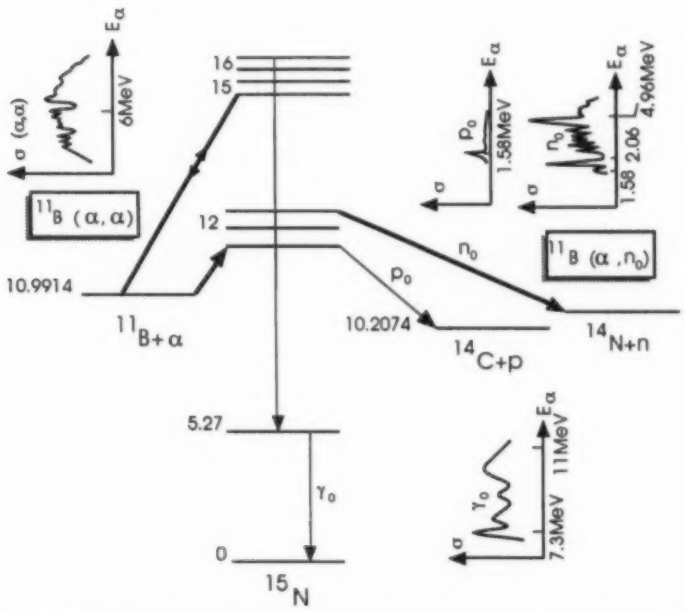

Fig. 5. Schematic representation of possible nuclear reactions with α-particles on ^{11}B.

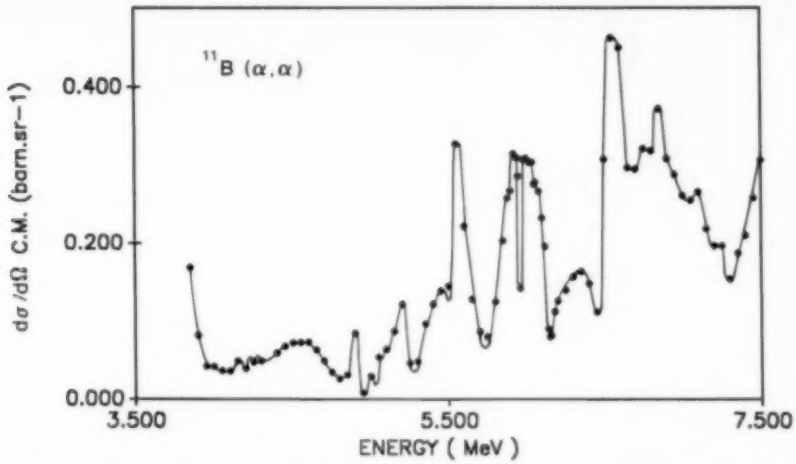

Fig. 6. Excitation function (at $\theta_{lab} = 172°$) of the $^{11}B(\alpha,\alpha)$ reaction between 3.5 and 7.5 MeV α incident energy.

quickly both the boron distribution and the isotopic composition.

Finally another method can be mentioned which is the nonclassical way to use elastic scattering and is called nuclear backscattering spectroscopy. It allows in particular to profile light elements in heavy matrices. This technique is based on the fact that at higher energies it is possible to take advantage of the increased cross sections (σ) due to the formation of compound nuclei. It has been shown for example that σ could be increased by a factor of 80 at 5.7 MeV and of 150 at 7.5 MeV for $^{12}C(\alpha,\alpha)^{12}C$ and $^{16}O(\alpha,\alpha)^{16}O$ reactions respectively [42]. In the case of boron analysis it has been shown [27] that an energy region ranging between 5.92 and 6.04 MeV could be used for analytical applications. Fig. 6 represents the excitation func-

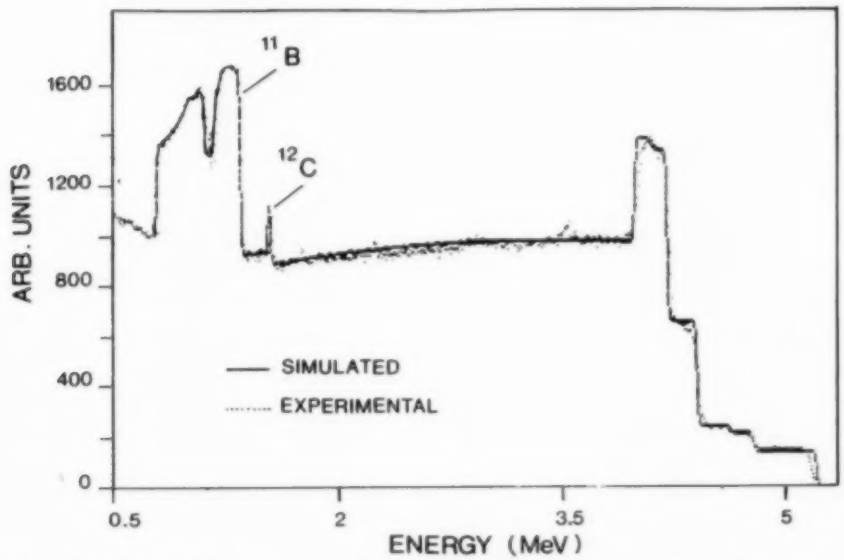

Fig. 7. Analysis of a TiB_x layer deposited on AISI M2 steel using the $^{11}B(\alpha,\alpha)$ reaction at 6.04 MeV. Comparison of experimental and simulated spectra.

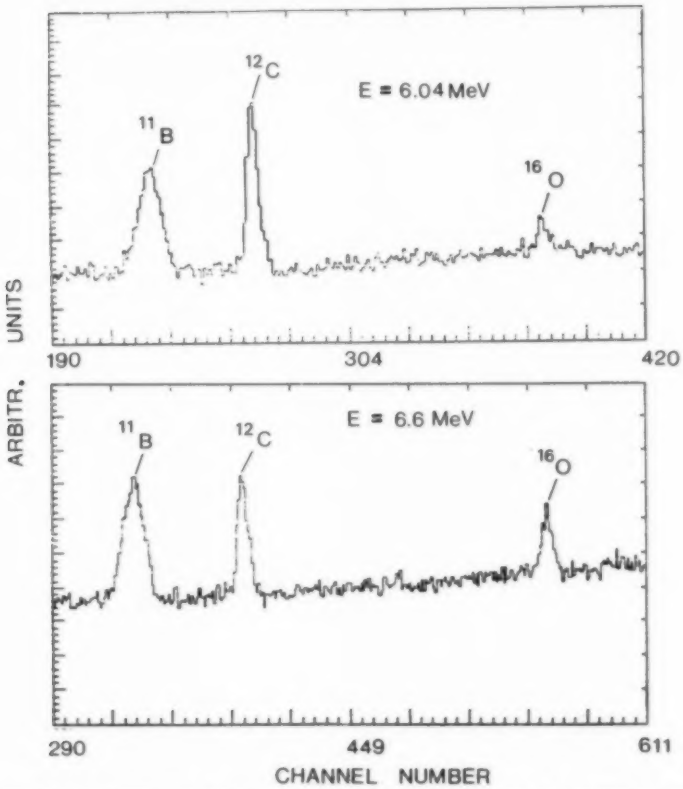

Fig. 8. Experimental spectra of backscattered α-particles on a boron implanted steel at two energies of incident α-particles: E = 6.04 and 6.60 MeV. O and C contaminations appear clearly.

tion of the $^{11}B(\alpha,\alpha)^{11}B$ reaction. The σ value at 6.04 MeV is 45 times the $\sigma_{Rutherford}$ which allows a good sensitivity (4 at.% in nickel) and the depth resolution has been found to be 20 nm in Ni. This reaction was used to determine the stoichiometry of TiB_2 layers deposited on steels (fig. 7) as well as implanted boron profiles in steels (fig. 8). The results and performances obtained with this reaction, when compared with those of $^{11}B(p,\gamma)$ reaction at 163 keV, offer a good agreement. The great advantages of nuclear backscattering are the rapidity, the practical aspect of the technique, and the use of internal standards for quantitative measurements.

7. Reactions with ^{3}He

Pillay et al. [43] have examined the possibility of analyzing light elements and in particular boron by detecting the prompt high energy γ-rays (> 4 MeV) originating from $^3He^+$ ions bombardment [$(^3He,n\gamma)$, $(^3He,p\gamma)$, $(^3He,\alpha\gamma)$ reactions]. They present in these proceedings the applicability of the technique in high purity metallurgical matrices.

8. Recoil nuclei detection

The elastic recoil detection analysis (ERDA) is now a well-established technique [44,45] for providing high depth resolutions. This technique is suitable for light element analysis and consists in bombarding the light target nuclei to be detected by heavier nuclear projectiles. There are several possible methods to identify unambiguously the recoil atoms in addition to their energy determination:

(a) By time of flight.

(b) By differential energy loss (E, ΔE) as for instance described by Petrascu et al. [46], who used high energy S beams (70 MeV) to analyze boron. The sensitivity obtained in silicon wafers for boron was 3.4×10^{16} atoms cm^{-3} and the profiles could be performed on 4 μm.

(c) By measuring the energies of both the scattered and the recoiled atoms in time coincidence, it is possible to increase the sensitivity of the technique. Already in 1975 this technique was used under the name CMCP in particular by Coetze et al. [34] to determine the boron isotopic ratio. Höfsäss et al. [4,5] have proposed to use this method, which they call ERCS (elastic recoil coincidence spectroscopy), to profile simultaneously different light elements like B, C, N, and O, in thin film samples, with a 2 MeV $^4He^+$ incident beam. More precisely, in ref. [5], they have analyzed a thin silicium crystal implanted with boron. Compared with ERDA, the sensitivity can be increased by 2-3 orders of magnitude; on the other hand, in the case of the ERCS technique the samples have to be in the form of self-supporting films (≤ 2 μm thickness) and this constitutes an important limiting factor. A limiting factor for depth resolution is also the energy resolution of surface barrier detector for heavy ions. In the mentioned example, the depth resolution is about 50 nm. Since very low beam currents are available (< 1 nA) the use of microbeams is achieved.

(d) By magnetic analysis which can significantly increase the depth resolution. In ref. [3] Gossett reports the study of BN thin films using 3 MeV ^4He particles. At this energy where σ are nuclear, a quantification of the composition profiles requires standards for each analyzed element. The obtained surface depth resolutions can be as good as a few nanometers.

9. Comparison with other techniques – Discussion

The nuclear reaction analysis presents some very interesting advantages that make it a powerful technique:

- it allows quantitative analysis;
- it provides good depth resolutions and high sensitivities under well-chosen conditions;
- it is nondestructive;
- it can give crystallographic information by lattice localization on single crystal using channeling;
- with microprobe facilities it enables the determination of elemental surface distributions.

However this technique does not bring any chemical information for instance and is often considered as complicated and expensive. We will now examine the use that has been made of other boron analytical methods using low energy ions (secondary ion mass spectroscopy (SIMS), resonance ion mass spectroscopy (RIMS)), electrons (electronic microprobe, Auger electron spectroscopy (AES)) and photons (X-ray photoelectron spectroscopy (XPS)).

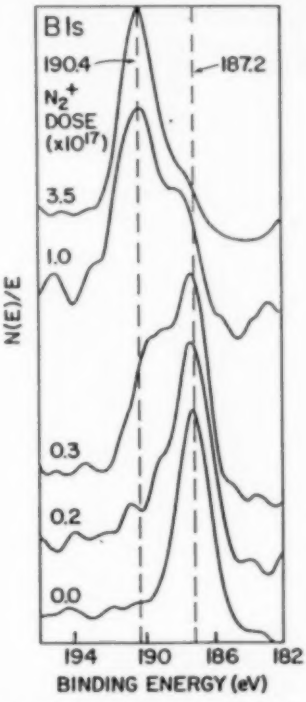

Fig. 9. From ref. [49]: XPS B 1s peaks of a 4 keV N_2^+ bombarded boron sample after different exposures indicated.

SIMS has been extensively used for investigation of boron concentration in semiconductors [31,38,47] since it can probably offer the lowest detection limits. The depth profiling detection limits for ion implants in silicon obtained by SIMS using O_2^+ bombardment are in the 10^{14}–10^{15} atoms cm^{-3} range [48].

SIMS is supposed to provide an excellent depth resolution (potentially) but its main disadvantage is its nonreliability in this field (uncertainty in rate speed, hence in depth scale).

Stiller [47] has demonstrated the existence of boron both in the matrix and at grain boundaries in nickel alloy containing boron impurities (0.08 wt.%). In fact using O_2^+ primary ions, he was able to show the boron distribution at grain boundaries.

With the same primary beam, Oosterhoff [38] has performed boron implantation profiles (10^{15}/cm^2, from 100 to 900 keV boron energy). This technique was used together with two complementary techniques: capacitance voltage profiling and NRA.

XPS and to a lower extent AES can give chemical information. Their use is illustrated in ref. [49]. The authors have put forward the BN formation when bombarding boron with N_2^+ ions (0.5–4 keV). Fig. 9 illustrates the XPS B 1s peak of a 4 keV N_2^+ bom-

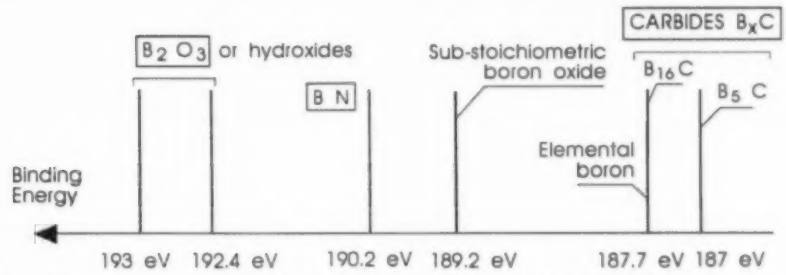

Fig. 10. Binding energies corresponding to the various chemical states of boron (B 1s peaks) for X-ray photoelectron spectroscopy experiments.

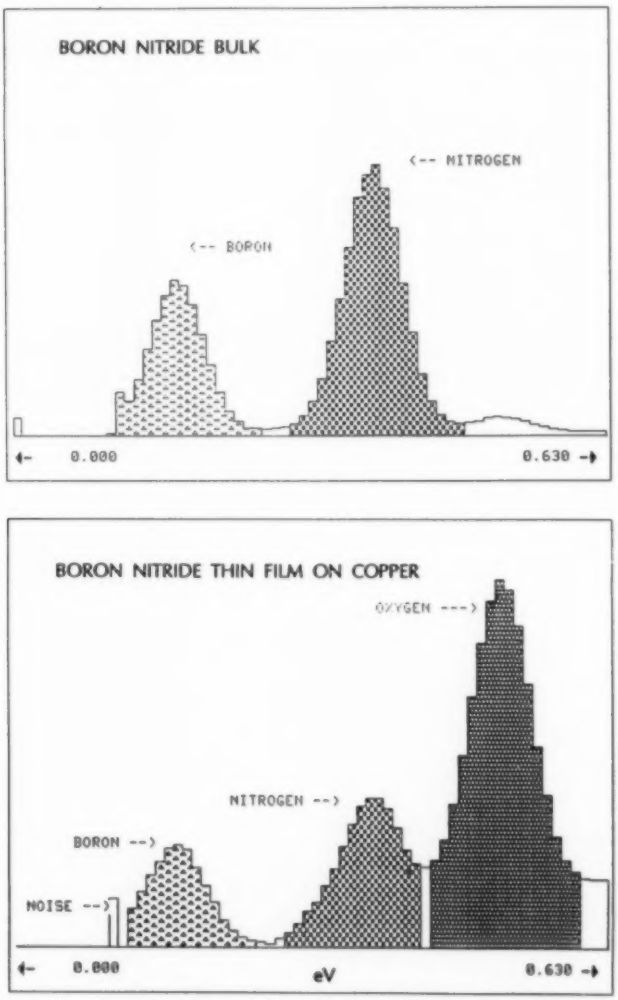

Fig. 11. Kα peaks corresponding to the analysis of a boron nitride bulk and a boron nitride thin film deposited on copper using the analytical electron microprobe [50].

barded boron sample at different doses. The shift of the B 1s peak characteristic of the elemental state of B to the BN chemical form clearly appears when the dose is increased up to 3.5×10^{17} N_2^+ cm^{-2}. The B 1s peaks of the different boron compounds are shown in fig. 10. Mezentzeff et al. [11] have been able to determine with both AES and XPS the [N]/[B] ratio using standard procedures. The detection limits of the AES technique are however much higher than those provided by SIMS (10^{19} atoms cm^{-3} under the same conditions as mentioned above [48]).

The analytical electronic microprobe can also provide interesting information, although it is used under limiting conditions in the case of boron analysis (necessity to use a windowless or a very thin window detector). The fluorescence yield is extremely weak ($w_k = 7.1 \pm 1.8 \times 10^{-4}$) and the X-ray peaks appears around 180 eV.

Fig. 11 illustrates the possibility of determining the stoichiometry of a thin BN layer deposited on copper using a bulk BN standard sample (from ref. [50]). The detector used in this experiment is a quantum detector from KEVEX with a 142 eV resolution. The stoichiometry determination necessitates the background subtraction from oxygen and carbon peaks (which are strong contaminations) and a deconvolution of the B and N peaks. By integrating these last 2 peaks under the same conditions on both the bulk and the thin layer samples, it is possible to demonstrate that the BN thin layer has a stoichiometric composition.

The increase use of the GDOS technique in the industry can be mentioned. It suffers from the same difficulties as SIMS for quantitative analysis. However in a few minutes it allows to obtain simultaneously the distribution profiles on several μg depths of around 15 elements. The detection limit for boron analysis is of the ppm order of magnitude.

Acknowledgement

I would like to thank Professor J. Tousset for his crucial help in the organization of this paper.

References

[1] P.J. Scanlon, M.C. Ridgway and H.H. Brongersma, Nucl. Instr. and Meth. B45 (1990) 615.
[2] O. Herniksen, T. Laursen, E. Johnson, A. Johansen and L. Sarholt-Kristensen, Nucl. Instr. and Meth. B15 (1986) 356.
[3] C.R. Gossett, Nucl. Instr. and Meth. B15 (1986) 481.
[4] H.C. Hofsäss, N.R. Parikh, M.L. Swanson and W.K. Chu, Nucl. Instr. and Meth. B45 (1990) 151.
[5] H.C. Hofsäss, N.R. Parikh, M.L. Swanson and W.K. Chu, Nucl. Instr. and Meth. B58 (1991) 49.
[6] S.E. Nonie and K. Randle, J. Radioanal. Nucl. Chem. Lett. 118(4) (1987) 269.
[7] G. Beurton, F. Dugain, Revue de l'Aluminium, No. 494 (1980) 202.
[8] A.E. Pillay and M. Peisach, these Proceedings (3rd Int. Conf. on Chemical Analysis, Namur, Belgium, 8–12 July 1991), Nucl. Instr. and Meth. B66 (1992) 226.
[9] Ch. Engelmann, Int. Conf. on Analysis of Non-metals in Metals, Berlin, 1980.
[10] R.G. Fairchild, D. Gabel, B.H. Laster, D. Greenberg, W. Kiszenick and P.L. Micca, Med. Phys. 13(1) (1986) 50.
[11] F. Martini, C. Heurteaux, J.C. Wissocq, M. Thellier and A. Stampfler, J. Radioanal. Nucl. Chem. 91 (1985) 3.
[12] R.L. Fleischer and P.B. Price, Science 140 (1963) 1221.
[13] D. Fink, J.P. Biersack, H. Grawe, J. Riederer, K. Müller and R. Henkelmann, Nucl. Instr. and Meth. 168 (1980) 453.
[14] M. Behar, M. Weiser, S. Kalbitzer, D. Fink and F.L. Grande, Nucl. Instr. and Meth. B34 (1988) 316.
[15] C. Vandecasteele, Activation Analysis with Charged Particles (Wiley, New York, 1988) p. 84.
[16] Ch. Engelmann, J. Radioanal. Chem. 7 (1971) 281.
[17] R.W. Michelmann, J. Krauskopf, J.D. Meyer and K. Bethge, Nucl. Instr. and Meth. B51 (1990) 1.
[18] R. Mortier, C. Vandecasteele, K. Strÿckmans and J. Hoste, Anal. Chem. 56 (1984) 2166.
[19] C. Friedli, B.D. Lass and E.A. Schweikert, J. Radioanal. Chem. 54 (1979) 281.
[20] B. Borderie, J.N. Barrandon and J.L. Debrun, J. Radioanal. Chem. 37 (1977) 297.
[21] Ph. Albert, J. Radioanal. Chem. 55(2) (1980) 453.
[22] I. Golicheff, M. Loeuillet and Ch. Engelmann, J. Radioanal. Chem. 12 (1972) 233.
[23] E. Ligeon and A. Bontemps, J. Radioanal. Chem. 12 (1972) 335.
[24] M.J. M. Pruppers, F. Zijderhand, K.M.H. Maessen, J. Bezemer, F.H.P.M. Habraken and W.F. Van der Weg, Nucl. Instr. and Meth. B15 (1986) 512.
[25] C. Boni, E. Cereda, G.M. Braga Marcazzan and V. de Tomasi, Nucl. Instr. and Meth. B35 (1980) 8.
[26] R.B. Boulton and G.T. Ewan, Anal. Chem. 49(9) (1977) 1297.
[27] N. Moncoffre, N. Millard, H.Jaffrezic and J. Tousset, Nucl. Instr. and Meth. B45 (1990) 81.
[28] R. Lappalainen, J. Raisanen and A. Anttila, Nucl. Instr. and Meth. B9 (1985) 55.
[29] I.C. Vickridge, R.J. Sparks and D.M. Bibby, Fuel 69 (1990) 660.
[30] P.J. Scanlon, G. Farrell, M.C. Ridgway and R. Valizadeh, Nucl. Instr. and Meth. B16 (1986) 479.
[31] M.C. Ridgway, P.J. Scanlon and J.L. Whitton, J. Appl. Phys. 62 (1987) 3682.
[32] P.J. Scanlon, M.C. Ridgway and H.H. Brongersma, Nucl. Instr. and Meth. B45 (1990) 615.
[33] X. Lu, Y. Xie, Z. Zheng, W. Jiang and J. Liu, Nucl. Instr. and Meth. B43 (1989) 565.
[34] P.P. Coetzee, R. Pretorius and M. Peisach, J. Radioanal. Chem. 25 (1975) 283.

[35] C. Olivier and M. Peisach, J. Radioanal. Chem. 11 (1972) 105.
[36] B. Borderie, M. Basutcu, J.N. Barrandon and J.L. Pinault, J. Radioanal. Chem. 56 (1980) 185.
[37] B. Borderie, Nucl. Instr. and Meth. 175 (1980) 465.
[38] S. Oosterhoff, Nucl. Instr. and Meth. B30 (1988) 1.
[39] M. Vos, D.O. Boerma, P.J.M. Smulders and S. Oosterhoff, Nucl. Instr. and Meth. B17 (1986) 234.
[40] J.C. McIntyre, Jr, J.A. Leavitt and M.D. Ashbaugh, Z. Lin and J.O. Stoner, Jr., these Proceedings (3rd Int. Conf. on Chemical Analysis, namur, Belgium, 8–12 July 1991), Nucl. Instr. and Meth. 366 (1992) 221.
[41] C. Olivier, J.W. McMillan and T.B. Pierce, J. Radioanal. Chem. 31 (1976) 515.
[42] A. Chevarier, N. Chevarier, P. Deydier, H. Jaffrezic, N. Moncoffre, M. Stern and J. Tousset, J. Trace Microprobe Tech. 6 (1988) 1.
[43] A.E. Pillay and M. Peisach, these Proceedings (3rd Int. Conf. on Chemical Analysis, Namur, Belgium, 8–12 July 1991), Nucl. Instr. and Meth. B66 (1992) 43.
[44] J. L'Ecuyer, C. Brassard, C. Cardinal, J. Chabbal, L. Deschênes, J.P. Labrie, B. Terreault, J.G. Martel and R. Saint-Jacques, J. Appl. Phys. 47 (1976) 381.
[45] J. Tirira, P. Trocellier and J.P. Frontier, Nucl. Instr. and Meth. B45 (1990) 147.
[46] M. Petrascu, I. Berceamu, I. Brancus, A. Buta, M. Duma, C. Grama, I. Lazar, I. Mihai, M. Petrovici and V. Simion, Nucl. Instr. and Meth. B4 (1984) 396.
[47] K. Stiller, J. Phys. Coll. C6, 49 (1988) 347.
[48] H.W. Werner, Mater. Sci. and Eng. 42 (1980) 1.
[49] P. Mezentzeff, Y. Lifshitz and J.W. Rabalais, Nucl. Instr. and Meth. B44 (1990) 289.
[50] J.M. Mackowski, unpublished results.

Nuclear Instruments and Methods in Physics Research B66 (1992) 139–145
North-Holland

Nuclear Instruments & Methods in Physics Research
Section B

On the determination of carbon using charged particle accelerators

R.D. Vis

Faculty of Physics and Astronomy, Free University, Amsterdam, The Netherlands

In this paper, various aspects of the determination of carbon with beams of charged particles are discusse.l. Although initially analyses were performed with several forms of activation analysis, at present the majority of the work is done with in beam techniques, such as nuclear reaction analysis and prompt radiation analysis. Some methods for the determination of isotopic ratios will also be described.

1. Introduction

Quantitative determination of carbon and its distribution are of importance in various areas of science. The quality of steel, weldings and resistance against corrosion depend for a great deal of the proper carbon concentration and its homogeneous distribution.

In biology, carbon is of course a major element. Nevertheless, the determination of carbon in the hard tissues bone and teeth is of importance as the organic fraction plays an important role in these tissues. A nice example of the use of a stable tracer to follow biochemical processes is the use of ^{13}C build in a suitable compound and analyzed after the metabolic process of interest with a suitable nuclear reaction. Especially if one can obtain the distribution of ^{13}C in a biological section, one can study these metabolic processes in great detail. Sometimes, signals originating from carbon are used for the normalization of trace element determinations in biological samples. Nuclear backscattered protons are used to normalize the trace element signals to the amount of biological material irradiated.

In geology, inclusions, and especially the fluid ones are analyzed for carbon compounds. Also in meteorites, the abundance of carbon is extensively studied to reconstruct the cooling history of carbonaceous and ordinary chondrites. In archeology, carbon of course is crucial for the determination of the age of a variety of subjects, for which purpose accelerators are being used as sophisticated mass spectrometers capable of determining ultra-traces of ^{14}C.

2. Nuclear reactions used

2.1. Charged particle activation analysis

Initially, activation analysis with charged particle beams has been used to determine carbon. On ^{12}C reactions of the type (d, n), (^{3}He, α) and (p, pn) were commonly used. The (p, pn) reaction has been studied in great detail, the excitation curve is known within an accuracy between 3 and 5% [1] and this reaction has been used as a standard for measuring other excitation functions. The disadvantage of these reactions is that the products are pure positron emitters, necessitating unfolding procedures to extract the isotope with the right half life. Standardization has been done with the numerical integration method [2] using excitation functions from literature or by using appropriate standards.

An attractive option for activation analysis is the use of the (^{3}He, n) reaction on ^{12}C, leading to ^{14}O with a half-life of 71 s which emits 2.31 MeV γ-radiation during its decay. Activation analysis with ^{3}He particles was described in detail by Ricci et al. [3] who reported detection limits down to 1 ppm for carbon.

The $^{12}C(^{3}He, \alpha)^{11}C$ reaction has been used by Misaelides et al. [4] for the determination of C in semiconductors. In this work, and more extensively in the work of Liebler et al. [5] the excitation function of this reaction is given. The (d, n) reaction, leading to ^{13}N as final nucleus, was investigated by Michelmann et al. [6]. The cross section of the latter reaction is slightly smaller than the values for the ^{3}He induced one.

For these analyses, high beam currents are needed to introduce sufficient radioactivity. Real microanalysis is not conceivable since the currents in microbeams of charged particles are generally too low for activation analysis. Therefore, in beam reactions are commonly used for microanalysis and for the measurement of the distribution of carbon in given samples.

2.2. In beam techniques

In beam techniques are characterised by the fact that measurement of radiation occurs during the irradiation. Rather arbitrarely, a subdivision is made in nuclear reaction analysis (NRA) in case particles are

0168-583X/92/$05.00 © 1992 – Elsevier Science Publishers B.V. All rights reserved

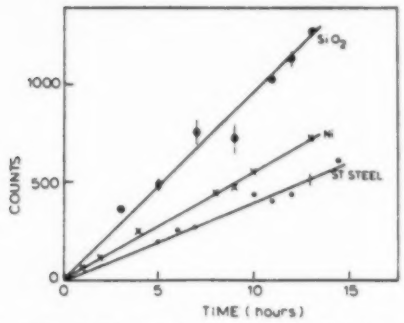

Fig. 1. Carbon build up during deuteron irradiation on different surfaces. Measurements were done using the $^{12}C(d, p_0)^{13}C$ reaction. 1.4 MeV deuterons were used with a beam current of 100 pA.

detected and prompt radiation analysis (PRA) in case γ-radiation is detected. A further division is made into resonant and nonresonant reaction analysis, dependent of whether or not a resonance in the excitation function is used.

Before going into the details of these reactions, two problems associated with the in beam analysis of carbon are mentioned. As most nuclear microprobes does not operate under ultrahigh vacuum conditions, inevitably carbon build up will occur caused by cracking of thin layers of hydrocarbons on the sample surface during the irradiation. Makjanic [7] studied this build-up in the Amsterdam nuclear microprobe during different conditions and on different surfaces. Cleaning the vacuum chamber and placing a cold trap near to the sample holder gave some improvement but, although the whole system was pumped with turbomolecular pumps down to 10^{-5} Pa still a deposition rate of 5 ng cm^{-2} min^{-1} was observed. For the results obtained on different surfaces, see fig. 1. It is most likely, that differences found for different materials are caused by the different emission rate of secondary electrons by these materials. These electrons are the main cause of cracking of adsorbed organic material. The build-up rate is also known to be temperature dependent; cooling of the target will reduce the deposition rate.

A rather peculiar phenomenon has been observed by Freund et al. [8] and Van der Stap [9]. In an olivine matrix, carbon tends to occur in a concentration gradient with higher values near to the surface of the olivine crystals. The temperature dependence of these gradients has been studied by Freund et al. while Van der Stap measured that after polishing the fresh surface which is initially low in carbon becomes carbon richer just by waiting several hours. The higher matrix carbon concentration in the carbonaceous chondrite Allende as compared with the C-concentration in inclusions as chondrules was explained by the finer grain size of the matrix with an associated larger surface area accommodating more carbon. This increase of surface carbon after polishing could clearly be distinguished from the carbon build up mentioned before, because it is a much larger effect.

2.2.1. Proton induced reactions

One of the first examples of the use of in beam analysis of C was the proton capture reaction on ^{12}C, producing around 2.3 MeV γ-radiation [10]. This $^{12}C(p, \gamma)^{13}N$ reaction was used to analyze steel samples. Rudolph et al. [11] used the same reaction for the simultaneous investigation of carbon layers on the surface and at the interfaces of solids, the so called buried layers. The large resonance at 0.457 MeV ($\Gamma = 36$ keV) and depth dependent proton energy within a thick target lead to the emission of γ-ray quanta whose energies are also depth dependent. In fig. 2 results of these measurements are shown. Note, that at beam energies well above the resonance the γ-ray caused by the $^{13}C(p, \gamma)^{14}N$ reaction shows up clearly opening up possibilities for the measurement of isotopic ratios, especially since the cross section of the latter reaction is considerably higher.

2.2.2. Deuteron induced reactions

For NRA with particle detection, virtually only exothermic reactions have potential use for trace analysis. With a positive Q-value, the emitted particle has a higher energy than the incoming beam, which consequently facilitates detection of these emitted particles interference free from nuclear or Rutherford scattered particles. Options available are the use of deuteron beams (by far the most widespread method for C-analysis) and ^3He beams.

Deuteron induced reactions on carbon has been studied in detail [12–14] for bombarding energies between 0.5 and 2.0 MeV. The (d, n) reaction was studied by Bennett at al. [15] but this reaction is due to its negative Q-value ($Q = -0.28$) not very suitable for in beam analysis. Of much more interest are the $^{12}C(d, p_0)^{13}C$ ($Q = +2.73$) and $^{12}C(d, p_1\gamma)^{13*}C$ ($Q = -0.37$), the latter being used for the PRA method using the γ-emission. In fig. 3 the excitation function for the reaction to the ground state is given for 4 different scattering angles. It is clear from the figure, that backward angles are favourite. This is because both the cross section reaches its highest values and the number of elastically scattered deuterons is decreasing towards backward angles. Kashy et al. [14] also give angular distributions of the ground state protons and the excitation function for the $^{12}C(d, p_1\gamma)^{13*}C$ reaction measured at $\varphi = 80.5°$.

Pollard et al. [16] give proton spectra for the deuterium induced reaction on $BaCO_3$, both natural and

enriched in ^{13}C. The bombarding energy was 1.3 MeV. Studied were also possible interferences which were quantified for the elements Li, N, B and F for bombarding energies between 1.2 and 1.6 MeV. The sensitivity for the analysis of ^{13}C is, however, more than one order of magnitude lower than for ^{12}C, which reduces the possibility of measuring small enrichements of the ^{13}C isotope while f.i. used as a stable tracer.

A very selective reaction for the detection of ^{13}C is $^{13}C(\alpha, n)^{16}O$. In forward direction neutrons are emitted of 3.7 MeV while irradiating with 2.8 MeV $^4He^+$-ions. Only ^9Be produces higher energetic neutrons but with a very small cross section. Measuring neutrons above a threshold of about 3.5 MeV enables to measure ^{13}C selectively. If no B is present in the sample one is able to lower the threshold to 2 MeV (to avoid neutrons from ^{18}O to be detected) which increases the sensitivity considerably opening possibilities to detect small variations in the $^{12,13}C$ isotopic ratio.

γ-detection during deuteron bombardment increases the selectivity and can avoid possible interferences while detecting protons. γ-detection, however, leads to a poorer sensitivity, partly as a consequence of the reaction cross sections involved and partly as a consequence of γ-ray detector efficiency. Pollard et al. [16] studied interferences and found spectral interference from deuteron induced reactions on Be, S and Mg. At the price of less sensitivity, one may choose other γ-transitions to avoid these overlaps. Lenglet et al. [17] used (d, pγ) reactions on C and O to measure mass loss during the irradiation of biological samples to be analyzed for trace elements.

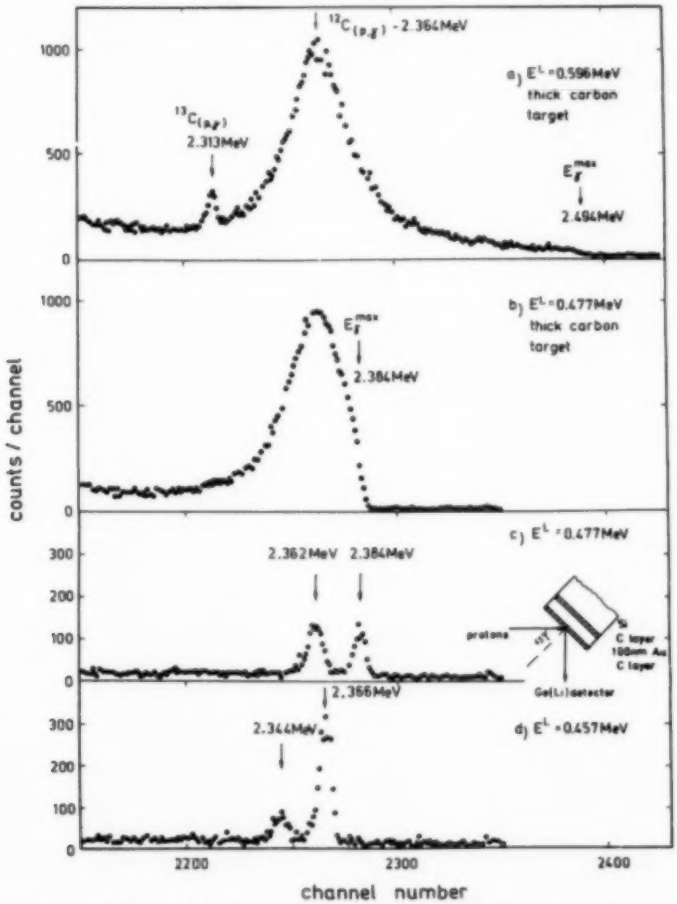

Fig. 2. Measured γ-ray spectra from $^{12}C(p, \gamma)^{13}N$, taken at incident energy (E^L) near the 0.457 MeV resonance. Clearly separated γ-ray peaks are observed for the sandwich target (insert in c) at proton energies 0.477 (c) and 0.457 (d). (Data taken from ref. [11]).

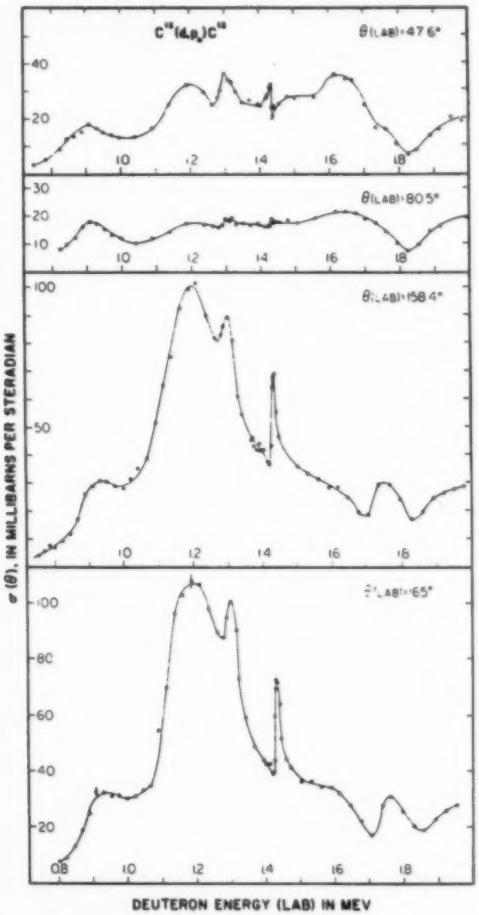

Fig. 3. The excitation function for the (d, p_0) reaction on ^{12}C at 4 different angles. (Data taken from ref. [14]).

2.2.3. ^{3}He-induced reactions

Reactions of the type (^{3}He, p) on both C isotopes have lower cross sections than the deuteron induced ones. The cross section for the reaction $^{13}C(^3He, p)^{15}N$ increases slowly with increasing beam energy [18,19]. Spectral interference occurs between the ground state protons from ^{12}C and the p_2 and p_3 groups from ^{13}C. Interferences from other elements under ^{3}He bombardment are studied by Bromley et al. [20] and are most severe for the elements Be, Li, B and N.

2.2.4. Elastic scattering

Cross sections for Rutherford scattering increase with increasing atomic number Z. Therefore, detection of light elements is not very sensitive, especially not if the matrix is from a higher Z material. To avoid the C-peak riding on a huge background, specimens should be very thin. For RBS, ^{4}He-beams from 1 or 2 MeV are commonly used. It should be noted, that, especially at large scattering angles, strong deviations can occur from Rutherford cross sections due to nuclear effects and for C the acronym NBS is more appropriate [21,22].

The situation for the light elements can be improved considerably by performing elastic recoil detection (ERD) during which beams are impinging at oblique angles and recoil atoms ejected from the sample are measured at forward angles. During this technique, it is possible by placing a thin foil in front of the detector to stop heavy recoil atoms and find an optimum in the sensitivity curve around carbon. This method works satisfactorily in case surface layers have to be analyzed; due to the small angles of incoming and outgoing particles, the probed layer is very thin. To avoid particles from the beam reaching the detector, for light element analysis very often beams of heavy ions such as $^{28}Si^{6+}$ are used. These ions will also stop in the absorber foil placed in the detection path.

2.2.5. Position information

Information about the position of carbon can be obtained by using a well focussed incoming beam. Beams below 1 μm with sufficient current for analysis are now available at a few places [23,24]. Scanning procedures in combination with advanced software packages enable to produce elemental maps with this lateral resolution.

All techniques described above also give depth information. Using NRA, detailed knowledge of the excitation function combined with a known composition of the matrix and thus a known stopping power enable to reconstruct the concentration profile along the range of the projectiles. In general, these procedures have a limited depth resolution, due to straggling of the beam and the limited detector resolution. If, however, one is able to use a preferentially sharp resonance in the excitation function, one can obtain a much better depth resolution by probing in depth using beam energy changes [25]. The resolution is for a great deal determined by the width of the resonance; if this width is small, resolutions down to 10–20 nm are achievable in favourable cases, but these small resonances are not available in the excitation function of the commonly used reactions on carbon. ^{3}He-induced reactions for depth profiling of C and O were used by Gossett [26]. The author improved the depth resolution using glancing incident beams. D'Agostino et al. [27] used a 1.6 MeV deuterium beam and obtained a depth resolution of 0.25 μm studying a welding joint.

ERD features a very good depth resolution. The analysis goes along the same ways as RBS (which in itself also produces depth information) and the formalism for ERD has been well described by Doyle et al.

[28] with a view on computer application. By selecting carefully the experimental parameters, a depth resolution for carbon of 10 nm can be reached.

3. Other accelerator based techniques

For the determination of isotopic ratios of $^{12,13,14}C$, accelerators are used. The technique is called AMS (accelerator mass spectrometry) and in cases a tandem accelerator is used (TAMS). Basically, the sample is brought into the ion source where it is bombarded with Cs^+-ions, which not only sputter away carbon atoms but also promote the formation of C^--ions by means of a thin surface film of Cs on the sample. The C^--ions are accelerated and stripped in the stripper canal of the tandem to C^{3+}- or C^{4+}-ions which again are accelerated, separated by means of a combination of electrostatic and magnetic fields and measured. The advantage of the accelerator is that isobaric molecular species do not survive the stripping avoiding mass spectral interferences and that ^{14}C atoms can be counted individually giving very high sensitivity. Nitrogen does not interfere, as no negative ions are produced in the ion source. A good description of a modern TAMS facility can be found in ref. [29]. Cyclotrons also have sufficient mass separating power to be used for this purpose [30]. The method is so sensitive that one is able to determine a ratio of $^{14}C/^{12}C$ of 10^{-15} which opens possibilities to backdate objects down to 50000 years.

A completely different technique is bombardment of a sample with a low intensity heavy ion beam in order to sputter away molecular fragments from the surface which are detected with a time of flight mass spectrometer. Initially ^{252}Cf spallation sources were used but the flexibility of an accelerator offers advantages. The technique is able to measure C-compounds on the sample surface up to very high molecular weights. The method is known as PDMS (particle desorption mass spectrometry) [31].

4. Applications

It is not the intention of this paper to review all sorts of applications of C analysis. Suffice it to give a few examples in which nuclear techniques have contributed to improve knowledge. Very extensively, steel has been analyzed for carbon. One of the earliest applications of in beam reactions was the determination of C in steel at Harwell (UK) by measuring the prompt γ-radiation emitted during the reaction $^{12}C(p, \gamma)^{13}N$ ($E_\gamma = 2.3$ MeV) [10]. Shortly later, deuterons were used for the same purpose, also performing γ-ray spectroscopy [32]. Since then, a large

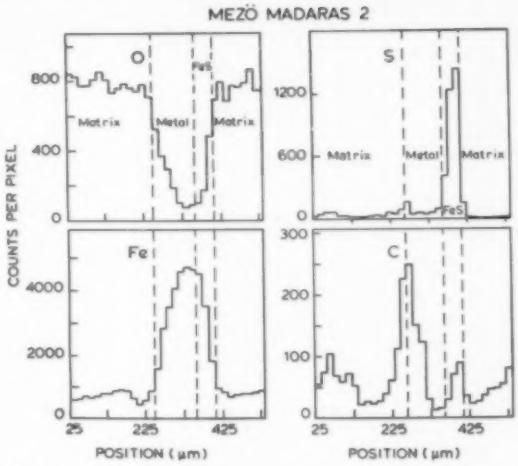

Fig. 4. Results of line scans made on Mezö Madaras (see text).

number of C-analyses have been done to analyze metals, alloys or welding joints [33–41]. Also in plasma fusion research and catalysis, there has been a notably increase in the exploitation of nuclear techniques [42].

At our institute, a large number of analyses have been performed on meteorites [43–47]. During a study of different classes and types of ordinary chondrites, it was found that in spite of large variations in the bulk C-concentrations reported in literature, the matrices of all these chondrites have a remarkably constant C-concentration. This has lead to an assumption that the matrix is common and was formed separately and presumably earlier than inclusions such as chondrules. In a later stage mixing occurred between these 2 phases [7]. During scanning, a peculiar C-distribution was observed. In fig. 4, results of line scans are displayed from Mezö Madaras. It is shown that C is present preferentially at the edges of Fe or FeS inclusions. The asymmetry in the distributions is caused by the different positions of the small inclusions with respect to the surface of the sample which, in combination with the different range of X-rays used to detect Fe and S and of protons used to detect C and O explain the results (fig. 5). It has been assumed that Fe acts as a catalyst for a Fischer–Tropsch type of reaction followed by pyrolysis to form elementary carbon as jackets around these inclusions.

Neelmeyer et al. [48] used the d, p_0 reaction on ^{12}C in combination with RBS to improve the understanding of the high wear resistance of tool steel after carbon implantation. Depth profiling was performed within a 200 nm thick near surface layer structure, modified by carbon in beam assisted deposition of C together with carbon-substrate ion beam mixing. These

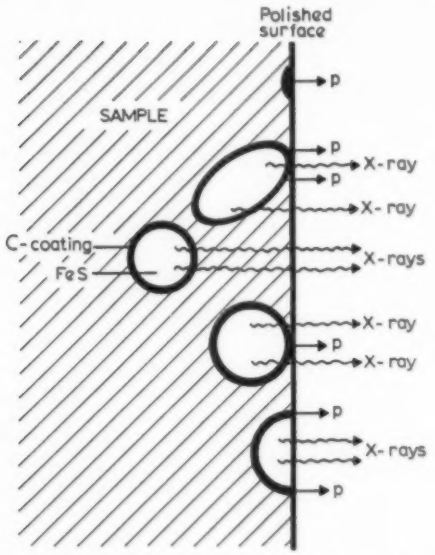

Fig. 5. Possible positions of FeS grains in the sample with respect to its surface and the corresponding outcoming radiation.

modifications were done in order to obtain new types of wear resistant coatings.

In biology, sometimes C-distributions are measured with RBS to normalize trace element concentrations present in these sections [49]. Other fields of application include the semiconductor industry and other forms of materials science.

5. Conclusions

Nuclear techniques for the determination of carbon are well developed. It is nowadays possible to detect trace concentrations of carbon and also to measure the C-distribution present in the sample in three dimensions. The resolution obtained is determined by the C-concentration and its chemical surrounding. With advanced techniques such as resonant nuclear reactions, elastic recoil detection or coincidence techniques to measure exactly the kinematics of the projectile–atom collision, a depth resolution of 10 nm is feasible. Also for the determination of the isotopic ratio of C, accelerator based techniques have contributed considerably. For the most commonly used reactions on carbon, data are available from the very comprehensive compilation on nuclear cross section data from Jarjis [50].

References

[1] E. Bruninx, CERN report 62-9 (1962).
[2] C. Van die Casteele and K. Strijckmans, J. Radioanal. Chem. 57 (1980) 121.
[3] E. Ricci and R.L. Hahn, Anal. Chem. 37 (1965) 742.
[4] P. Misaelides, J. Krauskopf, G. Wolf and K. Bethge, Nucl. Instr. and Meth. B18 (1987) 281.
[5] V. Liebler, K. Bethge, J. Krauskopf, J.D. Meyer, P. Misaelides and G. Wolf, Nucl. Instr. and Meth. B36 (1989) 7.
[6] R.W. Michelmann, J. Krauskopf, J.D. Meyer and K. Bethge, Nucl. Instr. and Meth. B51 (1990) 1.
[7] J. Makjanic, Thesis, Free University, Amsterdam (1990).
[8] F. Freund, H. Kathrein, R. Knobel, G. Oberheuser, H. Wengeler, G. Demortier and H.J. Heinen, Nucl. Instr. and Meth. 197 (1982) 27.
[9] C.C.A.H. van der Stap, Thesis, Free University, Amsterdam (1986).
[10] T.B. Pierce, P.F. Peck and W.M. Henry, Nature (London) 204 (1964) 571.
[11] W. Rudolph, C. Bauer, P. Gippner and K. Hohmuth, Nucl. Instr. and Meth. 191 (1981) 373.
[12] G.C. Phillips, Phys. Rev. 80 (1950)164.
[13] J.M. Blatt and L.C. Biedenharn, Phys. Rev. 86 (1952) 399.
[14] E. Kashy, R.R. Perry and J.R. Risser, Phys. Rev. 117 (1960) 1289.
[15] W.E. Bennett and T.W. Bonner, Phys. Rev. 58 (1940) 183.
[16] P.M. Pollard, J.W. McMillan and D.J. Malcolme-Lawes, J. Radioanal. Chem. 70 (1982) 349.
[17] W.J.M. Lenglet, F. van Langevelde, A.J.J. Bos, R.D. Vis and H. Verheul, Spectrochim. Acta. Part B 40 (1985) 763.
[18] J. Schiffer, Nucl. Phys. 15 (1976) 1064.
[19] H.J. Kim, W.T. Milner and F. McGowan, Nucl. Data Tables 2 (1966) 148.
[20] D. Bromley and E. Almqvist Rep. Prog. Phys. (1960) 544.
[21] J.F. Ziegler and J.E.E. Baglin, J. Appl. Phys. 42 (1971) 2031.
[22] J.F. Ziegler and J.E.E. Baglin, J. Appl. Phys. 45 (1974) 1888.
[23] G.W. Grime, M. Dawson, M. Marsh, I.C. McArthur and F. Watt, Nucl. Instr. and Meth. B54 (1991) 52.
[24] G.R. Moloney, D.N. Jamieson and G.J.F. Legge, Nucl. Instr. and Meth. B54 (1991) 68.
[25] G. Amsel, J.P. Nadai, E. D'Artemare, D. David, E. Girard and J. Moulin, Nucl. Instr. and Meth. 92 (1971) 481.
[26] C.R. Gossett, Nucl. Instr. and Meth. 218 (1983) 149.
[27] M.D. D'Agostino, E.A. Kamykowski, F.J. Kuehne, G.M. Padawer, E.J. Schneid, R.L. Schulte, M.C. Stauber and F.R. Swanson, J. Radioanal. Chem. 43 (1978) 421.
[28] B.L. Doyle and D.K. Brice; Nucl. Instr. and Meth. B35 (1988) 301.
[29] K.H. Purser, T. Smick, A.E. Litherland, R.P. Beukens, W.E. Kieser and L.R. Kilius, Nucl. Instr. and Meth. B35 (1988) 284.
[30] K.M. Subotic, D. Novkovic, M.S. Stojanovic and L.S. Milinkovic, Nucl. Instr. and Meth. B50 (1990) 267.

[31] E.A. Schweikert, W.R. Summers, D.J. Keith, P.E. Filpus-Luyckx and M.U.D. Beug Deeb, J. Trace and Microprobe Techn. 5 (1987) 1.
[32] T.B. Pierce, P.F. Peck and W.M. Henry, The Analyst 90 (1965) 339.
[33] T.B. Pierce, J.W. McMillan, P.F. Peck and I.G. Jones, Nucl. Instr. and Meth. 118 (1974) 115.
[34] D. Heck, Nucl. Instr. and Meth. 197 (1982) 91.
[35] F.C.W. Pummery and J.W. McMillan, Nucl. Instr. and Meth. 168 (1980) 181.
[36] J.W. McMillan and F.C.W. Pummery, Corros. Sci. 20 (1980) 41.
[37] T.B. Pierce, J. Radioanal. Chem. 17 (1973) 55.
L38]J.F. Singleton and N.E.W. Hartley, J. Radioanal. Chem. 48 (1979) 317.
[39] J.W. McMillan, P.M. Hirst, F.C.W. Pummery, J. Huddleston and T.B. Pierce, Nucl. Instr. and Meth. 149 (1978) 83.
[40] T.B. Pierce and J. Huddleston, Nucl. Instr. and Meth. 144 (1977) 231.
[41] T.B. Pierce, J. Radioanal. Chem. 37 (1977) 285.
[42] J.W. McMillan, Nucl. Instr. and Meth. B30 (1988) 474.
[43] D. Heymann, C.C.A.H. van der Stap, R.D. Vis and H. Verheul, Meteoritics 22 (1987) 3.
[44] C.C.A.H. van der Stap, D. Heymann, R.D. Vis and H. Verheul, J. Geophys. Res. 91 (1986) 373.
[45] J. Makjanic, D. Heymann, C.C.A.H. van der Stap, R.D. Vis and H. Verheul, Nucl. Instr. and Meth. B30 (1988) 466.
[46] J. Makjanic, J.L.R. Touret, R.D. Vis and H. Verheul, Meteoritics 24 (1989) 49.
[47] J. Makjanic, D. Heymann and R.D. Vis, Nucl. Instr. and Meth. B49 (1990) 514.
[48] C. Neelmeijer, E. Hensel, P. Knothe, M. Posselt and E. Richter, Nucl. Instr. and Meth. B42 (1989) 369.
[49] F. Watt, A.J. Brook and G.W. Grime, Nucl. Instr. and Meth. B49 (1990) 465.
[50] R.A. Jarjis, Nuclear cross section data for surface analysis, Department of Physics, Schuster Laboratory, University of Manchester, England (1979).

Nuclear Instruments and Methods in Physics Research B66 (1992) 146–157
North-Holland

Nuclear Instruments & Methods in Physics Research
Section B

Ion beam analysis of nitrogen

K. Bethge

Institut für Kernphysik, Johann Wolfgang Goethe-Universität, W-6000 Frankfurt am Main, Germany

Nitrogen plays an important role in almost all materials. In metals its presence influences the tribology. In semiconductors nitrogen compounds act as insulating layers. The less abundant isotope ^{15}N can be used as tracer element to investigate biological processes. Thus the analysis of materials concerning the nitrogen content needs adequate methods. Nuclear reactions on both isotopes reveal an appropriate tool, if the cross sections are known to a high degree of accuracy.

1. Introduction

Nitrogen, the first element in the fifth group of the periodic table is an ever present elements in nature, because of its 80% abundancy in the earth's atmosphere. The stable isotopes ^{14}N and ^{15}N are abundant to 99.63% and 0.366%, respectively. Thus its properties may advantageously or disadvantageously affect all natural materials exposed to air. The possible effects can be of quite different physical character. Nitrogen can be just an adhesive layer on the surfaces without strong chemical reactions. In some materials, however, nitrogen also penetrates into the bulk of the material reacting chemically in the near surface region. This effect becomes drastic enhanced if nitrogen ions are implanted into materials because of the strong atomic reactivity compared to the dominant passivative role of the N_2 molecule. A few of these effects will be mentioned subsequently separated to different classes of materials ordered according to their electric conductivity.

It should, however, be emphasized that the results of ion beam analyses can only contribute some information to understand the features and properties of materials, full understanding has to emerge from comparison with other methods of investigation.

1.1. Metals

Nitrogen in metals plays an important role in tribology. It has been shown [1–5] that the implantation of nitrogen into metals, e.g. steels, titanium, and titanium alloys, increases the wear resistence, an important fact for cutting tools. The process of nitrogen diffusion into the metal under mechanical stress is still investigated at many laboratories. For optimal conditions a fairly high dose has to be implanted. During the implantation also sputtering takes place. The sputtering rate depends, however, also on the implanted dose [6]. Under the influence of mechanical stress nitrogen diffuses into larger depths of the material which changes the materials properties also in the near surface bulk region [7].

For the full understanding of the processes it is necessary to determine quantities as well as profiles of nitrogen in the depth. That process as a production process in industry has still to be accepted in industry [8].

1.2. Semiconductors

The technique of doping semiconductors, e.g. silicon with elements of the fifth group, phosphorus and arsenic has become a common technique to produce n-type semiconductors. Nitrogen plays not a similar role in silicon as other elements of the fifth group for doping the material to produce n-type material because its solubility is very small. That implies that diffusion into the material is difficult to achieve. The implantation of nitrogen is a possible effect [9] to surmount the difficulties, but instead of forming shallow donator states, as expected, its shows a quasi Jahn–Teller effect which leads to a deep level in the middle of the gap at about 0.7 eV.

In high temperature semiconductors, like SiC, nitrogen is used as a dopant. Its content has to be known to a high degree of accuracy [9,10]. However, nitrogen became dominant in other respects. It forms in silicon passivation layers, e.g. Si_3N_4. A layer of this material can prevent the diffusion of oxygen. Thus it is an objective of nitrogen implantation to form insulating layers. This process is called SIMNI (separation by implantation if nitrogen). It is a two step process which starts with a high dose nitrogen implantation at elevated temperatures $T \approx 350°C$ and a subsequent annealing at high temperatures ($T_a \approx 700°C$). The process

0168-583X/92/$05.00 © 1992 – Elsevier Science Publishers B.V. All rights reserved

results in buried insulating layers for SOI structures (silicon on insulator) [11,12]. Nitrogen is also used as an addition to the argon atmosphere during the crystall growing process. A passivation layer of nitrogen prevents during the annealing process the increase and penetration of displacements [13].

In all the forementioned cases it is important to determine quantity and profile of nitrogen, because all effects begin to function if a threshold has been surmounted. An additional problem is the determination of the stoichiometry which is not the same as in the gaseous phase.

1.3. Insulators

Nitrogen implantation was used to study the change of properties of optical wave guides like $LiNbO_3$ [14]. Nitrogen is one of the constituents of frequently used ceramic material as Si_3N_4 or BN. Little is known how a deviation of the stoichiometry influences the properties of the material. The role of nitrogen in ceramic superconductors is presently also investigated [15]. The behaviour of diamond, particular its specific electric resistance has been studied after nitrogen ion implantation [16]. The nitrogen concentration of industrial glasses, its repartition from the surface, its influence on oxidation and reduction conditions have been studied [98].

1.4. Polymers

Polymers are built from molecules which contain nitrogen as constituents, thus a uniform distribution is expected, so far no change of concentration according to nitrogen implantation has been observed. A recent development for nitrogen detection was caused by the need to detect nitrogen containing explosives particular as a service method on airports [17].

1.5. Biological samples

The abundance of nitrogen in biological samples can vary according to metabolic processes. Thus the determination of both nitrogen isotopes can be of valuable help in biological and medical research and for routine measurements [19,73].

2. Experimental methods

The ion beam analysis of nitrogen as well as of other elements requires three carefully understood main components which features determine the successful work, an accelerator, appropriate sample or target handling and a highly sensitive and high resolution detection system.

The accelerators should provide sufficient beam intensities and particle energies, e.g. up to 15 MeV, depending on the Q-value of the specific nuclear reaction used. Many analyses have been performed at energies in the low MeV range. In many laboratories electrostatic accelerators of the Van de Graaff-type in both versions, single ended and tandems are being used [20]. High accuracy analyses need ion beams with as small as possible beam energy straggling. The primary energy straggling originates in the ion source. Therefore ion sources which fulfill that requirements are preferable. Furthermore the voltage fluctuations of the generating system impose additional energy straggling to the beam. Without any precaution these fluctuations in energy are in the order of 1 keV. They can, however, be minimized by electronic feedback circuits [21] or by stabilizing the beam via a second beam component, e.g. a molecular component and its deflection through a highly stabilized magnetic field. That principle allowed to achieve energy stability in the order of 100 eV [22–24].

The second component in an analysis experiment which deserves special care is the sample or target itself. Energy loss introduces statistical fluctuations which have to be taken into account because that quantity determines the spatial resolution [25]. Even despite the fact that good compilations on energy losses and ranges exist [26], in many cases, particular for heavier projectiles than α-particles, the energy loss and their ranges have to be determined experimentally. The maximum achievable depth of analysis can be expressed as follows.

$$W = \frac{\xi E_0 \, \Delta k}{C \, \mathrm{d}E/\mathrm{d}x \,|_{E_0}}, \tag{1}$$

where

E_0 = energy of the incident beam,
ξ = adjustment parameter (for α-particles in silicon ≈ 0.9),
C = $f(k, \theta)$ function of the kinematical factor and angle,
Δk = difference of kinematical factors for the masses of host and impurity element.

The depth resolution δx achievable in the analysis depth is given by

$$\delta x = \delta E / C(k, \theta) \, \mathrm{d}E/\mathrm{d}x, \tag{2}$$

where δE is the energy straggling of the primary incident beam from the accelerator. $C(k, \theta)$ is the same function as in eq. (1).

The Doppler broadening, known from the analysis of light elements, like hydrogen, if using nitrogen beams [27], may limit the depth resolution. In special combinations of nitrogen and the host material that effect might be considered particular, if ERDA is applied [28]. In general, however, the effect will be within the

detector resolution. The detector resolution is a further component which influences the accuracy of the measurements. Surface barrier detectors cause an additional energy straggling, because the particles have to penetrate different front layers before stopping [29], which limits the resolution to 3 to 4 keV. A special detection system is a time-of-flight detector [30]. For ERDA measurements detector systems with particle identification are necessary to be used.

The other necessary equipment is that of nuclear physics, vacuum chambers, conventional pulse electronic and data handling equipment. Improvements for further analysis work should aim to larger solid angles for the detectors, increased detection efficiency, thinner windows for the detectors which could improve the energy resolution still further, improved electronics which should reduce the pileup background [31].

3. Analysis with accelerated beams

The majority of the analyses of nitrogen has been done with accelerated light particles, thus we restrict that review to reactions performed with light projectiles up to mass 4 (α-particle) and also to nonradioactive beams (no tritium). The nuclear data for most of the available reactions are listed in numerous compilations [32].

3.1. Rutherford backscattering (RBS)

The Rutherford backscattering has reached a leading position in the analysis of materials. The respective scattering of charges is element specific, it allows to determine elemental profiles, the sensitivity is for N in a heavy matrix in general about 1 at.%. With special care for the shielding and special detectors [29] the ppm region can be reached. RBS is, however, not specifically related to nitrogen. Moreover the information about the quantity of nitrogen is in many cases needed if nitrogen is incorporated in a heavy matrix. According to the statistical nature of the measuring principle (counting) the separation of signals from nitrogen from those of the matrix materials implies difficulties if the nitrogen content is small.

The detection limits of RBS have been extrapolated, for which the following expression holds [31].

$$N_{\square} = nE_0^2/Q\,\Delta\Omega Z_1^2 Z_2^2, \qquad (3)$$

with

$N_{\square}$ = minimal areal impurity concentrations [at/cm^2],
n = number of counts,
$\Delta\Omega$ = detection solid angle,
E_0 = incident energy,
Q = analysing ion dose/point.

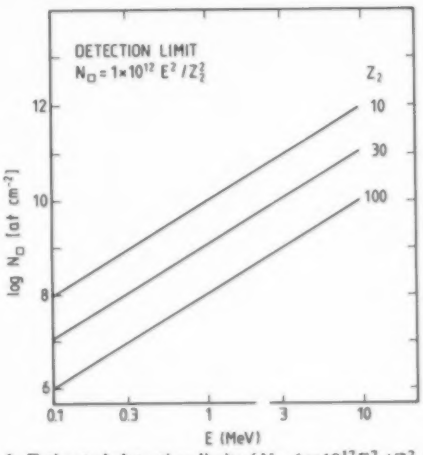

Fig. 1. Estimated detection limits ($N = 1\times10^{12}E^2/Z_2^2$ for a substrate heavier than carbon with the following parameters: ^{4}He Z_2/C, $I = 1$ μA, $n = 70$ counts, $\Delta\Omega = 0.3$ sr, $t = 2$ h. Background contributions were neglected (from ref. [31]).

The diagram shown in fig. 1 was obtained using realistic values for the detector solid angle and measuring times. Nitrogen analysis of thin silicon nitride layers using RBS have been reported [101].

3.2. Elastic recoil detection

The measurement of the recoiling particle from an elastic collision is the complementary method to RBS. It is preferentially used for detecting light elements in a heavy matrix using heavier projectiles than the element to be analysed. That procedure allows to select the detection angle such that only the light recoil can be detected. In case for nitrogen analysis heavy projectiles like Ar, Kr or Xe should be used at energies high enough to reach a sufficient analysis depth. The method further requires a particle identification for the recoils because many different elements may be present in the sample which recoil all simultaneously under heavy particle bombardment [96].

3.3. Nuclear resonance scattering

Some excitation functions of the elastic scattering of light projectiles, like protons and α-particles show in the accessible energy range at specific energies pronounced resonances. These resonances are caused by the nuclear structure of the compound nucleus formed during the collision, thus they appear with different strength at different scattering angles. They can be very versatile in analysing materials because the width of the resonance can be directly correlated to the

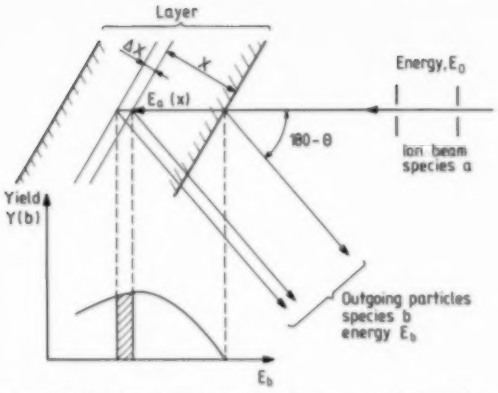

Fig. 2. Principle of NRA analysis for cross sections without resonances.

depth resolution in the material. Thus the smaller the width of the resonance the better the depth resolution. The achievable depth resolution depends, however, on the depth itself and the energy loss the projectile experiences in penetrating the host matrix. Detailed values can be obtained from formulas compiled in ref. [26].

3.4. Nuclear reaction analysis (NRA)

Most of the reactions listed in table 1 and 2 have been investigated in the past, mainly angular distributions have been measured, so that differential cross sections for these prompt reactions are available [32]. If projectiles penetrate into the material they loose energy, the reaction thus takes place at energies smaller than the incident energy, therefore excitation functions in the laboratory system are needed for the application of a specific reaction for materials analysis.

The proceedure is shown in fig. 2 for a nonresonant reaction. The measured yield $Y(E_b)$ can then be analysed using the following expression:

$$Y(E_b)\,dE_b = I N_A(x) \frac{d\sigma(E_a(x), \theta)}{d\Omega} \times \frac{\Delta\Omega\, dE_b}{(dE/dx)\cos\theta}, \quad (4)$$

with

I = number of beam particles,
$N_A(x)$ = distribution of atoms A in the target at depth x,
$d\sigma/d\Omega$ = differential cross section,
$\Delta\Omega$ = detector solid angle.

Even that the method is in principle applicable in all cases, practical restrictions exist which make some reactions less favourable, particular if the spectra of ejectiles overlap considerably. The limitations are mainly caused by the quantity and availability of cross sections. As can be seen from the tables some reactions require high projectile energies due to the large negative Q-values. Furthermore reactions with smooth excitation functions are easier to apply than those with a few or many very pronounced resonances because cross sections have to be integrated along the penetration path of the particle in the material which may give rise to ambiguities causing larger errors. On the other hand, resonances in the cross section allow very accurate depth profilings.

The detection limits for NRA can be estimated [31], resulting in the following expression

$$N = Y_m E/Q\Gamma\eta\,\Delta\Omega(d\sigma/d\Omega), \quad (5)$$

with

Y_m = $[1 + (1 + 8U(\Delta S/S)^2]^{1/2}/Q(\Delta S/S)^2$ maximum yield,
S = $Y_m - U$ number of signal counts,
ΔS = standard deviation in S,
U = number of background counts,
$\eta\Delta\Omega$ = incident intrinsic efficiency of the detector times solid angle,
Γ = resonance width [eV] (Lorentzian).

3.5. Nuclear resonance reaction analysis (NRRA)

Resonances in the excitation function of a nuclear reaction allow to profile the elements to be analysed. The procedure is shown to fig. 3. The upper left figure shows the excitation function with one resonance occuring at the energy E_R. The lower right part of the figure shows the experimental condition, an ion beam penetrates into the sample. The upper right hand part

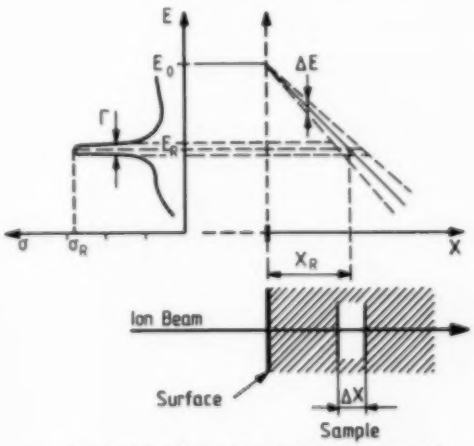

Fig. 3. Principle of NRRA analysis (details see text).

connects the two parts of the figure, showing the slow down in energy of an ion beam.

The moment the projectile energy approaches the resonance energy E_R, the increasing cross section causes a larger yield of the measured quantity, which can be a particle yield or a γ-ray yield. Thus the width of the resonance determines the depth resolution.

A relevant example is the detection of ^{15}N in a host matrix using the $^{15}N(p, \alpha\gamma)^{12}C$ reaction. The width of the first resonance has been measured to be 120 ± 30 eV [33]. This figure leads to a depth resolution of about 20 nm in a depth of about 10 μm.

It is, however, less favourable, if several resonances occur, as in the above mentioned example (cf. fig. 10). The depth profiling is unambiguously possible as long as a second resonance at higher incident energies has not reached the surface according to the energy loss of the projectiles, or if the strength of resonances are considerably different.

3.6. Charged particle activation analysis

As indicated in tables 1 and 2 a few nuclear reactions produce radioactive final nuclei. Most of the products of nuclear activation in the nitrogen region are positron emitters with reasonably long half-lives. That allows to use them to determine the amount of nitrogen in a given sample.

The procedure of analysis is shown in fig. 4, where the activation of a sample is plotted against measuring time on a semilog scale. Three periods have been distinguished. Period 1 is the activation period which should last long enough to produce a sufficient large number of decaying nuclei. In general it is sufficient to activate for about 5 times the half-life of the radioactive nucleus.

Also under very good vacuum conditions material is deposited on the surface during the irradiation, which will thus also be activated. The surfaces have thus to be cleaned. If these layers contain atoms of the element under investigation it is necessary to remove such layers from the surface before measuring the activity. This period 2 is indicated as sample handling.

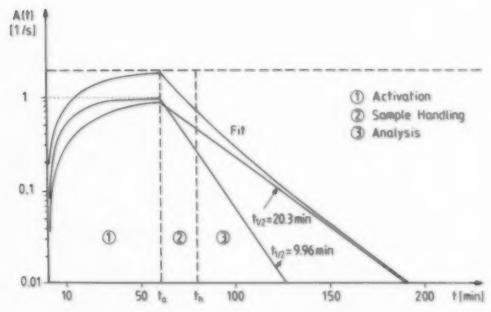

Fig. 4. Principle of CPAA (details see text).

After the cleaning process the measuring period 3 starts. The measurement itself is a counting procedure as long as reasonably long half-lives exist. For the analysis of nitrogen this is the case, if ^{11}C, ^{13}N and ^{18}F are produced. The other radioactive nuclei ^{14}O, ^{15}O, ^{16}N and ^{17}F can be used for the analysis if a fast automatized sample handling is available and the surface cleaning can either be fast, or surface contaminations can be avoided at all. The advantage would be the short analysis time, however, for the reactions producing ^{14}O and ^{17}F, the energy of the activating particles has to be sufficiently large. The measured quantity is then calculated from the following expression

$$K = \frac{N_0 A l}{\dot{i}\epsilon\bar{\sigma}R(1 - e^{-\lambda t_a})N_A} \left[\mathrm{kg/m^3}\right],$$

with

N_0 = counting rate at time t_a (extrapolated),
A = atomic mass number,
l = isotope abundance,
$\dot{i}$ = averaged projectile current,
ϵ = efficiency of the measurement system,
$\bar{\sigma}$ = cross section averaged for the activation,
R = projected range of the projectiles,
λ = decay constant,
N_A = Avogadro's number,
t_a = time of activation.

The quantity determined is an integral quantity for the volume irradiated, profiling is in general not possible unless the sample is irradiated several times under different incident angles [34]. That procedure is similar to a tomography. The beam diameter should therefore be small and the time between two successive irradiations should be long enough to allow the decay of the preceeding activation. By charge particle activation quantities of impurity or doping elements in the ppb range can be determined.

Difficulties arise if the trace element under analysis is incorporated into a matrix which can also be activated such that the signals from the radioactive decay of the trace nucleus is buried in the signals from the abundant activity. A comprehensive article [35] contains almost all reactions used for the detection of light particles by CPAA.

4. Nuclear reactions for nitrogen analysis

4.1. Reactions for the detection of ^{14}N

Nuclear reactions with ^{14}N as target material are listed in table 1. They produce stable as well as ra-

Table 1
Nuclear reactions on ^{14}N

Reaction	Q-value [MeV]	Half-life	Ref.
$^{14}N(n, p)^{14}C$	0.625	5730 a	[36,37]
$^{14}N(p, \gamma)^{15}O$	7.286	122.24 s	[39,40]
$^{14}N(p, n)^{14}O$	−5.926	70.6 s	[46]
$^{14}N(p, p)^{14}N$	0	prompt	[41–44]
$^{14}N(p, d)^{13}N$	−8.329	9.96 min	[47]
$^{14}N(p, \alpha)^{11}C$	−2.923	20.3 min	[48–51]
$^{14}N(d, n)^{15}O$	5.072	122.24 s	[52–56]
$^{14}N(d, p)^{15}N$	8.609	prompt	[57,58]
$^{14}N(d, \alpha)^{12}C$	13.574	prompt	[58,59]
$^{14}N(^3He, p)^{16}O$	15.242	prompt	[61,62]
$^{14}N(^3He, d)^{15}O$	1.802	122.24 s	not reported
$^{14}N(^3He, \alpha)^{13}N$	10.024	9.96 min	[63]
$^{14}N(\alpha, \gamma)^{18}F$	4.416	109.7 min	[64]
$^{14}N(\alpha, n)^{17}F$	−4.735	64.8 s	[66]
$^{14}N(\alpha, p)^{17}O$	−1.192	prompt	[64,67]
$^{14}N(\alpha, d)^{16}O$	−3.111	prompt	[70]
$^{14}N(\alpha, \alpha)^{14}N$	0	prompt	[18,67,71]

dioactive final nuclei. The first group can be used for the analysis with prompt NRA, the second one for the CPAA. Subsequently all reactions with ^{14}N as target material are listed despite their previous use for analysis. Some characteristics of the reactions will be mentioned.

$^{14}N(n, p)^{14}C$ [36,37]
Cross sections have been measured for $E_n = 61$ meV to 34.6 keV. At $E_n = 25$ keV, $\langle\sigma\rangle = 0.81$ mb, at $E_n = 52.4$ keV, $\langle\sigma\rangle = 0.52$ mb. The reaction has been used for depth profiling [38] in metals like vanadium and in archaeometric pottery samples.

$^{14}N(p, \gamma)^{15}O$ [39,40]
Excitation functions have been measured in the energy range $E_p = 0.2$ to 3.6 MeV. Resonances have been observed at 1.06, 1.74, 2.36 and 2.49 MeV. The short half-life of ^{15}O limits the reaction in its applicability for CPAA.

$^{14}N(p, p)^{14}N$ [41–44,97]
Excitation functions have been measured from 0.9 to 4.1 MeV at different angles. Under 160° sharp resonances appear at 1.061, 1.744 ($\Gamma \approx 6$ keV), 3.192 ($\Gamma \approx 11$ keV, $d\sigma/d\Omega = 340$ mb/sr), 3.878 MeV ($d\sigma/d\Omega \approx 300$ mb/sr). For an analysis of thin GaN layers on Al_2O_3 the proton scattering in the energy range 1.7 to 2.3 MeV has been used [45]. The differential scattering cross sections measured under 170° show an enhancement over the Rutherford cross section of more than a factor 10 in the energy range 2.7 to 3.1 MeV [96].

$^{14}N(p, n)^{14}O$ [46]
Excitation functions have been measured in the range $E_p = 6$ to 12 MeV. Broad resonances appear at 8 MeV (100 mb), 8.2 MeV (100 mb), 10 MeV (115 mb). The extreme short half-life of ^{14}O reduces the feasibility for CPAA. The large negative Q-value limits the applicability of the reaction for materials analysis further.

$^{14}N(p, d)^{13}N$ [47]
Angular distributions have been measured for deuteron groups at many energies up to $E_p = 155.6$ MeV. The large negative Q-value limits the applicability of the reaction for nitrogen detection in CPAA, however, with sufficient high energies e.g. of tandem accelerators a larger depth can be scanned. Particles with very high energies from cyclotrons are less suited.

$^{14}N(p, \alpha)^{11}C$ [48–51]
Excitation functions have been measured from $E_p = 4$ to 22 MeV (fig. 5). The reaction has been used for CPAA analysis preferentially because the half-life of

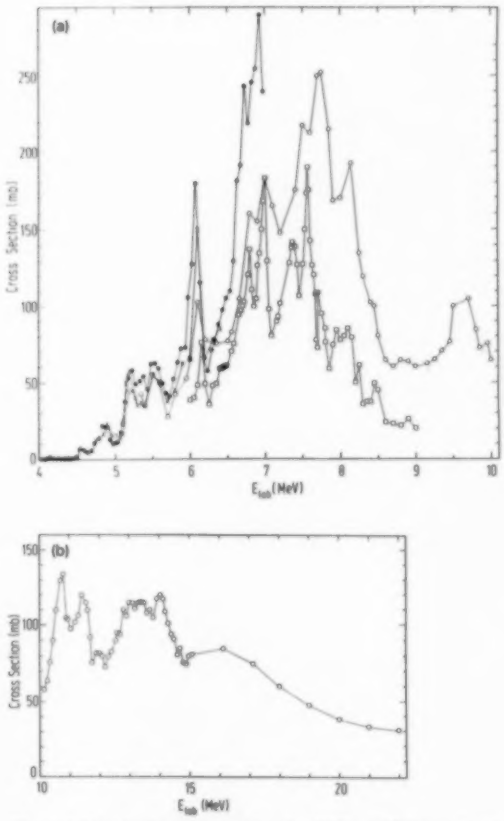

Fig. 5. (a) Excitation function for the $^{14}N(p, \alpha)^{11}C$ reaction in the energy range $E_p = 4$ to 10 MeV taken from different references (●) [48], (□) [49], (×) [50], (○) [51]. The reaction is well suited for CPAA. (b) Same as fig. 5a, energy range $E_p = 10$–22 MeV [48].

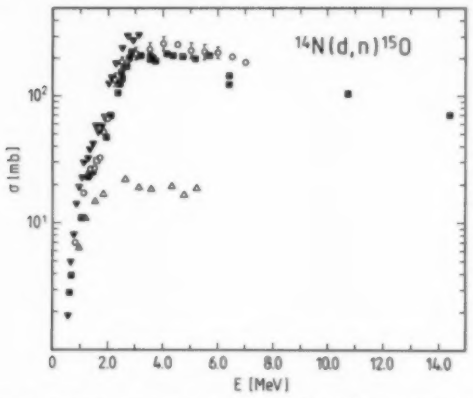

Fig. 6. Excitation function for the ^{14}N(d, n)^{15}O reaction (○) [53], (△) [54], (▼) [55], (■) [56].

^{11}C is very favourable. It has been used for the analysis of semiconductor materials.

^{14}N(d, n)^{15}O [52–56]
Excitation functions measured for $E_d = 0.6$ to 14 MeV, are compiled in ref. [53] (fig. 6). The short half-life of ^{15}O limits the reaction in its applicability for CPAA.

^{14}N(d, p)^{15}N [57]
Cross sections for different proton groups have been measured. For p_0 a small resonance appears at $E_d = 2.3$ MeV. For p_5 a maximal cross section of 160 mb/sr has been observed at $E_d = 2.0$ MeV. Absolute calibrations are reported [58], analysis of thin tantalum layers on glass at a bombarding energy of 650 keV have been reported [99].

^{14}N(d, α)^{12}C [59]
Excitation functions for α_0 and α_1 have been measured in the energy range $E_d = 0.6$ to 1.4 MeV. A resonance appears at 1.2 MeV in α_0. Spectroscopy of α-groups have been used in tracer technique after nitrogen implantation, in metallurgical applications [60,100] and for the analysis of semiconductor material like silicon [94].

^{14}N(^{3}He, p)^{16}O [61]
Differential cross sections have been measured in the energy range $E_{^3He} = 2.5$ to 5.5 MeV at angles 30, 90 and 150°. Excitation functions for several proton groups have been reported in the energy range $E_{^3He} = 3$ to 11 MeV [62].

^{14}N(^{3}He, d)^{15}O, not reported

^{14}N(^{3}He, α)^{13}N [63]
Differential cross sections for several α-groups have been measured in the energy range $E_{^3He} = 2.5$ to 8.5 MeV at 50, 90 and 165°. Maxima appear for α_0 at 165°: 4.5 MeV (2.5 mb/sr) and 5.5 MeV (3.0 mb/sr). In nuclear physics studies mainly the α-ejectiles have been measured, whereas for analysis of materials the decay properties of ^{13}N are more important. The reaction would be suitable for CPAA because of a reasonably long half-life of ^{13}N, but the production cross section is fairly small.

^{14}N(α, γ)^{18}F [64]
Excitation function has been measured up to 3 MeV. Three resonances appear at 1.39 MeV, 2.34 MeV and 2.87 MeV with sufficient intensity to use the reaction for analysis purposes (fig. 7). A resonance at 1.531 MeV has been used [65] for studies of dynamical behaviour of nitrogen diffusion in metals for tribological investigations.

^{14}N(α, n)^{17}F [66]
Excitation function has been measured between 6 and 20 MeV incident energy. Strong resonances appear at 9 MeV (120 mb) and 10 MeV (100 mb). The strengths would be sufficient for analysis but the short half-life of 64.8 s and the high threshold energy complicates the use. Analyses using that reaction have not been reported.

^{14}N(α, p)^{17}O [18,64,67,68]
Differential cross sections have been measured for incident energies $E_\alpha = 3.5$ MeV at 89 and 163.5°. Resonances appear at 3.7 MeV (24 mb/sr) and 4.5 MeV (20 mb/sr) in the 163.5° spectrum. Monotonous be-

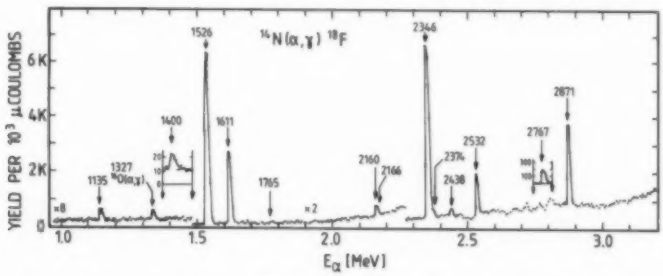

Fig. 7. Excitation of states in ^{18}F for the ^{14}N(α, γ)^{18}F reaction (from ref. [64]).

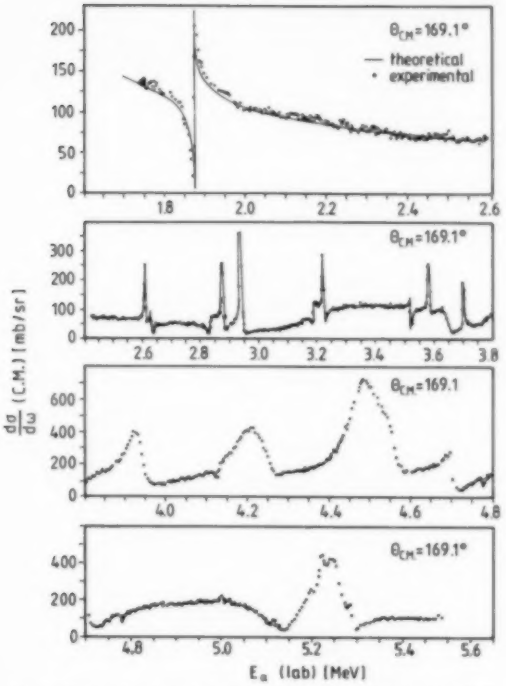

Fig. 8. Excitation function for the $^{14}N(\alpha, \alpha)^{14}N$ reaction [70].

haviour between $E_\alpha = 5$ to 6 MeV and a resonance at 6.55 MeV (30 mb/sr) has been observed at 172° [18]. The reaction can be used for NRA, in particular the resonance at 3.7 MeV ($\Gamma_p = 53 \pm 6$ keV). Thin layers of $Nb_xTi_{1-x}N$ on carbon substrates have been analysed using the energy range $E_\alpha = 5$ to 6 MeV.

$^{14}N(\alpha, d)^{16}O$ [69]
Spectra measured at 47 MeV incident energy. No application has been reported.

$^{14}N(\alpha, \alpha)^{14}N$ [18,67,70]
Differential cross sections have been measured for $E_\alpha = 1.6$ to 5.8 MeV (fig. 8). Several well separated resonances have been observed, which can be used for nitrogen analysis. E.g. resonance at 3.58 MeV ($\Gamma_\alpha = 4$ keV), resonance at 3.72 MeV (220 mb/sr, $\Gamma_\alpha = 53 \pm 6$ keV) (fig. 9). Nitrogen-implanted steel samples have been analysed, a depth resolution of 20 nm has been reported [18].

4.2. *Nuclear reactions for the detection of ^{15}N*

Nuclear reactions with ^{15}N as target material are listed in table 2. In most reactions stable nuclei are produced. Many excitation functions show pronounced

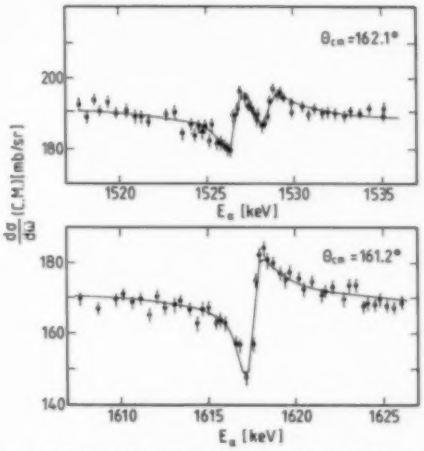

Fig. 9. Excitation function for two prominent resonances in the $^{14}N(\alpha, \alpha)^{14}N$ reaction [68].

resonances which allow to use these reactions for profiling nitrogen, however, not many reactions have been used for analyses. Some characteristics will be mentioned subsequently.

$^{15}N(p, \gamma)^{16}O$
The high excited level of ^{16}O (at 12.530 MeV) decays mainly by α emission into an excited state of ^{12}C. The γ-width Γ_γ is about 21×10^{-3} eV whereas the α-width Γ_α amounts to 120 eV. Thus the small γ-transition probability does not allow to use the capture reaction for materials analysis.

Table 2
Nuclear reactions on ^{15}N

Reaction	*Q*-value [MeV]	Half-life	Ref.
$^{15}N(p, \gamma)^{16}O$	12.127	prompt	[71]
$^{15}N(p, n)^{15}O$	−3.537	122.24 s	[74]
$^{15}N(p, p)^{15}N$	0	prompt	[75]
$^{15}N(p, d)^{14}N$	−8.609	prompt	not reported
$^{15}N(p, \alpha)^{12}C$	4.966	prompt	[71]
$^{15}N(d, n)^{16}O$	9.903	prompt	[52]
$^{15}N(d, p)^{16}N$	0.266	7.13 s	[76]
$^{15}N(d, \alpha)^{13}C$	7.687	prompt	[77]
$^{15}N(^3He, p)^{17}O$	8.55	prompt	[79]
$^{15}N(^3He, d)^{16}O$	6.633	prompt	[80]
$^{15}N(^3He, \alpha)^{14}N$	9.744	prompt	[81]
$^{15}N(\alpha, \gamma)^{19}F$	4.012	prompt	[82]
$^{15}N(\alpha, n)^{18}F$	−6.419	109.7 min	not reported
$^{15}N(\alpha, p)^{18}O$	−3.981	prompt	[76]
$^{15}N(\alpha, d)^{17}O$	−9.801	prompt	[69]
$^{15}N(\alpha, \alpha)^{15}N$	0	prompt	[70]

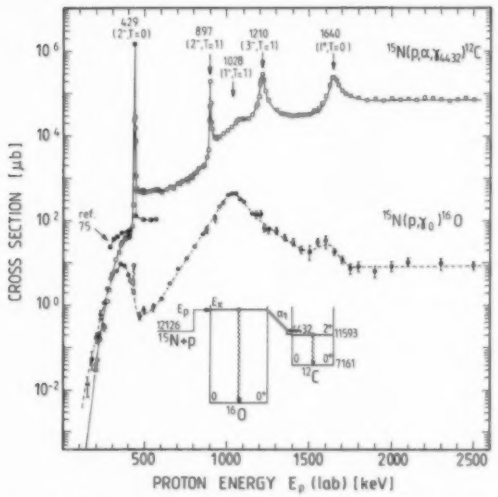

Fig. 10. Excitation function for the $^{15}N(p, \alpha\gamma)^{12}C$ reaction [71]. The detailed improved analysis of the first resonance is indicated as from ref. [72].

$^{15}N(p, n)^{15}O$ [74]
Excitation functions have been measured for $E_p = 3.8$ to 19.0 MeV. Differential cross sections have been measured under 0° for $E_p = 3.8$ to 6.4 MeV. Pronounced resonances appear at 4.37 MeV ($\Gamma_p = 19$ keV, 40 mb/sr) and 6.33 MeV ($\Gamma_p = 26$ keV, 40 mb/sr).

$^{15}N(p, p)^{15}N$ [75]
Differential cross sections for $\theta = 159.5°$ have been measured for $E_p = 1.0$ to 3.7 MeV. The main resonances appear at 1.02 MeV ($\Gamma_p = 100$ keV, $d\sigma/d\Omega =$ 260 mb/sr) and 3.5 MeV ($\Gamma_p = 15$ keV, $d\sigma/d\Omega = 220$ mb/sr).

$^{15}N(p, d)^{14}N$, not reported.

$^{15}N(p, \alpha)^{12}C$, $^{15}N(p, \alpha\gamma)^{12}C$ [71]
This reaction is most frequently used for nitrogen analysis because of its large cross section. According to the high positive Q-value the reaction produces a high lying level in ^{16}O which decays by α-emission to the first excited level in ^{12}C which than decays by γ-emission into the ^{12}C ground state. This reaction is very extensively used in materials analysis. The resonance at 0.429 MeV (cf. fig. 10) has a width of 120 eV [33]. The peak cross section exceeds the average cross section by more than five orders of magnitude [72]. This extremely strong resonance allows to determine ^{15}N in many host matrices despite the fact that ^{15}N has a natural abundance of 0.366%. The next resonance at 0.898 MeV ($\Gamma_\alpha = 600$ eV) has then to be considered because it may interfere in the analysis beyond a depth of about 5.5 μm (SiC). The yield has been measured for $E_p = 0.15$ to 27.4 MeV. The reaction is also applied to trace nitrogen circulation in biological and medical samples [73].

$^{15}N(d, n)^{16}O$ [52]
Excitation functions have been measured for $E_d = 0.5$ to 5.9 MeV at 0°. Pronounced peaks have been observed at 1.8 MeV (6 mb/sr), 3 MeV (4 mb/sr) and 5 MeV (3 mb/sr). Differential cross sections measured at 153.5° for $E_d = 4.3$ to 6.4 MeV show no pronounced structure.

$^{15}N(d, p)^{16}N$ [76]
Differential cross sections have been measured in the angular range 0 to 160° and the energy range $E_d = 4$ to 6 MeV. Some indications of resonances.

$^{15}N(d, \alpha)^{13}C$ [77]
Yield curves have been measured for $E_d = 0.8$ to 2.7 MeV. Structures are reported at $E_d = 1.06$, 1.25 and 1.8 MeV. The reaction has been applied for analysis to determine nitrogen in steel [78] to study the wear resistance.

$^{15}N(^3He, p)^{17}O$ [79]
Angular distributions measured for $E_{^3He} = 18$ MeV.

$^{15}N(^3He, d)^{16}O$ [80]
Angular distributions measured for $E_{^3He} = 11$ MeV.

$^{15}N(^3He, \alpha)^{14}N$ [81]
Angular distributions measured for $E_{^3He} = 2.7$ MeV.

$^{15}N(\alpha, \gamma)^{19}F$ [82]
Excitation functions have been measured for $E_\alpha = 5.2$ to 8.4 MeV.

$^{15}N(\alpha, p)^{18})$ [83]
Excitation function for $^{15}N(\alpha, p\gamma)^{18}O$ has been measured for $E_\alpha = 5.2$ to 8.4 MeV.

$^{15}N(\alpha, d)^{17}O$ [69]
Angular distributions for several deuteron groups measured at $E_\alpha = 47$ MeV.

$^{15}N(\alpha, \alpha)^{15}N$ [70]
Excitation functions have been measured for several angles and incident energies $E_\alpha = 1.6$ to 5.5 MeV. Several strong resonances have been observed under 170°.

4.3. Interfering reactions

If host materials which contain different impurity or doping elements are analyzed by ion beam methods special care has to be taken for interfering nuclear reactions which is an obvious fact for the CPAA. Table 3 contains a few reactions which can interfere if boron or carbon is present in the host sample. The (p, d) reaction on carbon is very unlikely to interfere because

Table 3
Nuclear reactions on ^{10}B, ^{11}B and ^{12}C

Reaction	Q-value [MeV]	Half-life	Ref.
$^{10}B(p, \gamma)^{11}C$	8.689	20.3 min	[83]
$^{11}B(p, n)^{11}C$	−2.764	20.3 min	[84]
$^{10}B(^3He, \gamma)^{13}N$	21.64	9.96 min	[85]
$^{11}B(^3He, n)^{13}N$	10.18	9.96 min	[86]
$^{12}C(p, d)^{11}C$	−16.497	20.3 min	[87]
$^{12}C(^3He, d)^{13}N$	−3.55	9.96 min	[88]

of its large negative Q-value which plays a role only at high energy analyses.

Other impurities and also the host material might cause interferences which has to be checked in each case separately. If the cross sections of the reaction used for analysis is small, a long activation time may also cause a considerable matrix activation, which in general might have larger decay times. In such cases the analysis becomes more complicated because of the background corrections.

5. Other methods of analysis

In industrial processes the analysis of materials has to be a routine procedure. Accelerator based method remain to a large extend in the domain of research and development departments. Thus efficient other methods of analysis are employed which in most cases are closely related to the final objectives for which the material should be used, e.g. conductivity measurements for conductors, semiconductors and insulators, hardness and wear tests for metals.

The use of mass spectrometers, however, is appropriate also to analyse materials and to measure profiles. For routine measurements the secondary ion or neutral particle mass spectrometry (SIMS, SNMS) have been successfully used. High resolution and very high sensitivity can also be achieved with glow discharge mass spectrometry (GDMS) for single element detection and with spark source mass spectrometry (SSMS) for simultaneous multielement detection. In case of GaAs analysis a detection limit for nitrogen of < 5 at. ppb has been obtained [89].

6. Selected examples of analysis

As indicated in the introduction nitrogen plays an important role in many different materials. Therefore the analysis of these materials is an essential contribution to the understanding of the material and its behaviour.

In metal physics it is of interest to profile nitrogen in different alloys in order to pursue tribological investigations. These profiles depend, however, on many parameters which have to be checked separately in order to understand their influence.

As an example a profile of ^{15}N is shown in fig. 11. The enriched isotope has been implanted under different conditions into Ti and Cr containing alloys. The profiles have been measured after implantation of nitrogen of different fluences. According to the sputtering of the material the profile changes into an asymmetric shape [90,91].

For semiconducting material the nitrogen content has also to be known quantitatively. Nitrogen is most probably incorporated as molecule in the silicon lattice, which causes vibrational lines in the absorption band. Two frequencies have been observed, at 767 cm^{-1} and at 963 cm^{-1}. The peak hight of these absorption lines is correlated to the concentration [N] of nitrogen in the crystal

$$[N] = \frac{\alpha}{\ln 10} F = E F_m / d = \alpha F_\infty,$$

where α is the absorption coefficient, E the extinction, d the sample thickness, $F_\infty = F/\ln 10$.

For the calibration it is necessary to measure the concentration [N] in independent experiments [51] which sensitivity should be about equal. For silicon this has been done by using the CPAA with the reaction $^{14}N(p, \alpha)^{11}C$, as well as in a separate IR absorption experiment using the absorption line at 963 cm^{-1} where the extinction E was measured.

The calibration factor F_∞ was then determined from the two independent measurements on the same sample

$$F_\infty = (1.72 \pm 0.27) \times 10^{17} \quad cm^{-2}.$$

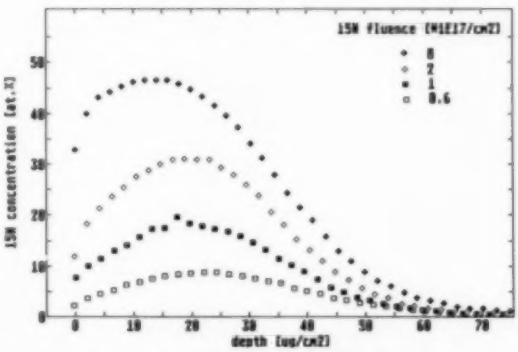

Fig. 11. Profile of nitrogen, implanted with different fluences into chromium at 30 keV [92].

This value is in good agreement with other published calibration factors [92].

Nitrogen has also been used as a marker to determine sputtering rates [93,94] in silicon. For that purpose nitrogen was implanted into the material. Its depth profile was measured using the $^{14}N(d, \alpha)^{12}C$ reaction before and after sputtering with argon ions. From three different α-groups (α_0, α_1, α_2) the difference in the thickness of the material layer to be sputtered could be estimated. The sputtering coefficients agreed with calculated values [95].

7. Concluding remarks

The survey of nuclear reactions presented in the preceeding chapters was restricted to nuclear reactions and scattering of light projectiles. Though these projectiles are used overwhelmingly in the present analyses of nitrogen, it might be possible that future trends of analyses tend towards heavier projectiles. Then ERDA (elastic recoil detection analysis) might become more important also for the analysis of nitrogen if projectiles like Kr or Xe are used at high energies. In addition to the accelerator development (energy resolution, stability) also a further development of the particle detection has to be pursued because reaction products with neighbouring masses have to be separated particular for ERDA. Especially the sensitivity of the detectors has to be improved for this method. Furthermore a need exists for better and more reliable data for the energy loss of heavy projectiles.

For additional reactions as well as for some of those mentioned above it is necessary to improve the nuclear data (values of cross sections as well as energies of resonance) as it was indicated in fig. 5a for the open and full symbols or to measure them for the first time to be able to use the full frame of reactions for the ion beam analysis of nitrogen.

The preceeding listing of reactions is not complete in the sense that it does not contain all references for these reactions. Many references from the compilation of F. Ajzenberg [32] did appear in Russian or Japanese journals which are not available in all libraries, to which the author had access.

Acknowledgements

In the course of preparing the contribution to the third conference on chemical analysis Dr. H. Baumann and Dr. G. Wolf contributed considerably which is greatly acknowledged. I wish to thank S. Kalbitzer, C. Rolfs, and W.A. Lanford for the permission to use some of their graphics of published results.

References

[1] G. Dearnaley et al., Nucl. Instr. and Meth. B7/8 (1985) 188.
G. Dearnaley, Nucl. Instr. and Meth. B50 (1990) 358 and references therein.
[2] D.M. Follstaedt et al., Nucl. Instr. and Meth. B12 (1985) 359.
[3] C.M. Preece and J.K. Hirvonen, Ion Implantation Metallurgy (AIME, Warrendale, PA, 1980).
[4] J.P. Hirvonen et al., Appl. Phys. Lett. 51 (1987) 232.
[5] H.J. Brading et al., these Proceedings (3rd Int. Conf. on Chemical Analysis, Namur, Belgium, 8–12 July 1991), Nucl. Instr. and Meth. B66 (1992) 230.
[6] B. Hoffmann et al., Nucl. Instr. and Meth. B28 (1987) 336.
[7] G. Terwagne et al., these Proceedings (3rd Int. Conf. on Chemical Analysis, Namur, Belgium, 8–12 July 1991), Nucl. Instr. and Meth. B66 (1992) 262.
[8] R.B. Alexander, Nucl. Instr. and Meth. B40/41 (1989) 575.
[9] W.J.M.J. Josquin, Nucl. Instr. and Meth. 218 (1983) 581.
[10] C.J. McHargue et al., Nucl. Instr. and Meth. B46 (1990) 79.
[11] N. Hatzopoulos et al., Nucl. Instr. and Meth. B55 (1991) 734.
[12] Lin Chenglu et al., Nucl. Instr. and Meth. B55 (1991) 742.
[13] W. Schröder, private communication.
[14] G. Goetz and H. Karge, Nucl. Instr. and Meth. 218 (1983) 1079.
[15] D. Bäuerle, private communication.
[16] M. Iwaki et al., Nucl. Instr. and Meth. 218 (1983) 1129.
[17] L. Grodzins, Nucl. Instr. and Meth. B56/57 (1991) 829.
[18] H. Artigalas et al., these Proceedings (3rd Int. Conf. on Chemical Analysis, Namur, Belgium, 8–12 July 1991), Nucl. Instr. and Meth. B66 (1992) 237.
[19] Z. Szökefalvi-Nagy and J. Räisänen, these Proceedings (3rd Int. Conf. on Chemical Analysis, Namur, Belgium, 8–12 July 1991), Nucl. Instr. and Meth. B66 (1992) 258.
[20] K. Bethge, Nucl. Instr. and Meth. A287 (1990) 210.
[21] R. Bloch et al., Nucl. Instr. and Meth. 59 (1968) 325.
[22] G. Bilpusch et al., Phys. Rep. 28 (1976) 145.
[23] J.B. Schroeder et al., Nucl. Instr. and Meth. B56/57 (1991) 1033.
[24] G. Amsel et al., Nucl. Instr. and Meth. 205 (1983) 5.
[25] P. Oberschachtsiek et al., Nucl. Instr. and Meth. B45 (1990) 20.
[26] J. Ziegler et al., The Stopping and Range of Ions in Solids (Pergamon New York, 1980).
[27] G. Amsel, B. Maurel, Nucl. Instr. and Meth. 218 (1983) 193.
[28] W. Lanford, these Proceedings (3rd Int. Conf. on Chemical Analysis, Namur, Belgium, 8–12 July 1991), Nucl. Instr. and Meth. B66 (1992) 65.
[29] T. Maisch et al., Nucl. Instr. and Meth. A288 (1990) 19.
[30] T.M. Stanescu et al., Nucl. Instr. and Meth. B50 (1990) 167.
[31] T. Maisch et al., Nucl. Instr. and Meth. B50 (1990) 1.
[32] F. Ajzenberg,
for $A = 13$–15: Nucl. Phys. A268 (1976) 1, A360 (1981) 1, A449 (1986) 1, A523 (1991) 1;

for $A = 16–17$: A281 (1977) 1, A375 (1982) 1, A460 (1986) 1;
for $A = 18–20$: A300 (1978) 1, A392 (1983) 1, A475 (1987) 1.
[33] B. Maurel and G. Amsel, Nucl. Instr. and Meth. 218 (1983) 159.
[34] E. Hanna Bakraji et al., Nucl. Instr. and Meth. B56/57 (1991) 896.
[35] J. Hoste and C. Vandecasteele, Nucl. Instr. and Meth. B40/41 (1989) 1182.
[36] P.E. Koehler and H.A. O'Brien, Phys. Rev. C39 (1989) 1655.
[37] K. Brehm et al., Z. Phys. A330 (1988) 167.
[38] D. Fink et al., Nucl. Instr. and Meth. 218 (1983) 171.
[39] A.E. Evans et al., Phys. Rev. 149 (1966) 863.
[40] U. Schroeder et al., Nucl. Phys. A467 (1987) 240.
[41] M.L. Wert et al., Phys. Rev. 179 (1969) 1047.
[42] E. Rauhala, Nucl. Instr. and Meth. B12 (1985) 447.
[43] S. Bashkin et al., Phys. Rev. 114 (1959) 1552.
[44] J. Olness et al., Phys. Rev. 112 (1958) 475.
[45] N.R. Parikh, Mater. Res. Soc. 128 (1989) 375.
[46] H.M. Kuan, J.R. Risser, Nucl. Phys. 51 (1964) 518.
[47] H. Curtis et al., Nucl. Phys. A165 (1971) 19.
[48] W.W. Jacobs et al., Phys. Rev. C9 (1974) 2124.
[49] P.D. Ingalls et al., Phys. Rev. 169 (1968) 842.
[50] P.N. Shrivastava et al., Phys. Rev. C13 (1976) 524.
[51] F. Köhl et al., Nucl. Instr. and Meth. B53 (1991) 80.
[52] J.L. Weil and K.W. Jones, Phys. Rev. 112 (1958) 1975.
[53] F. Köhl et al., Nucl. Instr. and Meth. B50 (1990) 19.
[54] T. Retz-Schmidt and J.L. Weil, Phys. Rev. 119 (1960) 1079.
[55] K. Wohlleben and E. Schuster, Radiochim. Acta 12 (1969) 75.
[56] H. Vera Ruiz and A.P. Wolf, Radiochim. Acta 24 (1977) 65.
[57] V. Gomes Porto et al., Nucl. Phys. A136 (1909) 385.
[58] J.A. Davis et al., Nucl. Instr. and Meth. 218 (1983) 141.
[59] G. Amsel et al., Nucl. Instr. and Meth. 92 (1971) 481.
[60] C. Neelmeijer et al., these Proceedings (3rd Int. Conf. on Chemical Analysis, Namur, Belgium, 8–12 July 1991) Nucl. Instr. and Meth. B66 (1992) 242.
[61] S. Gorodetzky et al., Nucl. Phys. 43 (1963) 92.
[62] P. Guazzoni et al., Phys. Rev. C4 (1971) 1086.
[63] A.R. Knudsen and F.C. Young, Nucl. Phys. A149 (1970) 323.
[64] C. Rolfs et al., Nucl. Phys. A199 (1973) 257, 300.
[65] G. Terwagne et al., Nucl. Instr. and Meth. B19/20 (1987) 145.
[66] W. Gruhle et al., Nucl. Phys. A186 (1972) 257.
[67] E. Kashy et al., Phys. Rev. 112 (1958) 547.
[68] H.B. Mak et al., Nucl. Phys. A343 (1980) 79.
[69] B.G. Harvey et al., Nucl. Phys. 39 (1962) 160.
[70] H. Smotrich et al., Phys. Rev. 122 (1961) 232.
[71] C. Rolfs and W. Rodney, Nucl. Phys. A235 (1974) 450.
[72] K.M. Horn and W.A. Lanford, Nucl. Instr. and Meth. B34 (1988) 1.
[73] Ph. Massiot et al., these Proceedings (3rd Int. Conf. on Chemical Analysis, Namur, Belgium, 8–12 July 1991), Nucl. Instr. and Meth. B66 (1992) 250.
[74] K.W. Jones et al., Phys. Rev. 112 (1958) 1252.
[75] S. Bashkin et al., Phys. Rev. 114 (1959) 1543.
[76] W. Bohne et al., Nucl. Phys. A196 (1972) 41.
[77] E.K. Warburton and N. McGruer, Phys. Rev. 105 (1954) 639.
[78] J.A. Sawicki et al., Nucl. Instr. and Meth. B15 (1986) 530.
[79] M.C. Lemaire, Phys. Rev. C5 (1972) 328.
[80] W. Bohne et al., Nucl. Phys. A128 (1969) 537; A160 (1971) 257.
[81] D.D. Clayton, Phys. Rev. 128 (1962) 2254.
[82] T.J.M. Symons et al., J. Phys. 64 (1978) 411.
[83] J. Peterson et al., Ann. Nucl. Eng. (GB) 2 (1975) 503.
[84] J.C. Overley and R.R. Borchers, Nucl. Phys. 65 (1965) 156.
[85] R.A.I. Bell et al., Nucl. Phys. A179 (1972) 408.
[86] T.H. Hsu et al., Nucl. Phys. A174 (1971) 365.
[87] E.K. Warburton and H.O. Funsten, Phys. Rev. 128 (1962) 1810.
[88] J.R. Comfort et al., Phys. Rev. C3 (1971) 1086.
[89] B. Wiedemann et al., 2nd Eur. Vacuum Conf., Trieste, 1990.
[90] T. Osipowicz et al., Nucl. Instr. and Meth. B18 (1987) 232.
[91] M. Rose, Diploma Thesis, Univ. Frankfurt, 1991.
[92] Y. Itoh and T. Nozaki, Appl. Phys. Lett. 47 (1985) 488.
[93] R. Weniger, Ph.D. Thesis, Univ. Frankfurt, 1984.
[94] K. Bethge, Nucl. Instr. and Meth. B10/11 (1985) 633.
[95] N. Matsumani et al, At. Data Nucl. Data Tab. 31 (1984) 1.
[96] Yang Guohua et al., Nucl. Instr. and Meth. B61 (1991) 175.
[97] I.M. Knox, these Proceedings (3rd Int. Conf. on Chemical Analysis, Namur, Belgium, 8–12 July 1991), Nucl. Instr. and Meth. B66 (1992) 31.
[98] G. Debras and G. Deconninck, J. Radiat. Anal. Chem. 38 (1977) 193.
[99] G. Weber and L. Quaglia, J. Radiat. Anal. Chem. 12 (1972) 323.
[100] J.C.B. Simpson et al., Nucl. Instr. and Meth. B24/25 (1987) 801.
[101] Y. Tamminga et al., Nucl. Instr. and Meth. 200 (1982) 499.

Nuclear Instruments and Methods in Physics Research B66 (1992) 158–190
North-Holland

Nuclear Instruments & Methods in Physics Research
Section B

Analysis of oxygen by charged particle bombardment

David D. Cohen and Edith K. Rose
Australian Nuclear Science and Technology Organisation, PMB 1, Menai NSW 2234, Australia

This review summarises the work done to mid 1991 on oxygen analysis using charged particle beams. Light ions (p, d, He) in the energy range 0 to 4 MeV are emphasised. Nuclear reaction analysis for the isotopes of oxygen are considered in detail particularly (p, α), (d, p), (d, α) and ^{3}He induced reactions and the latest nuclear and cross section data presented.

1. Introduction

In this paper we review the isotopic analysis of oxygen using low-energy light-ion bombardment. We have surveyed over 200 papers the majority of which we have referenced here [1–197]. They go back to the mid 1950's, however, we emphasise the more recent work done on ion beam analysis (IBA) of oxygen. Eighty-five percent of this published work refers to ^{16}O, about 4% to ^{17}O and about 37% to ^{18}O, the three stable isotopes.

Oxygen is a most important element, it forms 20.95% of the earth's atmosphere by volume and comprises nearly 50% by weight of the earth's crust. Approximate 65% of the human body and 90% of all water is oxygen. It is a very reactive element and forms stable oxides with many other elements. Oxygen is the third most abundant element found in the sun. It is essential for most life forms and for practically all combustion. Ozone (O_3) is a highly active form of oxygen formed by UV or electrical discharge action on oxygen. Its presence in the atmosphere, corresponding to about a 3 mm layer at sea level, is of vital importance in preventing UV from the sun reaching the planet's surface. It literally occurs everywhere, an ability to analyse for oxygen isotopes therefore is most important.

Oxygen has several isotopes, three are stable ^{16}O, ^{17}O and ^{18}O, while ^{14}O, ^{15}O, ^{19}O and ^{20}O are unstable with very short half lives which makes them of limited use as oxygen traces for analysis. Table 1 gives the abundances, isotope masses and half lives of oxygen isotopes. The average atomic weight is 15.9994. The atomic density of the gas at NTP is 4.302×10^{22} atom cm^{-3} and a mass density of 1.429 mg/cm^3 and 1.143 g/cm^3 for liquid oxygen at -183°C. It has a melting point of -218°C.

Stable isotopes of oxygen have been used in the studies of surface reactions and solid state phenomena

Table 1
Properties of isotopes of oxygen

Isotope	Mass	Abundance (%)	Half-life
^{14}O	14.0	–	71 s
^{15}O	15.0	–	124 s
^{16}O	15.994915	99.758	stable
^{17}O	16.999133	0.037	stable
^{18}O	17.999160	0.204	stable
^{19}O	19.0	–	29 s
^{20}O	20.0	–	14 s

such as oxidation of metals and semiconductors, diffusion in solids and high resistivity silicon. IBA techniques for oxygen are particularly applicable for thin oxide films involving small submicrogram quantities. For example thin silicon dioxide films are used extensively for insulation and masking devices during semiconductor manufacture. The thickness and composition of these structures determines the performance of these devices. Also many protective corrosion coatings and passifying coatings consist of inert oxide films. The properties of such films are well analysed by nuclear methods using low energy ion accelerators.

Kaim and Palmer [24] have used ^{3}He nuclear reaction analysis to analyse the light elements carbon, nitrogen and oxygen (up to 1 at.%) in niobium, a metal which has considerable importance in high-temperature applications in fission and fusion reactors. These light-element impurities play significant roles in the mechanical properties of niobium and its radiation damage behaviour.

^{18}O tracers have been used to study dispersion of water in consolidated porous medium such as reservoir rock core [97]. The collected fluids were turned into solid samples by standard anodizing techniques and analysed using ^{18}O(p, α)^{15}N reaction to give the rock dispersivity. Cohen et al. [98] have used similar meth-

0168-583X/92/$05.00 © 1992 – Elsevier Science Publishers B.V. All rights reserved

ods for ^{18}O tracers to monitor metabolic rates of lizards in Australian deserts using blood plasma samples as small as 150 μl.

Recently it has been suggested [103] that analysis of the three isotopes of oxygen in the atmosphere may serve as a unique tracer for stratospheric–tropospheric mixing, ozone–oxygen cycling and atomic oxygen protoproduction rates. Thiemens and Meagher [103] describe a nice method of cryogenic separation of oxygen and nitrogen in air for both isotopic ratio determination by mass spectrometry or other means [104].

Proton induced reactions on ^{16}O and ^{18}O play significant roles in oxygen burning in stars [5]. The $^{16}O(p, \alpha)^{13}N$ reaction produces ^{13}N which would subsequently be converted into ^{12}C via photodisintegration, hence providing additional sources of ^{12}C and alpha particles. To ascertain the significance of this reaction in explosive nucleosynthesis, its rate must be established at temperatures around 4×10^9 K. This corresponds to proton energies between 5 and 9 MeV, ideal for low-energy charged particle accelerators.

The study of oxygen in carbon–nitrogen–oxygen (CNO) cycle in stars with masses greater than one solar mass is important in understanding the nucleosynthesis of stars during their hydrogen burning phase [116,143,168]. Temperatures in stars can exceed 2×10^9 K. Lorenz et al. [116] have studied ^{18}O burning via $^{18}O(p, \gamma)$ and (p, α) reactions over the proton energy range 72–935 keV which covers the important temperature range $(0.5–25) \times 10^8$ K, while recent work by Landre et al. [143] uses the proton stripping reaction $^{17}O(^3He, d)^{18}F$ to study proton widths of states in ^{18}F near threshold. Their measurements lead to substantial changes in the stella reaction rate for $^{17}O(p, \alpha)^{14}N$ reaction, which in turn leads to a readjustment in the isotopic ratio $^{16}O/^{17}O$ in red giant stars. They also point out that they could find no experimental data before November 1989 below 400 keV for the specific reactions $^{17}O(p, \alpha)^{14}N$ and $^{17}O(p, \gamma)^{18}F$ which destroy ^{17}O in stars.

Many of the examples we have quoted do not easily lend themselves to conventional analytical techniques such as wet chemistry especially when high sensitivity, good depth resolution and nondestructive analysis of small samples are required. The nuclear techniques described below are an attractive alternative. Charged particle beams of light ions p, d and He, with energies 0 to 4 MeV, have ranges in most materials of much less than 100 μm and are readily tailored for nuclear reaction analysis (NRA).

We have restricted this review to the energy range 0–4 MeV for a good reason; it corresponds to ion energies below or near the Coulomb barrier for oxygen (2.3 MeV for protons, 4.6 MeV for helium ions), so we do not have to deal with too many resonant nuclear reaction processes or reaction channels. Furthermore, the energy and current range required is easily covered by the vast majority of the hundreds of charged particle accelerators found in physics laboratories around the world. Many of these accelerators were developed in the 1960's for nuclear structure studies and these, together with many recently purchased electrostatic accelerators, are now being used to great effect for nondestructive ion beam analysis.

In section 2 of this review we describe the IBA techniques required for oxygen analysis including reaction kinematics and yield calculations, in section 3 we provide detailed information on the most common nuclear reactions used for oxygen analysis, while in section 4 we describe how to prepare good reference standards for oxygen analysis.

2. IBA techniques

Historically oxygen was first studied using nuclear reaction analysis techniques by Amsel [189], in the early sixties, for the 1165 keV resonance in the $^{18}O(p, \alpha)^{15}N$ reaction. Much more pioneering work has followed this over the past three decades [67,82,86,138,139,157,180,187] on oxygen analysis and sample preparation.

Deconninck [156] points out that even as early as 1978 there were about one hundred original papers on the subject of IBA techniques for oxygen analysis, and quotes the six most popular reactions then as

$^{16}O(d, p)^{17}O$	$Q = 1.918$ MeV,
$^{16}O(d, \alpha)^{14}N$	$Q = 3.111$ MeV,
$^{17}O(^3He, \alpha)^{16}O$	$Q = 16.435$ MeV,
$^{18}O(p, \alpha)^{15}N$	$Q = 3.980$ MeV,
$^{18}O(\alpha, n)^{21}Ne$	$Q = -0.699$ MeV,
$^{18}O(p, n)^{18}F$	$Q = -2.438$ MeV.

Typical experimental conditions for these reactions were proton energies of a few MeV, deuteron energies between 0.8 to 1 MeV and ^3He energies between 2 and 5 MeV. Several MeV for (α, n) and (p, n) reactions with negative Q were most common.

In table 2 we have listed the common nuclear reactions used for oxygen analysis found in our survey of 200 or so references. We also give typical incident ion energies, analytical sensitivities and depth resolutions where information is given. Some of these more commonly used reactions for each isotope will be discussed in detail in the following sections. The table is set out in increasing incident ion mass then increasing isotope mass. The references quoted are not meant to be a comprehensive list of all references pertinent to that

Table 2
Typical incident ion energies, sensitivities and depth resolutions for nuclear reaction analysis of oxygen

Reaction	Incident energy [MeV]	Sensitivity [μg/g]	Typical resol. [nm]	References
$^{16}O(p, \gamma)^{17}F$	1–10	300		[29,40,45,51,70,117]
$^{16}O(p, p)^{16}O$	0.5–3	1–10 at.%	200	[34,54,56,61,122, 123,129]
$^{16}O(p, \alpha)^{13}N$	5.4–10	0.2–1.0 at.%	20–50	[5,71,114,161,162]
$^{16}O(d, p)^{17}O$	0.5–4.0	0.1–1.0 at.%	30–50 (×10 foils)	[2,3,8,10,13, 16,17,20,27, 38,48,55,65, 73,75,82,107, 110,112,114,120, 123,124,130,131,132, 135,147,150,153,155, 157,158,163,180,181, 182,187,195,196]
$^{16}O(d, \alpha)^{14}N$	0.5–2.0	0.3–1.0 at.%	20–50	[2,6,10,15,16, 37,39,44,74,107, 110,111,114,121, 132,147,150,153, 155,187,195]
$^{16}O(d, n)^{17}F$	2.5–3.5	0.1 μg/cm^2 100	450	[1,7,57,114,161, 187]
$^{16}O(t, n)^{18}F$	2–6	5 ppm, 5–25 ppb 4×10^{13} at/cm^2		[11,19,31,50,60, 64,71,114,161,162]
$^{16}O(^3He, p)^{18}F$	2–40	0.3 at.% 300 ppb at 18 MeV	150	[4,24,25,26,30, 33,36,38,41,52, 60,64,65,108, 118,125,126,127, 128,130,132,133, 162]
$^{16}O(^3He, \alpha)^{15}O$	2–10	0.1 at.%	10–30	[24,35,41,65,67, 108,124,125,126, 179,190,191,195]
$^{16}O(\alpha, \alpha)^{16}O$	2–3	3×10^{15} atoms/cm^2 1–10 at.%	5–15	[14,18,22,28,42,43, 49,53,56,58,59,60, 62,63,66,68,69,75, 106,109,115,119, 123,124,164,175,193 196]
$^{16}O(\alpha, n\gamma)$ $^{16}O(\alpha, n)$	2.4–3.5	875		[19,32]
$^{16}O(\alpha, p\gamma)^{19}F$	32			[69,76]
$^{16}O(\alpha, 'd)^{18}F$	45	5 ng/g		[30,64,162]
$^{16}O(\gamma, n)^{15}O$	16	1–35		[23,160]
$^{16}O(n, p)^{16}N$	14	1–3		[9,12,20,21, 46,47]
^{17}O		0.1–1.0 wt.%		[76,103,143, 166–169]
$^{18}O(p, p'\gamma)$	1.0–6.0	0.1 at.%	15–100	[5,76,80,86,91, 102,135,145,194]
$^{18}O(p, p)^{18}O$	1.0–6.0	1–10 at.%	200	[76,80,106,145,148]
$^{18}O(p, \alpha)^{15}N$	0.1–3.5	0.1 at.%	20	[2,24,79,82,83–87, 90,92–98,101,102, 105,106,111,113,116, 124,135,136,142,144, 145,146,151,156,157, 171,172,181,183,184, 185,187]

Table 2 (continued)
Typical incident ion energies, sensitivities and depth resolutions for nuclear reaction analysis of oxygen

Reaction	Incident energy [MeV]	Sensitivity [μg/g]	Typical resol. [nm]	References
$^{18}O(p, n)^{18}F$	2.5–20.0	70 ng/cm^2 0.01 at.%		[2,77,81,89,99,104, 114,135,144,161,176]
$^{18}O(d, p\gamma)^{19}O$				[76]
$^{18}O(d, \alpha)^{16}N$				[187]
$^{18}O(^3He, ^1d)^{19}F$	26.4			[88]
$^{18}O(\alpha, \alpha)^{18}O$	2.5–3.5	1–10 at.%	10–30	[7]
$^{18}O(\alpha, n\gamma)^{21}Ne$				[48,78]
SIMS		0.001 at.% 5×10^{17} cm^{-3}	1	[18,41,58,74,87,100, 149,154,184, plus lots more]
ERDA	2–5	5 at.%	50	[68,72,74]
Sample preparation				[2,90,92,96,97,98,105, 137,138,139,140,141, 142,157,180,183,184, 186,188]
Computer simulation				[124,152,172,190,197]

reaction but they should be a representative list that includes the majority of relevant data on that reaction.

The ^{16}O section contains 16 reactions and about 85% of the surveyed references, the ^{18}O section has nine common reactions and about 37% of the surveyed references, while all the ^{17}O reactions together contain only a handful of references on (p, γ), (d, pγ), (α, pγ), (p, α) and (^{3}He, d) reactions. These proportions strongly reflect the relative isotopic abundance and hence the usefulness of each isotope for oxygen analysis using ion beams. The fact that the ^{18}O abundance is a factor of 500 down on ^{16}O and the ^{17}O is nearly a factor of 2700 down on ^{16}O makes it no surprise that ^{17}O nuclear reactions would have to have particularly high cross sections to be useful for oxygen analysis.

The most population reactions for oxygen analysis are the $^{16}O + d$ reactions. These have the disadvantage that low deuteron energies and currents must be used to keep neutron production on light nuclei down. For this reason, recently the $^{16}O + {}^3He$ reactions and event the $^{16}O + \alpha$ elastic scattering reactions have become quite common. The $^{18}O + p$ reactions are by far the most common for this isotope.

Historically ^{3}He beams have only been used by relatively large accelerators, like cyclotrons. The earlier lower energy Van de Graaff accelerators, for example, operating below 2 MV or lower did not produce high enough yields for analysis of oxygen. Recently, however, with more accelerators operating in the 2 to 5 MV region both $^{16}O(\alpha, \alpha)^{16}O$ resonance scattering and $^3He + {}^{16}O$ reactions have become popular [24,35,65,67,124,179,190,191].

Abel et al. [67] quote the following advantages of ^{3}He-induced reactions: (1) lower neutron yields at medium energies than deuteron beams, and (2) possibility to carry out simultaneous ^{3}He RBS and NRA measurements which complement each other.

Rutherford Backscattering (RBS) using α particles for oxygen analysis routinely gives depth resolution 5–15 nm with sensitivity around 3×10^{15} atom/cm^2 with a small loss in depth resolution. (α, α) resonance scattering can increase this sensitivity by more than an order of magnitude which is particularly useful when looking at low level oxygen contained in thin layers such as GaAs–oxide interfaces in the study of passivation of GaAs surfaces by anodic or plasma oxidation [43].

A major drawback for the RBS analysis of oxygen is the fact that Rutherford cross sections are proportional to Z^2, the atomic number of the target. Hence small oxygen yields are superimposed on much larger high-Z backgrounds. However, as the incident energy is increased low-Z backscattering often becomes non Rutherford due to nuclear effects. For example, in oxygen at 2 MeV proton scattering is four times that of Rutherford [61]. Ref. [62] quotes cross sections for 2 to 5 MeV ^{4}He for elements above argon as being Rutherford but for lighter elements such as oxygen may be strongly non-Rutherford and should be measured, see Leavitt et al. [66] for example.

Similar measurements for oxygen on high temperature superconductors have also been performed by Barbour et al. [56] using 2.5 MeV protons and 8.7 MeV alphas with depth resolutions of 200 and 50 nm respectively giving ratios of cross sections to Rutherford of 5 for protons and 22 for alphas at these energies.

A quick survey of table 2 shows that an accelerator capable of producing p, d, ^{3}He and ^{4}He beams of a few

Table 3a
Q values for proton reactions

Target	Outgoing particle			
	n	d	t	α
^{16}O	−16.199	−13.439	−20.404	−5.2185
^{17}O	−3.544	−1.920	−11.326	1.191
^{18}O	−2.4379	−5.820	−3.7069	3.9804
^{12}C	−18.120	−16.497	−23.363	−7.551
^{14}N	−5.926	−8.329	−22.136	−2.923
^{19}F	−4.021	−8.206	−11.099	8.114

Table 3b
Q values for deuteron reactions

Target	Outgoing particle				
	p_0	p_1	n	t	α
^{16}O	1.9191	1.040	−1.623	−9.4065	3.1104
^{17}O	5.8199	3.836	3.384	2.113	9.7995
^{18}O	1.734	1.638	5.7685	−1.786	4.247
^{12}C	2.722	−0.367	−0.281	−12.465	−1.339
^{14}N	8.609	3.338	5.072	−4.296	13.574
^{19}F	4.377	3.721	10.624	−4.174	10.034

Table 3c
Q values for ^{3}He reactions

Target	Outgoing particle					
	p_0	p_1	n	d	t	α
^{16}O	2.0328	1.096	−3.196	−4.892	−15.435	4.915
^{17}O	8.321	8.209	4.298	0.113	−2.780	16.433
^{18}O	6.878	6.222	13.125	2.4998	−1.673	12.535
^{12}C	4.779	2.466	−1.147	−3.550	−17.357	1.856
^{14}N	15.242	9.193	−0.957	1.804	−5.162	10.025
^{19}F	11.890	11.540	7.562	7.355	−3.258	10.147

Table 3d
Q values for α reactions

Target	Outgoing particle					
	p_0	p_1	n	d	t	^{3}He
^{16}O	−8.114	−8.224	−12.1344	−16.321	−19.213	−16.433
^{17}O	−5.657	−6.313	0.590	−10.033	−14.208	−12.535
^{18}O	−5.598	−5.878	−0.693	−11.475	−11.8207	−16.620
^{12}C	−4.966	−10.236	−8.502	−13.574	−17.870	−15.632
^{14}N	−1.191	−2.062	−4.734	−3.111	−12.517	−9.745
^{19}F	1.676	0.401	−1.949	−6.463	−6.966	−13.976

MeV is a most useful tool for oxygen analysis to 1 at.% or better than with a depth resolution of 20 nm or so.

The table also lists a few key references on standard reference sample preparation and a few recent references containing computer simulation codes, such as RUMP [197], which are capable of fitting nuclear reaction spectra.

Secondary ion mass spectrometry (SIMS) [58,74,87, 149], is also a powerful low energy ion technique capable of low level oxygen analysis and depth profiling. However, this is considered to be outside the scope of this review and the references listed are for general interest only and only include references where comparisons for oxygen analysis have been made.

Several reactions listed in table 2 have more than one reaction channel which can proceed. For example, deutrons and ^{3}He ions not only produce p's and d's but also subgroups of these such as p_1 to p_8 or α_1 and α_2 depending upon the reaction kinematics, the Q for each reaction channel and the excited state of the product nuclei. In tables 3a–3d we list the Q values for proton, deuteron, ^{3}He and alpha reactions on oxygen producing the common outgoing particles α, p_0, p_1, n, d and t. We have also included other light nuclei ^{12}C, ^{14}N and ^{19}F which are often present in significant amounts in the target or detection systems and may produce interfering outgoing particles of similar energies. The reactions with negative Q values have thresholds for the incoming ion of energies at least as high as the Q value itself. For instance all (p, n) reactions listed in table 3a have negative Q values and hence, if neutron production is a problem, reactions involving proton energies below 2.4 MeV will not produce significant numbers of neutrons. High positive Q reactions are generally favoured for oxygen analysis as they produce outgoing particles of high energy which also are readily resolved in modern day detection systems. For example, the $^{16}O(^3He, \alpha)$ reaction below 3 MeV should be quite useful because it has a high Q value of 4.915 MeV but a negative Q value of −3.196 MeV for neutron production. The $^{16}O(d, \alpha)$ and $^{18}O(p, \alpha)$ reactions are similar but with somewhat lower Q values. This explains the relative recent popularity of these reactions for oxygen analysis. The $^{17}O + ^3He$ reactions have particularly high Q values and hence should be very useful for nuclear reactions analysis of this isotope. We see that reactions like $^{18}O(^3He, \alpha$ or p) are not so favoured because of the large positive Q value, 13.125 MeV for neutron production which means that even at low ^{3}He energies one has to cope with high energy neutrons. These tables are therefore very good for selecting appropriate nuclear reactions for analysis.

2.1. Reaction kinematics

We have already introduced the concept of Q value for a reaction and talked about incoming ion and outgoing particles energies. Nowadays for a full quantitative analysis using ion beams it is necessary to consider the nuclear reaction kinematics and yields. There

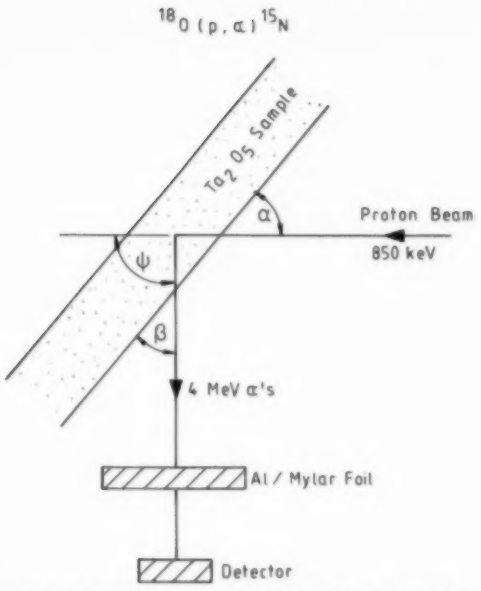

Fig. 1. Schematic of typical nuclear reaction analysis (NRA) experiment. The detector is usually a surface barrier detector and Mylar or Ni foils may be used to stop scattered particles reaching the detection system.

is nothing new about these concepts [55,170,173] and only the results are quoted here for completeness.

Consider a typical nuclear reaction experiment shown schematically in fig. 1. This particular reaction is the $^{18}O(p, \alpha)^{15}N$ reaction in $Ta_2^{18}O_5$ enriched target at the 846 keV resonance. The ion beam is incidence on the target at angle α shown, the outgoing particle is produced at depth in the sample, leaving the surface at angle β, resulting in a reaction angle $\psi = \alpha + \beta$. The outgoing particle may sometimes pass through a foil (such as Mylar or Al) used to stop scattering input ions from reaching the detector. Following the standard nomenclature of the Ion Beam Handbook [173] we have for the lab energy of the light product

$$E_3/E_T = B\left[\cos\psi \pm \left(D/B - \sin^2\psi\right)^{1/2}\right]^2, \quad (1)$$

where we use only the plus sign unless $B > D$, in which case $\psi_{max} = \sin^{-1}(D/B)^{1/2}$. Other parameters in eq. (1) are defined thus

$$E_T = E_1 + Q, \quad (2)$$

$$A = \frac{M_1 M_4 (E_1/E_T)}{(M_1 + M_2)(M_3 + M_4)}, \quad (3)$$

$$B = \frac{M_1 M_3 (E_1/E_T)}{(M_1 + M_2)(M_3 + M_4)}, \quad (4)$$

$$C = \frac{M_2 M_3}{(M_1 + M_2)(M_3 + M_4)}\left[1 + \frac{M_1 Q}{M_2 E_T}\right], \quad (5)$$

$$D = \frac{M_2 M_4}{(M_1 + M_2)(M_3 + M_4)}\left[1 + \frac{M_1 Q}{M_2 E_T}\right]. \quad (6)$$

Subscript 1 refers to incident ion, 2 to the target, 3 to the light product and 4 to the heavy product. Note also that $A + B + C + D = 1$ and $AB = BD$.

The centre of the mass angle of the light product θ is given by

$$\sin\theta = \left[\frac{E_3/E_T}{D}\right]^{1/2} \sin\psi, \quad (7)$$

and the ratio of the centre of mass cross section $\sigma(\theta)$ to lab cross section $\sigma(\psi)$ for the light product is given by

$$\frac{\sigma(\theta)}{\sigma(\psi)} = \frac{\sin^2\psi}{\sin^2\theta}\cos(\theta - \psi). \quad (8)$$

Table 4a
Oxygen-16 input/output energies and ranges in Mylar for selected reactions and angles

Reaction	Q [MeV]	Energy [MeV]			Range in Mylar [μm]			θ_{cm} [deg]	$\frac{\sigma_{cm}}{\sigma(160°)}$
		E_{in}	E_{out} 90°	E_{out} 160°	R_{in}	R_{out} 90°	R_{out} 160°		
(p, p)	0.0	1.0	0.881	0.783	18	15	12	160.0	1.00
(d, p_0)	1.9191	1.0	2.645	2.414	11	91	78	161.0	1.10
		2.5	3.893	3.456	53	175	143	161.3	1.13
(d, p_1)	1.049	1.0	1.823	1.633	11	49	41	161.2	1.12
		2.5	3.071	2.686	53	117	93	161.4	1.15
(d, α_0)	3.1104	1.0	3.085	2.607	11	14	11	161.8	1.19
		2.5	4.084	3.241	53	21	15	162.4	1.28
(^{3}He, p_0)	2.0328	2.5	3.896	3.394	12	176	160	161.4	1.15
(^{3}He, p_1)	1.096	2.5	3.009	2.572	12	113	87	161.6	1.18
(^{3}He, α)	4.915	2.5	5.457	4.327	12	32	23	162.4	1.28
(α, α)	0.0	2.5	1.499	0.927	11	6	4	160.1	1.01

Table 4b
Oxygen-17 input/output energies and ranges in Mylar for selected reactions and angles

Reaction	Q [MeV]	Energy [MeV]			Range in Mylar [μm]			θ_{cm} [deg]	$\frac{\sigma_{cm}}{\sigma(160°)}$
		E_{in}	E_{out} 90°	E_{out} 160°	R_{in}	R_{out} 90°	R_{out} 160°		
(p, p)	0.0	1.0	0.888	0.794	18	15	13	160.0	1.00
(p, α)	1.191	1.0	1.648	1.400	18	6.5	5.5	161.7	1.19
(d, p_0)	5.8199	1.0	6.351	6.006	11	411	375	160.6	1.06
		2.5	7.612	7.022	53	566	490	160.9	1.09
(d, p_1)	3.836	1.0	4.474	4.186	11	223	199	160.7	1.07
		2.5	5.735	5.226	53	343	292	161.0	1.10
(d, α)	9.7995	1.0	8.419	7.643	11	63	54	161.0	1.10
		2.5	9.444	8.175	53	76	60	161.5	1.16
(^{3}He, p_0)	8.321	2.5	9.898	9.116	12	902	779	160.9	1.09
(^{3}He, p_1)	8.209	2.5	9.793	9.016	12	885	763	160.9	1.09
(^{3}He, α)	16.433	2.5	14.767	12.912	12	147	122	161.4	1.15

Table 4c
Oxygen-18 input/output energies and ranges in Mylar for selected reactions and angles

Reaction	Q [MeV]	Energy [MeV]			Range in Mylar [μm]			θ_{cm} [deg]	$\frac{\sigma_{cm}}{\sigma(160°)}$
		E_{in}	E_{out} 90°	E_{out} 160°	R_{in}	R_{out} 90°	R_{out} 160°		
(p, p)	0.0	1.0	0.894	0.805	14	15	13	160.0	1.00
(p, α)	3.9804	0.84	3.761	3.424	14	19	16	161.0	1.10
(d, p_0)	1.734	1.0	2.495	2.293	11	82	71	161.0	1.09
		2.5	3.769	3.380	53	166	138	161.1	1.12
(d, p_1)	1.638	1.0	2.404	2.206	11	77	67	160.9	1.09
		2.5	3.678	3.294	53	159	132	161.2	1.12
(d, α)	4.247	1.0	4.097	3.592	11	21	17	161.4	1.15
		2.5	5.146	4.274	53	29	22	161.9	1.22
(^{3}He, p_0)	6.878	2.5	8.570	7.878	12	699	601	160.9	1.09
(^{3}He, p_1)	6.222	2.5	7.945	7.290	12	610	525	160.9	1.09
(^{3}He, α)	12.535	2.5	11.811	10.238	12	106	87	161.5	1.16

We have used eqs. (1)–(8) and the stopping power tables of ref. [177] to calculate outgoing particle energies $E_3 = E_{out}$ for given input ion energies $E_1 = E_{in}$ at two reaction angles 90 and 160°. The thickness of Mylar foil to just stop the incident ion and the outgoing light product and conversion factors from lab to centre of mass frame. These are listed in tables 4a–4d for ^{16}O, ^{17}O and ^{18}O reactions, respectively. The input ion energies of 1 and 2.5 MeV have been selected as those commonly used in the region 0–4 MeV covered by this review. Again we see the effects of the kinematics producing larger E_{out} values for larger Q values and lower E_{out} values for larger reaction angles as expected.

If the Mylar foil of fig. 1 is to be designed to just stop the scattered input ions but let the light product particle through then R_{in} must be significantly less than R_{out} in table 4. Otherwise a foil cannot be used for that reaction. Clearly foils are good for ^{3}He reactions with large Q values, but cannot be used for high energy, 2.5 MeV, (d, α) reactions because the range of α particles in the foil is less than the scattered deuteron at the appropriate energy. Foils that are necessarily thick enough to stop the incident ions may also produce large energy losses in the product particle and consequently large straggling losses which in turn effect depth profiling resolution for that reaction [178].

Table 4 also gives the conversion factors from lab frame to the centre of mass frame for the light product particle. Generally the angles differ by only a few degrees, however the cross sections can differ by more than 10%. It therefore becomes important to note which frame your measurements are quoted in, since modern nuclear reaction cross sections can be made to ±2 or 3% or better. Much of the more modern work performed since 1975 is quoted in the lab frame, while earlier work through the 1960's, by Amsel et al. see for example ref. [173], is in the centre of mass frame. However, many others have not bothered to note which frame their cross section results are quoted in. This

may explain some of the differences between graphical data presented later in this review.

2.2. Reaction yields

The nuclear reaction yields have been discussed at length for thin and thick targets, for resonant reaction cross sections, and for target concentration profiles in refs. [13,15,157,170,173]. As we expect Amsel to review this topic further in these proceedings we only quote the simple case of a uniform concentration profile in a thin target. Hence the counting rate N(Hz) into a peak for a given reaction of cross section σ(mb/sr) is given by

$$N = 10^{-27} I \Omega n \sigma \epsilon \quad \text{counts/s}, \tag{9}$$

where $I = i/(q \times 1.6 \times 10^{-19})$ is the beam current expressed as the number of incident particles/unit time. Ω is the detection solid angle (msr), n is the number of target atoms/cm^2 and ϵ is the detection efficiency (usually near 1). For a beam current $i = 1$ μA, $I = 6.25 \times 10^{12}$ particles/s of unit charge ($q = 1$), if $\Omega = 1$ msr, $\sigma = 1$ mb/sr and we have a count rate of 1 Hz into a peak, then for 100% detection efficiency, eq. (9) gives us a sensitivity of $n = 1.6 \times 10^{14}$ atoms/cm^2. Beam currents of 1 μA are typically quite high except for cooled or metal targets (1 μA at 1 MeV is 1 W), currents of 100 nA are typical for nuclear reaction studies so it is easy to see why resonant nuclear reactions with cross section of 10 mb/sr or higher are favoured for ultimate sensitivities around 10^{14} atoms/cm^2. For a 200 nm thick target of most materials we would expect between 10^{17} and 10^{18} atom/cm^2 so 10^{14} atoms/cm^2 oxygen atoms corresponds to 0.1 to 0.01 at.% sensitivity. A glance through table 2 shows that most practical sensitivities are an order of magnitude worse than this. This is mainly due to background or interfering reactions or reduced currents necessary to minimise target damage and heating effects.

The charged particle activation (CPA)-type reactions like ^{16}O(t, n)^{18}F, ^{16}O(^{3}He, p)^{18}F or ^{18}O(p, n)^{18}F require different yield calculations than those of eq. (9) because the heavier product (^{18}F) is a radioactive positron emitter decaying with a short half-life (109.7 min) to 511 keV annihilation γ-rays, which are used to analyse for the oxygen content. As shown in table 2, CPA analysis techniques can have particularly good detection limits for oxygen in the ppb region under favourable conditions. Bethge [38] gives the oxygen concentration (kg/m^3) for CPA as

$$C = \frac{N_0 W F_1}{i \epsilon \bar{\sigma} R (1 - e^{-\lambda T}) N_A}, \tag{10}$$

where N_0 is the initial counting rate (after activation), W is the mass number, F_1 is the isotopic abundance, i the average beam current, ϵ the detection efficiency, $\bar{\sigma}$ the average cross section, R the range of activating particles, T the irradiation time, λ the decay constant (ln $2.T_{1/2}$) and N_A Avogadro's number.

Table 5
Positron emitting (p, n) reactions may compete with the ^{18}O(p, n) reaction when using the 511 keV γ-rays for oxygen analysis. Taken from ref. [89]

Element	Reaction	Threshold [MeV]	$T_{1/2}$
O	^{18}O(p, n)^{18}F	2.4	109.8 min
	^{19}F(p, d)^{18}F	8.2	109.8 min
Ni	^{60}Ni(p, n)^{60}Cu	6.9	23.4 min
	^{61}Ni(p, n)^{61}Cu	3.0	3.4 h
	^{62}Ni(p, n)^{62}Cu	4.7	9.7 min
	^{64}Ni(p, n)^{64}Cu	2.5	12.7 h
Cu	^{63}Cu(p, n)^{63}Zn	4.2	38 min
	^{65}Cu(p, n)^{65}Zn	2.1	250 days
Zn	^{66}Zn(p, n)^{66}Ga	6.0	9.2 h
	^{67}Zn(p, n)^{67}Ga	1.8	3.3 days
	^{68}Zn(p, n)^{68}Ga	3.7	68 min

For the charge particle activation one has to be certain that oxygen is the only isotope activated and hence the only element contributing to the annihilation 511 keV γ-rays. These problems can be unfolded to some extent by looking at the decay of the 511 keV γ-ray with time and waiting for short-lived contributions, like ^{11}C (20.4 min) or ^{13}N (9.96 min), to decay away [38,89]. However, this also reduces the techniques sensitivity to oxygen analysis. Wai and Dysart [89] list potential interfering positron emitters produced during proton activation of oxygen. For example, the ^{18}O(p, n)^{18}F reaction has a threshold of 2.4 MeV and reaches a maximum cross section of about 0.5 b at around 5 MeV. At this proton energy, table 5 taken from their work, shows other (p, n) reactions in Ni, Cu and Zn which are positron emitters with half lives comparable to that of ^{18}F. They point out that radiochemical separation of ^{18}F may become necessary to obtain the best sensitivities.

3. Reference standards

One of the basic requirements of many analytical techniques is the production of stable, uniform, well characterised reference standards and ion beam analysis is no exception. For oxygen analysis using ion beams the reference standards typically used are Ta_2O_5, SiO_2 or Al_2O_3 [2,138–141,142,181,183,186], with Ta_2O_5 being the preferred standard [92,96,98,140,141]. Generally the nature of the target backing is unimportant provided it is a material with high enough atomic number to avoid interfering nuclear reactions and of high enough purity so that no unwanted signals appear

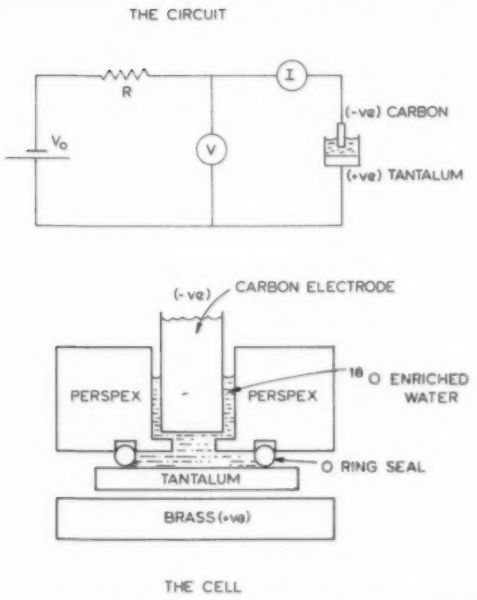

Fig. 2. The circuit and anodising cell used to prepare Ta_2O_5 reference standards of known thickness.

from trace elements in the backing. For high current ion beams (several hundred nanoamperes) tantalum metal is ideal because it withstands the heating and ionising effects of the beam, it is easy to obtain in the very pure state and it is easy to oxide in dilute aqueous solution. We have used Ta_2O_5 standards in our laboratory now for nearly nine years with very little deterioration. The standard deviation of several hundred results taken over this time is better than $\pm 2\%$. Similar long term stability under ion bombardment has been noted by Amsel et al. [138].

The Ta_2O_5 reference standard is prepared by normal anodic oxidation techniques [138]. The film thickness is strictly proportional to the voltage drop across the film during anodisation for a given cell current and temperature. The use of Ta_2O_5 reference standards for ion beam analysis work was pioneered by Amsel and the Paris group 30 years ago.

Fig. 2 shows a schematic of a typical cell and the simple electronics used to drive it. The current is limited to 1 to 2 mA/cm^2 since at higher values heating effects in solution may be detrimental. Cells of this type to anodise tantalum using aqueous solutions of as little as 150 μl have been used by Cohen et al. [92,98]. This may be important when using very small samples of the expensive rarer isotopes such as ^{18}O or ^{17}O enriched water. The tantalum foil is typically 1 cm^2 99.95% pure, 0.2 mm thick and good electrical contact is ensured by polishing the brass electrode and pressing the Ta backing firmly onto it using the perspex cell block and rubber O-ring to seal.

It is most important to polish the Ta metal before anodising. Firstly, degrease in acetone and then rub gently with 1200 wt and dry paper under flowing water. Do not overdo this as the surface may work harden or you may reveal grain boundaries and affect the oxide layer's adhesion properties. Chemically polish for 15 to 20 s in a mixture of 50 cc of 95% H_2SO_4, 20 cc of 50–70% HNO_3 and 20 cc of 45–48% HF. If the oxide layer is to stick properly to the substrate it is most important to then wash this thoroughly for 5 min in boiling triple-distilled water to completely remove all traces of acid.Amsel et al. [138] stress that chemical polish is essential to obtain reliable standards as unpolished or ill-polished samples will produce electronic losses during anodising that will affect the results.

The cell electrolyte should be triply distilled water (^{16}O) with 5% by weight ammonium citrate solution buffered to pH = 6 with ammonia. The temperature should be constant and noted. Other electrolyte solutions work just as well, e.g. 0.01N H_2SO_4, 1% NaCl or KCL, and 0.0016M orthophosphoric acid [2,140,188].

Using the cell and circuit of fig. 2, the oxide thickness (t(Å)) is given by

$$t = a(V+b)(T+c), \tag{11}$$

where a, b and c are constants and T is temperature (°C) and V is the voltage across the film. Oxide thickness (^{16}O) before anodising and after polishing is typically 40–50 Å thick. Recent values for the film density $\rho = 8.20$ g cm^{-3} [140] are higher than previously quoted values of 8.03 g cm^{-3} [138] and 7.93 g cm^{-3} [142]. The conversion from thickness t(Å) to n(atoms/cm^2) for Ta_2O_5 is:

$$n = (5N_0\rho t/W) \times 10^{-8} \quad \text{atoms/cm}^2 \tag{12}$$

$$= 5.5874 \times 10^{14} t(\text{Å}) \quad \text{atoms/cm}^2, \tag{13}$$

where $N_0 = 6.022 \times 10^{23}$ and $W = 441.893$ for $Ta_2^{16}O_5$.

Eq. (11) shows that for a given temperature T the thickness t(Å) is proportional to the voltage V. A plot of t, as measured by standard ellipsometry techniques [174], versus V is indeed a good linear fit. Such a plot is shown in fig. 3 and taken from ref. [98]. It assumes the complex refractive index of tantalum is $n_1 = 2.145$ and for Ta_2O_5 $n_2 = 3.3–2.25i$ and gives a slope of 16.42 Å/V at 20°C.

Eqs. (11)–(13) then show that for say a 120 V target (1970 Å) at 20°C we have ~4% change per 10°C change in temperature and it contains 1.10×10^{18} atoms/cm^2. This demonstrates the need to maintain the temperature constant to within a few degrees if targets of 1% precision are to be made.

Recent work by Nwosu and Fischbeck [96] show that this constant of proportionality is a function of the

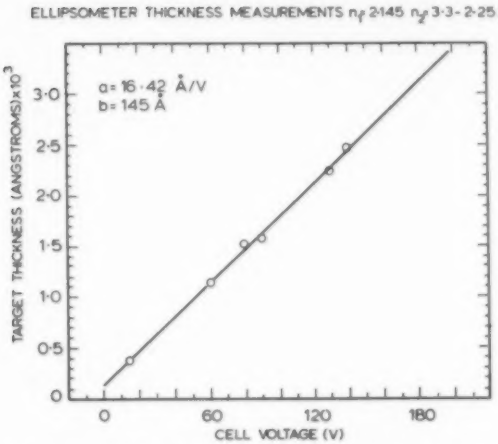

Fig. 3. Typical plot of Ta_2O_5 thickness as measured by ellipsometry techniques versus cell voltage. The complex refractive index for Ta was 2.145 and its oxide 3.3–2.25i.

electrolyte and its pH being only 15.7 ± 0.3 Å/V for distilled water and 16.3 ± 0.2 Å/V for 3% by weight ammonium citrate (pH = 6.5). Their values for serum, plasma and urine samples at pH values from 6 to 8 are given in table 6 and show that this constant increases with increasing pH.

Targets from 0 to 150 V corresponding a few nanometres to 250 nm are readily prepared on tantalum. Hence thin targets can easily be prepared for nuclear reaction cross section work. For instance, for the 846 keV proton resonance in $^{18}O(p, \alpha)^{15}N$ reaction the stopping power of protons in Ta_2O_5 is around 103 MeV cm^2 g^{-1} giving an energy loss of ~8.4 keV/100 nm of oxide film. So for a 10 V $Ta_2^{18}O_5$ target the proton loss in the target is only 1.4 keV at 846 keV more than sufficient to measure the 47 keV wide resonance at this energy, even at small reaction angles.

The oxide layers formed on tantalum by this technique are very stable and uniform and their thickness is well characterised by their colour [92]. These colours are clearly visible, if a perspex cell is used, as the film voltage drop increases. Colours for the first order processes are straw brown, mauve, deep blue, corresponding to 12–38 V then blue becoming lighter and finally disappearing and becoming colourless (38–62 V). At about 60 V the second order appears starting with gold, yellow, orange, mauve and then sky blue (62–125 V). At around 105 V the third order appears before the second has reached the infrared from 105–135 V the second and third orders overlap mixing colours producing green. At greater thickness overlapping of many orders occurs more frequently and at around 300 V four bands overlap and the colour is an uninteresting matt grey.

Seah et al. [141] recently compared the measurements of 6 international laboratories on a round robin of two Ta_2O_5 standards prepared using the above methods and found that results agreed to better than $\pm 2.2\%$ on the thin 30 nm sample and $\pm 1.9\%$ on the 100 nm sample. Analysis techniques include $^{16}O(d, p)^{17}O$, RBS and ERDA and this close agreement shows that we can can, with care, prepare standard reference oxide layers for ion beam analysis using these analysing techniques on tantalum.

In a similar fashion to that described above aluminium and silicon can be anodised [2]. For aluminium the electrolyte is usually ammonium citrate and yields film thicknesses of 13.7 Å/V with base oxide thicknesses of between 5 and 10 nm. For high purity silicon wafers dry glycol containing 0.4% KNO_3 in water yields film thickness of 6.2 Å/V. The SiO_2 films are a little more difficult to prepare.

Having prepared the reference standard one can use these to calibrate the experimental geometry, if the cross sections are known, or measure other unknown reaction cross sections relative to known ones for a given experimental geometry. Section 2.2 shows that the target yield from such a standard can be expressed as

$$Y = 3.75872 \times Q\Omega\sigma F_1 F_2 / \sin \alpha, \qquad (14)$$

where x (μg cm^{-2}) is target thickness, σ is the cross section (mb/sr), Q (μC) is total charge hitting the target, Ω (msr) is the detector solid angle, F_1 is the isotopic enrichment fraction, F_2 is the number of isotope atoms per molecule of atomic weight W and α is the angle between the incoming beam and the target surface. For example, for a 10 V $Ta_2^{18}O_5$ made from 87% enriched ^{18}O water we have $x = 13.45$ μg cm^{-2}, $F_1 = 0.87$, $F_2 = 5$, $W = 450.592$ and hence the yield/μC msr at normal incident is 0.488σ (mb/sr). A typical 15 min run on these metal targets can accumulate 200 μC of charge, so with a 10 msr solid angle one requires nuclear reactions with cross sections greater than 1 mb/sr or so in order to acquire more than 1000 counts in the spectrum.

Table 6
Anodic constant [Å/V] for Ta_2O_5 targets made from biological fluids at 22°C. Taken from ref. [96]

	Water		Plasma		Serum	Urine
pH	6	6.0–6.4	6.8–7.3	7.0–8.0	7.0–8.0	7.0–8.0
Anodic constant	15.7±0.4	16.2±0.4	16.7±0.4	17.5±1.2	17.3±1.2	17.3±0.8

Table 7
Rutherford elastic scattering cross sections [mb/sr] for 2 MeV ^{4}He on ^{16}O, ^{18}O, Al, Si and Ta

Isotope	Angle		
	90°	135°	165°
^{16}O	321	103.5	75.8
^{18}O	324	105.7	77.8
^{27}Al	866	291	217
^{28}Si	1006	338	253
^{180}Ta	27617	9472	7141

Studies on RBS of ^{4}He on ^{16}O [175] and ^{18}O [105] have shown that the elastic scattering on ^{4}He on these isotopes obeys the Rutherford scattering law for energies below 2 MeV to a few percent. Since RBS experiments are easily set up it is reasonably common practice to normalise results to 2 MeV ^{4}He backscattering yields, using eq. (14) and hence eliminate common errors such as those associated with solid angle, charge measurement and target thickness. The Rutherford cross sections for 2 MeV ^{4}He on ^{16}O, ^{18}O, Si, Al and Ta are given in table 7 to assist in this process.

The (p, p) scattering results are clearly non Rutherford as shown below in figs. 4 and 31 especially above 1 MeV on both ^{16}O and ^{18}O and hence are not too useful for standardisation purposes.

4. Nuclear reactions for oxygen analysis

In table 2 we have listed many reactions for the analysis of oxygen isotopes. The list of references shows that some of these have been more popular than others. We now consider a selected few of these in more detail in an attempt to show the state of recent data and where there are gaps in the current data. Much of the cross section data in the ion energy range 0–4 MeV is now quite old. Recent measurements have tended to concentrate on particular resonances or even on peak cross sections of particular resonances. The best resonance for nuclear reaction analysis is one which has a high peak cross section that falls to zero at energies for several hundred keV above and below the resonance energy. narrow resonances are best for profiling, while broader resonances give larger yields and hence better sensitivities.

All nuclear reactions tend to be angular dependent, experimentally backangles are generally favoured ($\psi >$ 90°). However, some reactions like ^{18}O(p, α)^{15}N at the 846 keV resonance have higher yields at smaller reaction angles. In order to keep the graphic representation of the data manageable we have restricted it to a couple of common angles and in some cases combined similar angles on the one graph. The nomenclature used for the data in the graphs is author/year/reference/angle. Hence ABE90[67]160 refers to Abel et al. 1990, ref. [67] and a reaction angle of 160°. No attempt has been made to separate out lab frame from centre of mass cross sections. Only data quoting differential cross sections (mb/sr) have been used, total cross sections were not used.

The data displayed has been obtained from published tabulations where possible ref. [115] for example. However, tabulated data are scarce and much of the data have been laboriously read from published graphs. With modern personal computers and the portability of information stored on diskette we think it highly desirable that future nuclear reaction cross section measurements made over significant energy ranges should be made available in this format to all those who are interested. Modern data has tended to concentrate on peak resonance cross sections, whereas for a full depth profile simulation on modern computers the complete resonance shape with angle and energy is often required to some degree of precision.

4.1. $^{16}O(p, p)^{16}O$

Rutherford scattering techniques have been popular for some time [55,170,173], alpha particles are more commonly used as already stated, however (p, p) scattering also has its uses for oxygen analysis. The references listed in table 2 are by no means complete but they are representative of recent applications for oxygen analysis and these and the references therein form a good starting point to quantify this reaction.

The data cross section for ^{16}O(p, p)^{16}O scattering are presented in figs. 4a to 4c for reaction angles 110, 135 and 160°. In the region 1 to 2.5 MeV the data is similar in shape to Rutherford predictions but generally lies well above it.

There exists very little reliable (p, p) data below 2 MeV before the work of Braun et al. [34] in 1983 shown on our plots. The experimental data shows the basic $1/E^2$ dependence for the cross section but Braun et al. give $\sigma/\sigma_R = 3.5$ at 2 MeV and 160° or 83 ± 3 mb/sr compared with Chu et al. [55] 94 ± 2 mb/sr in centre of mass system at 160°. Barbour et al. [56] give $\sigma/\sigma_R = 5$ at 2.5 MeV and 165° with ^{16}O analysis to a depth of 4 μm and a depth resolution of 200 nm. They also demonstrate that there are no large resonances below 2 MeV and suggest that minor resonances occur at 2.66, 3.47 and 4.35 MeV in our energy range of interest.

Luomajarvi et al. [122] recently measured σ/σ_R at $\psi = 170°$ for proton energies between 0.77 and 2.48 MeV. Their results together with the earlier work of Chow et al. [129] are reproduced in fig. 5 together with a polynomial fit to this data namely

$$\sigma/\sigma_R = 1.21 - 1.06 \times 10^{-3}E + 11.50 \times 10^{-6}E^2 - 1.44 \times 10^{-10}E^3, \quad (15)$$

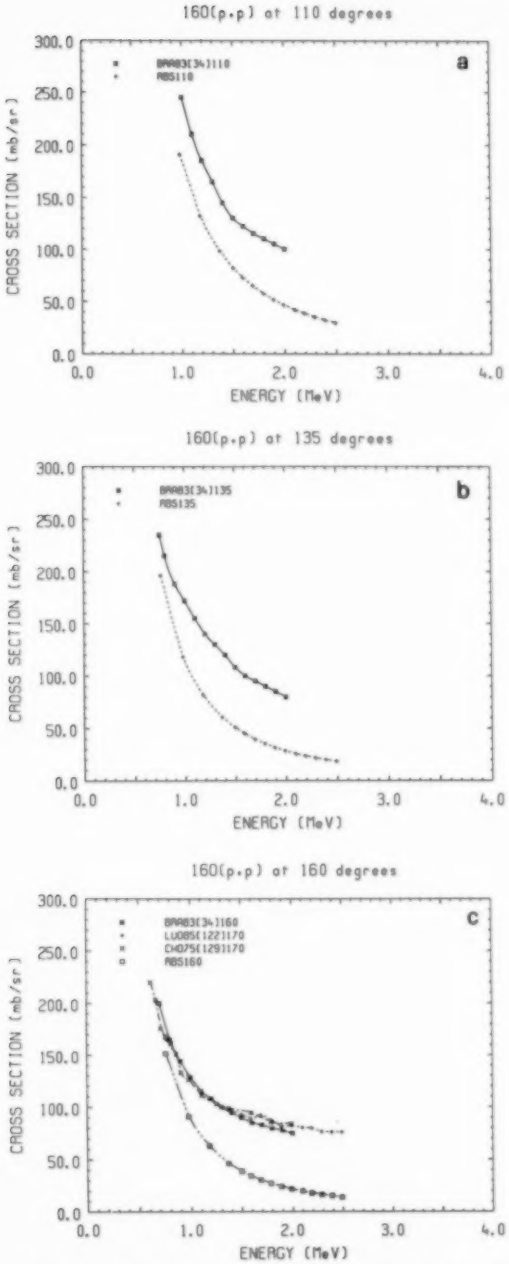

Fig. 4. $^{16}O(p, p)^{16}O$ cross section data for (a) 110°, (b) 135° and (c) 160°.

with E in keV. Fits for four energies at angles between 80 and 170° were also given by them. Eq. (15) gives $\sigma/\sigma_R = 3.938$ at 2 MeV and $\psi = 170°$ compared with

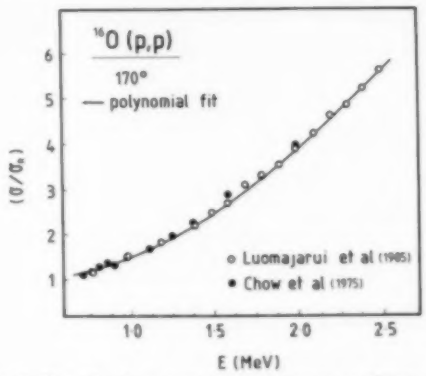

Fig. 5. Plot of σ/σ_R versus proton energy at 170° for (p, p) scattering. Taken from ref. [122].

the experimental value of Chow et al. [129] of $\sigma/\sigma_R = 3.98$ at 171.5° lab angle at 1.991 MeV with $\sigma = 83.9$ mb/sr.

Generally (p, p) cross sections on ^{16}O are 13–20 times larger than the equivalent (d, p), (d, α) at 0.9 MeV or (^{3}He, α) at 2.4 MeV cross sections. Typical spectra produced are shown in fig. 6. These are taken from Xie et al. [61] at proton energies of 0.87 and 1.63 MeV where σ/σ_R are about 1.3 and 2.8, respectively. The target is 0.5 mm thick CuO. The sampling depths

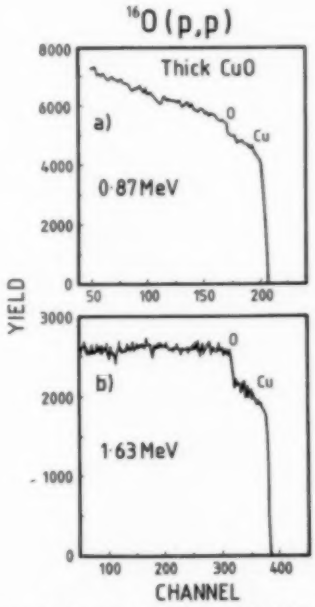

Fig. 6. Proton backscattering spectra of CuO (a) at 0.87 MeV and (b) at 1.63 MeV. Taken from ref. [61].

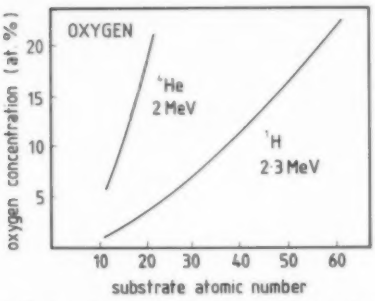

Fig. 7. Backscattering detection limits for (p, p) and (α, α) scattering on ^{16}O versus atomic number of the substrate. Taken from ref. [54], no reaction angle given.

of these two energies are 2 and 7 μm respectively. Fig. 6a with a cross section closer to Rutherford shows similar $1/E^2$ dependence with depth, however for the higher energy proton plot of fig. 6b the spectra is considerably flatter, the yield is reduced but the height of the oxygen edge is improved relative to copper.

Fig. 7, taken from the work of Rauhala et al. [54], shows the (p, p) and (α, α) detection limits on ^{16}O as the atomic number of the bulk impurity in a heavier substrate increases. For 2.3 MeV proton scattering the minimum detectable limit increases from around 1 at.% for magnesium oxide to over 20 at.% for tin oxide. This is a direct consequence of the Z^2 dependence of RBS on scattered ion yield. This figure also shows the superior detection limits for proton scattering over alpha scattering at the same energy. The price one pays for this is significantly poorer depth resolution of protons relative to alphas (200 nm compared with 10 nm).

4.2. $^{16}O(d, p)^{17}O$

Deuterons of energy around 1 MeV have been extensively used for oxygen analysis with good sensitivity and depth resolution. The Q values for this reaction are fairly high so proton energies are reasonable and table 4a shows that 10 to 50 μm Mylar foils may be used to stop scattered deuterons with energies up to 2.5 MeV and still allow the proton groups through to the detection system.

Several proton groups are possible for the (d, p) reaction over the energy range 0 to 4 MeV depending on the excited states of ^{17}O. The Q values for these are given in table 8 together with selected (d, p) reactions that may interfere for deuteron energies of 1.10 Mev and reaction angle of 135°. The p_2 to p_5 groups from ^{16}O have negative Q values and hence thresholds for proton production require deuteron energies above their corresponding Q values. This is another good

Table 8
Selected (d, p) reactions and emitted proton energies for (d, p) reaction at 1.1 MeV. Adapted from ref. [27] and ref. [10]

Nuclide	Q [MeV]	E_d = 1.10 MeV, 135°	
		E_{out} [MeV]	Proton group
^{16}O	1.9191	2.541	p_0
	1.049	1.728	p_1
	−1.141	–	p_2
	−1.929	–	p_3
	−2.634	–	p_4
	−3.163	–	p_5
^{14}N	1.455	2.065	p_4
	1.309	1.934	p_5
	1.038	1.697	p_6
^{10}B	1.244	1.737	p_8
^{11}B	1.145	1.694	p_0

reason for using deuteron energies below 1.1 MeV. The other reason is that $^{16}O(d, n_0)$ (d, n_1) reactions have Q values of −1.627 and −2.127 MeV, respectively, and hence there is minimal neutron production from ^{16}O below those thresholds. Although D(d, n) reactions from implanted deuterium produces some neutrons at all energies. It is generally advisable to minimise neutron production at all energies.

The interferences from ^{14}N, ^{10}B and ^{11}B should also be considered when using the (d, p_1) reaction on ^{16}O since the $^{16}O(d, p_1)$ reaction around 1 MeV has by far the largest differential cross section at backward angles which makes it a favourite for analysis. Debras and Deconninck [10] also show that the $^{14}N(d, p_5)$ reaction with E_{out} = 1.79 MeV, the $^{19}F(d, p_{12})$ reaction with E_{out} = 1.79 MeV, and the $^{9}Be(d, p_1)$ reaction with E_{out} = 1.55 MeV, for E_d = 0.9 MeV at 135° can possibly interfere with the $^{16}O(d, p_1)$ reaction.

Fig. 8, taken from ref. [141], shows a typical spectrum for the (d, p) reaction at the 973 keV resonance

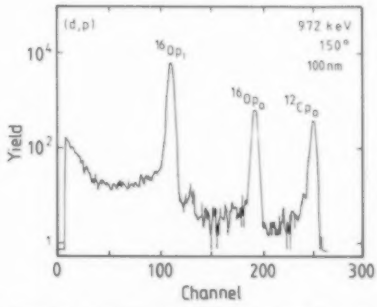

Fig. 8. Typical spectrum for $^{16}O(d, p)$ reaction at 972 keV and 150° on Ta_2O_5, 100 nm thick. Taken from ref. [141], a 15 μm Mylar foil has been used to stop the α_0 particles reaching the detector.

and 150° for a 100 nm Ta_2O_5 film. The carbon peak arises from the $^{12}C(d, p_0)$ reaction on a 1 nm thick surface layer. This is a fairly simple spectrum with the larger (d, p_1) peak well clear of interferences. A 15 μm Mylar foil has been used to stop the α_0 particles from the (d, α_0) reaction reaching the detector.

Figs. 9a to 9d show the $^{16}O(d, p_0)$ and (d, p_1) cross section data for reaction angles of 135 and 150–170°, respectively. Angular distributions for (d, p_0) and (d, p_1) for energies from 0.8 to 2.0 MeV are given in refs. [144,155]. The 973 keV resonance in (d, p_1) rises from ~13 mb/sr at 165° to 15 mb/sr at 127° falling rapidly to between 8 and 5 mb/sr for forward angles below 66°. For (d, p_0) below 1.66 MeV resonance variations are small with angles above 120°. Forward angles below 66° increase the cross section in this region by about a factor of two or so. Generally for deuteron energies above 2 MeV (d, p_0) cross sections for small reaction angles are larger than for large backward angles.

The (d, p) cross sections fall away to values less than 1 mb/sr quite rapidly below 1 MeV. This together with the resonances near 1 MeV for (d, p_0) and (d, p_1) have made this reaction a popular choice for oxygen profiling and analysis.

Low energy differential cross sections and their angular distributions have been studied by Longequeue et al. [150] for both (d, p_0) and (d, p_1) reactions down to 300 keV deuteron energies. However, Turos et al. [6,153], Seah et al. [141] and Vizkelethy [124] have used the small plateau at 800–900 keV, in the (d, p_1) reaction at around 145° with a cross section of ~5 mb/sr for oxygen analysis. Vizkelethy [124] find the yields for p_1 are approximately $8p_0$ yields at 135° and 834 keV. A typical spectrum taken from ref. [6] is shown in fig. 10 for 600 nm SiO_2 target at a deuteron energy of 900

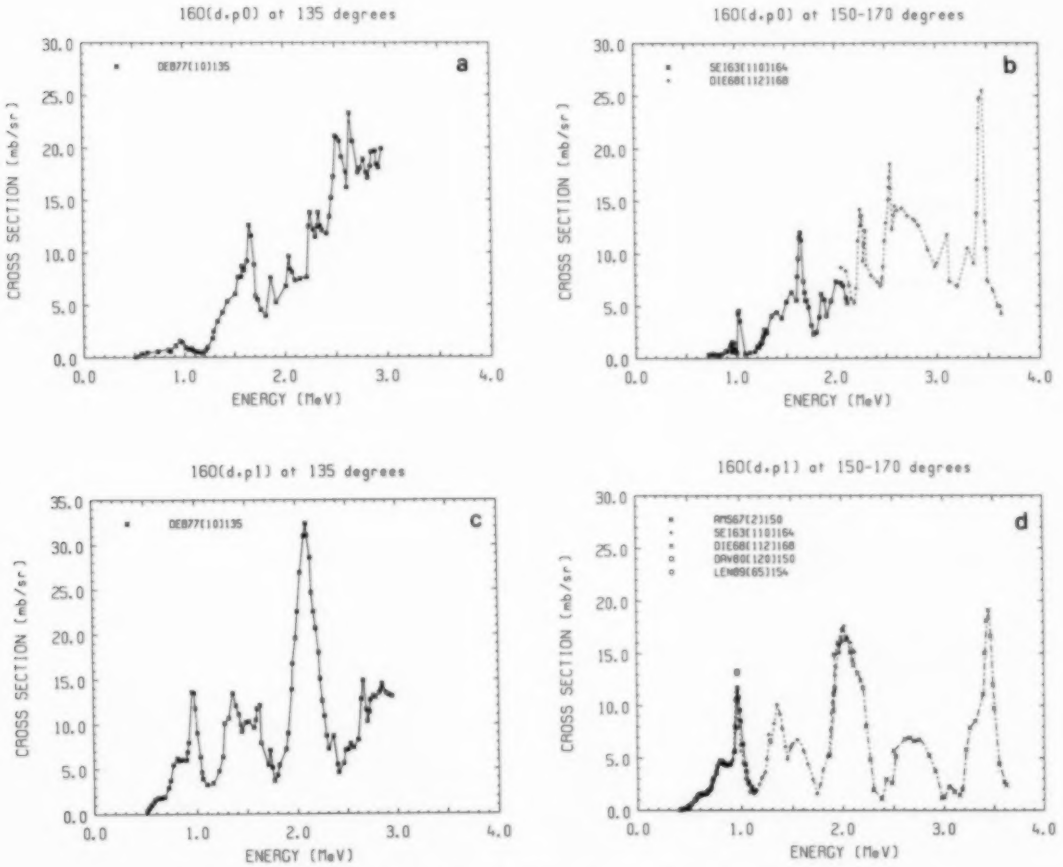

Fig. 9. $^{16}O(d, p)$ cross section data from (a, b) (d, p_0) and (c, d) (d, p_1) at 135° and 150–170°.

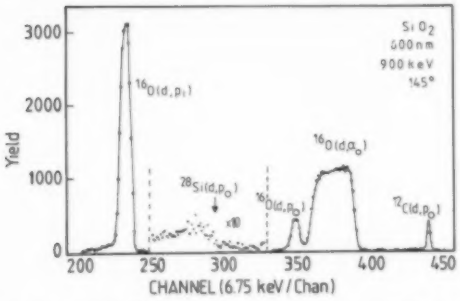

Fig. 10. A typical $^{16}O + d$ spectrum, taken from ref. [6] for 900 keV deuterons on 600 nm thick SiO_2 target. No foils were used in front of the detector.

keV. Unlike the spectrum shown in fig. 8, this one does not use a Mylar foil to stop the (d, α_0) products so they are clearly shown together with some $^{28}Si(d, p_0)$ contamination (×10) and the usual $^{12}C(d, p_0)$ contamination peak at high energies.

The two α-particle groups α_0 ($Q = 3.111$ MeV) and α_1 ($Q = 0.798$ MeV) from the (d, α) reaction are easily stopped by Mylar or Al foils which also stop the elastically scattered deuterons, whereas the proton groups lose typically 10 to 30% of their energy. The p_0 ground state group is much more energetic than the p_1 group so interference after traversing these foils are minimal for moderately thick targets.

Davies et al. [120] have used well characterised Ta_2O_5 anodised foils to measure the cross section of the (d, p_1) reaction at the 973 keV resonance. They find $\sigma = 13.3$ mb/sr at 150°. This compares well with Lennard et al. [65] $\sigma = 13.6$ mb/sr at 150° but is higher than the earlier work of Amsel and Samuel [2] $\sigma = 12.5$ mb/sr at 150°. Earwaker [75] has measured the (d, p_0) reaction at the 2.02 MeV resonance and gets 7.4 mb/sr at 174° and Amsel et al. [111] measured the (d, p_1) reaction at the 1.66 MeV resonances as 19 mb/sr at 90°. No recent measurements (since 1977) of the rather broad and large (d, p_1) resonance at 2.1 MeV have been found. The cross section for this resonance as measured by Debras et al. [10] is around 32 mb/sr at 135° larger than any other (d, p) resonance over our energy range of interest (0–4 MeV). Table 18.5 of ref. [132] gives maxima in the yields and peak widths for $^{16}O + d$ reactions including (d, p) and (d, α) for $E_d = 0.8$–11 MeV and the reader is referred to these for the other less commonly used (d, p) resonance energies.

Typical depth resolutions for (d, p) reaction on oxygen are around 30 to 50 nm [35], Turos et al. [153] quote 20 to 50 nm at 850 keV deuteron energy with no foils. Foils of course may degrade this resolution by as much as a factor of ten in some cases, depending on the thickness used, deuteron input energy and the target thickness and angle.

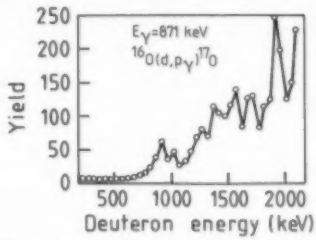

Fig. 11. Differential excitation function for the production of 871 keV γ-rays from $^{16}O(d, p\gamma)$ reaction. Taken from ref. [48].

Deuteron beams on ^{16}O also induce intense prompt γ-rays of 871 keV from the reaction $^{16}O(d, p_1\gamma)^{17}O$ and of 2.313 MeV from the reaction $^{16}O(d, \alpha_1\gamma)^{14}N$ and nothing from the (d, p_0) and (d, α_0) reactions [48]. Since ^{16}O is the major isotope of oxygen this reaction offers quite good sensitivity (10 μg g^{-1}) and depth solution (50 nm) for oxygen analysis using γ-rays. The excitation function for the 871 keV γ-ray is shown in fig. 11. Carstanjen et al. [73] recently used this γ-ray in coincidence with the p_1 group from $^{16}O(d, p_1)$ reaction to determine depth profiles of oxygen in the presence of nitrogen. This technique showed considerable improvement in backgrounds due to interferring reactions between gated and ungated spectra. These are shown in figs. 12 to 14 for 900 keV deuterons on aluminium, tantalum loaded with 1.5 at.% nitrogen and 0.5 at.% deuterium and a comparison of the (d, p_1) peak for surface oxygen on technical grade aluminium and bulk oxygen in potassium nitrate. Fig. 12 shows the Al target with the $^{16}O(d, p_1)$ and (d, p_0) peaks together with proton groups from $^{14}N(d, p_2, p_3, p_5)$ and $^{12}C(d, p_0)$. These groups are indicative of large amounts of C, O and N at the surface. Gating the spectrum by the 871 keV γ-ray reduces the background and reveals that the sample contains a thick oxide layer at the surface plus a small amount in the bulk (0.01 at.%). The $^{15}N(d, p_{4,5})$

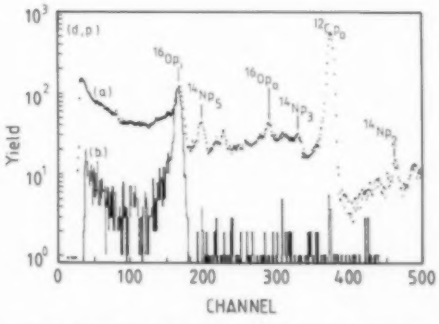

Fig. 12. Ungated (a) and gated (b) $^{16}O(d, p_1\gamma)$ spectra for 900 keV deuterons on Al using 871 keV γ-ray. Taken from ref. [73].

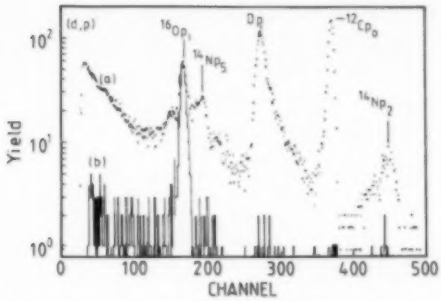

Fig. 13. As for fig. 12 for Ta loaded with 1.5 at.% nitrogen and 0.5 at.% deuterium. Taken from ref. [73].

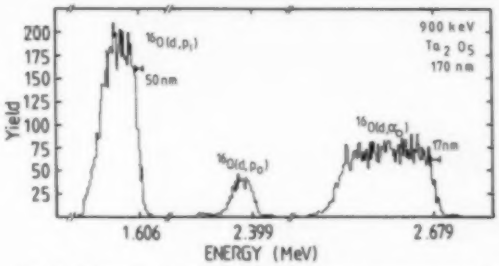

Fig. 15. Spectrum obtained using a magnetic spectrometer for the $^{16}O + d$ reaction on Ta_2O_5 at 135° and 900 keV. Taken from ref. [16].

cross sections are 1–7 mb/sr for 600 to 1400 keV deuterons very similar to $^{16}O(d, p_1)$ cross sections at these energies.

Fig. 13 is a similar gated and ungated spectra for a Ta target. The presence of 0.5 at.% deuterium produces a large peak from the D(d, p)T reaction, which is all but removed by this coincidence technique. Again nitrogen and carbon contaminants are also removed. Fig. 14 is a comparison of the coincidence spectra for potassium nitrate, containing bulk oxygen and Al containing surface oxygen, demonstrating that oxygen profiling is also possible with this coincidence technique.

4.3. $^{16}O(d, \alpha)^{14}N$

The $^{16}O + d$ reaction produces both proton groups (discussed earlier) and alpha groups. The Q for α_0 is 3.1104 MeV, for α_1 is 0.798 MeV and for α_2 is −0.835 MeV. Table 4a shows that the energy of the α_0 particle is generally not sufficient to allow the use of foils in this experiment to stop the scattered deuterons reaching the detector. This generally means that target currents must be lower to cope with count rates into the scattered deuteron peak in the spectrum. Also the pile up of the backscattered deuterons (twice E_d), if count rates are high, may overlap with the alpha energy. A typical spectrum for $^{16}O + d$ reaction using a surface barrier detector is shown in fig. 10. The (d, α_0) peak lies well above the (d, p_0) and (d, p_1) peaks but clearly depending on kinematics and target thickness, there is the potential for the (d, p_0) and (d, α_0) peaks to interfere. Some of the problems mentioned, associated with the detection of the particle products using a surface barrier detector, can be overcome by using a high resolution magnetic spectrometer [16]. These costly instruments are sometimes available in nuclear physics laboratories and overcome the need for absorber foils and significantly improve depth resolution however, count rates are generally low. Fig. 15, taken from ref. [16], shows the spectrum for $^{16}O + d$ at 900 keV and 135° for a 170 nm thick Ta_2O_5 target measured using the Washington NRL double focussing magnetic spectrometer. A position sensitive detector located in the image plane of the spectrometer was used. The spectrometer resolution ($\Delta E/E$) was 0.08% and the ultimate depth resolutions obtained 50 nm for (d, p_1) and 17 nm for (d, α_0) are shown on the figure.

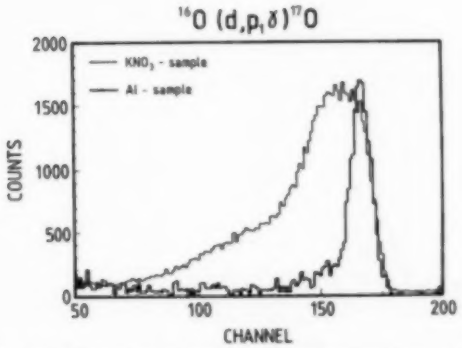

Fig. 14. Comparison of the coincidence spectra from KNO_3 and Al using 871 keV γ-ray. Taken from ref. [73].

Amsel et al. [2] point out that one advantage of the (d, α) reaction is that ^{16}O and ^{18}O can be analysed simultaneously. The $^{18}O(d, \alpha)$ $Q = 4.247$ MeV peaks (typically four of them) are usually 1 MeV higher in energy than the ^{16}O peak because of the higher Q for this reaction.

The cross section data for $^{16}O(p, \alpha)$ reaction at 90°, 135–145° and 160–170° are shown in figs. 16a to 16c, respectively, over the energy range 0 to 4 MeV. The scale of the plots has been kept the same so that direct comparisons can be made. For 90° the early work of Amsel [111] between 0.8 and 2 MeV is the only tabulated data. Above 0.8 MeV and 1.5 MeV the (d, α_1), (d, α_2) and (d, p_2) reactions are energetically possible but their cross sections are much smaller than the (d, α_0).

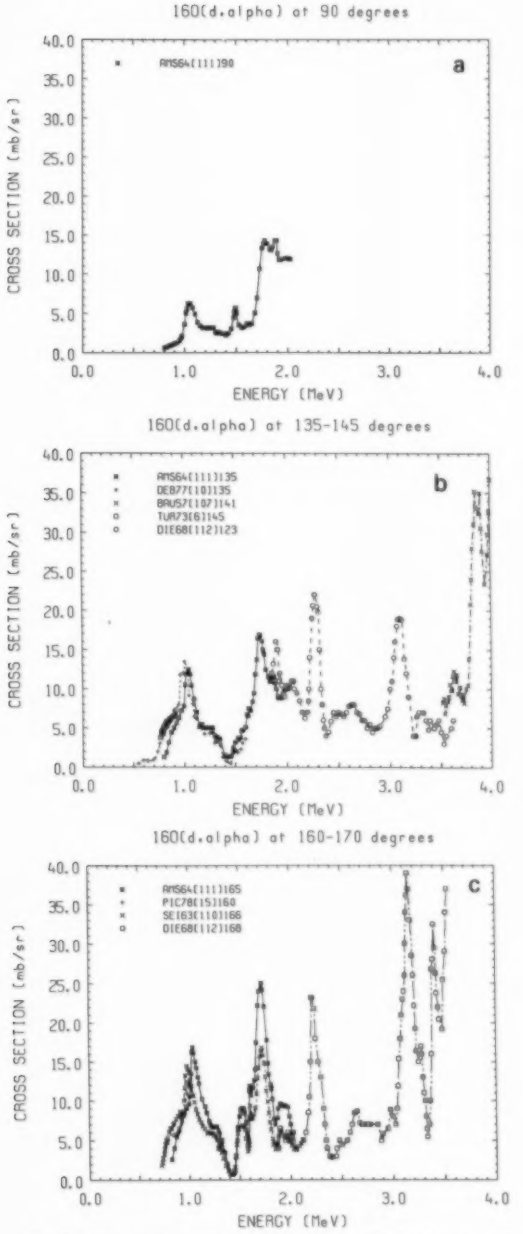

Fig. 16. Cross section data for $^{16}O(d, \alpha)$ at (a) 90°, (b) 135–145° and (c) 160–175°.

Figs. 16 show that there are five or six main resonance peaks between 0.5 and 4 MeV. These resonances tend to have larger cross sections for more backward angles. This is particularly so for the commonly used 1 MeV resonance being less than 7 mb/sr at 90° but 16 or 17 mb/sr for angles greater than 160°. Angular distributions for the (d, α_0) between 1 and 2 MeV have been given in refs. [147,155].

Ref. [132] table 18.15 gives maxima yields for (d, α) reaction and their widths for E_d from 0.8 to 11 MeV. For example, the five main resonances in our figures occur at 1.048, 1.765, 2.28, 3.13 and 3.68 MeV and the widths of the 1.048 and 1.765 MeV resonances are 88 ± 10 and 141 ± 10 keV, respectively. Baumgartner et al. [107] measured the two major resonances at 3.85 and 4.0 Mev with widths of 100 keV and 35 keV and ref. [135] gives these as 3.80, and 3.95 MeV with a width of 35 keV also.

The cross section of the most commonly used resonance at 1.048 MeV has been measured by Debras [10] as 13.5 mb/sr at 135°, Picraux [15] at 12.5 mb/sr at 160° and by Longegueue et al. [150] as 6 mb/sr at 90° and 19 mb/sr at 160°. Figs. 16b and 16c show considerable shift (50 keV between results of Amsel [111] and others near the 1 MeV resonance. Amsel gives 12.5 mb/sr at 135° and 17 mb/sr at 165° for this resonance. The results of Amsel [111] and Seiler [110] also differ considerably around the 1.765 MeV resonance even though the reaction angles are within a degree of one another (165°, 166°).

Dietzsch et al. [112] have measured the higher 2.28 and 3.13 resonances as 23 mb/sr and 39 mb/sr at 168° and 3.95 MeV resonance at 35 mb/sr at 145° with a width of 35 keV. The (d, α_2) peak for this reaction lies between the (d, p_3) and (d, p_2) peaks.

The main disadvantage of the $^{16}O(d, \alpha)$ reaction, as with most deuteron reactions, is the neutron production from such reactions as $^{12}C(d, n)^{13}N$ ($Q = -0.281$ MeV) with small Q and the D(d, n)T from implanted deuterons in the target. There are also interferences from (d, p) reactions such as $^{12}C(d, p_0)^{13}C$ ($Q = 2.722$ MeV) and $^{16}O(d, p_0)^{17}O$ ($Q = 1.9191$ MeV) which, as tables 4 and 8 and fig. 10 show, produce proton energies close to the α energy. However, low bias detector voltages, thin depletion layers of surface barrier detectors can be used to suppress the interfering proton signals with some loss in detector resolution [15,37,153]. Fig. 17, taken from Simpson et al. [37] shows how, if the geometry and deuteron energy are optimised then the depletion thickness can be adjusted to minimise $^{16}O(d, p_0)$ interferences. For $E_d = 1.08$ MeV with incidence beam 30° to the normal and exit angl of 45°, reaction angle of 135° and a 24 μm depletion detector rather than 316 μm gives depth resolution of better than 40 nm in Ta_2O_5 and SiO_2 targets and very little contribution from the (d, p_0) group. Haas and Khubeis [39] arrive at similar conclusions and eliminate (d, p) interferences by using thin surface barrier detectors. For example, for 22 μm depletion detectors 5.2 MeV

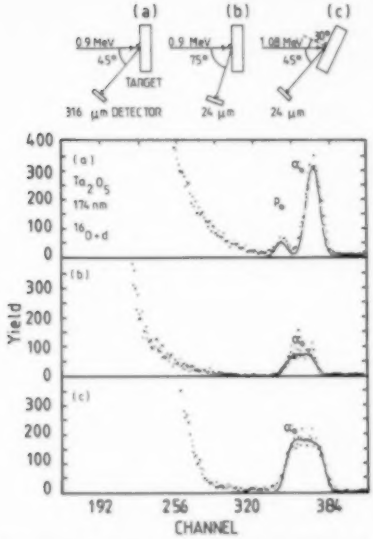

Fig. 17. Typical spectra for $^{16}O+d$ reaction at the three geometries shown and with surface barrier depletion thickness of 316 μm and 24 μm. Taken from ref. [37].

α's are stopped but protons and deuterons can deposit only a maximum of 1.3 and 1.8 MeV, respectively. They also improved the depth resolution of this reaction to 13 nm and the sensitivity to 0.01 at.% by using improved pile up rejection with 30 ns pulse pair resolution.

4.4. $^{16}O(^3He, p)^{18}F$

The latest definitive work on this reaction has been performed by Lennard et al. [65] at the University of Western Ontario. They suggest ^3He reactions are the most plausible alternative for users not wanting to use deuteron beams for oxygen analysis as they have high Q. ^3He has a low binding energy 7.7 MeV compared with ^4He 28.3 MeV hence many of the simpler nuclear reactions which it undergoes are exoergic. However, unlike deuterons binding energy of only 2.2 MeV, ^3He is not a prolific neutron producer.

Early work on the $^3He + ^{16}O$ reaction by Bromley et al. [108] was performed before the advent of silicon surface barrier detectors and its accuracy is limited by the poor resolution of gas counter spectrometers. To detect both the p_0 and α_0 groups from oxygen and carbon with a modern silicon surface barrier detector a partial depletion depth of at least 300 μm is required.

Up to eleven proton groups have been observed by Kuehner et al. [64] for this reaction. The first six, their Q values and cross sections for four angles are shown in table 9 and taken from ref. [65] for the 2.4 MeV resonance.

The majority of these proton groups are observed as shown in fig. 18. although typically the p_{1-4} groups are not resolved. Table 4a demonstrates that the (^3He, p) are ideal for the use of Mylar foils in front of the detection system and the thickness of this foil can be adjusted to move the α_0 peak around so as not to interfere with the p_0 peak from ^{16}O. The spectra of fig. 18 were taken at the 2.4 MeV resonance on thin (25 nm) and thick (230 nm) Ta_2O_5 target using 14.5 μm Mylar filter and a 100 μm partially depleted surface barrier detector. Again the p_{1-4} groups from $^3He + ^{12}C$ reaction are clearly visible.

Good cross section data over the range 0 to 4 MeV is virtually non existent. We have plotted available data in figs. 19a and 19b for reaction angles 90 and 150°. This clusters around 2 to 3 MeV region and there is some disagreement between the recent data of Lennard et al. [65] and the earlier work of Kaim and Palmer [24] and Bromley et al. [125]. At the 2.4 MeV resonance Kaim and Palmer [24] give p_{1-4} as 0.45 mb/sr and Lennard et al. [65] give 1.40 mb/sr at 150°. For the p_0 group at 2.4 MeV ref. [24] gives 1.13 mb/sr and ref. [65] gives 1.73 mb/sr. The work of Lennard et al. [65] is more recent and his measurements on $^{16}O(d, p_1)^{17}O$ at 150° and 973 keV agree well with the Davies et al. [120], namely 13.6 ± 0.4 mb/sr and 13.3 ± 0.4 mb/sr so

Table 9
Proton groups, Q values and cross sections for $^3He + ^{16}O$ reaction at 2.392 MeV and at 4 angles in lab frame. The cross sections are taken from the recent work of Lennard et al. [65]

Group	Q [MeV]	Cross section [mb/sr] at 2.392 MeV				E_γ [keV]
		93.4°	113.8°	133.9°	153.7°	
p_0	2.0321	1.21	1.41	1.59	1.73	937
p_1	1.096	0.496	0.632	0.865	1.08	1041
p_2	0.992	0.411	0.244	0.125	0.0394	1080
p_3	0.953	0.0121	0.0775	0.190	0.265	
p_4	0.914	0.0095	0.0152	0.0135	0.0157	
p_5	0.332	0.125	0.174	0.189	0.157	
p_6	−0.067	0.147	0.0944	0.0794	0.0888	

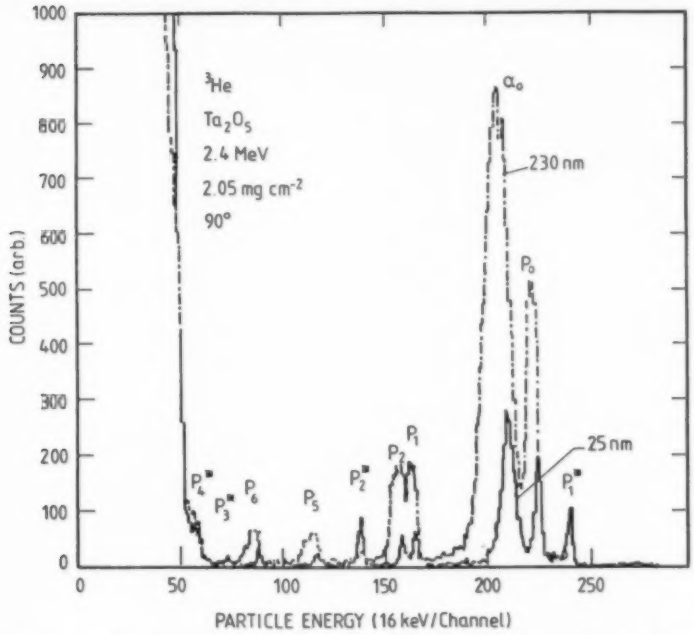

Fig. 18. Spectra of $^3He + ^{16}O$ at 2.4 MeV for thin (25 nm) and thick (230 nm) Ta_2O_5 target using 14.5 μm Mylar foil and 100 μm partially depleted detector. (*) groups are from carbon.

more weight must be put on the work of Lennard et al. in these plots. Even so cross sections are only of the order of a few mb/sr. Below 2 MeV cross sections are less than 200 μb and hence not much use in ^{16}O analysis. The sum of all α_0 and p_{0-6} groups is only 7.86 ± 0.4 mb/sr at 90° and 3.68 ± 0.15 mb/sr at 150° [65].

The angular distributions of α_0 and p_0 to p_6 groups for $^3He + ^{16}O$ reactions are given in fig. 20 for centre of mass angles between 80° and 160° and the relative intensities of the p_1 to p_4 groups for the four reaction angles used by Lennard et al. [65] are given in fig. 21. Note the α_0 contributions are much reduced for backward reaction angles.

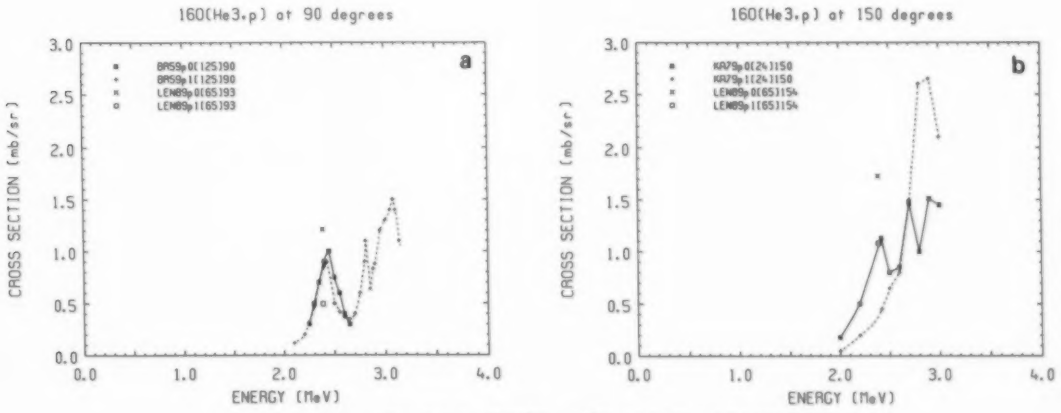

Fig. 19. Cross section data for $^{16}O(^3He, p)^{18}F$ at (a) 90° and (b) 150–160°.

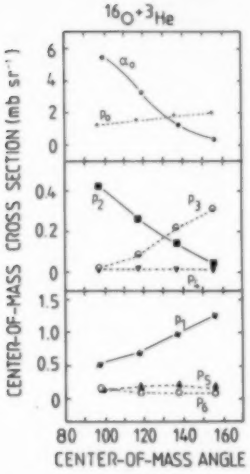

Fig. 20. Angular distributions of α_0 and p_0 to p_6 groups of $^3He + ^{16}O$ reaction at the 2.4 MeV resonance. Taken from ref. [65].

The $^{12}C(^3He, p_{0-4})^{14}N$ reaction can interfere with the ^{16}O p_0 to p_4 group. The carbon ^3He cross sections rise almost linearly from about 0 to 3.5 mb/sr from 2 to 3 MeV ^3He energies and hence has a relatively high yield compared with $^{16}O + ^3He$. Since carbon is nearly always present in vacuum systems with pressures above 0.1 mPa this reaction may be used to monitor the C buildup on the target. Fig. 22 shows the spectrum of 2.4 MeV ^3He on a mixture of thick Al_2O_3 and carbon. The reaction angle of 169° means the α_0 contributions from ^{16}O and ^{12}C are much reduced. The foil thickness was 15 μm of Mylar. The $^{12}C(^3He, p_1)$ and $^{16}O(^3He, p_0)$ peaks overlap considerably but the ^{16}O p_1 to p_4 groups are well separate even for this high degree of carbon contamination. This shows the importance of proper selection of reaction angle and experimental conditions to optimise for ^{16}O analysis.

When using ^3He reactions above 1.45 MeV on targets containing carbon one should be aware of neutron production from $^{12}C(^3He, n)^{14}O$ $Q = -1.147$ MeV reaction. Abel et al. [67] have measured this neutron production at ^3He energies of 2.6 MeV (~ 200 nA) and obtain dose levels of around 4 mrem/h from bulk carbon at 45 cm and several mrem/h near surrounding apertures and collimators. Also above 3.5 MeV the $^{16}O(^3He, n)^{18}Ne$ reaction with $Q = -3.196$ MeV will contribute to neutron production. ^{18}Ne decays by β^+ to ^{18}F with half-life of 1.67 s and produces 511 keV annihilation γ-rays.

The $^{16}O(^3He, p\gamma)^{18}F$ reaction has special appeal compared to the (d, pγ) reaction because it avoids contaminating the accelerator ion source and beamline components with deuteron gas whilst still providing a satisfactory high γ-ray yields for ^{16}O analysis. Raisanen [45] also points out that the effective threshold for the (p, p'γ) reaction on ^{16}O is 6.8 MeV so it too is limited to the higher energy accelerators. Heggie et al. [26] have measured the $^{16}O(^3He, p\gamma)^{18}F$ reaction for the production of 937, 1040 and 1080 keV γ-rays deexciting the first three states of ^{18}F. Their cross sections are shown in figs. 23a and 23b. The 937 keV γ-rays has the highest cross section but the summed cross section of all three γ-rays rises from 10 mb at 2.6 MeV to 90 mb at 4 MeV and has been applied by them to study oxygen in chrome black solar collectors.

The $^{16}O(^3He, p)^{18}F$ reaction is one method of producing accelerator based ^{18}F, one of the most important radionuclides in nuclear medicine today. ^{18}F has a half-life of 109.7 min and is a positron emitter used extensively in PET facilities. Cross sections for this reaction peak sharply around a ^3He energy of 7.8 MeV, dropping rapidly below 5 MeV [60].

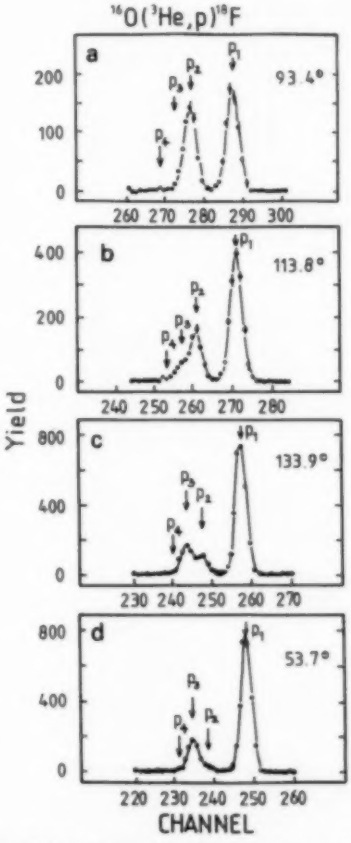

Fig. 21. Relative intensities of the p_1 to p_4 proton groups from $^{16}O(^3He, p)^{18}F$ at (a) 93.4°, (b) 113.8°, (c) 133.9° and 9d) 53.7° lab angle. Taken from ref. [65].

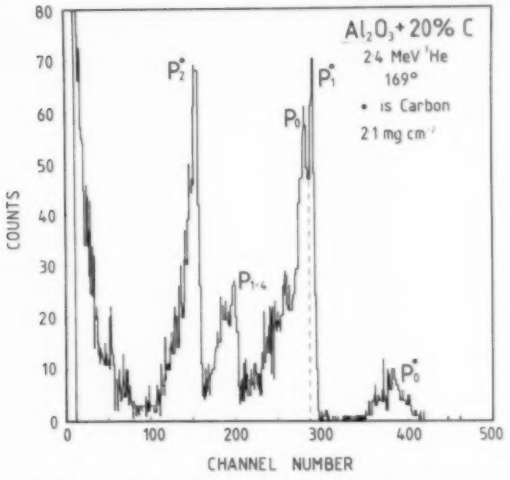

Fig. 22. Typical spectrum for 2.4 MeV ^{3}He ions on a mixture of thick Al_2O_3 and 20 wt.% carbon at 169° with 2.1 mg cm^{-2} of Mylar foil. The detector was 100 μm depleted surface barrier.

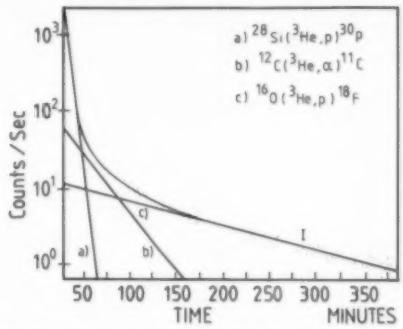

Fig. 24. Decay curves for CPA of silicon containing carbon and oxygen (a) ^{30}P, (b) ^{11}C and (c) ^{18}F add up to produce curve I. Taken from Bethge [38].

As a method of oxygen detection this charged particle activation (CPA) technique is quite sensitive if the two annihilation γ-rays are detected in coincidence. Other competing reactions producing 511 keV γ-rays are $^{19}F(^3He, \alpha)^{18}F$ ($Q = 10.1$ MeV), $^{10}B(^3He, d)^{11}C$ ($Q = 3.2$ MeV, $T_{1/2} = 20.3$ min) $^{12}C(^3He, \alpha)^{11}C$ ($Q = 1.9$ MeV). Total activation cross sections for all of these reactions have been given by Gass and Muller [118]. A comprehensive table of ^{3}He reactions, their half-lives and Q values is given by Markowitz and Mahoney [126].

CPA analysis using ^{3}He beams at high energy and looking for the annihilation peaks requires plotting of the decay curves with time after irradiation to look for slopes characteristic of ^{18}F decay [33]. Fig. 24 shows such a plot for CPA on silicon containing carbon and oxygen. The contributions from Si (a), C (b) and O (c) add up to the decay curve I. Ref. [33] has used this technique for oxygen analysis in Fe and Cr at 15.2 MeV and quoted sensitivities of around 100 ppb of oxygen after chemical separation of the ^{18}F. A full discussion of CPA analysis techniques is beyond this review.

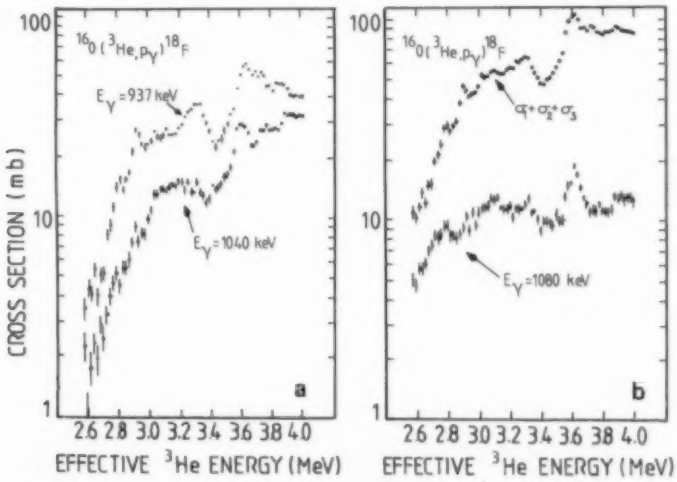

Fig. 23. Cross sections for $^{16}O(^3He, p\gamma)^{18}F$ reaction for the production of (a) 937 keV and 1040 keV and (b) 1080 keV and total γ-rays, taken from ref. [26].

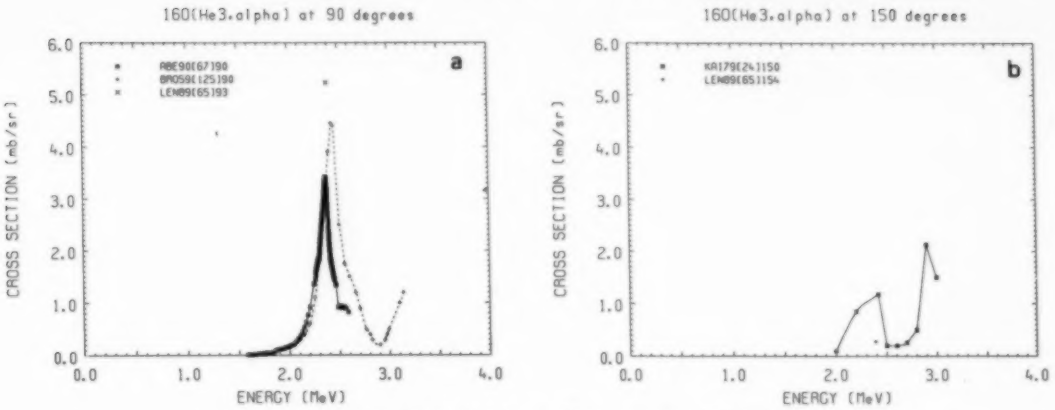

Fig. 25. Cross section data for $^{16}O(^3He, \alpha)^{15}O$ reaction at (a) 90° and (b) 150°.

4.5. $^{16}O(^3He, \alpha)^{15}O$

This reaction goes hand in hand with the $^{16}O(^3He, p)$ reaction and some data for it was given in the $(^3He, p)$ section. The $(^3He, \alpha_0)$ reaction has a Q value of 4.915 MeV which for 2.4 MeV ^3He ions produces alphas of ~5.4 Mev at 90° and ~4.3 at 160°. The scattered ^3He ions are readily stopped by 12 μm of Mylar leaving the alphas with sufficient energy to reach the detector. The reaction produces ^{15}O which has a short half-life of 124 s.

The cross section data for this reaction at 90 and 150° is shown in figs. 25a and 25b. The reaction cross section has a strong peak near 2.4 MeV width ~170 keV at 90° reaction angle, falling quickly towards zero at lower energies, being essentially zero below 2 MeV. The early work of Bromley et al. [125] found this resonance at 90° to be much broader than recent measurements of Abel et al. [67]. At larger back angles, however, this resonance falls towards zero also, a fact that was used to reduce the α_0 interference contributions in the $(^3He, p)$ reaction, discussed in the previous section. The angular distribution for this reaction has been given in fig. 20 for reaction angles from 80 to 160° [65]. Other earlier angular distributions have been given by Bromley et al. [108].

At 90° reaction angle and 2.4 MeV ^3He energy, the cross section for this reaction is several times that for the $(^3He, p_{0,1})$ reaction so, as fig. 26 shows, the α_0 peak dominates the spectrum. The spectrum of fig. 25 was obtained at the 2.4 MeV resonance for a thick ZrO target using 2.1 mg/cm^2 Mylar filter. Clearly even in this thick target situation the sum of the p_0, α_0 and p_1 to p_4 ^{16}O peaks are well separated from the carbon contamination peaks and could be used for quite sensitive oxygen analysis. Lennard et al. [65] have produced a plot of the α_0 plus p_{0-6} cross sections for the 2.4

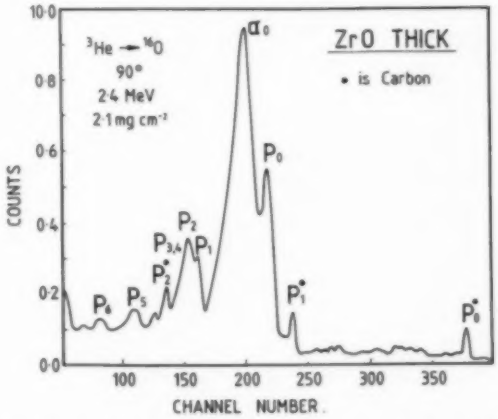

Fig. 26. Typical spectrum for $^3He + ^{16}O$ reaction at 2.4 MeV and a reaction angle of 90°. The target was thick ZrO and a 2.1 mg/cm^2 Mylar foil was used to absorb the scattered ^3He ions.

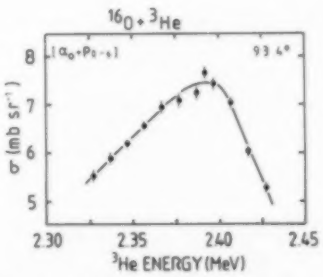

Fig. 27. Plot of the sum cross sections for the α_0 plus p_2 to p_6 groups from the $^3He + ^{16}O$ reaction at the 2.4 MeV resonance and a reaction angle of 93.4°. Taken from ref. [65].

Table 10
Peak cross section measurements for the 2.4 MeV $^{16}O(^3He, \alpha_0)$ resonance

Energy [MeV]	σ [mb/sr]	Angle	Reference
2.392	5.23	93.4°	Lennard [65]
	2.90	153.8°	
	1.01	133.9°	
	0.279	153.7°	
2.370	3.4	90°	Abel [67]
2.42	4.4	90°	Bromley [108]
2.38	3.7	90°	Cohen [179]
2.42	1.18	150°	Kaim [24]

MeV $^3He + ^{16}O$ resonance at 93.4°, which is reproduced in fig. 27. The peak cross section has a value of (7.86 ± 0.4) mb/sr at reaction angle of 90°, a very reasonable value for sensitive oxygen analysis.

Very little tabulated recent data exists outside the 2 to 3 MeV ^3He energy range. Table 10 gives measured peak cross sections for this reaction at the 2.4 MeV resonance. The values vary from the low 3.4 mb/sr of Abel et al. [67] to the high recent value of Lennard et al. [65] of 5.23 mb/sr which may be the more reliable value. Kaim and Palmer's [24] value at 150° is also significantly larger than Lennard's value at the corresponding angle.

4.6. $^{16}O(\alpha, \alpha)^{16}O$

The $(\alpha, '\alpha)$ elastic scattering technique at backward angles is a very popular technique for elemental profiling and near surface analysis for low energy alphas. It is called Rutherford backscattering (RBS) [55,170,173]. However, the yields for RBS are proportional to Z^2, the atomic number of the target. So for oxygen analysis in the presence of heavier substrate elements yields and hence sensitivities are poor. The sensitivity of the (α, α) reaction for oxygen analysis is typically worse than the corresponding (d, p), (p, α) and (d, α) reactions.

The cross sections for $^{16}O(\alpha, \alpha)$ scattering at angles around 90 to 130° and 165° are shown in figs. 28a and

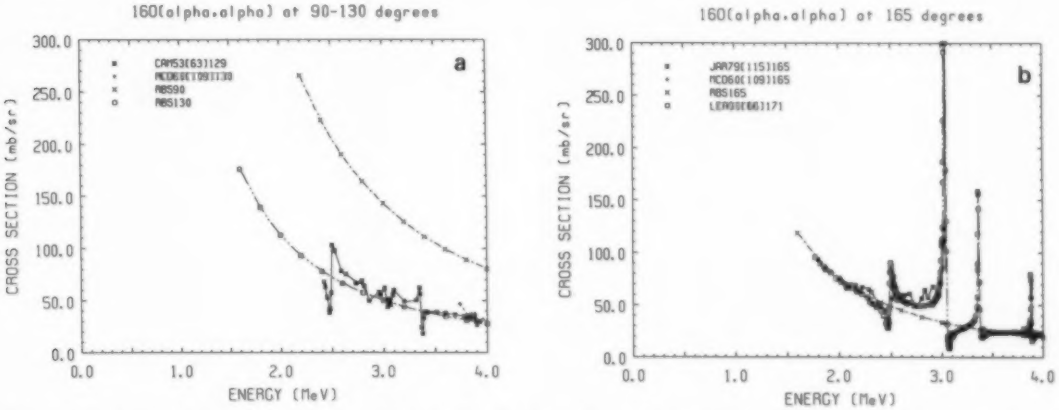

Fig. 28. Cross section data for $^{16}O(\alpha, \alpha)$ scattering at (a) 90–130° and (b) around 165°. The smooth curves are the Rutherford cross sections at 90°, 130° and 165°, respectively.

Table 11
Resonance parameters associated with resonances between 1 and 5 MeV in $^{16}O(\alpha, \alpha)$ cross section

l	1953 Cameron [63]		1987 Ajzenberg [133–135]		1990 Leavitt [66]	
	E_R [MeV]	Width [keV]	E_R [MeV]	Width [keV]	E_R [MeV]	Width [keV]
1	–	–	1.3174	0.028	–	–
0	2.490	24	2.522	19.0	2.484	24
3	3.045	10	3.0382	8.1	3.034	10
0	3.090	5	3.082	3.4	3.078	5
2	3.380	10	3.372	15.1	3.365	10
2	3.885	3	3.885	2	3.878	2
5	–	–	4.653	0.013	–	–
1	–	–	5.002	2.5	4.966	–

28b. These figures show that below 2 MeV the cross section is essentially Rutherford [55] showing large resonances especially at large back angles above 2 MeV. Alkemade et al. [94] have confirmed that (α, α) resonances with cross sections larger than 6% of Rutherford cross sections are not present below 2 MeV.

Extensive lists of known resonances from 1.3 to 29.4 MeV are listed in ref. [135] table 20.18. For our region of interest, 0–4 MeV these, together with the more recent measurement of Leavitt et al. [66] and the earlier work of Cameron [63] are listed in table 11.

Leavitt et al. [66] have done a comprehensive study of these non-Rutherford $^4He + ^{16}O$ cross sections normalising to ^4He + Ta cross sections. Other energy measurements of the main resonance near 3.04 MeV include Wang et al. [159] giving 3.042 ± 0.003 MeV, Berning et al. [59] giving 3.039 MeV and Sie et al. [165] giving 3.0359 MeV.

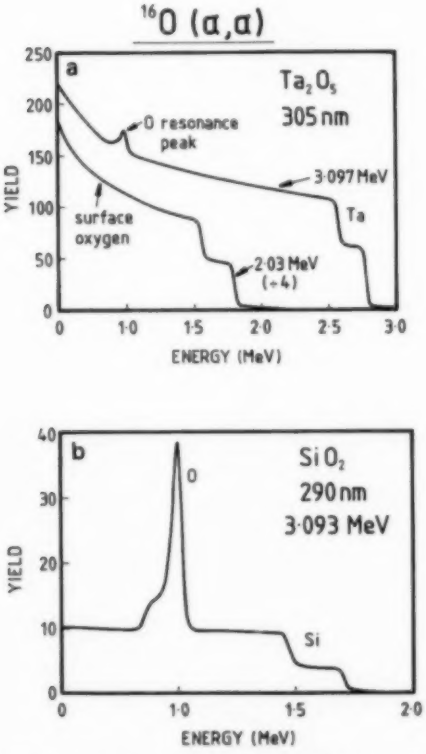

Fig. 29. (a) Shows the effects of the 3.04 MeV resonance on (α, α) scattering in Ta_2O_5 target at energies below (2.03 MeV) and above (3.097 MeV) this resonance. (b) Typical spectrum showing the effects of 3.04 MeV resonance for three different ion energies. Taken from ref. [53].

The Rutherford cross section at the 3.04 MeV resonance is 32.0 mb/sr at 170.5° and ref. [66] gives the peak cross section of 22.66 times Rutherford for a 6 keV thick target, that is 725 mb/sr, way off the top of our plot fig. 28b.

Blanpain et al. [53] give a good example of the use of (α, α) resonance scattering to enhance the oxygen signal in a Ta_2O_5 sample and an SiO_2 sample. These are shown in figs. 29a and 29b. The standard RBS yields falling steadily as $(Z/E)^2$ are shown in fig. 29a for a ^4He energy of 2.03 MeV. The surface oxygen signal in this spectrum for Ta_2O_5 305 nm thick is completely swamped, only being present in the step down in the Ta edge. While at 3.097 MeV an oxygen peak is clearly visible as well as the step down in the Ta edge. Fig. 29b shows 3.093 MeV ^4He in SiO_2 layer (290 nm) here Si and O are closer in atomic number and the oxygen resonance peak is well above the Si signal that it sits on.

Another example is shown in figs. 30a and 30b, taken from the work of Li et al. [69]. It clearly demonstrates the effects on RBS spectra when the helium ion energy is above and below the large 3.04 MeV resonance. These spectra are both for 300 nm CuO films on Si substrate. In fig. 30b the incident energy has been varied from 3.068 to 3.155 MeV to demonstrate the broadening of this peak due to energy straggling at depth.

Leavitt et al. [62] also demonstrate with their analysis of several YBaCuO films, the further kinematic advantage of using ion energies above 2 MeV where cross sections cease to be Rutherford. Figs. 31a and 31b show their work for 1.892 and 3.776 MeV ^4He ions on 250 nm YBaCuO films containing Ba and W impurities. Clearly at the higher alpha energies the Cu, Y, Ba and W signals are better resolved. The price you pay for this is poorer depth resolution and a lower yield.

Hofsass et al. [68] have developed the elastic recoil coincidence (ERC) method with high sensitivity to profile light elements up to oxygen in thin polymer foils or thin samples containing heavier elements. In this technique the forward scattered ^4He ion and the elastically recoiled heavy atom are detected in coincidence. Target thicknesses less than 2 μm are required to detect light elements like B, C, N and O using this technique. For 2 MeV He ions depth resolutions of up to 50 nm were obtained for oxygen analysis up to depths of 1 μm polycarbonate films.

Mezey et al. [119] have compared Auger/RBS/SIMS and resonance scattering techniques for oxygen analysis in silicon. The results are given in table 12. They conclude normal RBS is severely restricted in its ability to detect even buried oxide layers. SIMS is by far the most sensitive but needs high vacuums. The resonance scattering and SIMS are both isotopically

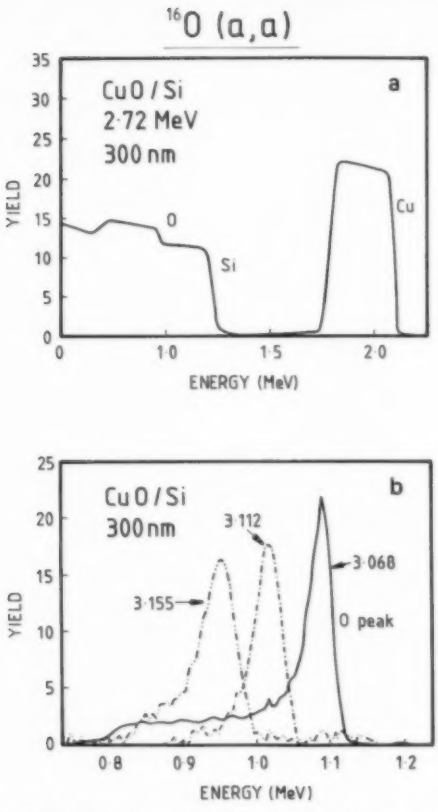

Fig. 30. Typical spectra for 300nm CuO layer in a Si substrate for $^{16}O(\alpha, \alpha)$ reaction at (a) below the resonance and (b) above the resonance for three different ion energies. Taken from ref. [69].

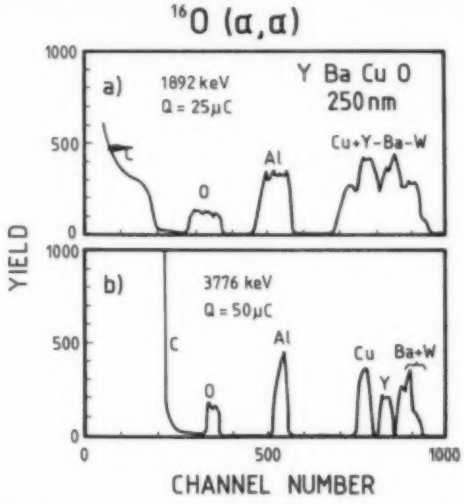

Fig. 31. Typical spectra for $\alpha + ^{16}O$ reaction on YBaCuO films (a) at 1.892 MeV and (b) at 3.776 MeV. Taken from ref. [62].

Table 12
A comparison of RBS, Auger, SIMS and (α, α) scattering for oxygen analysis

Technique	Sensitivity	
2 MeV He RBS	≥ 10 at.%	5×10^{21} cm^{-3}
3.04 MeV (α, α)	0.5–1 at.%	10^{20} cm^{-3}
Auger	< 0.1 at.%	$\leq 5 \times 10^{19}$ cm^{-3}
SIMS (10^{-7} T)	0.001 at.%	5×10^{17} cm^{-3}
SIMS (10^{-10} T)	0.0002 at.%	10^{16} cm^{-3}

sensitive and RBS and scattering can both be used in channelling mode to obtain crystallographic information. Correction procedures for Auger and SIMS techniques for oxygen are complicated and require standards.

4.7. $^{18}O(p, p)^{18}O$

Unlike the $^{16}O(p, p)$ reaction, which has few resonances below 3 MeV, the $^{18}O(p, p)$ reaction has both a large number of resonance above 1.5 MeV and is non Rutherford in magnitude. The common resonances with their widths are given in table 19.18 of ref. [132]. Many of these correspond to proton resonances in the $^{18}O(p, \alpha)^{15}N$ reaction which has the same compound nucleus ^{19}F. The stronger resonances in our region of interest (0 to 4 MeV) are listed in table 13.

The cross section data for $^{18}O(p, p)$ scattering at 90° and 140–160° are shown in figs. 32a and 32b. Above the 846 keV resonance the (p, p) cross sections generally lie above Rutherford by significant amounts depending on the reaction angle.

Carlson et al. [145] give the angular dependence of major resonances between 840 keV and 2 MeV. These generally peak at two to three times Rutherford at backward angles. Except for the 1.766 MeV resonance

Table 13
Major resonances in the $^{18}O(p, p)^{18}O$ reaction between 0.5 and 4 MeV and their widths taken from ref. [135]

E_p [MeV]	Γ_{lab} [keV]	E_p [MeV]	Γ_{lab} [keV]
0.6326	2.1	2.2289	33
0.846	47	2.387	24
1.2390	6.1	2.644	4.6
1.4025	5.2	3.029	19.5
1.766	3.6	3.165	–
2.001	31	3.479	2.3

which is close to Rutherford at 90° and about seven times Rutherford at large backward angles. Below the 846 keV resonance cross sections are near or below Rutherford. On the low energy side of the 846 keV resonance, fig. 32a shows that at 90° the cross section is at 50% Rutherford rising slowly back to Rutherford at about 750 keV. Yagi [171] measured the (p, p) cross section at the high side peak of the 846 keV resonance (857 keV) as 360 ± 26 mb/sr for centre of mass reaction angle of 140.8°. Carlson [145] gives this high side peak cross section as 285 ± 15 mb/sr for $\psi_{lab} = 159.5°$ and 565 ± 30 mb/sr for $\psi_{lab} = 86.8°$. This compares with the Rutherford cross section at 857 keV of 143, 120 and 506 mb/sr for reaction angles of 140.8, 159.5 and 86.8°, respectively.

The 846 keV resonance is an s($l = 0$) wave resonance in the elastic scattering cross section as characterised by a dip then rise at backward angles and a dip then small rise at 90°. Similarly, the 1.766 MeV resonance is due to an even l value ($l = 2$) but the rise then dip at backward angles with a dip then small rise at 90° for increasing energy suggests a d wave excitation.

Other resonance parameters for E_p between 3.4 and 6.2 MeV for over 20 resonances have been measured by Almanza et al. [80] and Orichara et al. [148].

For sufficiently thin targets (< 250 keV) the energy region 1.0 to 1.5 MeV is a reasonably smooth region with cross sections roughly two times Rutherford for reaction angles greater than 90°. This may be useful for probing ^{18}O depth profiles to μm depths. Just above this region at 1.766 MeV there is a sharp resonance with a total width of only 3.6 keV which is good for depth profiling at backward angles (160°) to large depths also. Carlson et al. [145] give the peak cross section (lab frame) for this resonance as (205 ± 11) mb/sr at $\psi_{lab} = 159.5°$.

Early work by Carlson et al. [145] and later by Din [102] show there is a 1.982 MeV γ-ray from the inelastic proton scattering reaction $^{18}O(p, p\gamma)$. Din [102] gives the γ-ray yield as a function of energy over the range 3 to 6.5 MeV. The yields from this γ-ray are sufficient to use it also for oxygen analysis.

There appears to be no advantages in using $^{18}O(p, p)$ scattering over $^{16}O(p, p)$. The increased cross section and hence yield from the 846 keV or the 1.766 MeV resonances in ^{18}O over the ^{16}O cross sections at these energies is not compensated for by the factor of 50 reduction in the natural abundances of the two isotopes. So unless the samples are significantly ^{18}O enriched no advantage is obtained. The depth resolutions and sensitivities are also very similar for similar experimental conditions.

4.8. $^{18}O(p, \alpha)^{15}N$

The most favoured reaction for ^{18}O analysis is the $^{18}O(p, \alpha)^{15}N$ reaction since it requires relatively low bombarding energies (usually around 1 MeV) for relatively high count rates enabling isotopic abundance on or near the surface to be determined very rapidly. For incident proton energies between 0.5 and 1.0 MeV this reaction produces one group of alpha particles and there are few interfering proton induced reactions, hence backgrounds are low and sensitivities high. Fig. 33 shows typical (p, α) spectra versus alpha energy for four different levels of ^{18}O-enriched tantalum oxide. Table 4c gives $Q = 3.9804$ MeV and for 846 keV protons, the outgoing alpha has an energy of 3.761 MeV at 90°. The scattering 846 keV protons are stopped by about 14 μm of Mylar. The alpha energies of fig. 33 lie between 0.6 and 1.1 MeV after traversing 16 μm of Mylar foil between the target and the detector. That it

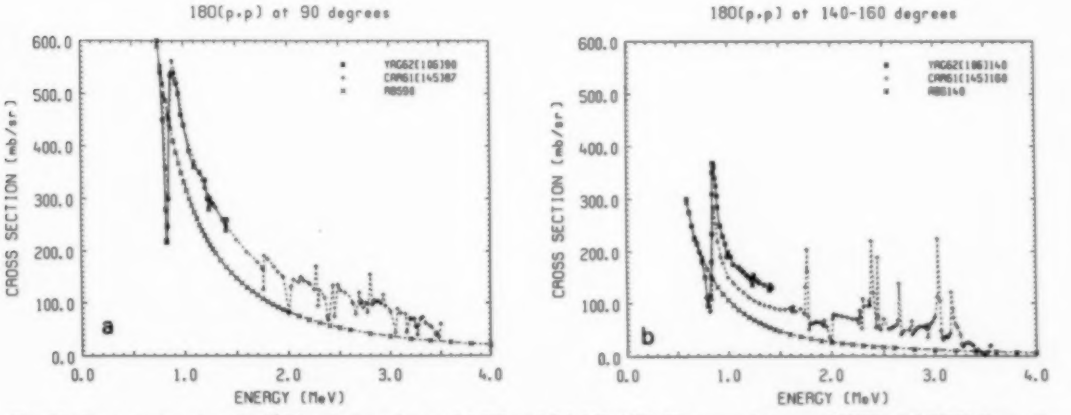

Fig. 32. Cross section data for $^{18}O(p, p)$ scattering at (a) 90° and (b) 140–160°. The smooth curves RBS90 and RBS140 are the Rutherford values for 90 and 140°, respectively.

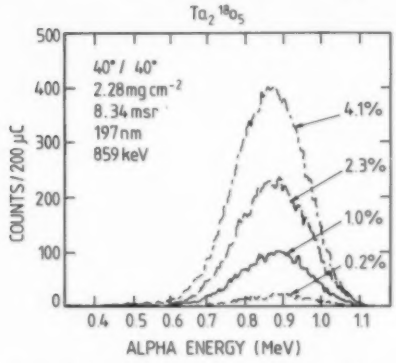

Fig. 33. Typical $^{18}O(p, \alpha)^{15}N$ spectra for 859 keV protons on a 197 nm thick $Ta_2^{18}O_5$ target at a reaction angle of 80°. The data is shown for four levels of ^{18}O enrichment and taken from ref. [98].

they lose about 70% of their energy traversing the foil. The peaks clearly sit on essentially a zero background for several hundred keV either side. This large energy loss of the alpha particles in traversing the foil generally limits the depth resolution to about 20 nm or more for the 846 keV resonance.

In figs. 34a to 34d we show the cross sections data for the $^{18}O(p, \alpha)^{15}N$ reaction at 30, 80–90, 135–145 and 155–170° reaction angles. The key feature of this data for small reaction angles is the 846 keV resonance rising to over 100 mb/sr at forward angles (< 30°). At backward angles other key resonances increase in size, noticeably the 633 and 1.766 keV resonances both being larger than the 846 keV for angles greater than 160°.

Carlson et al. [145] measured (p, α) cross sections from 0.8 to 3.5 MeV as early as 1961 for reaction angles of 87 and 160° and identified 35 resonances.

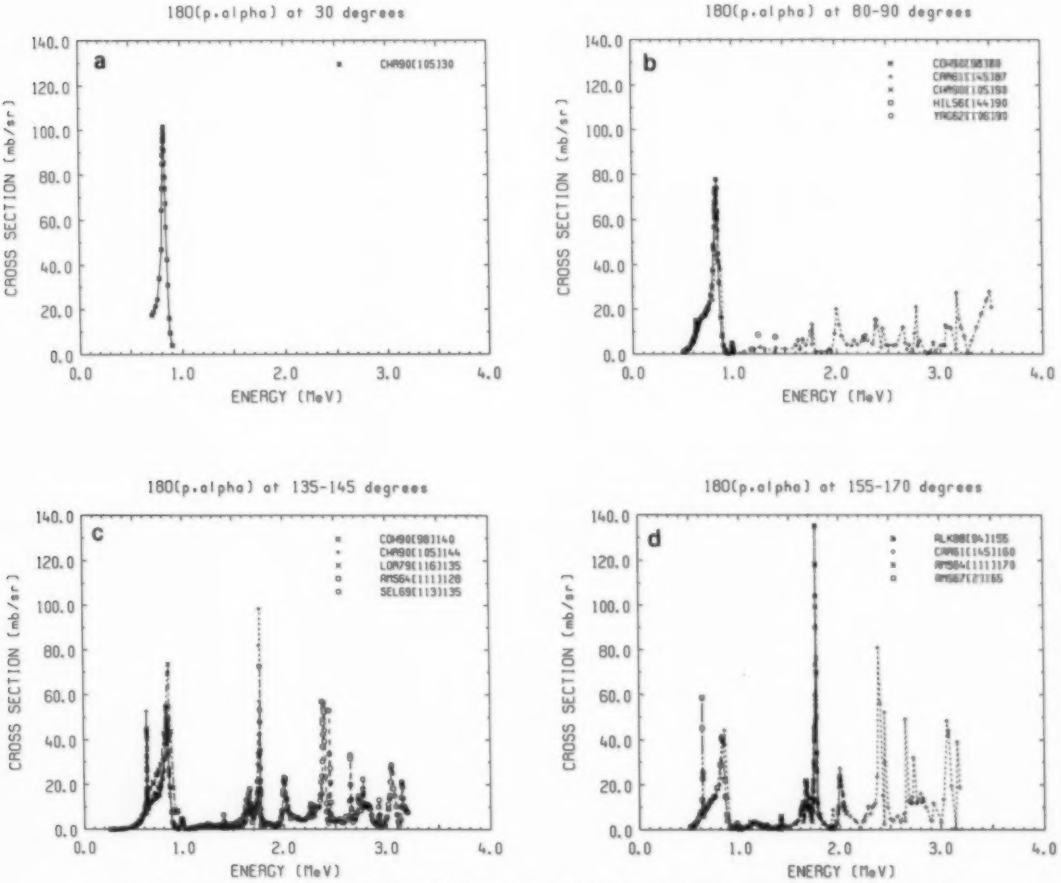

Fig. 34. Cross section data for $^{18}O(p, \alpha)^{15}N$ reaction at (a) 30°, (b) 80–90°, (c) 135–145° and (d) 155–170°.

Table 14
Resonances, widths and centre of mass cross sections for major resonances in the $^{18}O(p, \alpha)^{15}N$ reaction. Adapted from refs. [135,187]

E_p [MeV]	Γ_{lab} [keV]	$\sigma(170°)$ [mb/sr]	E_p [MeV]	Γ_{lab} [keV]	$\sigma(170°)$ [mb/sr]
0.152	0.050	–	1.766	4.5	~135
0.6326	2.1	–	1.928	0.16	6.7
0.846	47	~60	2.001	31	22
0.987	3.8	~45	2.387	24	~80
1.135	140	2.84	2.644	4.6	~50
1.1685	0.6	–	3.029	19.5	~50
1.2390	6.1	2.05	3.479	23	
1.4025	5.2	5.37			
1.620	30	10.7			
1.668	27	19.7			

This was ten more than the earlier work of Hill and Blair [144] and Clarke et al. [146] at 90°. Amsel [2,187] also measured resonances and cross sections for this reaction and these are displayed graphically in the Ion Beam Handbook and used extensively today [173]. In 1979 Lorentz et al. [116] studied the (p, α) reaction at stellar energies from 72 to 935 keV and reaction angles of 90 and 135° and observed resonances for proton energies as low as 95 and 152 keV. Recently Battistig et al. [188] and the group from France have revisited this narrow (50 eV) 152 keV resonance in the (p, α) reaction and shown that it looks very promising for high depth resolution profiling of ^{18}O.

Table 14, adapted from ref. [135] table 19.17 and table 7 of ref. [187], lists proton resonances, their widths and centre of mass cross sections for major resonances in the $^{18}O(p, \alpha)^{15}N$ reaction.

In the proton range 0 to 4 MeV the 1.766 MeV narrow resonance has by far the largest cross section. Recent measurements of this resonance by Alkomade et al. [94] give 135 ± 5 mb/sr and a width of 4.5 keV at 155°. They also measured the cross section of a 20 keV wide plateau between 1.740 and 1.760 MeV as 45 ± 1.5 mb/sr and then fitted a split Breit Wigner, as suggested by Cohen et al. [90] to obtain the peak resonance and width. The early work of Carlson [145] found 83 ± 7 mb/sr, Amsel [111] 95 mb/sr at 155° for the peak and 41 ± 4 mb/sr and 36 mb/sr, respectively, for the low energy plateau. The most recent work by Christensen et al. [105] found the peak cross section was 98 ± 3 mb/sr at 144°.

The relative high energy of the protons and narrow width of the 1.766 keV resonance together with the low cross sections either side of this resonance made it well suited for oxygen profiling to depths of several micrometres. The big disadvantage is that no foils can be used to stop the scattered protons (see table 4c) as their energy is too high and the foil would not allow the alpha through either, especially at backward angles where this resonance is largest.

Foils can be used for the lower 633 and 846 keV resonances and these have also been commonly used for ^{18}O analysis [79,82–85,87,95,96,98,105,116,142].

In 1990 Christensen et al. [105] analysed both these resonances in detail. They concluded that the nominal 846 keV resonance energy as given by ref. [135] should be 833 keV. Recent energy measurements by us confirm this shift to lower energies and we obtained 837.1 ± 1.4 keV and 630.6 ± 1.8 keV for the lower resonances and 982.6 ± 1.8 keV for the nominal 987 keV resonance. These are all lower than the nominal values of ref. [135] table 19.17 given in our table 14.

The peak cross section for the 846 keV resonance at various angles has been measured by several authors. The results are shown in table 15.

The recent work of Christensen et al. [105] confirms the cosine dependence of this reaction and agrees well with the early theoretical calculations of Yagi [106] at 90°. The cross section peaks around 100 mb/sr at small reaction angles and falls to just above 40 mb/sr near 180°. Christensen points out that the value of Cohen

Table 15
Peak cross section measurements for the $^{18}O(p,\alpha)^{15}N$ 846 keV resonance.

Author	Year	Ref.	Cross section [mb/sr]	
			90°	140–160°
Hill and Blair	1956	[144]	25	–
Carlson	1961	[145]	60 ± 4	44
Yagi	1962	[106]	74	–
Amsel	1967	[2]	–	41
Lorenz	1979	[116]	62 ± 8	–
Kaim	1979	[24]	–	37
Cohen	1990	[98]	47 ± 6	42 ± 5
Christensen	1990	[105]	72	45

Table 16
Cross section values for the $^{18}O(p, \alpha)$ reaction at 750 keV

Author	Year	Ref.	Cross section [mb/sr]	Angle
Amsel	1967	[2]	15.5	165°
Lorenz	1979	[116]	26.0	90°
Kaim	1979	[24]	14	150°
Cohen	1990	[98]	20	80°
			15	140°
Christensen	1990	[105]	19.5	144°
			17.9	165°

[98] is systematically low and so we have normalised this data only over the energy range 0.55 to 1.0 MeV in the plots of figs. 34b and 34c to the value of Yagi of 74 mb/sr at 90°.

The narrow 633 keV resonance has opposite angular dependence to the 846 keV resonance peaking at backward angles and almost disappears altogether at angles below 90°. Christensen [105] gives 53 mb/sr at 144°, Amsel [2] 58 mb/sr at 165°, Cohen [98] 45 mb/sr at 140°, Lorenz [116] 46 mb/sr at 135° and Kaim [24] 26 mb/sr at 150°. At around 750 keV the (p, α) cross section is almost independent of angle and table 16 gives values for this region. There is quite a spread in results for a relatively flat portion of this cross section spectrum.

Amsel and Samuel [2] quote $\sigma(\text{mb/sr}) = 3.38 \times 10^{-4} \exp[E/58\ \text{keV}]$ for 400 keV < E < 600 keV which gives 0.334, 1.87 and 10.5 mb/sr at 165° at 400, 500 and 600 keV, respectively, over the 200 keV range relatively free of resonances and independent of angle in this region.

As already stated there are only a few (p, α) reactions that may interfere with the $^{18}O(p, \alpha)$ reaction. These together with their Q values are listed in table 17 and have been discussed by Lappalainen et al. [192]. In general the differing Q values to the $^{18}O(p, \alpha)$ reaction ($Q = 3.9804$ MeV) means these alpha groups will have significantly different energies to the ^{18}O group and have with sufficient resolution can be easily distinguished.

Table 17
(p, α) reactions that may interfere with the $^{18}O(p, \alpha)$ reaction, their Q values and abundances

Reaction	Q [MeV]	Abundances [%]
$^{15}N(p, \alpha)^{12}C$	4.966	0.37
$^{11}B(p, \alpha)^{8}Be$	8.590	80.22
$^{19}F(p, \alpha)^{16}O$	8.115	100
$^{9}Be(p, \alpha)^{6}Li$	2.125	80.22
$^{7}Li(p, \alpha)^{4}He$	17.347	92.58

Table 3a shows that the ^{12}C and ^{14}N (p, α) reactions have large negative Q values and for proton energies below 2.4 MeV are of no consequence.

Din [102] shows that there are two γ-rays associated with the $^{18}O(p, \alpha\gamma)$ reaction. These have energies of 5.276 and 5.304 MeV and for proton energies between 3 and 7 MeV give sufficient yields to also be used to analyse for ^{18}O. However, for energies above 2.5 MeV the $^{18}O(p, n)$ channel is available and neutrons will be produced as well.

Clearly, there are many other charged particle reactions, for the analysis of oxygen, which we have not discussed in detail here. For example, Wood et al. [81] use the $^{18}O(p, n)^{18}F$ ($Q = -2.4379$ MeV) reaction. Where they look at the ^{18}F positron annihilation γ-rays to analyse very small (20 μl) liquid samples of ^{18}O enriched water, using 8.5 MeV protons. Hill and Blair [144] show that there are also several large lower energy $^{18}O(p, n)$ resonances at 2.65, 3.04 and 3.26 MeV with widths of 10, 33 and 29 keV, respectively, whose peak cross sections lie between 10 and 25 mb/sr for neutron production. These less frequently used reactions have been referenced in table 2 for information. In this review we have restricted ourselves mainly to the common charged particle reactions in the energy range 0 to 4 MeV which produce particles readily detected by modern surface barrier detectors.

5. Conclusion

In this review we summarised the work in about 200 references on charged particle analysis of oxygen. Oxygen is obviously a most important element in the periodic table and techniques that can detect its presence from a few atomic percent upwards are most useful. The nuclear reaction techniques described in this review are not exhaustive, but are representative, of methods that have unique capabilities. They are, fast, nondestructive, good sensitivity, can analyse very small samples and have the ability to depth profile oxygen in the near surface regions of solid samples with resolutions down to 10 nm or so under favourable conditions.

Typically the best results are obtained when an isolated resonance, with a high peak cross section is chosen, such as the 973 keV resonance in the $^{16}O(d, p_1)$ reaction is used. The chosen reaction should be free of other large resonances below the input ion energy for thick targets or the targets should be sufficiently thin so that lower energy resonances do not interfer. In the past the (d, p) reactions have been favoured, however, with many more modern accelerators being placed in laboratories without neutron shielding, the ^{3}He reactions together with resonant elastic scattering reactions

have become popular, since these are not prolific neutron-producing reactions.

The recent upsurge in nuclear reaction analysis of oxygen has meant that many of the old cross section measurements carried out in the 1950's and 1960's are being repeated more precisely. In many of these cases measurements are now being made using modern surface barrier particle detectors for the first time. If precise and accurate measurements to a few percent are to be achieved it is necessary to have confidence in these reaction cross section measurements and exchange of standard targets and round robin type measurements between international laboratories should be encouraged. Oxide standards are easily prepared by anodising tantalum, aluminium, silicon or even zirconium. Tantalum is the most common, and standards from a few nanometres to hundreds of nanometres thick, which are durable and stable over many years, have been used to calibrate experimental systems and measure cross sections.

The advent of modern high speed personal computers means that simulation codes like RUMP [197], or our GENUREAC [152], are becoming quite common. These codes require not only resonant peak cross sections but also resonant shapes near the peak and more reliable measurements of this type should be encouraged.

References

[1] E. Möller, L. Nilsson and N. Starfelt, Nucl. Instr. and Meth. 50 (1967) 270.
[2] G. Amsel and D. Samuel, Anal. Chem. 39 (1967) 1689.
[3] G. Amsel, B. Béranger, B. de Gélas and P. Lacombe, J. Appl. Phys. 39 (1968) 2246.
[4] J.F. Lamb, D.M. Lee and S.S. Markowitz, Anal. Chem. 42 (1970) 212.
[5] A.V. Nero and A.J. Howard, Nucl. Phys. A210 (1973) 60.
[6] A. Turos, L. Wielunski and A. Barcz, Nucl. Instr. and Meth. 111 (1973) 605.
[7] J. Lorenzen, Nucl. Instr. and Meth. 136 (1976) 289.
[8] R.L. Schulte, Nucl. Instr. and Meth. 137 (1976) 251.
[9] H. Münzel, F. Michel, P.P. Coetzee and V. Krivan, J. Radioanal. Chem. 37 (1977) 267.
[10] G. Debras and G. Deconninck, J. Radioanal. Chem. 38 (1977) 193.
[11] M. Valladon and J.L. Debrun, J. Radioanal. Chem. 39 (1977) 385.
[12] G. Beurton and R. Pillon, J. Radioanal. Chem. 40 (1977) 189.
[13] J.A. Borders and J.M. Harris, Nucl. Instr. and Meth. 149 (1978) 279.
[14] S. Petersson and H. Norde, Nucl. Instr. and Meth. 149 (1978) 285.
[15] S.T. Picraux, Nucl. Instr. and Meth. 149 (1978) 289.
[16] J.K. Hirvonen and W.H. Lucke, Nucl. Instr. and Meth. 149 (1978) 295.
[17] A. Niiler and R. Birkmire, Nucl. Instr. and Meth. 149 (1978) 301.
[18] J.P. Ponpon, J.J. Grob, A. Grob, R. Stuck and P. Siffert, Nucl. Instr. and Meth. 149 (1978) 647.
[19] B. Borderie and J.N. Barrandon, Nucl. Instr. and Meth. 156 (1978) 483.
[20] R.L. Schulte and E.A. Kamykowski, J. Radioanal. Chem. 43 (1978) 233.
[21] M.D. D'Agostino, E.A. Kamykowski, F.J. Kuehne, G.M. Padawer, E.J. Schneid, R.L. Schulte, M.C. Stauber and F.R. Swanson, J. Radioanal. Chem. 43 (1978) 421.
[22] L.O. Norlin, B. Orre, G. Possnert and K. Johansson, Phys. Scripta 17 (1978) 439.
[23] D.R. Williams, J.S. Hislop, A.P. Mead, T.W. Sanders and D.A. Wood, J. Radioanal. Chem. 48 (1979) 213.
[24] R.E. Kaim and D.W. Palmer, J. Radioanal. Chem. 48 (1979) 295.
[25] P. Debefve, H.P. Do, C. Friedli, P. Lerch and M. Renaud, Radiochem. Radioanal. Lett. 40 (1979) 389.
[26] J.C.P. Heggie, Z.E. Switkowski and G.J. Clark, Nucl. Instr. and Meth. 168 (1980) 125.
[27] J.W. McMillan and F.C.W. Pummery, Corrosion Sci. 20 (1980) 41.
[28] E. Kótai, G. Mezey, T. Lohner, A. Manuaba, F. Pászti and J. Gyulai, Nucl. Instr. and Meth. 180 (1981) 619.
[29] A. Anttila, R. Hänninen and J. Räisänen, J. Radioanal. Chem. 62 (1981) 293.
[30] P. Debefve, H.P. Do, C. Friedli and P. Lerch, J. Radioanal. Chem. 64 (1981) 213.
[31] H. Yonezawa, T. Shigematsu and K. Kudo, J. Radioanal. Chem. 68 (1982) 135.
[32] R. Lappalainen, A. Anttila and J. Räisänen, Nucl. Instr. and Meth. 212 (1983) 441.
[33] M. Isshiki, K. Arakawa, S. Satoh, M. Nagano, Y. Fukuda, K. Chiba and K. Igaki, Trans. ISIJ 23 (1983) 796.
[34] M. Braun and T. Fried, Z. Phys. A311 (1983) 173.
[35] C.R. Gossett, Nucl. Instr. and Meth. 218 (1983) 149.
[36] H.J. Dowell, E.A. Schweikert and T.H. Ramsey, J. Radioanal. Chem. 81 (1984) 125.
[37] J.C.B. Simpson, J.M.C. Groves and L.G. Earwaker, Nucl. Instr. and Meth. B9 (1985) 321.
[38] K. Bethge, Nucl. Instr. and Meth. B10/11 (1985) 633.
[39] E.L. Haase and I. Khubeis, Nucl. Instr. and Meth. B10/11 (1985) 727.
[40] A.Z. Kiss, E. Koltay, B. Nyakó, E. Somorjai, A. Anttila and J. Räisänen, J. Radioanal. Chem. Articles 89 (1985) 123.
[41] R.L. Hahn and E. Ricci, Phys. Rev. 146 (1966) 650.
[42] J.A. Leavitt, P. Stoss, D.B. Copper, J.L. Seerveld and L.C. McIntyre, Nucl. Instr. and Meth. B15 (1986) 296.
[43] P. Person, A. Chevarier, N. Chevarier, P. Clechet, D. Lamouche, J.R. Martin and M. Stern, Nucl. Instr. and Meth. B15 (1986) 425.
[44] M. Dubus, J. Margail and P. Martin, Nucl. Instr. and Meth. B15 (1986) 559.
[45] J. Räisänen, Nucl. Instr. and Meth. B17 (1986) 344.
[46] B.W. East, T. Preston and I. Robertson, Proc. Int. Symp. on In-vivo Body Composition Studies, Upton, USA, 1986, p. 155.
[47] M.E. Anderson, J. Radioanal. Chem. 100 (1986) 373.

[48] D. Gihwala and M. Peisach, J. Radioanal. Nucl. Chem. Lett. 106 (1986) 9.
[49] R.G. Musket, Nucl. Instr. and Meth. B24/25 (1987) 698.
[50] N. Bordes, G. Blondiaux, C.J. Maggiore, M. Valladon, J.L. Debrun, R. Coquille and M. Gauneau, Nucl. Instr. and Meth. B24/25 (1987) 722.
[51] J. Räisänen, T. Witting and J. Keinonen, Nucl. Instr. and Meth. B28 (1987) 199.
[52] M. Iwamoto and T. Nozaki, J. Radioanal. Nucl. Chem. Articles 125 (1988) 143.
[53] B. Blanpain, P. Revesz, L.R. Doolittle, K.H. Purser and J.W. Mayer, Nucl. Instr. and Meth. B34 (1988) 459.
[54] E. Rauhala, J. Keinonen and R. Järvinen, Appl. Phys. Lett. 52 (1988) 1520.
[55] W. Chu, J.W. Mayer and M.A. Nicolet, Backscattering Spectrometry (Academic Press, New York, London, 1978).
[56] J.C. Barbour, B.L. Doyle and S.M. Myers, Phys. Rev. B38 (1988) 7005.
[57] Z. Tao, D.E. Alburger, K.W. Jones, Y.D. Dao and Y.H. Kao, Appl. Phys. Lett. 53 (1988) 1440.
[58] H.A. Ras and R. Pretorius, Nucl. Instr. and Meth. B35 (1988) 488.
[59] P. Berning and R.E. Benenson, Nucl. Instr. and Meth. B36 (1989) 335.
[60] T. Nozaki, M. Iwamoto and T. Ido, Int. J. Appl. Radiat. Isotopes 25 (1974) 393.
[61] T. Xie, S.R. Ryan and H.J. Fischbeck, Nucl. Instr. and Meth. B40/41 (1989) 766.
[62] J.A. Leavitt and L.C. McIntyre, Jr., Nucl. Instr. and Meth. B40/41 (1989) 797.
[63] J.R. Cameron, Phys. Rev. 90 (1953) 839.
[64] J.A. Kuehner, E. Almqvist and D.A. Bromley, Phys. Rev. 122 (1960) 908.
[65] W.N. Lennard, S.Y. Tong, I.V. Mitchell and G.R. Massoumi, Nucl. Instr. and Meth. B43 (1989) 187.
[66] J.A. Leavitt, L.C. McIntyre Jr., M.D. Ashbaugh, J.G. Oder, Z. Lin and B. Dezfouly-Arjomandy, Nucl. Instr. and Meth. B44 (1990) 260.
[67] F. Abel, G. Amsel, E. d'Artemare, C. Ortega, J. Siejka and G. Vizkelethy, Nucl. Instr. and Meth. B45 (1990) 100.
[68] H.C. Hofsäss, N.R. Parikh, M.L. Swanson and W.-K. Chu, Nucl. Instr. and Meth. B45 (1990) 151.
[69] J. Li, L.J. Matienzo, P. Revesz, G. Viskelethy, S.Q. Wang, J.J. Kaufman and J.W. Mayer, Nucl. Instr. and Meth. B46 (1990) 287.
[70] J. Keinonen and J. Räisänen, Nucl. Instr. and Meth. B50 (1990) 39.
[71] E.H. Bakraji, A. Giovagnoli, G. Blondiaux and J.L. Debrun, Nucl. Instr. and Meth. B50 (1990) 65.
[72] B. Gebauer, D. Fink, P. Goppelt, M. Wilpert and Th. Wilpert, Nucl. Instr. and Meth. B50 (1990) 159.
[73] H.D. Carstanjen, W. Decker, J. Diehl, Th. Enders, R.M. Emrick, A. Föhl, E. Frieland, D. Plachke and H. Stoll, Nucl. Instr. and Meth. B51 (1990) 152.
[74] J.P. Stoquert, E. Fogarassy, R. Stuck, G. Guillaume and P. Siffert, Surf. and Interf. Anal. 15 (1990) 57.
[75] L.G. Earwaker, Nucl. Instr. and Meth. 197 (1982) 41.
[76] A.E. Pillay and D.K. Bewley, J. Appl. Radiat. Isotopes 34 (1983) 1571.
[77] M. Peisach, R. Pretorius and P.J. Strebel, Anal. Chem. 40 (1968) 850.
[78] A.W. Rosenstein and A. Nir, Anal. Chem. 45 (1973) 1707.
[79] R. Robin, A.R. Cooper and A.H. Heuer, Anal. Chem. 44 (1973) 3770.
[80] R. Almanza and G. Murillo, Nucl. Phys. A248 (1975) 214.
[81] R.A. Wood, K.A. Nagy, N.S. MacDonald, S.T. Wakakuwa, R.J. Beckman and H. Kaaz, Anal. Chem. 47 (1975) 646.
[82] E. Rosencher, A. Straboni, S. Rigo and G. Amsel, Appl. Phys. Lett. 34 (1979) 254.
[83] J.M. Calvert and D.G. Lees, J. Radioanal. Chem. 48 (1979) 287.
[84] J.F. Singleton and N.E.W. Hartley, J. Radioanal. Chem. 48 (1979) 317.
[85] A.M. Pritchard, N.E.W. Hartley, J.F. Singleton and A.E. Truswell, Corrosion Sci. 20 (1980) 1.
[86] B. Maurel, G. Amsel and Nadai, Nucl. Instr. and Meth. 197 (1982) 1.
[87] E.W.A. Young and J.H.W. de Witt, Oxidation of Metals 26 (1986) 351.
[88] A.E. Champagne and M.L. Pitt, Nucl. Phys. A457 (1986) 367.
[89] C.M. Wai and M.E. Dysart, Anal. Chem. 58 (1986) 3266.
[90] D.D. Cohen, A. Katsaros and D. Garton, Nucl. Instr. and Meth. B15 (1986) 555.
[91] A. Wriekat, Mater. Sci. Eng. 85 (1987) 181.
[92] S.D. Bradshaw, D. Cohen, A. Katsaros, J. Tom and F.J. Owen, J. Appl. Physiology 63 (1987) 1296.
[93] J.R. Campbell, O.A. Abou-Zeid, W.R. Falk, R. Abegg, S.K. Datta and S.P. Kwan, Nucl. Phys. A467 (1987) 205..
[94] P.F.A. Alkemade, C.A.M. Stap, F.H.P.M. Habraken and W.F. van der Weg, Nucl. Instr. and Meth. B35 (1988) 135.
[95] L.F.R. Ferreira, J.M. Calvert, C. Gleave, D.G. Lees and P.C. Rowlands, Proc. R. Soc. London A422 (1989) 279.
[96] S.N. Nwosu and H.J. Fischbeck, Nucl. Instr. and Meth. B40/41 (1989) 833.
[97] S.N. Nwosu and H.J. Fischbeck, Nucl. Instr. and Meth. B40/41 (1989) 857.
[98] D.D. Cohen, S.D. Bradshaw, F.J. Bradshaw and A. Katsaros, Nucl. Instr. and Meth. B50 (1990) 43.
[99] J.R. Speakman, K.A. Nagy, D. Masman, W.G. Mook, S.D. Poppitt, G.E. Strathearn and P.A. Racey, Anal. Chem. 62 (1990) 703.
[100] G. Stingeder, S. Gara, S. Pahlke, H. Schwenk, E. Guerrero and M. Grasserbauer, Fresenius Z. Anal. Chem. 333 (1989) 576.
[101] P.P. Matyash, N.A. Shakun and N.P. Dikii, ZhETF Pis. Red. 19 (1974) 31.
[102] G.U. Din, Nucl. Phys. A134 (1969) 655.
[103] M.H. Thiemens and D. Meagher, Anal. Chem. 56 (1984) 201.
[104] A. Schimmelmann and M.J. DeNiro, Anal. Chem. 57 (1985) 2644.

[105] N.S. Christensen, F. Jensen, F. Besenbacher and I. Stensgaard, Nucl. Instr. and Meth. B51 (1990) 97.
[106] K. Yagi, J. Phys. Soc. Japan 17 (1962) 604.
[107] E. Baumgartner and H.W. Fulbright, Phys. Rev. 107 (1957) 219.
[108] D.A. Bromley, J.A. Kuehner and E. Almqvist, Nucl. Phys. 13 (1959) 1.
[109] L.C. McDermott, K.W. Jones, H. Smotrich and R.E. Benenson, Phys. Rev. 118 (1960) 175.
[110] R.F. Seiler, C.H. Jones, W.J. Anzick, D.F. Herring and K.W. Jones, Nucl. Phys. 45 (1963) 647.
[111] G. Amsel, Annal. Phys. (Paris) 9 (1964) 247.
[112] O. Dietzsch, R.A. Douglas, E. Farrelly Pessoa, V. Gomes Porto, E.W. Hamburger, T. Polga and O. Sala, Nucl. Phys. A114 (1968) 330.
[113] D.L. Sellin, H.W. Newson and E.G. Bilpuch, Nucl. Phys. 51 (1969) 461.
[114] A. Haddou, M. Berrada and G. Paic, J. Radioanal. Nucl. Chem. Articles 102 (1986) 159.
[115] R.A. Jarjis, Nuclear Cross Section Data for Surface Analysis, Department of Physics, University of Manchester, Vol I and II (1979).
[116] H. Lorenz-Wirzba, P. Schmalbrock, H.P. Trautvetter, M. Wiescher and C. Rolfs, Nucl. Phys. A313 (1979) 346.
[117] T. Joy and D.G. Barnes, Nucl. Instr. and Meth. 95 (1971) 199.
[118] J. Gass and H.H. Müller, Nucl. Instr. and Meth. 136 (1976) 559.
[119] G. Mezey, E. Kótai, T. Nagy, L. Lohner, A. Manuba and J. Gyulai, Nucl. Instr. and Meth. 167 (1979) 279.
[120] J.A. Davies and P.R. Norton, Nucl. Instr. and Meth. 168 (1980) 611.
[121] C-D. Lien, L. Wielunski and M-A. Nicolet, Nucl. Instr. and Meth. 213 (1983) 463.
[122] M. Luomajärvi, E. Rauhala and M. Hautala, Nucl. Instr. and Meth. B9 (1985) 255.
[123] G. Demortier, F. Bodart, G. Deconninck, G. Terwagne, Z. Gabelica and E.G. Derouane, Nucl. Instr. and Meth. B30 (1988) 491.
[124] G. Vizkelethy, Nucl. Instr. and Meth. B45 (1990) 1.
[125] D.A. Bromley and E. Almqvist, Rep. Prog. Phys. 23 (1960) 544.
[126] S.S. Markowitz and J.D. Mahoney, Anal. Chem. 34 (1962) 329.
[127] J.F. Lamb, D.M. Lee and S.S. Markowitz, Anal. Chem. 42 (1970) 209.
[128] T. Iizuka, S. Takasu, M. Tajima, T. Arai, T. Nozaki, N. Inoue and M. Watanabe, J. Electrochem. Soc. 132 (1985) 1707.
[129] H.C. Chow, G.M. Griffiths and T.H. Hall, Can. J. Phys. 53 (1975) 1672.
[130] F. Ajzenberg-Selove, Nucl. Phys. A300 (1978) 1.
[131] F. Ajzenberg-Selove, Nucl. Phys. A360 (1981) 1.
[132] F. Ajzenberg-Selove, Nucl. Phys. A392 (1983) 1.
[133] F. Ajzenberg-Selove, Nucl. Phys. A449 (1986) 1.
[134] F. Ajzenberg-Selove, Nucl. Phys. A460 (1986) 1.
[135] F. Ajzenberg-Selove, Nucl. Phys. A475 (1987) 1.
[136] D.W. Palmer, Nucl. Instr. and Meth. 38 (1965) 187.
[137] D. Phillips and J.P. Scott Pringle, Nucl. Instr.a nd Meth. 135 (1976) 389.
[138] G. Amsel, J.P. Nadai, C. Ortega, S. Rigo and J. Siejka, Nucl. Instr. and Meth. 149 (1978) 705.
[139] G. Amsel, J.P. Nadai, C. Ortega and J. Siejka, Nucl. Instr. and Meth. 149 (1978) 713.
[140] M.P. Seah, M.W. Holbourn, C. Ortega and J.A. Davies, Nucl. Instr. and Meth. B30 (1988) 128.
[141] M.P. Seah, D. David, J.A. Davies, T.E. Jackman, C. Jeynes, C. Ortega, P.M. Read, C.J. Sofield and G. Weber, Nucl. Instr. and Meth. B30 (1988) 140.
[142] L. Young, Anodic Oxide Films (Academic Press, London, 1961).
[143] V. Landre, P. Aguer, G. Bogaert, A. Lefebvre and J.P. Thibaud, Phys. Rev. C40 (1989) 1972.
[144] H.A. Hill and J.M. Blair, Phys. Rev. 104 (1956) 198.
[145] R.R. Carlson, C.C. Ki, J.A. Jacobs and A.C.L. Barnard, Phys. Rev. 122 (1961) 607.
[146] R.L. Clarke, E. Almqvist and E.B. Paul, Nucl. Phys. 14 (1959) 472.
[147] H.C. Ki, R.F. Seiler, D.F. Herring and K.W. Jones, Nucl. Phys. 57 (1964) 526.
[148] H. Orihana, G. Rudolf and Ph. Gorodetzky, Nucl. Phys. A203 (1973) 78.
[149] K. Wittmaack, Vacuum 34 (1984) 119.
[150] N. Longequeue, H. Beaumevielle, E. Ligeon, J.P. Longequeue and M. Sandon, J. Physique 26 (1965) 367.
[151] D.J. Neild, P.J. Wise and D.G. Barnes, J. Phys. D 5 (1972) 2292.
[152] D.D. Cohen and E.K. Rose, Proc. 6th Australian Conf. on Nuclear Techniques of Analysis (1989) p. 156.
[153] A. Turos, L. Wielunski, A. Barcz and J. Olenski, J. Radioanal. Chem. 16 (1973) 627.
[154] J.B. Clegg, A.E. Morgan, H.A.M. de Grefte, F. Simonde, A. Huber, G. Blacmore, M.G. Dowsett, D.E. Sykes, C.W. Magee and V.R. Deline, Surf. Interf. Anal. 6 (1984) 162.
[155] S. Cavallaro, A. Cunslo, R. Potenza and A. Rubbino, Il Nuovo Cimento 14A (1973) 692.
[156] G. Deconninck, Introduction to Radioanalytical Physics (Elsevier, New York, 1978).
[157] G. Amsel, J.P. Nadai, E. D'Artemare, D. David, E. Girard and J. Moulin, Nucl. Instr. and Meth. 92 (1971) 481.
[158] Z.Y. Hua, H.S. Cheng, C.L. Jia, A.R. Jiang and B.C. Miao, Int. J. Mod. Phys. B1 (1987) 1035.
[159] Z.L. Wang, J.F.M. Westendorp and F.W. Sais, Nucl. Instr. and Meth. 211 (1983) 193.
[160] C. Engelmann, G. Filippi, J. Gosset and F. Moreau, J. Radioanal. Chem. 37 (1977) 559.
[161] A. Ait Haddou, M. Berrada and G. Paic, J. Radioanal. and Nucl. Chem. Articles 102 (1986) 159.
[162] J. Hoste and C. Vandecasteele, Nucl. Instr. and Meth. B40/41 (1989) 1182.
[163] D.E. Arafah and J.D. Meyer, J. Appl. Phys. 64 (1988) 1557.
[164] K.G. Prasad, M.B. Kurup, P. Singh, A.K. Grover, G.V.S. Rao, Nucl. Instr. and Meth. B36 (1989) 485.
[165] S.H. Sie, D.R. McKensie, G.B. Smith and C.G. Ryan, Nucl. Instr. and Meth. B15 (1986) 525.
[166] L.M. Polsky, C.H. Holbrow and R. Middleton, Phys. Rev. 186 (1969) 966.

II. REVIEW PAPERS

[167] I. Berka, K.P. Jackson, C. Rolfs, A.M. Charlesworth and R.E. Azuma, Nucl. Phys. A288 (1977) 317.
[168] C. Rolfs and W.S. Rodney, Nucl. Phys. A250 (1975) 295.
[169] C. Rolfs, W.E. Kieser, R.E. Azuma and A.E. Litherland, Nucl. Phys. A199 (1973) 274.
[170] J.R. Bird and J.S. Williams, Ion Beams for Material Analysis (Academic Press, New York, 1989).
[172] K. Yagi, K. Katari and H. Ohn Uma, J. Phys. Soc. Japan 17 (1962) 595.
[172] W.R. Allen and M.B. Lewis, Nucl. Instr. and Meth. B51 (1990) 330.
[173] J.W. Mayer and E. Rimini, Ion Beam Handbook for Material Analysis (Academic Press, New York, London, 1977).
[174] F.L. McCrackin, NBS Technical Note 479 (1969).
[175] J.R. MacDonald, J.A. Davies, T.E. Jackman and L.C. Feldman, J. Appl. Phys. 54 (1983) 1800.
[176] W. Fritsch, K.-D. Büchs, E. Finckh, P. Pietrzykr and B. Schreiber, Z. Physik 262 (1973) 65.
[177] J.F. Ziegler, J.P. Biersack and U. Littmark Stopping and Range of Ions in Solids, vol. 1 (Pergamon, New York, 1985).
[178] D.D. Cohen and E.K. Rose, Proc. 10th Int. Conf. on Ion Beam Analysis, Eindhoven, July 1991, Nucl. Instr. and Meth. B64 (1992).
[179] D.D. Cohen, G.M. Bailey and N. Dytlewski, Proc. 10th Int. Conf. on Ion Beam Analysis, Eindhoven, July 1991, in Nucl. Instr. and Meth. B64 (1992).
[180] G. Amsel and J. Davies, Nucl. Instr. and Meth. 218 (1983) 177.
[181] J. Peirriere, J. Siejka and R.P.H. Chang, J. Appl. Phys. 56 (1984) 2716.
[182] I.C. Vickridge, Nucl. Instr. and Meth. B34 (1988) 470.
[183] R.S. Alwitt, C. Ortega, N. Thorne and J. Siejka, J. Electrochem. Soc. 135 (1988) 2695.
[184] I. Montero, B. Pelloie, J. Perriere, J.C. Pivin and J.M. Albella, J. Electrochem. Soc. 136 (1989) 1869.
[185] O. Jaoul and B. Houlier, J. Geophys. Res. 88 (1983) 613.
[186] J. Siejka, J.P. Nadai and G. Amsel, J. Electrochem. Soc. 118 (1971) 727.
[187] G. Amsel, Ph.D. Thesis, Faculty of Science University of Paris (1964).
[188] G. Battistig, G. Amsel and E. D'Artemare, private communication, submitted for publication in Nucl. Instr. and Meth. B.
[189] G. Amsel, private communication, 10th Int. Conf. on Ion Beam Analysis, Eindhoven, July 1991, by J. Davies, Nucl. Instr. and Meth. B64 (1992).
[190] J.C. Wong, J. Li, C. Ortega, J. Siejka, G. Vizkelethy and Y. Lemaitre, 10th Int. Conf. on Ion Beam Analysis, Eindhoven, July 1991, Nucl. Instr. and Meth. B64 (1992).
[191] C. Ortega, A. Sacuto, J. Siejka, I. Trimaille and G. Vizkelethy, 10th Int. Conf. on Ion Beam Analysis, Eindhoven, July 1991, Nucl. Instr. and Meth. B64 (1992).
[192] R. Lappalainen, J. Raisanen and A. Anttila, Nucl. Instr. and Meth. B9 (1985) 55.
[193] A. Turos, Hj. Matzke, J. Chaumont and L. Thomé, these Proceedings (3rd Int. Conf. on Chemical Analysis, Namur, Belgium, 1991), Nucl. Instr. and Meth. B66 (1992) 280.
[194] W.H. Schulte, H. Ebbing, H.W. Becker, S. Wüstenbecker, M. Berheide, M. Buschmann, C. Rolfs, G.E. Mitchell and J.S. Schweitzer, these Proceedings (3rd Int. Conf. on Chemical Analysis, Namur, Belgium, 1991), Nucl. Instr. and Meth. B66 (1992) 11.
[195] K.K. Bourdelle, these Proceedings (3rd Int. Conf. on Chemical Analysis, Namur, Belgium, 1991), Nucl. Instr. and Meth. B66 (1992) 274.
[196] G. Demortier, these Proceedings (3rd Int. Conf. on Chemical Analysis, Namur, Belgium, 1991), Nucl. Instr. and Meth. B66 (1992) 51.
[197] L.R. Doolittle, Nucl. Instr. and Meth. B9 (1985) 344.

Nuclear Instruments and Methods in Physics Research B66 (1992) 191–204
North-Holland

Nuclear Instruments & Methods in Physics Research
Section B

Ion beam analysis of fluorine: Its principles and applications

G.E. Coote

Nuclear Science Group, DSIR Physical Sciences, P.O. Box 31312, Lower Hutt, New Zealand

I review the nuclear reactions which are suitable for ion beam analysis of fluorine in materials and for profiling fluorine in the outer few μm. The $^{19}F(p, \alpha\gamma)^{16}O$ and $^{19}F(p, p'\gamma)^{19}F$ reactions have proved the most suitable. The remarkable crystal structure of calcium hydroxyapatite, which encourages the uptake of fluoride ions during the formation or subsequent changes to a bone or tooth, results in important applications of the scanning proton microprobe. I describe applications of these techniques in research on teeth and bones, materials science, geochemistry and archaeometry.

1. Introduction

Fluorine is the most reactive chemical element, and cannot be freed from its compounds by chemical means. It is not a rare element, as it makes up an estimated 0.065% of the earth's crust. ^{19}F is the only stable isotope, and ^{18}F the longest-lived radioisotope (109.9 min). Applications of ion beam analysis are therefore restricted, since no other stable isotope with different nuclear properties can be separated and used as a tracer.

I review briefly the history of this subject, giving credit to the pioneers of new advances. I summarize the studies of nuclear reactions with F as the target, referring to those papers which provide fundamental data for ion beam analysis and depth profiling.

I review applications of fluorine analysis in the inorganic world, of geochemistry, meteoritic material and man-made materials such as alloys. Much of this work was concerned with measurements of fluorine contamination of surfaces. The review of biological studies begins with a short introduction to that essential and remarkable mineral calcium hydroxyapatite, which in some circumstances may be converted partially or completely into fluorapatite. I explain why fluorine in calcified tissues is almost always associated with this mineral, modifying its chemical properties significantly, and why we can study changes in calcified tissues by determining the fluorine distribution. I discuss the small amount of research on bone development. The study of human and animal teeth has been much more extensive; I mention the questions we are trying to answer and important advances which have occurred.

In recent years interesting results have sprung from the study of fluorine distributions in teeth and bones which had been buried for long periods. The processes which occur in the animal body occur also in these quite different conditions, and on different time scales. They can provide new information for the anthropologist and the archaeologist. There is a a brief mention of fish scales, which also contain hydroxyapatite, so it is not surprising that fluorine is there also. The fluorine occurs in remarkable patterns which differ from one species to another, and might provide better understanding of the growth patterns and life histories of fish.

2. A brief history

The gamma-rays from proton bombardment of fluorine were discovered in the 1950s. The high energy radiations from the $^{19}F(p, \alpha\gamma)^{16}O$ reaction interfere with gamma-ray spectroscopy, since they are produced prolifically from minute amounts of fluorine in collimators, targets or backings. It is pleasing that for the same reasons they have proved valuable in other branches of science. As we gain further experience and devise improved instruments we can expect many more fruitful applications.

Honour for the first application of ion beam analysis of fluorine goes to Sippel and Glover [1] in 1960. They needed new techniques for determining light elements in silicate rocks and the measurement of 6–7 MeV gamma-rays from proton bombardment was their chosen method for fluorine. They calculated stopping power corrections but showed that errors which arose from variations in stopping power of the matrix were less than 2%.

They were ahead of their time and there was no further work reported until 1967. Möller and Starfelt [2] applied the same technique to studying fluorine contamination of Zircaloy cladding for reactor fuel. They used a resonance in the reaction to measure a

0168-583X/92/$05.00 © 1992 – Elsevier Science Publishers B.V. All rights reserved

depth profile, possibly the first team to do so. In the same year Pierce et al. [3] published a list of resonances below 0.5 MeV in the elements from lithium to chlorine, and the resulting gamma-rays which could be detected in NaI or the relatively new Ge(Li) detectors.

In 1969 Bewers and Flack published a comprehensive paper on the theory and practice of fluorine determination by proton bombardment [4,5]. They presented an analysis of those factors important for quantitative determination, including the important part played by the stopping cross section. By passing the beam through a transmission foil they could analyze powders, liquids and gases.

Tooth enamel was an obvious target and the first application of depth profiling to tooth enamel was published in 1973. Mandler et al. [6], observing 6.13 MeV gamma-rays with a Ge(Li) detector, measured the fluorine concentration to a depth of 2.1 μm in teeth treated with several fluorine compounds. Studies of the inner enamel and dentine of sectioned teeth, measured with a 1 mm^2 beam, were published by Chaudhri and Crawford in 1981 [7], and depth profiling was extended to cementum in 1983 [8]. By 1984 the power of proton microprobes was being extended to sound teeth [9] and to precarious lesions [10].

The first investigation of fluorine in archaeological bones was published in 1981 [11], extended to archaeological teeth in 1982 [12], and the absorption of fluoride ions from groundwater into teeth was clarified in 1988 [13]. Proton microprobes, even rather simple ones, were able to provide unexpected information.

In recent years studies of teeth have become more sophisticated, with joint projects on tooth development in animals [14–16], and the interaction of fluorine in different chemical forms with lesions in teeth [17]. The potential of bone studies was demonstrated in an experiment on rats, which revealed the changes in fluorine distribution with age in rat femurs and vertebrae, with possible relevance to the monitoring and treatment of osteoporosis [18].

Investigations of fluorine have recently been extended to further materials: fish scales [19] and archaeological flints [20].

3. Experimental methods

Ion beam analysis of fluorine is simplified, although applications are circumscribed, by the fact that ^{19}F is the only stable isotope. Ion beam analysis can be performed with a number of reactions, although the simplicity and sensitivity of two reactions have led to their dominance.

$^{19}F(p, \alpha)^{16}O \quad Q = 8.115$ MeV

Golicheff et al. [21] measured $\sigma(p, \alpha_0, 150°)$ for E_p from 500 to 1800 keV, with a further detailed study between 1000 and 1400 keV, which includes the broad resonance at 1355 keV. For protons between 1350 and 1500 keV the detection limit was 5 $ng\,cm^{-2}$.

Dieumegard et al. [22] studied this reaction in detail over the extended energy range 300 to 2000 keV. They measured $\sigma(E, 150°)$ and $\sigma(E, 90°)$ for the α_0 group in great detail, especially in the vicinity of resonances, where automatic energy scanning was used. They list seven resonances, from 777 to 1901 keV, with the most prominent at 1347 and 1713 keV. The resonance widths were 7 keV for the narrowest resonance (777 keV) and 72 keV for the strongest (1713 keV). The 150° yield curve is reproduced in the compilation of Mayer and Rimini [23]. The high Q value, 8.115 MeV, ensures that the alpha peaks are well separated from those from other elements and their detection is practically background-free, even for thick targets.

Giles and Peisach [24] introduced an electromagnet between the target and a position-sensitive particle detector, then bombarded a CaF_2 target with 3 MeV protons. After measuring the positions of the peaks they adjusted the magnetic field to move the proton peak right off the detector, leaving only the α_0 peak. The beam current could then be increased by seven times, with the deadtime still at an acceptable level.

$^{19}F(p, \alpha\gamma)^{16}O \quad Q = 8.115$ MeV

The gamma-rays of interest from this reaction pertain to the α_1, α_2, α_3 groups, with energies 6.129, 6.917 and 7.117 MeV, respectively. These are easily detected with a NaI(Tl) or BGO crystal, and there is

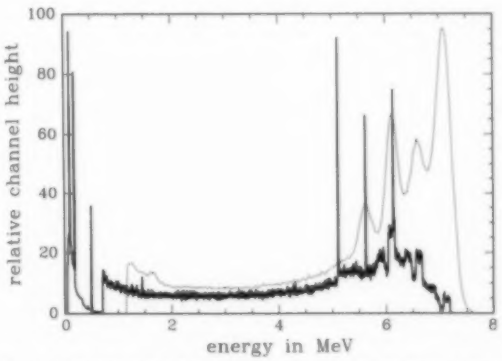

Fig. 1. Spectra of the 6.129, 6.917 and 7.117 MeV gamma-rays from the $^{19}F(p, \alpha\gamma)^{16}O$ reaction, recorded in a BGO crystal (75 mm by 75 mm) and in an HPGe detector of 9.5% relative efficiency. The 110 and 197 keV gamma-rays can be seen in the HPGe spectrum.

normally no need to resolve them. A window is normally set over the whole group (here denoted as 6–7 MeV), with a lower limit of about 4.5 MeV. In fig. 1 spectra collected with an HPGe and a BGO detector are superimposed. The two higher energy peaks show Doppler broadening. Several groups have measured excitation curves for this reaction, usually for the group but in a few cases for the individual peaks. Fig. 3 illustrates a low-resolution thick-target excitation curve measured by the author. See section 3.1.

Osman et al. [25] measured total cross sections for transitions from the 6.13, 6.92, 7.12 and 8.88 MeV states in ^{16}O for proton energies between 1.9 and 4.16 MeV. Ge(Li) and Na(Tl) detectors were each placed at 55° to the beam axis. The excitation functions for the separate transitions are quite different. They derive a total cross section by summing the four transitions, which shows resonances at approximately 2.05, 2.34, 2.6, 2.8, 3.17 and 4.03 MeV.

Golicheff et al. [26] measured the yield of 6.13 MeV gamma rays from a thick teflon target with E_p from 400 to 1700 keV. They listed 16 resonances from 224 to 1691 keV. Golicheff and Engelmann [27] continued this work, and measured the yield of the 6.13 MeV gamma-ray from a thin target between 800 and 1000 keV. For the ten strongest resonances they list the relative emission of the three gamma-rays. Demortier et al. [28] bombarded a thick CaF_2 target with protons between 0.3 and 2.5 MeV and detected the 6–7 MeV gamma-rays with a NaI crystal at 90°. They plot and tabulate the yield for a thick target of pure F in $N\gamma/st./\mu C$, and identify 22 resonances. Stroobants et al. [29] extended this work by investigating the sensitivity limit for bulk analysis and possible interferences with other gamma-rays, particularly that at 4.43 MeV from $^{15}N(p, \gamma)^{15}O$.

Jarjis [30] bombarded a thin target of CaF_2 with protons between 0.8 and 2.05 MeV and detected the 6–7 MeV gamma rays with a NaI(Tl) detector at 0°. He plotted the relative yield curve in this region in 4 keV steps.

In an extensive study, Dieumegard et al. [22] measured the thin target excitation curve, using an electrostatic energy scanning system. The gamma ray detector was 76 mm by 76 mm NaI(Tl) at 70 mm from the target, and the energy window was 4.7–10 MeV. Their plot of the yield curve has been reproduced in a compilation of data for ion beam analysis [23]. They concluded that the width of a very narrow resonance was best determined by fitting the thick target yield curve; in this way they obtained for the rather weak 1088 keV resonance a width of 150 ± 50 eV. They tabulated 17 resonances from the literature, revising some of the energies and widths from their own work. For the first 15 resonances they list the relative intensity, with the 872.1 keV resonance taken as 100%. They include scans of three strong, relatively broader resonances (872, 934, 1370 keV), comparing the latter with a simultaneous measurement of $^{19}F(p, \alpha)^{16}O$ at 150°. They discuss how to choose among the nuclear reactions and resonances to achieve the best sensitivity, depth resolution and speed of measurement.

$^{19}F(p, p'\gamma)^{19}F \quad Q = 0$ MeV

This method has been commonly used for the determination of F, and is likely to become more widely used as larger HPGe gamma-ray detectors become available. Demortier et al. [28] placed a Ge(Li) detector at 90° to a proton beam and measured the yield of the 110 and 197 keV gamma-rays from a thick target (CaF_2 mixed with graphite). They plot and tabulate both yield curves in the range 0.9–2.4 MeV. The two curves are significantly different but the identified resonances coincide (12 for 110 keV and 14 for 197 keV). Stroobants et al. [29] present similar data and consider the possible interference from $^{18}O(p, \gamma)^{19}F$ (197 keV); they concluded that it could be dealt with by comparing the 110/197 ratio with an F standard or by measuring the 495 keV gamma from $^{16}O(p, \gamma)^{17}O$.

Grambole et al. [31] measured the thin target excitation functions for the 110 and 197 keV radiations for $E_p = 0.7$ to 2.9 MeV. They showed that the resonances are isolated and narrow below 1.5 MeV but above that they are much broader. Prominent resonances are 872 and 1088 keV (for 197 keV radiation) and 934 and 1420 for 100 keV. They show also thick-target yield curves from 0.8–1.55 MeV for these radiations and a gamma-ray window 3.0–7.2 MeV from $^{19}F(p, \alpha\gamma)^{16}O$. From further measurements they concluded that the narrow 1088 keV resonance in the 197 keV yield curve is suitable for shallow depth profiling of solids.

Boni et al. [32] wished to analyze several elements, including F, in thin and intermediate specimens. To this end they measured the excitation functions for the 110 and 197 gamma-rays in the proton energy range 2.2 to 3.8 MeV, searching for energy intervals in which the cross section was as as high and constant as possible. Their published data show much irregularity but some regions between 3.5 and 3.8 MeV where at least one of the cross sections is reasonably constant.

Bird and Clayton [33] noted that the elements Al and Na were those most likely to contribute a background to the 6–7 MeV window used for determining F via the $^{19}F(p, \alpha\gamma)^{16}O$ reaction. However, intense gamma rays of lower energy were emitted in the $(p,p'\gamma)$ reactions. The detection limit of the $(p, \alpha\gamma)$ reaction could therefore be reduced by collecting a spectrum of the low energy window (with a Ge detector) simultaneously with a spectrum of the high energy window (with a scintillation detector). The intensity of the low energy

radiations could be used to calculate the contributions from these elements to the high energy window. This technique could prove valuable when determining F in mineral grains, since their content of Al or Na is usually much higher than that of F.

$^{19}F(d, p)^{20}F \quad Q = 4.379$ MeV
$^{19}F(d, \alpha)^{17}O \quad Q = 10.038$ MeV

In a detailed paper, Maurel et al. [34] considered deuteron-induced reactions from two standpoints: when other light nuclei are to be measured along with some light nuclei it could be advantageous to do so with a deuteron beam; it is also desirable to know how peaks from fluorine may interfere with measurement of other elements. They publish $\sigma(E, 150°)$ for the α_0 and α_1 groups of the $^{19}F(d, \alpha)^{17}O$ reaction from 0.7 to 1.95 MeV.

In their discussion of the (d, p) reaction they list the Q values for 14 proton groups and the energy of the protons at 150° for $E_0 = 1.5$ MeV. They illustrate the interference effects between fluorine and other light nuclei in the rather complex spectra arising from deuteron beams. They emphasize the importance of selecting optimal bombarding and detection conditions, including the depletion depth of the detector and the thickness of the filter which blocks the deuterons. They plot spectra which show proton peaks from F and their relation with peaks from ^{12}C, ^{14}N, and ^{16}O.

Bondarenko and Rudenko [35] determined F in zirconium by an activation method: detecting 1.63 MeV gamma-rays from the decay of ^{20}F (11.4 s). The specimens were bombarded by 3 MeV deuterons for 30 s then automatically delivered to the counting position, where a series of counts was taken over 160 s. The decay curve was fitted to remove interference from the 1.78 MeV gamma from ^{28}Al, produced by the (d, p) reaction on Al impurities. The lower limit for F detection in zirconium was 0.5 ppm.

$^{19}F(\alpha, p)^{22}Ne \quad Q = 1.675$ MeV

McIntyre et al. [36] employed resonances in the $^{19}F(\alpha,p)^{22}Ne$ reaction to detect and depth profile ^{19}F in solid targets. They bombarded a MgF_2 film with alpha particles in the range 2100–2500 keV and detected protons at 135° with a silicon detector covered with a 25 μm Mylar film to stop elastically scattered alpha particles. They observed two proton peaks, from reactions leaving ^{22}Ne in its ground and 1.28 MeV first excited state, and two strong resonances in the yield curve, at 2190 and 2315 keV, in general agreement with the results of Kuperus et al. [37]. They showed that this method provided a simple, specific probe for ^{19}F in the presence of heavier elements such as Ga and As, where Rutherford backscattering was ineffective. The low background in the proton spectra resulted in good sensitivity for F detection, of the order of 10^{19} F atoms cm^{-3}. A smaller resonance at 2443 keV had been used for near-surface analysis by Smulders [38] and Kuper [39].

$^{19}F(\alpha, \alpha'\gamma)^{19}F \quad Q = 0$ MeV
$^{19}F(\alpha, n\gamma)^{22}Na \quad Q = -1.950$ MeV
$^{19}F(\alpha, p\gamma)^{23}Ne \quad Q = 1.675$ MeV

Giles and Peisach [40] bombarded CaF_2 targets with high energy alpha particles and recorded with a Ge(Li) detector the resulting gamma spectrum. There were significant peaks from each of the above reactions: from the first 110, 197, 1236 and 1349 keV; from the second 583, 891 and 1528 keV; from the third 1275 keV. They measured the excitation functions for the 110 and 197 keV gamma-rays from $E_\alpha = 3$ to 5 MeV. Both of these increase by about 100 times over this interval. The minimum detectable amount of F, using the 197 keV gamma-ray, was about 100 ng.

3.1. Depth profiling

Since the pioneering work of Möller and Starfelt [2], depth profiling of fluorine has been carried out extensively on man-made materials and on tooth enamel. A number of narrow resonances in the $^{19}F(p, \alpha\gamma)^{16}O$ reaction have been employed. The work of Dieumegard et al. [22] is a good summary of these resonances and their properties, from which the experimenter can choose according to the required yield, depth capability and depth resolution at the surface. The resonance with the highest yield (872 keV) has been commonly used [8,41], as has the slightly less intense 1375 keV resonance [41]. The weak but isolated resonance at 672 keV has been used [6], as has the very narrow resonance at 1088 keV [31]. The lowest resonance at 340 keV is narrow ($\Gamma = 2.85$ keV), is 140 keV below the next resonance and has a low background. For these reasons it has been applied by several groups in recent years [42–45].

It appears that, until 1983, resonances in the $^{19}F(p, p')^{19}F$ reaction were not used for depth profiling. By measuring the 197 keV gamma rays in the vicinity of the 1088 keV resonance, Grambole et al. [31] profiled F in glass and in implanted silicon, and in a surface layer on ZrNb.

Methods for extracting the depth profile from a nuclear excitation curve have been described in a number of papers, for example [22,31,43,44,47,48]. Nuclear reaction data for ion beam analysis have been reviewed by Bird [49], and in a book edited by Bird and Williams [50].

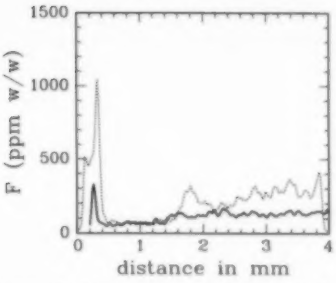

Fig. 2. F scans of a human tooth (full line) and a bovine tooth (dotted line) showing that the concentration in the inner enamel is about 50 ppm, so any interference from reactions with other elements must be no greater than this and may be much less.

3.2. Summary

Ion beam analysis of fluorine has been dominated by the (p, αγ) and (p, p′γ) reactions, both of which are simple to use and have high sensitivity. The 6–7 MeV radiations from the first reaction are readily detected with a NaI(Tl) or BGO crystal, since high resolution is not required. This method is very suitable for measuring fluorine distributions in sections of bones or teeth, since the background is very small. There is some interest in determining very low levels in teeth, so the sources of background must be examined. Calcite provides zero background, which eliminates Ca, C and O, but P and N should be tested further. Fig. 2 shows that the background from hydroxyapatite cannot be equivalent to more than 50 ppm of F, but it may be much less. In the study of rocks other elements could generate a higher background under the high energy window, which could be calculated from the spectrum of low energy gamma rays, as described above. The numerous and well-characterised resonances in the yield curve are diverse in their characteristics and the experimenter must select the best for his purposes.

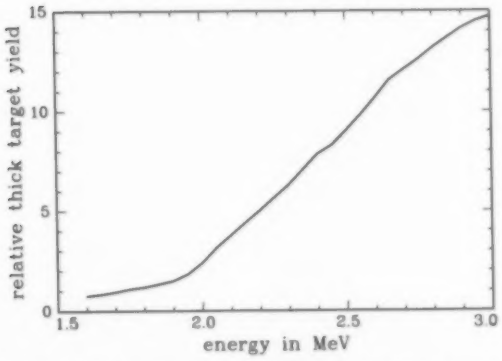

Fig. 3. A thick-target yield curve of the high energy gamma-rays of fig. 1, with a window set between 4–7.2 MeV. The target was a crystal of fluorapatite.

To use the (p, p′γ) reaction requires a high resolution detector, but these are available with high efficiency. The two peaks sit on high backgrounds, so spectra must be collected so that the peak areas can be extracted. Although this means that the reaction is less suitable for measuring distributions in biological material it could provide lower limits in studies of rocks. Only a limited amount of depth profiling has exploited this reaction.

The (p, α) and (α, p) reactions could prove valuable in measuring very low levels of F in metals and rocks. Other α-induced reactions require a high energy beam and are likely to remain little used.

The basic information on the reactions induced by deuteron bombardment of ^{19}F is known but these reactions have been little used for analysis of materials.

4. Applications to inorganic materials

4.1. Geochemistry

Sippel and Glover [1] wished to develop a rapid analytical technique for the analysis of sedimentary rocks, which would allow analysis of the light elements not accessible to the XRF technique. Their targets were prepared from powdered sedimentary rocks mixed with binders of KBr, KCl or graphite. They regarded the most promising method for F as the detection of the 6–7 MeV gamma-rays. They discussed the corrections for stopping power of the matrix and calculated the stopping powers for the main constituents of sedimentary rocks.

Clark et al. [51] developed these techniques further, and by this time the Si(Li) and Ge(Li) detectors were available. They analyzed a USGS standard rock for a total of 28 elements. For fluorine they used 1.375 MeV protons, detected the same gamma-rays and claimed a thick-target detection limit of 1 ppm.

Allen and Clark [52] analyzed F in different phases of meteorites. The samples were crushed and homogenized as much as possible with a graphite binder; in some instances the magnetic and nonmagnetic portions were analyzed separately. Using the same techniques as before they found significant variations within each sample. They concluded that about 20% of meteoric F is in the metal or a phase closely associated with it, but in the non-magnetic phase it was associated with plagioclase.

Hanson et al. [53] made careful determinations of F in NBS Standard Reference Materials for comparison with determinations by chemical methods. They chose

SRM91 (opal glass), SRM120b (phosphate rock) and SRM2671a (freeze-dried urine). These materials, with F concentrations in the few percent range, provided the opportunity for a stringent test of the nuclear technique. They detected with a Ge(Li) detector the 110 and 197 keV gamma-rays excited by 3.1 MeV protons. Their results, corrected for stopping power differences, agreed to 5% or better with the NBS certified values.

A team from Liege has explored further the analysis of F in rocks, with clear ideas of the information it may provide. They bombarded their targets with a broad beam of 1.5 MeV protons and detected the 6–7 MeV gamma-rays with a standard NaI crystal [54]. They did not use all the peaks, only the full-energy peak at 6.1 MeV. Their corrected results for geochemical reference samples were within 10% (or better) of the certified values. They estimated their lower limit of detection as 25 ppm. An advantage of the PIGE method is that calibration may be based on pure chemical standards and independent of reference materials. They proceeded to analyse 15 geochemical standards from the Geological Society of Japan [55], for which F data was very limited. They estimated the precision of their results as 10% at the 100 ppm level and 6% at the 1000 ppm level.

In a third paper [56] they reported on more than 200 specimens from an igneous complex and surrounding metamorphic rocks in SW Norway. Fluorine is an important constituent besides CO_2 of the fluid phase in equilibrium with igneous and metamorphic rocks. There was a good correlation between the concentration of fluorine and of phosphorus for igneous rocks, suggesting that fluorine is esentially contained within the mineral calcium apatite. The trends on F with position in the complex could be explained in this way.

A study based on fluorine analysis in serpentinite rocks from Lower Silesia was reported by Prybylowicz et al. [57]. The 110 and 197 keV gamma-rays were detected, as were gamma-rays from Li, Na, Mg and Al. Rocks representing different degrees of alteration of primary peridotite into sepentinite were analyzed, and F contents varied from 140 to 300 ppm. They observed no correlation between the F content and degree of alteration of the primary rock.

The studies described so far measured the F level in pellets of homogenized rock. This is a limited source of information, most of which is retained in the detailed contents of individual mineral grains. This has been done with great thoroughness by using the PIXE method, e.g. ref. [58]. Coote et al. [59] reported measurements of F in individual grains of epidote, hornblende, biotite and apatite in eight igneous and metamorphic rocks. They were interested in using these ratios as a geothermometer, recording the maximum temperature ever reached by these rocks. Thermodynamic theory [60] predicts the variation with temperature of the equilibrium ratio of F levels in coexisting various pairs of minerals. More recently, Mosbah et al. [61] determined F in natural glasses and in melt inclusions trapped in minerals of different origins. They consider fluorine to be a good tracer of magmatic evolution, as it can be concentrated in silicate melts as fractional crystallization progresses. They used 3.4 MeV protons focused to a 30 μm spot, detected the 110 and 197 keV gamma rays, and investigated the change in yield with thickness of the specimen. The measured lower limit of detection for an integrated charge of 500 nC was 30 ppm.

4.2. Materials

Möller and Starfelt [2], involved in the development of nuclear power, were concerned at the possible contamination by fluorine of Zircaloy-clad fuel elements; if this occurred when the Zircaloy was pickled or electropolished it could lead to excessive corrosion. With their interest in the depth distribution they devised a method to measure it. They varied the proton energy over the 1375 keV resonance and detected 6–7 MeV gamma-rays with a NaI detector. They developed sufficient profiling theory to enable them to derive the depth distributions, including the effects of straggling. On unoxidized samples the fluorine was only on the surface, but in oxidized samples it was distributed to depths of several micrometers.

In England, Jarjis [62] was concerned with fluorine contamination of Magnox (magnesium alloy) reactor fuel canning material. He used the same reaction, after measuring its excitation function on a thin CaF_2 target. He varied the proton energy from 1.25 to 1.55 MeV, which includes the resonances at 1.283, 1.348 and 1.375 MeV. Analysis was done with a convolution program in which he inserted estimated profiles.

O'Connell and Crumpton [63] applied the same technique to the micronalysis of fluorine in microcracked chromium plate. Microcracking occurs if fluorosilicates are added to standard plating solutions. The surface concentration of F was constant to within 5% independent of plating conditions, while the bulk concentration was independent of the presence or quality of microcracking and was inversely proportional to the rate of electrodeposition of chromium.

For their measurements of fluorine contamination of Al, Si, Zircaloy and stainless steel, Gippner et al. [64] used the low energy gamma-rays because an unambiguous background separation was possible. They observed the 110 keV gamma-ray with a Ge(Li) detector, and varied the proton energy over the 872 and 935 keV resonances. They studied fluorine contamination of the surfaces of silicon wafers after procedures such as etching and polishing.

In a continuation of this work [31], the same group investigated implanted silicon samples as well as ZrNb plates and Cr–Al layers after HF treatment. They also measured thin target excitation yields for the 110 and 197 keV gamma-rays from 0.7 to 2.9 MeV, and investigated in detail the 1088 keV resonance, which they regarded as well suited to the measurement of profiles in the near-surface region of solids.

Depth profiling was applied by Derry et al. [65] to trace the diffusion of fluorine ions which had been implanted into diamond. The fluorine diffused via interstitial positions to the surface. Further insight was gained by implanting and profiling ^{13}C.

Hirvonen and Yang [66] pioneered a new field of application: the tribology of polymers. They investigated the transfer of polytetrafluoroethylene (PTFE) during unidirectional sliding on a stainless steel surface. To determine the minute amount of material transferred they measured the 6–7 MeV gamma rays at the 340 keV resonance. The transfer was examined from the first pass (when the highest transfer rate occurred) and was followed for the first ten passes. The average transfer rate was in most cases less than a monolayer, which indicates an uneven deposition.

The 340 keV resonance was employed by Rickards [67] to detect fluorine at high sensitivity, and to determine shallow depth profiles. He measured fluorine in F-doped films of SnO_2 used as conducting electrodes in solar cells [45]. The distribution and amount of F were related to the film growth parameters. Further studies concerned the corrosion of aluminium and stainless steel in an atmosphere of UF_6, and the stability of a Teflon target under proton bombardment.

Caridi et al. [68] studied fluorine enrichment phenomena in the coal combustion cycle, a topic of concern because fluorine is associated with corrosion in power plants and with the environmental impact of fly ash. Fly ash was collected at the input and output of a pilot electrostatic precipitator installed at a power plant, as well as samples of the coal. From the measurements they derived enrichment factors in the pathway from coal to fly ash and observed the influence of different operating modes of the electrostatic precipitator.

5. Applications in biology and medicine

5.1. Calcium hydroxyapatite and fluorapatite

The importance of fluorine in biology and in studies of living things arises from the structure and properties of the essential and remarkable mineral calcium hydroxyapatite $Ca_5OH(PO_4)_3$, which, by exchange of F for OH can become partially or completely fluorapatite, containing 3.77% F by weight. The structure of the two minerals is exactly the same except that the first has a slightly larger unit cell. The structure is quite complex, with vertical symmetry axes of three kinds. Beevers and McIntyre [69] take several pages to describe it, but for our present purpose the following points are of importance: the basic structure is made up of the ions of Ca, P and O; the OH^- or F^- ions lie in channels along the c-axis defined by planar triangles of Ca ions; the fit in these channels is critical and no other ions are known to fit into them. A slight increase in order in the structure which occurs when hydroxyl ions are replaced by fluoride is believed to be the cause of the relative instability of hydroxyapatite (HAP) compared to fluorapatite (FAP) [70].

From a study of the exchange reaction, Hagen [71] concluded that the conversion of HAP to FAP requires only small concentrations of fluoride, and is strongly favoured under acid conditions. A calculation of the thermodynamic constant for this reaction implies that, under physiologic conditions, FAP will always form at the expense of HAP. The crystallization of apatites in living things is a complex process, involving intermediate minerals such as octacalcium phosphate. Structures of biological minerals are reviewed by Young and Brown [72], calcium phosphate crystallization by Nancollas [73], vertebrate tooth mineralization by Veis [74] and proposed mechanisms of dental caries by Arends [75].

Much effort has been devoted to the study of diffusion of fluoride ions in apatites. Tse et al. [76] point out that because the fluoride distribution is one-dimensional, ions cannot enter the crystal by a simple diffusion process as would be the case in a material with 3-D diffusion paths. Even if fluoride ions could enter the channels they would be able to leave at the same rate. The uptake of fluoride ions would become possible in the presence of an electric field, which would produce a flux of vacancies within the hydroxyl sublattice [77].

5.2. Bone

Ion beam studies of fluorine in bone are very few compared to those of teeth. Hyvönen-Dabek [78] determined a number of elements in bone samples by irradiating freeze-dried samples with 2.4 MeV protons, and recording gamma-rays with a Ge(Li) detector. She estimated a detection limit of 1 ppm for fluorine, and found in her samples a range from 170 to 1630 ppm. Kajfosz and Szymczyk [79] used the same technique to determine fluorine in fresh and ashed human bones. Ash samples gave better reproducibility because ashing is a homogenization process. The bones of rabbits were powdered and their fluorine content determined by Chaudhri et al. [80]; the fluorine content was 0.073%

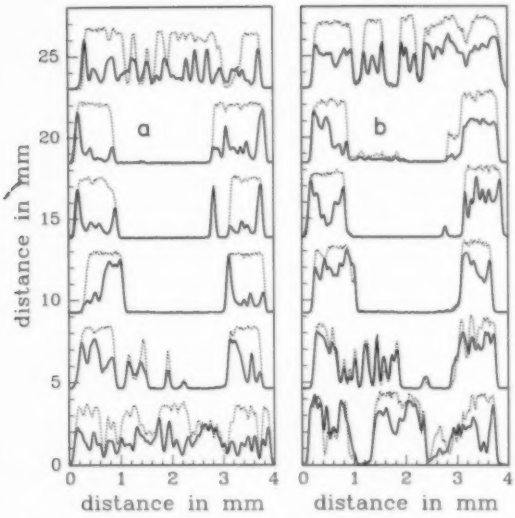

Fig. 4. Distributions of F (full line) and Ca (dotted line) from linear scans across sections of two rat femurs; (a) at age 4 weeks, (b) at age 12 weeks. The maximum F concentration is about 0.5%. The scan was from front to back of the femur.

for control animals but 0.63% for those kept on fluoridated water for 45 days.

A recent investigation [18] shows that ion beam analysis can reveal details of growth processes in the bones of an experimental animal, in both cortical (solid) bone and trabecular (cross-bracing) bone. If an animal is fed a diet rich in fluoride much of it will be incorporated into those parts of a bone which are growing rapidly or are being remodelled by special cells. The fluorine distribution will therefore depend on the age of the animal and its age when fluoride was first ingested. Measurements on rat femurs and vertebrae were performed to show if remodelling of cortical and trabecular bone occurred at the same or at different rates.

The goal was a practical one in that the results are relevant to the monitoring and treatment of osteoporosis, a disease in which the total amount of bone is reduced although the quality remains good. Fluoride therapy for this disease has been found to improve bone mass, if the fluorine is retained in the body. Nuclear resonance techniques can measure the fluoride level in the cortical bone of the finger of a patient who has ingested F in the treatment of osteoporosis. But does uptake in cortical bone tell anything about uptake in the critical trabecular bone? They concluded from their studies that, in the rat, uptake by cortical bone indicates uptake by trabecular bone, so put forward the working hypothesis that NMR measurement of F in the finger is a useful way to monitor changes in trabecular bone. A selection from the extensive measurements which led to this conclusion may be of interest. Fig. 4 shows fluorine and calcium scans at different positions on two rat femurs. There are marked changes with position along each femur, and between the two femurs. Three-dimensional distributions (fig. 5) were measured to ensure that the usual 1-D scans were providing a representative picture. The distributions in trabecular bone of two vertebrae are shown in fig. 6.

5.3. Teeth

Studies of teeth by ion beam techniques have naturally been very extensive, and the fluorine in the outer layer of enamel has been the main target of depth profiling measurements.

The first paper on the fluoride profile in enamel was published by Mandler et al. [6]. Using the 672 keV resonance and a Ge(Li) detector to observe the 6.13 MeV gamma rays, they profiled to a depth of 2.1 μm.

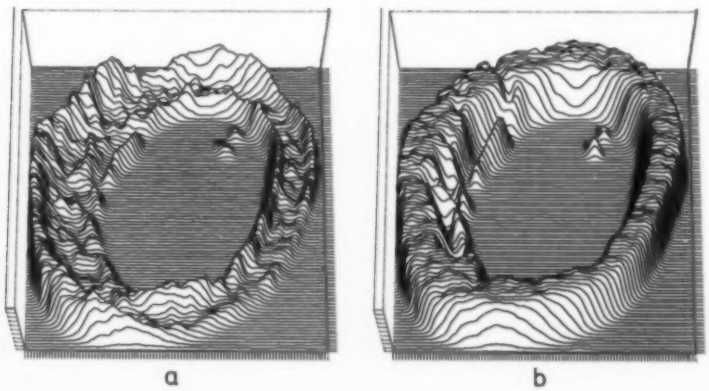

Fig. 5. 2-D distributions in a section of a rat femur; (a) F, (b) Ca. The maximum F concentration is about 0.5%.

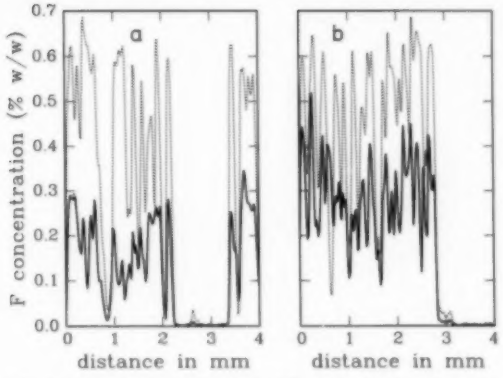

Fig. 6. F (full line) and Ca (dotted line) distributions from line scans across sections of two rat vertebrae; (a) at age 4 weeks, (b) at age 12 weeks.

The uptake of fluoride into enamel from several fluorine compounds was examined in this way. Thomas and Grea [81] devised a method, using large energy steps, for profiling deeper into the enamel. Stroobants et al. [29] also performed depth profiling of enamel. In a thorough paper, Lindh and Tveit [47] discussed the theory of depth profiling and applied it to enamel.

Stroobants et al. [82] describe their external proton beam method for in vivo analysis of a human tooth. They concluded that there was no radiation hazard or modification to the crystallite structure. This procedure was used intensively for studies of topical applications of fluoridated compounds [83]. Chaudhri and Crawford [7] investigated the influence of trace elements on the fluoride uptake by teeth, by collecting PIXE spectra from 1 mm^2 areas of sectioned teeth. Crawford et al. [8] applied fluorine depth profiling to the study of cementum, in a study of peridontal disease. Bodart et al. [84] carried out a large scale study of enamel of primary teeth, collected in different localities in Belgium. They calculated a table of correlation coefficients between fluorine and nine other elements.

The Heidelberg proton microprobe was applied by Svalbe et al. [9] to a study of fluorine and other trace elements in the full depth of enamel and into the dentine. Of particular interest were the concentration variations at the enamel surface and at the enamel-dentine junction. Dentine showed more variation in composition than enamel. A similar technique was used to scan the enamel surface at the positions of pre-carious lesions [10]. Fluorine was strongly enhanced within the lesion area, and showed marked variations in concentration at about 1 μm intervals.

With the various techniques established, recent work has concentrated on two main areas of dental research, the influence of fluoride on the development of teeth and on the reduction of dental caries. Lenglet et al. [14] examined the effect of a single fluoride dose on pre-eruptive enamel mineralization of hamster tooth germs. Using a proton microprobe, they measured distributions of F, Ca and P. The largest concentration of fluoride was found at the enamel-dentine junction.

The sheep is commonly used as an experimental animal in research on tooth development. Nelson et al. [15] published microprobe measurements on teeth from five sheep, which had been exposed to enhanced levels of fluoride daily for six months. Fluorine, calcium and zinc distributions were measured along multiple scans of enamel and dentine, at 1 mm intervals down each tooth, to provide a complete picture. The pattern of calcification, downwards from the tip and in both directions from the enamel–dentine junction, showed clearly in those animals given a high dose for a short time. Sheep teeth from a related experiment have recently been examined in the same way. A series of F scans from one tooth is illustrated in fig. 7.

Angmar-Månsson et al. [16] report on an experiment in which female rats were given a single dose of fluoride, at four different concentrations. Even animals killed 70 days later had fluorosis in their incisors, though they had been renewed nearly twice. The results support the hypothesis that sufficient F can be mobilized from bone adjacent to a tooth to affect the formation of enamel.

Nelson et al. [17] exposed extracted human teeth to weak acid alternated with fluorine-containing compounds (two toothpastes and a mouthwash). The exposed areas were scanned with the proton microprobe

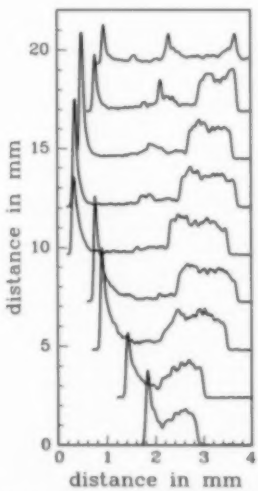

Fig. 7. F distributions from scans across a sheep tooth, with enamel on the left and dentine on the right. The maximum F concentration was about 0.7%.

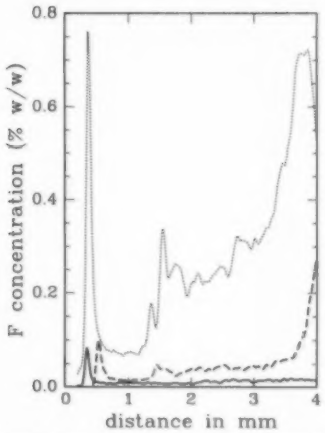

Fig. 8. F distributions from lateral scans about halfway down sections of three human premolars. Full line: New Zealand, about 1940; dashed line: New Zealand, 1987; dotted line: from Kenya.

to reveal differences in fluorine and calcium distributions, in comparison with masked control areas. Microhardness testing and the calcium profiles were used to determine the extent of lesion progression. A NaF dentifrice and mouthwash were observed to induce a considerably higher uptake of fluoride in the lesion (up to five times the original level) than a toothpaste containing morofluorophosphate. Each product was equally effective in reducing the extent of lesion

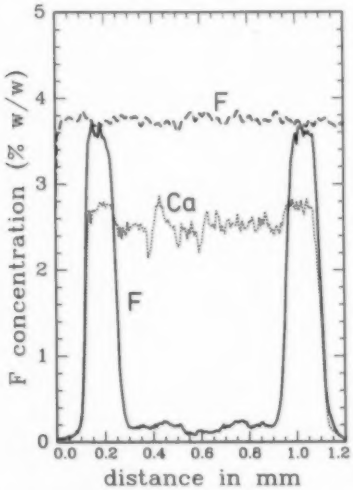

Fig. 9. F (full line) and Ca (dotted line) scans of a sectioned shark tooth, compared with the F scan of an FAP crystal (dashed line).

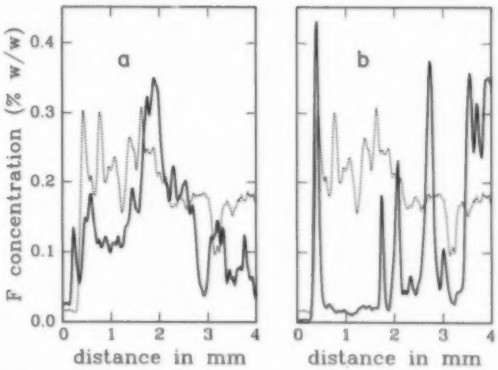

Fig. 10. F (full line) and Ca (dotted line) distributions along the centre line of a fish scale; (a) bream, (b) orange roughy.

progress, although the mineral content profiles of their lesions differed. Some of the F and Ca scans from this work were published earlier [85].

Cutress and Coote [86] have embarked on a comprehensive proton microporobe study of tooth collections from a number of periods and places, to provide information which should help answer remaining questions on the role of fluoridated water and toothpastes in the prevention of caries and the causes of fluorotic markings in enamel. Some early results from this study (fig. 8) illustrate the large range in fluoride levels in enamel and dentine which do exist. However they do not compare to that in a shark tooth (fig. 9) which near the tip is almost pure FAP.

5.4. Fish scales

A fish scale consists of layers of protein strengthened with mineral. X-ray diffraction analysis shows that most of this is calcium hydroxyapatite, so it is not surprising that significant amounts of fluorine have been found in all scales examined so far [19]. The distributions are highly variable and often are quite different from those of the calcium. They have been described and interpretated by Gauldie et al. [96,97]. Scans along the centre line of scales from two species are illustrated in fig. 10.

6. Applications in archaeology

6.1. Bone

The application of ion beam techniques in archaeology and the arts is reviewed by Bird et al. [87].

The first radial profiles of fluorine in archaeological bone were published by Coote and Sparks [11]. Their

intention had been to compare the ratio of nitrogen to fluorine, measuring these with a deuteron and proton beam, respectively. Nitrogen was detected but disappeared rapidly under the beam, but the fluorine was completely stable. It later became evident that useful information was contained in the radial profile of the fluorine, which diffused inward from the outside of the bone, or from an internal surface which had become exposed to groundwater. The distance scale is large – up to 10 mm, and may be up to 1 mm after only a few years. There were some suggestions regarding possible applications of these profiles. These included: as a dating technique, with perhaps low accuracy but a useful range extending from a few years to tens of thousands; as a quick method for selecting bones suitable for radiocarbon dating; or a quick way of separating bones of different age or provenance (since the surface concentrations might be different).

Haddy and Hanson [88] measured nitrogen and fluorine concentrations in a number of bones, using a chemical method for nitrogen and inelastic scattering for fluorine.

The mechanism for diffusion of fluorine into the bone was not known. The radial profiles suggest that there are two: a fast process which introduces only about 0.1%, presumably onto crystal surfaces; and a slower process which can result in concentrations of 1% or more. An equus bone from the Olduvai Gorge (1.75 Ma) had almost attained the composition of fluorapatite (3.77% F). The slow process cannot be solid state diffusion into the canals of the apatite structure. We believe that it is an example of bone remodelling, in which HAP crystals dissolve and are partially replaced by the less soluble FAP. In completely dry conditions, as in some caves, F does not diffuse into the bone or outwards from its higher concentrations around the Haversian canals. The same situation applies if the bone had been heated in a fire before burial, but this must have a different explanation.

Profiles of bones from a burial ground in coral of the Solomon Islands were published [59]. Surface concentrations ranged from 0.2–1.0% F, which was typical of bones from quite different soils in New Zealand. A further paper [12] included profiles of animal bones which had been buried for only a few years, and of moa bones from an arid area of New Zealand, including some which had been burnt before being discarded. Aware that important bones could not be cut in half, two methods were suggested for removing a section from one side of a bone, so that after microprobe analysis it could be glued back into place with a gap-filling glue.

A quantitative treatment of these profiles was introduced by Coote and Nelson [89]. Diffusion theory [90] shows that diffusion into a circular cylinder can be described by two dimensionless parameters, the "scaled radius" and the "scaled time", which contains the product Dt (diffusion constant by time elapsed). The fitting process was done visually on a screen, adjusting Dt until the best fit was obtained. A value for D was obtained by profiling bones dated by radiocarbon, hence t could be derived for a selection of bones. Some of the fits are remarkably good, others show deviations which may indicate changes in groundwater fluorine concentrations over time; the program could be modified so that such changes could be introduced and tested empirically.

Examples of bone profiles are included in a more recent paper [85]. The profile of a moa bone dated by radiocarbon at 16000 y is compared with calculated profiles for 1600 y and 100000 y, suggesting the large range of application. The method could prove most useful in the range 0–500 y, where radiocarbon dates are not very reliable.

Applications of these methods to forensic science and Pacific archaeology were described by Coote and Dennison [91]. The forensic application concerned human bones discovered under a shed in pumice soil which did not retain moisture. Quite different apparent ages from bones discovered only a few inches apart emphasized the importance of moisture in fluorine diffusion. A collection of finger bones from one Pacific island all gave ages of about 70 y, supporting other evidence of a fatal epidemic on the island. A museum collection of bones from the Marquesas Archipelago showed a much wider range, some perhaps too old to be accepted. It did identify bones whose radiocarbon date would be important, and this could become the primary use of the relatively simple and cheap fluorine profile method.

6.2. *Teeth*

The first fluorine profile of an archaeological tooth was published by Coote and Holdaway [12]. The 800 y old tooth from the Solomon Islands revealed for the first time the characteristic internal profiles of excavated teeth; they slope downwards from the inner surface of the dentine, showing that fluoride ions in ground water enter the tooth through the nerve canal and are deposited on the walls of the pulp cavity; they diffuse outward through the dentine and in a few thousand years may reach the enamel. Since there are no canals in dentine the profiles are much smoother than those in bone, and can be fitted accurately by numerical simulation [85,41].

The proposal to use these interior profiles for the relative dating of burials was tested by Vickridge et al. [41], on archaeological human teeth from the Solomon Islands and pig teeth from Vanuatu. In identifying the sequence of pairs of human burials interior profiles in dentine were less successful than outer profiles (diffu-

sion inward from the cementum.) In pig teeth the internal profiles were much less prominent than in human teeth. An unexplained feature of the profile, as if from diffusion inward from a spike at the enamel-dentine junction, was not present in modern pig teeth. The results from depth-profiling of pig enamel did not show promise as an alternative dating method. The authors concluded that there was much to be learned about fluoride diffusion into buried animal teeth and that other species should be investigated.

Can the interior profiles of human teeth be used to study the sequence of burials in an ancient cemetery? Coote and Molleson [13] attempted to answer this with teeth from a fourth century Roman settlement, Poundbury Camp in Dorset. Scans of medial sections of these teeth showed clearly the interaction of fluoride with the constituent parts of a tooth. Fluoride may enter enamel but it diffuses extremely slowly and for most purposes is blocked. The thin layer of cementum is almost as effective, though it shows concentrations two or three times higher at the surface. But if the enamel or cementum layer has been removed by disease so that dentine is exposed, fluoride diffuses quickly into it as if it were bone. An undamaged tooth is therefore well sealed from fluoride, and presumably other elements, apart from entry with water through the nerve canal.

The profiles in this study proved unsuitable for dating, since the true diameter of the pulp cavity for each scan could not be measured from these sections. It will be necessary to section the tooth transversely, so that the scan can be directed precisely across the centre. Work will continue along these lines.

The same workers have begun a study of eighteenth century human teeth, not from a cemetery but the crypt of an English church [92]. Some bodies were in wooden coffins, others sealed in lead. The anthropological information stored in these teeth is the main source of interest, but there might be some surprises. For example, fig. 11 shows two scans of a premolar from a wooden coffin. It seems clear that fluorine diffused from the pulp cavity into the dentine, but where did it come from? It was also present outside the tooth, as shown by the high level in the cementum; the contrast with enamel is clear. Post-mortem uptake of fluorine and other elements by teeth has been reviewed by Molleson [93].

6.3. Obsidian and quartz

In an early application of ion beam analysis of fluorine Coote et al. [94] bombarded obsidian (volcanic glass) with protons and detected the low energy gamma-rays from the minor elements sodium, fluorine and aluminium. Examination of these ratios for 120 specimens showed that the fluorine/sodium ratio gave

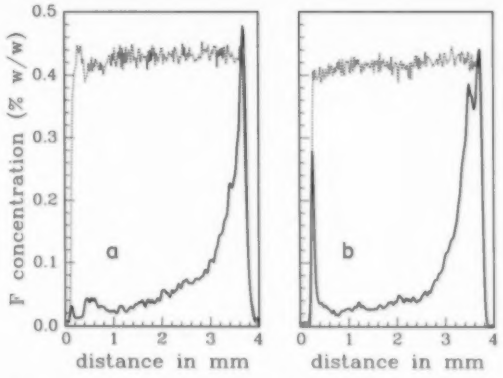

Fig. 11. F (full line) and Ca (dotted line) distributions across a section of a human tooth from a church crypt (burial date about 1750); (a) from enamel (left) to pulp cavity, (b) from cementum (left) to pulp cavity.

the best separation of source sites. The method was further developed by Bird and collaborators and used in extended studies of Melanesian obsidians [95]. Sample geometry was not critical and high precision could be attained in automated measurements lasting 3 to 5 min. Although a successful method it was eventually supplanted by the PIXE method with which more elements could be measured.

The very slow diffusion of fluorine from groundwater into quartz was investigated by Walter et al. [20] by depth profiling at the 872 keV resonance, detecting 6–7 MeV gamma rays with a BGO detector. They concluded that the profile width was roughly proportional to the time since the flint was worked. They applied the technique to a particular archaeological problem at a site in France which had been occupied from the neolithic to the Roman period. Their evidence supported the view that the inhabitants had smelted bronze and worked flint contemporaneously.

7. Discussion

The examples given here illustrate the wide range of applications of the ion beam analysis of fluorine. The scanning proton microprobe enables detailed research on bones and teeth, but physicists will need to find keen collaborators who have experience in biology, medicine or archaeology and know which important questions require an answer. The methods for determining fluorine in materials are well established, while BGO and HPGe gamma-ray detectors now have high efficiency and excellent resolution. Applications in geochemistry, materials science and environmental studies should advance rapidly in the future.

Acknowledgements

I am grateful to Ian Vickridge for help with the preparation of this paper, and Peter Johnson for lending a HPGe detector. I wish to express my gratitude to those students and colleagues who have helped me in studies of fluorine over a number of years, in particular Foss Leach, John Dennison, Theya Molleson, Grace Suckling, Terry Cutress, Dennis Nelson, Rodger Sparks and Charley McGill. The preparation of this paper was supported by the Foundation for Research, Science and Technology.

References

[1] R.F. Sippel and E.D. Glover, Nucl. Instr. and Meth. 9 (1960) 37.
[2] E. Möller and N. Starfelt, Nucl. Instr. and Meth. 50 (1967) 225.
[3] T.B. Pierce, P.F. Peck and D.R.A. Cuff, The Analyst 92 (1967) 143.
[4] J.M. Bewers and F.C. Flack, The Analyst 94 (1969) 1.
[5] J.M. Bewers and F.C. Flack, The Analyst 94 (1969) 7.
[6] J.W. Mandler, R.B. Moler, E. Raisen and K.S. Rajan, Thin solid Films 19 (1973) 165.
[7] M.A. Chaudhri and A. Crawford, Nucl. Instr. and Meth. 181 (1981) 327.
[8] A.W. Crawford, W.J. Sampson and H.J. de Bruin, J. Dent. Res. 62 (7) (1983) 806.
[9] I.D. Svalbe, M.A. Chaudhri, K. Traxel, C. Ender and A. Mandel, Nucl. Instr. and Meth. B3 (1984) 648.
[10] I.D. Svalbe, M.A. Chaudhri, K. Traxel, C. Ender and A. Mandel, Nucl. Instr. and Meth. B3 (1984) 651.
[11] G.E. Coote and R.J. Sparks, New Zealand J. Archaeology 3 (1981) 21.
[12] G.E. Coote and S. Holdaway, in: Archaeometry: an Australasian Perspective, eds. W. Ambrose and P. Duerden (Australian National University, Canberra, 1982) pp. 251–261.
[13] G.E. Coote and Theya Molleson, in: Archaeometry: Australasian studies 1988, ed. J.R. Prescott (Physics Department, University of Adelaide, Adelaide, S.A.) pp. 99–104.
[14] W.J.M. Lenglet, C.J.J. Stoof, D.M. Lyaru, R.D. Vis and H. Verheul, Nucl Instr. and Meth. B30 (3) (1988) 429.
[15] D.G.A. Nelson, G.E. Coote, I.C. Vickridge and G. Suckling, Archs. Oral. Biol. 34 (6) (1989) 419.
[16] B. Angmar-Månsson, U. Lindh and G.M. Whitford, Caries Res. 24 (1990) 258.
[17] D.G.A. Nelson, G.E. Coote, M. Shariati and J.D.B. Featherstone, Caries Res., in press.
[18] K.G. McNeill, G.E. Coote and A.J.W. Hitchman, J. Bone Min. Res. 6 (1991) 859.
[19] G.E. Coote, R.W. Gauldie and I.F. West, Nucl. Instr. and Meth. A54 (1991) 144.
[20] P. Walter, M. Menu and I.C. Vickridge, Nucl. Instr. and Meth. B45 (1990) 119.
[21] I. Golicheff, M. Loeuillet and Ch. Engelmann, J. Radioanal. Chem. 22 (1974) 113.
[22] D. Dieumegard, B. Maurel and G. Amsel, Nucl. Instr. and Meth. 168 (1980) 93.
[23] Ion Beam Handbook for Material Analysis, eds. J.W. Mayer and E. Rimini (Academic Press, New York, 1977).
[24] I.S. Giles, C. Olivier and M. Peisach, J. Radioanal. Chem. 37 (1977) 141.
[25] C.H. Osman, D.M. Rosalky and D.J. Baugh, ANU/P-450 (Department of Nuclear Physics, Australian National University, Canberra, 1970), unpublished.
[26] I. Golicheff, M. Loeuillet and Ch. Engelmann, J. Radioanal. Chem. 12 (1972) 233.
[27] I. Golicheff and Ch. Engelmann, J. Radioanal. Chem. 16 (1973) 503.
[28] G. Demortier, J. Stroobants, G. Deconninck and F. Bodart, Report LARN 724 (1983).
[29] J. Stroobants, F. Bodart, G. Deconninck, G. Demortier and G. Nicolas, in: Ion Beam Surface Layer Analysis, eds. O. Meyer, C. Linker and F. Kappeler (Plenum, New York, 1976) pp. 933–943.
[30] R.A. Jarjis, Nucl. Instr. and Meth. 154 (1978) 383.
[31] D. Grambole, C. Bauer, P. Gippner, C. Heiser, W. Rudolph and H.-J. Thomas, J. Radioanal. Nucl. Chem. 83 (1) (1984) 107.
[32] C. Boni, E. Cereda, G.M. Braga Marcazzan and V. de Tomasi, Nucl. Instr. and Meth. B35 (1988) 80.
[33] J.R. Bird and E. Clayton, Nucl. Instr. and Meth. 218 (1983) 525.
[34] B. Maurel, G. Amsel and D. Dieumegard, Nucl. Instr. and Meth 191 (1981) 349.
[35] Yu. I. Bondarenko and V.S. Rudenko, J. Radioanal. Chem. 52 (1) (1979) 127.
[36] L.C. McIntyre Jr., J.A. Leavitt, M.D. Ashbaugh, B. Dezfouly-Arjomandy, Z. Lin, J. Oder, R.F.C. Farrow and S.S.P. Parkin, Nucl. Sci. Techniq. 1 (1–2) (1990) 56.
[37] J. Kuperus, Physica 31 (1965) 1603.
[38] P.J.M. Smulders, Nucl. Instr. and Meth. B14 (1986) 234.
[39] F.G. Kuper, J. Appl. Phys. 60 (1986) 985.
[40] I.S. Giles and M. Peisach, J. Radioanal. Chem. 32 (1976) 105.
[41] I.C. Vickridge, G.E. Coote and S. Wood in: Archaeometry: Further Australasian Studies, eds. W.R. Ambrose and J.M.J. Mummery (Australian National University, Canberra, 1987) pp. 79–89.
[42] F. Bodart and G. Deconninck, Nucl. Instr. and Meth. 197 (1982) 59.
[43] B. Maurel, G. Amsel and J.P. Nadai, Nucl. Instr. and Meth. 197 (1982) 1.
[44] G. Deconninck and B. van Oystaeyen, Nucl. Instr. and Meth. 218 (1983) 165.
[45] E.P. Zironi, J. Rickards, A. Maldonado and R. Asomoza, Nucl. Instr. and Meth. B45 (1990) 115.
[46] H.-E. Zschau, F. Plier, G. Otto, C. Wyrwich and A. Treide, these Proceedings (3rd Int. Conf. on Chemical Analysis, Namur, Belgium, 8–12 July 1991), Nucl. Instr. and Meth. B66 (1992) 292.
[47] U. Lindh and Anne B. Tveit, J. Radioanal. Chem. 59 (1) (1980) 167.
[48] V.A. McGlone and P.B. Johnson, Nucl. Instr. and Meth. B61 (1991) 201.
[49] J.R. Bird, Nucl. Instr. and Meth. 168 (1980) 85.

[50] Ion Beams for Materials Analysis, eds. J.R. Bird and J.S. Williams (Academic Press, Sydney, 1989).
[51] P.J. Clark, G.F. Neal and R.O. Allen, Anal. Chem. 47 (4) (1975) 650.
[52] R. O. Allen, Jr. and P.J. Clark, Geochim. Cosmochim. Acta 41 (1977) 581.
[53] A.L. Hanson, H.W. Kraner, R.E. Shroy and K.W. Jones, Nucl. Instr. and Meth. B4 (1984) 401.
[54] I. Roelandts, C. Robaye, G. Weber and J.M. Delbrouck-Habaru, Chem. Geol. 54 (1986) 35.
[55] I. Roelandts, G. Robaye, G. Weber, P. Aloupogiannis and J.M. Delbrouck-Habaru, J. Radioanal. Nucl. Chem. Lett. 108 (3) (1986) 175.
[56] I. Roelandts, G. Robaye, G. Weber, J.M. Delbrouck, J.C. Duchesne, J. Radioanal. Nucl. Chem. 112 (2) (1987) 453.
[57] W. Przybylowicz, S. Szymczyk and J. Kajfosz, Nucl. Instr. and Meth. B15 (1986) 573.
[58] C.G. Ryan, D.R. Cousens, S.H. Sie, W.L. Griffin, G.F. Suter and E. Clayton, Nucl. Instr. and Meth. B47 (1990) 55.
[59] G.E. Coote, R.J. Sparks and P. Blattner, Nucl. Instr. and Meth. 197 (1982) 213.
[60] S. Ludington, Am. Mineral. 63 (1978) 551.
[61] M. Mosbah, N. Metrich and P. Massiot, Nucl. Instr. and Meth. B58 (1991) 227.
[62] R.A. Jarjis, J. Radioanal. Chem. 48 (1979) 311.
[63] B. O'Connell and D. Crumpton, Nucl. Instr. and Meth. 163 (1979) 161.
[64] P. Gippner, C. Bauer, K. Hohmuth, R. Mann and W. Rudolph, Nucl. Instr. and Meth. 191 (1981) 341.
[65] T.E. Derry, J.F. Prins, C.C.P. Madiba, J. Ennis, R.A. Spits and J.P.F. Sellschop, Nucl. Instr. and Meth. B35 (1988) 431.
[66] J.-P. Hirvonen and E.-L. Yang, Mater. Lett. 8 (6,7) (1989) 197.
[67] J. Rickards, Nucl. Instr. and Meth. B56/57 (1991) 812.
[68] A. Caridi, E. Cereda, S. Fazinic, M. Jaksic, G.M. Braga Marcazzan, O. Valkovic and V. Valkovic, Nucl. Instr. and Meth., these proceedings (3rd Int. Conf. on Chemical Analysis, Namur, Belgium 8–12 July 1991), Nucl. Instr. and Meth. B66 (1992) 298.
[69] C.A. Beevers and D.B. McIntyre, Mineral. Mag. 27 (1946) 254.
[70] M.I. Kay, R.A. Young and A.S. Posner, Nature 204 (1964) 1050.
[71] Arne R. Hagen, Calc. Tiss. Res. 13 (1973) 259.
[72] R.A. Young and W.E. Brown, in: Biological Mineralization and Demineralization, ed. G.H. Nancollas (Springer, Berlin, 1982) pp.101–141.
[73] G.H. Nancollas, in: Biomineralization: Chemical and Biochemical Perspectives, eds. S. Mann, J. Webb and R.J.P. Williams (VCH, Weinheim, 1989).
[74] A. Veis, ibid. ref. [73].
[75] J. Arends, in: Biological Mineralization and Demineralization, ed. G.H. Nancollas (Springer, Berlin, 1982) pp. 303–324.
[76] C. Tse, D.D. Welch and B.S.H. Royce, Calc. Tiss. Res. 13 (1973) 47.
[77] B.S.H. Royce, Annals. N.Y. Acad. Sci. 238 (1974) 131.
[78] M. Hyvönen-Dabek, J. Radioanal. Chem. 63 (2) (1981) 367.
[79] J. Kajfosz and S. Szymczyk, J. Radional. Chem. 58 (1980) 381.
[80] M.A. Chaudhri, G. Burns, E. Reen, J.L. Rouse and B.M. Spicer, J. Radioanal. Chem. 37 (1) (1977) 243.
[81] J.-P. Thomas and J. Grea, Nucl. Instr. and Meth. 126 (1975) 303.
[82] J. Baijot-Stroobants, F. Bodart and G. Deconninck, Health Phys. 36 (1979) 423.
[83] J. Baijot-Stroobants and J. Vreven, Archs. Oral. Biol. 25 (1980) 617.
[84] F. Bodart, G. Deconninck and M. Th. Martin, IEEE Trans. Nucl. Sci. NS-28 (1981) 1401.
[85] G.E. Coote and I.C. Vickridge, Nucl. Instr. and Meth. B30 (1988) 393.
[86] T.W. Cutress and G.E. Coote, to be published.
[87] J.R. Bird, P. Duerden and D.J. Wilson, Nucl. Sci. Appl. 1 (5) (1983) 357.
[88] A. Haddy and A. Hanson, Archaeometry 24 (1) (1982) 37.
[89] G.E. Coote and P. Nelson, in: Archaeology at ANZAAS, Canberra, ed. G.K. Ward (Canberra Archaeol. Soc., C/- Australian National University, 1987) pp. 22–27.
[90] J. Crank, The Mathematics of Diffusion, 2nd ed. (Oxford University Press, Oxford, 1975).
[91] G.E. Coote and K.J. Dennison, in: Archaeometry: Australasian studies 1988, ed. J.R. Prescott (Physics Department, University of Adelaide, Adelaide, S.A.) pp.157–163.
[92] Theya Molleson and G.E. Coote, to be published.
[93] Theya Molleson, in: Trace Elements in Environmental History, eds. G. Grupe and B. Herrmann (Springer, Berlin, 1989) pp. 67–82.
[94] G.E. Coote, N.E. Whitehead and G.J. McCallum, J. Radioanal. Chem. 12 (1972) 491.
[95] J.R. Bird, L.H. Russell, M.D. Scott and W.R. Ambrose, Anal. Chem. 50 (1978) 2082.
[96] R.W. Gauldie, G.E. Coote, I.F. West and R.L. Radtke, Tissue and Cell 22(5) (1990) 645.
[97] R.W. Gauldie, G.E. Coote, I.F. West and K.P. Mulligan, Tissue and Cell 23(5) (1991) 677.

Nuclear Instruments and Methods in Physics Research B66 (1992) 205–208
North-Holland

Nuclear Instruments & Methods in Physics Research
Section B

Analysis of neon by particle accelerators

A. Banse-Lefebvre [a], G. Deconninck [a], M. Dubus [b] and G. Terwagne [a]

[a] *LARN, Facultés Universitaires N-D de la Paix, 22, rue Muzet, B-5000 Namur, Belgium*
[b] *CENG, Grenoble, France*

Natural neon has three stable isotopes, ^{20}Ne (90.92%), ^{21}Ne (0,257%) and ^{22}Ne (8.8%) which can be detected by nuclear reactions. An experiment on the elastic scattering of 2 MeV ^{4}He ions from a solid neon target at 5.5 K is described, the spectrum is correctly fitted with a calculation using the Rutherford scattering cross section. Most applications are in the analysis of neon implanted metals. Depth profiling is possible by nuclear resonant reactions. A review is given of the main resonances used; in each case prompt γ-rays are detected. In the analysis of ^{20}Ne, the ^{20}Ne(p, γ)^{21}Na* reaction has a narrow resonance at 1168,8 keV which can be used with detection of annihilation γ-rays from the β^+ decay of ^{21}Na*.

The ^{22}Ne(p, γ)^{23}Na* reaction has a resonance at 1005 keV yielding 2640 keV γ-rays, the half-life (120 fs) is short enough to allow Doppler shift analysis.

PIXE using solid state detectors has few applications but dispersive X-ray spectroscopy of neon shows wide broadening of X-rays lines. This phenomenon is observed in metals implanted with neon ions. It can be used for the estimation of the pressure inside the bubbles formed by implantation.

1. Introduction

Neon has little reactivity [1] and solidifies at very low temperature (24.3 K). This atom, however, is often found in solids, as retained after different treatments: implantation into metals with bubbles formation, sputter deposition of thin amorphous films, etching and cleaning of solids surfaces namely in semiconductors fabrication.

This atom is sometimes used to estimate the chemical reactivity of the neighboring isoelectric F^- and Na^+ as implanted into solids, Ne is then implanted in same conditions and the temperature dependance of neon profiles is compared with F or Na profiles [2,3]. The hydrogen decoration of defects produced by implantation of Na and Ne in metals was also investigated having in view a search for NaH formation [3].

2. Analysis by backscattering

The analysis of neon can be made by SIMS or by nuclear reaction analysis (NRA). There are three stable isotopes: ^{20}Ne(90.92%), ^{21}Ne(0.257%) and ^{22}Ne(8.8%).

^{20}Ne is the most abundant isotope. This nucleus is of astrophysical importance because of resonances in the ^{20}Ne(α,γ)^{24}Mg capture reaction [4]. We have measured the backscattering (171° lab) of $^{4}He^+$ on ^{20}Ne on thin targets (400 Å) of neon present as bubbles formed after implantation of 50 keV Ne^+ in beryllium. A typical spectrum is shown on fig. 1, the ^{20}Ne signal is well separated from the other components (^{9}Be, ^{12}C, ^{16}O, ···). It is found that the cross section is Rutherford below 2.4 MeV, making the detection of ^{20}Ne possible by standard RBS analysis.

We have also measured the backscattering of 2 MeV protons and ^{4}He from a solid target of neon at a temperature of 5.5 K.

A solid neon target is produced by letting a jet of natural neon gas on an aluminum substrate cooled at 5.5 K by a circulation of liquid helium. This cryogenic target is rapidly growing by condensation, it is used for proton induced X-ray spectroscopy. This target can evaporate by sputtering or by heating, the target thickness is controlled by backscattering of 2 MeV protons from this sample. The backscattering spectrum shows the presence of resonances, as long as the target thickness is more than 2.9 mg/cm^2, this spectrum remains unmodified. The observation of protons scattered by the aluminum backing also indicates that the thickness is less than 2.9 mg/cm^2.

The backscattering of 2 MeV ^{4}He at 145° was recorded in a surface barrier detector, the spectrum shows the presence of ^{20}Ne and ^{22}Ne. A reasonable fit is obtained by a curve calculated with the backscattering formula [5] using Ziegler's stopping power coefficients [6] and the Rutherford cross section (fig. 2).

0168-583X/92/$05.00 © 1992 – Elsevier Science Publishers B.V. All rights reserved

3. Analysis by nuclear resonant reactions

The analysis of ^{20}Ne is possible by the capture reaction ^{20}Ne(p, γ)^{21}Na. Fortunately, there exists a well isolated resonance at 1168.8 keV ($\Gamma = 10$ eV) yielding a radiation of 3.545 MeV which can be used for depth profiling [8,9] of ^{20}Ne implanted into metals and oxides (fig. 3). Depth profiling is also possible by activation, in this case the radiation emitted by the residual nucleus ^{21}Na* (β^+ emitter, half-life 22.8 s) is detected. Using a NaI well crystal, 511 and 1022 keV sum γ-rays are observed with small background. Neon profiles of Ta (Ne) samples obtained by activation are shown in fig. 3b [8].

^{21}Ne is present in very small proportions, samples should be considerably enriched for eventual detection. High resolution (15 eV) measurements have been performed by Schulte et al. [9]. The 272 keV resonance in ^{21}Ne(p, γ)^{22}Na was studied using a monoatomic neon gas target at low temperature (25 K). γ-rays are detected in a 100% Ge detector, the energy window is 2–7 MeV. The resonance width is 3 eV, atomic effects due to L shell excitation are exhibited and the collision spectrum can be derived. These measurements bring new informations on the compound nucleus decay mechanism.

^{22}Ne isotope is best used for depth profiling of neon implanted into metals (fig. 4). The ^{22}Ne(p, γ)^{23}Na reaction has an intense resonance at $E_p = 851.4$ keV ($\Gamma = 6$ eV); capture γ-rays have energy between 2.6 and 9.6 MeV, they are detected in a large size Ge–Li detector or in a NaI well crystal [10]. The sensitivity of the detection is much better than for ^{20}Ne if isotopically enriched targets are used. For this reason, in the case of neon implantations it is advisable to use ^{22}Ne rather than ^{20}Ne as implanted species.

There exists a number of resonances in capture reactions and rearrangement collisions on neon isotopes. The most frequently used reactions are reported in table 1. Another resonance at 1005 keV in the ^{22}Ne(p, γ)^{23}Na reaction gives cascade γ-rays, the last member of the cascade is a 2.640 MeV transition

Table 1
Resonances used for depth profile analysis of neon

Isotope	Abundance [%]	E_R [keV]	Γ [eV]	E_γ [MeV]	Ref.
^{20}Ne	90.92	1168.8	10	3.545	[8,9]
		idem	idem	0.511, 1.022 [a]	[8]
^{21}Ne	0.257	272	3	3–7	[9]
^{22}Ne	8.8	851	6	2.6–9.6	[10]
		1005	–	2.640 [b]	[11]

[a] Activation analysis (half-life 22.8 s).
[b] Short half-life (120 fs), γ-ray spectra are used for Doppler shift attenuation analysis.

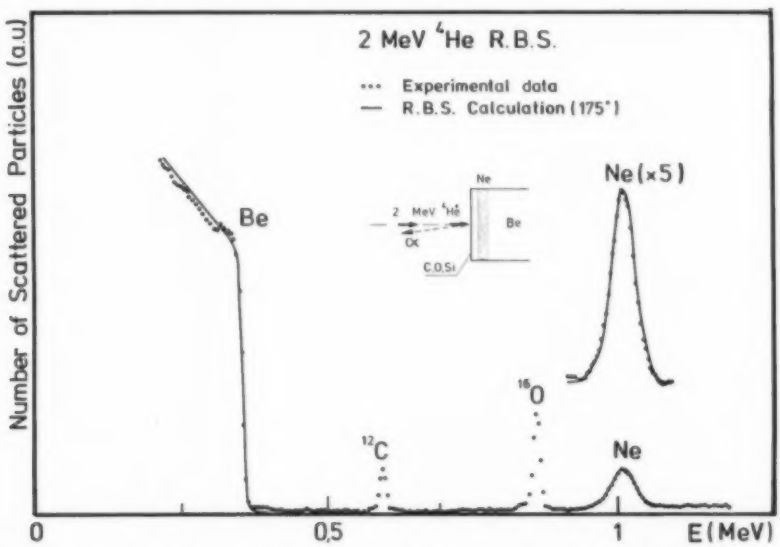

Fig. 1. Spectrum of 2.4 MeV He^+ ions scattered at 171°. The sample is a polished beryllium disk implanted with 50 keV Ne^+ ions, the concentration is 1.8 at.% at the maximum. ^{12}C and ^{16}O peaks are surface contaminants, the arrow indicates the position of surface ^{20}Ne.

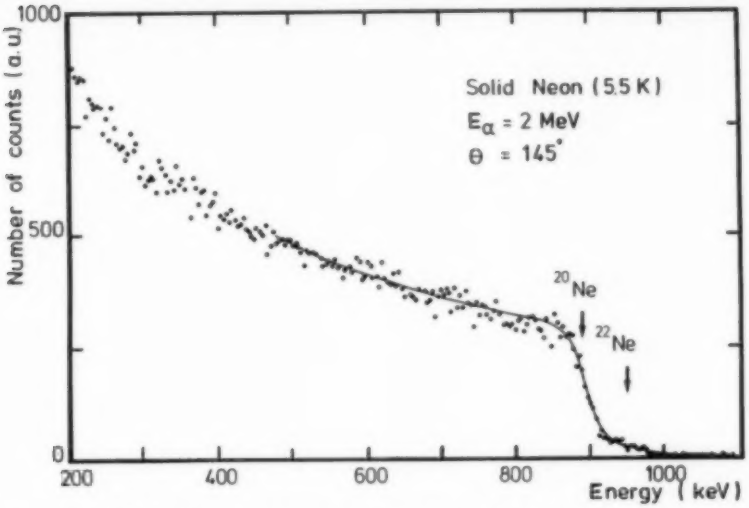

Fig. 2. RBS spectrum of 2MeV He^+ ions scattered at 145°. The sample is a layer of neon ice at 5.5 K on an aluminum backing. The curve is the result of a calculation using Rutherford cross sections.

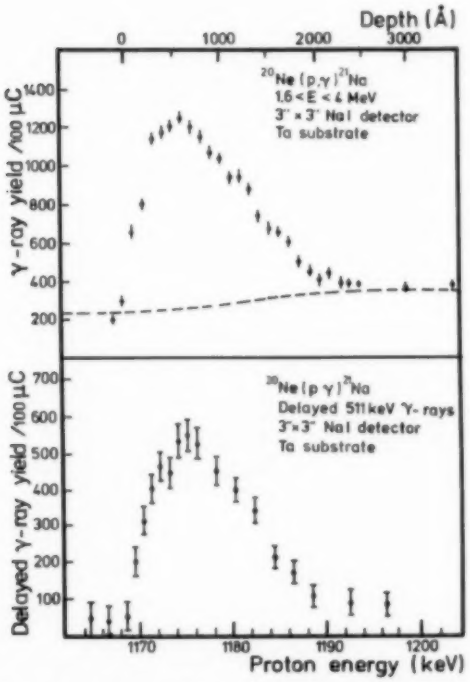

Fig. 3. Depth profiling of a sample of tantalum implanted with 50 keV ^{20}Ne ions (ref. [8]) using respectively prompt γ-rays (3.545 MeV) and delayed annihilation γ-rays from the residual nucleus ^{21}Na.

whose half-life is 120 fs. Such a short life-time allows Doppler shift analysis, a technique used by Keinonen et al. [11] for the estimation of the pressure of neon bubbles in molybdenum, tantalum and tantalum oxide.

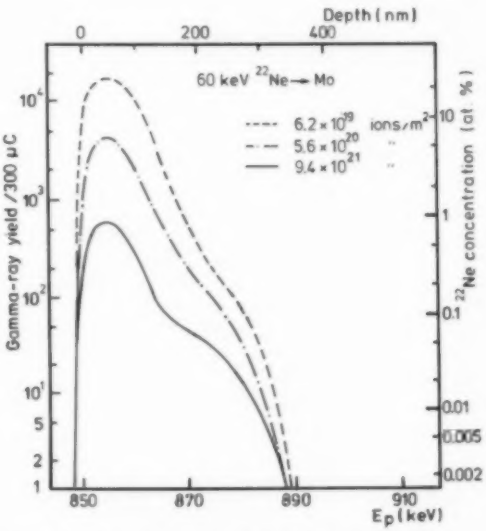

Fig. 4. Depth profiling of 60 keV ^{22}Ne ions implanted into molybdenum. The data are from ref. [10]. γ-rays (2.6–9.6 MeV) from the 851 keV resonance in the ^{22}Ne(p, γ)^{23}Na reaction are detected.

4. Dispersive X-ray analysis

PIXE analysis of neon is only possible with special windowless Si(Li) detector, the energy of the $K\alpha_{1,2}$ transition is 848.6 eV. The detection of Ne K X-rays is possible by energy dispersive techniques, using a flat crystal spectrometer equipped with a quartz or a beryl crystal [12]. The $K\alpha_{1,2}$ line (natural width 0.2 eV) and many satellites from multiple ionization are observed during ^{4}He irradiation (fig. 5). A considerable broadening of the $K\alpha_{1,2}$ line was observed when neon is implanted into metals. The FWTM of this line can be related to the metal shear modulus by a simple relation [12], this parameter is a measure of the neon bubbles pressure. In fig. 6a, the Ne $K\alpha_{1,2}$ band observed during irradiation of a sample of aluminum implanted with 50 keV $^+$Ne (solid line) is compared with the $K\alpha_{1,2}$ line from neon gas [13]. In fig. 6b, the effect of radiation damage is demonstrated, the solid line is from the same samples as fig. 6a; after a long irradiation, the bubbles have grown by coalescence, the pressure has decreased and the spectrum is typical of neon gas. This technique is a new way for the investigation of neon implanted into metals, the broadening has been attributed by the authors to the formation of a valence band in solid neon at very high pressure.

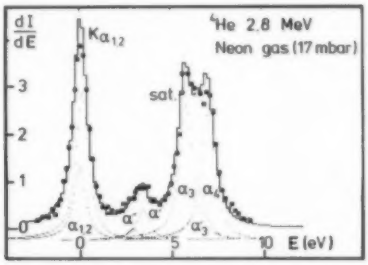

Fig. 5. High resolution X-ray spectrum from neon gas irradiated with 2.8 MeV ^{4}He ions. The dispersive analysis is made by diffraction on a beryl crystal. Zero energy corresponds to 848.6 eV which is the energy of the diagram Ne $K\alpha_{1,2}$ X-ray line.

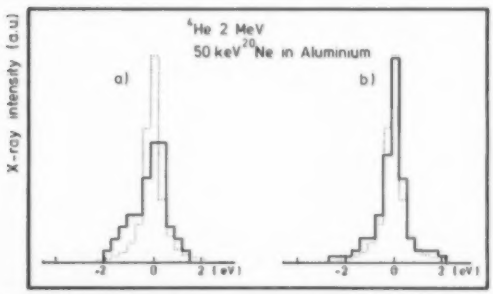

Fig. 6. X-rays spectra from neon irradiated with 2 MeV ^{4}He: (a) Broadening of the $K\alpha_{1,2}$ X-ray line when neon is implanted into an aluminum matrix (full line). The dotted line represents the spectrum from gas; (b) modification of the spectrum from Al(Ne) after irradiation with 300 μC of 2.8 He^+ (full line).

References

[1] W.A. Harrison, Electronic Structure and the Properties of Solids (Freeman, New York, 1980).
[2] G. Deconninck and B. Van Oystaeyen, Nucl. Instr. and Meth. 218 (1983) 165.
[3] J. Keinonen, A. Kehrel, K.P. Lieb and M. Uhrmacher, these Proceedings (3rd Int. Conf. on Chemical Analysis, Namur, Belgium, 8–12 July 1991), Nucl. Instr. and Meth. B66 (1992) 209.
[4] P.M. Endt and C. Van der Leeun, Nucl. Phys. A310 (1978) 100.
[5] G. Deconninck, An introduction to Radioanalytical Physics (Elsevier, Amsterdam, 1978).
[6] J.F. Ziegler, Helium Stopping Powers and Range in All Elements (Pergamon, New York, (1977).
[7] G. Deconninck, Y. Morciaux, M. Dubus and G. Bérard, LARN internal report no. 871 (1987).
[8] Z.E. Switkowski, J.C. Overley, S.-C. Wu, C.A. Barnes and J. Roth, J. Nucl. Energy 78 (1978) 64.
[9] W.H. Schulte, H. Ebbing, H.W. Becker, S. Wüstenbecker, M. Berheide, M. Buschmann, C. Rolfs, G.E. Mitchell and J.S. Schweitzer, these Proceedings (3rd Int. Conf. on Chemical Analysis, Namur, Belgium, 8–12 July 1991), Nucl. Instr. and Meth. B66 (1992) 11.
[10] J. Keinonen, A. Luukkainen, A. Antilla and M. Erola, Nucl. Instr. and Meth. 216 (1983) 249.
[11] A. Luukkainen, J. Keinonen and M. Erola, Phys. Rev. B32 (1985) 4814.
[12] A. Lefebvre and G. Deconninck, Nucl. Instr. and Meth. B15 (1986) 616.
[13] G. Deconninck and A. Lefebvre, Nucl. Instr. and Meth. B90 (1987) 167.

Section III
Contributed papers on the analysis of individual elements

Nuclear Instruments and Methods in Physics Research B66 (1992) 209–214
North-Holland

Nuclear Instruments & Methods in Physics Research
Section B

Hydrogen decoration of defects produced by Na implantation into polycrystalline Cr and Ta

J. Keinonen [a], A. Kehrel [a,b], K.P. Lieb [b] and M. Uhrmacher [b]

[a] *Accelerator Laboratory, University of Helsinki, Hämeentie 100, SF-00550 Helsinki, Finland*
[b] *II. Physikalisches Institut, Universität Göttingen, Bunsenstrasse 7–9, W-3400 Göttingen, Germany*

Polycrystalline Cr and Ta samples were implanted with 250 keV $^{23}Na^+$ ions to fluences of 1.5×10^{17} Na^+/cm^2. Due to the very low solubility of Na in metals this leads to Na precipitates which are potential sites for the agglomeration of implantation induced defects. Their trapping and detrapping was observed via decoration with H. The hydrogen depth distributions were measured with the nuclear resonance reaction $^1H(^{15}N, \alpha\gamma)^{12}C$, the Na depth distributions via $^{23}Na(p, \gamma)^{24}Mg$. Prior to any H or Na implantation, in both metals the H concentration was found to be below the detection limit of 0.2 at.%. After Na implantation (with or without additional H implantation) overlapping Na and H profiles were found, with the H profiles positioned somewhat deeper inside the samples. We interpret these results to indicate the formation of defect–hydrogen complexes at the Na precipitates, built from vacancies and hydrogen migrating to the implanted Na.

1. Introduction

In recent years, ion beam techniques are being used to modify or tailor new materials, making use of the radiation damage and the high energy deposited during the implantation process. Many studies have shown that defects in metals trap light gas atoms like O, He or H which are solved or implanted in the sample. Therefore, the "decoration" of defects with these atoms is a method to trace the defect concentrations and to study the trapping and detrapping mechanism. Mobile defects can be trapped at the implanted atoms, at inhomogenieties like grain bounderies or at inner surfaces which may occur between different phases.

Implantation of heavy inert-gas ions into metals leads to the formation of solid precipitates [1–6]. This observation has attracted experimental and theoretical studies on the precipitate formation, its physical properties, and physical and materials properties of metals [1–15]. The defect structure close to the precipitate–metal interface is of special interest. In spite of its importance and the fact that the precipitates have been produced by ion implantation and thus are subject to considerable defects, there are very few studies in the literature on the defects at the interfaces [8,14,16,17]. Trapping and annealing behavior of hydrogen provides a good method to study such open volume defects.

In this study we have continued our work on H trapping defects in Ne implanted Ta and Mo [8,16] and Na implanted Fe, Ni and Mo [17]. Sodium was selected due to its different electronic structure and larger atomic radius than those of Ne (2.23 Å for Na to be compared with 0.51 Å for Ne). Due to the very low solubility of Na in metals, Na implantation produces supersaturated solid solutions and results in Na precipitates already at concentrations well below 0.1 at.%.

2. Experimental procedure

Samples of typically 10×10 mm^2 area and 2 mm thickness were spark-cut from 99.99% pure Cr and Ta sheets. For the room-temperature implantations beams of $^{23}Na^+$ ions at 250 keV were produced in the University of Göttingen ion implanter IONAS [18]. The beams were swept by an electrical x–y-sweeping system over a 6 mm diameter circular aperture and homogeneously implanted into the water-cooled samples. The total implanted doses of 1.5×10^{17} $^{23}Na^+/cm^2$ were consistently determined by the integrated ion charges and the measured Na concentration profiles.

Depth profiling of ^{23}Na was performed by means of resonant nuclear reaction analysis (RNRA). The use of the reaction $^{23}Na(p, \gamma)^{24}Mg$ at $E_p = 309$ keV has been fully described in ref. [19], where details of the analysis can be found. In the calculation of the depth scale, the stopping power for the probing proton beam was taken from ref. [20]. The depth resolution was about 1 nm at the surface of a sample and about 30 nm at the depth of the projected Na range (about 200 nm). Proton beams of 30 μA were used; the targets were water-

0168-583X/92/$05.00 © 1992 – Elsevier Science Publishers B.V. All rights reserved

cooled. The γ-radiation from the capture reaction was detected in a 16 cm diameter ×14 cm long NaI(Tl) detector shielded by 5 cm of lead.

Hydrogen profiling by the RNRA technique was carried out at the University of Helsinki tandem accelerator EGP-10-II using a 100 nA $^{15}N^{2+}$ beam in conjunction with the 6.385 MeV resonance in the $^{1}H(^{15}N, \alpha\gamma)^{12}C$ reaction [21]. The use of this sharp ($\Gamma = 1.7$ keV [22,23]) resonance made it possible to profile H distributions with a depth resolution of about 10 nm at the surface and about 30 nm at 200 nm.

Room temperature irradiation of the samples with 300–400 keV H^+ ions to doses of 2×10^{18} H^+/cm^2 were done during the depth profiling of ^{23}Na atoms. Postirradiations with 1.0×10^{17} protons/cm^2 at 100 keV were performed at the 100 kV isotope separator of the University of Helsinki Accelerator Laboratory. The proton beam was swept by an electrical x–y-sweeping system to produce a homogeneous implantation over a 10 mm diameter area.

The 30 min isochronal annealings of the samples were carried out in a quartz-tube furnace in a low pressure atmosphere (< 1 μPa). The evolution of the H and Na concentration profiles was studied in the temperature range between 20°C and 920°C. Data on H chemisorption [24] indicate that hydrogen is released from the traps above about 150°C. The annealing behavior of H trapping defects was thus studied by measuring the hydrogen profiles at room temperature.

3. Experimental results

3.1. H profiling prior to any Na implantation

It is well known that many metals contain large quantities of dissolved hydrogen [25]. Previous experiments showed considerable high H concentrations at Ne precipitates in Mo and Ta without any H irradiation [8,16]. Similar observations were made at Na precipitates in Fe, Ni and Mo [17] and led to the conclusion that the trapped hydrogen came from the bulk. First the H concentration in the surface region of virgin Cr and Ta samples was measured. The upper limit of ≤ 0.2 at.% is based on the statistical uncertainty due to the laboratory background. In addition the samples were implanted with protons of 100 keV to a fluence of 1.0×10^{17} H^+/cm^2, but again the H concentrations were observed to be below 0.2 at.%. For H in Ta this "disappearing" is the consequence of the very fast H diffusion at room temperature: the preexponential factor is $D_0 = 4.4 \times 10^{-4}$ cm^2/s and the activation energy is only $Q = 0.14$ eV [26]. For H in Cr in addition a fast interstitial diffusion mechanism is expected [27].

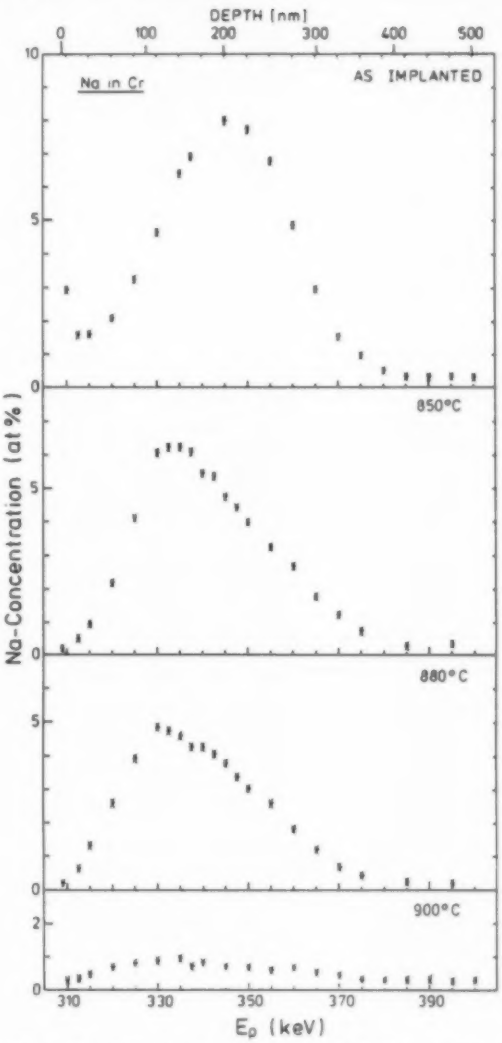

Fig. 1. Na profiles in chromium after 250 keV implantation and 30 min vacuum annealing at various temperatures T_A [28].

3.2. Na-implantation with subsequent H-irradiation

Implantation of 1.5×10^{17} Na ions at 250 keV results in depth profiles with concentration maxima of about 8 at.%. As an example fig. 1 shows Na profiles in Cr [28] after implantation and different vacuum annealing steps. In the corresponding figs. 2, 3 and 5, the Na profiles are given as solid lines. The measured concentration distributions compared to the known very low solubilities of Na in Cr and Ta (below 0.1

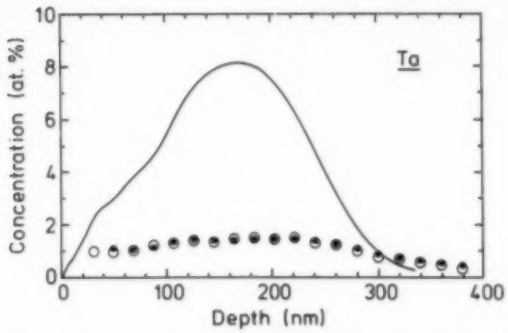

Fig. 2. Measured H profiles in Ta. The H profiles are for a Na-implanted sample (open circles) and the same sample annealed 30 min at 597°C and irradiated with 1×10^{17} 100 keV protons/cm^2 (closed circles). No H was observed in the sample after the annealing. The solid line shows the Na profile.

at.%, ref. [29]) suggest a strong damage in the implanted region.

After Na implantation the H profiles were scanned in the region of the implanted Na. In the case of Ta, the H profile with a maximum concentration of about 1.5 at.% was observed overlapping with the ^{23}Na profile (see fig. 2, open circles) After irradiating the Na implanted samples with 2×10^{18} 300–400 keV protons/cm^2 used to measure the implanted Na profiles, a similar H profile was found in Ta (fig. 2, black dots). In Cr the maximum H concentration was higher (4.0 at.%) and located somewhat deeper than the Na profile (fig. 3, open circles).

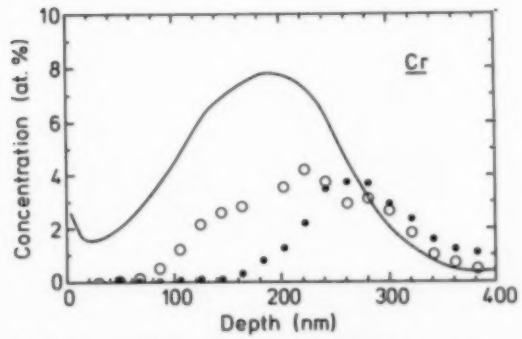

Fig. 3. H profiles in a Na implanted Cr sample annealed 30 min at 727°C and irradiated with about 2×10^{18} 300–400 keV protons/cm^2 (open circles) and in a sample irradiated with 1×10^{17} 100 keV protons/cm^2 (closed circles) after the Na implantation. The Na profile is shown by the solid line.

3.3. H detrapping and H postirradiation

Guided by the experiments on H trapping and detrapping at Ne precipitates in Ta [8,16] and on Na precipitates in Fe, Ni and Mo [17], we searched for the H detrapping temperature of Ta and Cr. For that reason, the Na-implanted and proton-postirradiated samples were annealed under low pressure (≤ 1 μPa) for 30 min. Outgassing of hydrogen started at 547°C for Ta and at 647°C for Cr, as proven by RNRA. On the other hand in Cr no Na is lost before heating up to 900°C [28].

When postirradiating Ta with 1×10^{17} protons/cm^2 at 100 keV, hydrogen distributions similar to those observed after 300–400 keV proton irradiation were observed. Post irradiation of the Cr sample with 1×10^{17} protons/cm^2 at 100 keV gave again a maximum H concentration of 3.8 at.%, but now the H profile was narrower and centered deeper in the bulk as compared to the high energy/high dose proton irradiation (fig. 3, black dots).

4. Discussion

4.1. Formation of Na precipitates

The formation of solid precipitates in heavy inert-gas implantation of metals is well known [1–8] The very low solubility of Na in metals [30] suggests that the Na implantation produces a supersaturated solid solution and hence Na precipitates. In fact, in our previous annealing experiments [17,19,28,29], we observed that the implanted Na first migrates into the region of the highest deposited damage energy from where it diffuses out of the sample and evaporates at the surface. Up to now, Na in Al is the clearest example known [19]: the first migration step is accompagnied by a narrowing of the Na profile, and the maximum Na concentration changes from 8 at.% to more than 12 at.%. This was explained by the formation of Na precipitates which fill up to 45% of the space available [19]. In the present experiments the existence of precipitates is concluded from fig. 1: at 850°C the Na profile in Cr has narrowed and is shifted somewhat towards the surface. Fig. 4 shows the results of computer simulations of the Na implantation into Cr which used a realistic stopping power for the $^{23}Na^+$ ions based on the recent experimental electronic and nuclear stopping powers for ^{26}Mg [31]. In fact, the simulated Na depth profile agrees with the "as-implanted" depth profile of fig. 1, whereas the maximum of the deposited energy (open dots in fig. 4) agrees with the center of the Na profile after heating at 850°C.

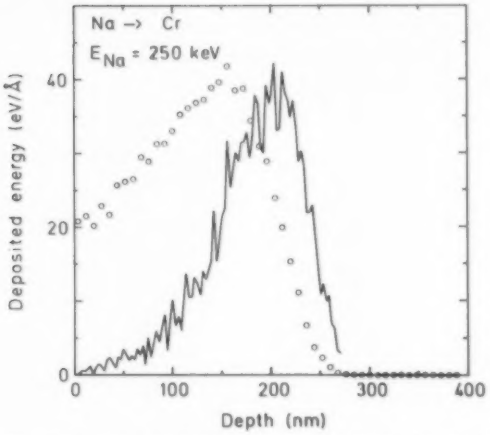

Fig. 4. Computer simulations of the range distribution (solid line) and the deposited energy distribution (open circles) in the implantation of Na into Cr at 250 keV.

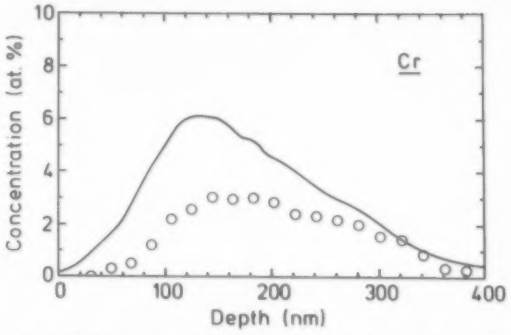

Fig. 5. Hydrogen concentration in a Na implanted Cr sample annealed 30 min at 850°C and irradiated with about 2×10^{18} 300–400 keV protons/cm^2. The Na profile is shown by the solid line.

4.2. Defect–hydrogen complexes

No hydrogen was observed in virgin samples irradiated at room temperature with 100 keV protons; but after the implantation of Na^+ ions a H profile is found which overlaps the Na profile. This fact proves that hydrogen from the bulk is trapped close to the Na distributions. As an example we present fig. 5, where H decorates a Na profile in a Cr sample, annealed for 30 min at 850°C: the Na profile had already moved towards the surface and the trapped H atoms are found at the same depth. On the other hand, in the as-implanted Na doped samples only a low H concentration is found for Ta, none for Cr. Furthermore, the H profile in postirradiated Cr (see fig. 3) shows that more H is trapped in that region which is less strongly damaged during the Na implantation. This implies that the high deposited energy in the Na implantation results in a strong dynamical annealing of the correlated damage. Similar observations were made in the experiments on Ne precipitates in Ta [8] and on Na precipitates in Ni, Fe and Mo [17]. Finally, the presence of vacancies can explain the higher H concentrations which are observed in Na implanted and H postirradiated Cr (4 at.%) compared to those in Ta (1.5 at.%). Adding the results of ref. [17]: Ni (4 at.%), Mo (3.5 at.%) and Fe (1.5 at.%) [17] we find two groups of metals (Cr, Ni, Mo/Ta, Fe) which differ in their vacancy-migration energies (~ 1.15 eV and ~ 0.7 eV, see table 1). Vacancies are thus mobile in Fe and Ta during the room temperature H postirradiation. They migrate freely through the whole sample and get lost as trapping centers at Na. On the other hand, in Cr, Ni and Mo vacancies migrate only during the heavy ion implantation inside the thermal spike and a considerable amount of them stays trapped at the precipitates.

NaH formation can be excluded from the H detrapping experiments. The decomposition-temperature of NaH is 797°C [32]. If NaH is embedded in different matrices a slight change of this temperature may occure, but H detrapping from Na implanted metals was observed to start in a very wide temperature range: at

Table 1
Summary of data relevant for the analysis of hydrogen–defect interaction in ion-irradiated Cr, Ta, Fe, Ni and Mo

Metal (crystal structure)	Activation energy of H diffusion [eV]	Activation energy of V migration [eV]	HV dissociation energy followed by migration of H and V [eV]
Cr (bcc)	[a]	1.1 [d]	[a]
Ta (bcc)	0.14 [b]	0.8 [g]	1.3 [g]
Fe (bcc)	0.11 [b]	0.6 [e]	[a]
Ni (fcc)	0.41 [b]	1.1 [f]	0.98 [f]
Mo (bcc)	0.77 [c]	1.3 [c]	1.4 [h]

[a] To our knowledge no literature data are known.
[b] Ref. [26], [c] ref. [25], [d] ref. [33], [3] ref. [34], [f] ref. [35], [g] ref. [36], [h] ref. [37].

647°C in Cr and at 547°C in Ta to be compared with 327°C (Fe), 97°C (Ni) and 277°C (Mo) [17]. Furthermore, for Mo [16] and Ta [8] the same type of experiment was done at Ne precipitates which cannot build any chemical compound with H. Comparing the two sets of experiments a much better agreement of the H-detrapping temperatures is found (NeMo: 227°C NaMo: 277°C and NeTa: 577°C NaTa: 547°C). These results rule out a possible NaH-formation and indicate that the H traps associated with Na implantation are quite similar to those observed after Ne, implantation, which were interpreted as vacancies trapped at the Ne precipitate/metal interface [8].

5. Conclusions

In the course of the discussion of the present experiments, similarities between the H trapping at Ne and Na precipitates [8,16] were shown for several details. The advantage of the Ne experiments were the higher concentrations of Ne precipitates (28 at.%) and trapped hydrogen (20 at.%) which clearly showed that the hydrogen profile coincides with the Ne profile, but not with the damage distribution. Although the results with Ne precipitates favor H trapping at the Ta/precipitate interface, a final answer could not yet been given as to whether H is trapped at the interface or within the precipitate [8,16]. One of the reasons is the missing lateral resolution of the RNRA method, despite its excellent depth resolution.

In the present study only much smaller H concentrations are found at Na precipitates. Nevertheless, depending on the host metal, H detrapping occurs at the same temperature for Na and Ne precipitates which hints to a similar H defect–precipitate complex in both cases. At higher deposited energy – i.e. during the heavy ion implantation – the H trapping defects anneal. Applying ion beam techniques supersaturated solid solutions of the implants can be achieved. If inmiscible compounds are prepared a similar complex behavior can probably be expected.

Acknowledgements

This work was supported by the Academy of Finland and the Deutsche Forschungsgemeinschaft.

References

[1] A. vom Felde, J. Fink, Th. Müller-Heinzerling, J. Pflüger, B. Scheerer, F. Linker and D. Kalella, Phys. Rev. Lett. 53 (1984) 922.
[2] C. Templier, C. Jaanen, J.-P. Riviére, J. Delafand and J. Grithé, C.R. Acad. Sci. 299 (1984) 613.
[3] J.H. Evans and D.J. Mazey, J. Phys. F15 (1985) L1.
[4] J.N. Evans and D.J. Mazey, Scripta Metall. 19 (1985) 621.
[5] J.H. Evans and D.J. Mazey, J. Nucl. Mater. 138 (1986) 176.
[6] G. Deconninck and A. Lefebre, Mater. Sci. Eng. 90 (1987) 163.
[7] A. Luukkainen, J. Keinonen and M. Erola, Phys. Rev. B32 (1985) 4814.
[8] J. Keinonen, V. Karttunen, J. Räisänen, F.-J. Bergmeister, A. Luukkainen and P. Tikkanen, Phys. Rev. B34 (1986) 8981.
[9] K.O. Jensen and R.M. Nieminen, Phys. Rev. B35 (1987) 2087.
[10] H.E. Hansen, R.M. Nieminen and M.J. Puska, J. Phys. F14 (1984) 1299.
[11] H.E. Hansen, J. Rajainmäki, R. Talja, M.D. Dentzon, R.M. Nieminen and K. Petersen, J. Phys. F15 (1985) 1.
[12] S.E. Donelly, Radiat. Eff. 90 (1985) 1.
[13] R.C. Frank, C.E. Rehn and P. Baldo, J. Appl. Phys. 57 (1985) 845.
[14] R.C. Frank, S.P. McManus, L.E. Rehn and P. Baldo, J. Appl. Phys. 59 (1986) 2747.
[15] V. Karttunen, J. Ignatius, J. Keinonen and R.M. Nieminen, J. Phys. Condens. Matter 1 (1989) 4885.
[16] J. Keinonen and V. Karttunen, Phys. Rev. B37 (1988) 8440.
[17] A. Kehrel, J. Keinonen, P. Haussalo, K.P. Lieb and M. Uhrmacher, Radiat. Eff. and Def., to be published.
[18] M. Uhrmacher, K. Pampus, F.J. Bergmeister, D. Purschke and K.P. Lieb, Nucl. Instr. and Meth. B9 (1985) 234.
[19] N. Scapellato, M. Uhrmacher and K.P. Lieb, J. Phys. F18 (1987) 232.
[20] H.H. Andersen and J.F. Ziegler, The Stopping and Ranges of Ions in Matter, vol. 3 (Pergamon, New York, 1977).
[21] H.J. Whitlow, J. Keinonen, M. Hautala and A. Hautojärvi, Nucl. Instr. and Meth. B5 (1984) 505.
[22] G. French, G.K. Wolf, H. Damjantschitsch, A. Wieser and S. Kalbbitzer, Nucl. Instr. and Meth. 218 (1983) 500.
[23] B. Maurel and G. Amsel, Nucl. Instr. and Meth. 218 (1983) 159.
[24] P. Nordlander, S. Holloway and J.K. Norskov, Surf. Sci. 136 (1983) 59.
[25] N.A. Galaktionowa, in: Hydrogen–Metal Systems Databook (Ordentlich, Holon, 1981) p. 185.
[26] J. Völkl and G. Alefeld, in Hydrogen in Metals I, Topics in Applied Physics, vol. 28, eds. J. Völkl and G. Alefeld, (Springer, New York, 1978) p. 331.
[27] J.D. Fast, in: Interaction of Metals and Gases, vol. 2, Philips Technical Library (Macmillan, Eindhoven, 1965) p. 88 ff.
[28] A. Kehrel, K.P. Lieb and M. Uhrmacher, Mater. Sci. Eng. A115 (1989) 43.
[29] A. Kehrel, K.P. Lieb, N. Scapellato and M. Uhrmacher, J. Nucl. Mater. 173 (1990) 284.
[30] W.G. Moffat, in: The Handbook of Binary Alloys (General Electric Co., New York, 1978).
[31] K. Arstila, J. Keinonen and P. Tikkanen, Phys. Rev. B41 (1990) 6117.

[32] CRC Handbook of Chemistry and Physics, eds. R.C. Weast and M.J. Astle (CRC Press, Florida, 1981) B-148.
[33] J. Johansson, A. Vehanen, J. Yli-Kauppila, P. Hautojärvi and P. Moser, Radiat. Eff. Lett. 58 (1981) 31.
[34] P. Hautojärvi, T. Judin, A. Vehanen, J. Yli-Kauppila, J. Johanson, J. Versane and P. Moser, Solid State Commun. 29 (1979) 855.
[35] H. Rajainmäki, S. Linderoth, H.E. Hansen and R.M. Nieminen, J. Phys. F18 (1988) 1109.
[36] P. Hautojärvi, H. Huomo, M. Puska and A. Vehanen, Phys. Rev. 832 (1985) 4326.
S.-J. Kim, M.-A. Nicolet, R.S. Averback and D. Peak, Phys. Rev. B37 (1988) 38.
B.M. Paine an R.S. Averback, Nucl. Instr. and Meth. B7/8 (1985) 666.
[37] A.R. Gorodetsky, A.P. Zakharov, V.M. Sharapov and Y.Kh. Alimov, J. Nucl. Mater. 93 & 94 (1980) 588.

Nuclear Instruments and Methods in Physics Research B66 (1992) 215–220
North-Holland

Nuclear Instruments & Methods in Physics Research
Section B

Depth profiling of hydrogen isotopes in thin, low-Z films by scattering recoil coincidence spectrometry

J.S. Forster

AECL Research, Chalk River Laboratories, Chalk River, Ontario, Canada K0J 1J0

J.R. Leslie and T. Laursen

Queen's University, Department of Physics, Kingston, Ontario, Canada K7L 3N6

The technique for profiling light elements in thin, low-Z foils, by means of a coincidence measurement over large solid angles, is demonstrated for hydrogen and deuterium in two separate geometries. A beam of 2.0 MeV ^{4}He particles was used to bombard foils of (i) evaporated carbon, (ii) evaporated carbon which had been implanted with 10^{17}/cm^2 7.5 keV H^+ ions and, (iii) evaporated carbon which had been implanted with 5×10^{16}/cm^2 7.5 keV D^+ ions. Measurements were made, in the latter two cases, with the implanted region facing the beam and away from the beam. Plots of E_α versus $E_{H(D)}$, as well as plots of total energies ($E_\alpha + E_{H(D)}$) clearly show the H (and D) distributions within the foil.

1. Introduction

One traditional method of profiling light elements in heavy substrates employs elastic recoil detection (ERD) [1]. Unfortunately, in order to obtain good depth resolution it is essential that the scattering angle be well defined and hence that the detector solid angle be small. As a consequence, probe beam intensities used are sufficiently high that they can radiation damage some materials such as polymers.

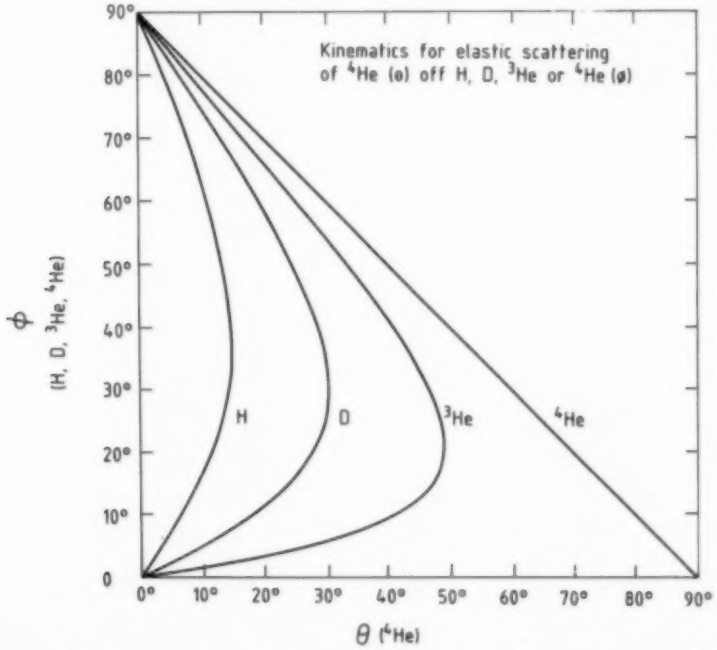

Fig. 1. Kinematics for elastic scattering of ^{4}He, through an angle θ, off H, D, ^{3}He or ^{4}He which recoils at an angle ϕ.

A new spectrometry, scattering recoil coincidence spectrometry (SRCS), proposed by Chu and Wu [2] overcomes this problem through the use of detectors with solid angles of the order of steradians instead of millisteradians. The loss of depth resolution, which would normally occur because of the large solid angles, is prevented, to a reasonable extent, by a coincidence measurement of the scattered-beam particle and the recoiling light ion; since this technique relies on the difference in stopping power before and after scattering, the depth resolution is inferior to that obtained by conventional ERD.

In a previous paper [3], we demonstrated that the experimental geometry suggested by Chu and Wu [2] is feasible for detecting hydrogen in thin carbon foils. Their technique requires two annular silicon detectors downstream from a thin foil, in which the recoiling light ions (H or D) are detected in coincidence with scattered ^{4}He ions. In the present work, we have made further measurements for hydrogen in carbon as well as for deuterium in carbon.

2. Experiment

The kinematics showing ^{4}He scattering off H, D, ^{3}He and ^{4}He are shown in fig. 1; after a binary collision between a ^{4}He ion and an H, D, ^{3}He or ^{4}He target atom the bombarding ^{4}He ion goes at an angle θ with respect to the beam direction while the recoiling atom goes at an angle ϕ. It can be seen from fig. 1 that a careful choice of angles θ and ϕ makes it possible to identify H, D, ^{3}He or ^{4}He.

The experimental layout is shown schematically in fig. 2. We used the setup that was used in our liquid–solid interface measurements [4], for which the beam-spot size at the target was ~ 0.5 mm as defined by upstream apertures. A further aperture, with a 1.5 mm diameter hole, was mounted directly in front of the target as shown in fig. 2. Two annular surface-barrier detectors of 300 mm^2 active area were used to detect coincidences between scattered ^{4}He ions and recoiling

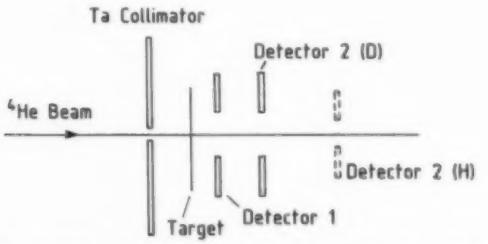

Fig. 2. Experimental geometry, drawn to scale, for coincidence measurements of ^{4}He scattering off H or D in thin carbon films.

D atoms. The detectors had a 6 mm diameter hole through their centres with an outer diameter of 19 mm. Detector 1, which measured recoiling D atoms, was placed ~ 3.5 mm downstream of the target in order to subtend an angular range ϕ from 45° to 66°. Detector 2, which measured scattered ^{4}He ions, was placed ~ 10.5 mm downstream of the target and subtended angles θ between 14° and 35°.

To profile H atoms, detector 2 was removed and replaced by an annular detector with inner and outer diameters of 4 mm and 15 mm, respectively. It was positioned ~ 20 mm downstream of the target and subtended angles θ between 8° and 15°; scattered ^{4}He ions were then detected in detector 2 and recoiling H atoms in detector 1.

The beam was carefully directed through the centres of the two detectors in order to avoid damage to them. The aluminum holder which held the target and detectors was mounted on a two-axis goniometer with x–y translation [4]. With the target and detectors removed, an insulated aperture with a 2 mm diameter hole was mounted at the downstream end of the holder and the goniometer was rotated in angle about the beam direction and translated in x and y until the beam passed cleanly through the 1.5 mm entrance and the 2 mm exit apertures. The target and annular detectors were then replaced in the aluminum holder and measurements made.

When measuring ^{4}He–H coincidences, the beam was kept between 5 and 10 pA which was determined by the count rate in detector 2 from ^{4}He elastically scattered off the carbon substrate; the rate was kept at ≤ 7000 counts per second in order to avoid pileup. When measuring ^{4}He–D coincidences we increased the beam current to ~ 25 pA because of the larger angles subtended by detector 2 and the consequent reduced rate in elastic scattering from the carbon foil.

Coincidence measurements for ^{4}He bombardment of the hydrogen implanted foil were made for the implant facing upstream and for the implant facing downstream. As well, a measurement was made for an unimplanted, evaporated carbon foil, to check on residual hydrogen in the foil. The hydrogen-implanted carbon foil had a thickness of 68 μg/cm^2 while the unimplanted foil was 60 μg/cm^2 thick. The ^{4}He–D coincidence measurements were also made with the implant facing upstream and with the implant facing downstream; the foil thickness was 115 μg/cm^2. Target thicknesses were determined from energy-loss measurements of alpha particles from a ^{241}Am source and the stopping powers of Ziegler et al. [5]; thickness uncertainties are estimated to be $\pm 10\%$.

Data were collected, event by event, on the Queen's University PDP-15 computer. An event consisted of the energy signal from each detector and the time correlation between them. The data were analyzed

later with the Concurrent Computer Corporation 3230 minicomputer at Chalk River. During analysis, the individual energy spectra, the time spectrum and the total energy spectrum, defined as the sum of the energies in detectors 1 and 2 and divided by 2, were generated. Two dimensional spectra of total energy versus time were generated as well; finally, total-energy spectra were generated for windows on the associated time spectra, as well as two-dimensional spectra of E_1 versus E_2 for windows on time and total energy.

3. Results

3.1. Hydrogen

The data for hydrogen profiling are straightforward to interpret because the experimental geometry ensures that only ^{4}He–H events are in true coincidence, as reported previously [3]; in that earlier work [3] we showed results for a thin cracked-ethylene carbon foil and for the hydrogen-implanted foil with the implant towards, and away, from the beam. In the present work, we have repeated measurements of the implanted foil and made a measurement of an unimplanted, evaporated carbon foil. Somewhat to our surprise, the unimplanted foil contained a considerable amount of hydrogen.

The three energy spectra for ^{4}He–H coincidences with a window on "real" time are shown in fig. 3 for (a) the unimplanted foil, (b) the foil with the implant facing the beam, and (c) the foil with the implant facing downstream. The experimental data are shown as solid squares.

We have made Monte Carlo simulations which are shown in fig. 3 as crosses. The Monte Carlo calculations used the stopping-power values of Ziegler et al. [5] and experimentally determined cross-sections for ^{4}He scattering from H [6] and for ^{4}He scattering from D [7]. For the unimplanted foil, the simulated spectrum has been normalized to the experimental one such that they have the same total number of counts; a uniform distribution of hydrogen throughout the foil was assumed. Inspection of fig. 3a shows that the calculations reproduce the data very well.

The implanted foil data in figs. 3b and 3c are more complex because there is a contribution from the hydrogen implant as well as from the residual hydrogen in the foil. Monte Carlo calculations were made for the implanted region with the hydrogen distribution taken from TRIM predictions [8] which give the peak of the implanted distribution at 17.6 μg/cm^2 below the surface with a straggle of 4 μg/cm^2. The simulated spectra were normalized to the experimental data at the maximum count, i.e. at channel 363 in fig. 3b and at channel 370 in fig. 3c. Inspection of figs. 3b and 3c shows that the position and shape of the implant are well reproduced. To fit the experimental spectra properly, calculations should be carried out that vary the ratio of the amount of residual hydrogen in the foil to the amount in the implanted region.

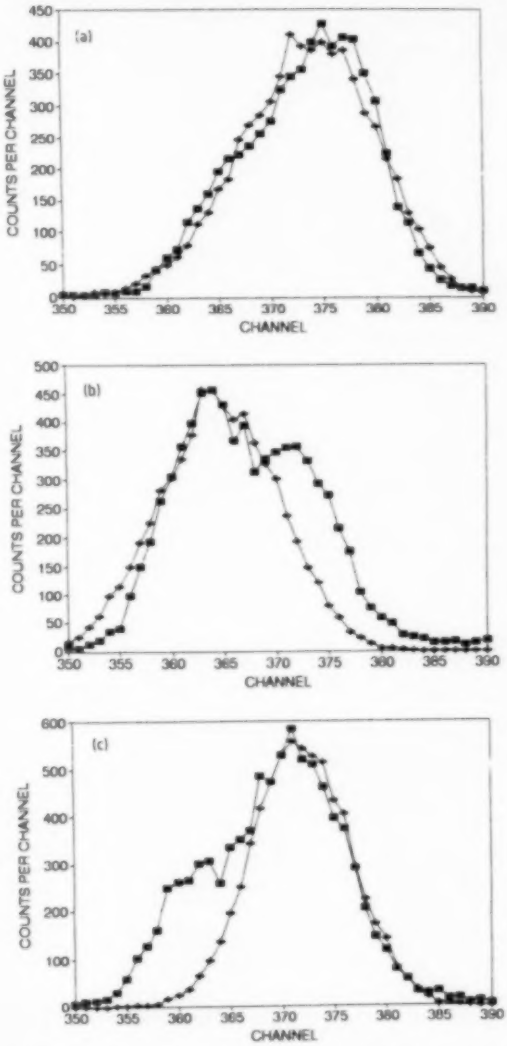

Fig. 3. Total-energy spectra, for a window on the prompt time peak, for (a) a 60 μg/cm^2 evaporated carbon foil, (b) a 68 μg/cm^2 hydrogen implanted carbon foil with the implant facing the beam and (c) the same foil as (b) but with the implant facing downstream. Experimental data (■ ——— ■) and Monte Carlo simulations (× ——— ×) are shown. The energy calibration is 5.06 keV/ch.

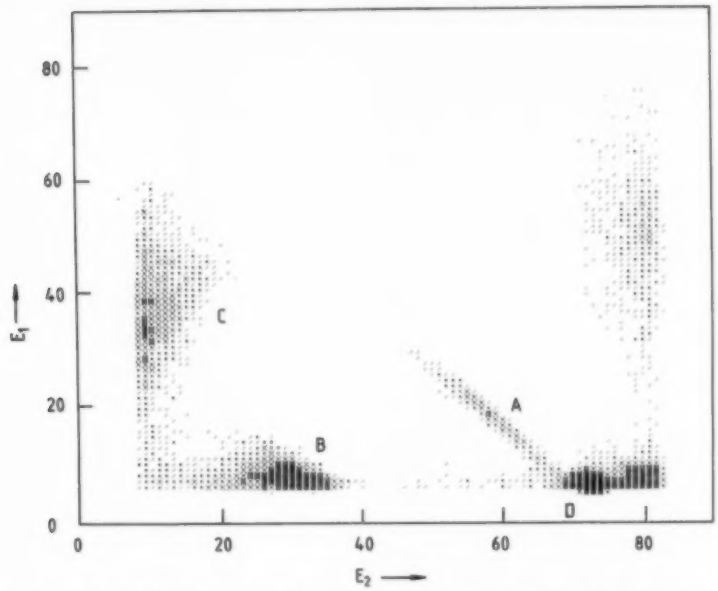

Fig. 4. Intensity as a function of E_1 and E_2 for 2 MeV ^{4}He ions scattered from a deuterium-implanted carbon foil. See text for details on the various regions marked A–D. The energy calibration is 22.68 keV/ch.

3.2. Deuterium

The data for deuterium profiling are more difficult to interpret because the experimental geometry allows other scattering processes to occur in real coincidences with the two detectors. As an example, the two-dimensional spectrum of intensity as a function of E_2 and E_1 with no gating conditions is shown in fig. 4. The region

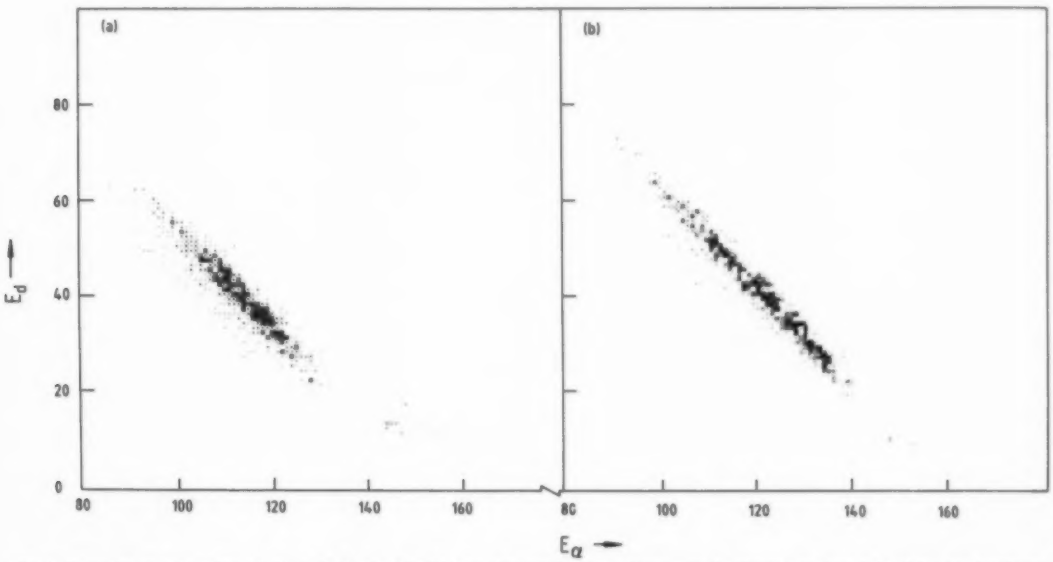

Fig. 5. Intensity as a function of E_α and E_d for 2 MeV ions scattered from a deuterium-implanted carbon foil (a) for the implanted region facing the beam and (b) for the implanted region facing downstream. The energy calibration is 11.34 keV/ch.

labelled A is the one of interest, namely $E_{^4He}$ versus E_D. Regions B and C result from carbon recoils, produced by head-on scattering of the beam, which subsequently scatter off carbon atoms in the target. The two distinct regions occur depending on whether the primary recoil scatters into detector 1 or 2, with the secondary recoil being detected in the other detector; both cases are kinematically allowed. Region D results from a small kinematically acceptable angular range for ^{4}He scattering off carbon, i.e. ^{4}He scattered at 35° to the beam and detected in counter 2 while the recoiling carbon atom is detected at 66° in detector 1. The other regions in the spectrum result from chance coincidences between the two detectors.

When proper windows are set on the "real" time peak and on the total energy, the two-dimensional spectra of intensity as a function of $E_{^4He}$ and E_d are obtained as shown in fig. 5. Fig. 5a is for the carbon foil with the D implant facing the beam while fig. 5b is for the implant facing downstream. A clear shift to higher energies is observed when the implant faces downstream (fig. 5b). This is a result of higher stopping powers for the ^{4}He and D after the collision as well as the longer path lengths for ^{4}He and D when the collision takes place near the entrance to the foil.

The deuterium implanted foil was checked with the D(^{3}He, p)^{3}He reaction with 0.8 MeV ^{3}He ions and the results are shown in figs. 6 and 7. Fig. 6 shows the proton energy spectra obtained with the implant facing the beam and with the implant facing downstream. A computer program [9] was used to produce the depth profiles that are shown in fig. 7; the profiles are given as deuterium per carbon atom (in atomic percent) as a

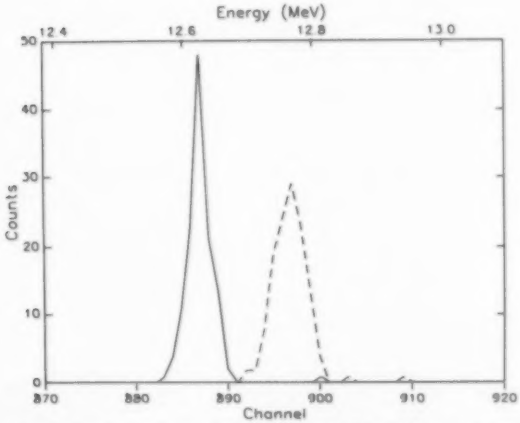

Fig. 6. Proton energy spectra from the D(^{3}He, p)^{4}He reaction for 0.8 MeV ^{3}He bombardment of the deuterium-implanted foil. Data are shown for the implant facing the beam (———) and for the implant facing downstream (— — —).

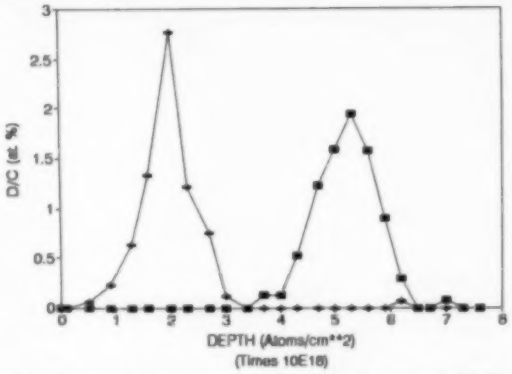

Fig. 7. Deuterium concentration versus depth profiles for the deuterium-implanted foil extracted from the proton spectra shown in fig. 6. Profiles are shown for the implant facing the beam (+ ——— +) and for the implant facing downstream (■ ——— ■).

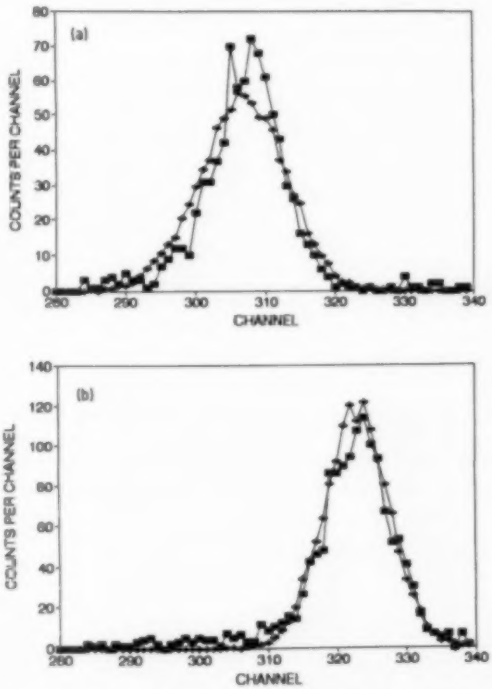

Fig. 8. Total-energy spectra, for a window on the prompt time peak, for (a) a 115 μg/cm^2 deuterium-implanted carbon foil with the implant facing the beam and (b) the same foil with the implant facing downstream. Experimental data (■ ——— ■) and Monte Carlo simulations (+ ——— +) are shown. The energy calibration is 5.67 keV/ch.

function of depth (in atoms/cm^2). Note the poorer depth resolution when the implant faces away from the beam because of straggling of the ^{3}He beam. These results agree well with TRIM [8] predictions, i.e. the implant peaks at a depth of 19 μg/cm^2 and has a straggle of 4 μg/cm^2.

The total-energy spectra corresponding to the two-dimensional spectra of fig. 5 are shown in fig. 8. Also shown are Monte Carlo calculations which have been normalized to each experimental spectrum such that the theoretical spectrum has the same total counts as the experimental one. The deuterium distribution was taken from the TRIM predictions [8] as mentioned above. Inspection of fig. 8 shows that the calculations reproduce the data very well.

4. Discussion

The data and calculations show that scattering recoil coincidence spectrometry is a powerful method for profiling light atoms in low-Z substrates. Very little beam current (10–30 pA) is required to make a statistically significant measurement in a reasonable amount of time (10–60 min).

From the spectra shown in figs. 3 and 8, it is possible to estimate the depth resolution for H and D in thin (50–125 μg/cm^2) carbon foils. Since SRCS is a combination of Rutherford scattering and ERD it is reasonable to use the same criteron for depth resolution as that used in backscattering spectrometry [10], namely that the depth resolution δx is defined by the energy width δE between the positions at 12 and 88% of the full height of a signal that corresponds to an abrupt change in sample composition and the relationship

$$\delta x = \delta E/[s], \qquad (1)$$

where $[s]$ is the energy loss factor; since the rate of energy loss in carbon is higher for ^{4}He than for H and D, we use the energy-loss factor for ^{4}He in carbon. This relation results in a depth resolution, for profiling H or D in carbon by SRCS, of 20–30 μg/cm^2 ($\sim$ 1000–1200 Å) based on the spectra shown in figs. 3b, 3c and 8.

To estimate the sensitivity limit for determining the deuterium content in carbon we note that the average area of the spectra shown in fig. 8 is 1000 counts and that the measurement took one hour at the maximum beam current permissible. The implanted dose was 5×10^{16} atoms/cm^2 of deuterium. If a total of 100 counts is considered reasonable, i.e. $\pm 10\%$ uncertainty because of statistics, and as much as four hours is allowed for data accumulation then a sensitivity limit of $\simeq 10^{15}$ atoms/cm^2 D is obtained for this particular geometry.

In conclusion, we have shown that the scattering recoil coincidence spectrometry technique of Chu and Wu [2] is indeed a viable technique for profiling light elements in thin, low-Z films where beam currents must be kept quite small to avoid radiation damage to the sample.

References

[1] J. L'Ecuyer, C. Brassard, C. Cardinal, J. Chabbal, L. Dechenes, J.P. LaBrie, B. Terrault, J.G. Martel and R.St. Jacques, J. Appl. Phys. 47 (1976) 881.
[2] W.-K. Chu and D.T. Wu, Nucl. Instr. and Meth. B35 (1988) 518.
[3] J.S. Forster, J.R. Leslie and T. Laursen, Nucl. Instr. and Meth. B45 (1990) 176.
[4] J.S. Forster, D. Phillips, J. Gulens, D.A. Harrington and R.L. Tapping, Nucl. Instr. and Meth. B28 (1987) 385.
[5] J.F. Ziegler, J.P. Biersack and U. Littmark, The Stopping and Range of Ions in Solids, vol. 1 (Pergammon, New York, 1985).
[6] Y. Wang, J. Chen and F. Huang, Nucl. Instr. and Meth. B17 (1986) 11.
[7] F. Besenbacher, I. Stensgaard and P. Vase, Nucl. Instr. and Meth. B15 (1986) 459.
[8] J.P. Biersack and L.G. Haggmark, Nucl. Instr. and Meth. 174 (1980) 257.
[9] T. Laursen and R.S. Koelbl, J. Nucl. Mater. 137 (1986) 241.
[10] W.-K. Chu, J.W. Mayer and M.-A. Nicolet, Backscattering Spectrometry (Academic Press, New York, 1978).

Nuclear Instruments and Methods in Physics Research B66 (1992) 221–225
North-Holland

Nuclear Instruments & Methods in Physics Research
Section B

Determination of boron using the B(α, p)C nuclear reaction at incident energies near 3 MeV

L.C. McIntyre, Jr., J.A. Leavitt, M.D. Ashbaugh, Z. Lin and J.O. Stoner, Jr
Department of Physics, University of Arizona, Tucson, AZ 85721, USA

A technique for determining boron content of thin films using the B(α, p)C reaction on both isotopes of boron is described. An incident alpha energy near 3 MeV is used and emitted protons are detected at 135° lab angle. A thin film containing a known areal density of boron is required for calibration. A comparison is made between this method and conventional elastic scattering of $^4He^+$ ions for boron determination in thin films containing heavy elements or backings. We also present relative yield data on protons from the $^{10}B(\alpha,p)^{13}C$ and $^{11}B(\alpha,p)^{14}C$ reactions at 135° lab angle between 1.4 and 3.3 MeV.

1. Introduction

Nuclear reaction analysis (NRA) has been extensively used to determine boron concentration in thin films and surface layers of bulk materials. This technique is more effective than standard elastic backscattering using ^4He ions, since boron's low Z and small mass results in a small yield of low energy scattered particles whose signals usually overlap those from heavier elements in the film or backing. An additional problem with ^4He backscattering measurements has been the uncertain elastic scattering cross section, even for incident alpha energies below 2 MeV [1].

A variety of nuclear reactions have been used in the analysis of boron. Materials analysis experiments observing emitted gamma rays have used the $^{11}B(p,\gamma)^{12}C$ reaction near a resonance at 163 keV [2] and the $^{10}B(\alpha,p\gamma)^{13}C$ reaction at 2.4 MeV [3] and 3.5 MeV [4]. Experiments observing outgoing charged particles have used the $^{10}B(d,p)^{11}B$ reaction at 2.7 MeV [5] and 1.47 MeV [6], the $^{11}B(p,\alpha)^8Be$ reaction near the 163 keV resonance [7–9] and at 660 kev [10], the $^{10}B(\alpha,p)^{13}C$ reaction near a resonance at 1.5 MeV [6] and at 2.67 MeV [11], and the $^{11}B(\alpha,p)^{14}C$ reaction at 2.67 MeV [11]. Reactions involving neutrons include the $^{10}B(n,\alpha)^7Li$ reaction [12,13] and the $^{10}B(p,n)^{10}Be$ reaction [14]. An overview of the general techniques of nuclear reaction analysis and lists of appropriate reactions for specific nuclides can be found in ref. [15–18].

We have found the $^{10}B(\alpha,p)^{13}C$ and $^{11}B(\alpha,p)^{14}C$ reactions to be particularly useful in quantifying the boron content of multilayer thin films (10–100 nm thick) used in soft X-ray optics applications [19]. In this paper we will describe the implementation of this technique. In addition, we present measurements of the relative yield of protons from the $^{10}B(\alpha,p)^{13}C$ and $^{11}B(\alpha,p)^{14}C$ reactions at incident energies between 1.4 and 3.3 MeV at a laboratory angle of 135°. A comparison will be made between ^4He backscattering and the B(α, p)C reactions in determining the boron content of thin films.

2. Experimental

Beams of $^4He^+$ ions were obtained from the University of Arizona 5.5 MV CN (High Voltage Engineering Corp.) Van de Graaff accelerator. A large area (450 mm^2) surface barrier detector was added to a standard backscattering setup [20] to detect protons from the (α, p) reaction. The detector was located 40 mm from the target at an angle of 135°. The angular acceptance was $135 \pm 17°$ and the solid angle subtended is about 0.3 sr. The detector was covered with a 25 μm Mylar foil to stop backscattered alpha particles. This is the same arrangement used in our previous work involving the $^{31}P(\alpha,p)^{34}S$ [21] and the $^{19}F(\alpha,p)^{22}Ne$ [22] reactions. The absolute uncertainty in the beam energy is estimated to be 5 keV and the beam energy spread is estimated to be less than 0.5 keV. Standard electronics and a multichannel analyzer were used to obtain energy spectra of emitted protons.

Fig. 1 shows a proton spectrum obtained with a self supporting 20 $\mu g/cm^2$ natural boron target bombarded with 3.0 MeV $^4He^+$ ions. The highest energy peak is due to the $^{10}B(\alpha,p_0)^{13}C$ reaction which has a Q value of +4.063 MeV. The other peaks are due to the $^{11}B(\alpha,p_0)^{14}C$ reaction and the $^{10}B(\alpha,p)^{13}C$ reaction leaving ^{13}C in excited states. The width of the peaks is almost entirely due to the large angular acceptance of the proton detector. The isolation of the $^{10}B(\alpha,p_0)^{13}C$ proton peak and its extremely low back-

0168-583X/92/$05.00 © 1992 – Elsevier Science Publishers B.V. All rights reserved

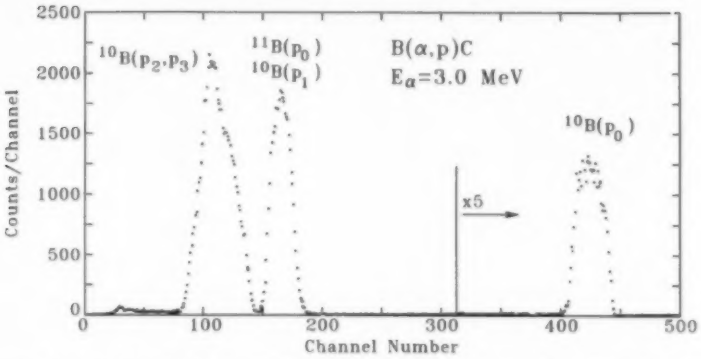

Fig. 1. Energy spectrum of protons from the $^{10}B(\alpha,p)^{13}C$ and $^{11}B(\alpha,p)^{14}C$ reactions using a 20 $\mu g/cm^2$ (84 nm) self-supporting natural boron target. The incident alpha energy was 3.0 MeV and the lab angle was 135°. Positions of protons leaving ^{14}C in the ground state and ^{13}C in the ground and several excited states are indicated.

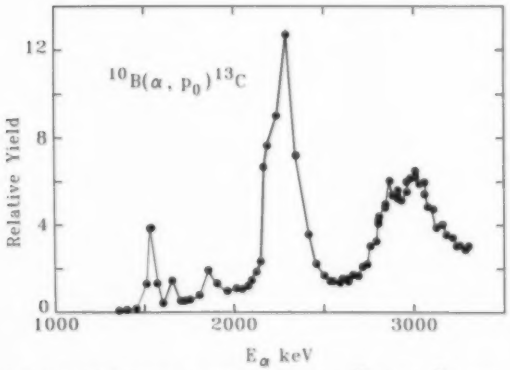

Fig. 2. Relative yield of protons from the $^{10}B(\alpha,p_0)^{13}C$ reaction at a lab angle of 135° as a function of incident alpha energy.

ground make it an attractive feature for boron analysis even though natural boron contains only 20% ^{10}B. For total boron determination we assume natural isotopic abundance in both unknown and calibration samples.

Figs. 2 and 3 show relative proton yield from the $^{10}B(\alpha,p_0)^{13}C$ and $^{11}B(\alpha,p_0)^{14}C$ reactions from 1.4 to 3.3 MeV incident energy. The target described above was used and data were taken in 25 or 50 keV steps. The energy loss of the beam in the target varied from 40 keV near 1.4 MeV to 20 keV near 3 MeV. The $^{11}B(\alpha,p_0)^{14}C$ yield includes the overlapping signal from the $^{10}B(\alpha,p_1)^{13}C$ peak which we believe to be small [5]. Another possible contributor to this peak is the $^{10}B(\alpha,d)^{12}C$ reaction [23]. These results are in reasonable agreement with previous nuclear physics experiments [23–28]. An advantage of the $^{10}B(\alpha,p_0)^{13}C$ reaction for boron analysis is the isolation and low background of the proton peak as mentioned above; however, the peak containing the $^{11}B(\alpha,p_0)^{14}C$ yield may also be used for thin films if the peak is completely resolved as in the case shown in fig. 1. This reaction has considerably higher yield, therefore greater sensitivity. Of course, both peaks are present in a given spectrum and both may be used.

The main features of the $^{10}B(\alpha,p_0)^{13}C$ excitation function are resonant behavior near 1500, 2300, and 3000 keV. Only the resonance near 1500 keV is narrow enough for depth profiling, however its width of about 25 keV results in rather poor surface depth resolution of about 100 nm [6]. Better depth resolution can be obtained using the 163 keV resonance in the $^{11}B(p,\alpha)^8Be$ or $^{11}B(p,\gamma)^{12}C$ reactions [2,7–9] or the $^{10}B(n,\alpha)^7Li$ reaction [12,13]. We limit ourselves in this paper to total boron determination in thin films.

We chose the region of relatively large and constant cross section near 3000 keV for boron analysis. The relative proton yield from both isotopes is approximately constant over the energy range 2950 to 3050 keV. This 100 keV range corresponds to a thickness of about 500 nm in either boron or silicon. The region of roughly constant cross section is actually much greater in the ^{11}B case as can be seen in fig. 3. Use of the larger peak near 2300 keV for the ^{10}B reaction or the peaks near 2600 keV or 3200 keV in the ^{11}B reaction would increase the sensitivity, but would complicate the analysis because of the rapidly changing cross section. A previous study used the B(α,p)C reactions to investigate boron in thick steel samples at an energy of 2.67 MeV, just above the resonance near 2600 keV in the ^{11}B reaction [11].

3. Results

In this section we will compare the determination of boron in thin films by ^4He backscattering and NRA

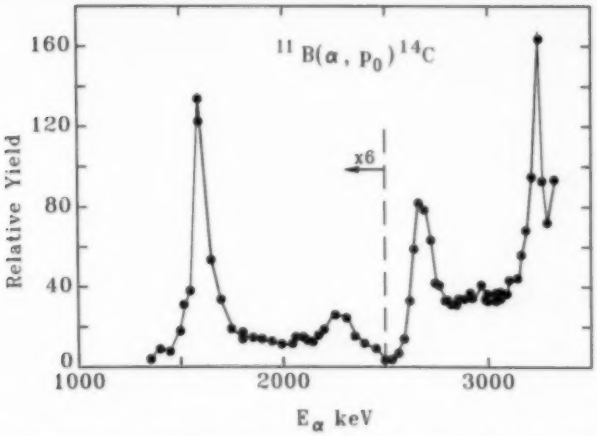

Fig. 3. Relative yield of protons from the combined $^{11}B(\alpha,p_0)^{14}C$ and $^{10}B(\alpha,p_1)^{13}C$ reactions at a lab angle of 135° as a function of incident energy.

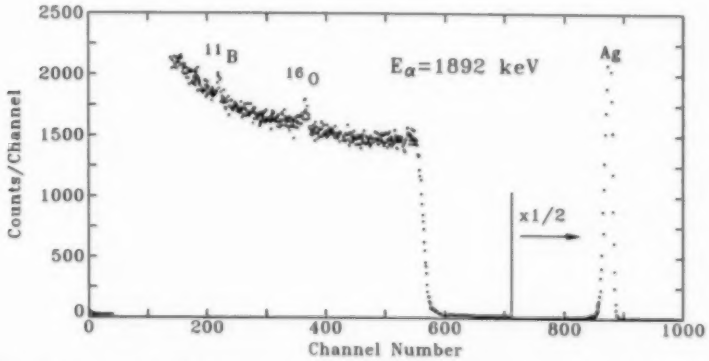

Fig. 4. Energy spectrum of backscattered (170.5° lab angle) 1892 keV $^4He^+$ ions from a two-layer thin film containing 15 nm of Ag on a Si backing with about 12 nm of boron on top.

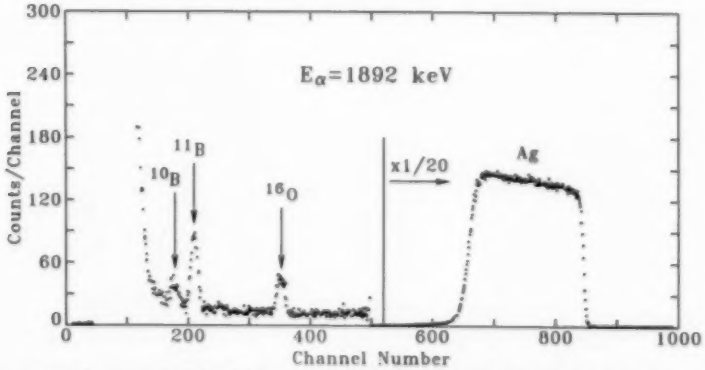

Fig. 5. Energy spectrum of backscattered (170.5° lab angle) 1892 keV $^4He^+$ ions from a 2 layer thin film containing 320 nm of Ag on a carbon backing with about 44 nm of boron on top.

using the $^{10}B(\alpha,p)^{13}C$ and $^{11}B(\alpha,p)^{14}C$ reactions at 3.0 MeV. Fig. 4 shows the backscattered spectrum of 1892 keV $^4He^+$ ions from a two-layer film consisting of a 15 nm Ag film on a Si backing with an overlayer of about 12 nm of boron. The boron peak is barely distinguishable on top of the Si signal and only a rough estimate of boron content is possible from these data. In samples with crystalline backings, the backing can be aligned for channeling to increase the sensitivity to boron [6].

Another backscattering technique we have used for boron is to use a carbon backing and a thick underlayer of Ag to suppress the carbon edge below the position of the boron peaks. Fig. 5 shows a backscattering spectrum of 1892 keV $^4He^+$ ions from a carbon backed film consisting of 320 nm of Ag with about 44 nm of boron on top. The boron peaks are visible, however the background is high and the boron content cannot be determined to better than about 10%. This technique is not generally applicable since it requires specially designed targets. As mentioned in the introduction, another problem with analyzing $^4He^+$ backscattering from boron has been the uncertainty in the cross section. We have recently reported measurments of the elastic scattering cross section of $^4He^+$ from both isotopes of boron at 170.5° lab angle from 1 to 3.3 MeV [1].

In order to use the $^{10}B(\alpha,p)^{13}C$ and/or the $^{11}B(\alpha,p)^{14}C$ reactions for determination of boron in samples like those mentioned above, it is necessary to calibrate using a thin film with a known boron content. We used, for this purpose, several self-supporting natural boron targets with nominal areal density of 10^{18} atoms/cm^2 (about 20 μg/cm^2). The areal density of these films was determined to about 5% as a result of our elastic scattering cross section measurements; the scattering from both isotopes was assumed to be Rutherford at 170.5° lab angle in the energy range 1 to 1.3 MeV [1].

Using these targets, and an incident $^4He^+$ energy of 3.0 MeV, we determined the number of protons detected per μC beam charge per atom/cm^2 of boron in the sample for our particular geometry. This calibration allowed us to determine total boron areal density in thin films containing heavy elements or backings to an accuracy between 7 and 10%. The areal density (Nt) of boron in an unknown thin film is given in units of 10^{15} atoms/cm^2 by the formula

$$Nt = K \times (\text{proton counts}/\mu\text{C beam charge}),$$

where K is a constant depending on geometry. In our case, K was determined to be 6.0 ± 0.5 for the ^{10}B reaction and 1.1 ± 0.1 for the ^{11}B reaction. The proton spectra from the silicon and carbon backed samples with Ag layers used in the elastic scattering experiments mentioned above are essentially identical in character to that shown in fig. 1.

Although we devised this technique for use with 10–100 nm thick boron films, it could be used to determine boron in thinner or thicker films of other elements containing boron as an impurity or implant. If we take as a minimum required signal 1 proton count per μC beam charge, the corresponding boron areal densities for our geometry are 6×10^{15} atoms/cm^2 for the ^{10}B reaction and 1.1×10^{15}atoms/cm^2 for the ^{11}B reaction. These areal densities represent a 1% and 0.2% boron content,respectively, in a 100 nm Si film, and is an indication of the relatively poor sensitivity of this technique in this energy range.

An advantage of the (α,p) reaction is that it has a negative Q value for many common contaminant and backing elements, e.g. carbon, oxygen, and silicon,

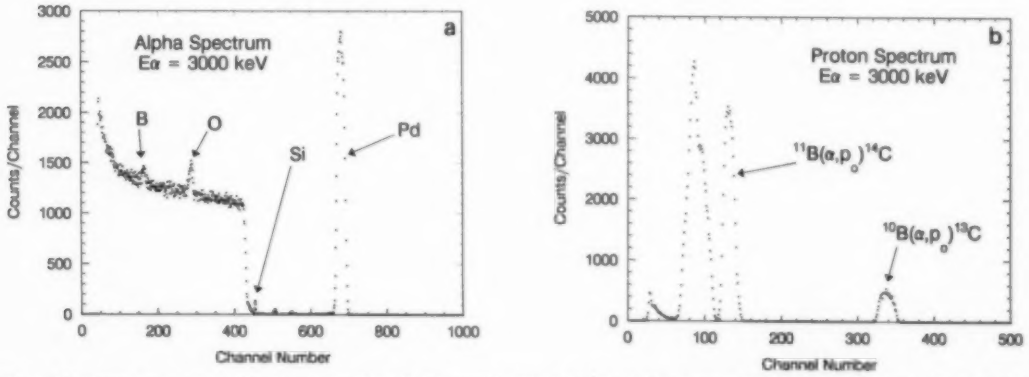

Fig. 6. (a) Energy spectrum of backscattered (170.5° lab angle) 3000 keV $^4He^+$ ions from a Pd(32 nm)/B(96 nm) thin film with a Si(4 nm) cap on a Si substrate. The collected charge was 50 μC. (b) Energy spectrum of protons (135° lab angle) taken simultaneously with the alpha spectrum of fig. 6a.

which therefore do not produce interfering signals. Another advantage of this reaction is that its implementation is easily adapted to a standard RBS experimental setup. It simply requires addition of a large area surface barrier detector which can be operated simultaneously with a ^{4}He backscattering measurement. In fact, many of the measurements of proton yield presented here were taken simultaneously with elastic scattering measurements at 170.5° lab angle [1]. An example of simultaneous ^{4}He backscattering and NRA data accumulation is given in fig. 6 which shows the alpha and proton spectra from 3000 keV $^4He^+$ bombardment of a Pd/B thin film.

In conclusion, we have described a simple and efficient method for determining the boron content of thin films using the B(α, p)C reaction on both isotopes of boron near 3.0 MeV incident energy. A typical application of this technique on a Pd/B or Ag/B multilayer on silicon results in simultaneous determination of the boron areal density from observation of emitted protons and determination of the Pd or Ag areal density from observation of backscattered alpha particles. Using a 100 nA beam of 3 MeV $^4He^+$, the boron areal density can be determined to about 10% and the Pd or Ag areal density can be determined to about 4% in less than 10 min. A boron film with known areal density is required for calibration.

Acknowledgements

The authors would like to thank J.M. Slaughter, P.A. Kearney and C.M. Falco for providing the Ag/B films. This work was partially supported by the Arizona Research Laboratory and the Optical Data Storage Center which is administered by the Optical Sciences Center, University of Arizona.

References

[1] L.C. McIntyre, Jr., J.A. Leavitt, M.D. Ashbaugh, Z. Lin and J.O. Stoner, Jr., Proc. 10th Int. Conf. on Ion Beam Analysis, Eindhoven, The Netherlands, 1–5 July, 1991, Nucl. Instr. and Meth. B64 (1992).

[2] M.J.M. Pruppers, F. Zijderhand, K.M.H. Maessen, J. Bezemer, F.H.P.M. Habraken and W.F. van der Weg, Nucl. Instr. and Meth. B15 (1986) 512.

[3] R. Lappalainen, A. Anttila and J. Räisänen, Nucl. Instr. and Meth. 212 (1983) 441.

[4] B. Borderie, M. Basutcu, J.N. Barrandon and J.L. Pinault, J. Radioanal. Chem. 56 (1980) 185.

[5] C. Olivier and M. Peisach, J. Radioanal. Chem. 11 (1972) 105; 12 (1972) 313.

[6] A. Armigliato, G.G. Bentini, G. Ruffini, G. Battaglin, G. Della Mea and A.V. Drigo, Nucl. Instr. and Meth. 149 (1978) 653.

[7] O. Henriksen, T. Laursen, E. Johnson, A. Johansen, L. Sarholt-Kristensen and J.L. Whitton, Nucl. Instr. and Meth. B15 (1986) 356.

[8] P.J. Scanlon, G. Farrell, M.C. Ridgway and R. Valizadeh, Nucl. Instr. and Meth. B16 (1986) 479.

[9] N. Moncoffre, N. Millard, H. Jaffrezic and J. Tousset, Nucl. Instr. and Meth. B45 (1990) 81.

[10] E. Ligeon and A. Bontemps, J. Radioanal. Chem. 12 (1972) 335.

[11] C. Olivier, J.W. McMillan and T.B. Pierce, J. Radioanal. Chem. 31 (1976) 515.

[12] J.F. Ziegler, G.W. Cole and J.E.E. Baglin, J. Appl. Phys. 43 (1972) 3809.

[13] M. Behar, M. Weiser, S. Kalbitzer, D. Fink and F.L. Grande, Nucl. Instr. and Meth. B34 (1988) 316.

[14] J.C. Overley, R.P. Ebright and H.W. Lefevre, IEEE Trans. Nucl. Sci. NS-26 (1979) 1624.

[15] L.C. Feldman and S.T. Picraux, in: Ion Beam Handbook for Materials Analysis, eds. J.W. Mayer and E. Rimini (Academic Press, New York, 1977) p. 112.

[16] G. Amsel, J.P. Nadai, E. D'Artemare, D. David, E. Girard and J. Moulin, Nucl. Instr. and Meth. 92 (1971) 481.

[17] G. Amsel and W.A. Lanford, Ann. Rev. Nucl. Part. Sci. 34 (1984) 435.

[18] J.R. Bird, in: Ion Beams for Materials Analysis, eds. J.R. Bird and J.S. Williams (Academic Press, San Diego, 1989) p. 149.

[19] P.A. Kearney, J.M. Slaughter and C.M. Falco, Opt. Eng. 30 (1991) 1076.

[20] J.A. Leavitt, Nucl. Instr. and Meth. B24/25 (1987) 717.

[21] L.C. McIntyre Jr., J.A. Leavitt, B. Dezfouly-Arjomandy and J. Oder, Nucl. Instr. and Meth. B35 (1988) 446.

[22] L.C. McIntyre Jr., J.A. Leavitt, M.D. Ashbaugh, B. Dezfouly-Arjomandy, Z. Lin, J. Oder, R.F.C. Farrow and S.S.P. Parkin, Nucl. Sci. and Tech. 1 (1990) 56 (China).

[23] R. A Dayras, Z.E. Switkowski and T.A. Tombrello, Nucl. Phys. A261 (1976) 365.

[24] E.S. Shire, J.R. Wormald, G. Lindsay-Jones, A. Lunden and A.G. Stanley, Philos. Mag. 44 (1953) 1197.

[25] E.S. Shire and R.D. Edge, Philos. Mag. 46 (1955) 640.

[26] S.J. Wilson, Phys. Rev. C11 (1975) 1071.

[27] L.L. Lee, Jr. and J.P. Schiffer, Phys. Rev. 115 (1959) 160.

[28] G.S. Mani, P.D. Forsyth and R.R. Perry, Nucl. Phys. 44 (1963) 625.

Nuclear Instruments and Methods in Physics Research B66 (1992) 226–229
North-Holland

Nuclear Instruments & Methods in Physics Research
Section B

Some studies on nuclear methods for boron determination

A.E. Pillay and M. Peisach [1]

Department of Chemistry, University of the Witwatersrand, P.O. Wits, 2050 South Africa

A summary of some studies of nuclear methods for the low-level determination of boron is presented. Since there is always need for an interference-free method, the study provides an impartial insight into the relative analytical capabilities of the methods of interest following intensive investigations in this area over prolonged periods. Of particular interest is the role played by interfering components such as carbon, nitrogen and oxygen which are invariably present in major concentrations in most sample matrices. A critical evaluation of the analytical potential of prompt, delayed and coincidence procedures is provided with emphasis on selective activation for boron in the presence of major interferences. Some future possibilities are proposed, and typical applications of the relevant methods for operation under routine conditions are discussed.

1. Introduction

The current demand for the determination of boron at all levels is widespread. The element occurs as an impurity in steels, as a major component in glass, as a thermalising agent in nuclear reaction materials, as a detecting system for neutrons, and as an important part of semiconductor devices. However, the main difficulty in the determination of boron is the serious problem of interference which arises mainly from the presence of carbon, nitrogen and oxygen in the sample matrix. These interferences are commonly present in major concentrations. Interference-free methods for such applications are, therefore, much sought after. Over the past few years a variety of nuclear methods (for this purpose) have been investigated at the University of the Witwatersrand and the National Accelerator Centre. This paper provides a comprehensive and critical view of the relative analytical potential of each method together with an overall evaluation of their individual merits and limitations for applications on a routine basis.

1.1. Gamma–beta coincidence spectrometry

This approach is particularly rapid and sensitive with proton irradiation and provides a unique method of monitoring boron at levels below 100 ppm [1]. It utilises the delayed mode in combination with weak decay cascades and is of especial significance as it works well in the presence of intense short-lived background from the matrix. A typical application is the detection of boron contamination in high purity aluminium. It was found that deconvolution of the 20 min decay from $^{11}B(p, n)^{11}C$ is almost impossible in the presence of oxygen which produces the 10 min ^{13}N half-life through the reaction $^{16}O(p, \alpha)^{13}N$. In addition, the 19s ^{10}C half-life from $^{10}B(p, n)^{10}C$ is strongly swamped by the intense 4s decay of ^{27}Si from the aluminium matrix produced by the reaction $^{27}Al(p, n)^{27}Si$. This impasse prompted the coincidence approach which uses the 717 keV γ-ray (98.3%) and beta energies in excess of 1 MeV from ^{10}C. Lower-energy betas from ^{10}C and ^{13}N can be excluded by the use of an appropriate absorber. Fig. 1 reproduces the pulse height spectrum recorded with the use of a NaI(Tl) detector for a 1 min irradiation. The figure shows that in cases where intense annihilation radiation occurs from activation of the matrix the sum peak (717 + 511) keV could alternatively be employed for analytical purposes.

1.2. Delayed gamma-ray spectrometry

The technique can be of great value in the absence of lithium impurities and is attractive because of its simplicity. It has been used [2] (with 10 MeV protons) for measuring boron impurities in steel where the lithium contamination was estimated to be negligible. Proton activation with high beam currents leads to the prolific production of the 478 keV γ-ray from $^{10}B(p, \alpha)^{7}Be$ ($Q = 11$ MeV). Of significance to analysts is that the 53 d half-life resulting from the decay of ^{7}Be offers the merit of extended off-line counting for the attainment of better detection limits. However, the method fails in the presence of lithium contamination which (in some cases) tends to occur concomitantly

[1] National Accelerator Centre, P.O. Box 72, Faure, 7131 South Africa.

0168-583X/92/$05.00 © 1992 – Elsevier Science Publishers B.V. All rights reserved

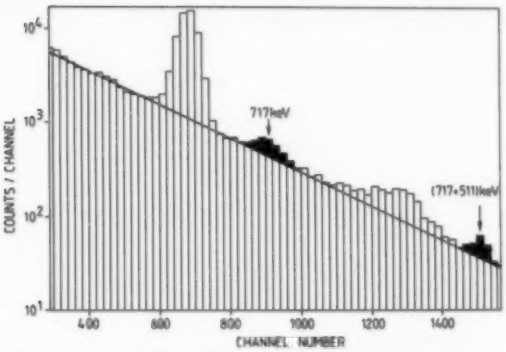

Fig. 1. Pulse height spectrum of gamma rays in coincidence with betas from ^{10}C emitted by a target of Al + 0.038% B irradiated by 8 MeV protons. The background drops off exponentially with energy as can be seen from the straight line across the logarithmic histogram. The shaded regions represent events due to the decay of the 717 keV state in ^{10}B and the sum peak at 717+511 keV due to true coincidences between a ^{10}B gamma and one annihilation photon. The unshaded peaks are due to 511 keV annihilation and 511+511 keV sum coincidences respectively. The arrows show spectrum calibration points at 717 and 1228 keV.

with boron. Under these conditions the interference from the reaction $^{6}Li(p, n)^{7}Be$ ($Q = -1.7$ MeV) presents an impasse which is impossible to resolve.

1.3. Prompt gamma-ray spectrometry

1.3.1. p, d and α activation

Protons, deuterons and alphas are the most popular projectiles used for charged particle activation. However, this particular area is beset with interferences and one way to approach the problem is indirectly by examining the level of interference rather than that of the element of interest, as a means of evaluating the strength of the interfering signal. Extensive studies [3–5] based on monitoring nuclear reactions from lithium, carbon, nitrogen and oxygen clearly demonstrate that interferences can be obviated by selective activation. Table 1 presents the possible interferences with the most likely boron reactions. The reactions marked with an asterisk are ones that can possibly be attained under interference-free conditions with a small accelerator (e.g. 5 MV Van de Graaff) if the activation proceeds below the energy threshold of the interference. Of these reactions of interest, the most eligible in the case of proton activation is Coulomb excitation of ^{10}B especially as the levels in this nucleus are comparatively low-lying (first excited state [6]: 718 keV). However, the proximity of the 718 keV line to the 511 keV annihilation radiation tends to produce undesirable background problems. With alphas, Coulomb excitation is indeed feasible but yields would evidently suffer if the activation proceeds below the energy threshold of $^{7}Li(\alpha, n)^{10}B$. Of the remaining reactions with alphas the one leading to ^{14}C is theoretically feasible but the high-lying levels in ^{14}C (first excited state [6]: 6.1 MeV) compromises the detection efficiency. $^{10}B(\alpha, n)^{13}N$ is safest although it has been shown [4] that in the presence of magnesium the first escape peak from the 2839 keV gamma-ray originating from $^{25}Mg(\alpha, n)^{28}Si$ may interfere. With deuterons, the reaction $^{10}B(d, n)^{11}C$ looks attractive theoretically but deuteron activation is usually not profitable mainly because of increased backgrounds resulting from neutron production. Overall, there are many such subtle factors (apart from the gross problem of interference) associated with nuclear phenomena in this area, which tends to restrict this approach and thus makes it unattractive for practical purposes.

1.3.2. ^{3}He activation

^{3}He is rarely used for activation mainly because of the complexity of the reactions with the matrix. However, this drawback can be turned to advantage when the exceptionally exoergic nature of ^{3}He beams with boron is considered. This particular factor led to a detailed study [7] of light elements, some of which were assessed as sources of potential interferences. Interference-free γ-rays having practicable yields and energies of 418, 718 and 1022 keV were observed with corresponding sensitivities of 9, 2 and 15 mg/(g m C), re-

Table 1
Possible interferences with boron during p, d and α activation

Reaction of interest	Q value [MeV]	Interfering reaction	Q value [MeV]
* $^{10}B(p, n)^{10}C$	−4.6	$^{12}C(p, t)^{10}C$	−23.5
$^{11}B(p, n)^{11}C$	−2.8	$^{14}N(p, \alpha)^{11}C$	−2.9
$^{10}B(p, \alpha)^{7}Be$	1.1	$^{7}Li(p, n)^{7}Be$	−1.6
$^{11}B(p, \alpha)^{8}Be$	8.6	–	–
* $^{10}B(p, p')^{10}B$	–	$^{13}C(p, \alpha)^{10}B$	−4.1
* $^{11}B(p, p')^{11}B$	–	$^{13}C(p, ^{3}He)^{11}B$	−31.2
$^{10}B(\alpha, n)^{13}N$	1.1	$^{12}C(\alpha, t)^{13}N$	−4.1
$^{11}B(\alpha, n)^{14}N$	0.2	$^{14}N(\alpha, \alpha')^{14}N$	–
$^{10}B(\alpha, p)^{13}C$	4.1	$^{13}C(\alpha, \alpha')^{13}C$	–
* $^{11}B(\alpha, p)^{14}C$	0.8	$^{13}C(\alpha, ^{3}He)^{14}C$	−12.4
* $^{10}B(\alpha, \alpha')^{10}B$	–	$^{7}Li(\alpha, n)^{10}B$	−2.8
$^{11}B(\alpha, \alpha')^{11}B$	–	$^{7}Li(\alpha, \gamma)^{11}B$	8.7
* $^{10}B(d, n)^{11}C$	6.5	$^{12}C(d, t)^{11}C$	−12.5
$^{11}B(d, n)^{12}C$	13.7	$^{14}N(d, \alpha)^{12}C$	13.6
$^{10}B(d, p)^{11}B$	9.2	$^{13}C(d, \alpha)^{11}B$	5.2
$^{11}B(d, p)^{12}B$	1.1	$^{13}C(d, t)^{12}B$	1.3
$^{10}B(d, \alpha)^{8}Be$	17.8	–	–
$^{11}B(d, \alpha)^{9}Be$	8.0	$^{7}Li(d, \gamma)^{9}Be$	16.6
$^{10}B(d, d')^{10}B$	–	$^{12}C(d, \alpha)^{10}B$	−1.3
$^{11}B(d, d')^{11}B$	–	$^{13}C(d, \alpha)^{11}B$	5.2

spectively. These lines originated collectively from the pick-up reaction $^{11}B(^3He, \alpha)^{10}B$ and Coulomb excitation of ^{10}B. A thorough evaluation of the analytical capabilities of this approach revealed that the peak-to-background ratios of the above lines were adequate to demonstrate that the method is potentially useful for the quantitative analysis of boron at all levels. Interference from the weak interaction $^7Li(^3He, \alpha)^{10}B$ was ignored.

1.4. Charged particle spectrometry

This approach is a variant of the ^3He/prompt γ technique above and represents a relatively unexplored territory. Here again, the technique exploits the highly exoergic nature of the reactions: $^{10}B(^3He, p)^{12}C$ (Q = 19.7 MeV), $^{10}B(^3He, \alpha)^9B$ (Q = 12.1 MeV), $^{11}B(^3He, p)^{13}C$ (Q = 13.1 MeV) and $^{11}B(^3He, \alpha)^{10}B$ (Q = 9.1 MeV). This factor formed the basis of a study [8] which led to the production of unique charged particle groups emitted from the relevant intermediate nuclear formations. The investigations, which included similar studies on C, N and O, revealed unambiguously that this technique is perhaps ideal for boron analysis at all levels. The uniqueness of the measured charged particle groups provides complete immunity to matrix effects and the advantage over the $^3He/\gamma$ method above is that backgrounds are very much reduced. Its applicability was examined by detecting boron contamination (trace and minor levels) in high purity metallurgical matrices and the results obtained were highly satisfactory, which makes the technique suitable for general applications with a small accelerator.

1.5. Neutron activation

The high $\sigma(n, \alpha)$ for ^{10}B ($\sim$ 4000 b) would have rendered this technique pre-eminently suitable for the routine analysis of boron. However, the reaction $^{10}B(n, \alpha)^7Li$ does not lead to a radioactive product and, therefore, activation with neutrons combined with delayed γ-spectrometry fails. Not all is lost, however, because the prompt γ-rays from ^7Li can be monitored, particularly the 478 keV line corresponding to the first excited state of this nucleus. The problem encountered though is the damage inflicted on the γ-ray detector by the neutron flux. Such damage can be quite considerable if the flux is high and this particularly adverse factor, therefore, does not make the method worthwhile. As a compromise, isotope sources with low fluxes could be employed for such purposes. However, in the study [9] where a 1 μg ^{252}Cf source was used to irradiate ore samples containing between 100 and 200 ppm of boron it was found that the flux from the source was inadequate to provide useful information, which renders this approach unsuitable for practical purposes.

Another approach [10], which is somewhat crude but was adopted as a feasibility study, was based on neutron absorption which essentially represented a variant of the Beer–Lambert law. A suitable BF_3 neutron detector was employed to monitor to original flux from a 1 μg ^{252}Cf source and subsequently the flux depression (due mainly to boron) when a sample was interposed. The problem encountered here was wide neutron scattering into the detector which led to serious statistical fluctuations in the recorded data. The technique is open to refinement though, if the scattering can be suppressed by application of suitable collimation. However, collimation itself tends to be problematical because of the high penetration of neutrons.

1.6. Future possibilities – β^+ spectrometry [1] / Cherenkov counting [11]

The reaction $^{10}B(^3He, n)^{12}N$ (Q = 1.6 MeV) possesses great potential for this particular approach. One of two modes can be adopted. Since ^{12}N emits 16.4 MeV betas (the highest recorded β^+ energy on the chart of radionuclides) they can be uniquely monitored by the use of an appropriate absorber (possibly Al) to exclude low-energy betas and Compton electrons, and a scintillator thick enough to stop the transmitted ^{12}N betas. For the analysis of boron the β^+ counting technique, therefore, offers the prospect of being a rapid and ultrasensitive method that is immune to matrix and background effects.

The second approach entails a variation of the above by monitoring the Cherenkov radiation, produced by ^{12}N betas in a suitable absorbing medium, with a simple photomultiplier tube. Here again Compton electrons and low-energy betas can be excluded as described above. This latter technique, however, offers the distinct advantage of a range of fluorescent absorbers that command good yields and short time constants.

2. Conclusion

Of the different approaches described here for the unique determination of boron in the presence of recalcitrant interferences, perhaps the best suited for most practical purposes is the ^3He/charged particle method. If offers the merit of a completely interference-free procedure and enjoys highly reduced backgrounds. The gamma–beta coincidence method, on the other hand, cannot be ignored because it is rapid as equally as it is sensitive. An interesting extension to this area of interest would be consideration of the proposed β^+ spectrometry and Cherenkov counting.

References

[1] U. Von Wimmersperg, J.P.F. Sellschop, A.E. Pillay and H.J. Annegarn, Nucl. Instr. and Meth. B28 (1987) 299.
[2] A.E. Pillay, unpublished results, 1986, Schonland Research Centre, University of the Witwatersrand, South Africa.
[3] A.E. Pillay and D.K. Bewley, Int. J. Appl. Radiat. Isot. 34 (1983) 1571.
[4] I.S. Giles and M. Peisach J. Radioanal. Chem. 50 (1979) 307.
[5] D. Gihwala and M. Peisach, J. Radioanal. Chem. 70 (1982) 287.
[6] F. Ajzenberg-Selove and T. Lauritsen, Nucl. Phys. 11 (1959) 1.
[7] A.E. Pillay and M. Peisach, to appear in the Proc. of the 1991 Int. Conf. on Activation Analysis, Beijing, China, J. Radioanal. Nucl. Chem. (1992).
[8] A.E. Pillay and M. Peisach, unpublished results, 1991, National Accelerator Centre, Faure, South Africa.
[9] A.E. Pillay, M.Sc. Thesis, University of the Witwatersrand, South Africa (1986).
[10] A.E. Pillay and J.I.W. Watterson, unpublished results, 1986, Schonland Research Centre, University of the Witwatersrand, South Africa.
[11] M. Peisach, private communication, 1990, National Accelerator Centre, Faure, South Africa.

Nuclear Instruments and Methods in Physics Research B66 (1992) 230–236
North-Holland

Nuclear Instruments & Methods in Physics Research
Section B

The structure and composition of plasma nitrided coatings on titanium

H.J. Brading, P.H. Morton and T. Bell
School of Metallurgy and Materials, The University of Birmingham, Birmingham B15 2TT, UK

L.G. Earwaker
School of Physics and Space Research, The University of Birmingham, Birmingham B15 2TT, UK

Titanium nitride layers on titanium metal have been produced by glow discharge plasma nitriding in nitrogen gas and the structure and composition of the layers has been investigated as a function of gas pressure and substrate temperature. Plasma nitriding is used as a surface treatment to improve the wear resistance of titanium alloys. The development of precise analytical techniques plays an important role in gaining a clearer understanding of the mechanism and kinetics of the coating formation. Light element analysis has been carried out using RBS and NRA and nitrogen concentration depth profiles obtained to a depth of 4–5 μm. The extent of oxygen contamination was measured using NRA and electronprobe microanalysis (EPMA). X-ray diffraction (XRD) was used to investigate the degree of preferred orientation in the coatings and also provide information on the amount of various nitride phases (TiN, Ti_2N) present in the coating.

1. Introduction

Titanium alloys have the inherent advantages of light weight and high strength. However since their tribological behaviour is characterised by a high coefficient of friction and poor wear resistance, their usefulness in many engineering applications is impaired. Recently a variety of surface engineering techniques have brought about improvements in these parameters [1,2] by the production of a hard surface coating of titanium nitride. Such protective coatings are being used increasingly on many industrial components – for example cutting tools and aeroengine turbine blades.

The glow discharge or plasma nitriding process [3] makes use of an abnormal glow discharge [4], which is associated with high current and charge densities. The components to be nitrided are electrically isolated and placed or suspended in a vacuum furnace which is evacuated and back filled with the treatment gas. A dc voltage is then applied between the components (cathode) and the furnace walls (anode) and the potential difference ionises the treatment gas producing a glow discharge. Positive ions in the treatment gas are accelerated towards the negatively connected components and hit the surface with high kinetic energy giving rise to sputtering of the surface, and heating of the components. In the plasma nitriding of titanium [5,6], nitrogen ions and/or accelerated neutral nitrogen atoms impinge on the surface and react to form a nitrogen rich film which results in both the formation of a compound nitride layer on the surface (δ-TiN and ε-Ti_2N phases) and the diffusion of nitrogen into the substrate. This has the effect of providing the titanium with a hard surface coating which adheres well to the substrate.

In order to produce titanium nitride coatings tailored to specific engineering tasks, it is necessary to characterise the coatings in terms of structure (thickness) and composition, as this allows for the optimization of the process parameters on which these depend. In this paper a number of surface analysis techniques have been applied to the characterisation of titanium nitride coatings which have been plasma nitrided with different substrate temperatures and plasma pressures. Nitrogen concentration profiles were measured to depths of 4 to 5 μm, the oxygen concentration in the coatings was investigated and the nitride phases present were identified.

2. Experimental procedures

A number of analysis techniques were used on the coatings in order to characterise different aspects of their structure.

2.1. Nitrogen concentration profiles

RBS and NRA experiments were carried out using the 3 MV Dynamitron accelerator at the School of Physics and Space Research in the University of Birmingham. Alpha particle backscattering was used to ob-

0168-583X/92/$05.00 © 1992 – Elsevier Science Publishers B.V. All rights reserved

tain high resolution (~ 0.01 μm) depth profiles of nitrogen in the first micron of the coating and the $^{14}N(d, p)^{15}N$ nuclear reaction was used to investigate nitrogen to a depth of 4 to 5 μm, which included the nitrogen diffusion zone. RBS measurements were carried out using 2.0 MeV normally incident α-particles together with a 100 μm depletion-depth silicon surface barrier detector (collimated to 2.5×10^{-3} sr) placed at 150° to the incident beam direction. Data were accumulated for a total incident charge of 4 μC. The NRA measurements [7] involved the use of 1.1 MeV normally incident deuterons together with a similar detection system placed at 150° to the incident beam direction (data were accumulated for a total incident charge of 150 μC). Scattered deuterons were eliminated from the detector by the use of a 12 μm aluminium absorber foil. The NRA experimental conditions were chosen so as to allow detection of protons from the $^{16}O(d, p_0)^{17}O$ reaction as well as from the nitrogen (d, p) and (d, α) reactions. The experimental data were analysed using computer codes developed at the School of Physics and Space Research [8] and cross sections taken from the compilation of Jarjis [9] and the following references contained therein [10–12].

2.2. Oxygen concentration measurements

Electron probe microanalysis measurements were carried out on a JEOL-JXA-840A (MODEL AN 10000 ZAF/4) electron probe microanalyser linked to a computer (Link Systems series 2 model 500 System running SPECTA ZAF-4/FLS Software). The electron microprobe analyser, which was run in wavelength dispersive mode (WDX) with an LDE_1 diffracting crystal, was used to measure the oxygen concentration in the first micron of the coatings. Measurements were made at several positions on each coating where the layer differed in colour. Counts were measured for the central channel of the oxygen Kα X-ray peak for 100 s and for 50 s at positions either side to account for background continuum radiation. These were compared to similar measurements made on a standard SiO_2 sample. The beam size was about 1 μm in diameter and had a 1 μm penetration depth [13]. A probe voltage of 10 kV and a current of 1×10^{-7} A were used. The $^{16}O(d, p_0)^{17}O$ reaction was also used to obtain an upper limit of the oxygen concentration (averaged over the first 4 to 5 μm of the coating) by comparing the oxygen p_0 peak height with the nitrogen $p_{1,2}$ peak height and adjusting for the difference in reaction cross section for these peaks.

2.3. X-ray diffraction measurements

XRD analysis, which was carried out on a Phillips PW 1050 X-ray spectrometer, linked to a BBC Master computer, using unmonochromated Co Kα radiation, was used to obtain information about the nitride phases present in the coatings. The specimens were scanned

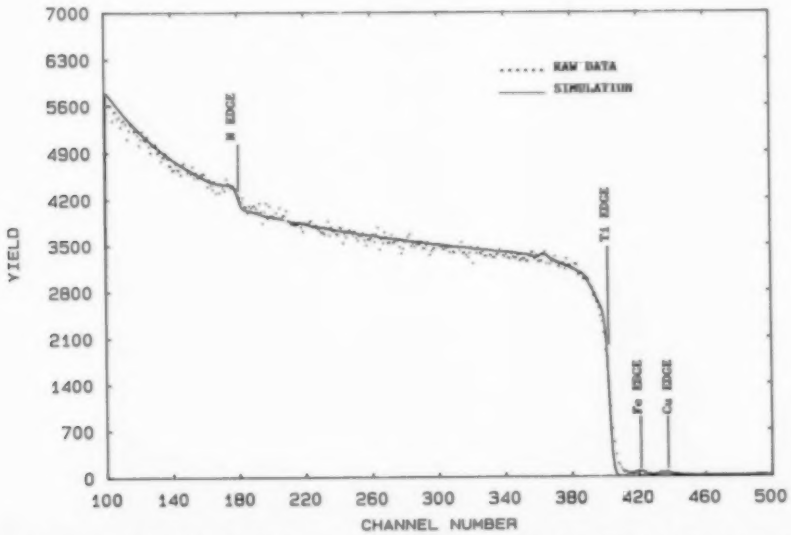

Fig. 1. RBS spectrum from sample 1 and the simulation used to obtain a nitrogen depth profile of the first micron (see fig. 3). Two small surface peaks corresponding to iron and copper can also be seen. (The energy width of the channels is 3.60 keV.)

for 2θ angles between 30° and 100° and the resulting X-ray diffraction peaks were identified using the JCPDS powder index files.

2.4. Analysis of RBS and (d, p) spectra

Fig. 1 shows the α-particle RBS spectrum obtained from sample 1 together with a simulation generated from an assumed nitrogen profile in the titanium. The process of producing a simulation is iterative. An initial nitrogen depth profile, in the form of titanium and nitrogen number densities changing with depth, is used to simulate the RBS curve; this is compared with the raw data, and the simulation is then changed by altering the nitrogen depth profile until a good match between simulation and raw data is achieved.

The emitted particle energy spectrum resulting from deuteron bombardment of sample 4 is shown in fig. 2. The choice of results for analysis by simulation was limited to the nitrogen $p_{1,2}$ peak as this was free from interference due to other peaks and cross section data for the reaction was available at this angle. The cross section used was that for the summed p_1 and p_2 groups.

The depth scale for this type of analysis depends on how well the absolute number densities of the elements within the coating are known. The number densities of the compounds TiN and Ti_2N and of the α-titanium substrate were known [14], and for compositions between these ratios of Ti : N it was assumed that the Ti and N number densities changed linearly. It is, however, frequently found that thin films have densities which differ significantly from that of the bulk compound [15]. The effect of this would be to increase the thickness of layers with a lower number density.

3. Sample investigated

All of the coatings investigated were produced by glow discharge plasma nitriding of "commercially pure"

Table 1
Processing parameters for the eight samples investigated. At a pressure of 1 mbar the maximum temperature achievable was 710°C

	Substrate temperature [°C]	Gas Pressure [mbar]	Applied voltage [V]	Treatment time [h]
Sample 1	700	5	425	10
Sample 2	775	5	500	10
Sample 3	850	5	520	10
Sample 4	700	3	520	10
Sample 5	775	3	665	10
Sample 6	850	3	680	10
Sample 7	700	1	920	10
Sample 8	710	1	950	42

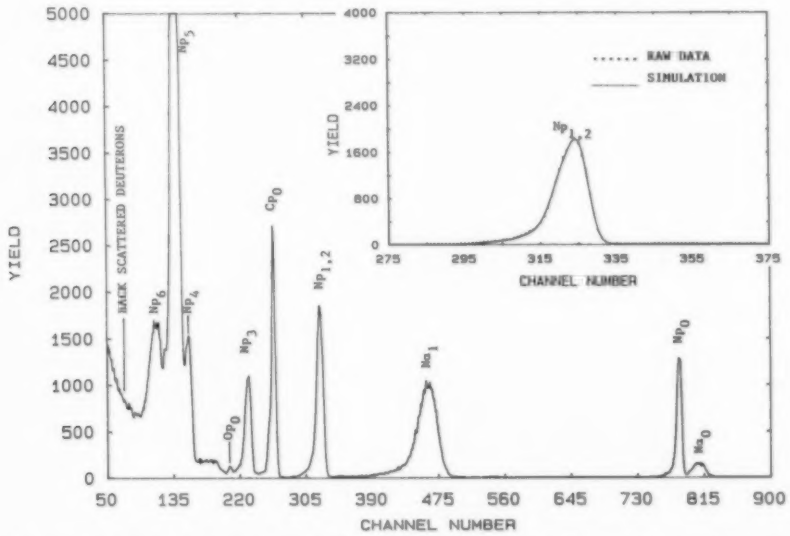

Fig. 2. NRA spectrum of sample 4 showing peaks from $^{16}O(d, p)^{17}O$, $^{14}N(d, p)^{15}N$, $^{12}C(d, p)^{13}C$ and $^{14}N(d, \alpha)^{12}C$ reactions. The N $p_{1,2}$ peak has been expanded to show the simulation of the nitrogen depth profile. A small O p_0 peak is also visible and gives an upper limit to oxygen contamination. (The energy width of the channels is 10.61 keV.)

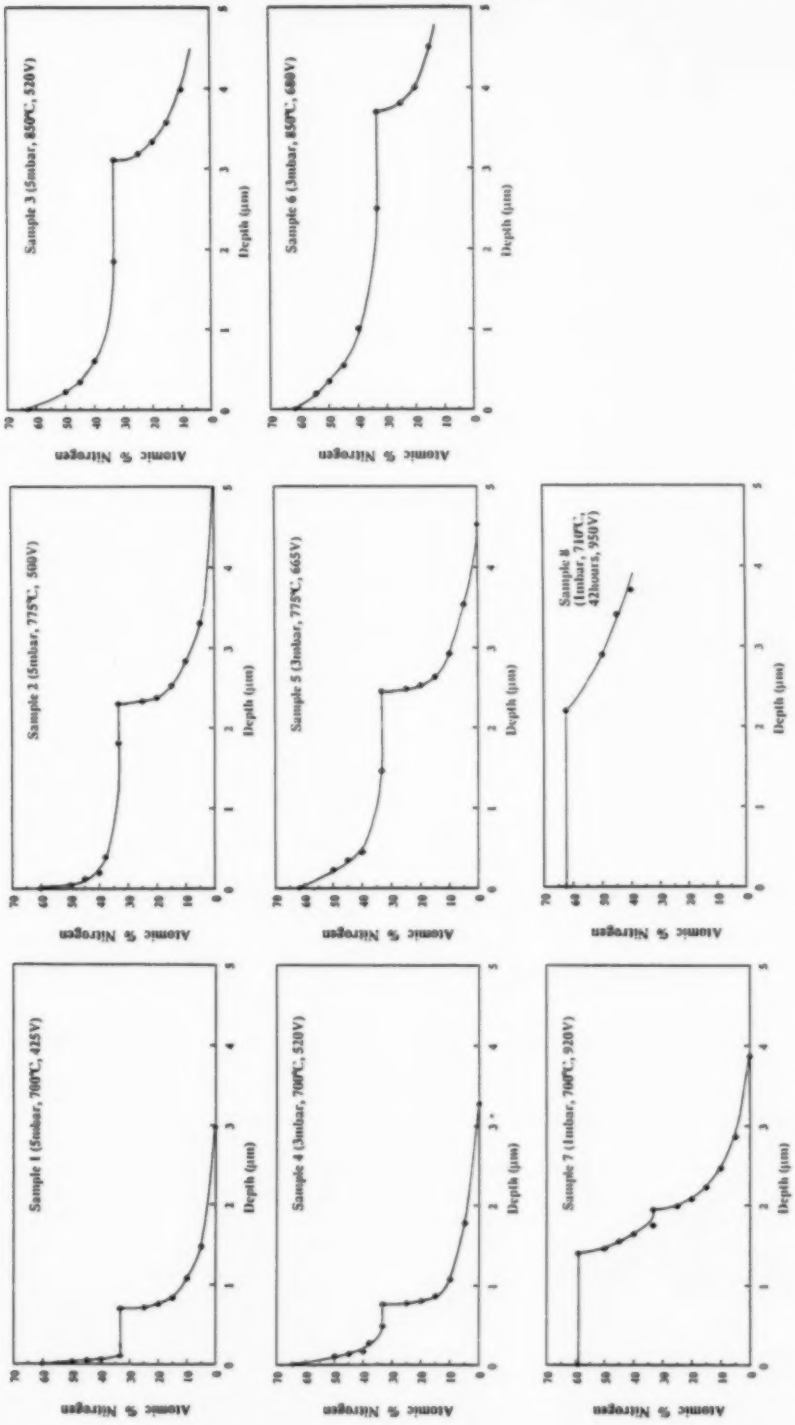
Sample 3 (5mbar, 850°C, 520V)
Sample 6 (3mbar, 850°C, 680V)
Sample 2 (5mbar, 775°C, 500V)
Sample 5 (3mbar, 775°C, 665V)
Sample 8 (1mbar, 710°C, 42hours, 950V)
Sample 1 (5mbar, 700°C, 425V)
Sample 4 (3mbar, 700°C, 520V)
Sample 7 (1mbar, 700°C, 920V)
Atomic % Nitrogen
Depth (μm)

Fig. 3. Nitrogen depth profiles for samples 1 to 8. These are a combination of the RBS profiles (first micrometer) and the NRA profiles.

titanium in a nitrogen atmosphere, the nitriding being carried out using a 40 kW (GZM40) Klöckner Ionon unit, designed specifically for the treatment of titanium components. The specimen support and current lead were made of titanium to reduce contamination of the atmosphere and specimen surface by sputtering from these components. The specimens were first heated to the treatment temperature in an inert argon atmosphere, all the heat being supplied by the glow discharge, and once the treatment temperature was achieved the argon was replaced by nitrogen at the treatment pressure. The plasma unit used did not allow direct control of the voltage and current of the glow discharge, V and I varying with the temperature and pressure settings. The samples produced and the treatment conditions are listed in table 1.

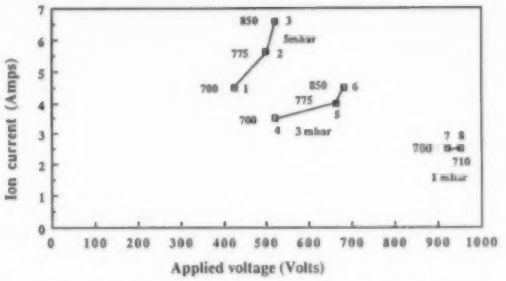

Fig. 4. Voltage and current characteristics of the plasma unit for the substrate temperature and pressure settings used for nitriding.

4. Results and discussion

4.1. Nitrogen depth profiles

The RBS and (d, p) spectra were measured for all the samples and analysed using the above method. The resulting RBS and (d, p) nitrogen depth profiles were then combined for each sample to give a nitrogen depth profile 4 to 5 μm deep from the (d, p) data, with a good near surface resolution (first micrometer) provided by the RBS data. The composite depth profiles obtained for the coatings are shown in fig. 3. All the profiles show the same general shape, an initial steep region where the nitrogen concentration is dropping rapidly, suggesting a thin TiN layer, a flattened region containing about 33 at.% nitrogen corresponding to the Ti_2N phase, followed by an exponential fall off in nitrogen corresponding to the region of nitrogen diffusion into α-titanium.

The solubility quoted for nitrogen in the δ-TiN structure is in the range 55 to 30 at.% [16]. The ε-Ti_2N phase exists only over a very small range of solubilities about 33 at.% of nitrogen. Nitrogen is soluble in α-titanium up to 22 at.%.

Several trends can be seen in these profiles. The width of the TiN layer is increased by raising the temperature and by lowering the pressure. Surface nitrogen concentrations of 59 to 63 at.% were observed on all of these samples, well above the previously assumed value corresponding to the stoichiometric nitrogen concentration for TiN (50 at.%) and also above the range of solubility quoted for nitrogen in TiN. On samples 7 and 8, thick layers ($1\frac{1}{2}$ to 2 μm) of over stoichiometric nitride with a constant titanium : nitrogen ratio were seen.

The width of the Ti_2N layer and the extent of nitrogen diffusion into the substrate both increase with the treatment temperature, but do not appear to be significantly effected by treatment pressure. The effect of temperature is to increase the rate of nitrogen diffusion through the coating, which increases the thickness of all the layers in the coating.

The increase in the TiN layer thickness due to decrease in pressure and, in particular, the amount of over stoiciometric nitride, is probably dependent on the availability and energy of nitrogen ions arriving at the specimen surface. Ions and accelerated neutrals at the surface cause physical sputtering, which increases with decreasing pressure and increasing ion current (current increases with temperature). They also hit and penetrate the top most atomic layers and have an energy that depends on the applied voltage.

Fig. 4 shows the current and voltage conditions that were observed for the temperatures and pressures used in the treatments. From this it can be seen that, current increases with increasing temperature and pressure, and that voltage increases with increasing temperature and decreasing pressure. Examination of the data in fig. 3 in the light of this information indicates that it is the higher applied voltage, required to operate at lower pressures that increases the width of the TiN layers; extra nitrogen appears to be forced into the titanium lattice by the bombardment of higher kinetic energy nitrogen ions. In fig. 3 an increase in voltage (samples 1 and 4, and again samples 2 and 5) gives rise to increased TiN layer thickness. This effect is most dramatic for samples 7 and 8 where the applied voltage is over 900 V and where a uniform layer over 1 μm thick is produced. The overstoichiometric TiN layer on sample 7 contains 59 at.% nitrogen whereas on sample 8 it is 63 at.%. This increase in the atomic percentage of nitrogen may be due to the increase in the applied voltage measured for sample 8 or alternatively to the longer treatment time of 42 h.

The RBS spectra show two small peaks due to surface contamination by iron and copper. This was temperature dependent and was therefore probably picked up during processing from sputtering of the

structure of the vacuum furnace, which contains both these elements.

4.2. Oxygen contamination measurements

Oxygen concentrations measured with the electron microprobe varied between 0.14 and 1.45 wt.%, but this variation appeared to be random, having no obvious correlation with processing temperature or pressure. An average was made of the measured oxygen concentrations (0.6 ± 0.4 wt.%) and this was converted to an atomic percent by assuming the ratio of titanium to nitrogen in the first micrometer of the coatings to be 3:2. The average oxygen concentration was $= 1.2 \pm 0.8$ at.% and the highest was 3.1 at.%.

The heights of the $^{16}O(d, p_0)$ peaks seen on the NRA spectra also indicated an upper limit of 2 to 3 at.% for the oxygen concentration averaged over the the first 4 to 5 μm of the coating.

There are several sources of this oxygen. The alloy used (commercially pure titanium – IMI 125)) contains 0.4 at.% oxygen. Also, the metal forms a surface oxide layer at room temperature. Some of this will be physically removed by sputtering in the plasma during processing. However some will also diffuse into the surface at the treatment temperature used. After processing, TiN is also known to form a TiO_2 oxide on its surface when exposed to the atmosphere at room temperature which is estimated to extend five to ten atomic layers into the surface [17].

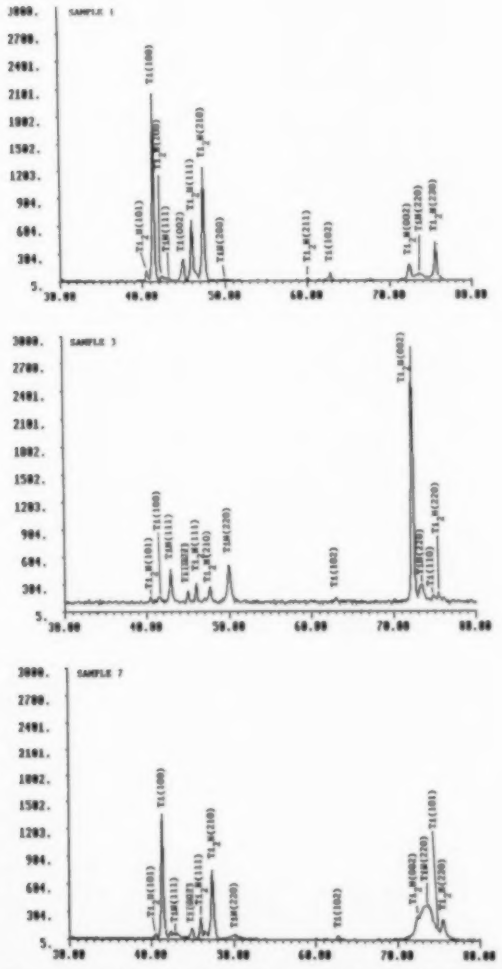

Fig. 5. X-ray diffraction traces for samples 1, 3 and 7. Sample 1 shows peaks from TiN, Ti_2N and α-Ti phases, sample 3 shows significant growth of the Ti_2N (002) peak due to the preferred crystallographic orientation in the Ti_2N layer, and sample 7 shows broadening of TiN peaks due to the presence of an over stoichiometric nitrogen concentration in this layer.

4.3. Phase identification using XRD

The XRD analysis confirmed the presence of the δ-TiN, ε-Ti_2N and α-titanium phases in the coating (fig. 5). The diffraction patterns show an enormous increase in the height of the Ti_2N (002) peak compared with the other Ti_2N peaks with increased treatment temperature [fig. 5 (sample 3)] which indicates that there is a preferred crystalographic orientation for the Ti_2N layer. In this case, the 002 planes of the Ti_2N lining up with the surface [5].

Fig. 5 (sample 7) shows the effect of a thick layer of over stoichiometric TiN on the diffraction patterns. The TiN peaks are broad in comparison with those for sample 1 (fig. 5). This is most likely to be caused by the extra nitrogen atoms being forced into the Ti lattice (which has a NaCl structure). These extra nitrogen atoms may fill tetrahedral sites [18] rather than the octahedral sites usually filled in TiN, or they may occupy vacant sites on the titanium lattice.

5. Conclusions

The $^{14}N(d, p)^{15}N$ reaction and RBS α-scattering measurements have been used to measure nitrogen depth profiles to a depth of 4 to 5 μm with a good resolution over the first micron. These profiles showed the effect of different plasma nitriding treatment parameters. Raising the substrate temperature increases the coating thickness and also increases the thickness of all the layers which make up the coating. The composition of the outermost surface of the outer TiN layer was found in all cases to be over stoichiometric, namely 59 to 63 at.% nitrogen. Lowering the treatment pressure has the effect of increasing the thickness of

the TiN layer, and at the lowest pressure investigated (1 mbar) gave rise to layers of over stoichiometric nitride (over 1 μm in thickness) with constant Ti:N ratios.

The beam parameters and detector geometries used allowed an estimate of the oxygen concentration in the coatings to be obtained in the presence of a large quantity of nitrogen. This was found to be in agreement with oxygen contamination measurements made with the electron microprobe. The level of oxygen contamination was found to be low, less than 3 at.%.

The presence of the TiN, Ti_2N and α titanium phases that make up the coating was confirmed by X-ray diffraction measurements. At the higher substrate temperatures, 775 and 850°C, preferred orientation of the Ti_2N phase occurred with the (002) planes aligning themselves parallel to the coating surface. The TiN peaks were found to broaden significantly when a large proportion of over stoichiometric TiN was present in the coating.

The above surface analysis techniques allow titanium nitride coatings produced by plasma nitriding a titanium substrate to be clearly characterised in terms of nitrogen depth profiles, titanium nitride compounds and the level of oxygen contamination and have revealed a compositional effect at high voltages (low pressures) not previously reported.

References

[1] M. Thoma, Proc. Conf. on Designing with Titanium (Institute of Metals, Bristol, 1986).
[2] T. Bell, Z.L. Zhang, J. Lanagan and A.M. Staines, Surface Treatments for Corrosion and Wear Resistance, eds. K.N. Strafford, P.K. Datta and C.G. Coogan, Chap. 12, p. 165.
[3] B. Edenhofer, Heat Treatment of Metals 1 (1974) 23.
[4] A. Von Engle, Ionised Gases, 2nd ed. (Oxford University Press, London, 1965) p. 217.
[5] K.T. Rie and Th. Lampe, Proc. Int. Conf. on Surface Modification of Metals by Ion Beams, Heidelberg, September 1987.
[6] T. Bell, H.W. Bergmann, J. Lanagan, P.H. Morton and A.M. Staines, Surf. Eng. 2 (2) (1986) 133.
[7] J.C. Simpson and L.G. Earwaker, Surf. and Coatings Technol. 27 (1986) 41.
[8] J.C.B. Simpson and L.G. Earwaker, Nucl. Instr. and Meth. B15 (1986) 502.
[9] R.A. Jarjis, Nuclear Cross Section Data for Surface Analysis, vols. 1–3, University of Manchester, Department of Physics Internal Report (1979).
[10] G. Debras and G. Deconninck, J. Radioanal. Chem. 38 (1977) 198.
[11] G. Amsel and D. David, Phys. Rev. 4 (1969) 383.
[12] V. Gomes Porto, N. Veta, R.A. Douglas, O. Sala, D. Wilmore, B.A. Robson and P.E. Hodgson, Nucl. Phys. A136 (1969) 385.
[13] M.H. Lorreto, Electron Beam Analysis of Materials (Chapman and Hall, London, 1984).
[14] Handbook of Chemistry and Physics (CRC Press, Boca Raton, 1986).
[15] See, for example, Electrochem. Soc. Ext. Abstr. 3 (1966) and papers therein.
[16] H.A. Wriedt and J.L. Murray, Phase Diagrams of Binary Titanium Alloys, ed. J.L. Murray (ASM Metals Park, OH, 1987).
[17] M. Wittmer, J. Noser and H. Melchior, J. Appl. Phys. 52 (11) (1981) 6659.
[18] R.R. Manory and G. Kimmel, Thin Solid Films 150 (1987) 277.

Nuclear Instruments and Methods in Physics Research B66 (1992) 237–241
North-Holland

Nuclear Instruments & Methods in Physics Research
Section B

Nitrogen profiling in nitride films and nitrogen-implanted samples using the $^{14}N(\alpha, \alpha)$ and $^{14}N(\alpha, p)$ reactions at 6 MeV incident energy

H. Artigalas, A. Chevarier, N. Chevarier, M. El Bouanani, E. Gerlic, N. Moncoffre, B. Roux, M. Stern and J. Tousset

Institut de Physique Nucléaire de Lyon, IN2P3-CNRS et Université Claude Bernard, 43, Bd du 11 Novembre 1918, F-69622 Villeurbanne Cedex, France

We investigate the nitrogen profiling potentiality using incident alpha particles from 5 to 7 MeV. In this energy range the alpha scattering cross sections on light elements are substantially larger than the Rutherford cross sections and therefore lead to competitive sensitivity. Moreover, another advantage is the high mass resolution which allows to profile simultaneously carbon, nitrogen and oxygen.

The analysis of TiN, NbTiN films and nitrogen implanted steel are presented. The inclusion, in the simulation program, of the $^{14}N(\alpha, \alpha)$ and $^{14}N(\alpha, p)$ cross sections allows to get a complete reproduction of the spectra and authorizes to determine accurately the nitrogen profile. Such a dual nitrogen analysis improves profile determination in case of thick analyzed layers. The sensitivity limits connected to the alpha scattered yield on steel substrate are 10^{16} and 5×10^{16} N atoms/cm^2 for the $^{14}N(\alpha, \alpha)$ and $^{14}N(\alpha, p)$ reactions, respectively.

1. Introduction

In the last few years there has been a great interest in the study of metal nitride films. This is due to the development of a reactive sputtering technique which authorizes the manufacturing of such compound films and leads to a variety of applications of these materials in several areas. Let us mention two typical examples: titanium nitride films [1] which are well known as wear-resistant surface coatings and as diffusion barriers, and niobium–titanium nitride films [2] which are studied for their superconducting properties. Besides nitrogen implantation [3] in metal alloys is a widely developped research area. It has already been established that the introduction of nitrogen in the near-surface region of metal alloys can improve their tribological characteristics. Since properties of nitride layers and nitrogen implanted alloys depend strongly on their composition, quantitative elementary analyses become very important.

Analytical procedures usually involve Auger electron spectroscopy (AES), X-ray photoelectron spectroscopy (XPS) and secondary ion mass spectrometry (SIMS). Some of these techniques provide informations on the chemical state of the elements, but the profiling of composition versus depth is accomplished by sputter erosion of the surface which may lead to confusing artifacts. Therefore energetic ion backscattering analysis which circumvents the sputtering problem and leads to quantitative mass concentration profiles, is an alternative probe for such materials.

In this work, the choice for energetic alpha backscattering analysis of nitrogen is first discussed. Then the measurements of $^{14}N(\alpha, \alpha)$ and $^{14}N(\alpha, p)$ excitation functions in the 5.2 to 7.5 MeV energy range are presented. Finally analyses of TiN, NbTiN films and nitrogen-implanted steel are discussed in order to underline the advantages and limitations of such analyses.

2. Nitrogen alpha backscattering analysis

In most cases RBS is not an adequate tool in profiling light elements in the presence of heavier elements. This arises because of the Z^2 dependence in the Rutherford cross section and the fact that the light element distributions are generally superimposed upon the matrix distribution. Nuclear reaction spectroscopy (NRS) is usually indicated when such difficulties in RBS occur. For the case of nitrogen the standard reaction used is the $^{14}N(d, \alpha)^{12}C$ reaction [4–8]. When high depth resolution is required, energy scan using either the $^{15}N(p, \alpha\gamma)^{12}C$ [9,10] or the $^{14}N(\alpha, \gamma)^{18}F$ [11,12] resonant reaction is performed. These reactions provide a very high depth resolution (less than 2 nm in

0168-583X/92/$05.00 © 1992 – Elsevier Science Publishers B.V. All rights reserved

steel) but generally the analyzed depth is limited to 200 nm due to the loss of resolution because of energy straggling.

In order to analyze up to micron depths and to profile simultaneously heavy and light elements, energetic ($E\alpha > 5$ MeV) alpha backscattering analysis is performed. Nevertheless such a technique requires accurate measured values of the cross sections for ^{4}He scattering by the light elements. A review of the experimental cross section data currently available for large angle ^{4}He scattering by the light elements ($4 \leq Z \leq 20$) has been published recently [13]. Cross sections on carbon and oxygen have been used in alpha nuclear backscattering spectrometry [14–16] but in case of nitrogen no cross section values have been published up to now for alpha energies higher than 5 MeV. Doyle et al. [17] have used nuclear microprobe device to analyse nitrogen by NBS, but as they referred to standards they did not need the cross section knowledge.

3. Cross section measurement

The ^{14}N(α, α) excitation function has already been studied [18–20] in the energy range from 2 MeV to 4.7 MeV incident energy. The cross sections are nearly similar to RBS up to 2.5 MeV. At higher incident energy the nitrogen alpha scattering cross sections are enhanced because of the nuclear interaction component. A smooth region between 3.2 and 3.5 MeV corresponding to 37 mb/sr cross section value (twice the Rutherford cross section) is observed. Nevertheless we are interested in incident energies higher than 5 MeV because they lead to an improved mass resolution and they enable, in most cases, to separate carbon oxygen and nitrogen components. A competitive reaction namely the ^{14}N(α, p)^{17}O reaction is observed for incident energies higher than 3.5 MeV. The excitation function shows a resonance at 3.7 MeV which has been used in nitrogen nuclear microprobe analysis [17]. As the (α, p) ground state Q value is equal to -1.193 MeV protons are emitted with less energy than the incoming particles and are thus detected in the energy range of the alpha backscattered particles. As both components will appear in the experimental spectra we measured the ^{14}N(α, α) and ^{14}N(α, p) excitation function between 5.2 to 7.5 MeV alpha incident energy at $\theta_L = 172°$ detection angle.

The cross section measurements have been performed using 0.2 μm thick $Nb_{0.34}Ti_{0.66}N_{0.93}$ film deposited on carbon wafer. The carbon substrate and the film thickness have been chosen in order to enable the film stoichiometry determination involving 2.2 MeV alpha RBS. Moreover the cross section values required in NBS have been checked using a standard TiN/Zr target. For each energy (the scan being performed in 50 kev or 100 keV steps) the N(α, α) and N(α, p) responses were taken as the height of the component spectrum front edge. The normalisation was achieved using Rutherford cross sections on bulk niobium. The (α, α) excitation function is shown in fig. 1. A rather smooth cross section variation is observed in the 5.8 to 6 MeV energy range, their values being around 100 mb/sr which corresponds to 18 times the Rutherford cross section. In the same energy range the (α, p) reaction cross sections (fig. 2) are much lower. They range between 8 to 13 mb/sr. At 6.57 MeV incident energy a narrow resonance has been observed in the (α, p) excitation function. Up to now we did not take advantage of this resonance for analytical purposes. The cross section values are given with an accuracy of 8% including uncertainties on the normalisation and the standard target stoichiometry. In order to take advantage of the 100 mb/sr cross sections in the 5.8 to 6 MeV energy range, nitrogen NBS has been performed at 6 MeV incident energy.

4. Backscattering analysis performed at 6 MeV alpha incident energy

The analytical characteristics namely mass separation, depth resolution, and sensitivity are discussed on

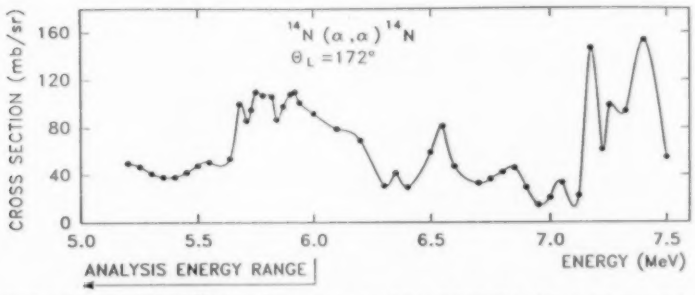

Fig. 1. Excitation function for the ^{14}N(α, α) reaction from 5.2 to 7.5 MeV incident alpha-particles energies.

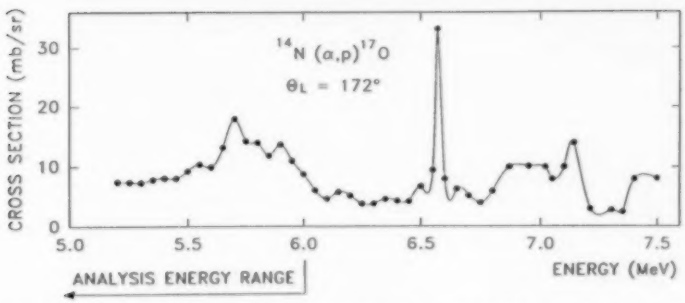

Fig. 2. Excitation function for the $^{14}N(\alpha, p)^{17}O$ reaction from 5.2 to 7.5 MeV incident alpha-particles energies.

the basis of typical sample profiling. Fig. 3 shows the NBS spectra of NbTiN film deposited on carbon substrates at 6 MeV alpha-particle energy. At this incident alpha-particle energy and for films of thickness thinner than 0.5 μm, carbon nitrogen and oxygen components are well separated. Then accurate film stoichiometry determination is easily achieved. Concerning the $^{14}N(\alpha, p)$ component, the front edge is at 2.37 MeV slightly higher in energy than the oxygen alpha backscattering component and could be superimposed to the fluorine component. Fortunately fluorine is not commonly introduced as contaminant neither in implantation nor in deposition technique. In such an analysis the depth resolution on Nb, Ti, O, N, C ranges from 23 to 26 nm. However we must point out that the nitrogen profiling obtained by the (α, p) reaction leads to worse depth resolution (80 nm) due to low proton stopping power values.

In case of bulk films overlaps between oxygen, nitrogen and carbon components are observed in the 6 MeV alpha backscattering spectra. Comparison of experimental and simulated distributions for a 2.6 μm NbTiN film analysis is given in fig. 4. The theoretical spectrum has been obtained assuming the same composition over the 2.6 μm film thickness. Discrepancies are observed mainly in the low energy parts of the titanium and nitrogen-components which can be explained by an interface contamination. The fit could be improved by taking into account carbon and oxygen contamination at the surface, in the inner film and at the film–substrate interface. Due to the fact that the carbon NBS component overlaps only with the low energy part of the nitrogen alpha NBS component while the oxygen profile overlaps with the N(α, p) component, the simulation of the whole spectrum is a quite severe test. Therefore the dual nitrogen analysis using both the $^{14}N(\alpha, \alpha)$ and $^{14}N(\alpha, p)$ components authorizes to determine accurately the nitrogen profile.

The NbTiN analyses are simplified by the choice of light carbon substrate. Let us examine the case of films deposited on heavy substrates. As an example the 6 MeV alpha backscattered spectrum for a 1.3 μm TiN film deposited on zirconium substrate is given in fig. 5. The comparison with simulated spectrum assuming a layer with 0.774% Ti and 0.226% N mass concentration is shown. The NBS nitrogen and $^{14}N(\alpha, p)$ components can be correctly analyzed as they are superimposed on a low alpha scattering zirconium yield since a 6 MeV incident energy has been used. The NBS nitrogen analysis for layer thicknesses larger than 2 μm should

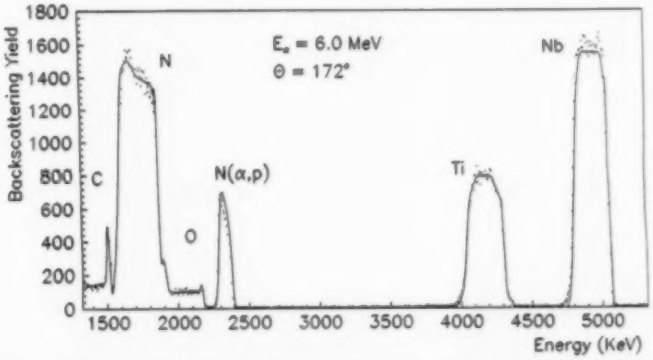

Fig. 3. Experimental (dots) and calculated (full line) backscattering spectra on a 0.5 μm NbTiN/C device.

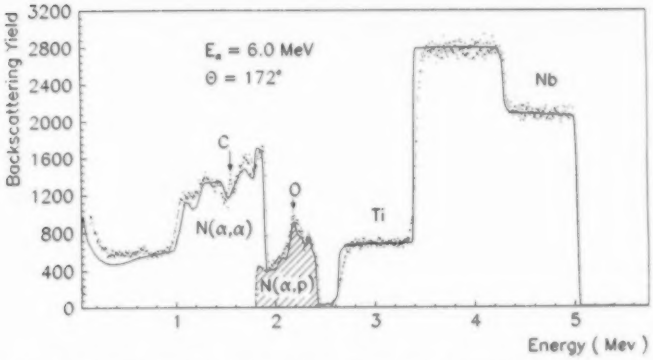

Fig. 4. Experimental (dots) and calculated (full line) backscattering spectra on a 2.6 μm NbTiN/C device. The individual simulated (α, p) contribution is hatched.

not be possible because of major increase of the low energy scattering yield on heavy matrix. One possible alternative should be to isolate the $^{14}N(\alpha, p)$ component using an absorber in front of the Si surface barrier detector in order to stop the alpha backscattered particles and to only transmit the protons produced by the nuclear reaction. Due to straggling and spreading in scattering angles the depth resolution should drop down to around 150 nm. Such a technique, adequate in case of bulk films deposited on heavy substrates, is in progress in our laboratory in order to profile nitrogen in thick (from 3 to 5 μm) NbTiN films deposited on copper.

To investigate the sensitivity that can be expected from the 6 MeV alpha backscattering analysis we used a nitrogen implanted steel sample. The implantation parameters are 160 keV energy and 9×10^{16} N/cm^2 dose. At this implantation energy the depth to profile is of the order of magnitude of 170 nm. The experimental spectrum is given in fig. 6. The measurement of the (α, α) and (α, p) nitrogen peak areas which allows

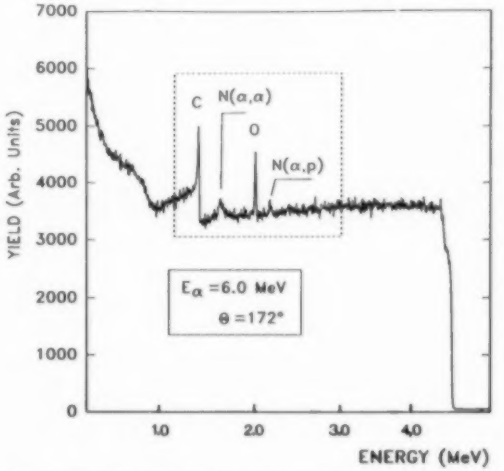

Fig. 6. Experimental backscattering spectra on a (160 keV energy and 9×10^{16} N/cm^2 dose) nitrogen-implanted steel sample.

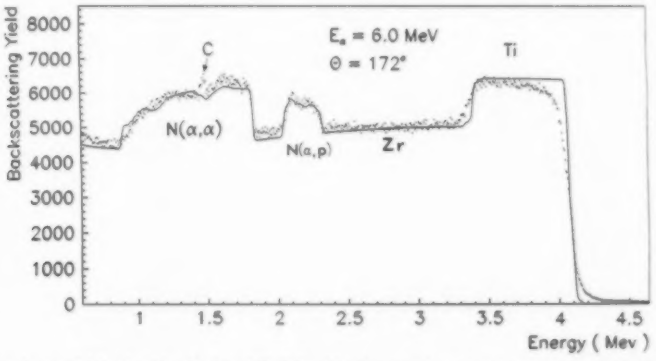

Fig. 5. Experimental (dots) and calculated (full line) backscattering spectra on a 1.3 μm TiN/Zr device.

the implanted dose determination is affected with at least 15% uncertainty due to the large background. In this case the implanted dose is close to the sensitivity limit estimated to 10^{16} and 5×10^{16} N/cm^2 for (α, α) and (α, p) nitrogen components, respectively.

However the nitrogen doses necessary to improve the steel tribological properties are larger than 10^{17}N/cm^2. Therefore the 6 MeV alpha backscattering analysis is very helpfull as it allows in one measurement to get nitrogen implantation profiles and to control carbon and oxygen incorporation during beam irradiation.

5. Conclusion

We have reported measured values of cross sections for both ^{14}N(α, α) and ^{14}N(α, p)^{17}O reactions in the energy range from 5.2 to 7.5 MeV. Simultaneous nuclear backscattering spectroscopy and nuclear reaction spectroscopy at 6 MeV alpha incident particles are shown to be powerful tools for profiling nitrogen in metallic nitride layers and in implanted samples.

References

[1] R. Buhl, H.K. Pulker and E. Moll, Thin Solid Films 80 (1981) 265.
[2] P. Bosland, F. Guemas and M. Juillard, 2nd ICMAS, Grenoble, 1990.
[3] N.E.W. Hartley, in: Ion Implantation, ed. J.K. Hirvonen (Academic Press, New York, 1980) p. 321.
[4] S. Lo Ruso, P. Mazzoldi, I. Santoni, G. Tosello and S. Tosto, Appl. Phys. Lett. 34 (1979) 627.
[5] G. Amsel, Revue de Phys. Appl. 3 (1968) 373.
[6] L.C. Feldman and S.T. Picraux, in: Ion Beam Handbook for Materials Analysis, eds J.W. Mayer and E. Rimini (Academic Press, New York, 1977) chap. 4.
[7] K. Bethge, Nucl. Instr. and Meth. B10/11 (1985) 633.
[8] L.M. Apatiga, E. Andrade, J. Richards, E. Belmont and F. Alba, Nucl. Instr. and Meth. B56/57 (1991) 799.
[9] B. Maurel and G. Amsel, Nucl. Instr. and Meth. 218 (1983) 15.
[10] T. Barnavon and J. Tousset, Radiat. Eff. 77 (1983) 249.
[11] C.R. Gossett, Nucl. Instr. and Meth. B10/11 (1985) 722.
[12] F. Bodard, G. Terwagne and M. Piete, Mater. Sci. Eng. 90 (1987) 111.
[13] J.A. Leavitt and L.C. McIntyre, Nucl. Instr. and Meth. B56/57 (1991) 734.
[14] J.C. Barbour, B.L. Doyle and S.M. Myers, Phys Rev. B38 (1988) 7005.
[15] J.A. Martin, N. Nastasi, J.R. Tesmer and C.J. Maggiore, Appl. Phys. Lett. 32 (1988) 2177.
[16] A. Chevarier, N. Chevarier, P. Deydier, H. Jaffrezic, N. Moncoffre, M. Stern and J. Tousset, J. Trace Microprobe Technol. 6 (1988) 1.
[17] B.L. Doyle, D.M. Follstaedt, S.T. Picraux, F.G. Yost, L.E. Pope and J.A. Knapp, Nucl. Instr. and Meth. B7/8 (1985) 166.
[18] D.F. Herring, Ren Chiba, B.R. Gasten and H.T. Richards, Phys. Rev. 112 (1958) 1210.
[19] D.F. Herring, Phys. Rev. 112 (1958) 1217.
[20] E. Kashy, P.D. Miller and J.R. Risser, Phys. Rev. 112 (1958) 547.

Nuclear Instruments and Methods in Physics Research B66 (1992) 242–249
North-Holland

Nuclear Instruments & Methods in Physics Research
Section B

Ion beam analysis of steel surfaces modified by nitrogen ion implantation

C. Neelmeijer, R. Grötzschel, E. Hentschel, R. Klabes, A. Kolitsch and E. Richter
Zentralinstitut für Kernforschung Rossendorf, Postfach 19, O-8051 Dresden, Germany

Conventional ERDA in combination with RBS and the $^{14}N(d, \alpha)^{12}C$ nuclear reaction has been applied to understand the wear behaviour of 210Cr46 tool steel after nitrogen implantation. However, the presence of the neighbouring elements ^{12}C and ^{16}O within the ^{14}N-implanted layers results in both strong limitations for the conventional ERDA and the necessity to registrate them analytically. The ERDA with Bragg ionization chamber proved useful allowing depth profile measurements with element separation in a single run. The solid-state lubrication caused by a nonmetallic carbon covering of the steel surface was deduced to increase the wear resistance drastically.

1. Introduction

The modification of steel surfaces by ion beams has been established as a favourable method to improve the mechanical properties as well as the resistance against chemical reactions [1]. For example, the mechanical and chemical abrasion of cutters chopping up plastic materials can be reduced by nearly an order of magnitude due to the implantation of nitrogen ions; the operating time of nitrogen-implanted extruder shafts increases strongly. In connection with the implantation process analytical methods which ascertain both the number of embedded nitrogen atoms and their real depth profile are necessary. For this reason the $^{14}N(d, \alpha)^{12}C$ nuclear reaction at $E_d = 1.4$ MeV deuteron energy [2] is suitable using oblique alpha-particle detection. However, the wear-resistance behaviour of steel surfaces was found [3] to be influenced not only by nitride formation but also favoured by the presence of C–N phases, where the carbon originates from the rest gas inside the implanter recipient. To correlate the mechanical steel properties with the chemical composition an analysis of both nitrogen and carbon atoms is of interest. Generally, the elastic recoil detection (ERD) [4] offers such a possibility and provides informations on further elements, i.e. oxygen, hydrogen, possibly incorporated within the nitride or carbonitride surface layers.

The present work reports on tool steel surfaces hardened by nitrogen-ion implantation at different implanter conditions. In dependence on the nitrogen fluency and the carbon partial pressure during implantation, pin-on-disk measurements informed on the characteristic layer resistance to wear. Corresponding compositional analysis by conventional ERD [5] turned out to be rather restricted due to strong overlaps of N, C and O signals. Separated nitrogen depth profiles deduced from complementary $^{14}N(d, \alpha_1)^{12}C$ experiments enabled a rough understanding of the complex ERD spectra. Moreover, Rutherford backscattering (RBS) [6] measurements allowed to distinguish between C and O surface deposition or matrix incorporation. The difficulties were overcome by using ERD in combination with a Bragg chamber [7] which allows to observe spectra well resolved in atomic number and energy of the recoiled species.

2. Experimental

2.1. Ion implantation

In our institute routine modification of steel surfaces takes place using a noncommercial high current implanter without mass separator. Nitrogen ions with 50 kV acceleration voltage were choosen to prepare a test series of polished 210Cr46 tool steel. Two samples labelled with I1 and I2 were implanted at high ion current density $I/A = 30$ $\mu A/cm^2$ and a low carbon partial pressure $p_C = 1.3 \times 10^{-3}$ Pa, adjusting the nitrogen fluency to $\phi_1 = 1 \times 10^{17}$ at/cm^2 and $\phi_2 = 8 \times 10^{17}$ at/cm^2, respectively. A further sample labelled with IC was prepared by $\phi_2 = 8 \times 10^{17}$ at/cm^2 operating with a moderate ion-beam intensity $I/A = 4.6$ $\mu A/cm^2$ but increased carbon partial pressure $p_C = 3.2 \times 10^{-3}$ Pa. A comparative sample labelled with M was implanted with 50 keV N^+ ($\phi_2 = 8 \times 10^{17}$ N/cm^2) ions of $I/A = 4.3$ $\mu A/cm^2$ current density at a commercial implanter including mass separation.

0168-583X/92/$05.00 © 1992 – Elsevier Science Publishers B.V. All rights reserved

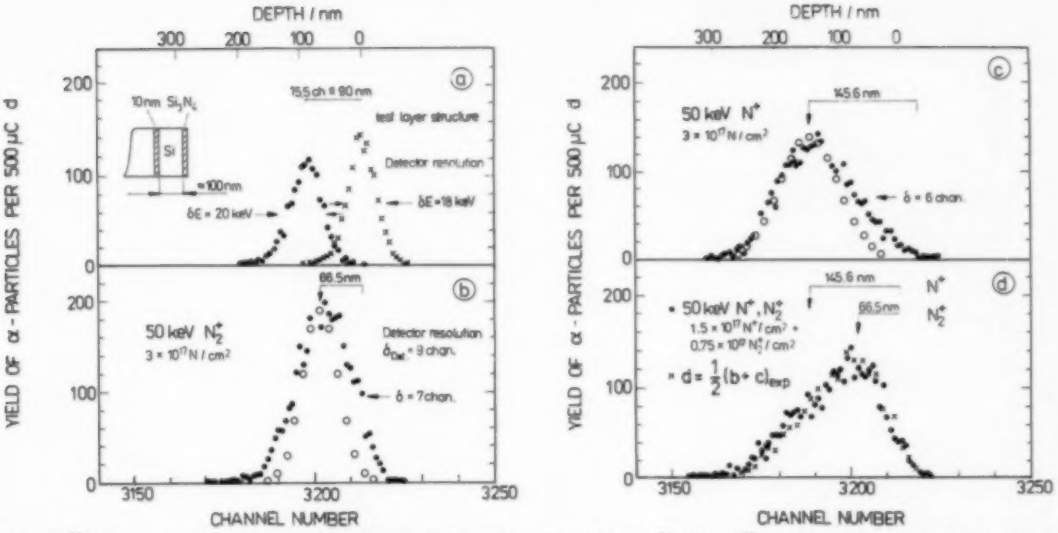

Fig. 1. ^{14}N test structure (a) and implantation profiles (b–d) examined by the $^{14}N(d, \alpha_1)^{12}C$ nuclear reaction at $E_d = 1.4$ MeV, oblique deuteron incidence $\alpha = 52.5°$ (target normal) and glancing α-particle detection $\vartheta = 168.5°$; angles are given with respect to the beam direction.

2.2. *Wear-resistance measurements*

The wear behaviour of the nonimplanted 210Cr46 tool steel and the nitrogen doped samples I1, I2, IC and M was examined by means of a pin-on-disk arrangement. The volume abrasion was determined as a function of the sliding distance of a fixed hardened ($HR_C = 60$) bearing ball (3 mm diameter) on the rotat-

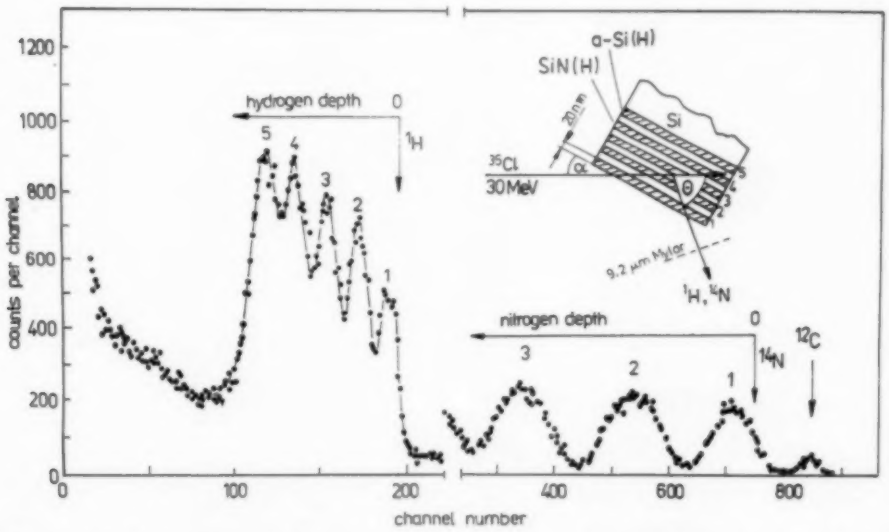

Fig. 2. ERD (conventional) energy spectrum of a sandwich structure produced by deposition of SiN(H) and a-Si:H layers of 20 nm thickness; $\alpha = 20°$, $\vartheta = 30°$.

ing steel disk. The pin ball moved on the disk with 1 m/s velocity and a load of 0.2 N. All wear experiments were performed at 30°C without lubrication.

2.3. Compositional analysis

2.3.1. Rutherford backscattering

To decide on the presence of surface coatings RBS spectra of both the nonimplanted steel and the implanted samples were recorded using a 1.7 MeV ^{4}He ion beam ($I = 50$ nA, $Q = 50$ μC, $\Omega/4\pi = 1.1$ msr) and a detection angle of $\vartheta = 170°$.

2.3.2. $^{14}N(d, \alpha_1)^{12}C$ analysis

The $^{14}N(d, \alpha_1)^{12}C$ nuclear reaction was applied in the vicinity of the local cross section plateau at $E_d = 1.4$ MeV deuteron energy ($Q_1 = 9.14$ MeV, $d\sigma/d\Omega = 2$ mb/sr, $\vartheta = 168.5°$) [8]. A target tilting angle of $\alpha = 52.5°$ – target normal with respect ot the incident beam – provided for a suitable depth resolution. This was tested by examining thin silicon nitride layers ($d = 10$ nm) deposited on a Si substrate or buried below a 100 nm Si film. The measured spectra of the α_1 group are depicted in fig. 1a. Moreover, fig. 1 presents the α_1 spectra gained from nitrogen depth profiles produced by 50 keV N_2^+ ($\phi = 1.5 \times 10^{17}$ N_2/cm^2, fig. 1b) or N^+ ($\phi = 3 \times 10^{17}$ N/cm^2, fig. 1c) implantation into Si. The profiles were found to agree well with the theoretical predictions [9]. Fig. 1d shows the analytical result of a 50 keV N^+ plus 50 keV N_2^+ double implantation into Si. As can be seen in this figure, the resulting α_1 spectrum correlates well with the energy distribution composed by a proportional superposition of the N^+ and N_2^+ profiles presented in figs. 1b and 1c.

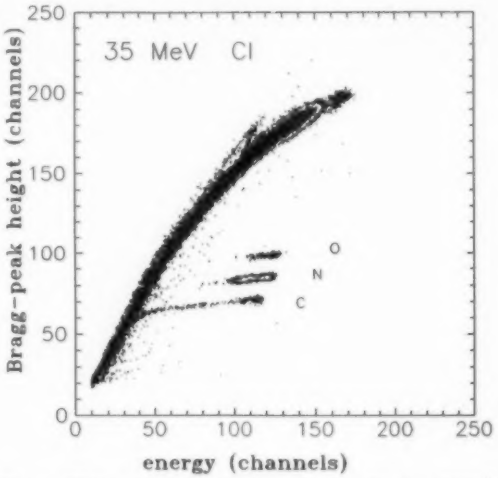

Fig. 3. ERD analysis of the steel sample IC ($\phi = 8 \times 10^{17}$ at/cm^2 nitrogen implantation without mass separation, 50 kV terminal voltage, increased carbon partial pressure $p_C = 3.2 \times 10^{-3}$ Pa). Bragg ionization chamber record for 35 MeV Cl^{7+}, $\alpha = 15°$, $\vartheta = 30°$.

2.3.3. ERDA – conventional

Our conventional ERD arrangement including a semiconductor detector with Mylar foil has been outlined recently [10]. A Cl^{6+} ion beam of 30 MeV energy was obtained from the 5 MV Rossendorf Tandem accelerator striking the target surface at $\alpha = 20°$ incident angle. The recoil atoms were observed at $\vartheta = 30°$ with respect to the projectile beam. A special target sandwich structure produced by plasma CVD, alternating SiNH and a-Si:H layers of 20 nm thickness (insert

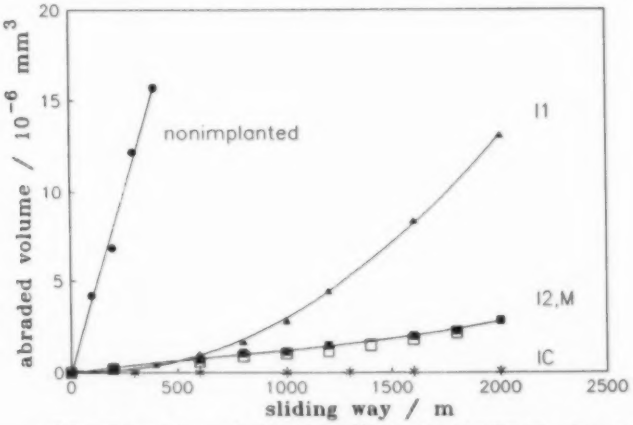

Fig. 4. Volume abrasion versus sliding distance for nonimplanted and ^{14}N-implanted 210Cr46 tool steel. Implantation without mass separation: I1 – $\phi = 1 \times 10^{17}$ at/cm^2, I2 – $\phi = 8 \times 10^{17}$ at/cm^2, IC – $\phi = 8 \times 10^{17}$ at/cm^2 with increased C partial pressure; with mass separation: M – $\phi = 8 \times 10^{17}$ N/cm^2.

of fig. 2), has served for estimating the depth resolution as a function of depth. Fig. 2 presents two regions of the corresponding ERD energy spectrum: the high energy part resolving the ^{14}N recoil signals of the upper three SiNH films and the low energy part originating from a superposition of the ^{1}H group and the ^{14}N signal of the deepest SiNH layer.

2.3.4. ERDA – Bragg ionization chamber

ERD analysis with a Bragg chamber [7] allows simultaneous depth profiling of atoms and separation with respect to the atomic number via the Bragg peak height. As an example, fig. 3 depicts the data set of the steel sample IC (8×10^{17} at/cm^2 nitrogen implantation at increased carbon partial pressure) for 35 MeV Cl ions at $\alpha = 15°$ and $\vartheta = 30°$. Besides a large number of elastically scattered projectiles the well separated branches of C, O and N recoils are discernable. Regarding ref. [7] the energy resolution was improved by using a more homogeneous polypropylene window of about 40 μg/cm^2 thickness. Now typical values $\Delta E/E$ are 0.7 to 0.9%. This corresponds to depth resolution values within 5 and 10 nm.

3. Results and discussion

3.1. Wear resistance

Fig. 4 shows the volume abrasion in relation to the sliding distance as measured by the pin-on-disk experiment. As obvious the wear decreases systematically with increasing fluency of implanted nitrogen atoms. Previous investigations [1] provided $\phi = 8 \times 10^{17}$ N/cm^2 as an optimum fluency for the nitrogen–steel system. At the same number of embedded nitrogen atoms a farther drastic wear reduction at increased carbon partial pressure during implantation was found as outlined by the curve IC in fig. 4. Such a behaviour had already been observed for carbon implantation in steel [11]. In connection with the following compositional analysis it is worth while to mention that implantation of $\phi = 8 \times 10^{17}$ at/cm^2 with mass separated N^+ ions (fig. 4, sample M) and implantation without mass separation does not induce marked differences in the wear characteristic.

3.2. Compositional analysis

Starting from the wear behaviour of the steel samples doped nominally with equal nitrogen fluencies of $\phi = 8 \times 10^{17}$ at/cm^2 but using different implantation conditions (see section 2) it had been important to get information on (i) the amount and the depth distribution of possibly incorporated carbon atoms, especially for the sample IC; and (ii) the composition identity or

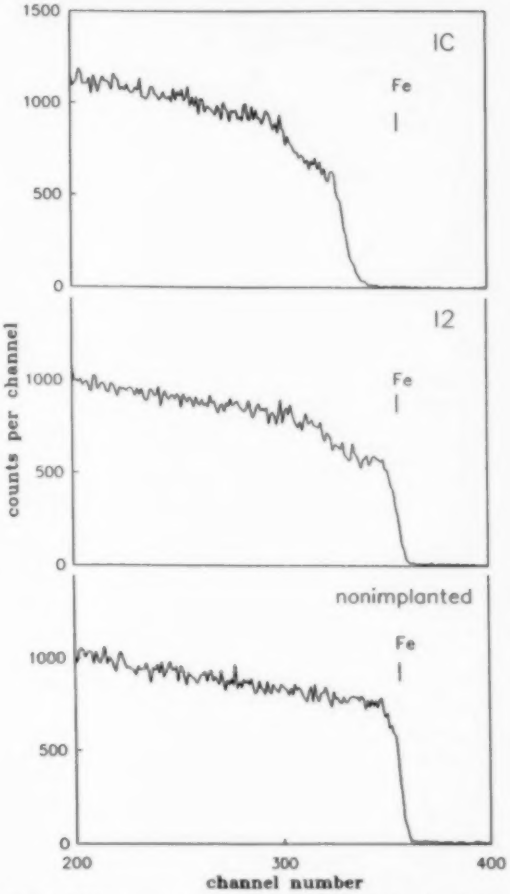

Fig. 5. RBS spectra observed for 1.7 MeV ^{4}He bombardment of nonimplanted and ^{14}N-implanted tool steel (see text), random incidence, $\vartheta = 170°$; sample characterization, see fig. 4.

the kind of differences within the surface region of the samples I2 and M.

For the samples of interest figs. 5, 6 and 7 compare corresponding spectra as observed by RBS, conventional ERD and $^{14}N(d, \alpha_1)^{12}C$ analysis.

As outlined in fig. 5 (RBS) the Fe surface signal is shifted towards lower energies only in the spectrum IC, note that the spectrum of sample M, here not shown, is quasi identical to that one of sample I2. To explain the shift of the Fe signal carbon growth was thought to take place during the implantation process. This assumption was confirmed regarding the corresponding ERD spectra in fig. 6. A broad carbon surface peak of high intensity dominates for sample IC in contrast to I2 and M. Supposing a pure carbon coating a layer thick-

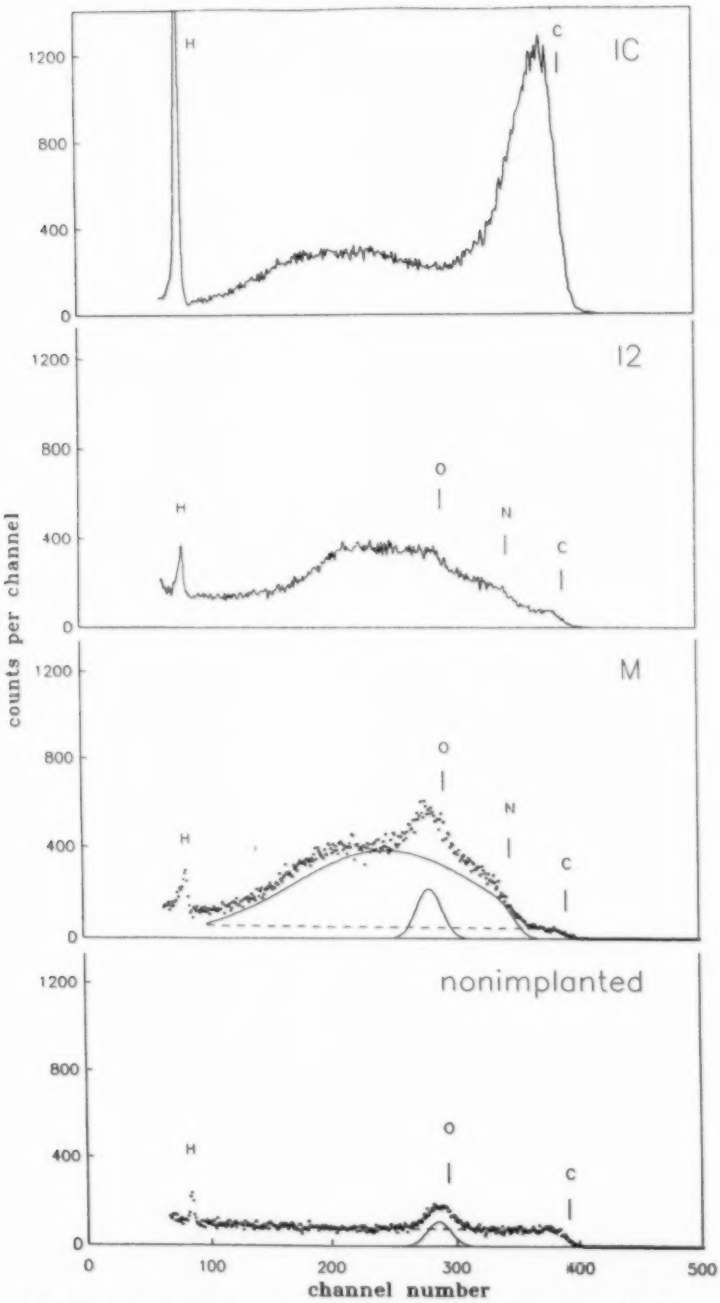

Fig. 6. Energy spectra of C, N and O recoiled atoms measured by conventional ERDA: 30 MeV Cl^{6+}, $\alpha = 20°$, $\vartheta = 30°$, 9.2 μm Mylar stopping foil. Samples: ^{14}N (50 kV) implantation into 210Cr46 tool steel, $\phi = 8 \times 10^{17}$ at/cm^2. M/I-implantation with/without mass separator, respectively; IC-increased carbon partial pressure. The dashed and solid lines in the spectra "nonimplanted" and "M" represent the fitting results for C and N/O, respectively.

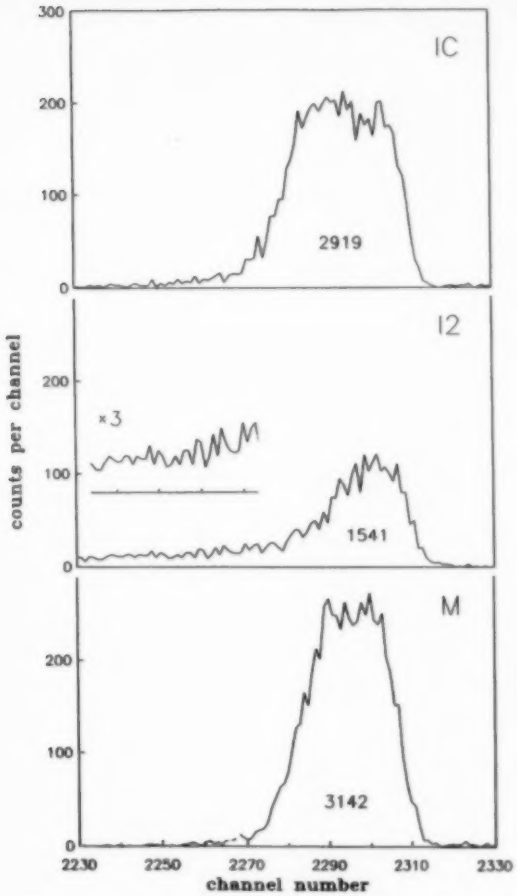

Fig. 7. Nitrogen depth profiles (implantation of 8×10^{17} at/cm^2, $\hat{U}$ = 50 kV) measured by means of the $^{14}N(d,\alpha_1)^{12}C$ nuclear reaction; E_d = 1.4 MeV, α = 52.5° (target normal) deuteron incidence, ϑ = 168.5° α-particle detection.

ness of 1.6×10^{18} C/cm^2 was estimated from the shift of the Fe edge in the RBS spectrum (fig. 5 sample IC). Strong overlaps of N, O and C signals, especially in the spectra I2 and IC, do not allow to deduce the nitrogen depth profiles by conventional ERDA (see fig. 6) without additional information. For this reason the ^{14}N selective results from the $^{14}N(d,\alpha_1)^{12}C$ nuclear reaction as depicted in fig. 7 were helpful. Taking spectrum M as the reference sample ($\phi = 8\times10^{17}$ N/cm^2, implanted with mass separation and a low current density I/A = 4.3 μA/cm^2, the C partial pressure $p_C = 1.3\times10^{-3}$ Pa) from fig. 7 it is obvious that only sample IC bears a rough resemblance to the amount and the depth profile of the N atoms. Remember that I2 was implanted with the same N fluency but using a high current intensity. Surely target heating during implantation results in a N diffusion as indicated in fig. 7, sample I2, by the loss of counts within the peak structure accompanied by the presence of an intense low energy tail.

This knowledge allows a better understanding of the complex ERD spectra of fig. 6. Spectrum M is composed by a superposition of signals caused from C inside the steel bulk material (compare fig. 6, nonimplanted), the implanted N depth profile and O (+H) surface peaks originating from a thin oxide (+water) film on the sample surface due to storing on air. To obtain concentration depth profiles a simulation procedure was developed which is discussed in more detail in ref. [10]. Starting from an initial depth profile described by an analytical function (e.g. Gaussian shape) for each element the program calculates the ERD energy spectrum. Adjustable parameters of these functions are changed and the process is iterated until satisfactory agreement between the experimental and calculated spectrum is achieved. Fig. 6, nonimplanted and fig. 6, sample M, include simulated energy spectra obtained under the assumption of a depth constant carbon content and an oxide surface layer. The N distribution in fig. 6, sample M, was assumed to be a Gaussian implantation profile. The quantitative analysis results in oxygen areal densities of 5.9×10^{16} O/cm^2 and 2.8×10^{16} O/cm^2 for the implanted sample (M) and nonimplanted steel, respectively. The range at the maximum value and the standard deviation of the N^+ ions (fig. 6, sample M) was found to be 60 and 45 nm, respectively.

Because of the more complex character of the other spectra in fig. 6 there was no chance to analyse those with the simulation program. The complexity of these spectra arises either from the surpassing carbon peak at the high energy part of the ERD spectrum IC or from the nitrogen diffusion into deeper regions (fig. 6, sample I2). Additionally, a substantial O content was present in the sample I2 originating from a higher oxygen partial pressure within the implanter ion source. The absence of mass separation allows the ionized oxygen to be also implanted into the sample.

The utilization of a Bragg ionization chamber [7] permits to overcome these difficulties. Figs. 8 and 9 show energy spectra recorded by the Bragg chamber, and depth distributions of N and O evaluated quantitatively by forward fitting [12] of adopted model functions. Supposing Rutherford cross section the number of projectiles scattered from the steel matrix atoms served for normalization.

The qualitative behaviour of the measured ^{14}N spectra is in correspondence with the results of $^{14}N(d,\alpha_1)^{12}C$ analysis (fig. 7). The calculated N distribution for the sample I2 shows the maximum shifted to

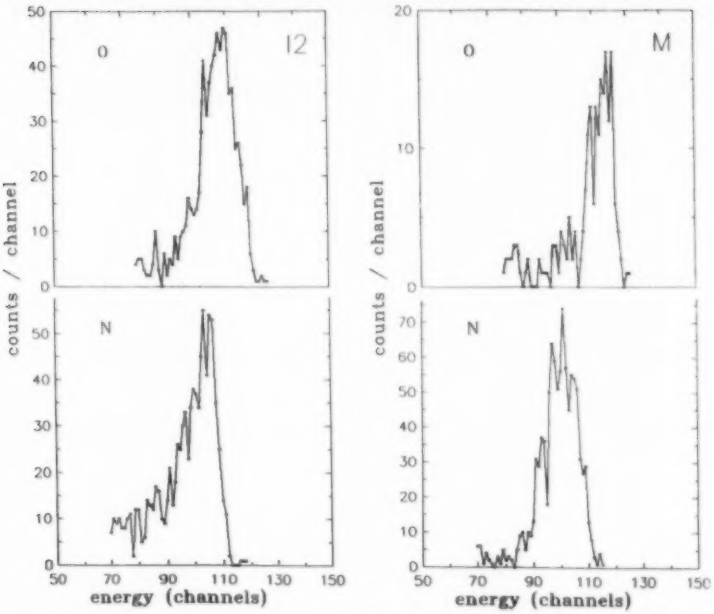

Fig. 8. Energy spectra of N and O recoiled atoms measured by ERDA with Bragg ionization chamber; 35 MeV Cl^{7+}, $\alpha = 15°$, $\vartheta = 30°$. Samples: ^{14}N (50 kV) implantation into 210Cr46 tool steel, $\phi = 8 \times 10^{17}$ at/cm^2, M/I-implantation with/without mass separation, respectively.

the surface and a drastic falling off with increasing depth. A comparable shape of the profile is also observed for the implanted oxygen atoms.

4. Conclusions

As known from the literature [13], wear-resistant surface regions are created in steel due to the implantation of N atoms which partly move towards the bulk during surface abrasion. Regarding the samples I2 and M it could be shown that in spite of significant differences in the shape of the N profile an identical wear behaviour was obtained. However, differences in the wear characteristic due to the different initial concentration of N atoms have to be expected when increasing the sliding way.

A completely changed wear behaviour occurs in the case of nitrogen-implanted steel covered with a carbon surface layer. The drastic growth of the wear resistance in the case of sample IC we attribute to a solid-state lubrication [14] effect. This assumption is supported by the RBS result (fig. 5, sample IC) which shows a nonmetallic C-coating free of coexistence with Fe atoms. Consequently, there is no formation of hard Fe carbonitrides but a soft carbon surface layer of lubricating properties.

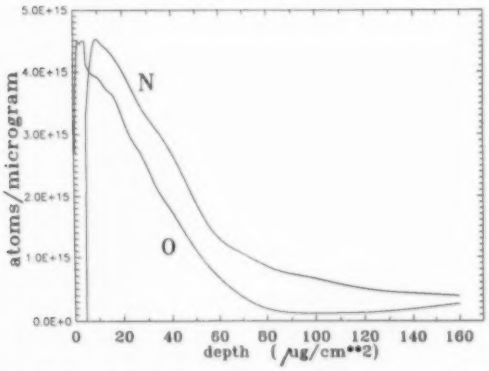

Fig. 9. N and O depth profiles for sample I2 deduced from the ERD energy spectra of fig. 8.

Acknowledgements

The authors express their thanks to the collaborators of the Rossendorf Accelerator Laboratory for high beam quality on both the 2 MV van de Graaff and the 5 MW Tandem accelerator. Moreover, we thank Mrs. L. Kumpf and Mr. K. Brankoff for fruitful cooperation in electronics and computer-assisted control of the experiments.

References

[1] U. Scholz, E. Richter and H. Reuther, Schmierungstechnik 20 (1989) 202.

[2] G. Debras and G. Deconnick, J. Radioanal. Chem. 38 (1977) 193.

[3] B. Rauschenbach and K. Hohmuth, Crystallogr. Res. and Technol. 10 (1984) 1425.

[4] J.P. Thomas, M. Fallavier and A. Ziani, Nucl. Instr. and Meth. B15 (1986) 443.

[5] C. Nölschner, K. Brenner, R. Knauf and W. Schmidt, Nucl. Instr. and Meth. 218 (1983) 116.

[6] W.-K. Chu, J.W. Mayer and M.-A. Nicolet, Backscattering Spectrometry (Academic Press, New York, 1978).

[7] E. Hentschel, R. Kotte, H.G. Ortlepp, F. Stary and D. Wohlfarth, Nucl. Instr. and Meth. B43 (1989) 82.

[8] R.A. Jarjis, Nuclear Cross Section Data for Surface Analysis, Department of Physics, Schuster Laboratory, University of Manchester (1979).

[9] J.F. Ziegler, J.F. Biersack and U. Littmark, The Stopping and Range of Ions in Solids (Pergamon, New York, 1985).

[10] C. Neelmeijer, R. Grötzschel, R. Klabes, U. Kreissig and G. Sobe, Proc. 10th Int. Conf. on Ion Beam Analysis, Eindhoven, The Netherlands, 1–5 July 1991, Nucl. Instr. and Meth. B64 (1992).

[11] C. Neelmeijer, E. Hensel, P. Knothe, M. Posselt and E. Richter, Nucl. Instr. and Meth. B42 (1989) 369.

[12] E. Hentschel, EBIC – A simulation program for fitting ERD energy spectra measured with a Bragg ionization chamber, to be published in Nucl. Instr. and Meth. B.

[13] G. Dienel, U. Kreissig and E. Richter, Vacuum 36 (1986) 813.

[14] J.M. Williams, Nucl. Instr. and Meth. B10/11 (1985) 539.

Nuclear Instruments and Methods in Physics Research B66 (1992) 250–257
North-Holland

Nuclear Instruments & Methods in Physics Research
Section B

Simultaneous determination of ^{14}N and ^{15}N by elastic backscattering and nuclear reaction: application to biology

Ph. Massiot [a], F. Sommer [b], M. Thellier [c] and C. Ripoll [c]

[a] *Laboratoire "Pierre Süe", CEA / DSM / DRECAM / CE Saclay, 91191 Gif-sur-Yvette Cedex, France*
[b] *Laboratoire "Pierre Süe" and Laboratoire de Biophysique, Faculté de Médecine de Créteil, France*
[c] *Laboratoire d'Echanges Cellulaires UA203 CNRS, Faculté des Sciences de Rouen, France*

The aim of this study is to use a nuclear microprobe for simultaneous localization and quantification of ^{14}N and ^{15}N in plant cells. A summary of the main nuclear reactions usually used for this purpose is presented. For ^{15}N, we tested the nuclear reaction $^{15}N(p, \alpha\gamma)^{12}C$. The yield curve was measured between 2.90 and 3.35 MeV; following the gamma ray at 4.439 MeV, it exhibited two resonances at 2.970 and 3.270 MeV. The choice of this energy range also made it possible to measure ^{14}N by proton elastic backscattering. The yield curve of the reaction $^{14}N(p, p)^{14}N$ was measured in the same energy range. The choice of a 3 MeV proton beam energy enabled us to optimize the ^{15}N detection limit and to have enough sensitivity for ^{14}N determination. The stability of nitrogen under the proton beam with these analytical conditions was tested.

1. Introduction

A better knowledge of the nitrogen metabolism in plants is necessary to optimize the use of fertilizers, thus improving harvests in quantity and quality and limiting the damages caused to the environment by excessive inputs of nitrate. Moreover, nitrogen determination is a useful tool to measure protein content [1,2]. For these reasons, the labelling of fertilizers with the stable isotope ^{15}N has already been successfully applied in agricultural research [3].

The average concentration of nitrogen in plant tissues is 1.5 wt.%. When plants are fed with an ^{15}N labelled substrate, the kinetic study of nitrogen incorporation requires the use of a microanalytical technique with a high sensitivity to ^{14}N, and an even better one to ^{15}N. The determination of ^{14}N and ^{15}N in bulk may be performed by mass spectrometry with a high rate of accuracy [4], but this method requires samples of at least 1 μg of pure nitrogen [5]. At the cellular level, the localization of labelled elements in biological specimens is usually performed by microautoradiography [6], but the half-lives of the radioactive isotopes of nitrogen are too short for application of this technique. Secondary ion emission mass spectrometry (SIMS) allows us to discriminate between ^{14}N and ^{15}N in order to visualize the distribution of both nitrogen isotopes with a good spatial resolution [7,8]. The method is fairly accurate for the determination of isotopic ratios, but absolute concentrations are difficult to measure in a biological matrix. To avoid the matrix effects in the quantification and visualization of nitrogen isotopes, nuclear methods offer an attractive alternative.

A nuclear reaction with thermal neutrons, $^{14}N(n, p)^{14}C$, may serve to map ^{14}N in a biological specimen [9], but it is not applicable to ^{15}N. In the present study, we have aimed to use a nuclear microprobe to simultaneously localize ^{14}N and ^{15}N in plant systems. Our final objective will be to achieve the subcellular localization of ^{14}N and ^{15}N, using the new nuclear microprobe of the Pierre Süe Institute in Saclay [10] when this instrument starts working (expected in a few months). In the meantime, we used the nuclear microprobe facilities of the Nuclear Center of Bruyères-le-Châtel and an optimal spatial resolution of 10 μm, in order to optimize conditions for the quantification of the stable isotopes of nitrogen. It was clearly preferable to detect both nitrogen isotopes simultaneously on the same sample, rather than perform successive determinations of these isotopes. We therefore had to begin by finding out which nuclear reactions were most appropriate for simultaneous quantitative microanalysis of ^{14}N and ^{15}N in plant samples.

2. Main nuclear processes used for the detection of stable nitrogen isotopes

Nuclear techniques such as prompt nuclear reactions (NRA: nuclear reaction analysis, PIGE: particle-induced gamma-ray emission) and elastic scattering (PESA: proton elastic scattering analysis, RBS:

0168-583X/92/$05.00 © 1992 – Elsevier Science Publishers B.V. All rights reserved

Rutherford backscattering sectrometry) have already been used to determine ^{14}N and ^{15}N, particularly with biological samples. We will briefly summarize the main reaction processes involved.

2.1. ^{14}N determination

The most sensitive nuclear reactions to detect ^{14}N are $^{14}N(d, p)^{15}N$ and $^{14}N(d, \alpha)^{12}C$ [3,11–14]. $^{14}N(d, p_0)^{15}N$ presents the major advantage of having a Q value higher than those for deuteron induced reactions on carbon and oxygen, which can interfere. Moreover, in biological matter, the influence of heavier elements present in traces can be neglected. The (d, p) and (d, α) reactions allow one to determine profiles of nitrogen contents in depth [2,15]. According to Pollard [3], the sensitivity in a urea matrix is 1150 counts per 1 wt.% ^{14}N per μC with a detection limit of 0.012 wt.% in urea.

Proton induced gamma ray emission has also been used for the determination of ^{14}N in biology. $^{14}N(p, \gamma)^{15}O$ exhibits prominent γ rays at 8.283, 5.242 and 3.042 MeV with a narrow proton resonance at 1061.6 keV [16]. This reaction is not sensitive enough for the measurement of nitrogen concentrations in plants.

With a 4.3 MeV proton beam, Xenoulis [17] used the $^{14}N(p, p'\gamma)^{14}N$ reaction, with $E_\gamma = 2.313$ MeV: this reaction has a high energy proton resonance [18] and a better sensitivity than the preceding one.

Deuteron induced gamma emission exhibits a few strong deexcitation γ rays, at $E_\gamma = 5.28$ and 5.31 MeV for $^{14}N(d, p\gamma)^{15}N$ [19] and at $E_\gamma = 7.3$ and 8.3 MeV for $^{14}N(d, n\gamma)^{15}O$ [20]. The sensitivities of the prompt gamma ray analysis of $^{14}N(d, p\gamma)^{15}N$ and $^{14}N(d, n\gamma)^{15}O$ reactions in urea were 140 and 80 counts per μC per 1 wt.% ^{14}N, respectively [3].

Elastic proton scattering $^{14}N(p, p)^{14}N$ may also serve to quantify ^{14}N: the cross section for backscattering of the light elements, carbon, nitrogen and oxygen, is enhanced by a factor of 4 to 7 over that expected from Coulomb scattering only, when the energy of the incident protons ranges from 2.0 to 2.5 MeV [21].

2.2. ^{15}N determination

For ^{15}N, the choice of nuclear reactions is more limited. Whereas the Q value for the $^{15}N(d, p)^{16}N$ reaction is only 0.265 MeV, that of $^{15}N(d, \alpha)^{13}C$ is 7.69 MeV. Interferences are very likely because of many reactions with other nuclide Q values of the same order of magnitude.

When one wishes to measure isotopic ratios $^{15}N/^{14}N$, deuteron induced gamma ray emission is not appropriate because the sensitivity of $^{15}N(d, n\gamma)^{16}O$ is extremely low (90 counts per μC per 1 wt.% ^{15}N in urea) and the transition $E_\gamma = 6.14$ MeV, due to the very weak peak, is at the limit of being discernable [3]. Sensitivity with the $^{15}N(d, n\gamma)^{16}O$ reaction is extremely poor compared with that of $^{15}N(p, \alpha\gamma)^{12}C$.

Matsumoto [22] investigated the elastic scattering analysis used to measure $^{15}N(p, p)^{15}N$ in several biological samples: the scattering yield with a 5.82 MeV proton beam, as detected at an angle of 165°, was shown to be adequate to analyze ^{15}N in natural adenine.

In fact, the proton capture resonance nuclear reaction $^{15}N(p, \alpha\gamma)^{12}C$ is the one most often used [23–25]. The 4.439 MeV gamma ray transition is extremely strong and the excitation function has numerous resonances at low and high energies [26]. Pollard measured ^{15}N in barley roots using this reaction with a 1.69 MeV proton energy, and she obtained a sensitivity of 4240 counts per μC per 1 wt.% ^{15}N in urea and a detection limit of 0.04 wt.% ^{15}N in urea [3].

2.3. Simultaneous determination of ^{14}N and ^{15}N

^{15}N and ^{14}N were simultaneously measured by proton induced gamma ray emission: $^{14}N(p, \gamma)^{15}O$ and $^{15}N(p, \alpha\gamma)^{12}C$, with a low proton beam energy [27]. These reactions are applicable to the analysis of samples containing large amounts of nitrogen, such as urea with ^{15}N enrichments in the range of 0.01% to 10%. In our present study, however, it was not possible to use the ^{14}N reaction for plant samples because the sensitivity was 1000 times below that of the reaction $^{15}N(p, \alpha\gamma)^{12}C$ [16].

^{14}N and ^{15}N were also simultaneously determined using the reactions $^{15}N(p, \alpha\gamma)^{12}C$ and $^{14}N(p, p'\gamma)^{14}N$ with a proton incident energy higher than 4 MeV [17]. By using a 5.82 MeV or, better still, a 6.7 MeV proton incident energy, Matsumoto obtained a kinematical energy dispersion of scattered protons adequate to discriminate the ^{14}N and ^{15}N peaks in a specimen containing methionine enriched to 95% in ^{15}N [22].

3. Choice of the reactions and the incident energy

The choice of suitable reactions with a high sensitivity to determine ^{15}N when using a maximum incident energy of 4 MeV is limited; we chose to use the proton capture resonant reaction $^{15}N(p, \alpha\gamma)^{12}C$. Once we had made our choice, our aim was to use the same incident particle with the same energy to detect also ^{14}N; this made it impossible to use the reactions with deuterons despite their good sensitivity. The only remaining possibility for ^{14}N quantification was thus proton elastic scattering. The other reactions are not sensitive enough, or they require an incident proton energy higher than that at our disposal.

3.1. Reaction $^{14}N(p, p)^{14}N$

Proton backscattering analysis of light elements with an incident proton beam of several hundred keV raises difficulties for quantification due to the non-Rutherford scattering cross section. However, a significant improvement of light-element detection sensitivity can be expected with a 3 MeV proton beam, particularly for thin target analysis. In addition, the stopping power in the medium being lower for protons than for heavier particles, this favours in-depths analysis of the sample and limits straggling. Another advantage is that protons induce less radiation damage in the sample than deuterons or helions.

Scattering with incident helium particles is a pure Coulomb process between two completely unscreened nuclear point charges. When using incident proton particles, the collision diameter is smaller and becomes comparable to the sum of three components: Rutherford scattering, nuclear potential scattering and nuclear resonance scattering [28]. Moreover, the proton scattering cross section on light elements is better than that expected for Coulomb scattering only [29,30].

The scattering cross section on ^{14}N for a proton energy in the range 1–4 MeV was measured a few years ago [31], and the theoretical calculation of the cross section of the p–p scattering can also be given with quite a high accuracy [32,33]. However, in order to limit the possibilities of experimental errors in the quantitative analysis, we shall calibrate our measurements using standards with a known nitrogen composition.

An incident proton energy has to be selected that is appropriate to the excitation function of $^{15}N(p, \alpha\gamma)^{12}C$, i.e. in the range of 2.9 to 3.35 MeV; it must also be compatible with a good elastic cross section of $^{14}N(p, p)^{14}N$ [31,34]. The excitation function of $^{14}N(p, p)^{14}N$ is more or less constant between 3 and 3.10 MeV, though it exhibits a strong narrow resonance towards 3.2 MeV. In this energy range, the cross sections for ^{12}C and ^{16}O, the main components of the biological matrix, are practically constant [35,36].

3.2. Reaction $^{15}N(p, \alpha\gamma)^{12}C$

The 4.439 MeV gamma ray issuing from the transition of the first excitation to the ground state of the ^{12}C atom nucleus may be detected by using the first and second escape peaks. A spectral interference is expected with $^{11}B(p, \gamma)^{12}C$ [37] but, given the low concentration of ^{11}B compared with that of ^{15}N in our future experiment on plants, it can be neglected.

The excitation function exhibits numerous well-defined resonances with high cross section values at low and high energies (table 1). They have been investigated over the past decades, in connection with studies of nuclear excited states [38,26]. Although, quite surprisingly, the high energy resonances at 3.0 and 3.3 MeV [26] with their respective cross sections of 750 and 535 mb have hardly been employed by previous authors, they are particularly well suited to our present problem. Using a proton beam with an energy between 2.9 and 3.35 MeV, it was thus possible to simultaneously optimize the detection of ^{14}N by elastic proton scattering and that of ^{15}N via the (p, $\alpha\gamma$) reaction.

Table 1
Resonance energies of the nuclear reaction $^{15}N(p, \alpha\gamma)^{12}C$ leading to the emission of the 4.439 MeV gamma ray [26,41]

Proton energy [keV]	Cross section [mb]	Resonance width [keV]
360	0.03	94
429	300	0.9
898	800	22
1040	15	130
1210	425	225
1640	340	68
1979	35	23
3000	750	45
3300	535	75

4. Experimental measurements

4.1. Experimental setup

The proton beam of the nuclear microprobe of Bruyères-le-Chatel was generated by a 4 MV Van de Graaff accelerator [39]. The proton energy was estimated with a degree of uncertainty of about 5 keV. For the present methodological study, the beam was defocused to an area of 200×200 μm^2. The integrated charge of protons was monitored by using a beam chopper placed just in front of the quadrupoles. The samples were irradiated in a collision chamber at an angle of 90° to the proton beam in a vacuum of 10^{-6} Torr.

The gamma radiations issuing from the nuclear reaction were detected with an ultrapure Ge detector Ortec (50.0×54.4 mm^2) set at 120° to the ion beam at a distance of 6.5 cm from the target and subtending a solid angle of approximativly 1.57 sr. The detector resolution and efficiency were 1.64 keV and 20.4% at 1.33 MeV (^{60}Co source), respectively. At 122 keV the resolution was 0.722 keV (^{152}Eu source). The Ge detector was placed in a sleeve-type stainless steel structure (thickness: 2 mm). It was protected from the surrounding background by three successive screens: Pb, Cd, Cu (thickness: 6.5 mm).

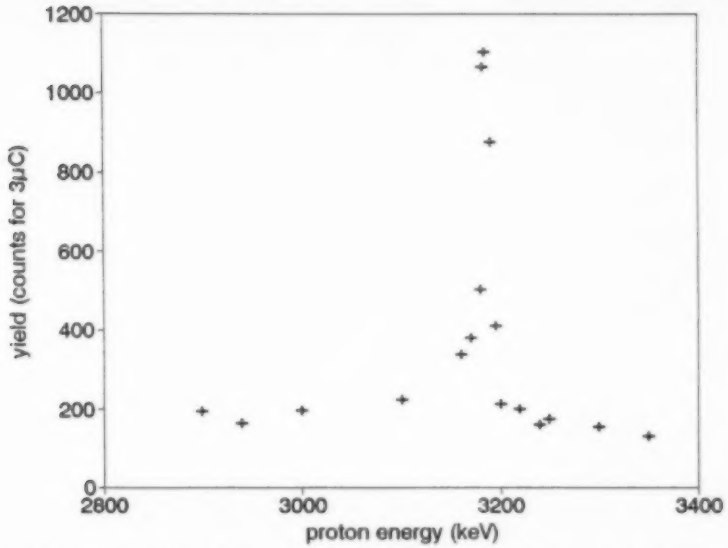

Fig. 1. Yield curve of the reaction $^{14}N(p, p)^{14}N$ measured between 2.9 and 3.35 MeV, showing the resonance at 3.185 MeV.

For the detection of charged particles issuing from the elastic backscattering reaction a silicon surface barrier detector was used. It was placed approximately at a scattering angle of 165° in relation to the direction of the beam. Due to our detection system, this maximum angle offers a good kinematic energy separation

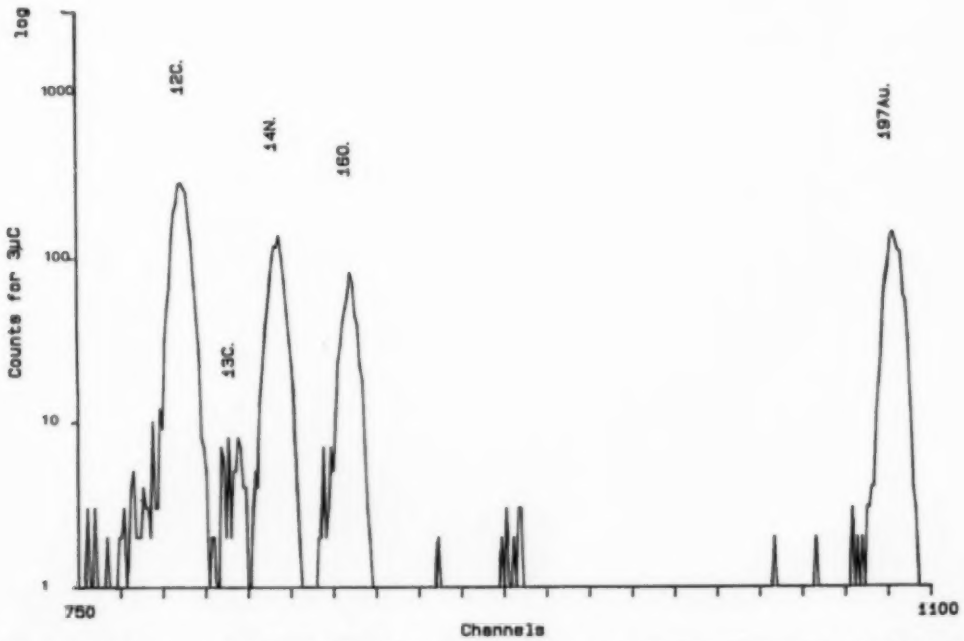

Fig. 2. Backscattering spectrum on a 0.3 μm thick Kapton foil, covered with a thin gold layer, obtained with a 3.185 MeV incident proton beam.

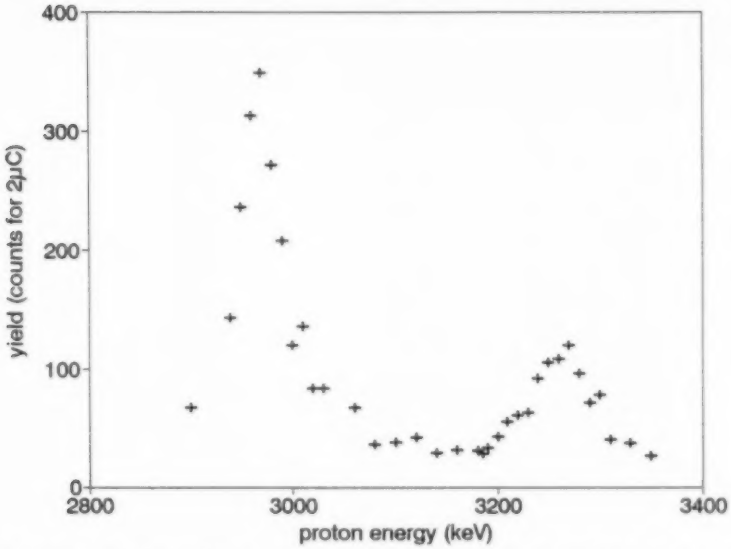

Fig. 3. Yield curve of the reaction $^{15}N(p, \alpha\gamma)^{12}C$ measured between 2.9 and 3.35 MeV, showing the two resonances at 2.970 and 3.270 MeV.

of adjacent masses [40]. The detector had an active area of 25 mm^2 and a sensitive depth of 100 μm, it was collimated to a diameter of 4 mm. Its resolution was 15 keV for 5.5 MeV alpha particles. The data acquisition system consisted of a Tracor TN4000 computer. Data handling for gamma ray and elastic scattering proton

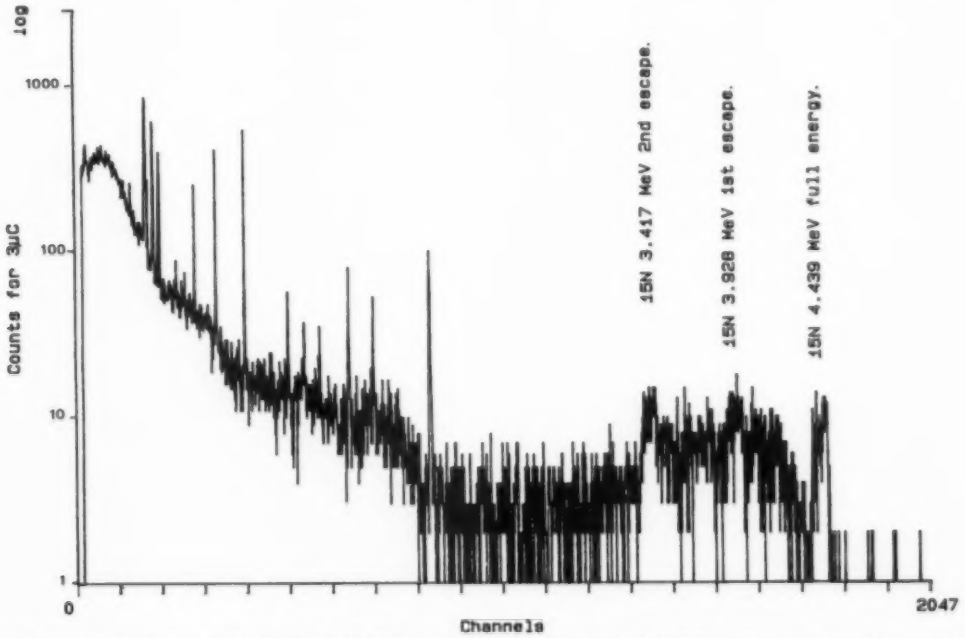

Fig. 4. Gamma ray spectrum obtained with a 3 MeV proton energy on a 0.5 μm thick Ni foil, implanted with ^{15}N ions at a dose of 10^{17} atoms/cm^2.

spectra were performed with VISPECT, a computer program developed in our laboratory by D. Piccot.

4.2. Excitation function of the reaction $^{14}N(p, p)^{14}N$

The incident proton energy was selected on the basis of the excitation functions of the two nuclear reactions $^{14}N(p, p)^{14}N$ [31] and $^{15}N(p, \alpha\gamma)^{12}C$ [25], in order to optimize the detection sensitivity of the two nuclides. This experiment was performed with a sample made of a thin Kapton foil ($C_{22}H_{10}N_2O_5$, 0.3 μm thick), which has the main advantage of being composed of the same major elements as plant tissues. It was covered with a thin gold layer to avoid charging problems.

The yield curve is shown in fig. 1. Each point was measured with an integrated charge of 3 μC. One narrow strong resonance is observed at 3.185 MeV with a width of 20 keV. The yield of energies below the resonance is approximately twice that afterwards.

A proton backscattering spectrum obtained with a Kapton foil at a proton energy of 3.185 MeV is given in fig. 2. Such an incident energy is high enough to prevent backscattering peaks on ^{12}C, ^{13}C and ^{14}N, ^{15}N from mixing, when the sample thickness is 0.3 μm and the detection angle 165° [40]. Due to the concentration of nitrogen in Kapton (7.3%) being much lower than that of carbon (69.1%), and to the isotopic abundance of ^{15}N in natural nitrogen being only 0.365%, it was not possible to detect the proton backscattering on ^{15}N.

4.3. Excitation function of the reaction $^{15}N(p, \alpha\gamma)^{12}C$

The yield curve of the $^{15}N(p, \alpha\gamma)^{12}C$ reaction, as presented in fig. 3, was measured in the same energy range as that of the yield curve of proton scattering on ^{14}N. For this experiment a 0.5 μm thick nickel foil (Goodfellow) was implanted with ^{15}N ions at a dose of 10^{17} atoms/cm^2. ^{15}N implantation was performed with 50 keV incident ions on a mean range of 54 nm and with a straggling of 24.5 nm. The integrated charge was 2 μC per point. The yield curve exhibits two well-defined resonances at 2.970 and 3.270 MeV with respective widths of 50 and 90 keV. The first resonance is about three times as high as the second one.

A typical spectrum of ^{15}N implanted in a nickel foil is shown in fig. 4. The 4.439 MeV gamma ray issuing from the reaction $^{15}N(p, \alpha\gamma)^{12}C$ is easily identified by is large peak width, which is due to the Doppler broadening caused by the alpha decay. Each gamma ray gives rise to three peaks, one corresponding to full energy and two, respectively, to the single and double escape peaks.

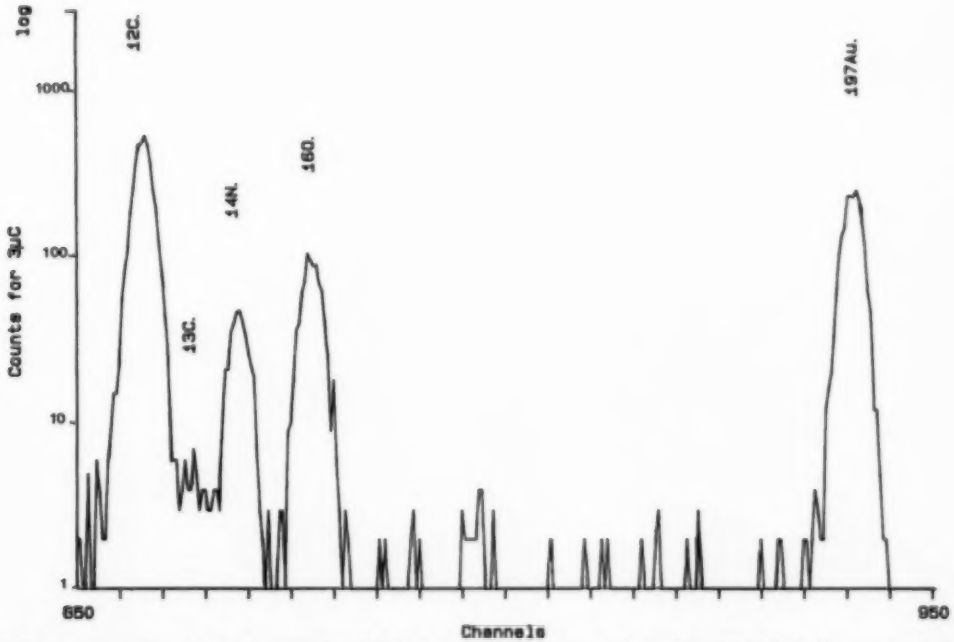

Fig. 5. The same sample as in fig. 2 was analyzed by backscattering spectrometry but with a 3.0 MeV incident proton beam. This proton energy, less favorable for detecting ^{14}N, was chosen for the simultaneous determination of ^{15}N.

4.4. Nitrogen stability under the proton beam

To check whether some migration of nitrogen occurred during the proton bombardment, we have performed 60 successive measurements of the intensity of the ^{14}N signal in Kapton and of the ^{15}N signal in nickel, at the same point in each sample under study. For each measurement, the specimens were irradiated with a 70 nC charge, a 7 nA beam intensity and a 3.185 MeV proton energy. The counting fluctuations observed could be put down to statistical error, which suggests that no nitrogen was released during analysis.

4.5. Detection limits

The detection limit was defined as the amount of the nuclide under study corresponding to three times the square root of the background. It was measured on Kapton foils. For ^{14}N, when using the 3.185 MeV resonance energy, the yield was enhanced by a factor of 5, compared with the neighboring energies. Two spectra obtained with a thin Kapton foil (0.3 μm), and using two different proton energies, are compared in figs. 2 and 5. The detection limit was estimated to be 53 pg at 3.000 MeV and 11 pg at 3.185 MeV for an integrated charge of 7 μC.

In order to estimate the detection limits for ^{15}N, we used three values of incident proton energy: 3.000, 3.185 and 3.300 MeV. The first and third values which are 30 keV above the top of the resonances of $^{15}N(p, \alpha\gamma)^{12}C$ reaction, were chosen to optimize the detection limits due to the effect of the target thickness. Energy calibration and stability of the calibration are all important to the reliability of the measurements.

On 7.5 μm thick Kapton foils, the detection limits measured with the full energy gamma ray at 4.439 MeV were respectively 19, 81 and 61 pg, for an integrated charge of 7 μC. Using a proton energy of 3.300 MeV did not improve the detection limits despite the resonance, due to the increased background.

Since the application of this technique to plants usually requires a better sensitivity for ^{15}N than for ^{14}N, we chose to perform the simultaneous detection of ^{14}N and ^{15}N with 3.000 MeV protons, thus favouring ^{15}N detection.

4.6. Application to plants and discussion

In order to illustrate the potential of the methodology described here, a plant sample (Lemna gibba L.) was analyzed. The calculation of the proton stopping

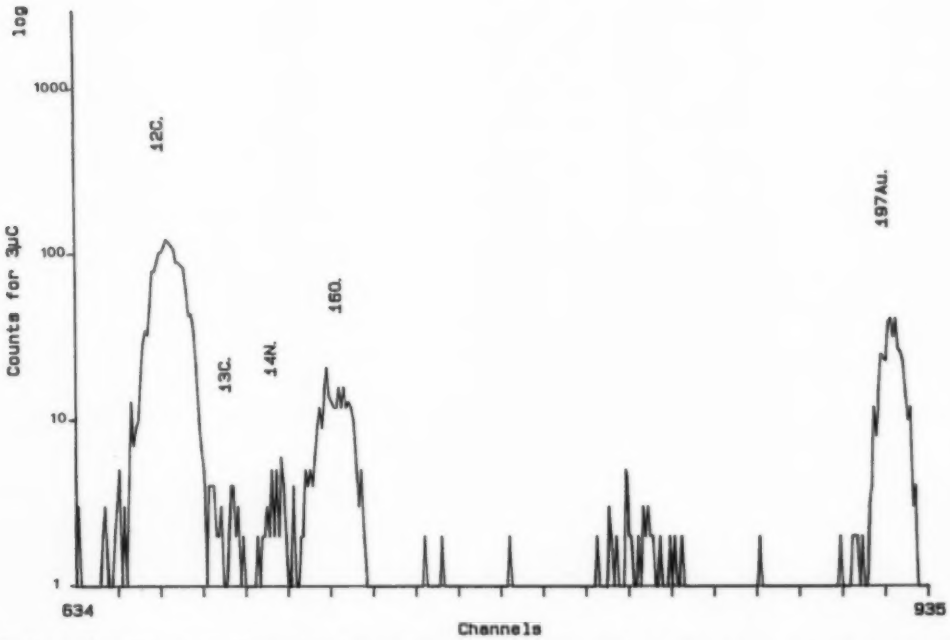

Fig. 6. Backscattering spectrum on a 2 μm thick Lemna gibba L. section, covered with a thin gold layer, obtained with a 3 MeV incident proton beam.

power in plant tissue allows us to estimate a maximum thickness for the plant section to obtain a good separation of C, N and O by backscattering spectrometry. A Lemna plant was therefore embedded in a resin and 2 μm thick sections were prepared.

A backscattering spectrum obtained on a plant section with an incident proton energy of 3 MeV is shown in fig. 6. The main elements (C, N, O) of the plant matrix are well separated and nitrogen can be determined with sufficient sensitivity. On this sample containing only natural nitrogen, a gamma spectrum for the determination of ^{15}N cannot be obtained because the amount of ^{15}N analyzed (5 pg) is too low, but the detection limits determined for ^{15}N will allow us to follow the metabolism of nitrogen in plant cells after culture of the plants on a nutrient medium containing ^{15}N nitrate. For this future experiment, we are now analyzing polymeric resins containing known nitrogen concentrations as standard samples, cut to the same thickness as the biological sections to obtain calibration curves in ^{14}N and in ^{15}N.

Acknowledgements

We are very grateful to Mr. Plantier, Institute of Nuclear Physic (Lyon), for the implantation of ^{15}N in Ni foils, and to Mr. Piccot and Mr. Martin for help with computer work.

References

[1] P. Rupnik, P. Kump, M. Budnar and I. Kreft, Nucl. Instr. and Meth. 142 (1977) 209.
[2] B. Sundquist, L. Gönczi, I.B. Koersner, R. Bergman and U. Lindh, Int. J. Appl. Radiat. and Isotopes 27 (1976) 273.
[3] P.M. Pollard, Ph.D. Thesis, University of Technology, Loughborough, England (1981).
[4] R. Fiedler and G. Proksch, Anal. Chem. Acta 78 (1975) 1.
[5] M. Chemardin and P. Gadal, Bull. E.N.S.A.I.A. XXII (1980) 61.
[6] L.H. Kroenberg, Anal. Biochem. 93 (1979) 189.
[7] L. Schaumann, P. Galle, W. Ullrich and M. Thellier, C.R. Acad. Sci. Paris 302, Ser. III, No. 3 (1986) 109.
[8] M. Thellier, C. Ripoll and J.P. Berry, Europ. Microsc. Analysis (May 1991) 9.
[9] E. Hennequin, M. Laurent-Petterson, T. Fernandez, B. Larsson and M. Thellier, J. Trace and Microprobe Techniques 7 (1990) 221.
[10] Ch. Engelmann and G. Revel, Nucl. Instr. and Meth. B54 (1991) 84.
[11] M. Mosbah, CEA Report R5456 (1986).
[12] F. Sommer and Ch. Engelmann, Nucl. Instr. and Meth. B22 (1987) 128.
[13] D. Heck, Nucl. Instr. and Meth. 197 (1982) 91.
[14] B. Sundquist, L. Gönczi, R. Bergman and U. Lindh, Int. J. Appl. Radiat. and Isotopes 25 (1974) 277.
[15] L. Gönczi, H. Berggren, R. Didriksson, B. Sundqvist and U. Lindh, Nucl. Instr. and Meth. 149 (1978) 337.
[16] J.J. Malanify and D.A. Close, Nucl. Instr. and Meth. 118 (1974) 293.
[17] A.C. Xenoulis and C.E. Douka, J. Radioanal. Chem. 54 (1979) 205.
[18] J.K. Bair, H.O. Cohn, J.D. Kington and H.B. Willard, Phys. Rev. 114 (1956) 1595.
[19] R.J. Sparks, Proc. Sec. Australian Conf. on Nuclear Techniques of Analysis (1978) p. 105.
[20] F. Bodart, G. Deconninck and J. Mengeot, IAEA-SM-227/98, 37.
[21] K. Takahiro, F. Nishiyama, T. Yamasaki and Y. Osaka, Nucl. Instr. and Meth. B51 (1990) 145.
[22] S. Matsumoto, Y. Hashimoto, H. Yamashita and I. Yamane, Nucl. Instr. and Meth. 174 (1980) 189.
[23] G. Amsel, C. Cohen and B. Maurel, Nucl. Instr. and Meth. B14 (1986) 226.
[24] L. Changgeng, W. Yongqiang, X. Jinzhong, M. Zhihui and Z. Zhihao, Vacuum 39 (1989) 119.
[25] R. Hänninen and J. Räisänen, Nucl. Instr. and Meth. B5 (1984) 34.
[26] S. Bashkin and R.R. Carlson, Phys. Rev. 106 (1957) 261.
[27] Ch. Engelmann, and M. Loeuillet, IEEE Trans. Nucl. Sci. NS-26 (1979) 1539.
[28] J.R. Bird, B.L. Campbell and P.B. Price, At. Energy Rev. 12 (1974) 275.
[29] E. Rauhala, Nucl. Instr. and Meth. B12 (1985) 447.
[30] M. Luomajärvi, E. Rauhala and M. Hautala, Nucl. Instr. and Meth. B9 (1985) 255.
[31] S. Bashkin, R.R. Carlson and R.A. Douglas, Phys. Rev. 114 (1959) 1552.
[32] R.G. Herb, D.W. Kerst, D.B. Parkinson and G.J. Plain, Phys, Rev. 55 (1939) 998.
[33] .D. Jackson and J.M. Blatt, Rev. Mod. Phys. 22 (1950) 77.
[34] G.R. Bolmgren, G.D. Freier, S.G. Likely and K.F. Famularo, Phys. Rev. 105 (1957) 210.
[35] H.L. Jackson, A.I. Galowsky, F.J. Eppling, R.W. Hill, E. Goldberg and J.R. Cameron, Phys. Rev. 89 (1953) 365.
[36] N. Jarmie and J.D. Seagrave, Los Alamos Report LA 2014 (1957).
[37] M.J.M. Pruppers, F. Zijderhand, K.M.H. Maessen, J. Bezemer, F.H.P.M. Habraken and W.F. Van der Weg, Nucl. Instr. and Meth. B15 (1986) 512.
[38] S. Bashkin, R.R. Carlson and R.A. Douglas, Phys. Rev. 114 (1959) 1543.
[39] Ch. Engelmann and J. Bardy, CEA Report R5340 (1986).
[40] W.K. Chu, J.W. Mayer and M.-A. Nicolet, Backscattering Spectrometry (Academic Press, New York, 1978) ch. 10, p. 288.
[41] A. Schardt, W.A. Fowler and C.C. Lauritsen, Phys. Rev. 86 (1952) 527.

Nuclear Instruments and Methods in Physics Research B66 (1992) 258–261
North-Holland

Nuclear Instruments & Methods in Physics Research
Section B

Location of protein bands in cellulose acetate electrophoretograms measuring nitrogen distributions by the $^{14}N(p,p'\gamma)^{14}N$ nuclear reaction

Zoltán Szökefalvi-Nagy [a] and Jyrki Räisänen [b]

[a] *Central Research Institute for Physics, Hungarian Academy of Sciences, P.O. Box 49, Budapest 114, H-1525 Hungary*
[b] *University of Helsinki, Department of Physics, Siltavuorenpenger 20 D, SF-00170 Helsinki, Finland*

The applicability of the resonance in the $^{14}N(p,p'\gamma)^{14}N$ reaction at about 4 MeV proton energy was demonstrated to detect the nitrogen content of proteins separated by nitrogen free cellulose acetate electrophoresis. Making use of a collimated proton beam of 4 MeV energy, N distributions were successfully detected along the protein bands by help of γ-ray spectroscopy. The possible uncertainties and present difficulties in the measurements as well as further perspectives are also discussed.

1. Introduction

Separation processes are key steps in the great majority of studies on molecules of biochemical or biological interest. Different versions of electrophoresis belong to the most widely used biochemical separation techniques. The term electrophoresis is used to describe the transport of a charged particle through a solvent (or supporting medium) by an electric field [1]. Molecules having different molecular weights migrate with different velocities, finally forming isolated narrow bands. The most common approaches to the detection of these bands involve the use of stains, autoradiography of radio labeled analytes, or immunoreaction with specially prepared antisera [2]. Recently the well known technique of particle induced X-ray spectrometry (PIXE) was proved to be enough sensitive to locate and even quantify bands formed in polyacrylamide gel electrophoresis (PAGE), provided that the protein of interest contains heavier metal ions in addition to the light major constituent [3]. In this measurement specially dried gel sections were directly bombarded by 3 MeV proton beam of about 10 nA intensity and X-ray spectra were taken at different gel positions. A simultaneous and independent quantitative measurement of both the total amount of protein and metal content would make this method more powerful. The protein content could be measured by determining the nitrogen content of the sample. Nitrogen, however, cannot be measured with conventional PIXE, but the strong resonance in the $^{14}N(p,p'\gamma)^{14}N$ nuclear reaction at (3903 ± 3) keV proton energy ($\Gamma = 106$ keV, $\omega\Gamma\gamma = 14$ eV) [4] offers another possibility, namely the use of the PIGE (proton induced gamma ray emission) technique [5]. Unfortunately, this idea obviously does not work with PAGE due to the large inherent nitrogen content of polyacrylamide [6]. In the case of nitrogen free supporting media, such as the routinely used cellulose acetate, this approach could be successful.

The purpose of the present study was to demonstrate the applicability of the above mentioned nuclear reaction to locate protein band in cellulose acetate supporting medium. In this paper the first exploratory measurements on native and stained transferrin, myoglobin and bovine serum albumin (BSA) samples obtained by cellulose acetate electrophoresis are reported.

2. Experimental

All of the electrophoretic sample preparations were carried out at the National Institute of Haematology and Blood Transfusion (NIHBT), Budapest, using a commercial low voltage separation apparatus and standard "Electrafor" cellulose diacetate membranes (Shandon Southern Products Ltd., Astmoor, UK). Transferrin, myoglobin and BSA stock solutions of 5% concentration were prepared and different volumes ranging from 0.15 to 1.2 μl were supplied for electrophoresis. Two parallel runs were always made, one membrane was dried on air without any further treatment, while the other one was stained for protein by Amido Black staining solution [1] and destained by 10% acetic acid. The strips selected for analysis were cut out from the dried membranes containing always eight independent strips. The photograph of both intact and bombarded stained strips is displayed in fig. 1.

0168-583X/92/$05.00 © 1992 – Elsevier Science Publishers B.V. All rights reserved

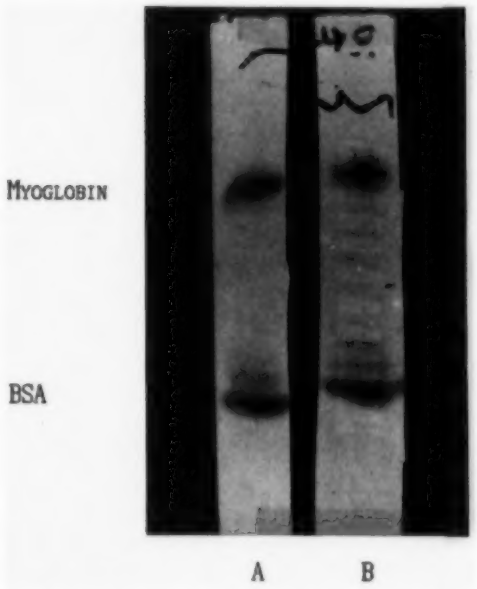

Fig. 1. Stained cellulose acetate strips (a) before and (b) after scanning by 4 MeV proton beam.

The two dark protein bands correspond to BSA and myoglobin having molecular weights of 67 and 17.5 kD, respectively.

The nitrogen analyses were performed in the Accelerator Laboratory of the University of Helsinki. The 4 MeV proton beam was provided by the 5 MV tandem accelerator EGP-10-II. Several preliminary measurements were carried out using different target chamber–detector combinations before the most suitable and convenient arrangement was found. The schematics of the final measuring setup is shown in fig. 2. The shape and size of the bombarding proton beam was

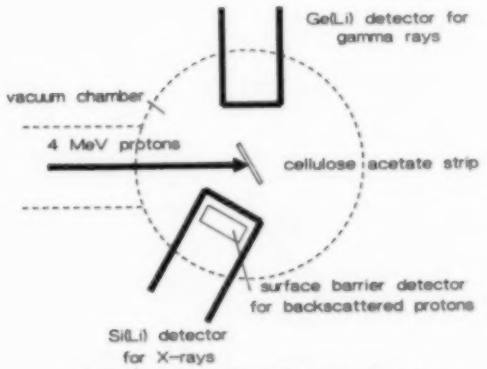

Fig. 2. The schematics of the measuring setup.

defined by the 0.5 mm wide and 4 mm long slit of a tantalum collimator positioned outside the cylindrical chamber having a deep port at 90° for the, Ge(Li) and another port at 135° for an auxiliary Si(Li) detector. Parallel to, but below this Si(Li) X-ray detector a thin surface barrier silicon detector was also added. This detector has detected the backscattered protons providing more reliable spectrum normalization. Signal processing were performed by conventional NIM electronics. The number of backscattered protons was monitored by an integral single channel analyzer–scaler combination, while γ- (and X-ray) spectra were collected by Nuclear Data and Canberra multichannel analyzers, respectively. The chamber has accommodated a vertical target holder rod making possible continuous target movement. The ~ 50 mm long and ~ 7 mm wide sample strips were glued onto a pure Al target holder frame which was fixed to the end of this rod.

3. Measurements and results

The correct proton energy setting and energy calibration of the Ge(Li) spectrometer was made by bombarding a thick bovine liver pellet observing the appearance of the γ-radiation of 2313 keV energy produced in the $^{14}N(p,p'\gamma)^{14}N$ nuclear reaction. Some estimation of the expected sensitivity could also be made from these spectra. As a result of this calculation it was obtained that protein bands containing about 0.8 μg N as a whole could be detected. In spite of the fact that even samples of the smallest supplied protein solution (0.15 μl) contain about two times more nitrogen, PIGE measurements were started on stained strips. Stained samples have two definite practical advantages. The protein bands are clearly visible making sample positioning straightforward, and the nitrogen contents of the bands are certainly higher due to the additional nitrogen atoms of the staining compound. (In real analyses, however, unstained native samples should be preferred to avoid evaluation uncertainties caused by the above mentioned N enrichment together with the possible loss of loosely bound metal ions in course of the staining procedure.) The relevant parts of γ-spectra measured in the centre of a stained myoglobin band and at a protein free position of the same strip are shown in fig. 3. The spectra clearly demonstrate that the 2313 keV γ-radiation from N has been successfully detected in the stained protein band, but on the other hand the empty cellulose acetate region contains no nitrogen. The 5 mg/cm^2 thick cellulose acetate membrane is rather fragile even in its intact form, further weakening could be ensued from the proton irradiation. In spite of low beam current (< 10 nA) and short bombarding time (~ 300 s) the definite

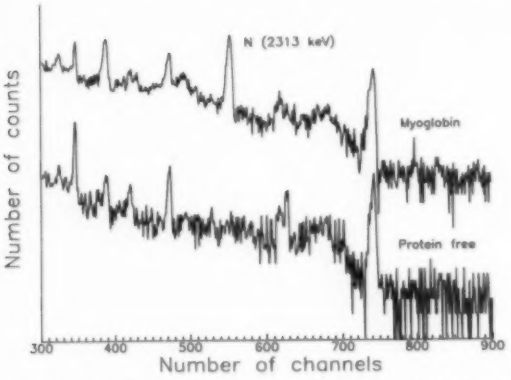

Fig. 3. γ-spectra obtained by bombarding the myoglobin band (upper curve) and a protein free region (lower curve) of a cellulose acetate electrophoretogram.

spot burned on the target indicates this danger. Repeated measurements proved that neither significant sample damage nor loss of nitrogen counts were observed when beam current density did not exceed the value of 5 nA/mm^2. If the stained proteins are uniformly distributed across the total width of the membrane, the sample should certainly be thick and no special attention should be paid to the accuracy and precision of the beam energy even in quantitative measurements. In fig. 4 the γ-ray yield of the $^{14}N(p,p'\gamma)^{14}N$ reaction is shown as a function of the bombarding proton energy. The yield was found to be constant in the 4.0–4.2 MeV proton range supporting the above mentioned assumption. In order to test whether this technique could be quantitative, measurements were made on samples containing different amounts of transferrin. The promising results are displayed in fig. 5. The N peak areas measured at the centre of each band were found to be proportional to the amount of transferrin supplied for electrophoresis. The linear relationship observed is more remarkable taking into account that the nitrogen content of a band was represented by the less accurate central position N counts instead of the integrated one along the whole band. A real scan was performed along a strip containing two protein bands (see fig. 1). The nitrogen distribution obtained is shown in fig. 6. The sharp peaks in the distribution correspond to the BSA and myoglobin bands, respectively.

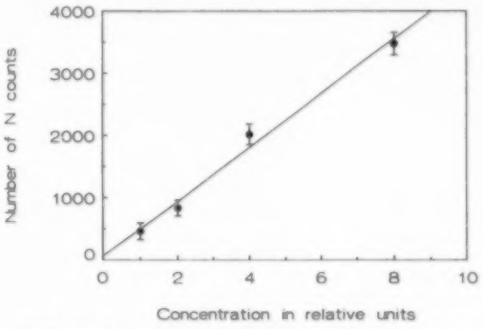

Fig. 5. Dependence of the γ-ray yield of N on the amount of transferrin supplied for electrophoresis.

In contrast to these reassuring results obtained with stained samples, measurements on unstained (native) strips have revealed serious difficulties. The basic problem is clearly seen in fig. 7 where nitrogen distributions along myoglobin bands in native and stained electrophoretograms are compared. Surprisingly enough, a more or less uniform nitrogen distribution was obtained along the unstained band. This strange result can be explained as follows. During electrophoresis the membranes were immersed in a so-called Barbital buffer [1]. Since no rinsing or washing procedures were made after electrophoresis, the nitrogen containing buffer molecules certainly remained to be absorbed in the membranes after drying. (PIGE measurements on

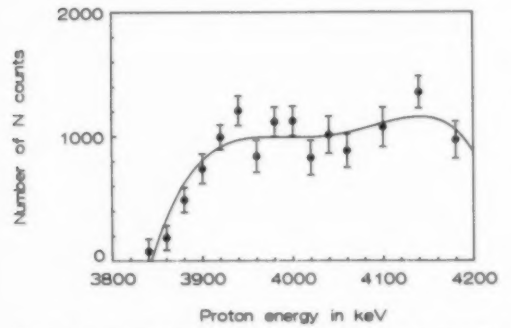

Fig. 4. The γ-ray yield of N as a function of the bombarding proton energy. (The full line is only drawn for eye guiding.)

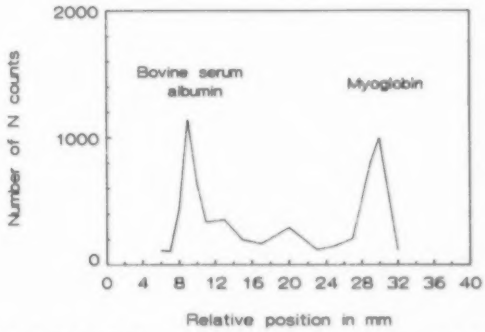

Fig. 6. N distribution along a cellulose acetate strip containing bovine serum albumin and myoglobin bands.

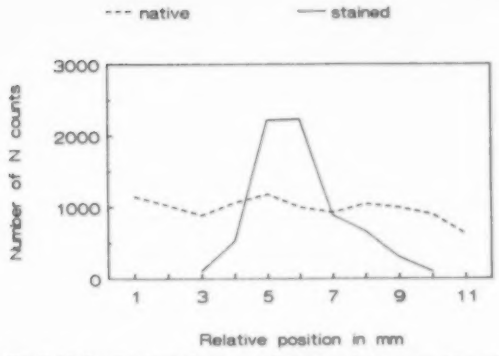

Fig. 7. N distributions along myoglobin bands in native (dotted line) and stained (full line) electrophoretograms.

blank membranes did not show nitrogen, and similar results were obtained at the protein free regions of stained strips.) In the sharp nitrogen peaks of the stained bands the nitrogen contribution from the bound dye molecules is probably dominating, while the nitrogen content of a native band was not sufficient to give rise to forming peaks over the background from the non-rinsed buffer solution. Details of the staining procedures are critical in conventional evaluation of electrophoretograms, too. The dye per protein molecule ratio, for instance is generally not known [1], therefore cumbersome standard addition is necessary even in the most common densitometric evaluations. The ultimate aim of our work is to combine PIGE and PIXE to analyze nitrogen and metal content simultaneously, but the complementing PIXE measurement could also be used to study the quantitative details of the staining.

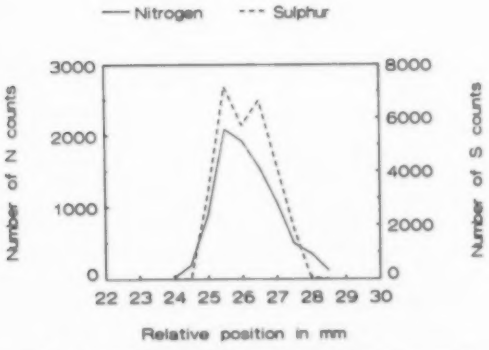

Fig. 8. N and S distributions of a stained transferrin band.

The molecules of the presently used Amido Black dye contain two sulphur atoms. These atoms can easily be detected by PIXE (see fig. 8), and the similarity of the simultaneously measured S and N distributions supports the assumption that the stained bands are mainly detected via their bound dye molecules.

4. Concluding remarks

The nuclear reaction chosen seems to be promising to locate or even quantify separated protein bands. Several problems, however, still have to be solved. Native, but washed samples have to be measured to find the minimum detectable amount of proteins. In order to use stained samples for quantitative purposes detailed experimental studies are necessary to reveal the binding characteristics of the most commonly used protein dyes with the aim of determining the excess nitrogen originated from the dye. The inclusion of simultaneous PIXE measurement will provide additional information to this staining problem, because dyes usually contain sulphur, as well.

Acknowledgements

This work was partially supported by the Hungarian National Science Foundation (OTKA) under Research Contracts nos. 1017 (OTKA 1/2) and 1819 (OTKA 1/3). The authors are indebted to Dr. J. Krammer, Dr. K. Hollós-Nagy, Mrs. J. Kopszándi and Mrs. Z. Zám for the sample preparations, one of the authors (Z.Sz.-N) is also grateful to the Finnish and Hungarian Academies for financing his visits to the University of Helsinki.

References

[1] A.T. Andrews, Electrophoresis (Clarendon, Oxford, 1988).
[2] J.W. Jorgenson, Anal. Chem. 58 (1986) 743A.
[3] Z. Szökefalvi-Nagy, I. Demeter, Cs. Bagyinka and K.L. Kovács, Nucl. Instr. and Meth. B22 (1987) 156.
[4] F. Ajzenberg-Selove, Nucl. Phys. A360 (1981) 1.
[5] R. Hänninen and J. Räisänen, Nucl. Instr. and Meth. B5 (1984) 34.
[6] Z. Szökefalvi-Nagy, Cs. Bagyinka, I. Demeter, K.L. Kovács and Le Huen Quynh, Biol. Trace Elem. Res. 26 (7) (1990) 93.

Nuclear Instruments and Methods in Physics Research B66 (1992) 262–266
North-Holland

Nuclear Instruments & Methods in Physics Research
Section B

High resolution depth profiling of nitrogen in AlN layers

G. Terwagne, S. Lucas and F. Bodart

Laboratoire d'Analyses par Réactions Nucléaires (LARN) and Institute for Studies in Interfaces Sciences (ISIS), Facultés Universitaires Notre-Dame de la Paix, 22, rue Muzet, B-5000 Namur, Belgium

Nitrogen implantation into aluminum offers many industrial applications. It has already been observed that the shape and the thickness of the layer formed depend strongly on the implantation doses for a given energy.

The aim of this work is to investigate the atomic movements of nitrogen during implantation which leads to the formation of the aluminum nitride layer. Resonant nuclear reaction analysis (RNRA) allows for the profiling of both stable nitrogen isotopes (^{15}N and ^{14}N) by means of the $^{15}N(p,\alpha\gamma)^{12}C$ reaction at 429 keV and the $^{14}N(\alpha,\gamma)^{18}F$ reaction at 1531 keV. Therefore, 100 keV $^{14}N_2^+$ and 100 keV $^{15}N_2^+$ were alternatively implanted into aluminum, and the behavior of each isotope was followed using the appropriate nuclear reaction.

The results indicate that some of the nitrogen atoms already present in the matrix are displaced and moved out the sample by the incident nitrogen atoms during the implantation. Consequently, the distribution of the original isotope is broadened due to the collisional processes occurring when nitrogen doses increase.

1. Introduction

Over the last decase, ion implantation has become a powerful tool for the modification of surface properties of materials. It is used extensively in tribology and in the particular case of nitrogen implantation into aluminum or iron, several interesting tribological modifications have been shown including hardness increase and friction reduction. In parallel with the studies of mechanical properties performed by other teams [1–3], we started, at the LARN, to study the dependence of implantation parameters (dose, temperature, flux, etc.) on the nitrogen depth profiles using resonant nuclear reactions. The use of nuclear techniques has several advantages over more conventional ones such as SIMS, Auger, etc.: it is non destructive, highly quantitative and very fast. These advantages have been successfully demonstrated in the discovery of a nitrogen surface peak [4,5].

To get nitrogen depth profiles, two nuclear reactions are used: $^{14}N(\alpha,\gamma)^{18}F$, $^{15}N(p,\alpha\gamma)^{12}C$. One particular feature of these nuclear reactions is the separate isotope measurements that can be done on nitrogen ^{15}N and ^{14}N. This is very useful for studying the atomic movements of nitrogen implanted into material. ^{14}N (or ^{15}N) can be initially implanted, followed by implantation of ^{15}N (or ^{14}N) in the same matrix. Using the above nuclear reactions, it is possible to follow the redistribution of the ^{14}N (or ^{15}N) due to ballastic process.

The aim of this paper is to present our investigation of nitrogen atomic movements in aluminum when it is implanted to high doses. The first part concerns the description of the characteristics of the nuclear reactions on ^{14}N and ^{15}N and the particular procedure to extract the actual depth profile. In the second part, we discuss the results of experiments carried out with successive implantations of ^{14}N and ^{15}N into aluminum. This experimental procedure has been used to study the formation of a buried aluminum nitride layer formed by ion implantation.

2. Nitrogen depth profile technique

^{14}N and ^{15}N distributions can be measured selectively using the two resonant nuclear reactions: $^{14}N(\alpha,\gamma)^{18}F$ and $^{15}N(p,\alpha\gamma)^{12}C$.

The capture reaction $^{14}N(\alpha,\gamma)^{18}F$ presents a narrow resonance at $E_\alpha = 1531$ keV. The natural width of this resonance Γ_R is 0.6 keV [6]. The emitted γ-rays have an energy between 3.5 and 5.3 MeV. The next resonance occurs at 1618 keV leaving a free region of bombarding energy of about 87 keV for profiling.

The ^{15}N distribution is measured using the well-known $^{15}N(p,\alpha\gamma)^{12}C$ resonant nuclear reaction which occurs at $E_p = 429$ keV. This very intense resonance is isolated and has a natural width of 120 eV [7]. Among the emitted particles, we detect the 4.43 MeV γ-rays of ^{12}C. The nearest resonance appears at 898 keV, which

0168-583X/92/$05.00 © 1992 – Elsevier Science Publishers B.V. All rights reserved

provides a large region of bombarding energy. In AlN matrix, we can profile an overall depth of a few μm under the surface.

To obtain an excitation curve at high resolution, we use an automatic energy scan system installed on our 2.5 MeV Van de Graaff accelerator [8]. The incident particle energy is varied by small increments from the resonance energy to a higher value correlated to the depth of the implanted layer.

In our system, the energy change is performed by a transverse electric field applied along the beam line and each step corresponds to a correction of the accelerator voltage of 150 eV for the proton beam at 429 keV, and of 1.5 keV for the α-particle at 1531 keV. For both nuclear reactions, γ-rays are detected in a 4 × 4 inches NaI well detector. A full description of the system can be found in ref. [9].

The depth resolution achieved for each nuclear reaction depends on the natural width of the resonance (Γ_R), the energy spread of the beam (Γ_B) and the straggling effect (Γ_S) due to unequal energy loss of identical incident particles. The latter can be estimated by a gaussian distribution at a depth greater than 400 nm for pure aluminum, and asymmetric distributions just below the surface which can be described by the Vavilov functions [10,11]. The overall effect of these three phenomena is to limit the depth resolution as observed in fig. 1. To compute the curves, we have chosen an energy spread of 400 and 1500 eV for the incident beam of our machine for proton and α-particles, respectively. It is clearly shown in fig. 1 that the depth resolution for the $^{14}N(\alpha,\gamma)^{18}F$ reaction is twice as good as for the other reaction.

As the measured excitation curve is the convolution of the actual depth profile, a function including the energy distribution of the beam ($\Gamma_B + \Gamma_S$) and the width of the nuclear reaction (Γ_R), a deconvolution procedure is necessary to obtain this actual concentration distribution. This deconvolution can be done with the help of a deconvolution program which uses a procedure developed by Deconninck et al. [12]. In addition, the depth profile is quantified by comparison with a TiN standard with a statistical accuracy on the concentration around 5%. The final accuracy on the depth profile expressed in at./cm^2 is better than 15%.

In the situation where we have to quantify the total amount of a species present in the matrix, we do not necessarily need to deconvolute the excitation curves. This amount can be roughly estimated by the following relation:

$$N = \frac{f_{St.}}{N_{St.}} \frac{1}{S_{St.}(E^*)} \Delta E \sum_{i=1}^{n} N_{\gamma i}, \qquad (1)$$

where N is the number of atoms (in 10^{17} at./cm^2), $f_{St.}$ is the atomic fraction of the measured isotope in the standard, $S_{St.}(E^*)$ is the standard stopping power in eV/(10^{15} at./cm^2) at E^*, ΔE is the energy change at each step of the profile, $\sum_{i=1}^{n} N_{\gamma i}$ is the total number of detected γ-rays in the profile (n channels), and E^* is the arithmetic mean energy over the whole energy scan.

One disadvantage of the $^{14}N(\alpha,\gamma)^{18}F$ reaction is the low cross section for the α capture reaction. To obtain an accurate profile over 2×10^{18} at./cm^2, high beam currents (≃ 500 nA) and long exposure times (≃ 2 h) are required. In this case, the accumulation of α-particles (≃ 5×10^{17} He$^+$/cm^2) into the sample can lead to the formation of blisters and radiation damages and as has been previously observed in the study of nitrogen implantation into iron [9].

However, on the opposite side, the $^{15}N(p,\alpha\gamma)^{12}C$ reaction has a high cross section which allows the measurement of a ^{15}N distribution on 200 nm in less than 10 min with a proton beam of 150 nA. Therefore, the influence of ^{14}N implantation will be preferentially studied by the measurement of the additional amount of ^{15}N.

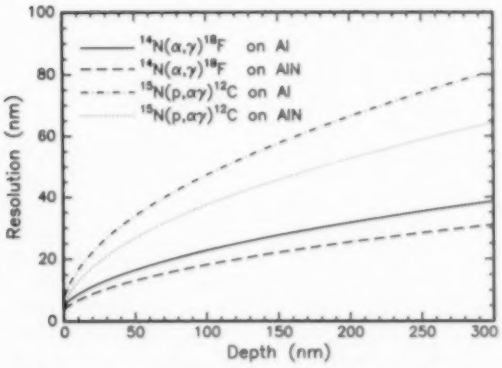

Fig. 1. Calculated depth resolution of the two nuclear reactions on ^{14}N and ^{15}N prior to the deconvolution for an aluminum and an aluminum nitride sample.

3. Study of the atomic movements of nitrogen implanted into aluminum

In previous work, we have shown that nitrogen implantation into aluminum leads to the formation of a nitride layer which is broadened when the implantation dose is very high [13,14]. It is possible to understand the mechanisms involved with the help of the isotopic selectivity of nuclear resonant reactions on ^{14}N and ^{15}N. To do this, we studied the migration of isotopic nitrogen atoms freshly implanted in a layer contaminated with nitrogen of the other isotope.

3.1. Sample preparation

Thick aluminum polycrystalline discs (15 mm diameter, 2 mm thick, 99.5% purity) were mechanically polished down to a grain size of 0.5 μm, and implanted with molecular $^{14}N_2^+$ or $^{15}N_2^+$ at 100 keV. We have shown previously that the depth distributions of the ^{14}N or ^{15}N are the same within the experimental errors [9].

For the rest of the paper, we shall define a sample preimplanted with A and postimplanted with B as a sample which is first bombarded with A ions, and afterwards implanted with B ions. In order to understand the evolution of the depth distributions during the implantation of nitrogen into aluminum, we have prepared two sets of specimens. The first one consists of a pre-implantation of ^{14}N to doses from 3.6×10^{17} to 11.4×10^{17} $^{14}N^+/cm^2$ followed by postbombardment of ^{15}N at a dose of 1.1×10^{17} $^{15}N^+/cm^2$. The second one consists of one implantation of ^{15}N at a dose of 3×10^{17} ions/cm^2, followed by postbombardment with ^{14}N to doses from 1.1×10^{17} to 11×10^{17} ions/cm^2 by steps of 1.1×10^{17} ions/cm^2. During all the implantation procedures, the temperature was monitored and maintained at 30°C and the residual vacuum was better than 2×10^{-6} Torr. The current density was about 10 μA/cm^2.

3.2. Depth distribution of the freshly implanted nitrogen

Fig. 2 shows the ^{15}N depth profile for the aluminum specimens preimplanted with different ^{14}N doses (between 3.6×10^{17} and 11.4×10^{17} $^{14}N/cm^2$), and one single implantation of ^{15}N (1.1×10^{17} $^{15}N/cm^2$). The shape of all depth distributions is nearly gaussian and we can calculate for those profiles: the projected range, the standard deviation of the distribution and the retained dose of ^{15}N (using eq. (1)). The results are presented in fig. 3. The retained dose versus the total implanted dose is constant (fig. 3c), meaning that all nitrogen post-implanted remains in the matrix whatever the dose of nitrogen already present.

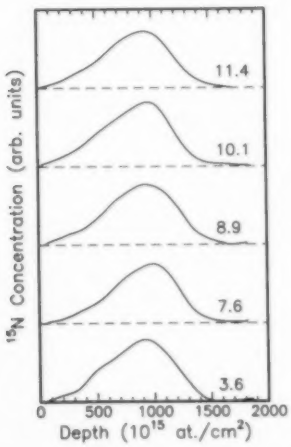

Fig. 2. Nitrogen depth profiles of ^{15}N (1.1×10^{17} $^{15}N^+/cm^2$) implanted into different aluminum matrices which have been pre-implanted to different doses of ^{14}N. The labels on the curves are the ^{14}N dose expressed in 10^{17} at./cm^2.

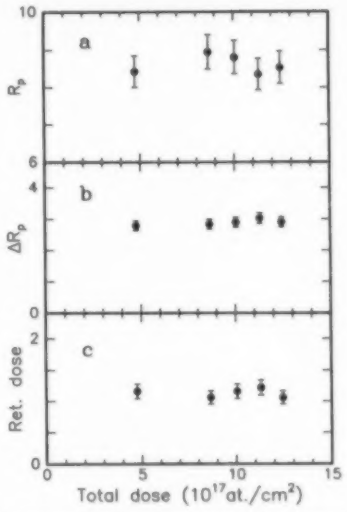

Fig. 3. Evolution of the projected range (R_p), standard deviation (ΔR_p), and retained dose of an 1.1×10^{17} $^{15}N/cm^2$ implantation into different aluminum samples containing ^{14}N. The units of the vertical scale see given in 10^{17} at./cm^2. The total dose is the sum of ^{14}N and ^{15}N.

The projected range R_p (fig. 3a) and the width ΔR_p (fig. 3b) of the distributions are also constant when the total dose is increased. Moreover, the mean projected range R_p (8.3×10^{17} at./cm^2) and the width of the distribution ΔR_p (2.8×10^{17} at./cm^2) are close to the data calculated with the TRIDYN code [15] for an aluminum nitride matrix implanted with 50 keV atomic ^{15}N ions, i.e. $R_p = 8.4\times10^{17}$ at./cm^2 and $\Delta R_p = 2.7\times10^{17}$ at./cm^2.

To prove the reliability of the profiling technique of ^{14}N and ^{15}N, we have measured successively the depth profile of ^{14}N and ^{15}N on an aluminum sample preimplanted with 8.9×10^{17} $^{14}N/cm^2$ and postbombarded with 1.1×10^{17} $^{15}N/cm^2$ (fig. 4). The measurements were performed after the implantation of both isotopes. We can observe that the ^{14}N concentration (triangles) does not exceed 40% and remains flat over the implanted layer, while the ^{15}N distribution (crosses) in fig. 4 is nearly Gaussian as discussed above.

Previous experiments have shown that the local nitrogen concentration of 50% is always reached when

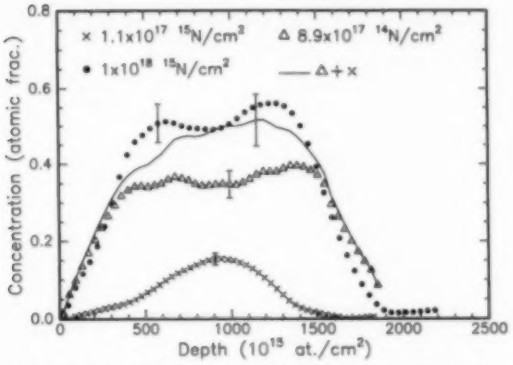

Fig. 4. Nitrogen depth profiles obtained using the two nuclear reactions, $^{14}N(\alpha,\gamma)^{18}F$ and $^{15}N(p,\alpha\gamma)^{12}C$. (+) and (△) sample pre-implanted with ^{14}N and post-implanted with ^{15}N; (———) algebraic sum of the ^{14}N and ^{15}N distributions; (●) nitrogen depth profile of a sample implanted with the same dose of ^{15}N than for the full circle profile.

the incident dose is greater than 3×10^{17} ions/cm^2 [13]. The nitrogen distribution observed for ^{14}N can be explained by a collisional process. The ^{14}N atoms are displaced by the incoming ^{15}N atoms which leads to a decrease of the maximum ^{15}N concentration and a broadening of the ^{14}N depth profile. The total amount of nitrogen present in this sample is the arithmetic sum of the ^{14}N and ^{15}N distribution (full line in fig. 4). We can compare this calculated depth profile with a ^{15}N distribution measured on a different sample, implanted with only ^{15}N at a dose equal to 10^{18} $^{15}N/cm^2$, the sum of both implantations with ^{14}N and ^{15}N in the same conditions (filled circles in fig. 4). Both depth profiles are the same within the experimental errors (10%).

3.3. Evolution of the depth distribution of nitrogen firstly implanted

By inverting the sequence of isotopic nitrogen implantations (preimplantation with ^{15}N followed by postbombardment with ^{14}N in the same conditions), we have measured the evolution of the depth profile of ^{15}N when more and more ^{14}N is implanted in the specimen and therefore the evolution of the depth distribution of ^{15}N which was firstly implanted. The results of such experiments are presented in fig. 5. The aluminum sample has been implanted first with ^{15}N at a dose of 3×10^{17} ions/cm^2. The depth profile, shown in the bottom of fig. 5, is nearly Gaussian and corresponds to the results obtained previously [13]. Afterwards, the same sample was postbombarded with different doses of ^{14}N between 1.1×10^{17} and 11×10^{17} ions/cm^2 by steps of 1.1×10^{17} $^{14}N/cm^2$ and the depth profile of ^{15}N was measured at each step.

At low doses of ^{14}N (lower than 3.3×10^{17} ions/cm^2), the depth profile of ^{15}N is broadened and for higher ^{14}N doses, the depth distribution of initially implanted nitrogen is split into two components. The first component "migrates" to the surface of the sample, whereas the second component penetrates deeper and deeper into the bulk. We can observe also in fig. 5 that the deeper component is larger than the one at the surface.

4. Discussion and conclusion

We have used the isotopic selectivity of resonant nuclear reactions on ^{14}N and ^{15}N to follow the atomic movements which take place when aluminum is bombarded with nitrogen.

An extensive description of the mechanism taking part in the formation of the buried nitride layer has already been reported elsewhere [16]. The results presented in fig. 5 suggest that when an incident nitrogen ion collides with nitrogen atoms bounded with aluminum, some of them move due to collisional processes. When they are free to move, they diffuse in the Al and AlN phases according to their diffusion coefficients. Therefore, at a depth where the number of collisional events is maximum, we expect a lower concentration for the preimplanted nitrogen distribution as observed in fig. 5. We conclude that the mechanisms taking place during broadening of the nitrogen distribution are purely ballistic and are followed by a diffu-

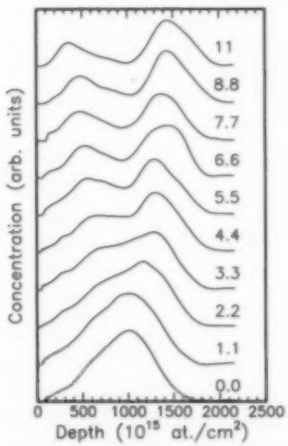

Fig. 5. Evolution of a pre-implantation of 3.3×10^{17} $^{15}N/cm^2$ into aluminum. The sample was post-implanted step by step with ^{14}N ions. The labels on the curves are the ^{14}N doses expressed in 10^{17} ions/cm^2.

sion of the delocalized atoms in either the Al or AlN phase.

Acknowledgements

The present research was supported by the Interuniversity Research Center (PAI) program of the Belgian Ministry of Science Policy. Special thanks are due to Y. Morciaux and J. Nackers for their technical support.

References

[1] G. Dearnaley, Mater. Sci. Eng. 69 (1985) 139.
[2] B. Doyle, D.M. Follstaedt and S.T. Picraux, Nucl. Instr. and Meth. B7/8 (1985) 166.
[3] B. Rauschenback, Nucl. Instr. and Meth. B15 (1986) 756.
[4] N. Moncoffre, G. Marest, S. Hiadsi and J. Tousset, Nucl. Instr. and Meth. B15 (1986) 620.
[5] G. Terwagne, M. Piette, P. Bertrand and F. Bodart, Mater. Sci. Eng. B2 (1989) 195.
[6] C.R. Gossett, Nucl. Instr. and Meth. B10/B11 (1985) 722.
[7] B. Maurel and G. Amsel, Nucl. Instr. and Meth. 218 (1983) 159.
[8] G. Amsel, F. D'Artemaere and F. Girard, Nucl. Instr. and Meth. 205 (1983) 5.
[9] G. Terwagne, M. Piette and F. Bodart, Nucl. Instr. and Meth. B19/20 (1987) 145.
[10] G. Deconninck, Introduction to Radioanalytical Physics, Akadémiai Kiado, Budapest (Elsevier, Amsterdam, 1978).
[11] P.V. Vavilov, J. Exp. Theor. Phys. 5 (1957) 749.
[12] G. Deconninck and B. Van Oystaeyen, Nucl. Instr. and Meth. 218 (1983) 165.
[13] S. Lucas, G. Terwagne and F. Bodart, Nucl. Instr. and Meth. B50 (1990) 401.
[14] S. Lucas, G. Terwagne and F. Bodart, Nucl. Instr. and Meth. B59/60 (1991) 925.
[15] W. Möller and E. Eckstein, Nucl. Instr. and Meth. B2 (1984) 814.
[16] G. Terwagne and S. Lucas, Proc. SM^{2}IB Conf., Washington, 1991, accepted for publication in Surf. Coat. Technol.

Nuclear Instruments and Methods in Physics Research B66 (1992) 267–273
North-Holland

Nuclear Instruments & Methods in Physics Research
Section B

Polarized nitrogen beams at LISOL

W. Vanderpoorten [a], J. Wouters [b], P. De Moor [a], P. Schuurmans [a], N. Severijns [b,*], J. Vanhaverbeke [a], L. Vanneste [a] and J. Vervier [b]

[a] *Instituut voor Kern- & Stralingsfysika, KUL, Celestijnenlaan 200D, B-3001 Heverlee, Belgium*
[b] *Institut de Physique Nucléaire, UCL, Chemin du Cyclotron 2, B-1348 Louvain-la-Neuve, Belgium*

A setup has been constructed which enables to produce nuclear polarized, mass separated beams at the Leuven Isotope Separator On Line (LISOL). First experiments demonstrate the existence of substantial atomic orientations, induced with both the tilted foil (TF) and the grazing surface scattering (GSS) technique. The results of the TF experiments being as good as optimal for our situation, the GSS results can still be enhanced. The setup could be used as a complementary method in material characterization studies and first experiments to use a polarized ^{13}N beam to determine site distributions of N implanted in Fe are being planned.

1. Introduction

During the past two years, a great deal of the on-line nuclear orientation activities at the Cyclotron Research Center in Louvain-la-Neuve has been devoted to the development of an in-beam nuclear orientation setup. The original motivation for this work was the orientation of short-lived radioactive nuclei which could not be oriented by the combination of very low temperatures and high electromagnetic fields (cf. conventional on line low temperature nuclear orientation (OL-LTNO) [1]) because of the too short half-life with regard to the spin lattice relaxation time and/or the too small hyperfine interaction after implantation in a host lattice. Two polarizing methods were incorporated in the already existing OL-LTNO setup, i.e. the tilted foil method (TF) [2] and the grazing surface scattering method (GSS) [3]. Both rely on the transfer of an atomic orientation to the nucleus of the beam ions via the hyperfine interaction. The atomic orientation is generated by an anisotropic Coulomb interaction at the surface of (a) a carbon foil which is tilted with respect to the beam axis in the TF geometry or (b) a Si(111) surface in the GSS geometry. Both geometries are drawn in fig. 1 and the preferential direction of the atomic angular momentum, which is generated, is indicated. These particular polarization methods were chosen because they are very polyvalent: no a-priori selection is made with regard to the atoms that can be polarized because the atomic orientation is purely a consequence of the dynamics of the beam–surface interaction.

During the development it became clear that the commonly available beam intensity at the Leuven Isotope Separator On Line (LISOL) would be the limiting factor with regard to the applicability of the technique. Indeed, although a rich variety of mass separated radioactive beams is available, the intensity of the beams is limited to typically 10^4 atoms/s, when the existing target–ionization systems are applied (FEBIAD source [4] or the Ion Guide based mass separation [5]). This beam intensity is the commonly accepted lower limit for nuclear magnetic resonance measurements on oriented nuclei (NMR/ON), which will be the first measurements to be performed. With the advent, however, of the radioactive ion beam (RIB) facility and the development of an electron cyclotron resonance (ECR) ion source at the separator – which is coupled to the RIB production area – this problem seems to be, at least partially, solved. In the present stage of development several light ion beams are available at intensities up to 10^{10} atoms/s (see below) and can be used for polarization experiments.

The tests of the polarization equipment were performed with a stable ^{14}N beam and will be described in the next section. The first radioactive beam which was successfully produced in the framework of the RIB project was a ^{13}N beam ($I = \frac{1}{2}$, $t_{1/2} = 10$ m) [12] and this beam will be used in a first polarization experiment as well. This will permit to use a great deal of the test results, obtained with ^{14}N, in the analysis. The final goal of the first experiments is then to implant a polarized ^{13}N beam in a metal host (e.g. Al) and to study site occupancies of N in this metal as a function of dose with NMR/ON.

Nitrogen implantation in Al has been studied quite extensively by Bodart and coworkers at the LARN

* Presently research associate for the NFWO/FNRS.

0168-583X/92/$05.00 © 1992 – Elsevier Science Publishers B.V. All rights reserved

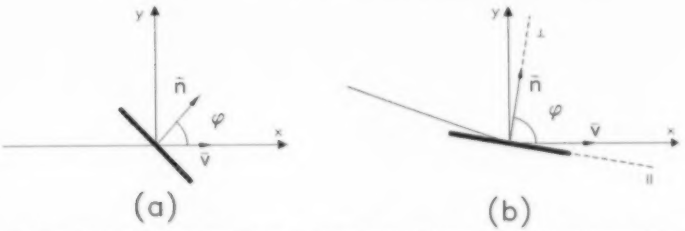

Fig. 1. Geometry of both the tilted foil (a) and grazing surface scattering (b) method. x is the beam direction and $\langle L \rangle = n \times v$ is pointing in the $-z$ direction (see text). φ is the angle between n and v.

laboratory in Namur [6]. They developed the IMPL code which calculates the ion distribution after implantation at high doses, taking into account the modification of the ion distribution during the implantation process [7]. The site occupancy, however, of N in Al is not known until now and NMR on the polarized ^{13}N nuclei probing the environment will clarify this situation. The same method has already proven to be very successful in earlier experiments with polarized ^{12}B in Al and Cu [8].

Besides NMR/ON, also cross relaxation experiments have yielded the same information, even somewhat more reliable [9]. The latter method consists in observing the changes of the polarization as a function of external magnetic field. These changes are introduced by the dipole–dipole interaction between the impurity nucleus and the host spins. Such measurements could, in principle, be carried out as well.

In the following, the experimental situation will be described in somewhat more detail together with the already obtained results.

2. The experimental setup

Fig. 2 shows an overview of the experimental area connected to the mass separator. The polarization setup is localized in the central beam line. At the end a ^{3}He–^{4}He dilution refrigerator is connected, which contains the sample. The technical details of the beam line are published elsewhere [10] and the discussion further will be limited to a short description of the experimental peculiarities.

2.1. The ion source

Recently, an ECR source has been constructed at the LISOL mass separator [11] to ionize the large number of radioactive nuclei which can be produced with the Cyclone 30 production facility [12]. The connection between the RIB production area and the ion source is made by a ± 30 m long tube constructed in 316 stainless steel, allowing the transport of several gases in an efficient way. Thus, to transport the radioactive nuclei a suitable carrier gas has to be found. Up to now already some very interesting activities are being produced: ^{13}N, ^{19}Ne, ^{15}O. Other are being tested and will be available in the near future (like e.g. ^{11}C). The ECR source will enable to ionize all these elements and the mass-separated beams can be used for polarization experiments. At present, the developments are concentrating on ^{13}N because this will be the first beam to be used. A gas handling system is incorporated as well to produce intense stable beams of several μA. After the ionization, the beams are extracted and accelerated up to 50 keV. Finally they are mass-analyzed and sent into the central beam line.

2.2. The central beam line

The beam line has a modular design to allow a certain flexibility, which is necessary because it is used for different experiments. Several beam manipulation and beam monitoring devices are incorporated [10].

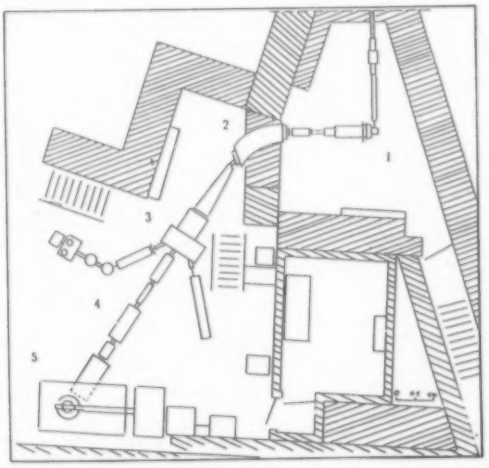

Fig. 2. Lay out of the experimental area at the mass separator, LISOL; (1) ion source area, (2) separator magnet, (3) beam switch, (4) central beam line, (5) ^{3}He–^{4}He refrigerator.

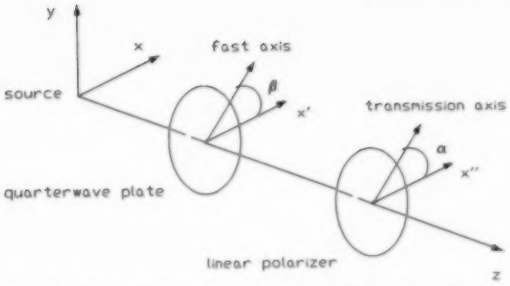

Fig. 3. Schematical drawing of the geometry of the optical detection device. In the complete system, some lenses and an interference filter are incorporated as well. The light is detected with a cooled Burle C31034 photomultiplier. For details see ref. [10].

The actual design is sufficient for our needs as was also shown by calculations with OOTRAN [13]. The beam line contains two interaction chambers, where the polarization is induced. This will be discussed in the next section. Each chamber can be connected to the ^{3}He–^{4}He dilution refrigerator. To reduce the amount of heat radiation from the beam line and to obtain the shortest possible distance between the interaction zone and the implantation zone, a very short side access (92 mm at room temperature) has been constructed [10]. The side access still allows an implantation temperature of about 15 mK. This is established by a series of diaphragms which reduce substantially the amount of heat radiation onto the cooled sample. The reduction of the distance between interaction region and implantation site is necessary for the most important factor of loss of intensity in the transport being the beam divergence after the interaction, due to the low energy of the beam. Since plans are being made to build a postaccelerator, this problem might be solved in the future.

2.3. The refrigerator

A dilution refrigerator is placed at the end of the beam line. Samples can be top loaded during its operation. At the sample site a static magnetic field up to 1.5 T can be applied with a superconducting magnet. An NMR coil is incorporated as well. Several side accesses have already been designed to allow continuous implantation in a cooled sample. The usual side access, with a length at room temperature of ± 1 m and which enables to reach implantation temperatures < 10 mK had to replaced by the very short side access, already mentioned before. Further, solid state detectors, i.e. 1 mm thick Si-PIPS particle detectors are mounted, which can operate at 4 K without window between source and detector. These detectors will be used to measure directly the nuclear polarization of the radioactive beams by means of the anisotropically emitted nuclear radiation. Since β-decay will be the main decay mode, β-particles can be detected at 0 and 180°, with respect to the external field simultaneously, ensuring a high sensitivity to the first order nuclear polarization.

3. Generation and detection of atomic orientation

3.1. Generation of the atomic orientation

3.1.1. General aspects

In the in-beam methods that will be discussed here, the atomic orientation is generated by an anisotropic Coulomb interaction of the beam ions with a surface which is tilted with respect to the beam axis. This tilting of the surface introduces a noncylindrical symmetry and is as such responsible for the generation of mainly a first order orientation of the electronic shell. A net angular momentum $\langle \boldsymbol{L} \rangle = \boldsymbol{n} \times \boldsymbol{v}$ is created, with $\boldsymbol{n}$ pointing parallel to the normal on the surface and $\boldsymbol{v}$ the beam velocity. Several authors have already tried to explain this effect and a first explanation was given by Schröder and Kupfer [14] who introduced the so-called e^--density gradient model, which describes the orientation as originating from the interaction of the beam ions with the e^--density gradient at the solid's surface. More specifically for the GSS geometry, Winter and coworkers [15] adopted current charge exchange models [16] to explain the observed orientation. They can explain the observed charge state distributions and polarizations fairly well, taking into account resonant electron transfer between the atom and the metal of which the Fermi sphere is Galilean-transformed. They show that long range interactions are very important for the production of the observed effects. This is an important difference compared to the TF geometry in which the velocity component, perpendicular to the surface, is generally larger ($v_\perp \propto v \sin \varphi$, in fig. 1). A detailed study, however, is not available for the TF case although it would be very interesting to see whether these long range interactions play a role in the TF geometry as well. With their model, also the energy dependence of the atomic orientation – in the case of N – could be explained, the result being that the polarization increased with the beam velocity up to a saturation value and the maximum of the nuclear polarization was reached at an energy of 50 keV [17].

3.1.2. The tilted foil setup

The TF method consists in directing a collimated beam through a foil which is tilted with respect to the beam axis. A major problem in our situation was that to transmit in a reasonable way a 50 keV beam of mass

≃ 15 through a carbon foil, the thickness of this foil is limited to ±150 Å which is about 4 μg/cm². Self supporting C-foils of 2–3 μg/cm² can be manufactured now and are mounted on stainless steel frames. The self supporting area is 20–50 mm². The foils stay intact for several hours in beams of 20–50 nA. The fragility of the foils is a major obstruction to use more intense beams and this is a drawback for the optical measurements (see further). When polarizing radioactive beams, however, the intensities are smaller and the problem of fragility should be less important.

The foils are subsequently mounted in a rotatable foil holder for normalisation purposes. In the actual construction including the small side access, the distance between the foil and the implantation zone is ±170 mm. Transmission tests showed that a transport efficiency of a few percent is possible in this configuration. Finally a diaphragm in front of the foil should enable to avoid as much as possible instrumental asymmetries.

3.1.3. The grazing surface scattering setup

For practical reasons the tilt angle in the TF geometry is limited to 60–70 degrees, although the first experiments in this regard showed that the degree of atomic polarization increases with the the sinc of the tilt angle [18], favouring large tilt angles. As a consequence of this result, Andrä proposed the scattering technique as an extension to larger angles and indeed larger polarizations were observed [3]. The method consists in the specular reflection of the beam at grazing incidence on very flat surfaces. The technique is slightly more complicated than the TF method and more extreme experimental conditions are required to obtain the best results. The considerable gain in polarization, however, makes it worthwile to try the effort.

A schematic drawing of the interaction region in this geometry is shown in fig. 4, together with the angular distribution of scattered $^{14}N^{+}$ ions. The latter was measured with a 1 mm ∅ needle at 60 mm behind the crystal. The measurements with the ECR source were performed at 40 kV. The angular distribution can thus still be somewhat enhanced going to 50 kV. The scattering crystal is attached to a high precision x–y–z positioner and the scattering angle can be adjusted with a precision of 0.25°, which is satisfying for our purposes. The first experiments were performed with a Si(100) crystal [10] but with a new Si(111) crystal having a better surface granularity (< 10 nm), higher polarizations were obtained (cf. next section). The positioner is mounted in an UHV chamber and during the experiments the on-line vacuum was 5×10^{-9} mbar. The improvement of the differential pumping should still lower this value since off-line a vacuum of 3×10^{-10} mbar is easily obtained.

3.2. Detection of atomic orientation

The atomic orientation is measured via the Stokes parameters of the fluorescence light of the excited atoms after the interaction. The Stokes parameters S, C, M, I define in a complete way the state of a light

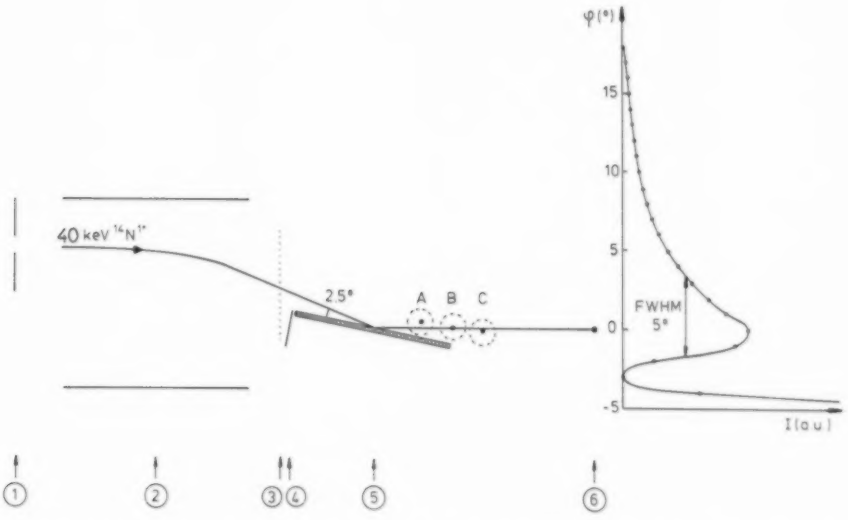

Fig. 4. Drawing of the interaction zone for the GSS geometry; (1) diaphragm, (2) deflection plates, (3) two-dimensional wire grid, (4) beam "skimmer", (5) scattering crystal, (6) 1 mm ∅ needle. The angular distribution of the scattered ions, measured with the needle, is also indicated.

beam. The parameter S is sensitive to the amount of circular polarization in the light beam and hence to the amount of first order polarization of the light source [19]. An optical detection system has been designed for this reason (fig. 4). It consists essentially of a quarter wave plate and a linear analyzer. The intensity of the light, measured as a function of the positions of these two optical instruments, can be written as (cf. fig. 3 for the definition of the angles) [20]:

$$I_t(\alpha,\beta) = \frac{1}{2}\left[I + \left(\frac{M}{2}\cos 2\alpha + \frac{C}{2}\sin 2\alpha\right)\right] + \frac{S}{2}\sin(2\alpha - 2\beta) + \frac{1}{4}\left[(M\cos 2\alpha - C\sin 2\alpha)\cos 4\beta + (M\sin 2\alpha + C\cos 2\alpha)\sin 4\beta\right]. \quad (1)$$

The second term contains the parameter S and has a periodicity 2β. This means that circularly polarized light, when measured with this system, will give rise to a π-periodic signal as a function of the position of the $\lambda/4$-plate. A $\pi/2$ periodicity is significant for linear polarization. The relative Stokes parameter, S/I, can be easily measured as

$$S/I = \frac{I(\alpha^-) - I(\sigma^+)}{I(\sigma^-) + I(\sigma^+)},$$

where $I(\sigma^*)$ are the intensities with positive and negative helicity. When the detection geometry is as described in fig. 3 (x is beam axis), S/I is proportional to the atomic orientation ($^L\rho_0^1/{}^L\rho_0^0$, as defined in ref. [21]), neglecting a small alignment contribution. To select the proper optical transition no monochromator was used for intensity reasons. Narrow band interference filters were used instead. As a consequence, the measured signal is an average over the hyperfine multiplets.

The first experiments were done with a $^{14}N^+$ beam from a FEBIAD source. Recently the ECR source has become operational and this source has been used from then on. The circular polarization of the NII $2s^2 2p3p^3D - 2s^2 2p3d^3F^0$ and of the NII $2s^2 2p3s^3P - 2s^2 2p3p^3D$ optical transitions was measured for both methods with filters, having a FWHM of 10 nm, centered respectively at 500 nm and 570 nm. The light was detected with a cooled RCA-31034 photomultiplier operating in single photon counting mode. After background subtraction, the light intensity was normalized in both cases to the beam current measured immediately behind the interaction zone.

3.2.1. The tilted foil result

Fig. 5 shows the intensity variation of the 500 nm fluorescence light after the interaction of a 50 keV ^{14}N beam with a 2 $\mu g/cm^2$ C-foil. From these data a value of $S/I = 10.2(1.9)$ is extracted. This result has to be compared with previous results polarizing a ^{15}N beam at 300 keV [22] with a single foil and it is seen that our value is in good agreement. This indicates that the optimum is practically reached unless more foils can be used but this is mainly an energy problem.

The fragility of the foils prohibited to use more than 50 nA of primary beam, resulting in a relatively small signal to background ratio ($\approx 1:1$). This explains part of the large error bars. The other part was due to an

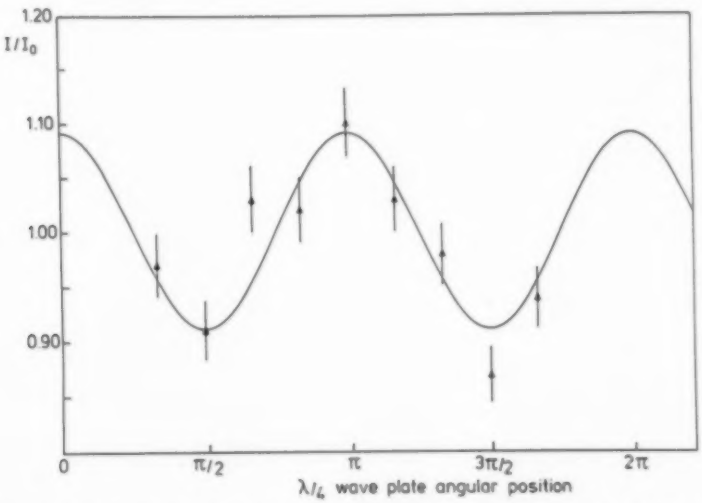

Fig. 5. Intensity as a function of quarter wave plate position for the TF case, as measured with the optical detection device of fig. 3. A value $S/I = 10.2(1.9)$ is deduced.

inaccurate normalization procedure at that time, a problem being solved at the moment. The use of 90% transparent wire grids to mount the foils should increase their strength. Tests to enhance the signal/noise ratio this way are now being carried out.

3.2.2. The grazing surface scattering result

Fig. 6 shows the result of the most recent scattering experiments. The three different curves were measured at three different positions (cf. fig. 4). Position C is relevant for the beam which is implanted, since at positions A and B there is a large contribution to the light intensity from atoms which have made violent collisions with a.o. adsorbates on the surface and which are consequently scattered at higher angles [23]. The degree of polarization of these atoms is in general smaller compared to the atoms which are specularly scattered. The value of 20% which has been obtained is already a good result since the measurements were done without cleaning the surface. This value is then to be compared with other measurements on "dirty" surfaces, obtaining about the same value [24]. Cleaning of the surface enhances considerably the amount of atomic orientation after GSS. S/I values of 63% are reported for the 567 nm line after sputtering of the surface. For cleaning purposes, a heating coil is installed under the crystal, to bake out the crystal in situ. A procedure of sputtering and heating is known to give good results. These tests will be done in the near future.

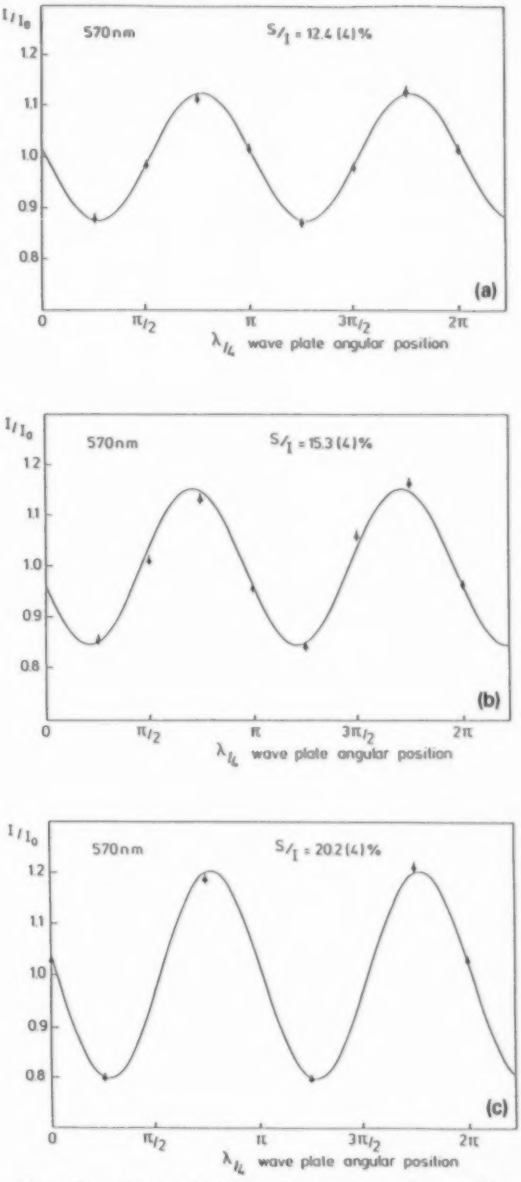

Fig. 6. Intensity as a function of quarter wave plate position for the GSS geometry, measured at three different positions relative to the crystal;cf. also fig. 4.

4. The nuclear polarization

The final goal of the development is the production of a nuclear polarized beam. The nuclear polarization is established by the hyperfine interaction. In low external field, the atomic angular momentum $\boldsymbol{J}$ and the nuclear spin $\boldsymbol{I}$ couple to a total angular momentum $\boldsymbol{F} = \boldsymbol{I} + \boldsymbol{J}$. $\boldsymbol{F}$ being conserved during the motion of the atom, $\boldsymbol{I}$ and $\boldsymbol{J}$ precess around $\boldsymbol{F}$ and this induces a polarization of $\boldsymbol{I}$ if $\boldsymbol{J}$ has been polarized before. The transfer efficiency depend on the angular momenta involved and the amount of nuclear orientation, $P_1 = \langle I_z \rangle / I$ is proportional to the induced atomic orientation and one can write [21]

$$P_1 = \sqrt{(I+1)/3I}\,\frac{{}^{\mathrm{I}}\rho_0^1}{{}^{\mathrm{I}}\rho_0^0} = C\,\frac{{}^{\mathrm{L}}\rho_0^1}{{}^{\mathrm{L}}\rho_0^0},$$

in terms of the tensorial components of the atomic and nuclear density matrices. The factor can be calculated for a given (LS)J term and a given nuclear spin [25]. Table 1 lists some of these factors. As can be seen is the transfer process most efficient when $I = J$ and no transfer occurs from a $J = 0$, atomic S-state.

The transfer of polarization goes via the stable and metastable terms of the atom. In the case of nitrogen, at low excitation energies, the relevant terms are the $2p^3\ {}^4S$, ${}^2P$ and ${}^2D$ terms. As can be seen from table 1, transfer coefficients of ± 0.3 can be expected. The

Table 1
Time-integrated transfer coefficients for transfer of atomic polarization to the nucleus [25]

		$I = 1/2$	$I = 1$
(LS)	^{x}S	0	0
	^{1}P	0.363	0.5
	^{1}D	0.226	0.353
	^{2}P	0.306	0.356
	^{2}D	0.217	0.335
	^{3}P	0.170	0.252
	^{3}D	0.198	0.299
	^{4}P	0.080	0.152

transfer is slightly less efficient for ^{13}N ($I = 1/2$) compared to ^{14}N ($I = 1$). This means that at present we are, in principle, capable of producing beams with $P_1 \cong 6$–7% with the GSS method, which could be enhanced after a proper surface treatment. Tests to detect this polarization are now being performed.

The potentiality to use the present technique in material characterization studies is then to be compared with other techniques. The degree of polarization, especially in the GSS case, should be high enough to perform reliable NMR/ON measurements. It can be remarked in this regard that NMR measurements have already been reported using degrees of polarization of the order of 1% [26].

Further, a big advantage is, as already stated, the large variety of possible probe nuclei. This could stimulate systematic studies of materials, doped with impurities as a function of valence number. This way, the present technique could be a nice enrichment in this field of research.

Acknowledgments

We acknowledge motivating discussions with H. Winter and we are very grateful for the Si(111) crystal he provided us with. The evaporator assistance of P. Demaret is also very much appreciated. Finally we want to thank the separator people for the help in preparing the beams. This work is financially supported by the Nationaal Fonds voor Wetenschappelijk Onderzoek and the Interuniversitair Instituut voor Kernwetenschappen.

References

[1] D. Vandeplassche et al., Nucl.Instr. and Meth. 186 (1981) 211.
Nuclear Orientation and Nuclei far from Stability, eds. B.I. Deutch and L. Vanneste (J.C. Baltzer A.G., Basel, Switzerland, 1985).
[2] H.G. Berry et al. Phys. Rev. Lett. 32 (1974) 751.
[3] H.J. Andrä, Phys. Lett. 54A 1975) 315.
[4] M. Huyse et al., Nucl. Instr. and Meth. B26 1987) 105.
[5] K. Deneffe et al., Nucl. Instr. and Meth. B26 (1987) 399.
[6] a.o. S. Lucas et al., Nucl. Instr. and Meth. B50 (1990) 401.
[7] M. Piette et al., J. Mater. Sci. Eng. B2 (1989) 189.
[8] R.E. Mc Donald and T.K. Mc Nab, Phys. Lett. 63A (1977) 177.
T.K. Mc Nab and R.E. Mc Donald, Phys. Rev. B13 (1976) 34.
[9] E. Jäger et al., Phys. Lett. A123 (1987) 39.
[10] W. Vanderpoorten et al., Vacuum 42 (1991) 789.
J. Wouters et al., Nucl. Instr. and Meth. B61 (1991) 348.
[11] P. Decrock et al., Rev. Sci. Instrum. 61 (1990) 279.
[12] M. Arnould et al., Nucl. Instr. and Meth. B40/41 (1989) 489.
[13] G. Vancraeynest, Master's Degree Thesis, K.U. Leuven, 1989, not published.
[14] H. Schröder and E. Kupfer, Z. Phys. A279 (1976) 13.
[15] H.J. Andrä et al., Nucl. Instr. and Meth. B9 (1986) 572.
[16] J.N.M. Van Wunnik et al., Surf. Sci. 108 (1981) 253.
[17] H. Winter, private communication.
[18] K.G.Berry, L.J. Curtis and R.M. Schektman, Phys. Rev. Lett. 34 (1975) 509.
[19] M. Born and W. Wolf, Principles of Optics (Pergamon, Oxford, 1970).
[20] H.G. Berry, G. Gabrielse and A.E. Livingston, Appl. Opt. 16 (1977) 3200.
[21] H. Winter, R. Zimny, Coherence in Atomic Collision Physics, ed. H.J. Beyer (Plenum, New York, 1988).
[22] B.I. Deutch, Hyperfine Interactions 24–26 (1985) 251.
[23] C. Marsch and H. Winter, Z. Phys. D18 (1991) 25.
[24] H. Winter, P.H. Heckman and B. Raith, Hyperfine Interactions 8 (1980) 261.
[25] H. Winter, Habilitationsschrift, Westfälischen Wilhelms-Universität, Münster (1987).
[26] W.F. Rogers et al., Phys. Lett. B177 (1986) 293.

Nuclear Instruments and Methods in Physics Research B66 (1992) 274–279
North-Holland

Nuclear Instruments & Methods in Physics Research
Section B

Oxygen measurements by elastic backscattering

K.K. Bourdelle [1]

Physics Laboratory, H.C. Ørsted Institute, University of Copenhagen, Universitetsparken 5, DK-2100 Copenhagen Ø, Denmark

The conventional Rutherford backscattering (RBS) method is often not sensitive enough for detection of oxygen when heavy elements are present. In recent years it has been found that the technique of elastic backscattering of protons and ^{4}He ions can provide advantages that are not attainable by RBS. The author considers the use of protons and ^{4}He ions in the energy regions of 1.0–4.0 MeV and 3.0–22.0 MeV, correspondingly, for oxygen profiling and lattice location in Si, YBaCuO, etc. Data on elastic scattering cross sections are reviewed. The most important characteristics of elastic backscattering such as minimum detectable concentration of oxygen, depth resolution, maximum depth of analysis are being addressed for the above-mentioned projectiles in various substrates. A comparison is made for the use of wide and narrow resonances. The problems associated with experimental data analysis are reviewed, and computer simulations including such effects as energy straggling, multiple scattering and possible Bragg rule violation are discussed. Estimations of the accuracy of elastic backscattering analysis are given. A comparison with RBS technique is made.

1. Introduction

The determination of the oxygen content in materials has been an important subject in materials analysis for a long time. The recent discovery of new high-T_c superconducting compounds with critical temperatures around 90 K and with properties that critically depend on their oxygen content has stirred a renewed interest in that field. There are a number of techniques available for oxygen detection in materials such as secondary ion mass spectrometry (SIMS), Auger electron spectroscopy (AES), etc. The main disadvantage of these methods is the necessity of the use of standards with compositions as close as possible to those of the materials in order to quantify the results of measurements. Furthermore in AES analysis, for example the chemical binding effects may influence outcome of the experiments.

The employment of methods based on the use of charge particle accelerators may often help to escape such difficulties and at the same time provides possibilities for nondestructive oxygen depth profiling. For instance, the conventional Rutherford backscattering (RBS) technique in combination with channeling analysis gives a wide variety of information (both chemical composition and crystal structure) about target materials, but in most cases, when heavy elements are present, it is not sensitive enough for detection of oxygen. This is due to a low kinematic factor and RBS cross section for oxygen [1]. Nuclear reaction analysis (NRA) is an attractive alternative to RBS for the analysis of light elements [2]. The principal advantage of using a nuclear reaction is that the detected reaction product usually has an energy greater than that of the projectiles elastically backscattered from the heavier matrix. The signal from the oxygen is thus confined to a region of the energy spectrum where the background normally is low, and NRA technique therefore provides enhanced sensitivity in comparison with RBS analysis. However, the NRA technique often requires a rather sophisticated data analysis of the experimental spectra and the use of standards is also often necessary.

An another alternative to RBS is based on the technique of elastic backscattering of protons and ^{4}He ions, and it has found wide application for detection of oxygen in recent years. This technique is based on the concept that when the energy of the analyzing beam exceeds a certain threshold, the cross sections of elastic scattering of protons and ^{4}He ions on ^{16}O becomes up to 1–2 orders of magnitude larger than corresponding values for Rutherford backscattering cross sections. In the present paper the main characteristics of this method will be discussed and the applications of the method will be reviewed.

2. RBS detection of oxygen, possibilities and limitations

Sigmon et al. [3] have shown that the minimum number of oxygen atoms on a silicon substrate that can be detected with channeled 2 MeV ^{4}He ions, is about

[1] On leave from: Institute of Nuclear Physics, Moscow State University, 119899 Moscow, USSR.

0168-583X/92/$05.00 © 1992 – Elsevier Science Publishers B.V. All rights reserved

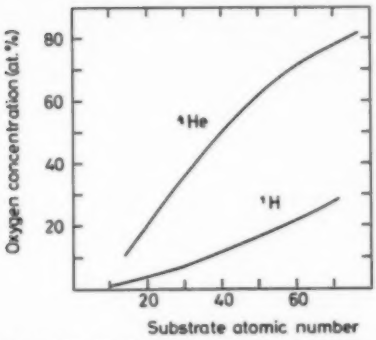

Fig. 1. Detection sensitivity of oxygen as a bulk impurity in a heavier elemental substrate by 2 MeV ^{4}He and 2.3 MeV ^{1}H backscattering (refs. [4,11]).

$(3–4) \times 10^{15}$ atoms/cm^2. Rauhala [4] has investigated the minimum detectable bulk concentration of oxygen by application of computer synthesis of RBS spectra. The results of this analysis are shown in fig. 1. The values of concentrations were found by varying the assumed target composition in order to produce a synthesized spectrum with a minimum detectable leading edge height of the oxygen $H_O = 3\sqrt{H_{sub}}$, where H_{sub} is the yield (10^4 counts/channel) from the heavier substrate element at the leading edge position of the oxygen.

In ref. [5] oxygen depth profiling in thermally-oxidized Ni where no direct oxygen signal could be detected has been performed in the following way. RBS spectra for pure Ni and for oxidized samples have been measured using the same dose of the analyzing ions. Due to additional energy losses of analyzing ions on the oxygen atoms the RBS yield for the oxidized samples was found to be less than for pure Ni. The stoichiometry of the Ni oxide has been determined from a comparison of these yields. This last method is illustrated in fig. 2, where RBS spectra from $Y_1Ba_2Cu_3O_{7-x}$ compounds synthesized by the program SANDV [6] are shown for $x = 0$ and 1. The data in fig. 1 indicate that for $Y_1Ba_2Cu_3O_7$ the bulk concentration of oxygen (54 at.%) slightly exceeds the minimum detection limit (about 50 at.%). The difference in the RBS yields for the heavier elements of about 4% seen in fig. 2 indicates the possibility of determining the bulk oxygen concentration in homogeneous $Y_1Ba_2Cu_3O_{7-x}$ samples with accuracy of about ±15%. However, to obtain such an accuracy a very precise beam current integration is needed.

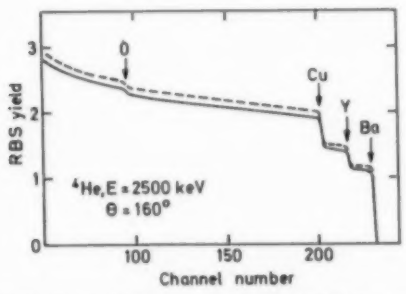

Fig. 2. Synthesized RBS spectra for 2.5 MeV ^{4}He ions incident on $Y_1Ba_2Cu_3O_{7-x}$ samples for $x = 0$ (full line) and $x = 1$ (dashed line).

3. Elastic backscattering analysis of oxygen

3.1. Proton backscattering in non-Rutherford region

Until recently proton beams are seldomly used in backscattering analysis. In spite of significantly larger accessible depths and smaller values of the straggling than for He ions, the method has some severe disadvatages, e.g. poorer depth resolution and lower mass resolution. In an early study [7] the broad and strong ^{16}O(p, p) elastic scattering resonance around 4 MeV (data on cross section see, e.g. ref. [8]) was used to determine the ^{16}O content in implanted and oxidized Ti films. In ref. [9] protons with $E = 3$ MeV (laboratory scattering angle $\theta = 165°$) permitted a determination of the oxygen concentration as a function of depth for anodized Al layers thicker than those which can be measured using standard RBS analysis.

The renewed interest in oxygen detection using protons beams originates mainly from the works of the Helsinki group [10,11]. In ref. [10] the ^{16}O(p, p) elastic scattering cross section σ_p has been remeasured (fig. 3). For $\theta = 170°$ the H-ion energy E was varied be-

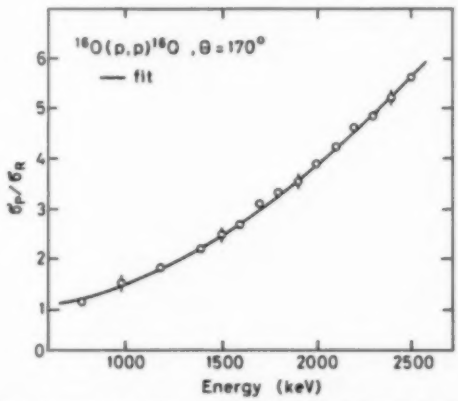

Fig. 3. Correction factor σ_p/σ_R for the ^{1}H Rutherford differential scattering cross section of oxygen as a function of ion energy [10]; (○) experimental, (———) fit to experimental data.

tween 0.8 and 2.5 MeV, and the angular dependence of σ_p for four different energies ($E = 1.8$–2.5 MeV) was investigated in the range $\theta = 80$–$170°$. The authors of ref. [10] have provided simple polynomial fits to their experimental data (fig. 3), which allows direct and easy use of the formulae for $\sigma_p(E, \theta)$ in computer programs treatment of the spectra. It is seen from fig. 3 that σ_p at a bombarding energy of 2.3 MeV is enhanced by a factor of 5 relative to the Rutherford cross section. The detection sensitivity of oxygen is then also enhanced by factor of 5 to 6 in comparison with the use of ^{4}He ions (fig. 1). In ref. [11] the method was applied to determination of the oxygen depth profile in YBaCuO samples. The analysis was made from the measurement of two spectra, using 2.0 MeV ^{4}He and 2.3 MeV H ions, respectively. The relative Y, Ba and Cu concentrations were determined from the corresponding heights of the leading edges of the ^{4}He spectrum (see e.g. fig. 2). The concentrations of all the elements (Y, Ba, Cu and O) were then extracted from the ^{1}H spectrum by fitting the yield from oxygen relative to the total yield from the heavier elements. The authors of ref. [11] claim that the accuracy of the method was better than $\pm 6\%$ for oxygen and the meaningful analysis of the concentration distribution could be made for depths up to 10 μm.

In ref. [12] the composition of polysilicon films (mixtures of Si, O and N) deposited on silicon substrates has been analysed by proton backscattering ($E = 1.68$ MeV). Sensitivities in determination of the concentrations of the light elements were found to be 2%. Yu et al. [13] have found that the use of 1.6 MeV H ions instead of a 2.0 MeV ^{4}He beam will decrease the error in determination of the stoichiometry of silicon dioxide deposited on GaAs from 25 to 9%. Other authors [14] used the 2 MeV protons to determine the concentration of oxygen in YBaCuO compounds, and in ref. [15] the oxygen content in CuO has been obtained with H ions in the energy region between 0.6 and 2.0 MeV.

3.2. Oxygen detection by elastic backscattering of ^{4}He ions

In conventional RBS analysis the energy of ^{4}He ions usually does not exceed values of 1–2 MeV. The backscattering cross sections in that energy region on elements heavier than carbon are very close to the Rutherford cross sections σ_R and they may be calculated accurately. The use of higher energy ^{4}He ions gives such advantages as enhanced mass resolution and reduction in overlap of backscattering peaks from different elements of the targets, which are particularly important in analysis of thin films composition.

Early experimental data [16] show that ^{4}He elastic backscattering cross sections on ^{16}O σ_α begin to deviate from σ_R at ^{4}He laboratory energy of about 2.2 MeV. The results of recent measurements of σ_α in the region of $E = 1.8$–5.0 MeV for $\theta = 170.5°$ are shown in fig. 4 [17]. It is seen from the figure that σ_α has a strong narrow resonance around 3 MeV. The data on the parameters of this resonance, i.e. energy of the resonance E_r, the half-width Γ and the maximum cross section σ_α^{max}, obtained so far are contradictory [16–20]. However, the data of refs. [16] and [17] in the resonance region are similar and provide the following parameters: $E_r = 3045 \pm 10$ keV, $\Gamma = 10$ keV and $E_r = 3034 \pm 4$ keV, $\Gamma = 10$ keV, respectively. Today most research is based on the the application of the data and calculations from ref. [16], which have recently been incorporated into computer programs for treatment of the spectra [21,22].

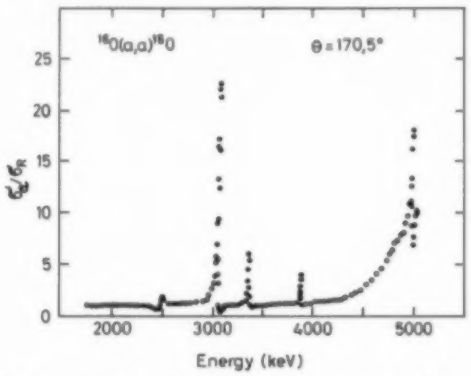

Fig. 4. Measured elastic scattering cross section for ^{4}He ions on oxygen for ^{4}He laboratory energies between 1.8 and 5.0 MeV, expressed in terms of the Rutherford cross section σ_R at the same energies [17].

The bibliography of application of this resonance for oxygen depth profiling counts many publications [19,21,22–33]. Wang et al. [19] have found that the sensitivity for detection of oxygen in crystalline silicon by this resonance is enhanced by a factor of 10 as compared with conventional RBS analysis, i.e. it is about 2×10^{14} at/cm^2. The depth profiling of oxygen was performed with a resolution of about 30 nm in Si (the depth resolution is defined mainly by the half-width of the resonance). Using glancing angle geometry, Kotai et al. [25] have achieved the best depth resolution of 6 nm (in silicon) obtained near the surface region. Besides, for thin oxide layers, the sensitivity was found to increase with increasing tilt angle of the target.

In refs. [23,30–33] this resonance has been employed to study the oxygen content in various metal oxides, and in refs. [21,22,29,32] the YBaCuO compounds have been investigated. Blanpain et al. [21] claim that a typical accuracy for quantifying oxygen concentration in high-Z oxides is about 5%. The dam-

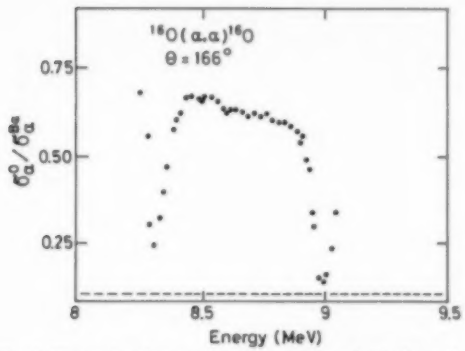

Fig. 5. The ratio of scattering cross sections for helium elastic scattering from ^{16}O and Ba as a function of incident ion energy. The dashed line shows the ratio of the Rutherford scattering cross sections [39].

age accumulation in the oxygen sublattice of ion-implanted single crystal garnets has been studied by the channeling method ($E = 3.1$ MeV) [26]. Stoffel et al. [29] determined the channeling characteristics (minimum normalized yield, half-angle of channeling) for the oxygen sublattice in an $Y_1Ba_2Cu_3O_{7-x}$ single crystal.

In ref. [34] ^4He beams with energies of 3.8 and 4.7 MeV, respectively, (see fig. 4) have been used to obtain oxygen content in various high-T_c superconducting thin films. Boyarko et al. [35] have determined the relative concentrations of all elements in epitaxial garnet films ($Y_3Fe_5O_{12}$, $Gd_3Ga_5O_{12}$, etc.) by using a ^4He beam with $E = 4.5$–5 MeV.

The cross section for elastic scattering of ^4He ion on ^{16}O between 5 and 12 MeV have been measured by several groups over the past 30 years [36–38]. A number of sharp resonances were found in that energy region. An energy range associated with a relatively constant cross section was found between 8.4 and 8.8 MeV, with dips on both sides [36–38]. Recently σ_α has been remeasured by two groups for $E = 8.2$–9.1 MeV [39,40]. Scattering angles were $\theta = 166°$ [39] and $\theta = 160°$ [40]. The results of ref. [39] shown in fig. 5 disagree significantly in absolute values of σ_α with data from ref. [40]. This is obviously connected with the difference in θ and is documented from data on the angular dependence of σ_α [37]. For a ^4He energy of 8.8 MeV σ_α was observed to be about 25 times greater than σ_R for oxygen (fig. 5). The above energy region for ^4He ions has found an application in the analysis of high-T_c superconductors [39–41]. The absolute uncertainty in determination of the relative concentration of oxygen has been reported to be ±4% [41].

Differential cross sections for the elastic scattering of ^4He ions by ^{16}O have been measured in refs. [42] and [43] in the ranges from 14.0 to 22.7 MeV and from 20.0 to 24.5 MeV, correspondingly. Several resonances have been observed. The cross sections were found to be strongly enhanced for large scattering angles, and for $E = 20$–22 MeV (this region corresponds to the broad resonance) they are about three orders of magnitude larger than those for scattering on medium mass nuclei. Kryuchkov et al. [44] have reviewed the application of ^4He beams with $E = 21.4$ MeV ($\theta = 175°$) for oxygen detection. They report a depth resolution of 80–150 nm and a maximum depth of analysis of 5–10 μm for targets with masses in the range 40 to 140 amu. The detection sensitivity of oxygen as surface impurity has been calculated using the relation $A_O \geq (2\text{–}3) \times \sqrt{A_{sub}}$, where A_O is the peak area under the oxygen signal and A_{sub} is the area under the signal for the substrate at the position of the oxygen peak. The calculated (solid line) and experimental (dots) values of the detection sensitivity are shown in fig. 6. The larger values of the experimental data in comparison with calculations originate from contributions from nonelastically scattered ^4He ions and protons emitted in (α, p) reactions on substrate nuclei. It is seen from fig. 6, that a significant increase in sensitivity in comparison with e.g. resonance at 3.04 MeV is achieved for substrates with a mass of about 100 amu.

3.3. Experimental data analysis

The oxygen concentration is extracted from the elastic backscattering spectra by use of several methods. In refs. [39–41], where the broad $^{16}O(\alpha, \alpha)$ resonance around 8.8 MeV has been used, the oxygen content has been determined from the ratio of the surface yields for oxygen and heavier elements of the substrate. The depth profiling by narrow $^{16}O(\alpha, \alpha)$ resonance around 3.04 MeV is provided using the well known stoichiometry of the silicon oxide sample as

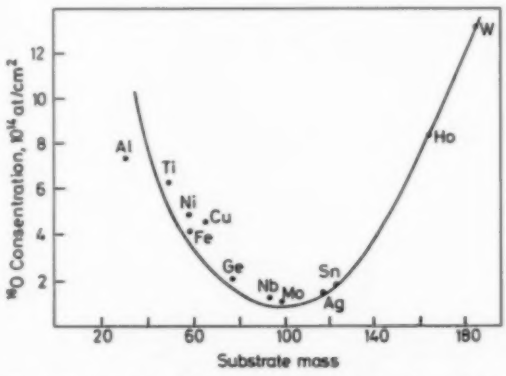

Fig. 6. Detection sensitivity of oxygen as a surface impurity in a heavier substrate, measured by elastic backscattering of ^4He ions with an energy of 21.4 MeV [44].

standard. The oxygen atomic abundance of the investigated sample is determined from the ratio of the normalized resonant yields in the sample of depth x, to that of SiO_2 standard of uniform concentration [30,32].

The opportunity of the computer reduction of the experimental data provides clear advantages, and the corrected oxygen cross sections for the elastic scattering of protons [10] have recently been incorporated into the computer programs [11,15]. In ref. [11] the good agreement between experimental and computer simulated spectra for YBaCuO samples was obtained. However, in ref. [15], where CuO samples were investigated, the agreement was rather poor for the low energy parts of the spectra. The simulated curves were found to uderestimate the experimental yields. The authors of ref. [15] associated this discrepancy with probable violation of the Bragg rule for heavy-metal oxides such as CuO.

The RUMP program [45] has been modified to handle various nuclear resonances (including the $^{16}O(\alpha, \alpha)$ resonance around 3.04 MeV), and it has been successfully applied to the investigation of metal oxides [21]. In spite of the reasonable agreement of experimental and simulated sprectra, a correct description of the background at lower energies was problematic because of such effects as energy straggling, multiple scattering and slit scattering. The correct description of energy straggling is critical for oxygen depth profiling with the use of narrow resonances.

Acknowledgements

It is a pleasure to acknowledge Dr. N.G. Chechenin and Dr. V.V. Zatekin for beneficial discussions. The author is indebted to Dr. E. Johnson for careful reading of the manuscript and useful comments.

References

[1] W.K. Chu, J.W. Mayer and M.A. Nicolet, Backscattering Spectrometry (Academic Press, New York, 1978).
[2] J.R. Bird, in: Ion Beams for Materials Analysis, eds. J.R. Bird and J.S. Williams (Academic Press, Sydney, 1989).
[3] T.W. Sigmon, W.K. Chu, E. Lugujjo and J.W. Mayer, Appl. Phys. Lett. 24 (1974) 105.
[4] E. Rauhala, J. Appl. Phys. 62 (1987) 2140.
[5] H.Y. Graham and M. Cohen, J. Electrochem. Soc. 119 (1972) 879.
[6] V.V. Zatekin and N.G. Chechenin, Algoritmy i Programmy, VINITI Centre, No. 7 (1989), in Russian
[7] G. Dearnly, P.D. Goode, W.S. Miller and J.F. Turner, in: Ion Implantation in Semiconductors and Other Materials, ed. B.L. Crowder (Plenum, New York, 1973) p.405.
[8] Ion Beam Handbook for Material Analysis, eds. J.W. Mayer and E. Rimini (Academic Press, New York, 1977).
[9] C.R. Gossett, Nucl. Instr. and Meth. 168 (1980) 151.
[10] M. Luomajarvi, E. Rauhala and M. Hautala, Nucl. Instr. and Meth. B9 (1985) 255.
[11] E. Rauhala, J. Keikonen and R. Jarvinen, Appl. Phys. Lett. 52 (1988) 1520.
[12] C. Jeynes, R.E. Miles, M. Bolt and J.G. Simmons, Nucl. Instr. and Meth. B15 (1986) 275.
[13] K.M. Yu, J.M. Jaklevic and E.E. Haller, Nucl. Instr. and Meth. B30 (1988) 551.
[14] N.R. Parikh, Z.H. Zhang, M.L. Swanson, M. Yu and W.K. Chu, Mater. Res. Soc. Symp. Proc. 128 (1989) 375.
[15] T. Xie, S.R. Ryan and H.J. Fiscbeck, Nucl. Instr. and Meth. B40/41 (1989) 766.
[16] J.R. Cameron, Phys. Rev. 90 (1953) 839.
[17] J.A. Leavitt, L.C. McIntyre, M.D. Ashbaugh, J.G. Oder, Z. Lin and B. Dezfouly-Arjomandy, Nucl. Instr. and Meth. B44 (1990) 260.
[18] J.D. MacArthur, H.C. Evans, J.R. Leslie and H.B. Mak, Phys. Rev. C22 (1980) 356.
[19] Z.L. Wang, J.F.M. Westendorp and F.W. Saris, Nucl. Instr. and Meth. 211 (1983) 193.
[20] J.A. Leavitt, P. Stoss, D.B. Cooper, J.L. Seerveld, L.C. McIntyre, R.E. Davis, S. Gutierrez and T.M. Reith, Nucl. Instr. and Meth. B15 (1986) 296.
[21] B. Blanpain, P. Revesz, L.R. Doolittle, K.H. Purser and J.W. Mayer, Nucl. Instr. and Meth. B34 (1988) 459.
[22] P. Berning and R.E. Benenson, Nucl. Instr. and Meth. B36 (1989) 335.
[23] G. Mezey, J. Gyulai, T. Nagy, E. Kotai and A. Manuaba, in: Ion Beam Surface Layer Analysis, eds. O. Meyer, G. Linker and F. Kappeler (Plenum, New York, 1976) p.303.
[24] S. Petersson, H. Norde, G. Possnert and B. Orre, Nucl. Instr. and Meth. 149 (1978) 285.
[25] E. Kotai, G. Mezey, T. Lohner, A. Manuaba, F. Paszti and J. Gyulai, Nucl. Instr. and Meth. 180 (1981) 619.
[26] G. Battistig, E.F. Kennedy, P. Revesz, J. Gyulai, G. Kadar, J. Gyimesi, G. Drozdy and G. Vizkelethy, Nucl. Instr. and Meth. B15 (1986) 372.
[27] S.H. Sie, D.R. McKenzie, G.B. Smith and C.G. Ryan, Nucl. Instr. and Meth. 15 (1986) 525.
[28] P.Person, A. Chevarier, P. Clechet, D. Lamouche, J.R. Martin and M. Stern, Nucl. Instr. and Meth. B15 (1986) 425.
[29] N.G. Stoffel, P.A. Morris, W.A. Bonner and B.J. Wilkens, Phys. Rev. B37 (1988) 2297.
[30] B.K. Pathaik, C.V. Barros Leite, G.B. Baptista, E.A. Schweikert, D.L. Cocke, L. Quinones and N. Magnussen, Nucl. Instr. and Meth. B35 (1988) 159.
[31] H.A. Bas, R. Pretorius, Nucl. Instr. and Meth. B35 (1988) 488.
[32] F.L. Freire, C.V. Barros Leite, B.K. Patnaik, G.B. Baptista, D. Naugle, R.K. Pandey and W. Kirk, J. Appl. Phys. 65 (1989) 400.
[33] J. Li, L.J. Matienzo, P. Revesz, Gy. Vizkelethy, S.Q. Wang, J.J. Kaufman and J.W. Mayer, Nucl. Instr. and Meth. B46 (1990) 287.
[34] J.A. Leavitt and L.C. McIntyre, Nucl. Instr. and Meth. B40/41 (1989) 797.
[35] E.Yu. Boyarko, I.E. Burkova, I.E. Evdokimov, O.N.

Dikarev, Yu.Yu. Kryuchkov and V.M. Malyutin, Sov. Tech. Phys. Lett. 15 (1989) 443.
[36] W.E. Hunt, M.K. Mehta and R.H. Davis, Phys. Rev. 160 (1967) 782.
[37] J. John, J.P. Aldridge and R.H. Davis, Phys. Rev. 181 (1969) 1455.
[38] O. Hausser, A.J. Ferguson, A.B. McDonald, I.M. Szoghy, T.K. Alexander and D.L. Disdier, Nucl. Phys. A179 (1972) 465.
[39] J.A. Martin, M. Nastasi, J.R. Tesmer and C.J. Maggiore, Appl. Phys. Lett. 52 (1988) 2177.
[40] S. Wu. H. Cheng, C. Zhang, X. Yao, G. Zhao, F. Yang and Z. Hua, Nucl. Instr. and Meth. B45 (1990) 227.
[41] J.C. Barbour, B.L. Doyle and S.M. Myers, Phys. Rev. B38 (1988) 7005.
[42] J.C. Jodogne, P.C. Macq and J. Steyaert, Phys. Lett. 2 (1962) 325.
[43] M. Takeda, S. Kato and T. Yamazaki, J. Phys. Soc. Japan 30 (1971) 56.
[44] Yu. Yu. Kryuchkov and I.P. Chernov, in: Ion Beams and Solids, vol. 2, ed. Yu.V. Martyenko (VINITI, Moscow, 1990), in Russian.
[45] L.R. Doolittle, Nucl. Instr. and Meth. B9 (1985) 344.

Nuclear Instruments and Methods in Physics Research B66 (1992) 280–282
North-Holland

Nuclear Instruments & Methods in Physics Research
Section B

Location of oxygen in leached UO_2 single crystals by resonant scattering of He ions

A. Turos [a,1], Hj. Matzke [a], J. Chaumont [b] and L. Thomé [b]

[a] *European Institute for Transuranium Elements, JRC, CEC, 7500 Karlsruhe, Germany*
[b] *Centre de Spectrométrie Nucléaire et de Spectrométrie de Masse, IN2P3-CNRS, 91405 Orsay Campus, France*

The resonant $^{16}O(\alpha, \alpha)^{16}O$ scattering was successfully used to determine the depth and lattice location of O atoms in UO_2 single crystals subjected to leaching. The results indicate that the transformed region has a O content ~20% higher than that in the virgin crystal. Moreover, the channeling dips for oxygen could be measured precisely enough to show that the lattice positions of oxygen atoms in the leached layer differ from those in the bulk material, as would be expected for the formation of higher oxides (U_3O_7, U_2O_5).

1. Introduction

Interaction of UO_2 with water leads to the formation of nonstoichiometric oxides and is of interest both in mineralogy and for the technique of disposal of spent nuclear fuel elements [1].

In the present study, UO_2 single crystals were leached in distilled water between room temperature and 200°C for different time periods. Rutherford backscattering of 2 MeV He^+-ions, with and without the channeling technique, revealed important changes in the surface layer of leached UO_2 single crystals. A peak of displaced U atoms was observed in the aligned spectra. This was attributed to the transformation of UO_2 into higher oxides of compositions between U_3O_7 and U_2O_5 [2].

The kinetics of U_3O_7 or U_2O_5 layer formation was indicated to be either controlled by the reaction at the UO_2/U_3O_7–U_2O_5 interface or by oxygen diffusion through the oxidized layer, depending on the pH value of water. The aim of the present work was to determine the depth and lattice location of O atoms in UO_2 subjected to leaching by using the resonant $^{16}O(\alpha, \alpha)^{16}O$ scattering associated to channeling.

2. Experimental

The samples used were single-crystalline UO_2 wafers of ⟨100⟩ orientation. They were preannealed to adjust the oxygen to metal ratio to the stoichiometric value of 2. Leaching was performed in water of different pH value in autoclaves between room temperature and 200°C.

The leached samples were analyzed by resonant $^{16}O(\alpha, \alpha)^{16}O$ scattering in ⟨100⟩ and random directions with the ARAMIS accelerator of the CSNSM-Orsay [3]. The energy of the He^{2+} beam was varied between 3.105 and 3.140 MeV in order to displace the sharp resonance at 3.045 MeV throughout the transformed layer. A counting rate lower than 2500 counts/s(corresponding to a beam current lower than 10 nA) was always used to prevent pile-up effects. The energy resolution was about 15 keV.

3. Results and discussion

One of the most important problems related to the leaching of UO_2 is the nature of the transformed surface layers. It is commonly accepted that the displacements of U atoms as seen in the channeling spectra are produced by the transformation of UO_2 to a higher U-oxide. The possibility of water incorporation can be ruled out for low temperatures or short leaching times. The hydrogen content of the layers has been measured before and after leaching using the ERDA technique [1]. Within the measurement accuracy, no uptake of hydrogen was noted. However, the direct proof can only be provided by the measurement of the oxygen content in the transformed layer.

This is a rather difficult task because of the very high atomic number of uranium. The ratio of the Rutherford scattering cross-sections for U and O amounts to: $(92/8)^2 = 132$. In such a case it is impossible to detect an O peak on the very intense back-

[1] On leave from the Soltan Institute for Nuclear Studies, Warsaw, Poland.

0168-583X/92/$05.00 © 1992 – Elsevier Science Publishers B.V. All rights reserved

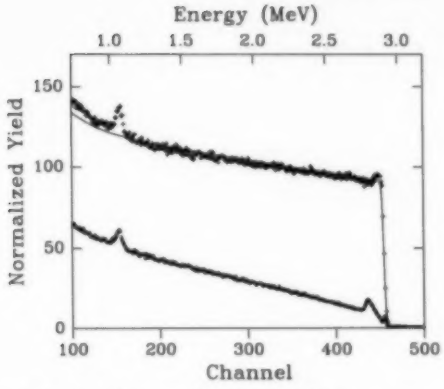

Fig. 1. Random (+) and ⟨100⟩ aligned (●) spectra measured at the incident ^{4}He energy of 3.105 MeV for a UO_2 single crystal subjected to leaching (200°C, 2 h, water of pH = 6).

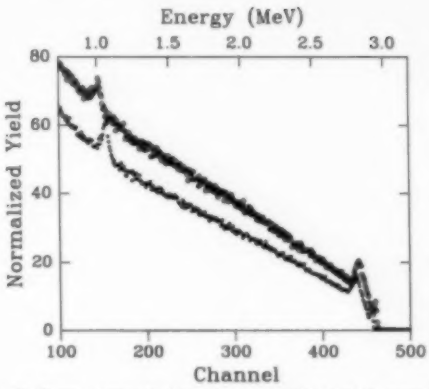

Fig. 2. Comparison of aligned spectra obtained at two different ^{4}He energies: 3.105 (●) and 3.140 (○) MeV for the leached UO_2 single crystal of fig. 1.

ground due to the scattering from U atoms. Also, nuclear reactions do not provide an acceptable tool. They do not offer a good depth resolution (e.g. the $^{16}O(d, p)^{17}O$ reaction) or require enrichment in $^{18}O(^{18}O(p, \alpha)^{15}N$ reaction). The only promising solution was to use the resonant $^{16}O(\alpha, \alpha)^{16}O$ scattering which presents a sharp resonance at 3.045 MeV with a scattering cross-section approximately 25 times higher than that for Rutherford scattering [4,5].

Fig. 1 provides a rather spectacular example of the application of resonant scattering for oxygen analysis in UO_2. Random and aligned spectra are shown for a ⟨100⟩ UO_2 single crystal leached at 200°C for 2 h in water of pH = 6. The energy of the incident ^{4}He ions was 3.105 MeV and exceeded the resonance energy by 60 keV. In such a case, the resonant scattering takes place at a depth corresponding to the maximum in the distribution curve of displaced U atoms. It is worth noting that quite a high intensity is obtained for the O peak in both random and aligned spectra. The intensity of the O peak in the aligned spectrum is comparable to that of the "damage peak" produced by displaced U atoms. The solid line following the experimental random spectrum is the result of the RUMP code simulation. A small step exists just below the leading edge of the experimental O peak. It represents the intensity of oxygen scattering in the absence of the resonant scattering.

In order to compare the influence of leaching on the O content and to determine the lattice location of the excess O atoms, another set of spectra was recorded at an incident ^{4}He energy of 3.140 MeV. At this energy, resonant scattering takes place just behind the transformed region. Fig. 2 shows the comparison of aligned spectra obtained at the two different energies: 3.105 and 3.140 MeV. It should be pointed out that the U front moves towards higher energies with increasing incident energy whereas the O peak is shifted in the opposite direction. The latter effect is due to the fact that the resonant scattering occurs at a greater depth. The integration of the numbers of counts in the oxygen peak of the random spectra corresponding to the different regions of the crystal indicates an increase of $(22 \pm 8\%)$ of the amount of O in the transformed layer compared to the nondistorted one.

The angular distribution of the scattering yield (channeling dip) can be obtained from such experiments by the appropriate choice of energy regions (windows) in the RBS spectra. A first window was located around the maximum of the U peak in the aligned spectrum whereas a second one was placed just

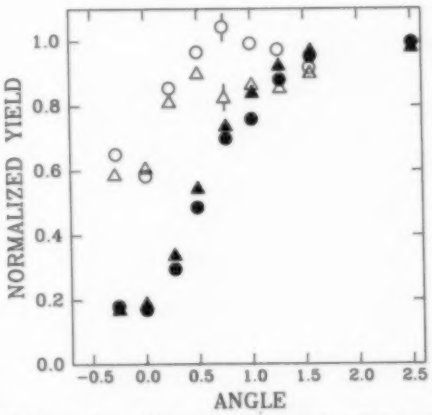

Fig. 3. Comparison of the channeling uranium (full symbols) and oxygen (open symbols) dips for virgin (circles) and transformed (triangles) regions of the leached UO_2 single crystal of fig. 1.

behind this peak (i.e. in a region of the crystal not affected by the leaching process). The O peak intensity was also measured in the two regions after subtraction of the background due to U scattering. Fig. 3 shows that the U dips do not reveal important differences whereas a substantial reduction of the scattering yield for the transformed region as compared to the virgin one was observed in the O dip for tilt angles ranging from 0.5 to 1.5°.

4. Conclusion

The results presented in this paper allow to conclude that the resonant $^{16}O(\alpha, \alpha)^{16}O$ scattering is a very efficient technique to determine the amount of oxygen and its location with respect to the surface of leached UO_2. It was shown that (a) the amount of O in the transformed region of a single crystal leached in water at pH = 6, 200°C, 2 h, is about 20% higher than that in the virgin crystal; and (b) the lattice positions of O in the transformed region of this crystal differ from those in the virgin one. However, the shape of the dips and the scattering yields are strongly dependent on the tilt plane in which the dip is measured. Thus, the precise evaluation of channeling dips is only possible by computer simulation. Because of the complex structure of atomic rows in compound crystals (UO_2, U_3O_7, U_2O_5) only computer codes based on the Monte Carlo method are appropriate. Relevant calculations will be done later.

References

[1] Hj. Matzke, G. Della Mea, F.Z.L. Freire and V. Rigato, Nucl. Instr. and Meth. B45 (1990) 194.
[2] Hj. Matzke and A. Turos, Solid State Ionics, in press.
[3] E. Cottereau, J. Camplan, J. Chaumont, R. Meunier and H. Bernas, Nucl. Instr. and Meth. B45 (1990) 293.
[4] B. Blanpain, P. Revesz, L.R. Doolittle, K.H. Purser and J.W. Mayer, Nucl. Instr. and Meth. B34 (1988) 459.
[5] P. Berning and R.E. Benenson, Nucl. Instr. and Meth. B36 (1989) 335.

Nuclear Instruments and Methods in Physics Research B66 (1992) 283–291
North-Holland

Nuclear Instruments & Methods in Physics Research
Section B

Depth profiling of light-Z elements with elastic resonances: Oxygen profiling with the 3.045 MeV $^{16}O(\alpha, \alpha)^{16}O$ resonance

W. De Coster, B. Brijs, J. Goemans and W. Vandervorst
IMEC vzw., Kapeldreef 75, B-3001 Leuven, Belgium

Depth profiling of light elements in high-Z substrates can be done with RBS using elastic resonances. With the resonant signal in the backscattered spectrum several parameters can be associated such as height, position, yield and FWHM. The dependence of the parameters on incident beam energy will be described. The influence of the energy spread and of the detector resolution, which limits the use and accuracy, is discussed. Computer calculations are given to establish the validity of the model and to illustrate the restrictions. A methodology which uses the different parameters is proposed. Experimental results are shown for the depth profiling of oxygen in 20 nm, 89 nm and 500 nm thick oxides with the elastic 3.045 MeV $^{16}O(\alpha, \alpha)^{16}O$ resonance.

1. Introduction

Detection of light elements ($Z < 10$) is very important in material analysis. Among the available analysis technique Rutherford backscattering spectroscopy (RBS) is interesting because it provides a quantitative depth profile without inducing major damage to the material [1]. However, due to low scattering cross sections for light elements, conventional RBS (2 MeV ^4He) is hampered by a low sensitivity for these elements. This is especially the case for the detection of light elements in high-Z substrates since then the low light-element signal is superimposed on a high "background" signal from the substrate.

While keeping the quantitative nature, depth profiling of light elements can be done by RBS with higher sensitivity by employing nuclear resonances in the elastic scattering cross sections. Although the background of the substrate is still present, the signal to background ratio can be highly enhanced. Compared to nuclear reaction analysis (NRA), where the background can be totally discarded in some cases, resonant RBS has the advantage that the same equipment as for conventional RBS is sufficient.

Oxygen is among the most important light elements in semiconductor industry. It is frequently present in processing, sometimes as an unwanted contaminant, other times as a necessary element to achieve the desired material properties. Depth profiling of oxygen by resonant RBS can be performed by employing the $^{16}O(\alpha, \alpha)^{16}O$ resonance at 3.045 MeV [2]. This resonance has recently been applied for the analysis of the oxygen contents in high-Z materials [3,4]. Compared to high energy scattering at 8.8 MeV where non-Rutherford scattering gives also an enhanced sensitivity for ^{16}O [5], the 3.045 MeV resonance has a better depth resolution and at these moderate energies, which can still be reached with small accelerators, no resonances will occur in substrates with $Z > 12$ (magnesium) [6].

Two methods can be applied for quantitative depth profiling when employing resonances. One method is to derive the depth distribution from the measured spectra by spectrum synthesis: An assumed sample composition is iteratively modified to obtain a good match of the predicted and the measured energy spectrum. This method, which is commonly used with conventional RBS analysis, has the disadvantage that it will become very difficult for complex samples and quickly varying cross sections. The second method is resonance scanning whereby the incident beam energy is step by step incremented to obtain resonant scattering at an ever increasing depth. The area of the resonance peak is measured at each energy to obtain a yield versus beam energy curve. This curve can then be converted to a concentration versus depth profile of the resonant element.

The second method requires that a sequence of RBS spectra is taken, out of which each time the yield is extracted. We will discuss here other parameters that can be extracted from the spectrum and which carry also information about the sample. The dependence of these parameters on the incident beam energy will be discussed. It will be shown that energy spread and especially the detector resolution tend to set a limit to the application of the parameters other than the yield.

0168-583X/92/$05.00 © 1992 – Elsevier Science Publishers B.V. All rights reserved

2. Resonance probing

2.1. Parameters

A commonly used resonance to "probe" the oxygen content is the well known $^{16}O(\alpha, \alpha)^{16}O$ resonance at $E_R \simeq 3.045$ MeV with a resonance width $\Gamma_R \simeq 10$ keV [2]. For a given incident beam energy, the presence of the light element at the depth where the beam energy is reduced to the resonance energy, will give rise to a peak in the backscattering spectrum. This light-element signal is usually superposed on a high background from the high-Z substrate, so that background subtraction is necessary to isolate the light-element signal. With the resulting peak four parameters can be associated: (1) The peak position E_P, the energy at which the resonance peak is detected. This is given by a channel number which has to be converted to energy. (2) The peak height H_P, the counts in the channel corresponding to the peak position. (3) The peak integral A_P, the area under the resonance peak or of the total light-element signal. To obtain only the contribution due to resonant scattering, the nonresonant contribution has to be subtracted. (4) The peak width Γ_P, the FWHM of the resonance peak or of the total signal. To obtain the FWHM of the resonance itself, the nonresonant background has to be subtracted. Measuring the FWHM of the total signal with the nonresonant contribution gives an additional increase of the FWHM. Fig. 1 shows measured RBS spectra of SiO_2 layers of different thickness on a silicon substrate. The inset shows the oxygen signal of the 5000 Å thick layer after (quadratic) background subtraction with the relevant parameters indicated.

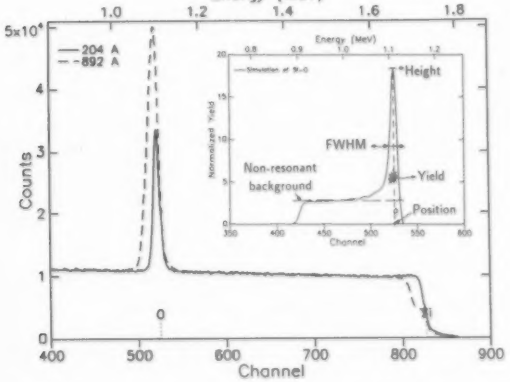

Fig. 1. Normalized 3.045 MeV ^4He spectra at 166.1° of different SiO_2 films on Si: 204 Å (solid line) and 892 Å (dashed line). The inset shows the simulated 5000 Å oxygen signal after background subtraction. Relevant parameters are indicated.

2.2. Peak parameters versus beam energy

The dependence of the peak parameters on beam energy will first be discussed from first principles, assuming ideal conditions. Afterwards the contributions of beam energy spread contributions and detector resolution will be discussed. We have worked without subtraction of the nonresonant background for the parameters because the presence of this nonresonant yield is the cause of some of the features which are observed. Also the oxygen profile is assumed to be contained in the top layer of thickness t.

With no energy spread of the beam and infinitely small detector resolution, the (integral) yield A and the channel height H for the element are given by (see chapters 3 and 4 of ref. [1]):

$$A(E_0) = \int_0^t \mathrm{d}A(x)\,\mathrm{d}x = \frac{Q\Omega}{\cos\theta_1}\int_{E_0-\Delta E_{eq}}^{E_0}\frac{\sigma(E)N(x(E))}{(\mathrm{d}E/\mathrm{d}x)_{in}(E)}\mathrm{d}E, \qquad (1)$$

$$H(E_1) = \sigma(E_x)Q\Omega\frac{N(x)\,\mathrm{d}x}{\cos\theta_1} = \frac{\mathscr{E}}{[\epsilon(E_x)]\cos\theta_1}\frac{\epsilon(KE_x)}{\epsilon(E_1)}. \qquad (2)$$

Here $\mathrm{d}A(x) = (Q\Omega/\cos\theta_1)\ \sigma(E_x)N(x)\,\mathrm{d}x$ is the scattering yield from the element in the slab between depth x and $x + \mathrm{d}x$. $N(x)$ is the atomic density of the element in the slab, E_x is the mean beam energy in the slab. ΔE_{eq} is the energy loss corresponding to the layer thickness $\Delta E_{eq} = \int_0^{t/\cos\theta_1}(\mathrm{d}E/\mathrm{d}x)\,\mathrm{d}x$. E_1 is the energy corresponding to the channel, K is the kinematic factor, ϵ is the stopping cross section and $[\epsilon(E_x)]$ the stopping cross section factor. Ω is the solid angle subtended by the detector, Q is the number of incident particles, θ_1 is the tilt angle and $\mathscr{E}$ is the width of a MCA channel. The backscattering angle θ is generally fixed in the case of resonance profiling: $\theta = 165°$ for $^{16}O(\alpha, \alpha)^{16}O$.

It is always possible to identify a maximum signal height in the spectrum. If a resonance is occurring in the sample, it will give rise to a peak in the signal height, which in any way will present a local maximum. To be able to assign the absolute maximum to the resonance, three energy regions have to be considered:

(a) $E_0 \leq E_R$. There is no resonance and since the cross section increases with E, the signal maximum will be situated at the front face of the oxygen containing layer. The position of this maximum is $E_M \sim KE_0$ and the height is $H_M \propto \sigma(E_0)N(0)\,\mathrm{d}x$. Both height H_M and position E_M will increase with energy. When $E_0 = E_R$ the resonant cross section

occurs in the top slab: $H_M = H_P \propto \sigma_R N(0)\,dx$ and $E_M = E_P \approx KE_R$.

(b) $E_0 > E_R$. The resonance will occur at the depth $\bar{x}_R$ where the incident beam energy is reduced to E_R. The resonance will present a local maximum with height $H_P \propto \sigma_R N(\bar{x}_R)\,dx$ and $E_P \backsim KE_R - \int_0^{\bar{x}_R/\sin\beta}(dE/dy)|_{out}\,dy$, where the integral is the energy lost by the ion on its outward path and β is the angle between the backscattered beam and the sample surface. Because of this additional energy loss the resonance will occur in the spectra at an energy $E_P < KE_R$. However, the height H_P will remain constant, neglecting the influence of straggling which will be discussed further on. If E_0 increases, the resonance will occur at ever larger depths and the peak position will shift to ever lower values, until the backside of the layer, containing the element, is reached at an energy $E_0 = E_R + \Delta E_{eq}$.

(c) $E_0 > E_R + \Delta E_{eq}$. Resonant scattering no longer occurs in the film. Since for energies above E_R the cross sections decrease, the highest cross section now occurs at the backside of the layer: $H_M \propto \sigma(E_0 - \Delta E_{eq})N(t)\,dx$ and $E_M \backsim K[E_0 - \Delta E_{eq}] - \int_0^{t/\sin\beta}(dE/dy)|_{out}\,dy$. Thus the height H_M decreases while the position E_M increases with energy.

The integral A_P is given by eq. (1) and this for every energy region. The FWHM Γ_P is determined by the convolution of the oxygen profile with the scattering cross section curve and with the energy loss function corresponding with the layer. In the ideal case the energy loss function would have a zero-width distribution. Even in this simplified case, there is no analytical solution for $\Gamma_P(E_0)$, so that it has to be extracted from numerical calculations of the oxygen signal for given beam energy. The dependence of the parameters on the beam energy will be discussed further in section 2.4.

2.3. Influence of energy spread and detector resolution

It is hereby assumed that, to an approximation, the energy loss function can be described by a Gaussian distribution function. However, for the small energy loss close to the surface the use of Vavilov distributions would be more correct [7]. The different contributions to the energy spread are also assumed to be described by independent Gaussian distribution functions, of which the variances at each depth can be calculated by the theory as outlined by Williams and Möller [8].

The inherent energy width of the beam together with straggling and multiple scattering along the inward path causes the particles at each depth x to be spread out over a number of energies. Resonant excitation will therefore occur from a certain depth interval δx_{exc}, around the mean depth $\bar{x}_R$. Since the different contributions to the energy spread $\delta E(x)$ at the depth x can be added in quadrature, this depth interval is equal to

$$\delta x_{exc} = \frac{\delta E(\bar{x}_R)}{(1/\cos\theta_1)(dE/dx)|_{in}} = \frac{\sqrt{\delta E^2_{beam} + \delta E^2_{str,in} + \delta E^2_{geo,in}}}{(1/\cos\theta_1)(dE/dx)|_{in}}. \quad (3)$$

Here is δE_{beam} the energy spread of the incident beam, $\delta E_{str,in}$ is the energy spread due to straggling with inclusion of multiple scattering along the incident ion trajectory and $\delta E_{geo,in}$ is the geometrical contribution for the incident path (generally negligible). The scattering yield $dA(x)$ from a slab between x and $x + dx$ then becomes

$$dA(x) = \frac{Q\Omega}{\cos\theta_1}\left\{\int_0^\infty\left[f_{beam}(E_0, E_i)\,dE_i \times \int_0^\infty\left(f_{spread}(E_i, E, x)\sigma(E)\right)dE\right]N(x)\right\}dx. \quad (4)$$

The first integral accounts for the incident beam energy spread with a Gaussian distribution function:

$$f_{beam}(E_0, E_i) = \frac{1}{s_{beam}\sqrt{2\pi}}\exp\left(-\frac{(E_i - E_0)^2}{2s^2_{beam}}\right),$$

with E_0 the mean beam energy and s_{beam} the standard deviation of the Gaussian with FWHM = δE_{beam}. The second integral accounts for the energy-loss straggling of a given component E_i of the incident beam. The energy spectrum inside the target is also described by a gaussian distribution function:

$$f_{spread}(E_i, E, x) = \frac{1}{s_{spread}\sqrt{2\pi}}\exp\left(-\frac{\left(E - \bar{E}(x)\right)^2}{2s^2_{spread}(x)}\right),$$

where $\bar{E}(x) = E_i - \int_0^{x/\cos\theta_1}(dE/dy)|_{out}\,dy$ is the mean energy at depth x to which an incident ion with energy E_i is reduced, $s_{spread}(x)$ is the depth dependent standard deviation, which includes energy-loss straggling as well as multiple scattering and geometrical contributions.

Calculation of eq. (4) at each depth will give us the excitation function for the light element (oxygen): this is the amount of backscattering at each depth. Integration of eq. (4) over the whole layer containing the light element, would give the integral yield of that element. The effect of energy spread is a smearing out: the oxygen contribution at a certain energy comes from a certain depth interval and the excitation function will broaden.

Since the elastically scattered particles have to travel backwards through the sample to reach the detector, contributions along the outward path as well as the finite energy resolution of the detector have to be taken into account to describe the actual shape in the spectrum. The additional energy spread of the outgoing particles, induced by straggling, multiple scattering and geometrical contributions from the effective detector acceptance angle, combined with the detector resolution δE_{det}, which will be under normal incidence the major component, can be described by a Gaussian energy distribution. Convolution of this gaussian with the excitation function gives an additional smearing out of the oxygen signal in the spectrum. The dependence of the peak parameters on the detector resolution is discussed in section 2.4.

2.4. Calculations and results

Spectrum simulations are performed with a modified version of the simulation package RUMP [9]. The program has been in-house adapted to handle the resonant scattering of $^4He^{2+}$ from oxygen. All sharp and broad resonances between 2.4 and 6.5 MeV have been included. The adaptation follows the scheme outlined in refs. [10,11]. To obtain the spectrum with energy spread inclusion, the idealized spectrum has to be convoluted with a Gaussian with depth(–energy)-dependent variance. The variance at each depth is calculated according to the theory as outlined by Williams and Möller [8]. For the geometrical contributions the beam diameter is taken to be 2 mm, the distance of the detector to the target is 10 cm and the detector width in the scattering plane is 7 mm. This corresponds to an effective detector acceptance angle of $> 4°$, which is too large to achieve good resolution, considering the rapid variation of the resonant cross section with backscattering angle θ.

In fig. 2 the calculated oxygen signals are shown for resonant scattering at 3.045 MeV from 892 Å thick SiO_2 layers on Si, and this for different values of the detector resolution. The height and yield are given in normalized units, according to the RUMP notation [9]. The 892 Å SiO_2 gives an equivalent energy loss $\Delta E_{eq} \approx 19$ keV for beam energies around 3 MeV. Also shown is a reference signal, calculated with inclusion of only the straggling contribution. As can be seen the signal tends to be smeared out with increasing detector resolution: the signal maximum shifts towards lower energies while the maximum height decreases. The signal integral yield, however, is independent of the detector resolution and thus remains constant. The total yield A depends only on the scattering excitation function and is obtained by integration of eq. (4) over the layer containing oxygen. A is thus only dependent on contributions along the inward path.

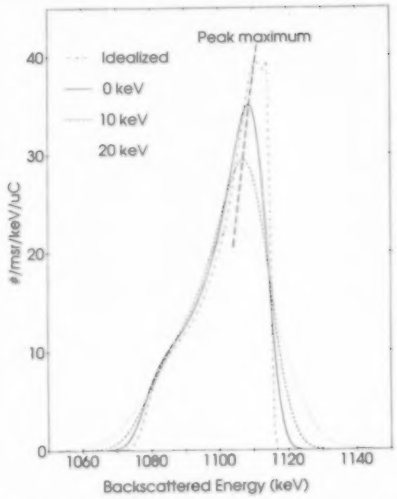

Fig. 2. Calculated contribution of the oxygen signal to 3.045 MeV ^4He backscattering spectra of a 892 Å SiO_2 film on Si for different δE_{det}: 0 keV (solid line), 10 keV (dashed line) and 20 keV (dotted line). The smearing out of the resonant signal is visible, yielding a decrease of the peak height and a shift in position to lower detected energies, as well as the increase in FWHM. However, the area of the signal remains constant.

It is important to notice that the shape of the resonance peak in the elastic cross section curve is not symmetrical. There is also a nonresonant 'background' to the sides of the resonance peak. Therefore the resonance can not be described by a Breit–Wigner dispersion formula, which is symmetrical. In fact a thin film with constant oxygen concentration will sample the cross section curve from the beam energy E_0 down to the energy $E_0 - \Delta E_{eq}$. This is clearly seen in fig. 2 where the reference signal (without energy spread) is proportional to the oxygen cross section curve, sampled by the 892 Å oxide from $E_R = 3.045$ MeV down to $E_R - \Delta E_{eq} = 3.027$ MeV. Thus the oxygen signal has clearly an asymmetrical shape with a median at an energy lower than E_R. Since the convolution of this signal with a Gaussian to include the energy spread and detector resolution, acts as a kind of smoothing and averaging through the nonzero tails of the Gaussian, the maximum of the convoluted signal will shift towards the median and will decrease in height.

Figs. 3a–3c show the dependence of the parameters on the beam energy for different detector resolutions δE_{det}. The signal height and the integral yield are shown in fig. 3a. Whereas the yield is independent of the detector resolution, the maximum signal height decreases with increasing δE_{det}. With increasing δE_{det} also the shape of the curves becomes more rounded

and the plateau, corresponding to the constant oxygen concentration, decreases in width. The yield curve, on the other hand, shows no plateau at all because the yield corresponds to a much larger "sampled" depth interval than for the height.

The position of the signal maximum exhibits the behaviour described in section 2.2 (fig. 3b). Around E_R the resonance occurs in the sample and the position decreases with increasing beam energy as the resonance is at fixed energy. Outside the energy interval $[E_R, E_R + \Delta E_{eq}]$ the position of the maximum increases. For larger detector resolution, the position is shifted towards the median and thus the backscattered energy interval between the two turning points, corresponding to the two interfaces, decreases. These turning points correspond to the interfaces and occur at fixed beam energy independent of δE_{det}.

Fig. 3c shows the FWHM of the oxygen signal measured without nonresonant background subtraction. This FWHM is a complex function of beam energy, determined by the convolution of the concentration profile with the scattering cross section curve. Although no measure of the resonance width, it gives an indication about the general shape of the oxygen

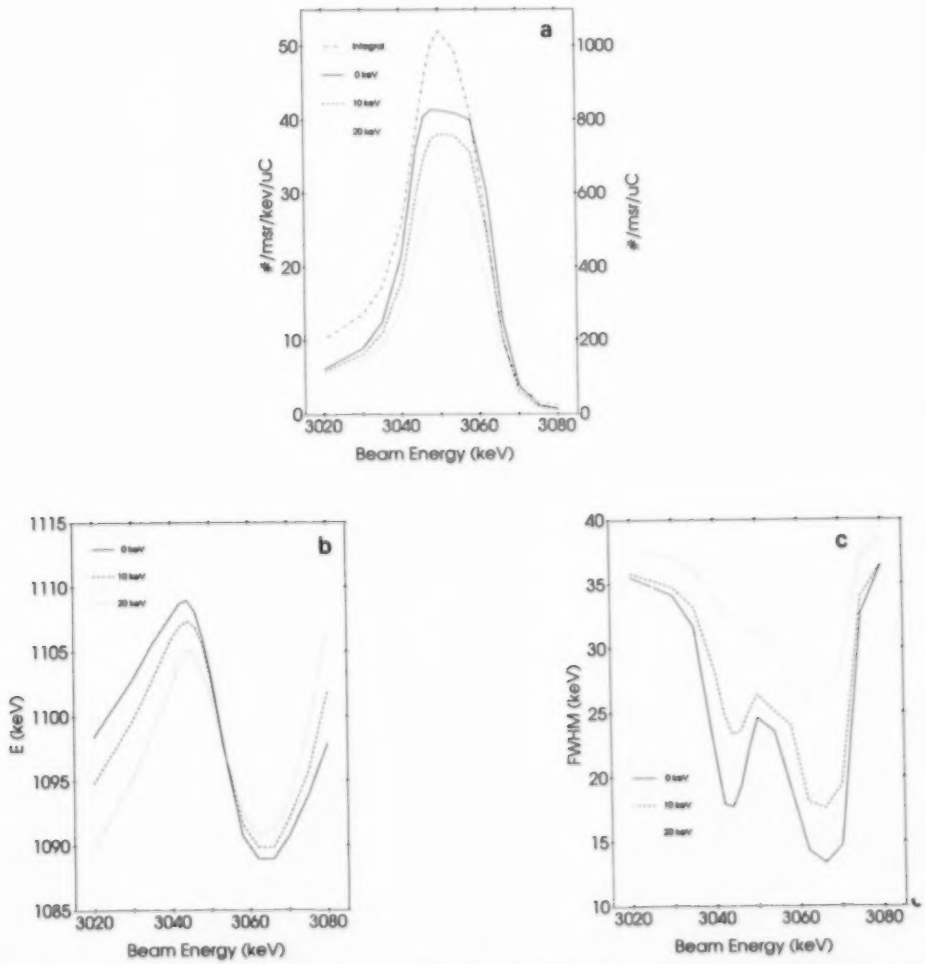

Fig. 3. Calculated peak parameters versus beam energy for a 892 Å SiO_2 film on Si for different δE_{det}: 0 keV (solid line), 10 keV (dashed line) and 20 keV (dotted line). (a) Resonance height and integral yield. The probing resolution decreases with increasing detector FWHM. The yield curve is independent of the detector resolution. (b) Resonance peak position. The decrease of the energy range between the turning points due to increasing detector is clear. (c) FWHM of the oxygen signal. The convolution of resonance and profile becomes more obscured with increasing δE_{det}.

signal in the spectrum. For $\delta E_{det} = 0$, the decrease of the FWHM for $E_0 < 3045$ keV and the increase for $E_0 > 3065$ keV with increasing energy is due to respectively the occurrence and the disappearance of resonant scattering in the oxide layer. Between these energies the signal is very peaked. With increasing δE_{det} the features are smeared out and the oxygen signal will have less sharp features.

The influence of the detector resolution on the parameters is shown in fig. 4. Various oxide thicknesses have been considered for a 3.045 MeV He beam at normal incidence. At low δE_{det} the FWHM is little influenced while at high δE_{det} it increases with the detector resolution (fig. 4c). With increasing δE_{det} the height decreases, the more rapidly the thinner the oxide is because then the tails of the Gaussian contribute less to the signal (fig. 4a). Also the peak position decreases with increasing δE_{det} (fig. 4b). It decreases towards the median of the profile until at high δE_{det} these become identical: the shape then is Gaussian, dominated by the detector resolution.

The former results are obtained in the assumption of perfectly flat samples. Surface topography will also influence the shape of the spectrum. Surface roughness (with random distribution) will contribute to a further degradation of the energy resolution. It can roughly be described by an additional Gaussian for both inward and outward path, to be included in the convolution. A

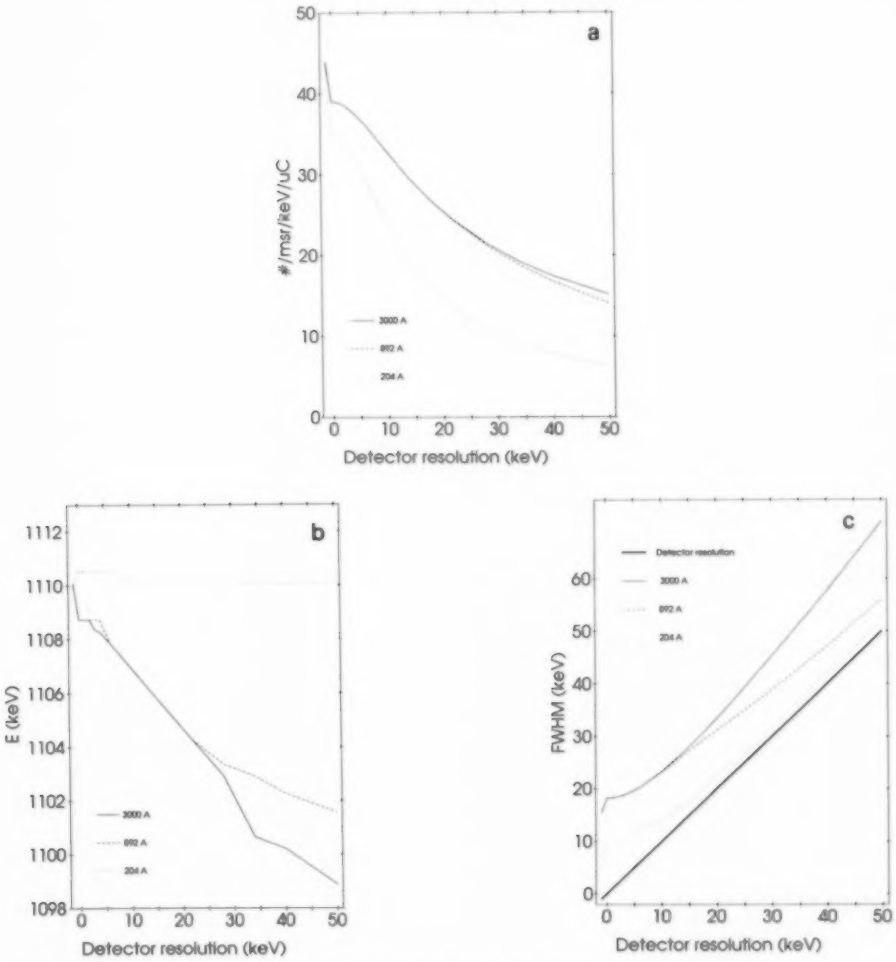

Fig. 4. The calculated influence of the detector resolution is shown for backscattering at 3.045 MeV from three oxide thickness: 3000 Å (solid line), 892 Å (dashed line) and 204 Å (dotted line). (a) Resonance peak height, (b) peak position and (c) FWHM of the oxygen signal.

detailed discussion is not attempted in this paper. Surface roughness is further not considered.

3. Methodology

In view of the previous, one could consider depth profiling methodologies using the different parameters. Both peak height and peak area (yield) can be used as a probe to determine the element concentration as a function of depth. The peak position would in principle allow to calculate the depth at which the resonance occurs. However, the depth scale can be determined more conveniently and more accurately from the incident beam energy. The peak position could be used to assign local maxima to the occurrence of a resonance in the case of a peaked profile. If the resonance occurs at low concentrations, the profile maximum can yield a higher nonresonant signal. Following the position as a function of beam energy allows to discard points that do not correspond to resonant scattering. The FWHM is of no direct use for determining a depth profile and will not be discussed further.

Compared to the integral yield, the use of the peak height has the following advantage: whereas the yield always samples a depth interval corresponding to Γ_R (+the energy resolution), the height allows in principle to probe a smaller depth interval (about the energy resolution along the inward path). The previous advantage is obstructed by the finite detector resolution (and outward path contributions), which are of no concern for the yield. The probing accuracy decreases with increasing detector resolution, due to shifts and a decrease in height. A clear disadvantage is that the statistics are much lower, so that scatter is greater and a larger dose has to be collected. This larger scatter can induce errors in the assignment of the signal maximum. Also is it more difficult to extract the correct height and position than to extract the yield from the spectrum.

For actual depth profiling, subtraction of the nonresonant background may be done, if one bears in mind the influence of it on the parameters. For the height, the subtraction would imply the subtraction of a constant from the determined value, for the integral this would yield subtraction of a nearly constant value and for the FWHM this certainly would give a much better measure of the convolution of the resonance peak with the profile.

Tracing the peak position as a function of energy would allow to unambiguously identify the resonant peak. However, the position can only be extracted with limited accuracy. The recorded spectrum should correspond as closely as possible to the true spectrum. Since the spectrum is discretisized into a series of channels and each channel corresponds to a certain energy interval over which the true spectrum is summed, this implies a small channel width $\mathscr{E}$. The channel containing the resonance, will present a local maximum. The smaller the channel width, the higher the accuracy with which the peak position can be identified. The uncertainty is in fact given by $\mathscr{E}$. On the other hand, the smaller $\mathscr{E}$, the lower the height per channel per beam dose. Thus statistical scatter will be larger and obscure the position of the maximum. For given statistical scatter, the required dose will be higher for smaller channel widths. A compromise between dose and accuracy is necessary.

4. Experimental results

The experiments are carried out on a tandem type accelerator, NEC 5SDH-2 1.7 MV terminal. The 3.045 MeV $^{16}O(\alpha, \alpha)^{16}O$ resonance is applied for the profiling of oxygen in SiO_2 layers, with various thicknesses: 204 Å ($\Delta E_{eq} \approx 4.3$ keV), 892 Å ($\Delta E_{eq} \approx 19$ keV) and 5000 Å ($\Delta E_{eq} \approx 109$ keV). The thicknesses have been obtained by spectroscopic ellipsometry. The samples have negligible surface roughness. The energy was calibrated by employing the $^{16}O(\alpha, \alpha)^{16}O$ resonance itself, due to the absence of other possibilities. The energy was determined from the energy scans which were performed. Inspection afterwards has revealed that this might have induced a systematic offset of a few keV. However, this only shifts the energy scale, without distorting it. The calibration was reproducible within the accelerator setting uncertainty for independent runs.

Two different setups were used for the experiments, both with a scattering geometry of $\theta_1 \approx \theta_2 \approx 166°$, solid angle $\Omega_1 \approx 1.6$ msr and $\Omega_2 \approx 3.8$ msr and effective acceptance angle $d\theta_1 \approx 2.8°$ and $d\theta_2 \approx 4.2°$. The data acquisition presents the main difference: in setup 1 the MCA has a fixed division of 1024 channels with $\mathscr{E}_1 \approx 1.9$ keV/channel and in setup 2 the division is 512 channels with $\mathscr{E}_2 \approx 3.66$ keV/channel. In view of the remark made on the channel width $\mathscr{E}$ in section 3 more accurate measurements of the energy position can be obtained with setup 1. The energy variation for the scan was carried out by manually varying the terminal setting (setup 1) or by application of the target biasing technique [12].

In fig. 5 the measured peak height and integral yield versus beam energy is shown for a 892 Å oxide on Si (experiment with setup 1). The yield curve is peaked around 3050 keV and as such does not give a good indication of the constant profile. The signal height, however, exhibits a kind of plateau which is more in correspondence with the constant oxygen profile. The detector resolution, extracted from the spectra is found to be about 25 keV. This high value is mainly due to

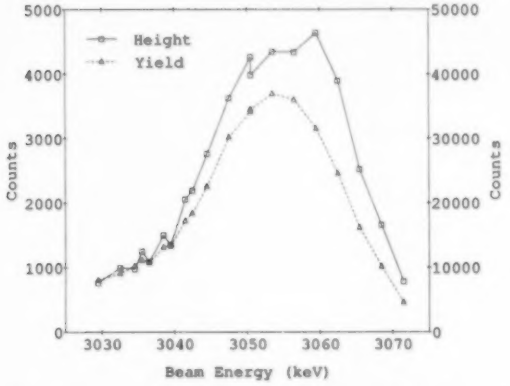

Fig. 5. Measured peak height and peak yield versus beam energy for a 892 Å SiO_2 film on Si with perpendicular beam incidence. In contrast to the yield curve, the height exhibits a kind of plateau in correspondence with the contrast oxygen concentration.

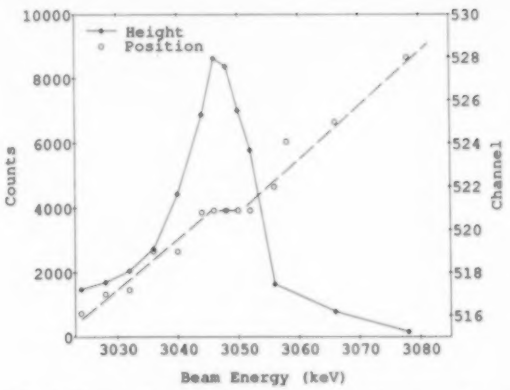

Fig. 7. Measured peak height and peak position versus beam energy for a 204 Å SiO_2 film on Si with perpendicular beam incidence. The height curve is very peaked, a plateau is not reached due to the to high energy increment. The position is a straight line, a decrease in energy not being measurable.

degradation of the long-used detectors. The measured peak position is not shown: there was a large scatter on the data due to the fact that $\mathscr{E} \simeq 4.7$ keV/channel, therefore the expected behaviour (fig. 3b) was hardly discernable. Fig. 6 shows the measured peak height and position for the same 892 Å oxide, but now measured with setup 1. The height curve is roughly the same, apart from the data scatter. The position clearly exhibits the expected behaviour, though also the scatter is relatively large. The discrepancy at 3055 keV is caused by a discontinuity in the manual energy scan, which could also be evidenced in the shift of the Si-leading edge. The extracted detector resolution is 14.8 keV.

The peak height and position versus beam energy of a thin 204 Å oxide are given in fig. 7 (experiment with setup 1.) No plateau is visible in the height. This is partly due to the influence of the detector resolution which is 14.8 keV. The spectrum for such a thin oxide was always nearly Gaussian without any distinct features. Apart from this, the expected plateau width is so narrow (4 keV) that it would not show up with the used

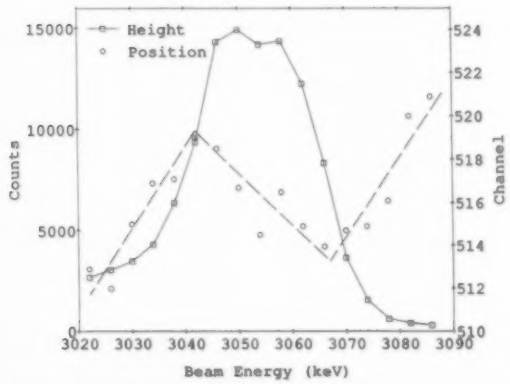

Fig. 6. Measured peak height and peak position versus beam energy for a 892 Å SiO_2 film on Si with perpendicular beam incidence. The position follows globally the expected behaviour, the large scatter is due to inaccurate position extraction limited by the finite energy scale $\mathscr{E}$.

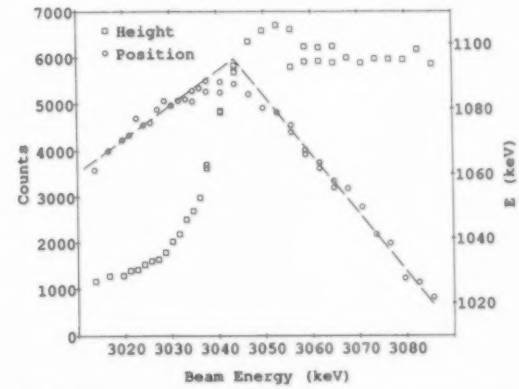

Fig. 8. Measured peak height and peak position versus beam energy for a 5000 Å SiO_2 film on Si with perpendicular beam incidence over a limited energy range. The peak position follows the expected behaviour. The variations in height around E_R are due to normalization errors.

energy increment of 3 keV. The position is almost a straight line with a plateau around 3.045 MeV. The moving towards lower energy of the position is not discernable.

Finally, results of position and height for a thick 5000 Å oxide are shown in fig. 8. Due to the large thickness, only a partial scan over 80 keV is performed. The results show the expected behaviour of peak height and position. The experiment is carried out in chamber 2 with the target biasing technique. The variations in height around E_R are due to a systematic error in the normalization of the spectra, necessary with the target biasing technique.

5. Conclusion

In depth profiling with elastic resonances, such as the $^{16}O(\alpha, \alpha)^{16}O$ resonance, different parameters can be extracted form the recorded spectrum at each energy. The variation of the peak height, position, yield and FWHM with incident beam energy is discussed for normal incidence. The influence of energy spread in the sample and of the detector resolution on the parameters is shown. Especially the detector resolution has a major influence on the shape of the backscattering signal.

A depth profiling methodology using the peak height as a probe has been proposed. Advantages and restrictions when compared with the use of the yield are discussed. It is clear that the detector resolution sets a practical limit to this application. With better detector resolution more accurate results can be obtained. The former has been experimentally illustrated for the depth profiling of SiO_2 layers of different thickness. However, better results can be obtained when the experiments are performed with higher resolution than in these preliminary experiments.

Tilting the target might yield an increase in accuracy since the profile will be stretched and will correspond to a greater energy interval. In principle this larger interval can be probed with higher accuracy and depth resolution. However, energy spread contributions will also increase for the larger path lengths involved. Also the surface roughness will become the limiting factor for the application of tilting. Further theoretical and experimental investigation of this is necessary.

Acknowledgement

W. De Coster is indebted to the Belgian IWONL for financial support.

References

[1] W.K. Chu, J.W. Mayer and M.-A. Nicolet, Backscattering Spectrometry (Academic Press, New York, 1978).
[2] J.R. Cameron, Phys. Rev. 90 (1953) 839.
[3] B.K. Patnaik, C.V. Barros Leite, G.B. Baptista, E.A. Schweikert, D.L. Cocke, L. Quinones and N. Magnussen, Nucl. Instr. and Meth. B35 (1988) 159.
[4] J. Li, L.J. Matienzo, P. Revesz, Gy. Vizkelethy, S.Q. Wang, J.J. Kaufman and J.W. Mayer, Nucl. Instr. and Meth. B46 (1990) 287.
[5] J.A. Martin, M. Nastasi, J.R. Tesmer and C.J. Maggiore, Appl. Phys. Lett. 52 (1988) 2177.
[6] M. Bozoian, K.M. Hubbard and M. Nastasi, Nucl. Instr. and Meth. B51 (1990) 311.
[7] J.R. Bird, R.A. Brown, D.D. Cohen and J.S. Williams, in: Ion Beam Material Analysis, eds. J.R. Bird and J.S. Williams (Academic Press Australia, 1989) p. 618.
[8] J.S. Williams and W. Möller, Nucl. Instr. and Meth. 157 (1978) 213.
[9] L.R. Doolittle, Nucl. Instr. and Meth. B9 (1985) 344.
[10] B. Blanpain, P Revesz, L.R. Doolittle, K.H. Purser and J.W. Mayer, Nucl. Instr. and Meth. B34 (1988) 459.
[11] P. Berning and R.E. Benenson, Nucl. Instr. and Meth. B36 (1989) 335.
[12] W. De Coster, B. Brijs, J. Goemans and W. Vandervorst, Proc. 10th Int. Conf. on Ion Beam Analysis, Eindhoven, The Netherlands, 1–5 July 1991, Nucl. Instr. and Meth. B64 (1992).

Nuclear Instruments and Methods in Physics Research B66 (1992) 292–294
North-Holland

Nuclear Instruments & Methods in Physics Research
Section B

PIGE – Resonance profiling applied to a clinical test of fluoride varnishes

H.E. Zschau [a], F. Plier [a], G. Otto [a], C. Wyrwich [b] and A. Treide [b]

[a] *Department of Physics, University of Leipzig, Linnéstrasse 5, Leipzig, O-7010 Germany*
[b] *Department of Stomatology, University of Leipzig, Nuernbergerstrasse 57, Leipzig, O-7010 Germany*

A clinical in-vivo experiment had been carried out to compare two caries preventing fluorine varnishes. The fluorine depth profiles in the near surface region of tooth enamel were measured using the 935 keV resonance of the nuclear reaction $^{19}F(p,p'\gamma)^{19}F$.

The results can be understood by studying the fluorine anamnese of the patients.

1. Introduction

One of the most efficient methods of caries prevention is the repeated local application of fluorine containing gels or varnishes in a certain time interval [1,2]. To optimize this procedure a knowledge of the time behavior of fluorine within the near surface region of the treated enamel is necessary. To study this in the case of two lacquers, a test was undertaken under comparable conditions followed by measurement of fluorine depth profiles using PIGE (proton induced gamma-ray spectrometry).

2. Sample preparation

Two different NaF-based anti-caries lacquers (the well-known Duraphat® and the newly developed Lawefluor®) were tested under clinical conditions. A group of 10 to 14 years old patients was chosen whose symmetrical premolars had been ordered for extraction because of jaw orthopedical problems.

Whereas 3 teeth were touched with the drug in vivo, one served as a control and was extracted before starting. According to a time interval of 1 day, 3 weeks and 3 months the 3 treated teeth were extracted, their roots were cut off and the labial sides were separated. In this regime 40 teeth from 10 persons were prepared for investigation, half of them for each varnish.

3. Experimental arrangement

The measurements were carried out at the 2 MeV Van de Graaff accelerator at the Physics Department of the University of Leipzig. The principle of depth profiling using resonance gamma reactions has been described by several authors, for instance see [3]. Here the nuclear reaction $^{19}F(p,p'\gamma)^{19}F$ at the resonance energy of 935 keV served as the tool [4]. This allowed a profiling depth of up to 3 μm with an initial depth resolution of 100 nm for protons incident at 45° to the target surface. Four samples mounted on the rotatable target holder enabled targets to be exchanged without breaking the vacuum of 10^{-4} Pa.

A beam collimated to 1 mm diameter was used to irradiate the centre of the labial sides of the premolars and a 55 cm^3 Ge(Li) detector with an energy resolution of 3.6 keV at $E_\gamma = 1332$ keV was used to record the

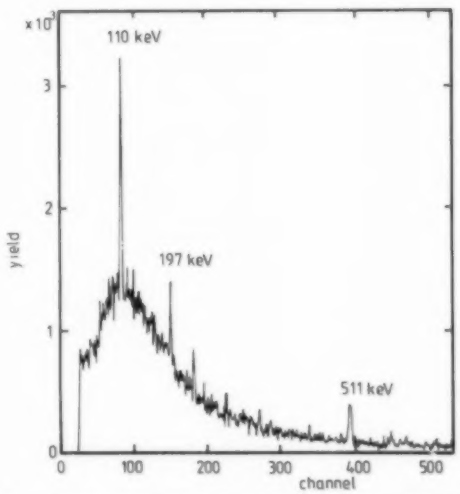

Fig. 1. Gamma spectrum of tooth enamel bombarded with 1 MeV protons recorded with a Ge(Li) detector.

0168-583X/92/$05.00 © 1992 – Elsevier Science Publishers B.V. All rights reserved

reaction gamma quanta (fig. 1). The detector was placed outside the scattering chamber at a distance of 5 cm to the beam spot. With a mean proton current of 100–150 nA a charge of 20 μC was collected for each depth point. CaF_2 crystals covered with a 15 nm thick Au layer to ensure electrical conductivity served as standards. A potential of −200 V at the scattering chamber suppressed secondary electron emission.

4. Results

Fluorine measurements were shown to be independent of the varnish type and can be summarized in 3 groups showing a very different behavior which is connected to the fluorine anamnese (figs. 2, 3 and 4).

Group 1 is characterized by a value of 500–1400 ppm F in the control samples. In this case the fluorine content after 1 day and also 3 weeks reaches values up to 4000–5000 ppm F followed by a strong decrease after 3 months. No person in this group had a clinical

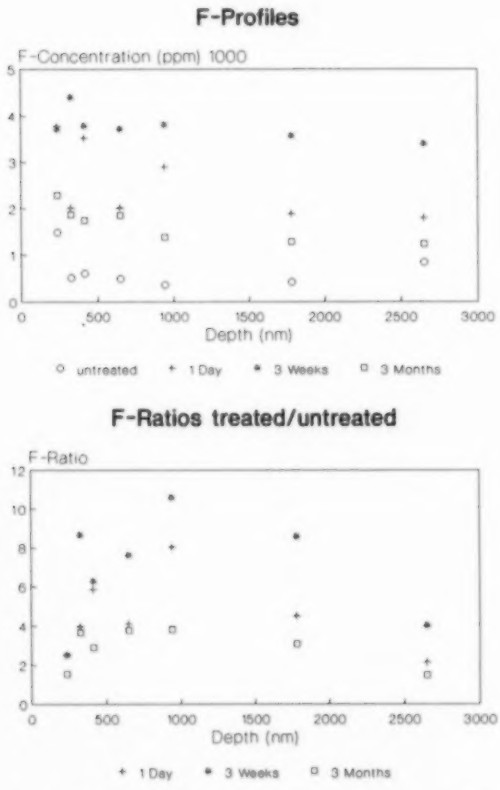

Fig. 2. Fluorine depth profiles and fluorine enrichment factor of treated/untreated enamel versus depth in group 1.

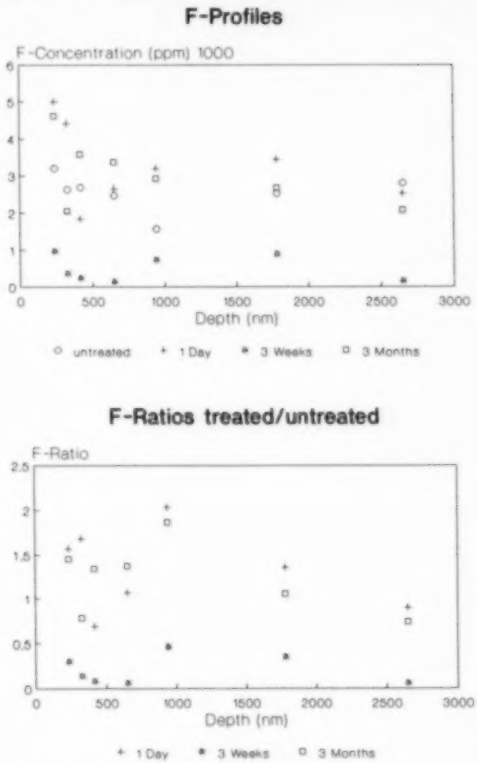

Fig. 3. Fluorine depth profiles and fluorine enrichment factor of treated/untreated enamel versus depth in group 2.

F-uptake prior to this experiment and therefore had a high enrichment compared to the control samples.

Members of the second group with concentrations in the range of 1500–3000 ppm F show no systematic behavior. Consequently the enrichment factor treated/untreated enamel varies very strong. From fluorine anamnese a noncontinuous clinical F-uptake was ascertained.

Members of group 3 show no influence of the varnish application to the fluorine profile. These children had received an intensive caries prevention treatment with fluoride tablets before this investigation. In this group the control samples show amounts of 2500–5000 ppm F.

5. Conclusions

Summarizing the results for both varnishes one can point out:

(a) The fluorine enrichment and time behavior of the fluorine profiles are very similar.

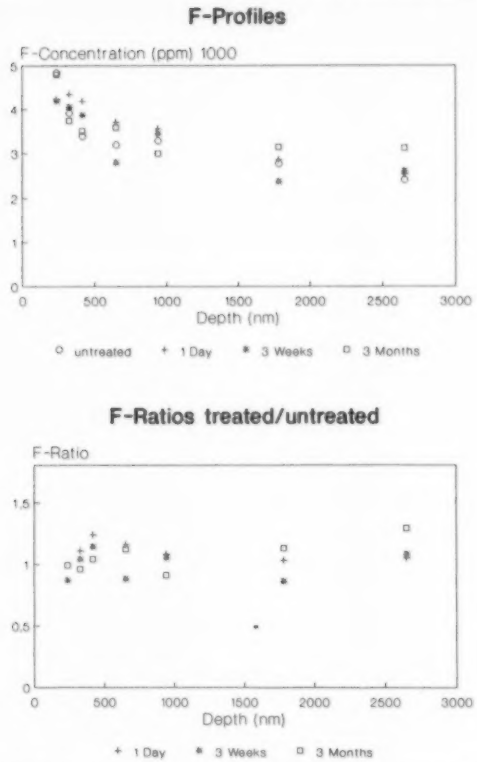

Fig. 4. Fluorine depth profiles and fluorine enrichment factor of treated/untreated enamel versus depth in group 3.

(b) The necessary time interval for a repeated varnish application is not lower than 3 months.
(c) The fluorine amount in the near surface region of tooth enamel before starting the lacquer application influences strongly the degree of enrichment.

References

[1] H.J. Maiwald and L. Geiger, Dtsch. Stomat. 23 (1973) 56.
[2] D.C. Clark, J.W. Stamm, T. Chi Quell and G. Robert, Commun. Dent. Oral Epidemid. 13 (1985) 2, 61.
[3] U. Lindh and A.B. Tveit, J. Radioanal. Chem. 59 (1980) 167.
[4] H.-E. Zschau, F. Plier, G. Otto, C. Wyrwich and A. Treide, Nucl. Instr. and Meth. B50 (1990) 74.

Nuclear Instruments and Methods in Physics Research B66 (1992) 295–297
North-Holland

Nuclear Instruments & Methods in Physics Research
Section B

The investigation of the fluorine uptake in tooth enamel after the application of a NaF containing varnish

F. Plier, H.E. Zschau and G. Otto

Department of Physics, University of Leipzig, Linnéstrasse 5, Leipzig, O-7010 Germany

The 935 keV resonance of the $^{19}F(p,p'\gamma)^{19}F$ nuclear reaction was used to determine fluorine depth profiles in human tooth enamel for three separate cases. These investigations allowed conclusions to be drawn about the interaction processes between the oral milieu containing fluorine, and the enamel surface.

1. Introduction

This paper summarizes the results of three studies designed to explore various interaction processes at the surface of tooth enamel after treatment with a varnish containing NaF. Depth profiling investigations were performed to examine the fluorine uptake in enamel using the $^{19}F(p,p'\gamma)^{19}F$ nuclear reaction, with particular attention paid to the processes that are responsible for the long term deposition of fluorine. This allowed conclusions to be drawn concerning the temporal cycling of NaF varnishes for caries prevention.

2. Materials and methods

The principle of fluorine depth profiling, using the PIGE technique, is discussed in detail in ref. [1]. The 935 keV resonance of the $^{19}F(p,p'\gamma)^{19}F$ nuclear reaction ($E_\gamma = 110$ keV) was used to determine the fluorine distribution in the enamel. The incident proton energy was varied from 940 to 1180 keV, in seven steps. The advantages of using this resonance are that the cross section is very high [2], thus facilitating the profile measurement, and that it allows fluorine to be profiled to a depth of 3 μm in enamel before next resonances disturb the results. The disadvantage of the chosen resonance is that the depth resolution is limited to $\Delta t = 120$ nm at the surface of smooth enamel. However, in practice the surface of the tooth enamel is not smooth and the influence of the surface roughness on the depth resolution must be considered [3]. The total depth resolution Δt_{total} is the result of the convolution of the surface roughness depth resolution and the ideal smooth target depth resolution [3]. For enamel Δt_{total} varies between 500 to 800 nm in the first 1 μm surface region of material at an incident angle of $\vartheta_i = 0°$.

The first experiment was designed to compare the fluorine uptake in sound enamel with the uptake in demineralized enamel. Four incisors were used. A piece of each incisor was removed and exposed to a demineralizing agent (hydroxylethylcellulose, pH = 5.1) for one hour to simulate the acidic action of bacteria in vivo. These demineralized samples, together with a second set of samples from each incisor, were then treated with the NaF containing "Duraphat®" varnish for one day. A third piece from each incisor was removed which acted as a control.

The second experiment investigated the relation between the fluorine uptake and fluorine concentration in enamel before the application of the varnish, the so-called fluorine preconcentration. This study was conducted using 4 premolars from each of 16 subjects. One of the premolars was removed before the NaF containing varnish was applied, the remaining premolars were removed 1 day, 3 weeks and 3 months, respectively after the application of the varnish.

The final experiment examined the uptake of fluorine in hydroxylapatit (hap) and enamel during demineralization in a hydroxylethylcellulose medium (pH = 5.1, fluorine content about $C_F = 0.2$ μg/g). During these measurements 24 pressed hap samples and 24 pieces of enamel, produced by cutting 6 incisors into quadrants, were analyzed. These quadrants from each tooth were separated to form four groups of six and the hap samples were also divided into four groups of six. A hap group and an enamel group were taken and then simultaneously exposed to the demineralizing agent for a set period of time. The times chosen for these exposures were 2, 72, 144 and 288 h. The changes in the enamel and hap matrix element concentration were revealed by Rutherford backscattering spectrometry (RBS) using 1.7 MeV He^+ ions at incident angles $\vartheta_i = 0°$ and $\vartheta_i = 30°$ and a scattering angle $\vartheta_s = 160°$,

0168-583X/92/$05.00 © 1992 – Elsevier Science Publishers B.V. All rights reserved

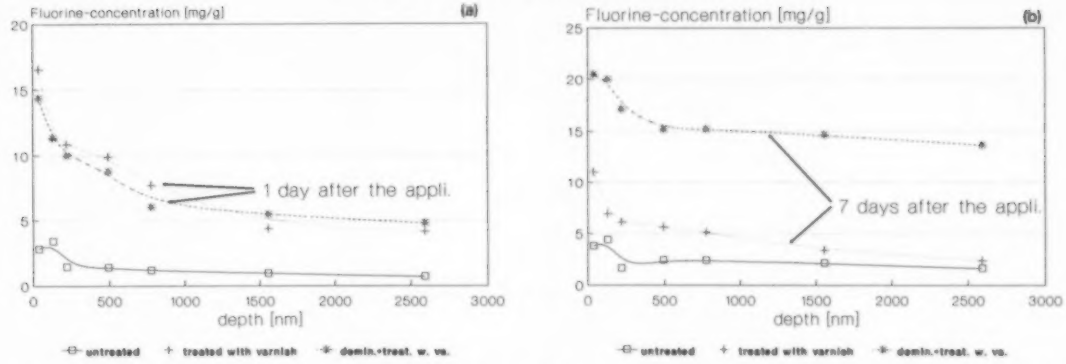

Fig. 1. A comparison of the fluorine uptake 1 day (a) and 7 days (b) after the in vitro application of a NaF containing varnish in sound and demineralized enamel.

and particle induced X-ray emission spectrometry (PIXE) using 1.7 MeV p^+ and He^+ ions.

3. Results

A typical example of the change in fluorine concentration after the varnish application in the untreated and demineralized enamel is shown in fig. 1. It can be seen that fluorine, from the NaF containing varnish, remained in the demineralized enamel for a longer time period than in the sound enamel.

The temporal changes in the fluorine concentration after the application of a fluorine containing varnish to teeth with different fluorine preconcentration are shown in fig. 2. Fig. 2a shows that immediately after the varnish application a strong increase in the fluorine concentration occurred in enamel containing a low fluorine preconcentration, and that this enamel had retained about 60% of the applied fluorine after a period of three months. Fig. 2b shows that for enamel with a high fluorine preconcentration no changes occurred in the fluorine concentration over the same three months time.

The results of the third experiment show that the chemical composition of the enamel changes with increasing demineralization time. The RBS and PIXE measurements, shown in fig. 3a, indicate that these changes are also depth dependent. Surprisingly, the fluorine concentration in the enamel increased with increasing demineralization time despite the low fluorine concentration in the demineralizing medium ($C_F = 0.2$ μg/g). No depth dependent changes in the matrix composition nor increases in fluorine concentration as a result of demineralization were observed in the hap samples.

4. Discussion

The main results of the three experiments are summarised as follows:

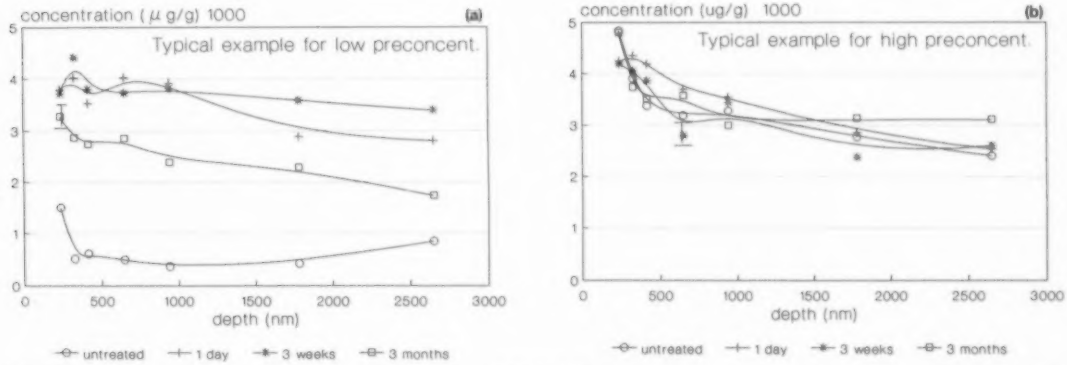

Fig. 2. The influence of (a) low fluorine preconcentration and (b) high fluorine preconcentration on the fluorine uptake in enamel after the application of a NaF containing varnish.

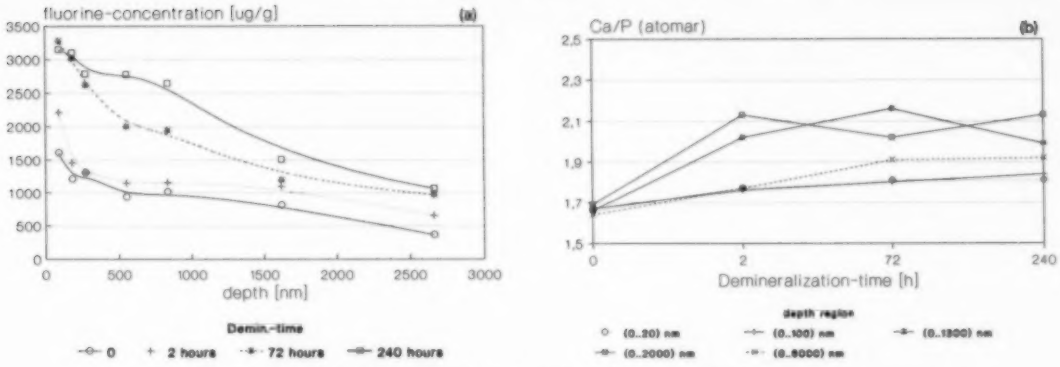

Fig. 3. The relation between the fluorine uptake and the mineralization processes.

(1) A short demineralization of enamel, before an application of a fluorine containing varnish, led to a long term deposition of fluorine in enamel.
(2) The fluorine uptake decreased as the fluorine preconcentration in the enamel increased.
(3) Fluorine was preferentially taken up in demineralized enamel.

These results show that the fluorine uptake, after the NaF varnish is applied, is directly connected with the mineralization processes at the enamel surface. This is demonstrated by the long term uptake of fluorine after a short term demineralization as shown in fig. 1, and can be explained by the production of soluble enamel components during demineralization which chemically react with fluorine to build stable compounds. These results allow the following model of fluorine uptake in enamel to be constructed:

1. The acidic action of bacteria causes the demineralization of enamel.

↓

2. Fluorine reacts with the soluble enamel components

↓

3. Stable compounds are built.

↓

4. The long term deposition of fluorine in the enamel results.

The practical consequence is that an acidic medium must be applied to the enamel directly before the application of the NaF containing varnish.

References

[1] G. Deconninck, Introduction to Radionalytical Physics (Akad. Kiado, Budapast, 1978).
[2] H.-E. Zschau, F. Plier and G. Otto, Fluor-Tiefenbestimmung in Zahnschmelz nach Applikation von Kariostatika, Wiss. Z. Univ. Leipzig, Math.-nat. wiss. Reihe, 39/90/1, Leipzig, 1990.
[3] F. Plier, H.-E. Zschau and G. Otto, these Proceedings (3rd Int. Conf. on Chemical Analysis, Namur, Belgium, 8–12 July 1991), Nucl. Instr. and Meth. B66 (1992) 38.

Nuclear Instruments and Methods in Physics Research B66 (1992) 298–301
North-Holland

Nuclear Instruments & Methods in Physics Research
Section B

Fluorine enrichment phenomena in coal combustion cycle

A. Caridi [a], E. Cereda [a], S. Fazinic [b], M. Jaksic [b], G.M. Braga Marcazzan [c], O. Valkovic [b] and V. Valkovic [b]

[a] *Cise, SpA, P.O. Box 12081, 20134 Milan, Italy*
[b] *R. Boskovic Institute, Zagreb, Yugoslavia*
[c] *Istituto Fisica Generale Applicata, University of Milan, Italy*

The use of nuclear techniques based on proton-induced gamma-ray emission for the detection of fluorine in coal and coal fly ash samples is presented. The method is applied to investigate fluorine enrichment phenomena in the coal combustion cycle taking into account the combustion itself and the abatement process. In particular, we analyzed coal samples as well as integral and size fractionated fly ash samples collected at the inlet and outlet units of a 3 MWe pilot electrostatic precipitator (ESP). This was installed in a slip stream derived from the flue gas duct of a power plant burning South African coal. Fluorine enrichment factors in the pathway from coal to fly ash and their dependence on the different ESP operating conditions have been studied.

1. Introduction

The assessment of environmental impact of particulate matter emitted by coal fired power plants and the technological research for the improvement of abatement systems require detailed information on element concentrations in coal and in emitted fly ash, in particular with respect to particle size distribution, and the characterization of element partitioning among coal products through the combustion cycle.

A lot of research work is carried out especially for toxic elements [1]. Among them, fluorine is of particular interest since its concentration in fly ash is enriched on the finest particles whose preferential penetration through emission control devices is relevant. The most important toxic effect of fluoride on human health is skeletal fluorosis, which is endemic in areas with soils and water containing high fluoride concentrations. In non-endemic areas, skeletal fluorosis has occurred as a result of industrial pollution. Besides the potential environmental and health risk, fluorine is of technological concern for its association with corrosion phenomena.

On the other hand fluorine has been studied less than many other elements because of analytical difficulties [2]. PIGE (proton-induced gamma-ray emission) technique, based on the detection of gamma rays following nuclear reactions, is effective for fluorine detection and has been extensively applied to the analysis of thick samples [3–7]. As for thin samples, no literature data have been found, although in this case PIGE would be quite convenient, taking into account that fly ash samples are generally available in small quantities. In this context we developed an experimental setup for PIGE analysis of thin samples, based on the use of an energy spread proton beam in order to overcome difficulties associated with nuclear cross section fluctuations [8].

In this work the PIGE technique was applied to fluorine analysis of pelletized coal and thin fly ash samples collected at the inlet and outlet units of a pilot electrostatic precipitator (ESP). Fluorine concentrations in emitted fly ash have been correlated with its concentration in coal and with the ESP operating conditions. In particular, the influence of the different ESP excitation modes as well as the dependence of fluorine concentration and enrichment phenomena on the ESP abatement efficiency for fly ash total mass have been studied.

2. Experimental

2.1. Sampling and sample preparation

Pulverized South African coal (Amcoal) samples were collected twice a day during the investigation period. Ash sampling was carried out at the inlet and outlet units of a 3 MWe pilot electrostatic precipitator (ESP) installed in a slip stream derived from the flue gas duct of a power plant [9]. In series in this ESP were two electric fields 5 m long and 3.75 m high. During the investigated period the precipitator was working in either conventional or pulsed energization mode and with different plate spacings from 300 to 500 mm. For integral sampling we used a standard isokinetic probe

0168-583X/92/$05.00 © 1992 – Elsevier Science Publishers B.V. All rights reserved

(with automatic flow control) connected to ceramic filters. Size fractionated fly ash samples were collected at the ESP inlet unit using an Andersen high-capacity stack sampler, with two impaction stages, a cyclone and a thimble backup filter.

We analyzed thick pellets of coal and thin samples of fly ash. A small quantity of fly ash, after grinding, was suspended in cyclohexane and filtered through a previously weighed Nuclepore filter, which was finally coated with a thin layer of polyvinyl acetate in order to prevent material loss. The thickness of filtered samples was in the range 0.1–1 mg/cm^2.

2.2. *Analytical technique*

For F analysis of coal samples, thick-PIGE has been applied. Coal samples were powdered and pelletized, and then bombarded with 6.5 MeV protons for a known recorded charge with 10–20 nA beam current. The ^{19}F(p, $\alpha_2\gamma$)^{16}O reaction (E_γ = 6129 keV) was used. The quality control was performed by the analysis of NIST reference materials 1633a and 1635.

Fly ash, prepared as thin samples, have been analyzed using the Cise 3.5 MV tandem VdG accelerator, whose PIXE–PIGE setup is extensively described in ref. [8]. Although more than twenty-five elements are simultaneously detected in an ordinary irradiation, in this work we restrict the presentation to fluorine results. The gamma rays are detected by a high purity Ge detector at 90° to the ion beam at a distance of 6 cm from the target. Within the energy range of the Cise accelerator and taking into account the efficiency of the gamma detector, the most suitable reactions for fluorine detection are ^{19}F(p, $p_1\gamma$)^{19}F (E_γ = 110 keV) and ^{19}F(p, $p_2\gamma$)^{19}F (E_γ = 197 keV).

The excitation functions of these reactions had been previously measured in the proton energy range 2.2–3.8 MeV (fig. 1) [10]. In order to carry out a straightforward quantitative analysis with respect to standard reference samples, an energy spread proton beam is used so that the fluctuations in the excitation functions are smoothed out. In particular, the proton beam, before entering the irradiation chamber, passes through a rotating aluminium disc whose sectors have different thicknesses so that the final energy distribution is a rectangle about 270 keV wide, which is the typical proton energy loss in samples as thick as 1 mg/cm^2 and made up of particles not larger than 20 μm. The resulting excitation functions are shown in fig. 2. Although the 197 keV fluorine peak has a higher yield, we chose the 110 keV one because its yield curve depends less on energy and can be easily taken into account in the quantitative analysis of samples with different thicknesses.

The irradiations were carried out at a proton primary energy (that is before the aluminium diffuser) of

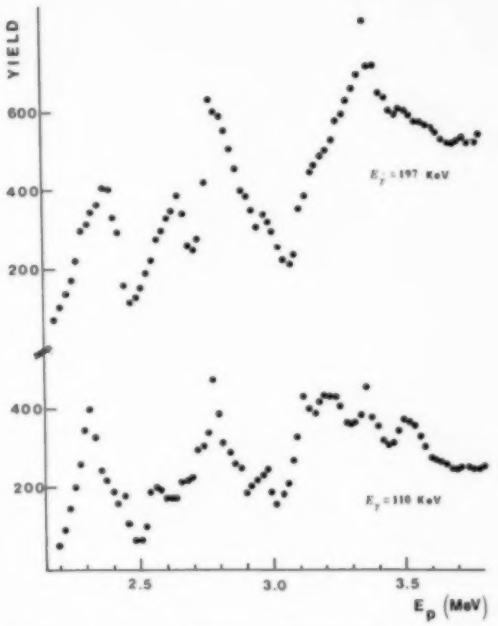

Fig. 1. Gamma-ray yields (counts/μC/μg/cm^2) for reactions ^{19}F(p, $p_1\gamma$)^{19}F (E_γ = 110 keV) and ^{19}F(p, $p_2\gamma$)^{19}F (E_γ = 197 keV) at θ_{lab} = 90° [10].

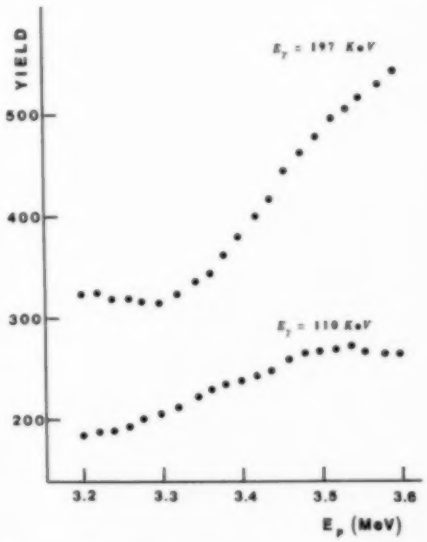

Fig. 2. Gamma-ray yields (counts/μC/μg/cm^2) for reactions on F, measured with a proton beam whose energy spread is about 270 keV. The energy scale refers to the primary energy (section 2.2).

Table 1
Properties (dry basis) of South African coal (Amcoal)

Moisture	8.1%
Ash content	15.7%
Volatile matter	28.7%
Sulphur	0.7%
Hydrogen	3.9%
Nitrogen	1.7%
Carbon	70.3%
Calorific value	6570 kcal/kg

3.52 MeV. System calibration was done by using Micromatter standard reference samples [11]. The detection limit for F in thin fly ash samples filtered through Nuclepore filters is 10 ppm. Both 110 and 197 gamma rays were produced by the $^{18}O(p, \gamma)^{19}F$ reaction. To check interference contributions, a Nuclepore filter (18% O) was irradiated; the $^{16}O(p, \gamma_1)^{17}F$ ($E_\gamma = 495$ keV) and $^{17}O(p, p_1\gamma)^{17}O$ ($E_\gamma = 871$ keV) lines were present but the ^{18}O lines were not detected. According to Demortier [3] and Bird [4] this contribution does not affect fluorine detection accuracy.

3. Results and discussion

We have investigated fluorine enrichment in two steps: first from parent coal to fly ash just before the ESP, and secondly through the abatement device.

Table 1 reports the properties of South African (Amcoal) coal. The average F concentration in coal was about 40 ppm while in fly ashes collected at the ESP inlet it was 255 ± 50 ppm. The normalized enrichment factor, defined as (F concentration in fly ash)/(F concentration in coal) normalized to coal/ash weight ratio, was about 1.1.

Table 2
F and Al average concentrations and F enrichment factors calculated with respect to Al in fly ash samples collected at the inlet and outlet units of the electrostatic precipitator (ESP). The enrichment factor (EF) is defined as $(F/Al)_{out}/(F/Al)_{in}$

ESP efficiency	F [ppm]		Al [%]		EF
	Inlet	Outlet	Inlet	Outlet	
92.73 [a]	270	580	18.2	18.2	2.15
96.75 [a]	210	720	17.3	18.9	3.14
97.90 [a]	320	740	18.2	19.0	2.22
98.06 [a]	260	730	17.3	19.3	2.52
98.74 [a]	340	770	17.2	18.3	2.13
99.15 [b]	180	940	16.5	19.0	4.54
99.21 [b]	270	830	17.5	17.9	3.00
99.46 [b]	240	1000	17.9	19.1	3.90
99.62 [b]	210	1000	18.5	18.6	4.74

[a] ESP conventional mode.
[b] ESP pulsed mode.

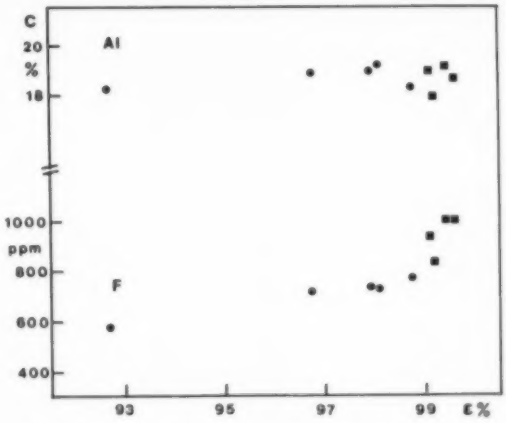

Fig. 3. F and Al concentrations (C) in fly ash collected at the outlet unit of the electrostatic precipitator, plotted against the abatement efficiency (ϵ) in conventional mode (circles) and pulsed mode (squares).

Table 2 shows F and Al concentrations in fly ash collected before and after the pilot ESP for a set of tests corresponding to different ESP conditions, in particular the two excitation modes (conventional and pulsed). The enrichment factors defined as $(F/Al)_{out}/(F/Al)_{in}$ are reported as well. We adopted Al as the reference element since it does not undergo partitioning through the combustion cycle.

Fig. 3 shows F and Al outlet concentrations as a function of the fly ash total mass abatement efficiency in conventional and pulsed excitation modes.

Total mass, F and Al penetration factors (100% − abatement efficiency (%)) and F, Al to total mass penetration ratios are reported in table 3. A preferential penetration for F is evident, especially in the ESP

Table 3
Penetration factors for total mass, fluorine and aluminium in fly ash samples collected at the inlet and outlet units of the electrostatic precipitator

ESP efficiency [%]	Penetration [%]			Elem. pen./Mass pen.	
	Mass	F	Al	F	Al
92.73 [a]	7.27	16.0	7.3	2.20	1.00
96.75 [a]	3.25	8.8	3.5	2.51	1.08
97.90 [a]	2.10	4.8	2.2	2.28	1.05
98.06 [a]	1.94	5.5	2.2	2.83	1.13
98.74 [a]	1.26	2.9	1.3	2.30	1.03
99.15 [b]	0.85	4.0	0.96	4.70	1.13
99.21 [b]	0.79	2.4	0.80	3.04	1.01
99.46 [b]	0.54	2.2	0.57	4.07	1.06
99.62 [b]	0.38	1.8	0.38	4.74	1.00

[a] ESP conventional mode.
[b] ESP pulsed mode.

Table 4
Mass, F and Al percentage and cumulative distributions with respect to particle size in fly ash collected at the ESP inlet unit

Range [μm]	Mass		F			Al		
	[%]	Cum. [%]	[%]	Cum. [%]	F/mass	[%]	Cum. [%]	Al/mass
> 6.8	55.1		25.4		0.46	57.2		1.04
3.6–6.8	12.4	44.9	18.3	74.6	1.48	10.0	42.8	0.81
0.86–3.6	23.5	32.5	33.5	56.3	1.43	26.3	32.8	1.12
< 0.86	9.0	9.0	22.8	22.8	2.53	6.5	6.5	0.72
Mass median aerodynamic diameter [μm]	6		2			6		

pulsed mode which is characterized by higher abatement efficiencies. It is interesting to observe that this preferential penetration with respect to the total mass seems to depend mainly on the operation mode rather than on the specific abatement efficiency of each test. As expected, for Al the penetration ratio is unity. A few reasons can account for the different behaviour found between Al and F. The most likely is that the volatile fluorine condenses on particle surfaces. Smaller particles, with a higher surface-to-volume ratio than large particles, have greater fluorine concentration. Mechanisms of homogeneous gas phase particle nucleation and coalescence can lead to small particle formation. Taking into account the higher ESP abatement efficiency for large particles, fluorine enrichment is further enhanced.

In table 4 the percentage size distributions for Al and F and total mass before the ESP are reported. Although the distributions are not detailed, being over only four size ranges, fluorine is enriched in the finest fraction. The resulting size distribution for a particular element depends upon the process of particle formation; in particular, for volatile elements, it depends on the gas to particle conversion mechanisms [12,13] leading to different trends with respect to particle diameter. The distribution reported here shows a flat trend for Al, while for F a $D_p^{-\alpha}$-like distribution ($\alpha \leq 1$) is obtained in the submicron range. A more detailed distribution would provide information about the number and kind of involved mechanisms.

4. Conclusions

The PIGE technique for the analysis of fluorine in coal and fly ash has been presented. Coals are analyzed as thick samples, to provide representative analytical results. For fly ash, available in only small quantities, thin sample analysis has been set up. The method is sensitive and reliable. In association with the PIXE technique it provides a multielemental analysis.

Fluorine enrichment phenomena from parent coal to fly ash and through the abatement process (ESP) have been studied for a particular coal (South African Amcoal) and in specific operational modes of the electrostatic precipitator. Similar studies for different coals should lead to estimates of fluorine emission, taking into account only the specific abatement conditions and the total mass penetration, which is more easily measured.

Fluorine concentration and enrichment data can also be used for validating statistical models aimed at estimating trace element enrichment factors, taking into account semiempirical particle size distributions and the ESP penetration function [14].

References

[1] V. Valkovic, Trace Elements in Coal (CRC Press, Boca Raton, 1983).
[2] E. Clayton and L.S. Dale, Anal. Lett. 18 (1985) 1533.
[3] G. Demortier, J. Stroobants, G. Deconnick and F. Bodart, Report L.A.R.N. 724.
[4] J.R. Bird and E. Clayton, Nucl. Instr. and Meth. 218 (1983) 525.
[5] M.A. Chaudri, Radiat. Eff. 94 (1986) 145.
[6] A. Anttila, R. Hanninen and J. Raisanen, J. Radioanal. Chem. 62 (1981) 293.
[7] A.Z. Kiss, E. Koltay, B. Nyako, E. Somorjai, A. Anttila and J. Raisanen, J. Radioanal. Chem. 89 (1985) 123.
[8] C. Boni, A. Caridi, E. Cereda and G.M. Braga Marcazzan, Nucl. Instr. and Meth. B47 (1990) 133.
[9] B. Bellagamba, G. Liberati, G. Malagnini and E. Riboldi, 3rd Int. Conf. on Electrostatic Precipitators, Abano, Italy, 25–29 October 1987.
[10] C. Boni, E. Cereda, G.M. Braga Marcazzan and V. De Tomasi, Nucl. Instr. and Meth. B35 (1988) 80.
[11] L.M. Heageny and J.S. Heageny, Nucl. Instr. and Meth. 167 (1979) 137.
[12] M.W. McElroy, R.C. Carry, D. Ensor and G. Markowski, Science 215 (1983) 13.
[13] E.I. Kauppinen and T.A. Pakkanen, Environ. Sci. Technol. 24 (1990) 1811.
[14] S. Cernuschi and M. Giugliano, Sci. Total Environ. 65 (1987) 95.

Workshop

Nuclear Instruments and Methods in Physics Research B66 (1992) 303–305
North-Holland

Nuclear Instruments & Methods in Physics Research
Section B

A workshop on cross-section data bases for IBA

I.C. Vickridge
Nuclear Sciences Group, DSIR Physical Sciences, P.O. Box 31312, Lower Hutt, New Zealand

The ideas presented and developed during a workshop on cross-section data bases for IBA are summarized and presented.

1. Introduction

This article has been written to summarize the workshop on cross-sections for IBA, proposed by G. Amsel, chaired by G. Amsel and G. Demortier, and held during the conference. The workshop was attended by about 30 participants, of whom about 20 participated actively. I have attempted to represent the views expressed by the participants as fairly as I can, and have tried to build on the spirit of those views where I go further than simply reporting the workshop.

The "raison d'être" for the workshop is best presented in the words of G. Amsel's proposition:

> "It is an increasingly widespread practice to use computer programs to interpret spectra or excitation curves, whether in RBS, resonant elastic scattering, ERDA, or NRA for extracting depth profiles from the experimental data. In NRA and PIGME a precise knowledge of all the possible reactions that may arise when analysing a given target is a necessity to identify the various peaks and to choose the best experimental conditions for optimising sensitivity, minimising interference effects between various isotopes, etc. These programs or optimisation procedures require reliable tabulated cross section values. To record and distribute such data has become an easy task with the recent personal computer revolution. It is therefore a vital problem for our scientific community to advance cross section and excitation curve data collection in the frame of an international well coordinated effort towards establishing a corresponding data base, which would serve as a firm basis of computer assisted IBA".

It was quickly established that some form of digital storage and communication of IBA cross sections was preferable to the publication of a book, or some other "hard-copy" system. All IBA laboratories that would access the proposed database would be able to produce local hard copy from digitally stored data. For the rest of the workshop I have tried to identify the main issues raised and summarise the discussion and conclusions reached.

2. What data should be included in the data base?

Apart from the purely practical aspects of limiting the ultimate size of the database, it is to be hoped that by specifying a scope for the data base, areas where it would be useful to measure or remeasure cross sections may be identified. The choice of which range of data to include in the data base may therefore be important in determining where future IBA cross-sections measurements should be made. The data base would be intended to include only data specific to the IBA community, with the exception that PIXE is now a mature specialised subfield of IBA with special cross-section needs adequately catered for elsewhere. Furthermore, the data base should be concerned only with prompt IBA. Whether any further resctrictions on reaction type or energy range would be needed to limit the amount of data remains an open question, however it was generally agreed that no cross-section data (except PIXE) useful for IBA should be excluded. Further discussion centered on whether or not to define preferred (laboratory) angles for cross sections to be measured in the future. There are good practical reasons for this for reactions which have cross sections which vary sufficiently slowly with reaction angle. For example, many IBA laboratories have charged particle detectors mounted at 150° or at 135°. However, the nature of nuclear reaction cross sections is such that, in a significant number of cases, the best angle at which to use a particular reaction will not be one of the preferred angles (whatever they happen to be), so the best option would probably be to recommend pre-

0168-583X/92/$05.00 © 1992 – Elsevier Science Publishers B.V. All rights reserved

ferred angles for those reactions where there is no advantage in using a specific angle, but to include data for any angle.

The question arose as to how to include both tabulated cross-section data, and also the much more compact semiempirical fits. A related question is how to include narrow resonance cross-section data? In both cases a mathematical expression is used to summarise experimental results in terms of a mathematical or physical model. In the case of the very narrow resonances used in resonance depth profiling, a thin target yield curve is not necessarily the best way to describe the cross section, which can only be expressed mathematically in the vicinity of a narrow resonance. These matters will need further discussion, however as an interim measure I have proposed a format for storage of cross-section data [1] that goes some way to accomodating these needs.

3. Should the data base organisation evaluate cross-section data reliability?

The evaluation of the reliability of cross-section data is by no means a trivial task, and needs a high degree of specialised knowledge and skill, which normally do not come cheaply. It is debatable whether it would be feasible to expend the necessary resources to do this job properly. However, one interesting proposition was that this job could be left for retired scientists from IBA, who may donate or discount their time to the benefit of their younger colleagues. Note however that the utility of a specialised IBA data base lies not only in having access to reliable data accepted by the IBA community as a whole (for those cases where absolute cross-section data are needed) but also in having rapid access to the entire range of available data even of poor precision or accuracy for the initial evaluation of the feasibility and major characteristics of a proposed IBA experiment. It would therefore be desirable not to exclude even poor quality data, especially where no other data exists.

Related to this question is that of whether the data base should include only absolute cross-section data or should also include relative data. Apart from the fact that even relative data is very useful, especially when an approximate practical indication of its overall magnitude (e.g., counts/μC) from a simple target for a given experimental geometry) accompanies it, absolute measurements of cross sections for the production of gammas are difficult to perform because of the necessity of accurately measuring detector efficiency for the gamma energy being considered. And in most applications of the use of ion-induced gammas for IBA, more than one gamma line, or in the absence of interferences the gamma plus escape and compton components may be used. It would therefore be desirable for the data base to be able to accomodate relative data as well as providing a source of high quality absolute data, and intelligent estimates of the accuracy and precision of the data. The proposal of ref. [1] treats this question in more detail, but in the final analysis the ultimate responsability for a reasonable assessment of the quality of the data must rest with the experimenter who performed the measurement.

4. Operational questions

Two basic questions arose concerning the operation of the data base. The first is: who will set up and pay for the data base? No conclusion could be reached, although it is to be hoped that this first step of recognising the need for, and identifying some of the important issues in the context of, a specific data base will stimulate further collaborative efforts on the part of the senior members of the IBA community. The second question was: what should be the relationship between the proposed data base and existing or proposed ones, such as the compilation of Jarjis [2], the IBA handbook [3], the new IBA handbook [4], or the existing nuclear physics data tabulations [5]? Firstly, it should be noted that refs. [2–4] provide only graphs or hard-copy listings of cross sections, so any use of these in simulation programs (such as RUMP [6] or SENRAS [7]) will require local redigitisation or manual entry of previously digitised data at each site, multiplying the work and introducing the opportunity for further digitisation or simple typing errors. The possibility of working with one of the larger organisations was raised at the workshop, and is an avenue to be explored, although whether it would be possible to arrange to meet all the special requirements of the IBA community remains to be seen.

5. Where to now?

Given that the need for a data base for IBA cross sections has been endorsed by the participants of this workshop, the next step requires the constitution of a small group of people to find practical ways of implementing an IBA cross-section data base embodying the main ideas summarised above, possibly under the umbrella of a larger international organisation, and to define the relevant operational and technical parameters for the data base. It is suggested that this group

might be made up, at least in part, of participants at the workshop.

Advice, comments and suggestions may be sent to:

Dr. Ian Vickridge
Nuclear Sciences Group, DSIR, P.O. Box 31 312, Lower Hutt, New Zealand
Tel.: + + 64 4 5666919
Fax: + + 64 4 5690657
Internet: SRGIICV@GRV.DSIR.GOVT.NZ

Dr. G. Amsel
Groupe de Physique des Solides, E.N.S., Universités Paris 7 et Paris 6, Tour 23, 2 Place Jussieu, F-75251 Paris Cedex 05, France
Tel.: + + 33 1 44274648
Fax: + + 33 1 43542878
Earnbitnet: GPS@FRLMCP61.BITNET

Prof. G. Demortier
LARN, Facultés Universitaires Notre-Dame de la Paix, 22 Rue Muzet, B-5000 Namur, Belgium
Tel.: + + 32 81 731267
Fax: + + 32 81 737938
Réseau EARN: LARN@BNANDP51

Acknowledgements

Thanks are due to G. Battistig and W. De Coster who took detailed notes during the workshop, and to G. Amsel and G. Demortier, who ably defined and chaired it.

References

[1] I.C. Vickridge, DSIR Physical Sciences Report 33, Nuclear Sciences Group, DSIR Physical Sciences, Lower Hutt, New Zealand.
[2] R.A. Jarjis, Nuclear Cross Section for Surface Analysis, vols. 1–3, University of Manchester, Department of Physics Internal Report (1979).
[3] Ion Beam Handbook for Materials Analysis. eds. J.W. Mayer and E. Rimini (Academic Press, New York, 1977) ISBN 0-12-480860-3.
[4] J. Tesmer, private communication.
[5] e.g., Nuclear Data Sheets (Academic Press, New York, 1966) ISSN 0090-3752.
[6] RUMP User's Manual, CGS Computer Graphics Services, Ithaca, NY, USA.
[7] G. Vizkelethy, Nucl. Instr. and Meth. B45 (1990) 1.

INSTRUCTIONS TO AUTHORS

Contributions to *Section B* of *Nuclear Instruments and Methods in Physics Research* must be in English and should have an abstract. The manuscript and copies of figures should be submitted in duplicate, together with one set of good quality figure material (for production of the printed figures), to one of the editors, Prof. H.H. Andersen or Dr. L.E. Rehn. It is suggested that manuscripts originating from Europe, India, The Middle East and Africa be sent to Copenhagen and manuscripts from The Americas, The Far East and Australasia, to Argonne.

Prof. H.H. Andersen
Physics Laboratory, H.C. Ørsted Institute
Universitetsparken 5, DK-2100 Copenhagen Ø
Denmark
Tel. +45 31 353133, ext. 322 FAX: +45 31 350628

Dr. L.E. Rehn
Materials Science Division, Bldg. 223, RM S231
Argonne National Laboratory, 9700 South Cass Ave
Argonne IL 60439, USA
Tel. +1 708 2529297 FAX: +1 708 2523308

Short contributions of less than 1500 words and not subdivided into sections may be published as Letters to the Editor in a shorter time than regular articles as the proofs will normally be corrected by the publisher.

Preparation of manuscripts

Manuscripts should be typed throughout with double line spacing and wide margins on numbered pages.

The *title page(s)* should contain, in addition to the article title, author(s)' names and affiliations, the text of related footnotes and the text of the abstract.

Tables should be typed on separate sheets at the end of the manuscript. In addition to its serial number, each table should have a sufficiently detailed heading or caption to explain the data displayed in it.

Figures should be numbered and their captions listed together at the end of the manuscript.

References in the text to other publications should be numbered consecutively within square brackets, for example: "Using a similar technique [1]..." or "As outlined in ref. [2],..." and listed together at the end of the text, for example:

[1] G.A. Smith, K.-H. Park, G.-C. Wang, T.-M. Lu and W.M. Gibson, Surf. Sci. 233 (1990) 115.
[2] T.Y. Tan, in: Defects in Semiconductors, eds. J. Narayan and T.Y. Tan (North-Holland, Amsterdam, 1981) p. 163.
[3] H. Yamazaki, Proc. 6th Int. Conf. on Ion Beam Modification of Materials, Nucl. Instr. and Meth. B39 (1989) 433.
[4] P. Bauer, F. Aumayr, D. Semrad and B.M.U. Scherzer, Nucl. Instr. and Meth. B1 (1984) 1.

In the case of multiple authorship all authors should be listed in the references provided they number less than ten. Only in case of more than ten authors is the first author et al. acceptable.

Formulae in the manuscript should be clearly written or typed with particular consideration given to characters that may be misinterpreted,

e.g. I (cap) l (el) 1 (one) ′ (prime)	c, C; p, P; s, S; etc
o (lower case) O (cap.) 0 (zero) ° (deg)	k, K, κ (kappa)
$\times$ (times) x (lower case) X (cap.)	Σ (sigma) $\sum$ (sum).

If necessary, unusual symbols should be explained in pencil in the margin.

Preparation of figures

The publisher requires a set of good quality drawings and photographs to produce the printed line figures and half-tone plates in the journal. Photographic copies ("glossy prints") of drawings are also acceptable for the line figures if they have been sharply focused and evenly exposed.

Line figures: The drawings or glossy prints supplied for the line figures should be 1.5–3 times larger than the printed size of the figures and should contain all the required lettering.

Figures are preferably reduced to a single column width (7.6 cm) unless their complexity, large width-to-height ratio, or need to display special detail makes a larger format necessary (max. printed width $\approx$ 20 cm). Inappropriately sized lettering on a figure may prevent its reduction to the size optimum for its information content. The lettering used on a drawing should be chosen so that after reduction, the height of numbers and (capital) letters falls within the range 1.2–2.4 mm. Care should be exercised in choosing the pen width of machine-plotted graphs. Frequently lines in these figures are too fine compared to the area of the figure.

Shaded areas in line figures should be shown by means of cross-hatching (or a matrix of dots) rather than a continuous grey "wash". Cross-hatching, after reduction, of density less than $\sim$ 25 lines/cm is satisfactory.

Half-tone plates: The photographs supplied for reproduction should be unmounted unless they form part of a composite figure and they should have a somewhat greater contrast than is desired in the printed figure. It is important that the photographs supplied are not already screened (overprinted with the point-matrix used by printers) or moiré patterns will form when they are screened for a second time. When necessary, the top side of a photograph should be marked. A reduction factor should be recommended for a photo when it is not obvious what detail in the photo is of interest.

Colour plates: Illustrations can be printed in colour when they are judged by the Editor to be essential to the presentation. Further information concerning colour illustrations and the costs to the author can be obtained from the Editors or the Publisher, or found at the end of volume B62.

IMPORTANT NEWS:

* Letters Section commencing 2nd quarter of 1992
* New Regional Editor for Europe:
  Joop Schoonman, Delft, The Netherlands
* New Regional Editor for Asia:
  Osamu Yamamoto, Tsu, Mie, Japan
* New Editor:
  Colin Vincent, St. Andrews, Scotland, U.K.

SCOPE:

This interdisciplinary journal is devoted to the physics, chemistry and materials science of diffusion, mass transport and reactivity of solids.

* physics and chemistry of defects in solids
* reactions in and on solids, e.g. intercalation, corrosion, oxidation, sintering
* ion transport measurements, mechanisms and theory

Related technological applications will also be included, provided their characteristics are interpreted in terms of the basic solid state properties. Review papers are welcome.

As of now, please submit your letters for our typeset Letters Section.

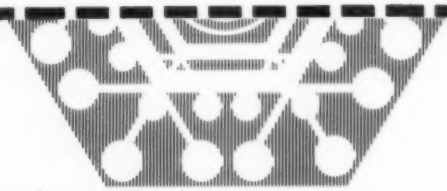

- ❑ please send me instructions to authors
- ❑ please send me a complimentary copy of Solid State Ionics
- ❑ please send me a descriptive brochure on Solid State Ionics

Name: _____

_____

Address: _____

_____

Return to:
Elsevier Science Publishers
North-Holland
Attn. Karien van der Harst
P.O.Box 103
1000 AC The Netherlands
The Netherlands

In the U.S.A. and Canada:
Elsevier Science Publishers Co. Inc.
Journal Information Centre
P.O.Box 882
Madison Square Station
New York, 10159 N.Y.
U.S.A.

SOLID STATE IONICS

DIFFUSION & REACTIONS

Principal Editor
M. Stanley Whittingham, Binghamton, NY, USA.

Regional Editor Europe
Joop Schoonman, Delft, The Netherlands

Regional Editor Asia
Osamu Yamamoto, Tsu, Mie, Japan

Editors
Louis-C. Dufour, Dijon, France
Gregory C. Farrington, Philadelphia, PA, USA
Klaus Funke, Münster, Germany
Yasutoshi Saito, Tokyo, Japan
Priya Vashishta, Baton Rouge, LA, USA
Colin Vincent, St. Andrews, Scotland, U.K.

NORTH-HOLLAND